NASA/CP–20220018789

International VLBI Service for Geodesy and Astrometry 2022 General Meeting Proceedings

Kyla L. Armstrong, Dirk Behrend, and Karen D. Baver

January 2023

NASA STI Program ... in Profile

Since its founding, NASA has been dedicated to the advancement of aeronautics and space science. The NASA scientific and technical information (STI) program plays a key part in helping NASA maintain this important role.

The NASA STI program operates under the auspices of the Agency Chief Information Officer. It collects, organizes, provides for archiving, and disseminates NASA's STI. The NASA STI program provides access to the NTRS Registered and its public interface, the NASA Technical Reports Server, thus providing one of the largest collections of aeronautical and space science STI in the world. Results are published in both non-NASA channels and by NASA in the NASA STI Report Series, which includes the following report types:

- TECHNICAL PUBLICATION. Reports of completed research or a major significant phase of research that present the results of NASA Programs and include extensive data or theoretical analysis. Includes compilations of significant scientific and technical data and information deemed to be of continuing reference value. NASA counterpart of peer-reviewed formal professional papers but has less stringent limitations on manuscript length and extent of graphic presentations.

- TECHNICAL MEMORANDUM. Scientific and technical findings that are preliminary or of specialized interest, e.g., quick release reports, working papers, and bibliographies that contain minimal annotation. Does not contain extensive analysis.

- CONTRACTOR REPORT. Scientific and technical findings by NASA-sponsored contractors and grantees.

- CONFERENCE PUBLICATION. Collected papers from scientific and technical conferences, symposia, seminars, or other meetings sponsored or co-sponsored by NASA.

- SPECIAL PUBLICATION. Scientific, technical, or historical information from NASA programs, projects, and missions, often concerned with subjects having substantial public interest.

- TECHNICAL TRANSLATION. English-language translations of foreign scientific and technical material pertinent to NASA's mission.

Specialized services also include organizing and publishing research results, distributing specialized research announcements and feeds, providing information desk and personal search support, and enabling data exchange services.

For more information about the NASA STI program, see the following:

- Access the NASA STI program home page at http://www.sti.nasa.gov

- E-mail your question to help@sti.nasa.gov

- Phone the NASA STI Information Desk at 757-864-9658

- Write to:
  NASA STI Information Desk
  Mail Stop 148
  NASA Langley Research Center
  Hampton, VA 23681-2199

NASA/ CP–20220018789

International VLBI Service for Geodesy and Astrometry 2022 General Meeting Proceedings

Kyla L. Armstrong (ed.)
NVI, Inc., Greenbelt, MD

Dirk Behrend (ed.)
NVI, Inc., Greenbelt, MD

Karen D. Baver (ed.)
NVI, Inc., Greenbelt, MD

Proceedings of the 12th General Meeting of the International VLBI Service for Geodesy and Astrometry
Hosted by the Finnish Geospatial Research Institute (FGI), NLS,
Helsinki, Finland
March 28 - April 1, 2022

National Aeronautics and
Space Administration

Goddard Space Flight Center
Greenbelt, MD 20771

January 2023

Level of Review: This material has been technically reviewed by technical management.

Available from

NASA STI Program
Mail Stop 148
NASA's Langley Research Center
Hampton, VA 23681-2199

National Technical Information Service
5285 Port Royal Road
Springfield, VA 22161
703-605-6000

Available in electronic form at https://www.sti.nasa.gov and https://ntrs.nasa.gov

Preface

This volume is the proceedings of the twelfth General Meeting (GM2022) of the International VLBI Service for Geodesy and Astrometry (IVS), held in Finnish Cyberspace, March 28 through April 1, 2022. The meeting was organized and hosted by the Finnish Geospatial Research Institute (FGI), National Land Survey of Finland (NLS).

Fig. 1 Logo of the twelfth IVS General Meeting.

The previous General Meeting (GM2020), which was organized for in-person participation, had to be cancelled on very short notice prior to taking place (two weeks before the opening) due to the onset of the coronavirus disease 2019 (COVID-19) pandemic. Hence, GM2022 was effectively held four years after the last successfully executed GM.

When starting the preparations of GM2022, we were hopeful that we would be at the tail end of the pandemic and could hold the GM as a hybrid event. However, the latter turned out not to be the case. The Omicron wave of the COVID-19 pandemic together with restrictions implemented by the Finnish government on organizing public events forced us to switch to a completely virtual format. Thus, GM2022 became the first GM that was held completely online.

The switch to a virtual meeting format was done about two months before the start of the event. The Local Organizing Committee, thus, was preparing a hybrid conference with an icebreaker, lecture room, coffee breaks, and meeting dinner for a significant time period for the in-person attendees—that is, with all the bells and whistles—as well as video and audio capabilities for the online folks. We would like to take this opportunity to thank the LOC for doing all this work and then being able to refocus the efforts to organize a purely virtual meeting. So, kudos to the **Local Organizing Committee** consisting of:

- Nataliya Zubko (Chair)
- Niko Kareinen
- Hannu Koivula
- Eliisa Nylén
- Markku Poutanen
- Renne Vantola

While a virtual setting largely removes the social interactions of an in-person meeting, it provides other opportunities. As there is no travel cost involved, groups are able to send more attendants. It is also possible to have recorded presentations that can be viewed asynchronously. On the other hand, the various time zones that the IVS community covers make for very awkward local times for some, resulting in partial attendance only.

The Program Committee had the task of organizing the scientific program taking the constraints of the virtual setting into consideration. In deliberation with the LOC, the result was a mix of oral sessions (via *Zoom*) and poster sessions in a virtual poster hall (via *Won-*

der). The outcome was an interesting and informative program for a wide cross-section of IVS members, including station operators, program managers, and analysts. We would like to thank the **Program Committee** consisting of

- Dirk Behrend, USA (Chair)
- James Anderson, Germany
- Johannes Böhm, Austria
- John Gipson, USA
- Anastasiia Girdiuk, Germany
- Megan Johnson, USA
- Lucia McCallum, Australia
- Chet Ruszczyk, USA
- Fengchun Shu, China
- Gino Tuccari, Italy
- Stuart Weston, New Zealand
- Alet de Witt, South Africa
- Nataliya Zubko, Finland

for their excellent work.

There were 177 registered participants from around the world that attended the meeting. In the five sessions of the meeting, the participants gave 98 presentations; 59 of these were talks, and 39 were posters or recorded presentations. The overall quality of the presentations was very high—a clear testament to the usefulness of the General Meeting as a knowledge exchange for all matters VLBI. In addition to the GM itself, there were several splinter meetings held before and after the GM. The 4th IVS Training School on VLBI for Geodesy and Astrometry took place from March 22–25, and an Analysis Workshop and a Correlator Workshop were held on April 1. Finally, the Directing Board had a meeting on April 5.

Given the circumstances, the meeting was very successful, showcasing the outstanding research that is done within the IVS community. The virtual format has its perks, but it is not a full replacement for an in-person event. The use of *Wonder* in the poster sessions enabled limited social interaction, alleviating somewhat the lack of not meeting in person. Still, we hope that the next GM can be held in person. As Arvo Kokkonen, Director General of National Land Survey of Finland, stated in his opening remarks, once the pandemic situation improves the IVS members are welcome to visit Helsinki and the Metsähovi Radio Observatory facilities when they are in the neighborhood.

The interested reader can find a feature article about GM2022 in the April 2022 issue of the IVS Newsletter. The Newsletter is available at

`https://ivscc.gsfc.nasa.gov/newsletter/issue62.pdf`

The next IVS General Meeting will be held in March 2024 in Tsukuba, Japan. As part of the GM, there will be festivities for the 25th Anniversary of the IVS. The host institution of GSI published their teaser video on the GGOS YouTube channel at https://www.youtube.com/watch?v=mQkA8VHKWD4.

This volume follows the session structure of GM2022 and contains the following:

- **The papers presented at the meeting.** There are five major sections of this volume, each corresponding to a meeting session. Poster/video and oral papers are mixed. The five sessions cover the following topics:

  1. Technical Developments at the Stations
  2. Observations, Operation, and Correlation
  3. Data Structures, Scheduling, and Analysis Strategies
  4. Interpretation of VLBI Results in Geophysics, Geodesy, and Astrometry
  5. Extending the Use of VLBI to Frame Ties, Deep Space Exploration, and Other Areas

  This volume includes 64 papers. All papers of this volume were edited by the editors for usage of the English language, form, and minor content-related issues.
- **An author index.**

The Proceedings volume is available on the IVS website from the URL

`https://ivscc.gsfc.nasa.gov/publications/gm2022`

The editors would like to thank the contributors to this volume.

Kyla Armstrong, Dirk Behrend, and *Karen Baver*
GM2022 Proceedings editors
Greenbelt, MD ⊙ November 2022

Fig. 2 IVS Chair Rüdiger Haas welcoming the online participants to GM2022.

Fig. 3 Markku Poutanen, IAG Secretary General, giving his welcome address.

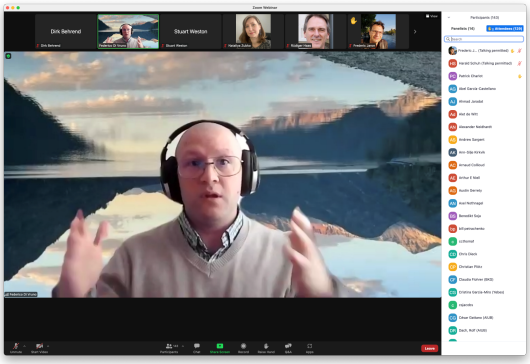

Fig. 4 Federico Di Vruno gave an invited talk on the potential impact of large satellite constellations on VGOS operations.

Fig. 5 A virtual poster hall was provided by *Wonder*. This online platform allowed the participants to have direct interactions in a convenient way. There were three poster sessions organized during the GM so that participants were able socialize as much as possible in this virtual setting.

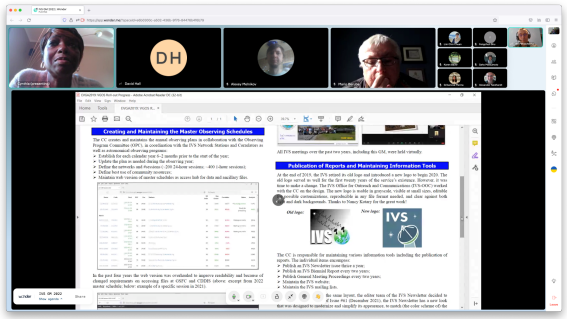

Fig. 6 During a poster session, the poster presenters could show off their work and interact face-to-face with interested participants.

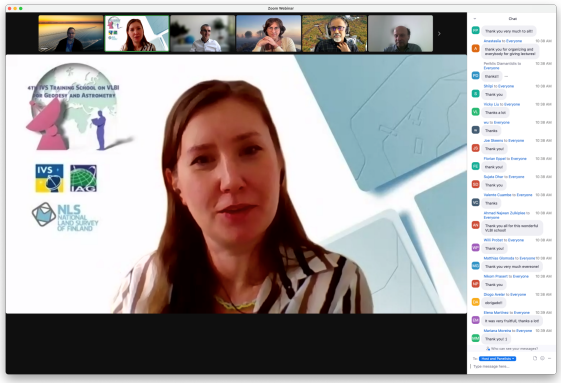

Fig. 7 Nataliya Zubko, lead of the local organizing committee, together with her entire team perfectly arranged the GM as well as the various splinter meetings for a very successful event week.

Table of Contents

Session 1

Technical Developments at the Stations

IVS IAG SUOMEN AKATEMIA

NLS FINNISH GEOSPATIAL RESEARCH INSTITUTE FGI

Dependency of Satellite Geodesy on UT1-UTC from VLBI

Rolf Dach

Abstract Satellite-based techniques need to know UT1 when Earth rotation parameters and orbital elements shall be estimated in a global solution because of the correlation between the ascending nodes of the satellite orbits with the UT1 parameter. In this context the satellite techniques depend on the UT1 results from VLBI. On the other hand, the estimated satellite orbits first established in inertial space are transformed back into the Earth-fixed frame using the estimated Earth rotation parameters. In this sense the quasi-inertial frame for the satellite orbit determination can also be seen as an intermediate frame for a particular solution.
The largest acceleration acting on the satellite, except for the gravitational attraction of the Earth, is the gravitational attraction by the Moon and the Sun. The positions of these celestial bodies are given in the inertial frame. As the satellites are usually observed from sites on the Earth's surface, the transformation from the terrestrial to the celestial reference system is required, including the correct UT1 value, in order to calculate the gravitational accelerations from Moon and Sun to the satellite orbit. Because of the large distances of the masses from the satellite, an error in UT1 of 10 ms can be accepted to limit the effect on the satellite orbit to a value smaller than 1 cm, also for longer satellite arcs containing several revolutions.

Keywords UT1, Satellite techniques, Satellite orbit modeling

Astronomical Institute, University of Bern

1 Introduction

The coordinates of the ground stations used for satellite technique solutions are normally expressed in an Earth-fixed, geocentric coordinate system, as defined by the ITRS (International Terrestrial Reference System), realized in the series of International Terrestrial Reference Frames (ITRF). This coordinate system is rotating with the Earth in space, which is why it is not an inertial system, as required for modeling the satellite motion. As the satellite orbits are primarily affected by interactions with the Earth's body, an Earth-centered coordinate system not rotating with the Earth but moving with the Earth around the Sun is best suited for satellite orbit modeling. Such a quasi-inertial system is the Geocentric Celestial Reference System (GCRS) formally realized by a GCRF (Geocentric Celestial Reference Frame).

All satellite techniques measure certain relations between the satellite positions and locations on the Earth's surface (e.g., the distance between a ground station and a satellite or the distance from the satellite to the ocean or ice surface) with different technologies. Therefore, all satellite-geodetic techniques have to take into account the relation between the two systems. When the elements on the Earth surface are expressed in the ITRF and the satellite position is available in the GCRF from orbit modeling, the transformation between both systems is necessary to process the satellite-based measurements related to the Earth surface. This transformation consists of the Earth orientation parameters as described in Chapter 5 of the IERS Conventions ([1], where IERS stands for International Earth Rotation and Reference Systems Service).

As all Earth-related information is expressed in the ITRF, it makes sense to transform the satellite posi-

tions at the epoch of the measurements (or with a regular sampling allowing for a numerical interpolation) from the GCRF into the ITRF as well. It is an advantage of this approach that only the ITRF needs to be maintained with regular realizations as ITRFxx and the GCRF can be kept as an intermediate system realized for satellite orbit modeling in the solutions using observations from a satellite-based technique.

In order to perform the transformation from the ITRF into GCRF (and vice versa) according to the IERS Conventions, the satellite techniques need in particular the UT1 values from VLBI (Very Long Baseline Interferometry). Subsequently we discuss the impact of missing or degraded UT1 values on satellite-geodetic analyses.

2 Transformation between ITRF and GCRF

The ITRS as well as the GCRS are both Cartesian, rectangular coordinate systems. The principal plane of the GCRS refers to the instantaneous rotation axis of the Earth, whereas the ITRS is defined by a long-term mean location of the rotation axis. The major difference is the definition of the coordinate axes within this plane: for the GCRS it is the vernal equinox and for the ITRS the zero-meridian pointing towards one particular meridian on the Earth surface, e.g., to the Greenwich meridian. The principle is illustrated by Figure 1.

UT1 is the central element to define the relation between the axes of the ITRS and GCRS. An error in UT1 results in a misorientation of the GCRF for the orbit computation in the quasi-inertial space with respect to the ITRF. The ascending node of the orbital plane is computed with respect to the X-axis of the GCRF and is therefore contaminated by such a misorientation of the coordinate axes. When using the erroneous UT1 value together with the corresponding contaminated angle for the ascending node, the orbital plane will keep the same orientation with respect to the Earth surface. The analysis of the satellite measurements related to the Earth-fixed frame is not affected.

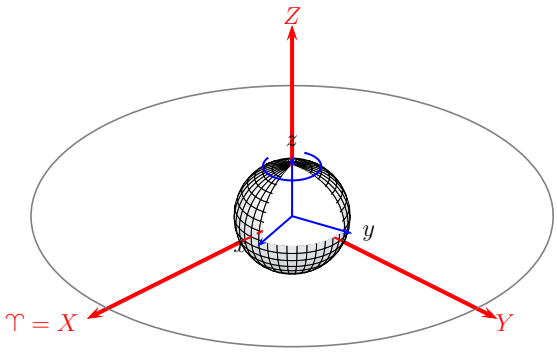

Fig. 1 Principle of ITRS (blue system) and GCRS (red system).

From a pure mathematical point of view, the two coordinate systems can be transformed with three rotations around each of the axes (Eulerian angles). The representation with polar motion, Earth rotation, precession, and nutation is a conventional one by considering the individual effects contributing to the physics of Earth rotation. When not following the convention but just estimating three angles instead, the representation of the satellite orbit with respect to the Earth-fixed frame is still possible—but the related rotation angles cannot be physically interpreted anymore if the error in UT1 becomes too large (e.g., hours).

Also, with a non-conventional realization of the GCRF, satellite measurements can be processed and used for the conventional ITRF realizations. Accelerations acting on the satellite and based on Earth-fixed models (e.g., the Earth gravity field) can also be transformed into a misaligned GCRF with the same effect on the satellite trajectory. In this sense a degraded UT1 series does not harm the satellite techniques.

The only remaining problems with a non-conventional realization of the GCRS are corrections to the Earth rotation parameters for effects with a higher resolution in time than that used for the estimation of the polar motion and Earth rotation angles. While a technique like Satellite Laser Ranging (SLR) is estimating not more than one offset per component and day, other techniques like GNSS (Global Navigation Satellite Systems) allow even for a higher resolution of up to 15 minutes [2].

As long as the UT1 errors are small (e.g., below a second) high frequency polar motion corrections can still be used without limitations. At this magnitude, UT1 errors do not harm the self-consistent use of Earth-fixed and quasi-inertial frames for analyzing satellite data.

3 Celestial Bodies other than the Earth

A degraded UT1 value may have an effect on the position of celestial bodies other than the Earth. Sun, Moon, and the most massive planets of the solar system are taken into account when analyzing measurements from satellite-geodetic techniques. The orders of magnitude of the most important accelerations acting on an artificial Earth satellite are listed in Table 1. The effects are discussed in detail in this section.

3.1 Solid Earth Tides for the Ground Stations

To compute the displacements of the ground stations due to solid Earth tides according to [1], the positions of the Sun and the Moon are needed. They are available in the ICRF, the inertial frame where the Earth (together with the satellites) is moving around the Sun. In order to obtain the positions of the celestial bodies in the Earth-fixed frame to compute the corrections for the station displacement, the transformation using the conventional definition of the Earth's orientation in space is needed. Otherwise the positions of the Sun and Moon are slightly misplaced.

The most important term in this context is UT1. An error in UT1 corresponds to an epoch error when the effect is computed. As a rough guess, we assume that the peak-to-peak deformation is about 40 cm with two minima and maxima per day — six hours for the transition from the minimum to maximum deformation. This results in a velocity of the ground station when following this deformation of $\frac{0.4}{6}\frac{\mathrm{m}}{\mathrm{h}} = \frac{400}{360}\frac{\mathrm{mm}}{\mathrm{min}} \approx 1\frac{\mathrm{mm}}{\mathrm{min}}$. This order of magnitude implies that even with an error of one minute in UT1 the deformations for ground stations due to Solid Earth tides can be computed with millimeter accuracy.

Table 1 Perturbing accelerations acting on a GPS satellite [3].

Perturbation	Acceleration m/s^2	Orbit Error after one day (m)
Two–Body Term of Earth's Gravity Field	0.59	∞
Oblateness of the Earth	$5 \cdot 10^{-5}$	10,000
Lunar Gravitational Attraction	$5 \cdot 10^{-6}$	3,000
Solar Gravitational Attraction	$2 \cdot 10^{-6}$	800
Other Terms of Earth's Gravity Field	$3 \cdot 10^{-7}$	200
Radiation Pressure (direct)	$9 \cdot 10^{-8}$	200
Y–Bias	$5 \cdot 10^{-10}$	2
Solid Earth Tides	$1 \cdot 10^{-9}$	0.3

3.2 Solar Radiation Pressure Modeling

Solar radiation pressure is an essential component for orbit modeling of many satellite types emerging from the interaction of solar radiation with the satellite surface. The direction towards the Sun from the illuminated surface area $\vec{r}_{sat} - \vec{r}_{Sun}$ with an intersection angle α are the input features for the computation of these accelerations (see Figure 2). Which of the effects matter for a given surface element depends on the optical properties. The impact on the orbit depends finally on the area of the surface elements and the mass of the satellite [4]. The largest uncertainty emerges from the level of detail in the decomposition of the satellite structure and the use of the correct inflight properties.

The location of the Sun with respect to the satellite is needed to compute the orientation of the particles interacting with a satellite surface. It appears in the vector difference $\vec{r}_{sat} - \vec{r}_{Sun}$ and the intersection angle α as indicated in Figure 2. As α is the angle between the normal vector $\vec{n}$ of the plane and the unit vector pointing from the satellite towards the Sun $\vec{r}_{Sun}$, we need only the angle α to assess the impact of a wrong location of the Sun when computing the effect of solar radiation. In the worst case the misorientation of the Sun resulting from a wrong UT1 value fully coincides with the intersection angle. The angle α appears in all formulas within a cos- or $\cos^2$-function. A 1% error in the $\cos\alpha$-term corresponds to 0.5 degrees (or two minutes in time). The uncertainty of the knowledge of the optical properties of the satellites after a certain time in orbit is usually more important.

Because GNSS satellites do orient their solar panels towards the Sun, the empirical parameters are typically also expressed in a Sun-oriented coordinate system at the satellite [5]. A displacement of the Sun as described above would also result in a misorientation of the principal axes of this coordinate system. As long as these are only fractions of a degree (as assumed above), the resulting discrepancy between the force acting on the satellite and the representation in the empirical orbit model is absorbed by the estimated orbit parameters.

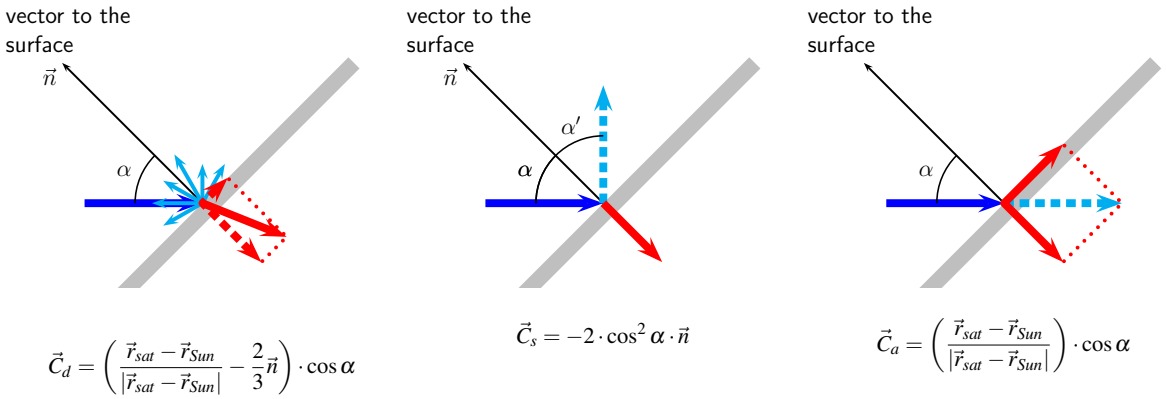

(a) Diffuse reflection (b) Specular reflection (c) Absorption

Fig. 2 Different versions of direct solar radiation pressure.

Other effects where the position of the Sun is needed in the context of solar radiation pressure modeling are the eclipse enter and exit epochs, when it is assumed that the radiation pressure due to the Sun is switched on or off. Assuming the worst constellation between Sun, Earth (or Moon), and satellite, the epoch is wrong by the full UT1 error. As long as the UT1 error is below one minute, this inconsistency can be absorbed by the empirical parameters of the Solar radiation pressure model.

3.3 Gravitational Force of the Sun and Moon

The gravitational attraction of the Earth is the most important component to keep a satellite on an orbit around the Earth. The oblateness of the Earth is causing an acceleration of $5 \cdot 10^{-5} \frac{\mathrm{m}}{\mathrm{s}^2}$ for a satellite with a semi-major axis of about 26,400 km (see Table 1). Satellites in a lower orbit (e.g., altimeter satellites with a height of about 1,000 km above the Earth surface) show a larger effect, by a factor of $\frac{(26{,}400\ km)^2}{(7{,}400\ km)^2} \approx 12$.

The Earth with a mass M_E, Sun, Moon, and other planets with masses M_i generate the following gravitational acceleration on a satellite at position $\ddot{\vec{r}}_{sat}$:

$$\ddot{\vec{r}}_{sat} = -GM_E \frac{\vec{r}_{sat}}{|\vec{r}_{sat}|^3} - G \cdot \sum_{i=1}^{n} M_i \frac{\vec{r}_i - \vec{r}_{sat}}{|\vec{r}_i - \vec{r}_{sat}|^3} \qquad (1)$$

Using the masses and the mean distances to the Sun and Moon, results in accelerations of $2 \cdot 10^{-6} \frac{\mathrm{m}}{\mathrm{s}^2}$ and $5 \cdot 10^{-6} \frac{\mathrm{m}}{\mathrm{s}^2}$, respectively (see Table 1). In this term the height of the satellite above the Earth surface is of secondary importance because the variation of the distance to the Moon or Sun due to the revolution of the satellite around the Earth is small compared to the mean distance to these celestial bodies.

The main effect from a degraded UT1 value is an erroneous direction to Moon and Sun in equation (1) resulting in an acceleration on the satellite misplaced by this angle. If the celestial body is located perpendicular above the orbital plane, a pure effect in the out-of-plane direction results, whereas along-track and radial effects are expected when the perturbing body is located in the orbital plane. With empirical accelerations estimated in orbit determination, the influence of potentially degraded positions of the celestial bodies on the solution can be greatly reduced.

Most of the analysis centers of the International DORIS Service (IDS, where DORIS stands for Doppler Orbit Determination and Radiopositioning Integrated on Satellite) include empirical once-per-revolution terms in along-track and cross-track directions in their solutions [6]. In this sense the related solutions are expected to be quite robust with respect to a dislocation of the Sun and Moon when computing the gravitational forces acting on these satellites.

As opposed to this setup, empirical accelerations are usually estimated in the Sun-oriented coordinate system located in the satellite when processing GNSS

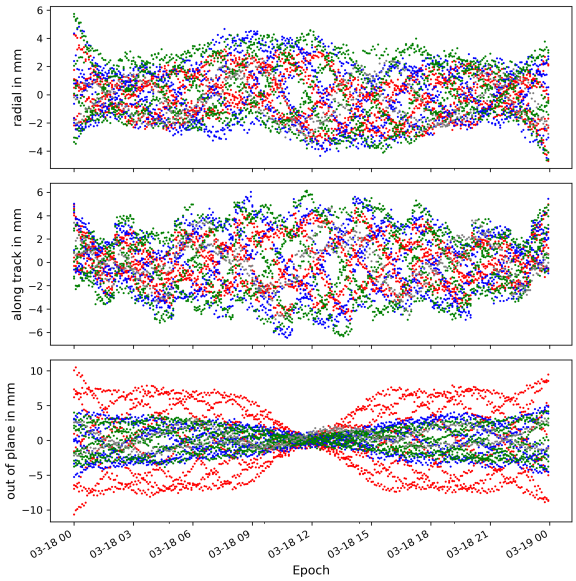

Fig. 3 Influence on the orbits of Galileo satellites in a one-day arc due to the direct gravitational forces by shifting UT1 by 100 ms in the positions of Moon and Sun.

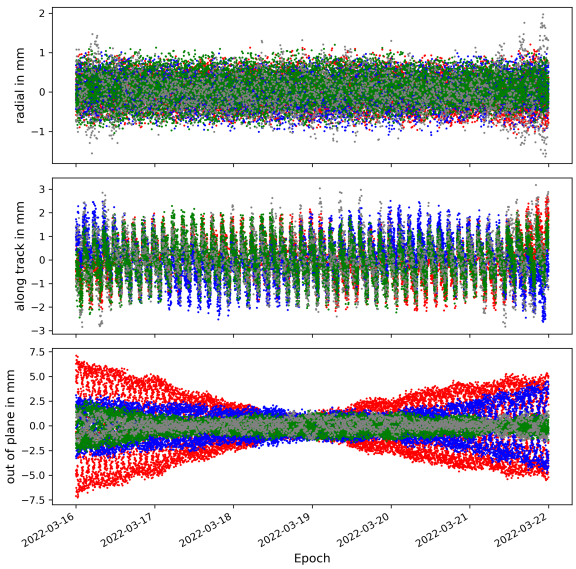

Fig. 4 Influence on the orbits of Galileo satellites in a six-day arc due to the direct gravitational forces by shifting UT1 by 10 ms in the positions of Moon and Sun.

data. Once-per-revolution terms are set up in one of the components of this coordinate system (see [7, 5]). Therefore, the effects caused by degraded UT1 values on the orbits and the solutions in general are larger for these satellites.

The errors introduced in the Galileo satellite positions by errors in UT1 are illustrated by Figures 3 and 4. An error of 100 ms in UT1 is underlying Figure 3, one of 10 ms Figure 4. Figure 3 shows the effect on a one-day orbit (about two revolutions of each satellite), Figure 4 on a six-day orbit (about 12 revolutions). In both cases the differences between the original (true) and the computed orbits with the modified positions of Moon and Sun do not exceed 1 cm.

The colors red, blue, and green in the figures correspond to the three orbital planes of the Galileo constellation (the gray dots represent the two satellites in specific elliptical orbits). The three planes show different effects as a result of the misorientation of the celestial bodies. Most prominent is the effect in the out-of-plane component. The satellites in the red plane show the largest effect, whereas the effects on the satellites in the green and blue planes are smaller. The elevation of the Sun above the orbital plane is about -56° for the red, $+25^\circ$ for the blue, and -20° for the green plane.

Two differences in the assumptions underlying Figures 3 and 4 matter: First, the size of the assumed UT1 error is increased by a factor of ten from Figure 4 to Figure 3 and the arc length is increased by a factor of six from Figure 3 to Figure 4. Finally, the comparison of the two figures confirms that the longer the arc (e.g., more revolutions shall be represented by one set of orbit parameter), the more the orbit solution becomes sensitive to the gravitational acceleration due to Moon and Sun. The computation of this impact is the most relevant influence of a potential error in UT1.

In conclusion, for GNSS solutions an error for UT1 below 10 ms is advisable in order to avoid a degradation of the results.

4 Earth Orientation Parameters from GNSS

As described in Section 2, satellite-based techniques are not able to contribute to UT1 because of the correlation with ascending node of the satellite orbit that need to be estimated for the orbit determination. Other components of the Earth orientation parameters can be obtained from GNSS, like polar motion (standard solutions from the International GNSS Service, IGS, contain daily offsets and rates) and in particular Length of Day (LOD). These GNSS-based estimates of LOD can

be used to define a GNSS-derived series of UT1-UTC relative to an initial epoch t_0:

$$(UT1-UTC)_{GNSS}(t_i) = (UT1-UTC)_{VLBI}(t_0) - \sum_{k=0}^{i-1}(LOD)_{GNSS}(t_k)$$

Such a series was created based on CODE contribution to the IGS repro3 [8] and is displayed in Figure 5. The series is based on a three-day long-arc solution as described in [9]. One set of orbit parameters covers 72 hours. The Earth rotation parameters in the three-day long-arc solution from CODE is generated using a piece-wise linear representation with nodal points at midnight (i.e., four per component). One of the UT1 values is fixed on the CO4 value, whereas the other three are estimated. From their variations in time, the LOD is derived. For the orbit and Earth rotation parameters the middle of the three days is extracted as the solution. For comparison, Figure 5 also contains the blue curve where the cumulated LOD series is extracted from the corresponding ony-day solutions.

Figure 5 indicates that it should indeed be possible to extract a GNSS-derived UT1-UTC time series of acceptable quality even over a long time span. It should be noted that the solution contains between 250 to 300 tracking stations and includes GPS (since 1994), GLONASS (since 2002), and Galileo (since 2012). Towards the end of the series, more than 80 satellites do contribute.

Already 20 years ago, [10] showed that it is even possible to extract information about precession and nutation from GNSS using the same principles as those outlined for UT1-UTC.

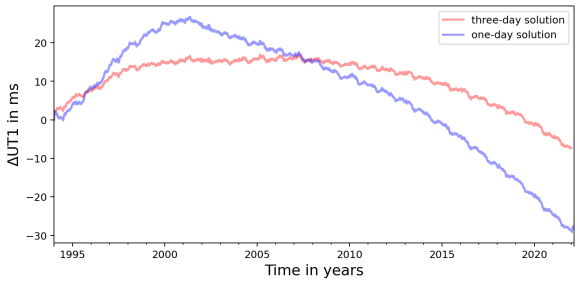

Fig. 5 Difference between UT1-UTC from C04(14)-series and the cumulated LOD series from CODE's contribution to IGS repro3 effort.

5 Summary

Most of the computations and modeling in the analysis of satellite orbits and related measurements is done either in the Earth-fixed (ITRS) or the quasi-inertial (GCRS) coordinate systems. For the transformation between the two systems Earth rotation matrices need to be applied. UT1 deficiencies can be absorbed to a large extent by the initial conditions and other parameters of the satellite orbits. In this way, both reference frames are mutually consistent where only a huge deficiency of several hours in UT1 leads to polar motion estimates that do not agree with the convention and that can therefore not be interpreted anymore. Moderate deficiencies in UT1 of less than one minute do not harm the consistency.

The biggest effect from celestial bodies from outside of this system is the gravitational force from the Moon and Sun on the satellite. Deficiencies in UT1 result in a wrong position of the Moon and Sun when the gravitational force is computed for orbit modeling. An error of up to 10 ms can be compensated by usually estimated orbit parameters and do not introduce a significant degradation of the obtained satellite orbit.

With a GNSS solution the cumulated LOD parameters may follow UT1 over years, in particular with a long-arc solution and continuity conditions on the Earth rotation parameters. GNSS solutions with few stations and satellites and in particular based on short arcs have noisier rates for the polar motion—and more relevant in this context—LOD estimates [11]. Other techniques, e.g., SLR with a limited number of tracking stations and non-uniformly distributed observations, have less favorable capabilities for reconstructing LOD.

Acknowledgements

Discussions with Gerhard Beutler and other colleagues at the institute about the sensitivity of satellite-geodetic techniques on UT1 deficiencies in general and on the results presented in this manuscript in particular have been very fruitful and helped to improve the paper.

References

1. G. Petit, B. Luzum, IERS Conventions (2010), IERS Technical Note 36, Bundesamt für Kartographie und Geodäsie, Frankfurt am Main, http://www.iers.org/IERS/EN/Publications/TechnicalNotes/tn36.html.
2. A. E. Sibois, S. D. Desai, W. Bertiger, B. J. Haines. Analysis of decade-long time series of GPS-based polar motion estimates at 15-min temporal resolution. Journal of Geodesy 91, doi:10.1007/s00190-017-1001-6, 965–983 (2017).
3. R. Dach, S. Lutz, P. Walser, P. Fridez (Eds). Bernese GNSS Software Version 5.2. User manual, Astronomical Institute, University of Bern, Bern Open Publishing. doi:10.7892/boris.72297; ISBN: 978-3-906813-05-9 (2015).
4. A. Milani, A. Nobili, P. Farinella. Non-Gravitational Perturbations and Satellite Geodesy. Adam Hilger Ltd., Bristol, UK (1987).
5. D. Arnold, M. Meindl, G. Beutler, R. Dach, S. Schaer, S. Lutz, L. Prange, K. Sośnica, L. Mervart, A. Jäggi. CODE's new solar radiation pressure model for GNSS orbit determination. Journal of Geodesy 89(8), doi:10.1007/s00190-015-0814-4, 775–791, 2015.
6. https://ids-doris.org/analysis-coordination/combination/contributions-to-itrf/contribution-itrf2014.html. Visited 12 July 2022.
7. T. A.. Springer, G. Beutler, M. Rothacher. A new solar radiation pressure model for GPS satellites. GPS Solutions 3(2), doi:10.1007/PL00012757, 50–62, 1999.
8. I. Selmke, R. Dach, D. Arnold, L. Prange, S. Schaer, D. Sidorov, P. Stebler, A. Villiger, A. Jäggi, U. Hugentobler. CODE repro3 product series for the IGS. Published by Astronomical Institute, University of Bern. URL: http://www.aiub.unibe.ch/download/REPRO_2020; doi:10.7892/boris.135946, 2020.
9. R. Dach, I. Selmke, A. Villiger, D. Arnold, L. Prange, S. Schaer, D. Sidorov, P. Stebler, A. Jäggi, U. Hugentobler. Review of recent GNSS modelling improvements based on CODEs Repro3 contribution. Advances in Space Research, 68(3), DOI:10.1016/j.asr.2021.04.046, 1263–1280, 2021.
10. M. Rothacher, G. Beutler, T. A. Herring, R. Weber. Estimation of Nutation using the Global Positioning System. Journal of Geophysical Research, 104(B3), DOI:10.1029/1998JB900078, 4835–4895, 1999.
11. S. Lutz, M. Meindl, P. Steigenberger, G. Beutler, K. Sośnica, S. Schaer, R. Dach, D. Arnold, D. Thaller, A. Jäggi. Impact of the arc length on GNSS analysis results. Journal of Geodesy, 90(4), doi:10.1007/s00190-015-0878-1, 365–378, 2016.

The Global VLBI Alliance

Francisco Colomer[1,2]

Abstract By its very nature, VLBI has always depended on international collaborations. These have led to the formation of several formal VLBI networks, which in turn regularly form combined arrays. In astronomy, "global VLBI" is the term often used for the coordinated observations of the European VLBI Network (EVN) and the Very Long Baseline Array (VLBA). In the past, the "Global VLBI Working Group" (GVWG) worked as an umbrella for the space VLBI and ground VLBI network collaboration (VSOP), organizing the logistics (time allocation of ground network resources was agreed in the GVWG) and technical compatibility. Nowadays, as several independent VLBI networks and instruments exist, we recover that spirit, by the establishment of a Global VLBI Alliance (GVA).
The GVA facilitates the flow of information between VLBI networks, including sharing strategies, technical developments for compatibility, logistics, operations, and user support. It also promotes, proposes, and coordinates common observational campaigns with these existing networks. Moreover, with the advent of the Square Kilometer Array (SKA) and its precursors, such global coordination of the various networks and their participating telescopes will be required. The next-generation Very Large Array (ngVLA) may also collaborate with a global VLBI array. In such scenario, the GVA will serve as contact point and framework of collaboration of the VLBI networks and these other facilities. Additionally, it can encourage and support new VLBI activities (like the African VLBI Network, AVN; Iniciativa VLBI IberoAmericana, IVIA; or developments in India and southeast Asian countries).
The GVA will also facilitate that adequate information is provided to the users. For this, a unique common portal will explain the characteristics of the different networks, and the options for users to access them or in combination.
Since there is a big synergy of developments with geodetic VLBI—and many radio observatories share their facilities and equipment between different VLBI applications—the discussions in the GVA will be very relevant to the IVS.

1. Joint Institute for VLBI ERIC (JIVE)
2. Instituto Geográfico Nacional (IGN)

Keywords VLBI networks, infrastructure, coordination, policy

1 Introduction

Very Long Baseline Interferometry (VLBI), by its very nature, has always depended on international collaborations. Currently, several formal VLBI networks exist, which in turn regularly form combined arrays. A Global VLBI Alliance (GVA) facilitates the flow of information between VLBI networks, including sharing strategies, technical developments for compatibility, logistics, operations, and user support. It also promotes and coordinates common observational campaigns with these existing networks, fosters and supports new VLBI activities, while increasing the visibility, as well as scientific and societal impact of VLBI. The GVA, moreover, facilitates the interaction with the users and serves as contact point and framework of collaboration of the VLBI networks and other astronomical facilities—in view of the growing need of multi-messenger studies.

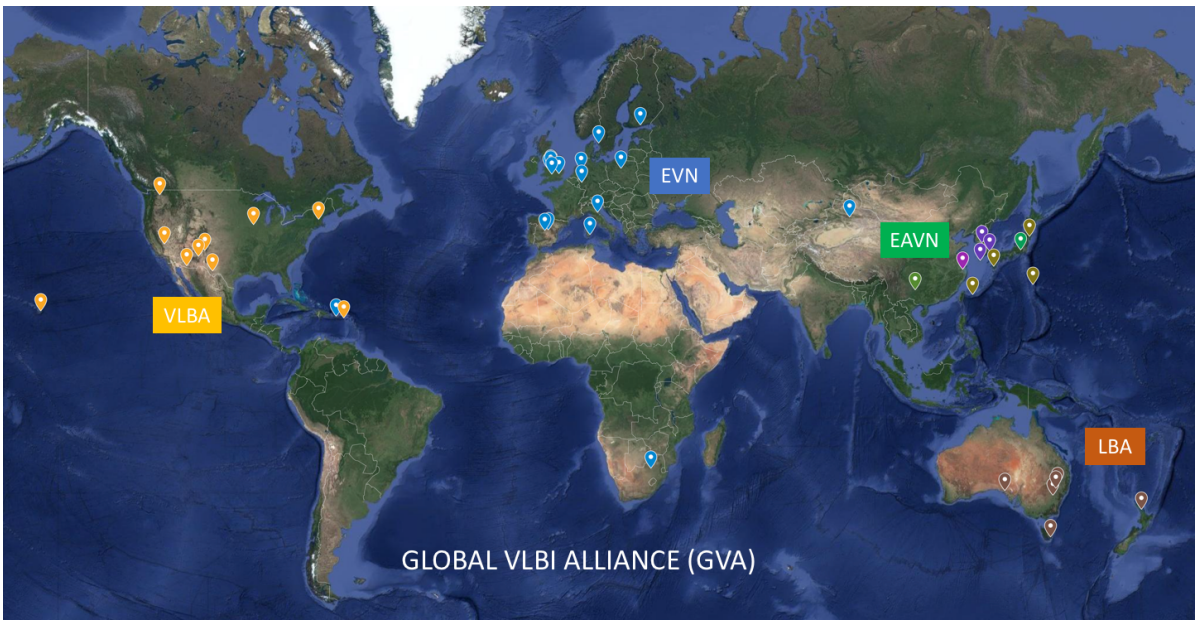

Fig. 1 VLBI networks in the Global VLBI Alliance.

2 VLBI Networks in the GVA

The Global VLBI Alliance is open to every VLBI network, and at this moment (March 2022) it includes those who can operate at some common frequencies. These networks are:

- The European VLBI Network (EVN),
- the East-Asian VLBI Network (EAVN), comprised of the Chinese VLBI Network (CVN), the Korean VLBI Network (KVN), and the Japanese VLBI Exploration by Radio Astronomy (VERA)—the last two also operating together as KaVa,
- the Very Long Baseline Array (VLBA) in USA, and
- the southern hemisphere Long Baseline Array (LBA), with radio telescopes in Australia and South Africa.

It is to note that several radio telescopes and institutional members of the networks above are also participating in IVS campaigns. Moreover, since there is a big synergy of developments with geodetic VLBI, and many radio observatories share their facilities and equipment between different VLBI applications, the discussions in the GVA will be very relevant to the IVS.

3 Structure of the GVA

The Global VLBI Alliance is structured as follows:

- GVA Director's Forum (GVAD): VLBI network directors or representatives (up to two per network) to discuss any aspect of the global cooperation.
- Science Forum (GVAS): evaluates and fosters the unique and complementary contribution of VLBI to astrophysical research. Members are active scientists, not necessarily linked to any of the VLBI networks in the GVA.
- Technical R&D Forum (GVAT): discusses opportunities and coordinates the development of new instrumentation or procedures.
- Operations and Logistics Team (GVAO): facilitates and coordinates observations scheduled with several VLBI networks, or with participation of third-party instruments (e.g., multi-wavelength/multi-messenger).
- Communication and Outreach Team (GVAC): coordinates activities and tools to increase the scientific and societal impact of VLBI.

The GVAS, GVAT, GVAO, and GVAC all report to the GVAD.

4 The GVA Science Forum

The GVA Science Forum (GVAS) evaluates and fosters the unique and complementary contribution of VLBI to astrophysical research. Members are active scientists, not necessarily linked to any of the VLBI networks in the GVA.

The GVAS provides the opportunity for scientists to identify needs and engage in discussions on how to keep the VLBI facilities responding to the latest astronomical challenges, participating and providing input to roadmap exercises. Recent examples are the excellent review of VLBI in the EVN science vision 2020–2030 document [1], "VLBI20-30: a scientific roadmap for the next decade – The future of the European VLBI Network," to optimize its unique role in the context of a rapidly evolving set of global astronomical facilities as planned for the next few decades. In the USA, the NSF Decadal Survey on Astronomy and Astrophysics 2020 (Astro2020) [2] supports the NSF to fund design and cost studies and prototyping for the next-generation Very Large Array (ngVLA), a potential replacement for the Jansky Very Large Array and the Very Long Baseline Array radio astronomy facilities.

The scientists involved can evaluate not only the synergies between VLBI facilities, but also exploit the unique and complementary characteristics that enhance the contribution of VLBI to astrophysical research, such as different frequency coverage, angular resolution, sensitivity, availability for studies that require observations with different cadences, real-time capabilities, access to different regions of the sky, and so on. Moreover, this will incorporate the VLBI aspect to roadmap exercises such as the Astronet Science Vision and Infrastructure Roadmap for European Astronomy [3], facilitating the coordination of VLBI networks with other astronomical instruments.

The GVAS is also a forum for cross-fertilization where scientists of some regional VLBI networks can meet with other colleagues and start global collaborations, in line with the true international nature of VLBI.

5 The Technical R&D Forum

The GVA Technical Research and Development Forum (GVAT) discusses opportunities and coordinates the development of new instrumentation or procedures. A primary goal is to make the VLBI networks sufficiently compatible as to allow joint observations, which requires capability for observing at common frequencies, using the same data transport and formatting protocols, storage, etc. Users also benefit from similar proposal tools and data reduction platforms.

The role of the GVAT is also to evaluate the best way to answer the expectations of the VLBI users, as described in the science vision documents, from the development of state-of-the-art instrumentation to the logistics of how the observations are made. Joint efforts to achieve increased sensitivity, survey speed, agility, frequency range, and post-processing capabilities are beneficial for all VLBI networks. For example, expected increases in correlator and data imaging capacity, possibly combined with Phased Array Feeds (PAFs) on the larger VLBI telescopes, would make imaging over large fields of view a standard capability, and flexible VLBI arrays and real-time capabilities will also allow follow-ups of transient events detected either in large field of view radio surveys or by instruments operating in other parts of the electromagnetic spectrum.

Currently there are several instances in which the staff responsible for R&D, scheduling, and logistics of VLBI networks regularly meet; the GVAT will extend the scope to the global scale and facilitate the exploration of not only the synergies but also the complementarity of the network characteristics, to fulfil the requirements of the user science cases.

6 Operations and Logistics Team

The GVA Operations and Logistics Team (GVAO) takes care of identifying and solving the details that facilitate coordinated observations with several VLBI networks, and/or with participation of third-party instruments (e.g. multi-wavelength/multi-messenger).

The team is composed of the officers responsible for operations and scheduling, in close collaboration with the chairs of the Time Allocation Committees (TACs), to discuss aspects such as proposal submission tools and deadlines, evaluation criteria, and other data policies which need to be consistent among the networks.

7 GVA Communications and Outreach

The results of VLBI, and its capacity to complement the information obtained in studies with other astronomical techniques, are made visible by the Communication and Outreach Team (GVAC), whose important mission is to promote the visibility of VLBI, its networks, making joint advocacy of VLBI. This is done by the maintenance of the GVA web portal [4], presence in social networks [5], organization or participation in conferences, workshops, schools and other events, among other things.

References

1. T. Venturi, M. Lindqvist, Z. Paragi et al., VLBI20-30: a scientific roadmap for the next decade – The future of the European VLBI Network, arXiv:2007.02347 (2020), https://arxiv.org/abs/2007.02347
2. USA NSF Decadal Survey on Astronomy and Astrophysics 2020 (Astro2020), see: https://nap.edu/resource/26141/interactive/ and https://www.aip.org/fyi/2021/astro2020-decadal-survey-arrives-priorities-major-facilities
3. Astronet Science Vision and Infrastructure Roadmap for European Astronomy (2021), see: https://www.astronet-eu.org/forums/roadmap-community-consultation
4. Website of the Global VLBI Alliance: http://www.gvlbi.org/
5. The Global VLBI Alliance in Twitter: @globalvlbi
6. EC H2020 "JUMPING JIVE" project, see: https://jumping.jive.eu/results.html
7. The Global VLBI Alliance, a working group in the International Astronomical Union, Commission B4, see: https://www.iau.org/science/scientific_bodies/working_groups/324/

Spectrum Management for the VLBI Global Observing System (VGOS) Observations

Juha Kallunki[1], Hayo Hase[2], Nataliya Zubko[3]

Abstract The wideband receiving system for 2–14 GHz of the VLBI Global Observing System (VGOS) challenges the spectrum management and the interference investigations. We share our experience with the new VGOS telescope, built at the Metsähovi Geodetic Research Station, as well as the long term experience of Aalto University Metsähovi Radio Observatory with spectrum management and radio interference monitoring. The following steps and measures should be made: (1) the registration of the VGOS site at the International Telecommunication Union – Radio Section to get a legal position for a radio astronomy site; (2) intentions to claim a protection zone for a RAS site; (3) possibilities of avoiding RFI; (4) an interference monitoring system to track the changes of the electromagnetic environment and eventually to give notice to the national spectrum administration, if unwanted RFI is detrimental to VLBI observations.

Keywords VGOS, RFI, spectrum management, spectrum allocation, interference monitoring, ITU-R registration

1 Introduction

VLBI Global Observing System (VGOS) is a passive user of the frequency range of 2–14 GHz. Active transmissions, e.g., by telecommunication such as 5G that has allocated frequency bands, cause interference and a conflict of interest when detrimental radiation disturbs the radio astronomy and VGOS observations. The Radio Astronomy Service (RAS) has only about 250 MHz of allocated bandwidth in the VGOS range, but VGOS uses four frequency blocks with eight channels each of 32 MHz bandwidth summing up to a demand of at least 1,024 MHz of bandwidth. In Table 1, the current IVS VGOS frequency band setups are shown. This causes various challenges for VGOS observations. More difficulties bring out the fact that the trial phase of experiencing different frequency sequences is ongoing and that the VGOS community has no clear consensus on the final frequency setup. Taking into account the general frequency allocation, it appears not to be realistic for VGOS to demand its own allocation for all VGOS channels. That is why striving for alternative protection methods is necessary. Local radio quiet zones (RQZ) are one possibility for getting protection for VGOS sites. However, in most cases the separation distances could be hundreds of kilometers, which cannot be achieved in populated areas. An important aspect is continuous radio frequency interference (RFI) monitoring, to track the ongoing changes of the electromagnetic environment and eventually give notice of RFI incidence detrimental to VGOS observation to the national spectrum administration. For the awareness of the VGOS requirements a fluent dialogue between the VGOS operator and the national frequency administration is required. In any case, it is also very important that each national administration register the VGOS sites at the International Telecommunication Union – Radio Section (ITU-R); thus the site will get a legal position as a radio astronomy service site. The registration improves possibilities of achieving acknowledgement by regulators and active services. In this paper, we

1. Aalto University, Metsähovi Radio Observatory, Finland
2. Bundesamt für Kartographie und Geodäsie, Geodätisches Observatorium Wettzell - AGGO, Germany
3. Department of Geodesy and Geodynamics, Finnish Geospatial Research Institute, National Land Survey, Finland

present some administrative spectrum management aspects and practical examples of RFI issues observed in Aalto University's Metsähovi Radio Observatory. Figure 1 shows the current frequency allocations among the different services between 2,500 and 5,000 MHz in Finland. This figure indicates the potential sources of disturbance of VGOS observations.

2 ITU Registration, Band Allocation, Protection Zones

The ITU-R (International Telecommunication Union – Radiocommunication Sector) main mission is to facilitate seamless and interference-free operation of radio communication services between member states. In other words, the ITU-R's main role is to coordinate the use of radio frequency spectrum and satellite orbit resources by the development of standards and regulations for radiocommunication systems with the objective of ensuring their effective use. ITU-R has recognized services such as RAS. This gives RAS an equal position to any other (active) service. Therefore, other radio spectrum users have to respect the requirements of frequencies allocated to RAS. Each radio service could have either primary or secondary allocations. In the case of RAS, the primary frequency allocation usually means that all transmissions are prohibited. The secondary allocation means that all practical steps must be done to protect RAS from harmful interference. However, there is only a limited number of RAS allocations. For instance, in a VGOS operation range there is only a total of about 250 MHz accumulated bandwidth allocated to RAS. This is a big challenge for VGOS operation as its frequency setup is not following the radio astronomy method of spectral line observations, but needs at least 1,024 MHz bandwidth in order to achieve millimeter accuracy for global reference frames.

Each observatory should be registered through its national administration to the ITU-R database. The initiative must come from the VGOS station owner. The registration contains the geographical location and the receiving capabilities. This is a first step for protection. The observatory is then listed officially as a RAS station and recognized as a passive user of radio spectrum. It is important to register as early as possible, as only future allocations or licenses will have to respect the VGOS site. For instance, future space mission owners may consult the ITU-R database to identify downlink areas avoiding illuminations of RAS sites.

The most effective protection which could be achieved would be VGOS' own frequency allocation either on the international or the national level. A more realistic option would be to achieve protection on the national level. For example, a public administration in Germany is tasked to perform contributions to the global geodetic tasks (VGOS observations), and therefore the frequency administration has to provide protection of the VGOS site when new licenses are emitted. Unfortunately, many VGOS sites are in another legal position. In general, VGOS' own frequency allocations would be best, but almost not achievable. For practical reasons it appears more likely to demand for the globally distributed VGOS network stations protection zones around the observatories, so that they can do their duties in an undisturbed manner. For instance, the RQZ concept is a rather effective method for protecting observations at maximum [1, 2] and is recommended wherever it is possible. The next alternative with fewer restrictions would be a coordination zone around VGOS sites, in which the regulators could introduce restrictions and conditions for other services in order to provide protection of the VGOS sites.

3 Interference Monitoring

The Aalto University Metsähovi Radio Observatory (MRO) has conducted continuous RFI monitoring for over 20 years. The monitoring covered especially the range of 500–1,000 MHz (often used as an intermediate frequency band) but also the S-band (2–2.5 GHz) used by legacy geodetic VLBI. In Figure 2, a typical radio spectrum between 400–2,400 MHz is shown. It was recorded with MRO's RFI monitoring system, which consists of a turnable log-periodic antenna, a pre-amplifier, and a backend. Ettus USRP N210 Software Defined Radio (SDR) is used as a backend. With the current instrumentation it is also possible to perform RFI monitoring in some narrower bands up to around 12 GHz. This is of special interest for first studies on the impact of various satellite services (e.g., geo-stationary satellites and OneWeb/StarLink satellite

Table 1 The current IVS VGOS frequency band setups. The individual channels have a width of 32 MHz. The values shown in the table are the upper edges of frequencies.

Band A	3032.4 MHz	3064.4 MHz	3096.4 MHz	3224.4 MHz	3320.4 MHz	3384.4 MHz	3448.4 MHz	3480.4 MHz
Band B	5272.4 MHz	5304.4 MHz	5336.4 MHz	5464.4 MHz	5560.4 MHz	5624.4 MHz	5688.4 MHz	5720.4 MHz
Band C	6392.4 MHz	6424.4 MHz	6456.4 MHz	6584.4 MHz	6680.4 MHz	6744.4 MHz	6808.4 MHz	6840.4 MHz
Band D	10232.4 MHz	10264.4 MHz	10296.4 MHz	10424.4 MHz	10520.4 MHz	10584.4 MHz	10648.4 MHz	10680.4 MHz

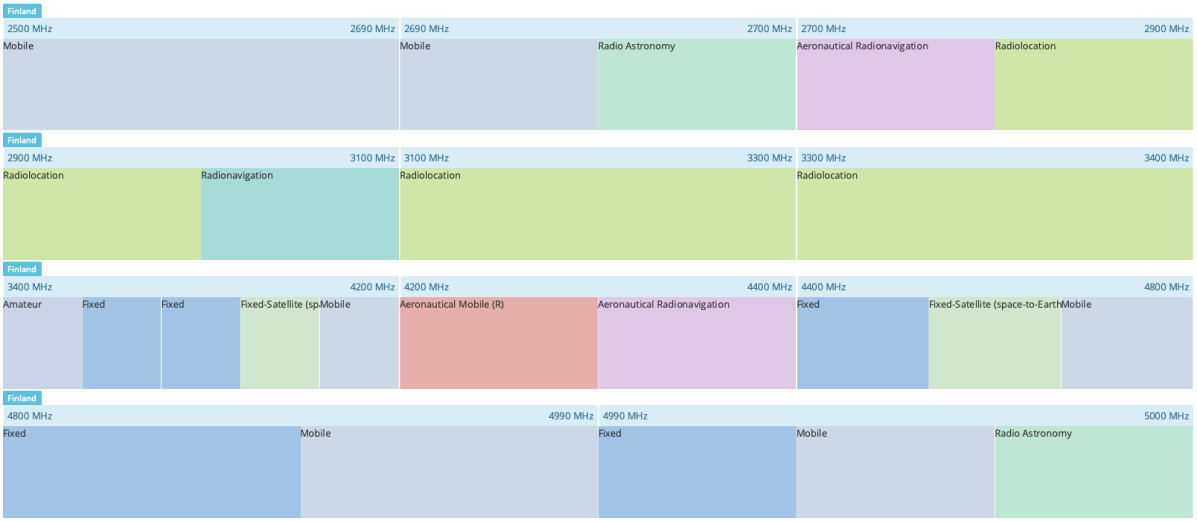

Fig. 1 The frequency allocation between 2500 and 5000 MHz in Finland.

service at 10.7–11.7 GHz) on radio astronomy or on broadband geodetic VLBI [3].

A dedicated RFI monitoring system that covers the VGOS broadband frequency range is developed at the Metsähovi Geodetic Research Station. It will allow us to detect harmful signals in real-time and take possible actions.

Geodetic VLBI observations in the legacy S-band (2,100–2,390 MHz) seriously suffer from active transmitters in many locations (seen also in Figure 2), such as mobile and military services. At higher VGOS frequencies (ca. 5–10 GHz), a new interference threat is the 5G cellular network. Various satellite mega constellations such as OneWeb or StarLink could be major problems for passive services in the future. In this decade we will see the launch of thousands of small satellites in low Earth orbits for communication [4]. In this scenario, it is very likely that satellites passing the radio telescope's beam will generate RFI. It is frightening that the satellite's transmission power could be so strong that the low noise amplifiers (LNA) of the radio astronomy receiver could be saturated. Figure 3 shows the spectrum of MRO's 1.8-meter solar telescope when a OneWeb satellite passes its beam. The power level rises more than 10 dB when the satellite passes the telescope's beam. This is a major interference noise contribution, and any kind of radio astronomical observation of faint extra-galactic radio sources will not be possible when such interference is present.

Another important aspect in interference monitoring and protection is a self-generated RFI inside the observatory. This is an increasing problem exposed by low-cost electronic devices, which can be found also in the observatories. The lower cost, unfortunately, means also less consideration to EMI (Electromagnetic interference) and EMC (Electromagnetic compatibility) issues. For instance, a single missing capacitor in the power feed could cause interference which is seen in the radio spectrum.

When executing RFI monitorings, the calibration of the system is an important issue. The readings from the spectrum analyzer give a first clue on signal strength. However, the parameters of the whole monitoring system chain should be known including system total gain and possible losses in RF cables. The calibrated RFI monitoring values should be compared with the ITU-R threshold interference level. The accepted threshold interference levels for the radio astronomy service bands

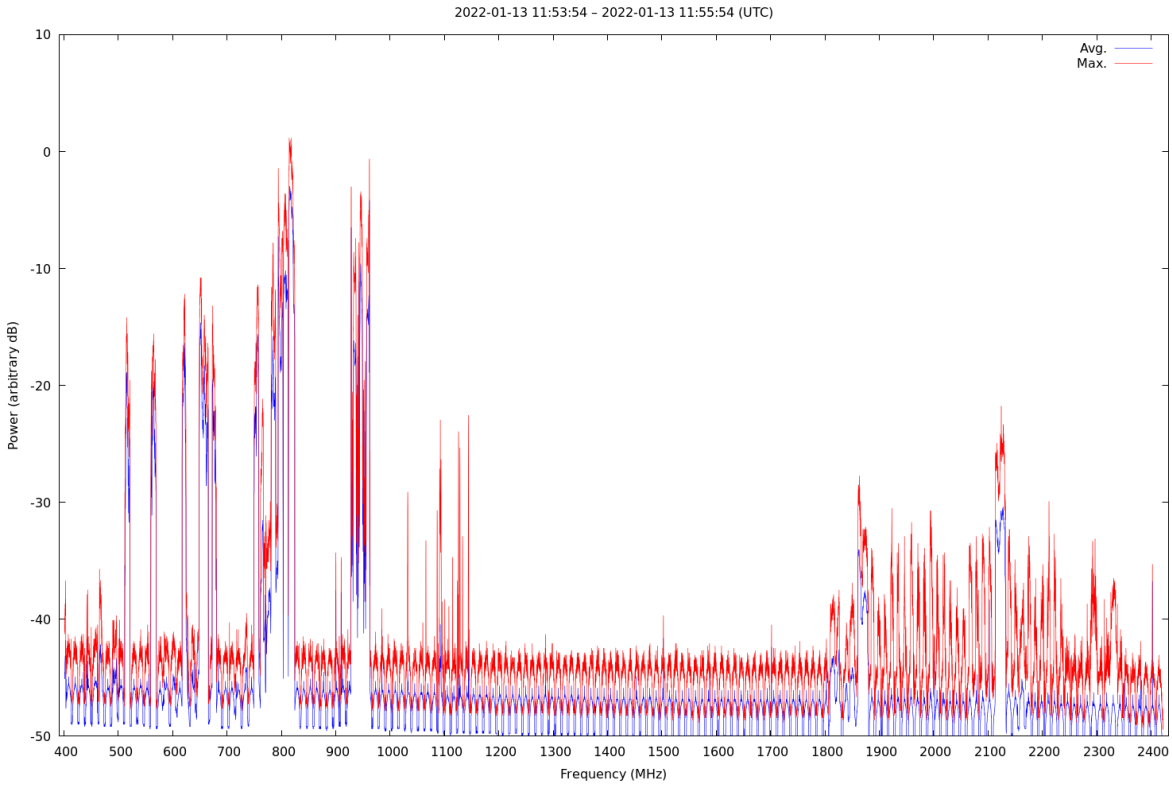

Fig. 2 The radio spectrum between 400 and 2,400 MHz. The spectrum has been observed by MRO's dedicated interference monitoring system. The spectrum clearly shows TV broadcasts and mobile telephone services (900 MHz and 18,000 MHz). The frequency band above 2 GHz is heavily used by active transmitters, which makes it almost impossible to execute undisturbed radio astronomy observations.

are presented in Recommendation ITU-R RA.769-2: Protection criteria used for radio astronomical measurements. This recommendation gives threshold interference levels of both continuum and VLBI observations [5].

4 Mitigation Methods

Besides spectrum management, there are also other mitigation methods to protect observations against harmful interference. There are several technical solutions such as additional notch filters in the receiver and software filters in the data post-processing phase either in the local recording or data correlation process. However, none supplies a perfect solution. The notch filter is not an optimal solution if several bands must be filtered out. Even increasing the dynamical range of the LNA may have an effect on its sensitivity. The best possible technical solution would be probably a combination of several mitigation techniques. Besides technical mitigation approaches, an operational approach for mitigation is the scheduling of the observations. Static scheduling considers a horizon mask where (terrestrial) interferers are excluded. Dynamic scheduling considers satellite orbits. The question remains whether this can be handled if many thousands of orbits have to be considered. Finally, an obvious method is to use only frequencies which are free from interference. However, the interference situation varies between different observatories/countries; thus a "good and clean" frequency setup does not work everywhere.

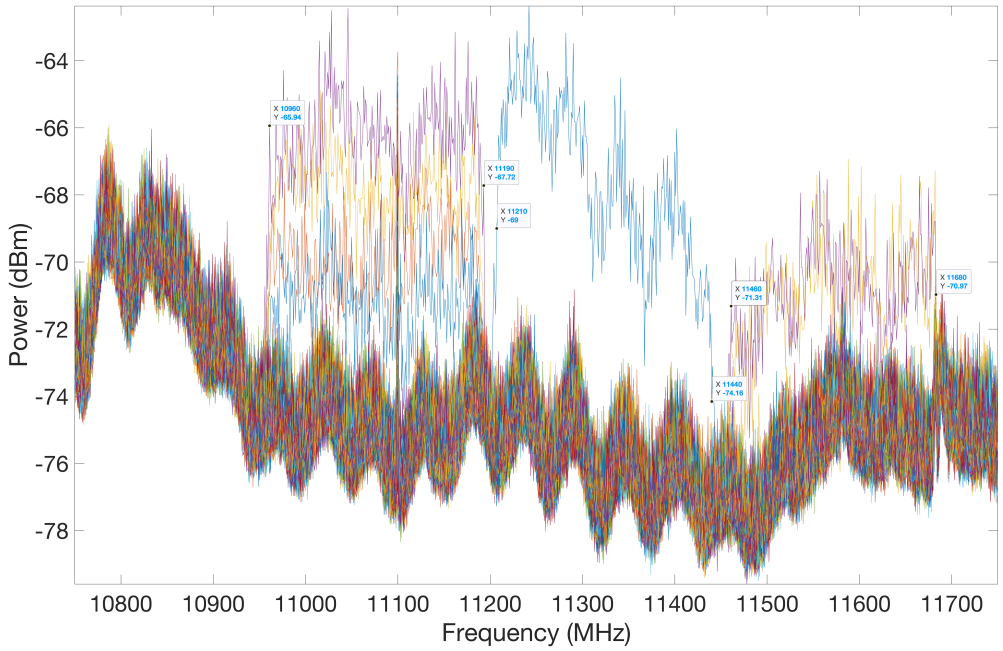

Fig. 3 OneWeb satellite interference monitored by MRO's 1.7-m solar telescope (10.7–11.7 GHz). When a OneWeb satellite passes the telescope's beam, the signal level rises by more than 10 dB.

5 Conclusions

As we have shown, frequency management and interference issues are especially challenging in VGOS operations. There are still some major open questions, especially a final VGOS frequency setup. This would facilitate further concrete actions in spectrum management. As long as the VGOS community has not decided on "its" frequency sequence, spectrum managers cannot request protection for the sequence from their national authorities. Likewise, VGOS radio astronomy is a passive service and must operate without interfering with other services. This weak position shall be altered by raising awareness (registration, ITU Report on Geodetic VLBI), agreeing on a VGOS frequency sequence in the near future, and searching for footnote protection in the radio regulations. In this regard, a close and fluent dialogue with national frequency administration is helpful. Each observatory should have a person responsible for spectrum management that could also be the link to one of the three regional spectrum management groups for radio astronomy such as CRAF (Europe/Africa), CORF (America), or RAFCAP (Asia-Pacific).

References

1. Hase, H., López-Pérez, J.A., Bautista-Duran, M., Kallunki, J., Kupiszewski, P., Tornatore, V., et al.: 2021, *Proceedings of the 25th European VLBI Group for Geodesy and Astrometry Working Meeting*, 43.
2. Hase, H., Tornatore, V., and Corey, B.: 2016, *New Horizons with VGOS*, 65.
3. Kirves, P., Kallunki, J., and Wagner, J.: 2010, *RFI Mitigation Workshop*, 27.
4. Gallozzi, S., Paris, D., Scardia, M., and Dubois, D.: 2020, *arXiv e-prints*, arXiv:2003.05472.
5. RA.769: Protection criteria used for radio astronomical measurements, https://www.itu.int/rec/R-REC-RA.769/en

Large Satellite Constellations and Their Potential Impact on VGOS Operations

Federico Di Vruno[1], Vincenza Tornatore[2]

Abstract Large LEO satellite constellations (or so-called Megaconstellations) will significantly change the view of the sky in some radio frequency bands. For VGOS telescopes, it is important to understand the potential impact these constellations will have on their operations, what the risk is of its receivers going into non-linear behavior, and how much additional power a telescope would receive if observing in the same frequencies where satellites are transmitting. This work describes three of these new constellations (as they would look fully deployed) and summarizes the results of a particular study considering two VGOS telescopes (Onsala and Wettzell).

Keywords VGOS, RFI, Megaconstellations, satellite constellations

1 Introduction

The industrialization of spacecraft construction and the lowering in costs of space launches have paved the way for big plans in Low Earth Orbit (LEO). Large satellite constellations like Starlink phase 1 (with 4,400 satellites) and OneWeb phase 1 (with 648 satellites) are already in the deployment phase. Others like Project Kuiper (from Amazon) or Guowang (from China) are in their development phase and yet others with even larger numbers are being filed into the International Telecommunication Union (ITU) system (see Table 1). With altitudes between 500 km and 1,200 km, these new constellations will surround the planet almost homogeneously. From a radio telescope point of view, the situation in the sky will change considerably. This change is already evident in the number of active satellites in LEO, from about 2,000 in 2018, to more than 5,000 in 2022, and the trend suggests that it may reach hundred of thousands in this decade [5].

Until now, most of the satellites for internet communication were located in the geostationary belt (at approximately 35,780 km altitude), appearing fixed in the sky for a terrestrial observer [7]. The new LEO satellites will orbit the Earth with a period of about 90 minutes and will be seen as hundreds to thousands of bright and fast-moving radio sources in the sky with downlinks in frequency bands from 10.7 GHz up to 76 GHz (see Section 2.2).

Contrary to the situation with terrestrial radio frequency interference (RFI), it is not possible to build radio telescopes far away from satellite transmissions [1]. The challenge is further increased by the opposite pointing direction of the radio telescopes and the user downlink antenna beams.

The typical power flux density (PFD) of satellite constellations is in the order of -146 dBW/m^2 [12, 6] in 4 kHz or an equivalent to 62×10^6 Jy, i.e., more than seven orders of magnitude brighter than a typical VGOS source [8]. These strong signals will require a radio astronomy receiver to have a large dynamic range to accommodate the RFI and still be able to detect faint cosmic sources in other frequency channels within the receiver band. This is normally possible for modern radio astronomy receivers. But it can be different in some particular situations such as total power bolometric receivers or receivers with a low effective number of bits (ENB) [3].

1. SKA Observatory, Jodrell Bank, Manchester, United Kingdom
2. Politecnico di Milano, DICA, Milano, Italy

2 Large LEO Constellations

Radio astronomy has been dealing with satellite transmissions since the very first satellites were launched back in the 1960s. Implementing different strategies, such as using analog receivers with large dynamic ranges, smart scheduling, and RFI flagging among others, radio telescopes have been more or less able to mitigate (or avoid) the effect of these strong radio transmissions towards Earth [1]. In conjunction with these strategies, spectrum management has also played a key role in dealing with the effects of satellites. Several radio astronomy groups have worked at regional, national, and international levels for the protection of the radio astronomy service (RAS) frequency bands allocated by the ITU. Some had successful results like the GLONASS example, while others are in battles that are ongoing for 20 years since satellite deployment like in the IRIDIUM case [2].

Table 1 Some of the large LEO constellations in deployment or planned.

Constellation	Number of Satellites	Altitude [km]
Starlink Phase 1	4,400	550
OneWeb Phase 1	648	1,200
Amazon Phase 1	3,200	~ 600
Guowang (GW)	13,000	590 to 1,145
Starlink VLEO	7,600	340
Telesat	298	1,000
Starlink Phase 2	30,000	328 to 614
OneWeb Phase 2	6,372	1,200
Cinnamon–937	327,320	550 to 643

The exponential growth in the number of active satellites in Low Earth Orbit [5] could result in more than 2,000 satellites above the local horizon at any moment in time. Radio telescopes are sensitive to any transmitter in line of sight through its main beam or antenna sidelobes.

2.1 Walker-Delta Constellations

All these new constellations follow a "Walker Delta" type of distribution, composed of orbital *shells* at a certain altitude. Each shell contains several *orbital planes*, with a certain inclination with respect to the equator and distributed homogeneously over the 360 degrees of right ascension. Each one of the constellation's planes contains N satellites. A representation of Starlink Phase 2 is given in Figure 1.

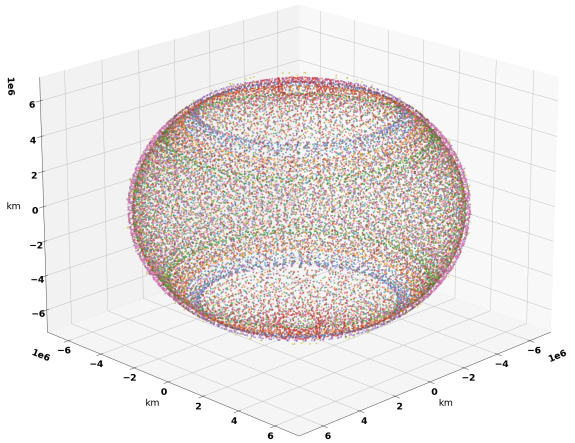

Fig. 1 View of Starlink Phase 2 constellation with 30,000 satellites. Different colors are used for each of the shells of the constellation frequency bands used by some of the satellite constellations.

A shell of a Walker-Delta constellation [17] is described by $i = t/p/f$ where i is the inclination, t is the total number of satellites, p is the number of equally spaced planes, and f is the relative spacing between satellites in adjacent planes. This description makes it very simple to simulate any of these constellations with the purpose of studying its geometric distribution in LEO as well as its effect on radio telescopes. It is also possible to use existing Two-Line Elements (TLEs) to obtain the approximate position of existing satellites in space, which can be useful to compare observations to simulation.

Figure 2 shows a qualitative view of the sky from the Wettzell VGOS station (lat 49 degrees), with the position of different satellite constellations simulated for 100 seconds. It is easy to see how the density of satellites in the sky will drastically change in the near future if all planned constellations are deployed.

2.2 Radio Frequencies

Satellite constellations transmit their downlink signals in frequencies allocated to the Fixed Satellite Service

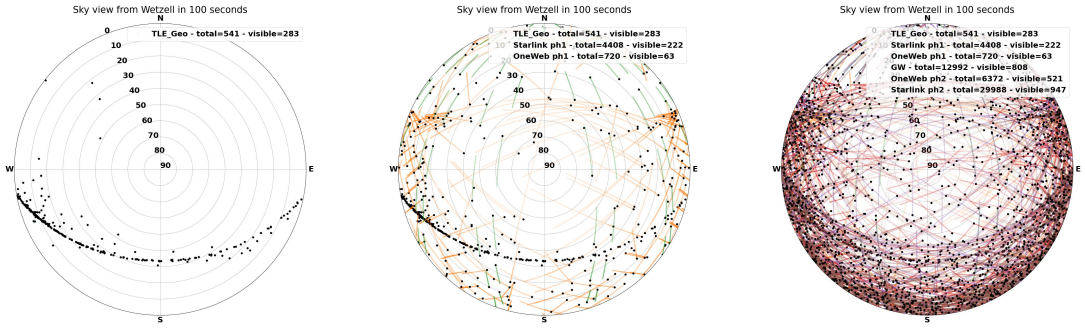

Fig. 2 Sky view from the Wettzell VGOS station with only geostationary satellites (left), simulation of SL1 and OW1 constellations fully deployed (middle), and simulation of six large LEO constellations fully deployed (right). The term "visible" is used for satellites above the horizon, as radio telescopes can detect satellites in any direction in the sky.

(FSS). Table 2 contains some of the currently in-use and planned FSS bands. It is important to note the proximity to some ITU protected RAS bands immediately adjacent or in very close proximity.

Table 2 Frequency bands used by some of the satellite constellations.

Frequency	Band name	Protected RAS bands (primary)
10.7–12.75 GHz	Ku	10.6–10.7 GHz
19.7–20.2 GHz	Ka	22.21–22.5 GHz
37.5–42.5 GHz	V	42.5–43.5 GHz
71.0–76.0 GHz	E	76–77.5 GHz

The close vicinity of the satellite's downlinks to radio astronomy bands is a matter of concern for radio astronomers and spectrum managers. For example, the protection of the 10.6–10.7 GHz Radio Astronomy Service (RAS) band, which includes a *passive band* in 10.68–10.7 GHz protected by the footnote RR No. 5.340 in the ITU-R Radio Regulations (RR), was studied for the Starlink Ph1 and OneWeb Ph1 constellations in [4]. The conclusion of the study was that both systems should not use the first 250-MHz channel to protect the RAS band. These signals cannot only impact sensitive observations in the RAS protected bands, but they can also affect wideband receivers which include the frequency range of user downlinks. Such wideband receivers (from 2 to 14 GHz in the case of VGOS) are necessary to conduct cutting-edge science or geodesy [8].

This paper focuses on the downlink frequency range 10.7 to 12.75 GHz where both OneWeb and Starlink have divided the band into eight channels of 250 MHz each. The study can be replicated for higher frequency bands with the appropriate modification of satellite and telescope characteristics.

3 Potential Impact on VGOS

By using large reflector antennas pointed towards the sky and wideband receivers covering the frequency range 2 to 14 GHz [8], VGOS telescopes can be impacted by downlinks of the large satellite constellations in different ways. In fact, the VGOS bandwidth is wide, while the protected radio astronomy band is very narrow, and Starlink and OneWeb use a considerable portion of the frequency spectrum. The severity of this impact depends on the interaction between the radio telescope beam and the satellite downlink beams. One of the most important aspects is how much a correlated baseline can be affected as the primary product of a VGOS observation. Nevertheless, the multidimensionality of this problem requires an analysis of the complete signal reception mechanisms and how each part of the signal chain may be impacted.

In a typical VGOS schedule, targets are observed with durations in the order of seconds to tens of seconds. The position of the target in the local sky and the density of satellites deployed will define how much interference will be seen by the telescope. The instantaneous received power from all satellites above the horizon may saturate the analog signal chain (e.g., low noise amplifiers, mixers), causing non-linearities

that would render the complete receiver band unusable, even if the digitizer band is tuned to a completely different frequency than the satellite downlinks channels. If the RFI power is not as strong and the analog signal chain remains linear, then there can be two possible scenarios:

- First scenario: the observed band is outside of the satellite downlink frequency range. In this case out-of-band emissions from the satellites could be a problem depending on their level. This work is not focusing on this, but [4] has studied that case.
- Second scenario: the observing band falls within one satellite downlink band (250 MHz channels) or vice versa. Strong RFI will be received by the VGOS antenna. This RFI can potentially be mitigated by correlation as long as the number of bits in the digitizer are enough to correctly digitize the signal. Since a VGOS digitizer has only two bits, the total integrated RFI needs to be lower (practically at least 10 dB lower or $1/10$) than the integrated noise power of the receiver [3].

Non-linearities and lack of headroom for RFI are transient phenomena and can be considered in terms of a data loss associated with the moments when a satellite is going through the main beam of the radio telescope. The issue of out-of-band emission is related to long integrations and needs a comparison between the level of integrated RFI vs. the integrated level of the astronomical source under observation. The following section describes a simulation method and presents a particular case for the Starlink phase 1, OneWeb phase 1, and Starlink phase 2 constellations to estimate data loss due to strong received power and the total aggregated RFI. The effects of the correlation are not included in this work but are currently under study by the authors.

4 Simulation Methodology

The simulation is based on the Equivalent Power Flux Density (EPFD) concept (see [11]), where the satellite constellation is propagated for a defined time duration, obtaining the coordinates and attitude of every satellite for each time step. Then the telescope antenna is pointed towards a defined *sky-cell* in azimuth and elevation, and for each of the simulated time steps the received power from all satellites above the horizon is calculated with the formula:

$$P_{rx_{(t,p)}} = \sum_{i=0}^{N_{sat}} (PFD_{sat_{(i,t)}} * A_{eff_{RAS_{(i,t,p)}}}) \qquad (1)$$

where:
t = time step
p = pointing direction
i = satellite index
PFD_{sat} = Satellite power flux density in W/m^2 towards the telescope location
$A_{eff_{RAS}}$ = Effective area of the telescope antenna in m^2 towards the satellite position

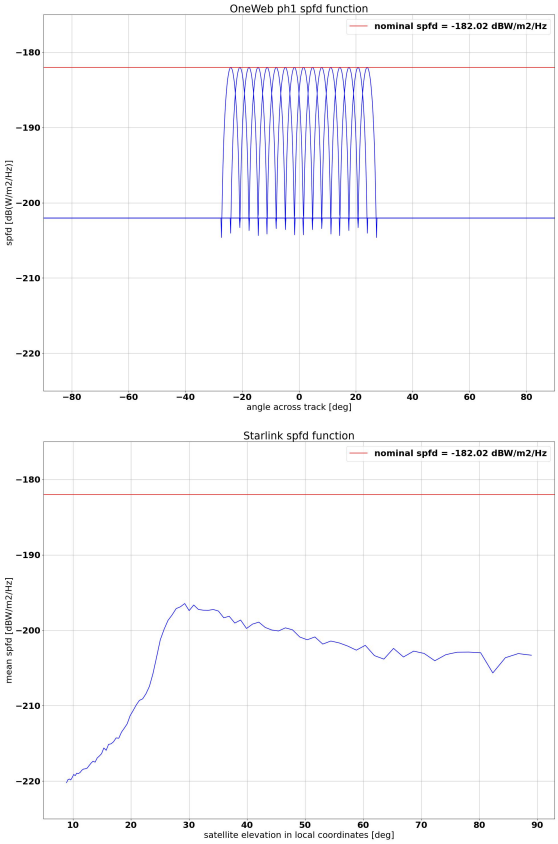

Fig. 3 OneWeb SPFD model (top) and Starlink SPFD model (bottom). The red line marks the maximum SPFD level of -182 dB/m^2/Hz.

This calculation is iterated for a number of *trials* (typically hundreds to thousands), where each try has a random start time of the constellation and, therefore, contributes to a statistically representative result. In sit-

uations where multiple frequencies are calculated, for example in the case of OneWeb with its 16 fixed-beams antenna (see Figure 3), the number of channels is added to the result. Therefore, the final calculation results in a data cube with four dimensions, namely the number of iterations N_{iters}, the number of pointing directions $N_{pointing}$, the number of time steps N_{time}, and the number of channels $N_{channel}$.

Although the original EPFD calculation as defined by the ITU uses telescope pointings in local coordinates (Alt, Az), this work considers pointings in celestial coordinates (Ra, Dec), because this allows to understand how celestial positions in different declinations can be impacted by satellite constellations transmissions.

4.1 Satellite Position Propagation

Using the Python package Cysgp4 [18] and the Astropy Coordinates package [14], the position of the satellites in horizontal coordinates (Alt, Az) and sky coordinates (Ra, Dec) are calculated for each timestep and each iteration (see Figure 5).

4.2 Satellite Power Flux Density (PFD)

The PFD from each satellite in a constellation is modeled based on publicly available information (ITU documents and FCC filings). To calculate the power flux density towards the telescope site, the coordinates of the telescope in the satellite reference frame are also calculated using the Python package cysgp4 [18].

OneWeb satellites are modeled based on the information available in the ECC report 271 [4], with eight channels in the range 10.7–12.75 GHz. A fixed beam antenna pattern, like the OneWeb system, makes it simpler to calculate the received power in a deterministic way.

The PFD from Starlink satellites is more complex to model since they have an antenna array that can produce, and electronically steer, several beams in one or multiple frequency channels. The mean PFD from a Starlink satellite is modeled as a function of the elevation of the satellite, obtained from a Monte-Carlo simulation in which the steering angle, the number of beams, and the position of satellite and observer were varied a large number of times. Starlink satellites are modeled as one frequency channel at a time.

4.3 Radio Telescope Antenna

The radio telescope antenna is modeled based on [10]. While this model is not a real measurement of the antenna pattern of a radio telescope, it is based on real measurements and is considered as a worst case for compatibility studies. To obtain the gain towards the satellite, the angle between the pointing direction and the position of the satellite is calculated.

The effective area of the antenna is calculated with the following equation:

$$A_{eff} = G_{RAS} * (\lambda^2/(4*\pi)) \quad (2)$$

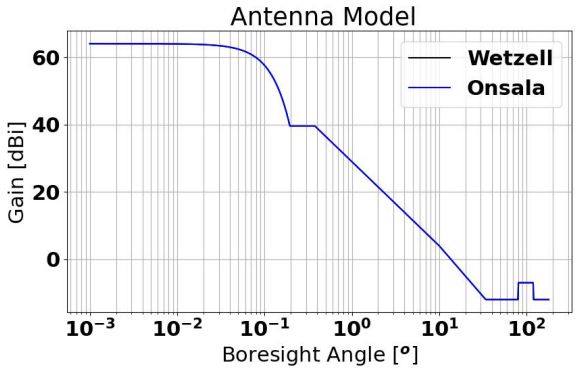

Fig. 4 Antenna pattern as defined in ITU-R RA.1631.

4.4 Correlation

Interferometry can greatly mitigate the effects of RFI, especially when the baselines are long like in the case of VLBI [16]. Although Thompson et al. have studied the effect that long baselines have over single (and stationary) RFI transmitters, the situation is not the same when potentially hundreds of transmitters using the same frequency and bandwidth are received simultaneously as can happen now.

For example in [7], Petrachenko identifies the 10.7–12.75 GHz range as a usable frequency range as only geostationary satellites were using that frequency at that time. Now the received RFI signal at an antenna will be the sum of the signals from all satellites above the horizon (of course, with different levels of attenuation). Such an analysis is deferred to a future update of this work.

4.5 Saturation Limit Threshold

Digital processing operations in a radio telescope can be applied as long as the analog and digital signal chains behave in a linear manner; strong enough signals will generate non-linearities corrupting the complete receiver band for the duration of the interference. Defining the level when a receiver goes non-linear is not a simple task and will depend on each particular receiver. In the case of the VGOS receivers a conservative value for total power of -50 dBm is considered to keep the analog signal chain within the linear regime.

If the received power is below this linearity threshold, the analog signal can then be correctly digitized with a bandwidth of 1 GHz. Two scenarios can be identified:

1. Digitizing a frequency range outside of 10.7–12.75 GHz. This should not have any complications since the signal chain behaves in a linear way. Therefore, this case will not be further studied.
2. Digitizing in a frequency range within 10.7–12.75 GHz. In this case it is interesting to understand when the RFI produces a significant amount of power compared to the RMS noise of the receiver.

Given the distinct characteristic of the VGOS system to use a 2-bit correlator, it is reasonable to consider that there is not much headroom in the digital signal chain to accommodate for RFI. This work considers that any signal above or equal to the receiver's noise power will result in a data loss. This defines the second threshold as a spectral power flux density equal to the RMS noise of a 20-K receiver system (-215 dBW/Hz).

These two thresholds are used in the simulation: a first set of flags is produced when the total integrated power (considering the eight channels of 250 MHz for each constellation) is higher than -50 dBm (representing a total data loss) and the second one representing a data loss in the case of observing in the same frequency range as the satellite transmissions.

After these two flagging stages, low level RFI will still be present. It is of interest to understand how this will affect the correlation of the baseline. This will be further studied in a future update of this work and compared to the thresholds defined in RA.769 [9].

4.6 Metrics

Based on the threshold limits defined in the previous section, the following metrics are used:

1. Full Band Data Loss (**FBDL**): percentage of time that the complete band is lost due to very strong RFI, where the total received power is > -50 dBm.
2. Digitizer Data Loss (**DDL**): percentage of the total observation time (single run multiplied by the number of iterations) that the instantaneous power spectral density is above 10% of the integrated noise power of the receiver. This can be calculated as a function of the declination of the source.
3. Average Equivalent Spectral Power Flux Density (**aESPFD**): average value of the equivalent Spectral Power Flux Density (eSPFD) during the observation time in each antenna. The eSPFD is calculated as the received spectral power flux density [W/m^2/Hz] divided by the maximum effective antenna area, and it is useful to compare to the SPFD (in units of Jy) of a celestial source in the main beam of the antenna.

5 Case Study Simulation

A specific study case was selected to understand the impact from several satellite constellations on two telescopes normally involved in VGOS observations. It is the intent to further expand this work into how correlation over the long baseline mitigates the RFI. The VGOS stations in Sweden (Onsala Space Observatory) and Germany (Geodetic Observatory Wettzell) were selected as the test stations using the parameters of Table 3 and the constellations Starlink phase 1, OneWeb phase 1, and Starlink phase 2 (Table 4). The simulated observations were run for 100 seconds in one-second timesteps with 100 iterations.

Table 3 VGOS station parameters used for the simulation.

Station	Wettzell	Onsala
Location (lon, lat) (deg)	(12.88, 49.14)	(11.92, 57.39)
Height (m)	600	20
Antenna Diameter (m)	13	13
Antenna Efficiency (%)	80	80
Receiver bandwidth (MHz)	1000	1000
System Temperature (K)	20	20
ITU-R RA.769 threshold (dBW/m^2/Hz)	−240	−240

Table 4 Parameters of satellite constellations used for the study [12, 13, 6].

Constellation	Altitude	Inclination	Number of planes	Satellites per plane
Starlink ph 1	550	53	72	22
	540	53.2	72	22
	570	70	36	20
	560	97.6	6	58
	560	97.6	4	43
OneWeb ph 1	1200	87.9	18	40
Starlink ph 2	340	53	48	110
	345	46	48	110
	350	38	48	110
	360	96.9	30	120
	525	53	28	120
	530	43	28	120
	535	33	28	120
	604	148	12	12
	614	115.7	18	18

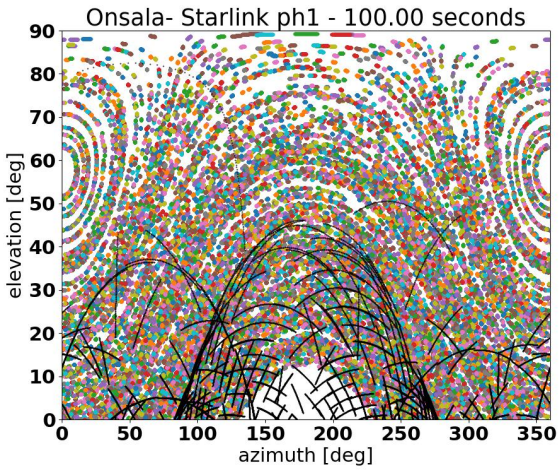

Fig. 5 Horizontal (Alt, Az) view of the pointing directions (in colors) and movement of the Starlink Phase 1 satellites (black) as seen from the Onsala Space Observatory for a time duration of 100 seconds.

Originally, we intended to use a real VGOS schedule, using the (Ra, Dec) values of the observed sources, but to get a more representative result of the impact as a function of source declination, the number of sources was increased artificially to 277 in a random fashion (see Figure 6 for a plot of the source distribution). Figure 5 shows the view of the local sky in (Alt, Az) and how the celestial sources and the satellite constellation (in this case Starlink Phase1) move across the sky in that timeframe.

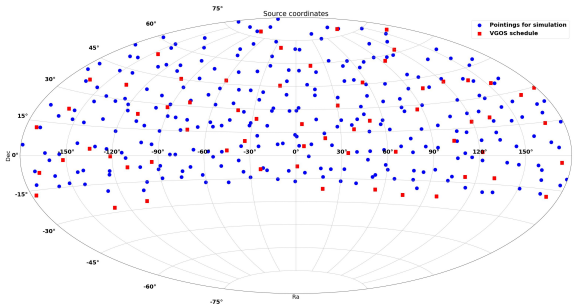

Fig. 6 VGOS schedule (2022Jan27) sources in red squares, selected telescopes pointings for the simulation in blue circles.

6 Results

The results for each one of the selected metrics are summarized here for each constellation simulated.

6.1 Full Band Data Loss (FBDL)

Notably, the analog saturation threshold was not reached due to the combination of maximum PFD from the satellites (−98 dBW/m^2 in 250 MHz) and maximum effective area of the VGOS antennas (106 m^2 or 20.3 dBm^2), as can be seen in Figure 7. This shows that even with large constellations such as Starlink phase 2 the analog receivers would still behave in a linear fashion.

6.2 Digital Data Loss (DDL)

When considering an observation coinciding in frequency with the downlinks of satellites (i.e., in within

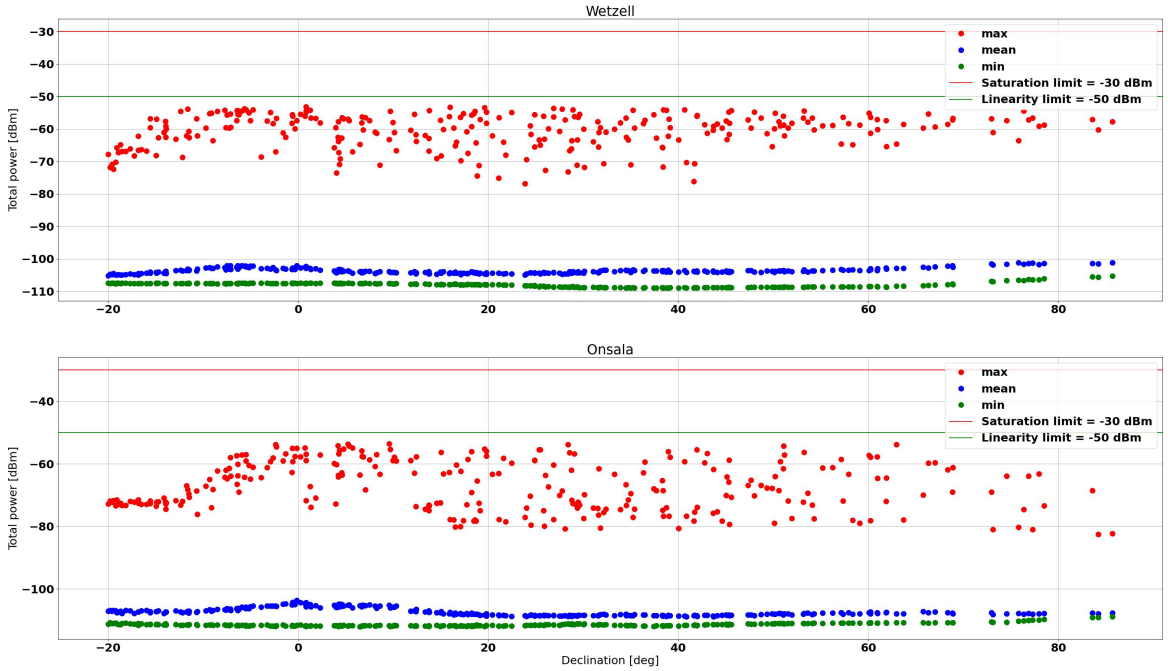

Fig. 7 Instantaneous power received by both VGOS antennas as a function of pointing declination with Starlink phase 2 constellation. The linearity threshold of −50 dBm was not reached in any situation.

the 10.7–12.75 GHz) the DDL varies as a function of declination of the observed source and observatory latitude. This effect is attributable to the different structures of each constellation's density of satellites around the Earth and the latitude of the observer. This shows that the impact on VGOS stations (and radio telescopes in general) strongly depends on the observatory latitude (Figure 8).

6.3 Average Equivalent Spectral Power Flux Density (aESPFD)

After a certain percentage of the observed data was lost as DDL (see Section 6.2), the aESPFD is calculated for each constellation as a function of declination. In this case the flagged percentage is calculated as the product of the flags from the previous section for each antenna.

Considering that the ITU-R RA.769 thresholds for harmful interference for VLBI are defined as -193 dBW/m^2/Hz, representing an ESPFD of 250 Jy for an antenna of 13 m in diameter, the results show that VGOS observations could in principle be conducted inside the satellite downlink bands considering the percentage of data lost (Figure 9).

7 Conclusions

This paper proposed metrics to evaluate the impact of large satellite constellations on VGOS operations by a simil-epfd simulation for Starlink ph1 and ph2, OneWeb ph1, and two European VGOS sites as receiving stations.

Through calculations and simulations it was proved that the maximum received power even in beam-to-beam coupling condition with satellites will not be enough to saturate the analog chain of a VGOS receiver. As for the digitized part, the simulations show that observations in the same band as the downlinks from satellites can have a significant percentage of data loss due to strong signals compared to the thermal noise of the receiver. Nevertheless, the results show that the ESPFD for both antennas and all constellations is lower than the threshold defined by ITU-R for VLBI. Observations outside of the satellite downlink

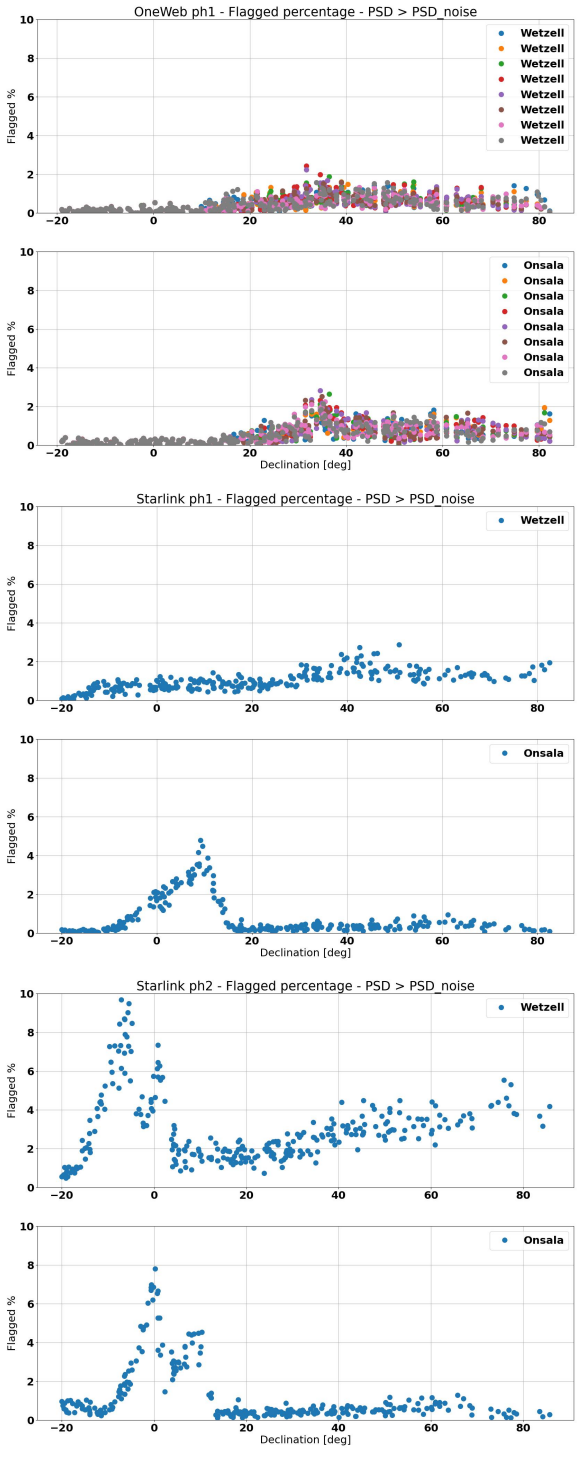

Fig. 8 Flagged percentage for each antenna and each constellation. A flag is raised when the power spectral density received is above the noise spectral density.

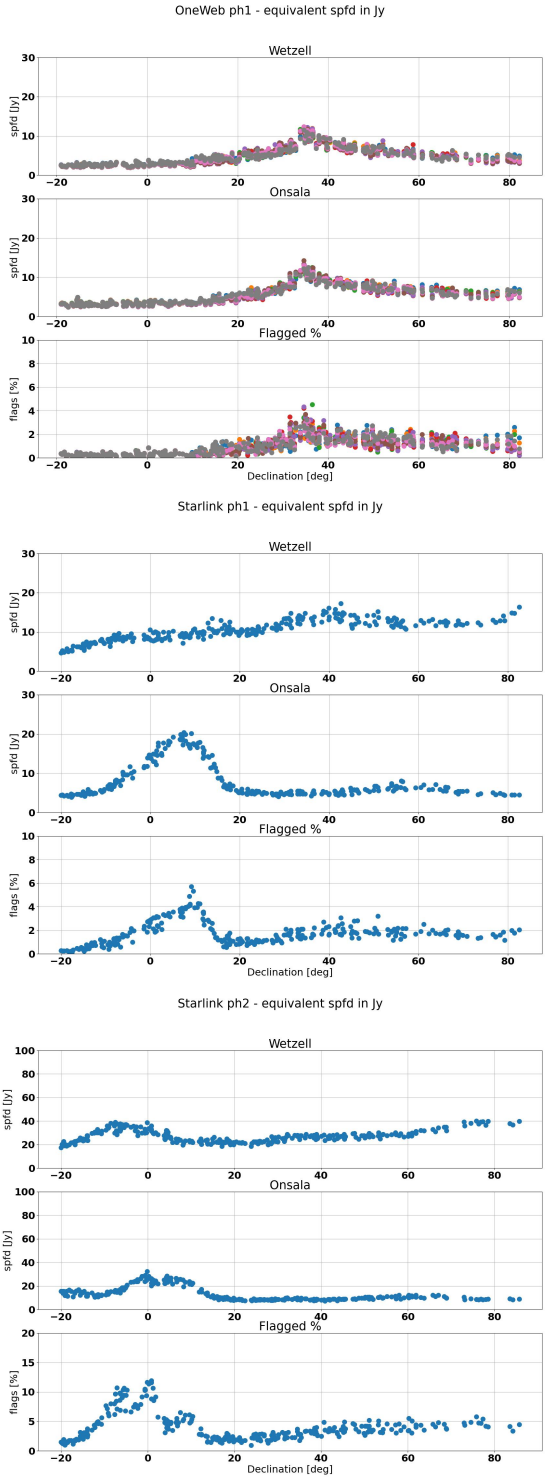

Fig. 9 Average Equivalent Spectral Power Flux Density (aESPFD) as a function of declination for each constellation.

bands should not be impacted by satellite downlinks in this frequency range.

As further work the authors will continue investigating how correlation can help mitigate the signals from satellite constellations and how the aggregation of all constellations scales the impact.

Acknowledgements

The authors would like to thank the IVS Coordinating Center at NASA Goddard Space Flight Center (GSFC) for taking the archive of IVS sessions. The schedule used in this work is available at the https://ivscc.gsfc.nasa.gov/sessions/2022/vo2027 web page. We are grateful to Salvo Buttaccio for the assistance with the VGOS schedule, to Dr. Benjamin Winkel for assistance with the use of the Cysgp4 Python package, and to Dr. Jose Antonio Lopez-Perez and Dr. Hayo Hase for useful discussions about VGOS receivers and operations.

References

1. W. A. Baan, 2011. “RFI mitigation in radio astronomy” RFI Mitigation Workshop 2010
2. J. Cohen, Iridium and Radio Astronomy in Europe Spectrum Management for Radio Astronomy: proceedings of the IUCAF summer school held at Green Bank, West Virginia, June 9–14, 2002.
3. Cooper, B.F.C., 1970. “Correlators with two-bit quantization”. Australian Journal of Physics, 23, pp. 521–527.
4. ECC Report 271, “Compatibility and sharing studies related to NGSO satellite systems operating in the FSS bands 10.7–12.75 GHz (space-to-Earth) and 14–14.5 GHz (Earth-to-space)”, European Communications Office, 2021.
5. A. Lawrence et al., 2022. “The case for space environmentalism”, Nature Astronomy, Vol. 6, pp. 428–435.
6. OneWeb phase 1 FCC filing, https://fcc.report/IBFS/SAT-MPL-20200526-00062/2379565
7. B. Petrachenko, “The Impact of Radio Frequency Interference (RFI) on VLBI2010”, IVS 2010 General Meeting Proceedings, pp. 434–438.
8. B. Petrachenko et al. 2010. “Final Report of the Observing Strategies Sub group of the IVS Working Group 3”, https://ivscc.gsfc.nasa.gov/about/wg/wg3/1_observing_strategies.pdf
9. Recommendation ITU-R RA.769 “Protection criteria used for radio astronomical measurements”
10. Recommendation ITU-R RA.1631 “Reference radio astronomy antenna pattern to be used for compatibility analyses between non-GSO systems and radio astronomy service stations based on the epfd concept”
11. Recommendation ITU-R S.1586 “Calculation of unwanted emission levels produced by a non-geostationary fixed-satellite service system at radio astronomy sites”
12. Starlink phase 1 FCC filing, https://fcc.report/IBFS/SAT-MOD-20200417-00037/2274316
13. Starlink phase 2 FCC filing, https://fcc.report/IBFS/SAT-AMD-20210818-00105
14. The Astropy Collaboration et al., “Astropy: A community Python package for astronomy”, A&A Volume 558, October 2013.
15. The Astropy Collaboration et al.,“The Astropy Project: Building an inclusive, open-science project and status of the v2.0 core package”, https://arxiv.org/abs/1801.02634
16. Thompson, 1982. “The Response of a Radio-Astronomy Synthesis Array to Interfering Signals”, IEEE Transactions on Antennas and Propagation, Vol. AP-30, No. 3, May 1982.
17. J. G. Walker, Satellite constellations, Journal of the British Interplanetary Society, Vol. 37, pp. 559–571, 1984.
18. B. Winkel, “A wrapper around the SGP4 package, for sat TLE calculations”, https://github.com/bwinkel/cysgp4

Status of the VGOS Infrastructure Rollout

Dirk Behrend[1], Chet Ruszczyk[2], Pedro Elosegui[2], Stuart Weston[3]

Abstract The legacy S/X system has been the production system of the IVS since the inception of the service. However, in 2020, after many years of development, the VGOS system was declared operational, and the fledgling VGOS network (of eight to ten stations) started contributing with operational sessions to the determination of IVS products. The VGOS observing program was expanded in 2021, and it is anticipated to grow further in 2022. In order to extend the observing program, aside from the growing observing network, other infrastructure components of the VLBI processing chain have been further developed. This includes the VGOS correlation and post-processing capabilities as well as VGOS data analysis. We provide a status overview of the infrastructure realization efforts of the VGOS station network and the correlation centers. Further, we outline the VGOS observing plan for 2022.

Keywords VGOS, infrastructure, correlator

1 Introduction

The member organizations of the International VLBI Service for Geodesy and Astrometry (IVS) operate an observational network of VLBI telescopes that currently consists of about 40 stations worldwide. This S/X VLBI network was developed mainly in the 1970s and 1980s. Due to the aging infrastructure but also because of demanding new scientific requirements, the larger IVS community planned and started to roll out the next-generation VLBI system called VGOS (VLBI Global Observing System) at existing and new sites over the last several years.

In 2020, these efforts culuminated in the VGOS system being declared operational. A fledgling network

Table 1 Individual VGOS station projects with recent milestones and projected broadband readiness.

Station	Recent milestone	Broadband
GGAO	VGOS-O, VGOS-R&D	ready
Westford	VGOS-O, VGOS-R&D	ready
Wettzell (Ws)	VGOS-O, VGOS-R&D	ready
Yebes (Yj)	VGOS-O, VGOS-R&D	ready
Ishioka	VGOS-O, VGOS-R&D	ready
Kokee Park (K2)	VGOS-O, VGOS-R&D	ready
Onsala (Oe, Ow)	VGOS-O, VGOS-R&D	ready
McDonald	VGOS-O, VGOS-R&D	ready
Hobart	VGOS-O tagalong	imminent
Sheshan	VGOS-O tagalong	imminent
Santa Maria	S/X observing	mid-2022
Katherine	S/X observing	mid-2022
Yarragadee	S/X observing	end 2022
Ny-Ålesund (Nn)	signal chain work	mid-2022
Ny-Ålesund (Ns)	S/X observing	2022
HartRAO	signal chain work	2022
Metsähovi	signal chain work	2022
Gran Canaria	RT in warehouse, civil works	2023
Urumqi	S/X observing	2023
Chiang Mai	site selected	2024
Fortaleza	site selected	2024
Matera	contract bid	2024
Badary	fixed broadband system	[S/X/Ka]
Zelenchukskaya	fixed broadband system	[S/X/Ka]
Svetloe	fixed broadband system	[S/X/Ka]
Tahiti	site selected, RFI survey	2025
Flores	RFI surveys	2025
Songkhla	site selected	2025
Kanpur	proposal	2025

[1]NVI, Inc./NASA Goddard Space Flight Center
[2]MIT Haystack Observatory
[3]Auckland University of Technology

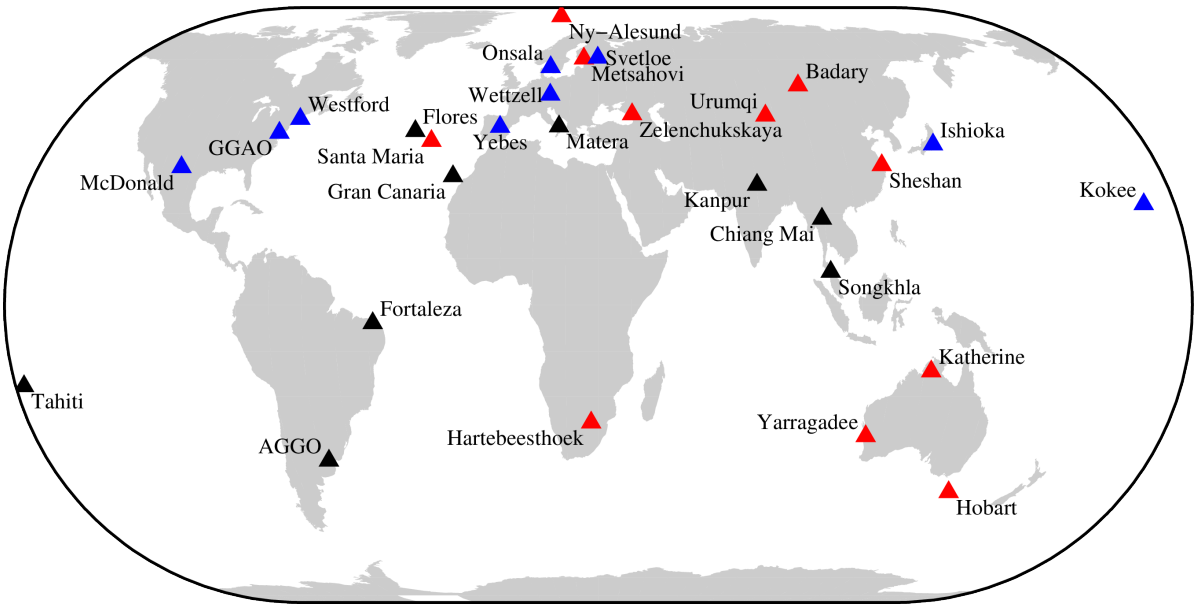

Fig. 1 Geographic distribution of the operational VGOS antennas (▲), built antennas with signal chain work in progress (▲), and VGOS projects in the planning stage (▲).

of up to eight to ten VGOS stations became part of the IVS observing program and, since then, has been contributing to the generation of IVS products. The nascent VGOS observing program has been expanded over the last two years. Prerequisites for this expansion, aside from the growing observing network, have been the further development of the VGOS correlation and post-processing capabilities as well as the VGOS data analysis, among other things. In the following, we summarize which VGOS station network is currently observing, which stations will be added soon, and which stations may be expected on a longer time horizon. In addition to the station infrastructure, we describe the network of operational VGOS correlators and its potential expansion. Finally, we describe the VGOS observing plan that the station and correlator resources in conjunction with data transport and storage capacities/limitations allow us to do in the observing year 2022.

2 Evolution of the VGOS Station Network

The network of VGOS stations currently observing in operational sessions consists of northern hemisphere sites only (Figure 1). This is anticipated to change in the course of 2022 when the three Australian AuScope telescopes will successively be converted to the VGOS signal chain. First among them, the Hobart antenna is on the cusp of being used operationally. In South Africa, the new antenna at Hartebeesthoek is expected to be integrated in the second half of 2022.

The further evolution of the VGOS station network is depicted in the global distribution map (Figure 1). Recent milestones and the state of the individual VGOS projects are listed in Table 1.

Beyond the projects listed, there are also efforts underway in other parts of the world. This includes undertakings in India, Malaysia, and Indonesia. Please do let the authors know of any other projects that may be in the discussion stage.

3 VGOS Correlation Capabilities

Over the past few years, correlation has advanced from developing VGOS capabilities to operational state and has recently evolved from a single correlator to a network of globally distributed correlators that can process VGOS sessions operationally (Figure 2). Currently, the turnaround time for 24-hour VGOS sessions is one to two months and is improving

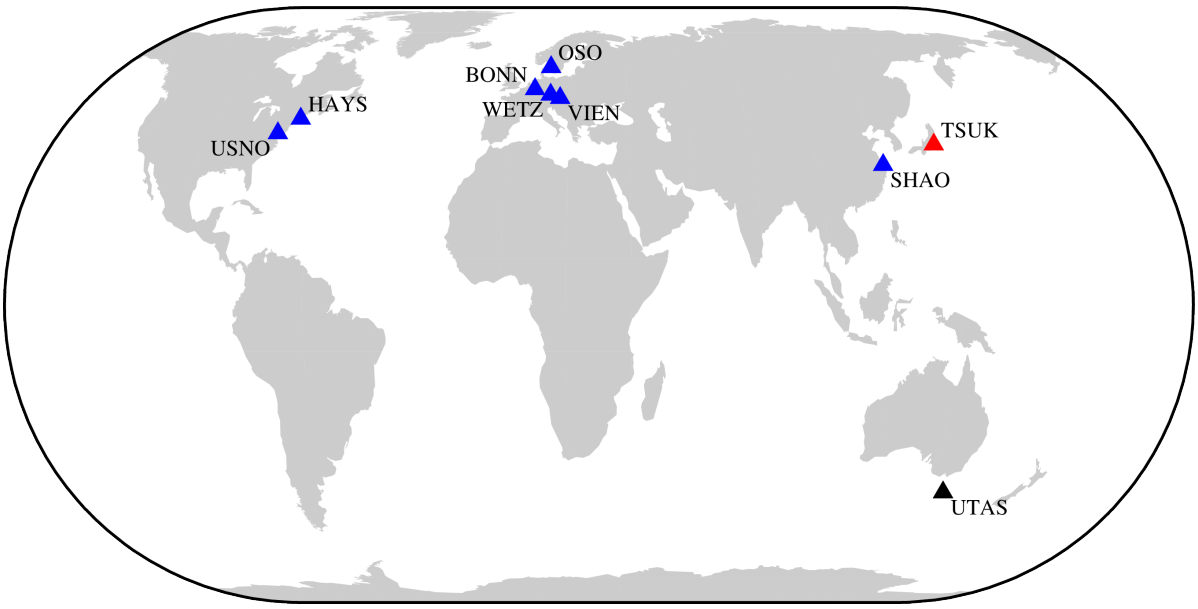

Fig. 2 Geographic distribution of the operational VGOS correlators (▲), correlators under verification (▲), and future correlation centers (▲).

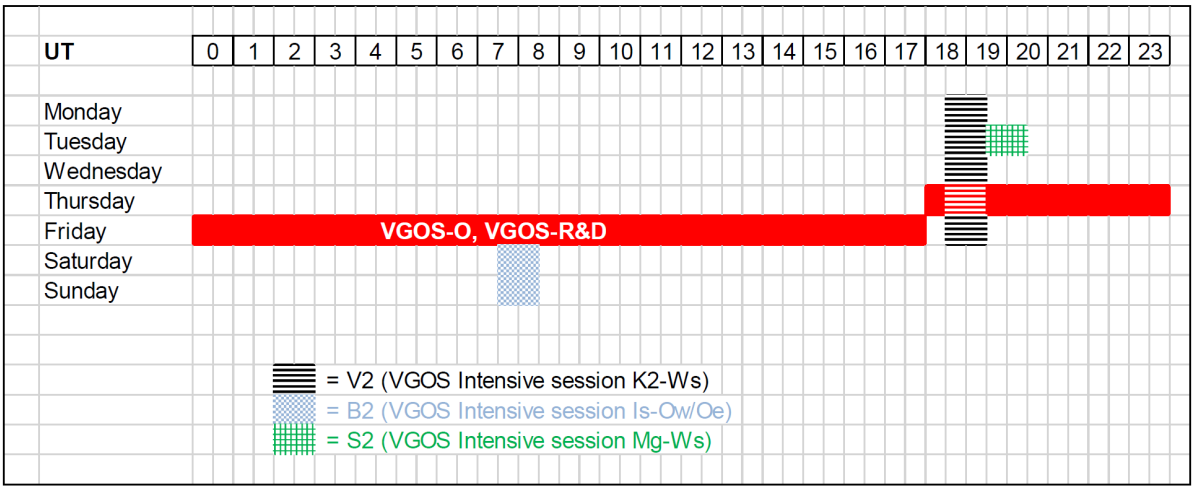

Fig. 3 Overview of the weekly VGOS observing plan for 2022.

as new Correlation Centers gain experience and as data transfer connections from stations to correlators increase capacity.

Other considerations include the need at correlator centers to match the storage capacity for the electronically transferred data of the entire observing network. A subset of the correlators can handle physically shipped Mark-6 modules, while some only support e-transfers. This entails that some data transports need an intermediary.

4 VGOS Observing Plan in 2022

The amount of VGOS observing in 2022 is governed by data transfer and storage limitations as well as correlation limits. The core observing program consists of one 24-hour session and five VGOS Intensives (V2) per week (Figure 3). There are six VGOS-R&D experiments (VR) planned with a cadence of two months replacing the regular VGOS-O sessions (VO).

In addition to the V2, there are two other Intensive series in the planning: B2 on the baseline Is-Ow/Oe (Ishioka–Onsala) to be processed at OSO/TSUK (Onsala/Tsukuba); and S2 on the baseline Mg-Ws (McDonald–Wettzell) to be processed at WETZ (Wettzell). Each VGOS-R&D session (VR) is paired with a one-hour VGOS Test session (VT) to prepare the subsequent R&D session. The VR/VT session pairs are run every other month with increasingly aggressive strategies to test the limits of VGOS (e.g., lower scan lengths in steps down to 3–8 s, reduced accumulation period (AP) times at the correlator from 1 to 0.25 s). Also, an improved frequency sequence that matches protected Radio Astronomy Service (RAS) frequencies of the International Telecommunication Union (ITU) will be employed (RAS matching). The pairing of the VR/VT may require the prioritization of the processing order and correlation time frame.

In short, there are well over 300 VGOS observing sessions planned for 2022, of which about 50 and 265 will be 24-hour and one-hour sessions, respectively.

5 Conclusions and Outlook

The rollout of the VGOS infrastructure is advancing steadily. Indeed, the VGOS network is expected to almost double from its fledgling state of nine northern hemisphere sites to up to sixteen global sites by the end of 2022. Importantly, several of those new sites are located in the southern hemisphere. The number of correlators capable of processing VGOS data has grown to seven centers—a most remarkable increase compared to only one a few years back.

The number of VGOS observing sessions planned for 2022 thrives relative to past years. However, data transport and storage as well as correlator time are the main resources that limit the current program. It is expected that processing efficiencies at the correlators will be improved over time resulting in an increased cadence of observing sessions. Nonetheless, this has to go hand in hand with enhancements of storage capacity and data transfer rates.

There is still work to be done to be able to transition from the legacy S/X system to the VGOS system as the production workhorse of the IVS. Having two systems in parallel, of course, also means that they compete for resources. It is however essential that the nascent VGOS time series are rigorously integrated with the existing S/X time series so that the long-lasting S/X series can be carried forward by VGOS without real lapse. The tie of the S/X and VGOS systems can be accomplished by mixed-mode sessions as well as local tie sessions at sites with co-located legacy S/X and VGOS stations.

Status at Ny-Ålesund Geodetic Earth Observatory

S. Garcia-Espada[1], R. Bolaño González[1], A. Meldahl[1], T. Gansmoe[1], S.A. Grøslie Wennesland[1], L.M. Tangen[2], A.-S. Kirkvik[2], G. Grinde[2], R. Kleiven[2], H.C. Munthe Kaas[2], P.E. Opseth[2]

Abstract We present the current status of the Ny-Ålesund Geodetic Earth Observatory. Special focus is placed on the status and future of the VGOS twin telescopes (Ns and Nn) and the legacy 20-meter antenna (Ny).

Keywords Network, stations, VGOS, Ny-Ålesund

1 Introduction

The Geodetic Observatory of the Norwegian Mapping Authority (NMA) is situated at 78.9° N and 11.9° E in Ny-Ålesund, Kings Fjord, on the west side of the island of Spitsbergen. This is the biggest island in the Svalbard archipelago. The Geodetic Observatory features a 20-meter legacy VLBI radio telescope at the Rabben site (see Figure 1), as well as fast-slewing VGOS (VLBI Global Observing System) twin telescopes at the new facility at Brandal (see Figure 2).

In addition to the 20-m VLBI telescope and the 13-m twin telescopes, the geodetic observatory has two GNSS receivers in the IGS system and a Super Conducting Gravimeter which is part of the International Geodynamics and Earth Tide Service. A second SCG is installed at the Brandal site, approximately 1.5 km away. A solar radio burst monitor is set up at Rabben, and a tide gauge is in operation at the harbor.

The observatory also hosts an accelerograph from the Instituto Geográfico Nacional in Spain and a GISTM (GPS Ionospheric Scintillation and TEC Monitor) receiver which is operated in the frame of ISACCO, an Italian research project on ionospheric scintillation observations, led by the Italian Institute of Volcanology and Geophysics (INGV). Another Real-Time Ionospheric Scintillation (RTIS) Monitor was set up and has been operated by the NMA since November 2012. A DORIS station is located approx-

Fig. 1 The geodetic observatory's Rabben site with the Ny 20-m telescope.

Fig. 2 The geodetic observatory's Brandal site with 13-m twin telescopes (Image: Bjorn-Owe Holmberg).

1. Kartverket, Ny-Ålesund Geodetic Earth Observatory
2. Kartverket, Hønefoss

imately 350 m from the new geodetic observatory at Brandal and is hosted by the French-German AWIPEV research base.

2 Legacy 20-m VLBI Telescope (Ny)

During the planning works of the new geodetic observatory at the Brandal site, it was agreed together with the airport authorities that due to safety reasons the 20-m radio-telescope (Ny) would be dismantled after a few years of parallel observations between the 20 m and the antennas at the new site in Brandal. The 20-m radio-telescope is close to the airport facilities in Ny-Ålesund and just a few meters from the runway, making landing and take off more challenging in bad weather conditions.

The 20-m antenna began operations in 1994, and it has operated regularly since then. After almost 30 years of operations, the maintenance of the antenna structure is a challenge in the harsh Arctic environment. It is difficult to find spare parts for both the mechanical structure and the S/X receiver. There are also economical reasons, including the budget to run this antenna plus two additional antennas; this triplicates the consumption of electricity, as well as the maintenance and human power needed.

The initial plan was to start the dismantling of the 20-m antenna during autumn 2022, but to make sure that there are enough parallel operations between the Rabben and Brandal sites, it was decided to extend the observing period and delay the dismantling until summer 2023 or whenever a big economical investment would be needed to keep the operations running.

Fig. 3 The 20-m VLBI telescope will be dismantled during summer 2023.

3 Legacy South (Ns) at the New Observatory at Brandal

The south antenna (Ns) at the Brandal site has an installed tri-band S/X/Ka receiver using the S/X bands for observations in the legacy network. Ns has been observing weekly in the IVS network as a regular station since November 2021. It is currently using a DBBC2 backend. An update of its flexbuff was done at the end of 2021. The CDMS (Cable Delay Measurement System) will be installed in the coming weeks.

When the legacy observations are finished, the Ns antenna's VGOS receiver will be upgraded at Yebes Observatory during 2023. The upgrade will consist of changing the LNAs from single-ended to a balanced configuration, resulting in a lower average receiver temperature and lower ripple across the frequency band. A DBBC3 is ready to be installed for when the Ns VGOS observing starts.

4 Parallel Operations of Ny-Ns

As mentioned above, the reason for Ns observing within the legacy S/X network is contributing to the parallel observations with the 20-m antenna before it is dismantled. It is important to have a long enough overlapping time series between the old 20-m antenna and the new antennas at Brandal in order to have a continuation of the Ny times series down at the new site with the Ns and Nn antennas. The Ns antenna was included in the legacy network to link the inter-comparison. Ny and Ns are observing the same sessions in the IVS legacy network (from 2–5 times per week). To run parallel observations with Ns and Ny is a challenge mainly due to the Ny faults. At the end of 2020 there was an elevation encoder fault that lasted four months until the encoder was repaired, and during 2022 the 20-m antenna's maser had a fault that lasted for over a month (see Figure 5).

It is planned that Ny and Ns are observing the NYTIE project (local VLBI sessions) in between official IVS sessions. The idea is to densify the parallel observation time series as much as possible and also to gain experience and learn to perform local VLBI tie sessions. We would like to thank E. Varenius from Onsala Observatory for his big support.

Ns and Ny are also participating in the VSBI (Very Short Baseline Interferometry) project by L. Petrov from NASA to whom we are grateful for his analysis performed so far.

After the parallel observations are finished with the dismantling of the 20-m antenna, it will be decided if the Ns antenna should continue observing a bit longer period in the legacy network or if it should join the VGOS network together with the Nn antenna and others.

Fig. 4 The distance between the Ny and Ns antennas is about 1.5 km.

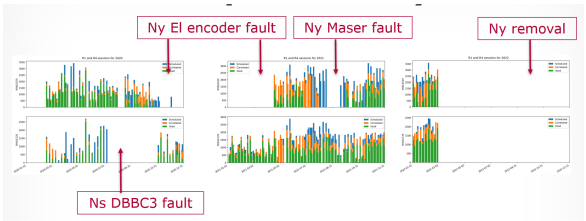

Fig. 5 Sessions observed by the Ny and Ns antennas, to show the periods of parallel observations.

5 VGOS North (Nn) at the New Observatory at Brandal

The new updated VGOS broadband receiver was installed in the north antenna (Nn) at the Brandal site in November 2021. The update in the receiver consisted of the installation of balanced LNAs instead of a single-ended one as mentioned before for the Ns VGOS receiver. The upgrade was performed at Yebes Observatory at the end of September 2021. The Ns VGOS broadband receiver will be sent to Yebes Observatory, and the same upgrade will be performed during 2023, so both VGOS broadband receivers will be equal.

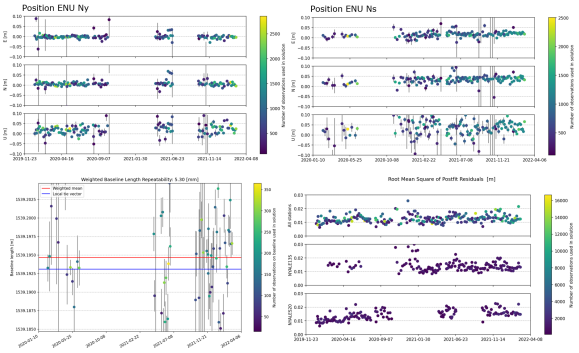

Fig. 6 Time series ENU positions for the Ny and Ns antennas. Weighted Baseline Length Repeatability and Root Mean Square of Postfit Residuals as analyzed by A.-S. Kirkvik using the *where* software.

The first fringe test was performed in summer 2022, and results are still to be analyzed at the production of these proceedings.

The aim is to join the IVS VGOS observation schedule by the end of summer 2022. The Nn antenna will join the network of the European EU-VGOS project.

Fig. 7 The Brandal site observatory as seen from the north. The Nn antenna is in the front.

6 RFI Measurement Campaign

Ny-Ålesund and the area 20 km around town is a radio silence area by Norwegian Parliament law (from 1994) to protect the VLBI antenna at the Geodetic Ob-

servatory at the Rabben site, and now it will protect the spectrum from 2–32 GHz for the VLBI antennas at the Geodetic Observatory at the Brandal site.

The use of WiFi and Bluetooth is not allowed in Ny-Ålesund and 20 km around. We have noticed RFI coming from WiFi in town, and during the summer season some tourist cruises use WiFi on board when staying in Ny-Ålesund. We are working on informing and making awareness for tourist cruises and permanent inhabitants in Ny-Ålesund to follow the protection rules. Reporting and advising about radio silence in Ny-Ålesund is a big challenge, as the number of tourist cruises has increased significantly.

7 Satellite Laser Ranging

The SLR installation is an ongoing project. The installation of the dome was delayed due to COVID travelling restrictions from EEUU in 2021. It was finally installed 1 April 2022. The installation of the gimbal telescope assembly is planned for the end of 2022. Laser installation is planned for 2024, and it will be fully operational by 2025.

Fig. 8 The SLR dome was installed in April 2022. The view from the control room. (Image: Bjorn-Owe Holmberg)

8 Other Monitoring Activities: Local Tie, Gravimeters, and GNSS

Local tie measurements are performed yearly using the local GNSS network at Brandal. The next local tie measurement is planned for the end of summer 2022.

Fig. 9 The SC Gravimeter at the gravimeter building at the Brandal site.

Fig. 10 GNSS antennas.

Russian New Generation VLBI Network

Dmitry Ivanov, Alexander Ipatov, Dmitry Marshalov, Gennadiy Ilin, Iskander Gayazov, Evgeny Khvostov, Andrey Mikhailov, Sergey Kurdubov, Sergey Serzhanov, Ilia Bezrukov, Viktor Stempkovsky, Alexander Vytnov, Igor Surkis, Valery Olifirov, Andrey Dyakov, Ismail Rahimov

Abstract In 2012, the new generation VLBI system VGOS project was launched in Russia. At the end of 2015 the two-element interferometer with 13.2–m multi-fast rotating antennas (RT-13) was completed at the Badary and Zelenchukskaya observatories. In 2020, the new generation VLBI network was replenished with the third antenna at the Svetloe observatory. Since then, observations are regularly carried out with the VLBI network in three band S, X and Ka mode. The radio telescopes have identical equipment, except for the installed multifunctional digital backend system at the RT-13 in Svetloe. Additionally, the RT-13 is equipped with the ultra-wideband receiver to provide compatibility with international VGOS observations. This paper presents the current state and the first results obtained with the VLBI network. The nearest prospects for the expansion of the network to the East will also be considered, taking into account the start of construction of a new co-location station.

Keywords VGOS, Quasar VLBI network

1 Intoduction

In 2010, the concept of the next generation VLBI Global Observing System (VGOS) network was finally formed [1]. The Institute of Applied Astronomy of the Russian Academy of Sciences (IAA RAS) started work on the VGOS radio telescopes in 2012. The radio telescopes are designed for routine 24/7 determination of Universal Time corrections UT1-UTC with highest accuracy. The first two new generation VGOS radio telescopes (RT-13) at Badary and Zelenchukskaya observatories were commissioned in 2015 and since then perform regular geodetic observations up to five sessions every day [2]. After the Svetloe radio telescope was commissioned in 2020 [3], regular observations began with the Russian new generation VLBI network (see Figure 1).

In 2021, we started the design of a co-located station in Ussuriysk, and upon completion of the project we will have a VLBI network with a baseline of about 6,500 km.

This became possible by our development of unique equipment for the new generation VLBI network. We have developed VGOS software correlator RASFX [4], tri-band and ultra-wideband receivers [5, 6, 7], digital backend systems [8, 9], and a data transferring and recording system [10]. Next, we will consider the key elements and technologies that made it possible to create and put into operation a new generation network.

2 RASFX GPU-based Software Correlator

The development of the RASFX correlator began in 2012. It was designed to be run on GPUs in high performance computing cluster under GNU/Linux. RASFX can process data of up to six VGOS-compatible stations in quasi-real time mode with the maximum input data rate of 96 Gb/s at the correlator input. RASFX is designed as based on all the requirements of VGOS-compatible broadband data processing, which also include the ability to process

Institute of Applied Astronomy RAS

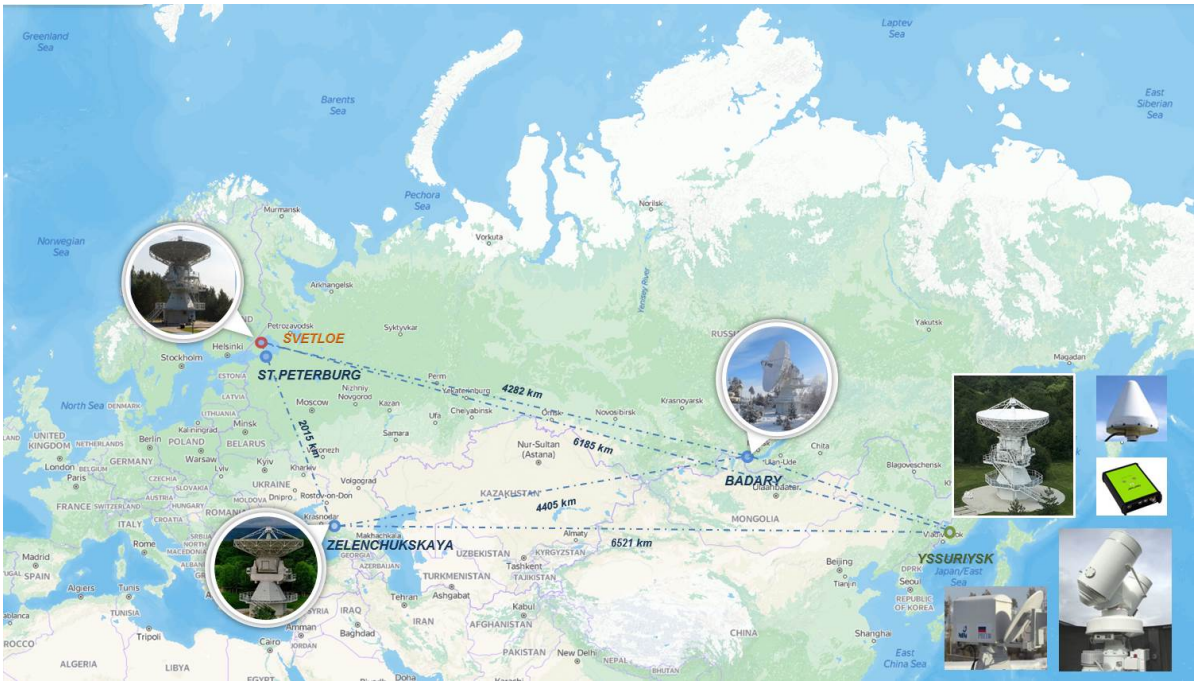

Fig. 1 Russian New Generation VLBI Network.

data recorded in circular and linear polarizations and to calculate high-resolution spectra.

The correlator hardware is a hybrid blade server cluster of the T-Platforms Corporation. It includes V200F blade servers, Intel R2216GZ4GCLX servers, network equipment, a high-speed RAID array, control and process synchronization systems, a power supply, and cooling systems. Each blade and Intel server is equipped with two Intel E5-2670 processors, two NVIDIA Tesla K20 GPUs, and InfiniBand network ports. The parallel LINPACK benchmark ranked the performance of the RASFX cluster as 85.34 Tflops.

Since 2016, RASFX has processed about 10,000 VLBI sessions.

Fig. 2 RASFX GPU-based software correlator.

3 Fast VGOS Radio Telescopes

The Russian new generation VLBI network consists of fast-rotating antennas manufactured by Vertex Antennentechnik GmbH. The antennas are built according to the Cassegrain scheme and have an alt-azimuth mount and a main reflector with a diameter of 13.2 m (see Figure 3). The hexapod is used for precise positioning of the 1.48 m counterreflector. An irradiation scheme with an ring focus was used. The antenna has velocities up to six degrees per second for elevation and up to 12 degrees per second for azimuth. The surface quality of the main mirror and counterreflector with a reserve provides performance to specification (see Table 1). The antennas are adapted for harsh climatic conditions. The temperature in the focal cabin is maintained within a few degrees. The receiving and processing equipment is located in the focal cabin of the radio telescope.

3.1 Receivers

The RT-13 radio telescope is equipped with a tri-band highly sensitive receiver capable of operating simul-

Fig. 3 VGOS antenna of the Svetloe Observatory.

Table 1 Specifications of the Fast VGOS Antenna

Mount	alt-azimuth
Configuration	Cassegrain
Subreflector scheme	ringfocus
Main mirror diameter	13.2 m
Subreflector diameter	1.48 m
Focal length	3.7 m
Azimuth speed	12°/sec
Elevation speed	6°/sec
Limits by Az	±245°
Limits by El	6°–109°
Operation	24 h / 7 d
Tracking accuracy	±15 arcsec
Surface accuracy (RMS)	< 0.15 mm
Frequency range	2–40 GHz
The surface efficiency	> 0.7
Polarization	LCP + RCP

taneously in two circular polarizations in the S/X/Ka bands. All input stages of the receiver including the feed and low-noise amplifier are cooled. Such design makes it possible to achieve high sensitivity in three frequency bands: S (2.2–2.6 GHz), X (7.0–9.5 GHz), and Ka (28–34 GHz) in both circular polarizations simultaneously [5].

The tri-band receiver has a dewar that has cooled combined S, X, and Ka feed horns and low-noise amplifiers. Double frequency conversion is used for the X- and Ka-bands. Single frequency conversion is used for the S-band. The frequency converters are placed in thermostatically controlled units, which are attached to the supporting structure frame. The total system noise temperature with the tri-band receiver is about 35 K in the S frequency band, 30 K in the X-band, and 75 K in the Ka-band. This corresponds to system equivalent flux densities of 1,000, 750, and 2,000 Jansky for the S-, X-, and Ka-bands.

The next step was the development of an ultra-wideband receiver compatible with the VGOS specification. The receiver operating frequency range is 3–16 GHz [6]. The signals are received in two linear polarizations. The design of the receiver is similar, but in this case a wideband quadruple-ridge flared horn is placed in the dewar together with low-noise amplifiers. Four dual channel frequency converters are used in the receiver. The bandwidth of each channel is 1 GHz. The total system noise temperature with the ultra-wideband receiver is about 35 K at most of the band and increases up to 50 K at the band edges.

3.2 Digital Backends

Digital backend systems were specially developed for recording signals in the frequency range over 500 MHz. The eight channel BRoadband Acquisition System was created for the two-element interferometer [8]. The system is plugged into the output of the receiving system and works with intermediate frequency signals from 1 to 1.5 GHz. Each channel of the system utilizes 512 MHz bandwidth and generates a digital data stream in the VDIF format. For two-bit data, the total data rate from the system is 16 Gb/s.

The next step was the development of the multifunctional digital backend system (MDBE), which was completed in 2020 [9]. MDBE has fully VGOS-compatible digital backends. The system is technologically more advanced. The input bandwidth is up to 2 GHz, and the sampling frequency is 4,096 MHz. The system is easy to reconfigure and supports different VLBI operating modes:

- broadband with 512 and 1,024 MHz bands,

- tunable digital converters – with 32, 16 MHz bands,
- old systems with narrow bands 8, 4 , 2 and 1 MHz.

There is a wide range of possibilities for adding new modes of operation.

3.3 Data Transferring and Recording System

We have developed the data transferring and recording system (DTRS) based on commercially available components and technology [10]. The DTRS hardware platform is made on the Dell PowerEdge R720/R740 servers with two Intel Xeon processors E5-2660v2 and SuperMicro disk chassis. Each server has four two-port Intel X520 network cards installed. Thus the DTRS has ten 10 Gb Ethernet network interfaces, eight of which are used to capture data from the digital backend and two of which are utilized to transfer data to the correlator at the processing center. It allows us to simultaneously record up to eight streams of 2 Gb/s data and transfer them for processing.

To process a high-speed packet stream on a 10 Gb/s Ethernet interface, PTC-CAPREC software uses the net API of the FreeBSD OS kernel. The netmap framework takes advantage of modern ethernet controllers directly, bypassing the OS network stack based on a classic memory buffer. The database runs under the FreeBSD operating system (Version 11); the ZFS file system is used to write data. The storage capacity of the DTRS at each station is about 200 Tbytes.

4 UT1 Results

Since the end of 2015, observations to determine UT1 have been regularly carried out up to five times per day. For such observations Tri-band receivers are used in dual band mode; these are the S- and X-bands. Figure 4 shows the UT1 obtained by the Russian VLBI network in comparison with the IERS finals series. It follows from the figure that with the addition of the third radio telescope (early 2019) errors of UT1 determination have decreased. The RMS for the series in the interval from 2015 to the end of 2021 varies from 18 μs up to 38.5 μs.

A comparison of our results with the VGOS-Intensive and IVS-Intensive series relative to the IERS finals series for 2021 is shown in Figure 5. The resulting RMS of 25.9 μs for our series is the same as for the VGOS-Intensive series. The difference in bias is 10 μs.

5 Future Plans

We have begun expanding our VLBI network to the East. Now we are developing a co-located station on the basis of the Ussuriysk Astrophysical Observatory. This observatory became part of IAA RAS in 2018. The Ussuriysk Observatory was founded in 1953 as a Solar Service. At present, there are several optical telescopes and some engineering infrastructure. In addition, the observatory has staff ready to learn and develop new techniques and insruments.

We hope that in the near future the station will acquire new space geodesy instruments.

6 Conclusions

The new generation VLBI network has been created in Russia. Since 2020, Russia's next generation three-element VLBI network has been in regular operation. A unique equipment for radio telescopes has been developed. The results obtained are in good agreement with international data. The errors of determining the UT1 are at the same level as the VGOS Intensive. In 2021, work began on the design of the co-location station in Ussuriysk. There is every reason to believe that in the near future the Russian VLBI network will include a new modern co-location station equipped with the latest means of space geodesy.

References

1. Petrachenko, B., Niell, A., Behrend, D., Corey, B., Böhm, J., Charlot, P., Collioud, A., Gipson, J., Haas, R., Hobiger, T., Koyama, Y., MacMillan, D., Malkin, Z., Nilsson, T., Pany, A., Tuccari, G., Whitney, A., Wresnik, J. "Design Aspects of the VLBI2010 System: Progress Report of the

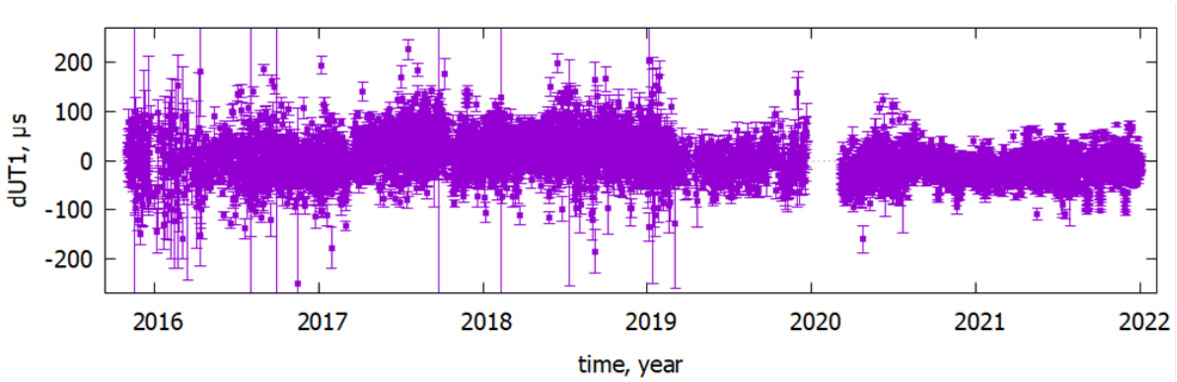

Fig. 4 Comparison of the UT1-UTC "R"-series vs. the IERS finals series.

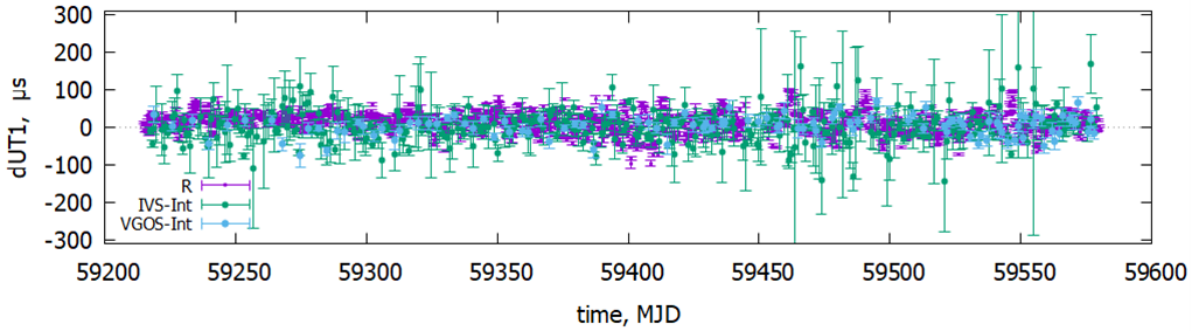

Fig. 5 Comparison of the UT1-UTC "R"-series vs. the IVS-Intensives and the VGOS-Intensives.

IVS VLBI2010 Committee", NASA/TM-2009-214180, 58 pp, 2009.

2. A. Ipatov, D. Ivanov, G. Ilin, S. Smolentsev, I. Gayazov, V. Mardyshkin, L. Fedotov, V. Stempkovski, A. Vytnov, A. Salnikov, I. Surkis, A. Mikhailov, D. Marshalov, I. Bezrukov, A. Melnikov, V. Ken, S. Kurdubov, New Generation VLBI: Intraday UT1 Estimations. *IVS 2016 General Meeting Proceedings. "New Horizons with VGOS"*. Edited by D. Behrend, K.D. Baver, and K.L. Armstrong. NASA/CP-2016-219016, pages 106–110, 2016.
3. E. Nosov, D. Ivanov, A. Ipatov, V. Mardyshkin, D. Marshalov, A. Mikhailov, I. Rakhimov, A. Salnikov, A. Vytnov, Extending of "Quasar" VLBI-Network: VGOS-compatible Radio Telescope in Svetloe. *IVS 2018 General Meeting Proceedings. "Global Geodesy and the Role of VGOS – Fundamental to Sustainable Development"*. Edited by K.L. Armstrong, K.D. Baver and D. Behrend. NASA/CP–2019-219039, pages 12–16, 2019.
4. I.F. Surkis, V.F. Zimovsky, V.O. Ken, Ya.L. Kurdubova, V.Yu. Mishin, N.A. Mishina, V.A. Shantyr, A Radio Interferometric Correlator Based on Graphics-Processing Units. *Instrum. Exp. Tech.*, 61, doi:10.1134/S0020441218060131, pages 772–779, 2018.
5. V. Chernov, A. Evstigneev, O. Evstigneeva, D. Ivanov, A. Ipatov, I. Ipatova, E. Khvostov, A. Lavrov, V. Mardyshkin, I. Pozdnyakov, Y. Vekshin, M. Zotov, The S/X/Ka Receiving System for Radio Telescope RT-13 of the 'Quasar' VLBI Network. *IAA RAS Trans.*, 41, pages 79–84, 2017.
6. A. Evstigneev, O. Evstigneeva, E. Khvostov, A. Lavrov, V. Mardyshkin, I. Pozdnyakov, The Ultra-Wideband Receiver System for RT-13 Radio Telescope IAA RAS 'Quasar' Network. *IAA RAS Trans.*, 41, pages 49–52, 2017.
7. E. Nosov, E. Khvostov, A. Vytnov. IAA Technology Development Center Report for 2017–2018, *International VLBI Service for Geodesy and Astrometry 2017+2018 Biennial Report*. Edited by K. L. Armstrong, K. D. Baver, and D. Behrend NASA/TP-2020-219041, pages 271–274, 2020.
8. E. Nosov, D. Marshalov, A. Melnikov. Operating Experience with the Broadband Acquisition System on the RT-13 Radio Telescopes. *IVS 2016 General Meeting Proceedings* Edited by D. Behrend, K. D. Baver, and K. L. Armstrong. NASA/CP-2016-219016. pages 53–57, 2016.
9. E. Nosov, D. Marshalov, L. Fedotov, Y. Sheynman, Multifunctional Digital Backend for Quasar VLBI network. *Journal of Instrumentation*, V.16, doi:10.1088/1748-0221/16/05/p05003, P05003, 2021.
10. I.A. Bezrukov, A.I. Salnikov, V.A. Yakovlev, A.V. Vylegzhanin, A Data Buffering and Transmission System: A Study of the Performance of a Disk Subsystem. *Instrum. Exp. Tech.*, 61, doi:10.1134/S0020441218040164, pages 467–472, 2018.

RAEGE Santa Maria: Station Overview

João Salmim Ferreira[1], Abel García-Castellano[1,2], José A. López-Pérez[2], Mariana Moreira[1,3], Diogo Avelar[1,4], Valente Cuambe[1,3], Francisco Wallenstein[1], Javier González-García[2], Carlos Albo-Castaño[2]

Abstract The RAEGE station of Santa Maria is part of the RAEGE network (Atlantic Network of Geodynamic and Space Stations), a cooperation project established between the National Geographic Institute of Spain (IGN) and the Regional Government of the Azores. It is a unique project at a geodetic and geodynamic level, in which there is commitment to the construction and operation of four Fundamental Geodetic Stations, namely: Yebes and Gran Canaria stations in Spain and Flores and Santa Maria stations in the Azores, Portugal. Santa Maria has a radio telescope equipped with a triband receiver (S, X, and Ka bands) and has been operating as a regular station within the IVS R1 and R4 sessions since May 2021. For the past two years, the radio telescope infrastructure and signal chain underwent a series of maintenance procedures and improvements that are described in this contribution. Currently, the station has a team of ten people (and growing) distributed among IT, maintenance, administrative, science communication, and R&D tasks. An overview of the state of the art of Santa Maria and its plans, which include the installation of a broadband VGOS receiver in the second half of 2022, are presented.

Keywords RAEGE, VGOS, Azores, Yebes, core site

1. RAEGE-Az – Associação RAEGE Açores, Santa Maria – Azores, Portugal
2. National Geographic Institute of Spain, Madrid, Spain
3. Atlantic International Research Centre, Terceira – Azores, Portugal
4. CoLAB +ATLANTIC – Cascais, Portugal

1 Introduction

The RAEGE network (Portuguese/Spanish acronym for the Atlantic Network of Geodynamic and Space Stations) is a cooperation project between the National Geographic Institute of Spain (IGN) and the Regional Government of the Azores (RGA) [1]. It is a unique project at a geodetic and geodynamic level, in which there is commitment to the construction and operation of four Fundamental Geodetic Stations, namely: Yebes and Gran Canaria stations in Spain and Flores and Santa Maria stations in the Azores, Portugal. Out of these, the RAEGE sites of Yebes and Santa Maria are fully implemented.

In 2018, the RGA created Associação RAEGE Açores (RAEGE-Az) to a) manage, develop, and disseminate the RAEGE project in the Azores; b) set up a research and development infrastructure for space and space geodetic related activities, and c) communicate space science within the Azores [2]. This entity intends to establish human resources, knowledge, and experience in the Azores in areas relevant for the RAEGE project (i.e. geodesy, radio astronomy, astrometry, etc.), while allowing for greater agility in this project's management in this region.

Building on the work developed previously, a new team in place since 2020, supported by the experienced partners from Yebes Observatory, carried out a great number of corrective maintenance procedures and improvements that allowed for RAEGE Santa Maria to become a regular station in the IVS S/X legacy sessions since May 2021.

In this contribution we intend to present the station's current configuration and equipment, describe the problems found and the procedures used to solve them, detail the signal chain improvements developed

in the past two years, and present the future prospects for the station.

2 Station Overview

The RAEGE station of Santa Maria has a team of ten people (and growing): one IT technician, two maintenance technicians, one administrative officer, one marketing and science communication officer, three engineers (electronics, telecommunications, and aerospace), one PhD astrophysicist for technical coordination and R&D project duties, and a station director, all based on Santa Maria island. Daily operations at this station comprise all the activities to ensure the supply of high-quality data for the network partners, technology development to support scientific challenges, and outreach activities.

The station has a 13.2-meter dish radio telescope (VGOS-like) equipped with a triband receiver designed by the Yebes Observatory. It is a low noise cryogenic receiver able to operate simultaneously in the S (2.2–2.7 GHz), X (7.5–9 GHz), and Ka (28–32 GHz) bands [3]. The Phase-Cal module injects tones shifted by 5 MHz. An active hydrogen maser generates the reference for the pulses and the local oscillators in the downconverters. The backend equipment is composed of a DBBC2 (Digital Base Band Converter) and two Mark 5b units for recording and transferring the sessions' data. Other than that, there is a relative gravimeter GRAVITON-EG installed since 2019, which has the purpose of gathering data to better understand which would be the most suitable gravimeter less prone to noise in an island environment. Also, there are two GNSS (Global Navigation Satellite System) stations, RAEG and AZSM, which are part of regional, national (both Portuguese and Spanish), and international networks (IGS, EUREF, EPOS, etc.). Finally, a seismograph Trillium 120 PA and a Silex accelerometer, designed by the IGN, are installed.

3 Corrective Maintenance Activities

The environment in the Azores is quite extreme in terms of humidity levels (above 78% relative humidity on average annually) and in terms of salinity due to the islands' dimensions, orography, and exposure to oceanic winds. Thereby, this is an environment extremely prone to corrosion, which degrades all the materials (especially the metal structures) much faster than in continental areas. An effective maintenance program is essential to keep the infrastructure in satisfactory condition. In the past two years, some corrective maintenance interventions were needed to recover the radio telescope functionality. In 2019, the radio telescope spent most of the time in park position due to a problem with the Low Noise Amplifiers (LNA) of the receiver installed at that time. In the beginning of 2020, when the triband receiver was repaired and reinstalled, the main gears of the radio telescope were found to be completely dry with a considerable layer of corrosion (see Figure 1).

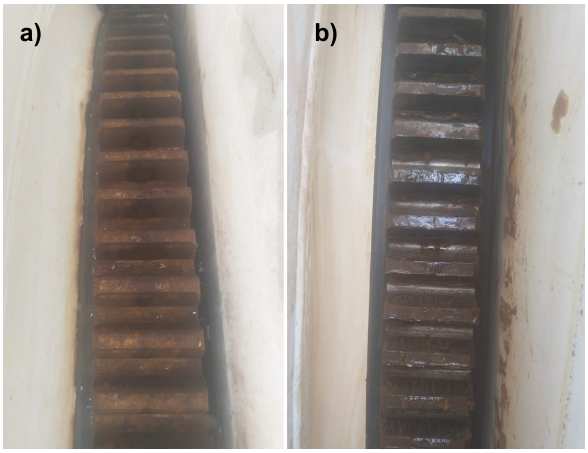

Fig. 1 Radio telescope main gears: a) before and b) after cleaning and lubrication.

Also, the automatic lubrication system in place (which works only with the motors running) wasn't supplying any grease to the lubrication gear wheels. These lubrication gear wheels are made of high-density polyurethane foam, and they are the greasing points of the system. They are critical for a correct lubrication process for both axis main gears. Due to the radio telescope's long stoppage time, these lubrication gear wheels were found completely dry and with cracks on some teeth (see Figure 2a). In two months, the accesses were opened, and all the main gears were cleaned and lubricated. It was decided to acquire a new standard of grease cartridges, to improve the pumping to the greasing points, and to replace all

the lubrication gear wheels. Nowadays the system is regularly inspected to ensure that all main gears are in good condition and well-lubricated.

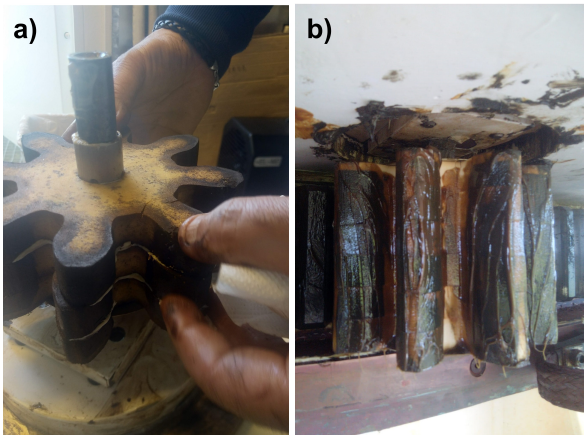

Fig. 2 Lubrication gear wheels: a) crack detail and b) after replacement by new parts.

Due to metal corrosion, several parts of the radio telescope had to be replaced by equivalent parts in stainless steel. Concerning this topic, the major intervention performed was the replacement of the servomechanism's container by a new one, in the beginning of 2021, as the floor started to collapse. The surrounding area had to be modified to improve the air flow on the structure and reduce condensation and zones with water accumulation. Every year from spring to early summer the radio telescope structure goes through a deep cleaning procedure to remove the moss that generally grows during winter, as well as general corrosion removal and repainting works.

Other major repairs consisted of the recovery of the positioning encoder system in the azimuth axis in the beginning of 2021. The system is composed of a large round tape and four encoder heads that read the tape marks at each axis of movement. The tape of the azimuth axis was found with scratches and with the marks faded in some areas, which caused the encoder heads to trigger errors at given radio telescope motion speeds. As no repair was possible, the encoder tape was replaced in a detailed procedure of installation and calibration. The source of the damages found on the tape was never truly understood.

The cable wrap is another system that needs to be inspected regularly for damages. After the rupture of the cable chain in the Yebes RAEGE antenna, an extensive assessment of the system in Santa Maria was made. It was found that in one of the extreme positions, the pins that support the wrap structure sometimes fail to hang the structure, and that could cause the rupture of the cable wrap chain. In order to ensure that the system behaves correctly, we were forced to limit the range of azimuth positions to 40°.

4 Signal Chain Improvements

The RAEGE station of Santa Maria began participating in the IVS S/X legacy sessions (R1 and R4) as a regular station from the end of May of 2021 to the present day with little interruption. The preparation of all signal chains to comply accordingly included the testing, updating, and debugging of all of the software of the different systems. The calibration of the DBBC and the pointing calibration sessions to determine the offsets and the gains in different sky positions, as well as all the works performed by the RAEGE team during the first months of operation (based on the correlators' and analysts' feedback), were vital to improve the quality of the data gathered by this station.

One of the improvements was to reduce the RFI (Radio Frequency Interference) detected on the channels. One of the sources was the radio telescope motor system injecting an 8 kHz tone through the electrical power supply line. On the DBBC channels, it was noticed that this tone only appeared with the active motors, and copies of it were being injected by the Phase-cal module on the receiver. To solve that, line filters were installed with the closest possible Phase-cal module. As a result, the tone disappeared.

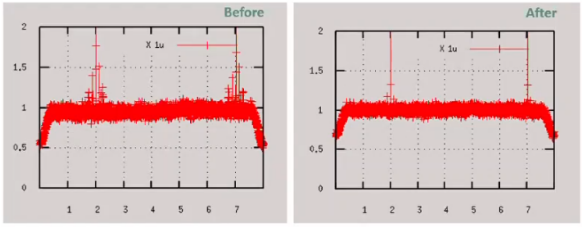

Fig. 3 RFI tones generated by the motors, before and after the installation of the line filters.

Another relevant RFI source was an external powerful link used by the civil protection with a carrier at

around 2,274 MHz, which sits in one of the channels of interest for the R1 and R4 sessions. Because of that, this specific channel was being successively discarded from correlation. After several months of conversations with all the entities, mediated by the Portuguese Authority for Communication, it was possible to move the carrier outside the frequency range of interest, and the channel started to be considered for correlation from October 2021 onwards.

During the first six months of operation, the correlators reported Phase-cal tone amplitude instabilities in some sessions, leading to the need to apply manual phase-cal for correlation purposes and a significant number of non-detections in both bands. It was discovered that leakage from the signal generators, used as local oscillators in the downconverters, was the cause of the problem. First, we found anomalies in the cabling of the 5 MHz reference signal from the ground to the receiver cabin, which were provoking the signal generators to not lock to this external reference signal. Hereafter, it was also found that, as the signal generators didn't have internal cooling systems installed, and because there isn't much space in the receiver cart, the units stopped generating an RF signal as a protective measure when the internal temperature rose above a given level. To solve these issues, different cables for the reference signals were used, and the IGN organized a retrofit campaign to upgrade all the signal generators used in the different receivers, to install an internal cooling system. From that point, to monitor the system behavior, a status message is printed in the session log file, during each scan, illustrating the signal generators' actual conditions.

In the past few months, one focus was the signal chain stability. During these months of operation, we found that the T_{sys} (System Temperature) measured varies a lot in the short term, even when observing the same reference source (such as TAU-A) successively at the same elevation. To confirm if the noise calibration diode was the reason for this issue, T_{sys} calibrations were compared with SEFD (System Equivalent Flux Density) calibrations carried out in sequence. Figure 4 presents T_{sys} and SEFD multiplied by a fix factor, just to be in the same scale, when the antenna is tracking TAU-A.

These tests were done only in X-band, where the RFI environment is more acceptable. Both curves present the same behavior (as the source is approaching the horizon, T_{sys} and SEFD rise), but the T_{sys} curve

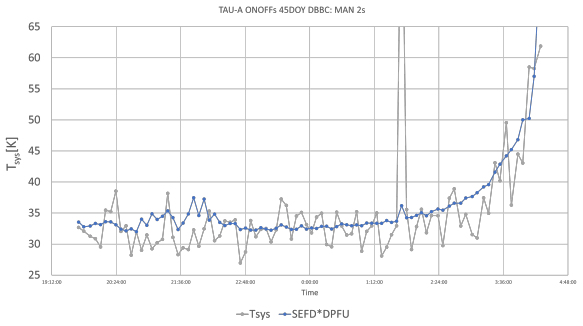

Fig. 4 System Temperature (gray) vs SEFD*DPFU (blue) measured observing TAU-A.

is noisier. At this point, two hypotheses could explain this effect: a) the noise calibration diode isn't stable or b) the sensitivity is limited and this is notable with the diode ($T_{cal} = 1.2\,\mathrm{K}$) and it isn't when tracking TAU-A (16 K approximately). To confirm this, the same test was done with a weaker source (3C84, with 50 Jy at X-band) as visible in Figure 5. Fluctuations in T_{sys} and SEFD are comparable, which suggests that gain stability is limiting the sensitivity, and this should be studied in more detail.

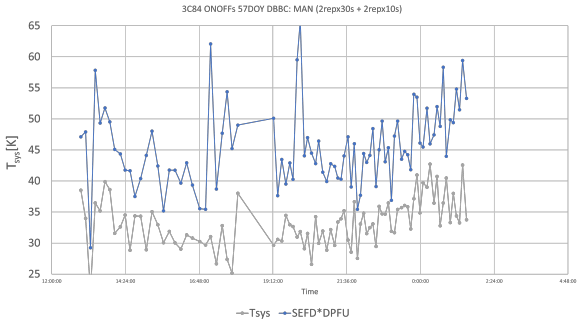

Fig. 5 System Temperature (gray) vs SEFD*DPFU (blue) measured observing 3C84.

5 Summary of IVS Operations

The RAEGE station of Santa Maria resumed operations on May 25, 2021. From that point on, the station has been participating regularly in the R1 and R4 S/X legacy sessions, and, in 2022, it is also scheduled in the

T2 and T2P sessions. The number of sessions in which the station participated is detailed in Table 1.

Table 1 IVS session summary from 2021-05-25 to 2022-03-31.

	R1	R4	T2	TOTAL
2021	29	27	–	56
2022	11	9	2	22

It must be noted that from the 90 sessions scheduled for Santa Maria to participate in from 2021-05-25 to 2022-03-31, 86.7% of them were indeed observed. From the observed sessions, 95% of the sessions were correlated. Concerning the correlators' statistics, the mean percentage of scheduled observations used per session was 68.7% for the Santa Maria data, which is considered as a successful performance.

6 Final Considerations

All the activities described in this contribution were performed by the Santa Maria station team in close collaboration with the staff from Yebes Observatory, as an expression of this RAEGE collaborative spirit across the Atlantic Ocean.

For 2022, as future major commitments for the RAEGE station of Santa Maria, all the RAEGE team is working to install a new Superconductive Gravimeter, to plan and build the GNSS–VLBI local tie pillar infrastructure, and to install a new VGOS broadband receiver, designed by Yebes Observatory, with all the corresponding backend equipment (Mark 6 and DBBC3), doing the best for the Santa Maria station to become a VGOS site by the end of 2022.

References

1. https://www.raege.eu
2. https://www.raege-az.pt
3. López-Pérez, J.A. et al. A Tri-Band Cooled Receiver for Geodetic VLBI. Sensors 2021, 21, 2662. https://doi.org/10.3390/s21082662

Description of RAEGE Yebes VGOS Receiver Upgrades

J. A. López-Pérez, F. Tercero-Martínez, J. D. Gallego-Puyol, I. López-Fernández, C. Albo-Castaño, I. Malo-Gómez, M. Díez-González, M. Patino-Esteban, P. García-Carreño, O. García-Pérez, J. González-García, G. Gómez-Molina, M. Bautista-Durán, R. Amils-Samalot, A. Rivera-Lavado

Abstract This contribution describes the upgrades to be implemented in the RAEGE Yebes VGOS receiver. Meanwhile, the Yebes radio telescope is operating with the VGOS receiver designed for the RAEGE Santa María station. The goal of these upgrades is to improve the overall receiver performance in terms of sensitivity, band-pass ripple, and phase calibration stability. For these purposes, the following components were redesigned and improved: 1) a new QRFH, with better input matching, 2) new balanced LNAs, with lower noise temperature and better input matching, 3) new cryogenic 30-dB directional couplers, more reliable than COTS units, 4) a new CDMS to improve the accuracy and stability of cable delay measurements, and 5) a new PhaseCal Antenna Unit with a new pulse generator and level control of calibration signals. Additionally, a new frequency converter is ready to be used with the R2DBEs. The upgraded receiver is expected to be installed in June 2022.

Keywords RAEGE, VGOS, VLBI, receiver, QRFH, LNA, PhaseCal, R2DBE, downconverter

1 Introduction

Yebes Observatory operates the 13.2-m RAEGE VGOS radio telescope located in the Iberian peninsula (see Figure 1). It is equipped with a broadband VGOS receiver for geodetic VLBI observations.

Yebes Observatory, Instituto Geográfico Nacional, Cerro de la Palera, sn, E-19141 Yebes, Guadalajara, SPAIN.

Fig. 1 The 13.2-m RAEGE Yebes VGOS radio telescope (Credit: M. Gómez).

This receiver is under an important upgrade program in order to improve the overall receiver performance in terms of sensitivity, band-pass ripple, and phase calibration stability.

While these upgrades are being implemented, the RAEGE Yebes radio telescope is operating with the VGOS receiver designed for the RAEGE Santa María station.

The upgrade program includes the following components that were redesigned and improved:

- a new QRFH, with better input matching;
- new balanced LNAs, with lower noise temperature and better input matching;
- new cryogenic 30 dB directional couplers, more reliable that COTS units;
- a new CDMS to improve the accuracy and stability of cable delay measurements; and
- a new PhaseCal Antenna Unit with a new pulse generator and level control of calibration signals.

Additionally, a new frequency converter is ready to be used with the R2DBEs.

The upgraded receiver is expected to be installed in June 2022. After this, the RAEGE Santa María VGOS receiver will also be upgraded.

2 QRFH Upgrade

The QRFH feed was redesigned to improve the port matching (see Figure 2).

Fig. 2 Upgraded QRFH antenna.

In Figure 3, it can be seen that the matching of QRFH version 3 (solid lines) is better than 10 dB across the whole VGOS band, as opposed to the former version (dashed lines).

Regarding the aperture efficiency, the new feed provides a flatter value around 60%, when the RAEGE radiotelescope is simulated using Physical Optics from actual QRFH measurements performed in the Yebes anechoic chamber. Details can be found in [1].

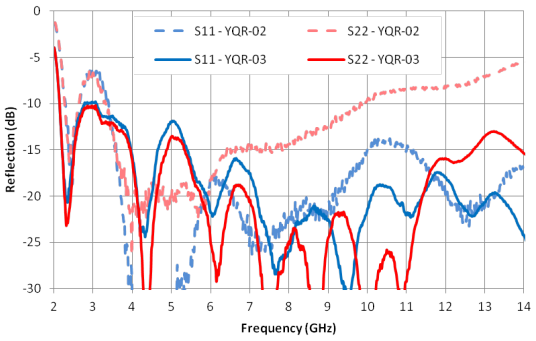

Fig. 3 QRFH matching.

The new QRFH implies a slightly larger dewar window to avoid edge effects, but it allows a 17% reduction in the dewar volume, from 59 to 49 liters.

3 Cryogenic 30-dB Directional Coupler

The next improvement is related to the directional couplers required for calibration signal injection in front of the LNAs. So far, we were using commercial units not specified for cryogenic temperatures. The connectors of these units may potentially fail, because they are not prepared for cooling.

Yebes has developed a specific cryogenic 30-dB directional coupler that solves these issues (see Figure 4). It was optimized in the range 3–14 GHz, but it is usable down to 2 GHz. It shows very good matching, flat coupling, and low insertion losses. Units are available to the community upon request.

Its performance is summarized as follows:

- Optimized in the range 3–14 GHz, usable down to 2 GHz;
- Specially designed to withstand thermal cycling and operate at cryo temps;
- Flexible location of the isolated vs. coupled ports;
- Port matching ≤ -20 dB;
- Coupling = -29.2 ± 1 dB;
- Insertion loss $\leq$ 0.3 dB @ 14GHz and 15K (connectors contribution $\sim$ 2 x 0.1 dB);
- Size: 21.3 x 14.5 x 17 mm;
- Weight: 22 grams.

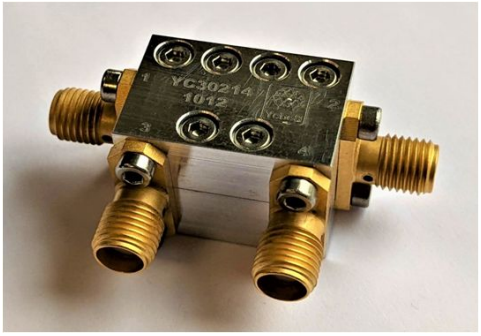

Fig. 4 The cryogenic 30 dB coupler developed in Yebes.

4 LNA Upgrade

Regarding the low noise amplifiers, we have decided to install balanced LNAs (see Figure 5) in all VGOS receivers developed at Yebes instead of single-ended ones, because of its better performance in terms of matching and band-pass ripple.

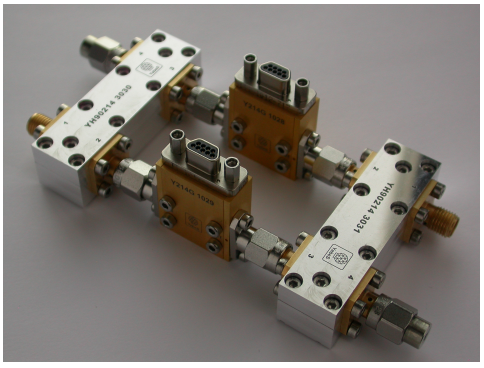

Fig. 5 Balanced LNA developed in Yebes.

Figure 6 shows that the input matching of the balanced configuration (red line) is much better than the singled-ended one (blue line). This is at the cost of a little extra noise of 1.5 K, due to the input hybrid. Details can be found in [2].

However, this penalty is largely compensated by the ripple reduction in the receiver's gain. Additionally, poor matching of LNAs will make phasecal tones to bounce back and forth between the QRFH and LNAs, and it may generate ghost pulses. For this reason we have improved the matching of both QRFH and LNAs.

Table 1 compares the performance of both types of LNAs.

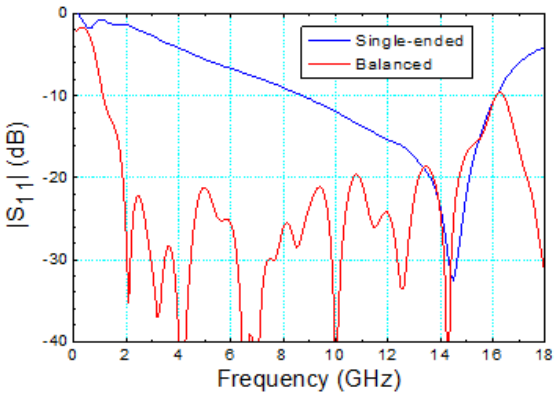

Fig. 6 Single-ended vs. balanced LNA input matching.

Table 1 Performance of single-ended vs. balanced LNAs.

Parameter	Single-ended LNA	Balanced LNA
Band	2–14 GHz	2–14 GHz
Noise Temp.	6.1 K	7.6 K
Gain	33.9 dB	33.8 dB
Input RL	−1.5 dB	−21 dB
Output RL	−16.9 dB	−23 dB

This balanced configuration was recently improved in terms of noise (from 7.6 to 5.6 K) with a flatter response across the band. A paper showing this improvement is in preparation.

5 PhaseCal Upgrade

Concerning the PhaseCal antenna unit, we have a new 10-MHz-spaced pulse generator with better phase stability. When the phase stability is measured in the center of each VGOS sub-band for 30 minutes at room temperature without thermal stabilization of the generator, the results shown in Table 2 were obtained. The worst value is 0.4° RMS at 10.46 GHz. In all cases, the drift during the measurement was lower than ±1° peak-to-peak.

Table 2 RMS phase noise of new pulse generator.

VGOS sub-band	RMS phase noise
A	0.11°
B	0.14°
C	0.2°
D	0.4°

Additionally, the spectrum of the pulses was equalized to get a flatter one. This will avoid large differences in pulse power between the VGOS sub-bands. Figure 7 shows the power of each single tone across the VGOS band with (red) and without (blue) the equalizer. The reduction in the spectrum slope is noticed.

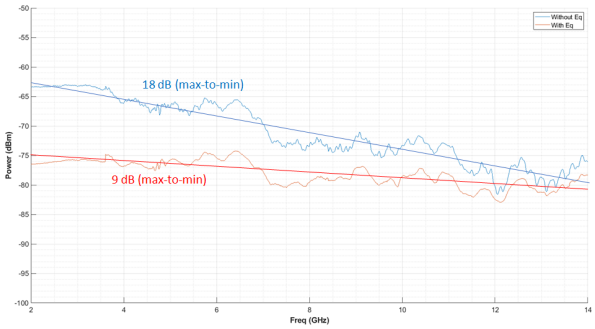

Fig. 7 Reduction of phasecal tones slope with equalizer.

Another upgrade of the PhaseCal antenna unit is the control of the power level for both NoiseCal and PhaseCal signals by means of variable attenuators. Using a chip from Analog Devices, we developed the module shown in Figure 8. It works from 0.1–40 GHz in steps of 0.5 dB up to 31.5 dB. It will be very convenient to optimize the level of the injected calibration signal in front of the LNAs.

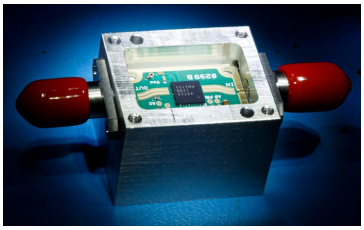

Fig. 8 Variable attenuator developed in Yebes.

6 CDMS Upgrade

Concerning the Cable Delay Measurement System, or PhaseCal Ground Unit, we have developed a new system which solves the issues of the previous one, in particular the digital noise associated with ultra-fast comparators.

Fig. 9 New CDMS developed in Yebes.

The new system is described in detail in [3] and shown in Figure 9. It is based in the design of Haystack from the 1980s, but the difference is that a 20-bit digital voltmeter reads the control voltage of the phase-locked loop, and this voltage is proportional to the two-way delay that we want to know. It incorporates a couple of electromechanical switches that insert an extra path of calibrated delay to compute the scale factor required for the conversion from volts to picoseconds.

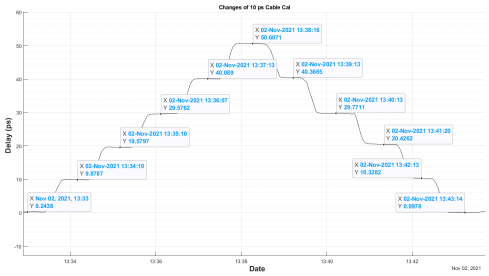

Fig. 10 CDMS response to 10-ps steps.

Figure 10 shows the delay measurements with a manual phase shifter in the cable path when 10-ps steps are applied. The system is very accurate and repeatable.

The RMS noise in a thermally controlled environment is lower than 1 ps.

Currently, we are developing a system using optic fiber only, instead of coaxial cable, similar to the system implemented at Onsala.

7 New Frequency Converter

Additionally, we have developed a new frequency converter that will be compatible with both R2DBE and dBBC3 backends.

It follows the approach proposed by Petrachenko some years ago. It has a single frequency conversion, as opposed to the current Up/Down converters, which have two (see Figure 11). As a result, the phase stability is much better. We have measured 3.4° RMS at 10.5 GHz over 30 minutes.

It is ready to be used with our R2DBEs as soon as we can get the firmware of this backend.

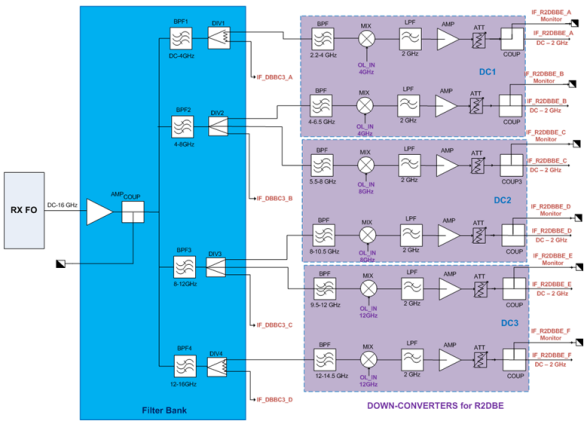

Fig. 11 Block diagram of new downconverter.

8 RFI Power Limiter

A very recent development began in Yebes labs related to an RFI power limiter based on a PIN diode (see Figure 12). The purpose is to protect the RF-over-fiber optic transmitters from strong RFI signals that could potentially destroy them.

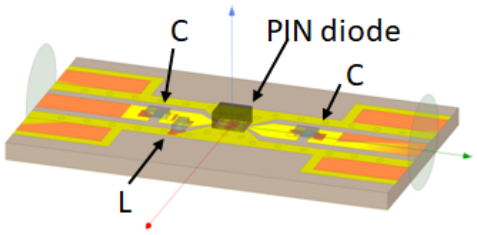

Fig. 12 Design of RFI power limiter.

9 Conclusions

Yebes Observatory is upgrading the VGOS receiver of the RAEGE radio telescope with new devices in order to improve the overal receiver's performance in terms of sensitivity, band-pass ripple, and phase calibration stability.

We are planning to install the upgraded receiver in June 2022. After this, the RAEGE Santa María VGOS receiver, currently in use at the Yebes VGOS antenna, will be upgraded, too, and shipped to Santa María to become a new VGOS station.

Acknowledgements

The authors want to thank the valuable work of all the technicians of Yebes Observatory in achieving the objectives of RAEGE and VGOS.

References

1. A. García, O. García-Pérez, F. Tercero, "QRFH antenna for VGOS receiver (YQR-03-002)", Yebes CDT Technical Report 2020-26.
2. I. Malo-Gómez, J. D. Gallego-Puyol, C. Díez-González, I. López-Fernández and C. Briso-Rodríguez, "Cryogenic Hybrid Coupler for Ultra-Low-Noise Radio Astronomy Balanced Amplifiers," IEEE TMTT, Dec. 2009.
3. García-Carreño, P.; González-García, J.; Patino-Esteban, M.; Beltrán-Martínez, F.J.; Bautista-Durán, M.; López-Espí, P.L.; López-Pérez, J.A., "New Cable Delay Measurement System for VGOS Stations", Sensors 2022, 22, 2308. https://doi.org/10.3390/s22062308

VGOS Station in the South of Thailand

N. Thoonsaengngam[1], P. Jareonjittichai[1], A. Leckngam[1], N. Kruekoch[1], J.A. López-Pérez[2]

Abstract Following the development of the 40-m Thai National Radio Telescope and the Thai VLBI Network, the project to build a VGOS station in the South of Thailand was approved for the years 2022–2025 to probe tectonic activities in the South East Asia region. The site is located in the vicinity of NARIT's Regional Observatory for the Public in Songkhla. A wideband 2–14 GHz receiver system is being developed in collaboration with Yebes Observatory.

Keywords VGOS, Thailand, wideband-receiver

Fig. 1 A map from google pinned positions of the Chiang Mai and Songkhla stations.

1 Introduction

The National Astronomical Research Institute of Thailand (NARIT) aims to expand the astronomy research horizon by developing national radio telescopes and related systems. This goal led to the proposal of a project called the Radio Astronomy Network and Geodesy for Development, or RANGD. The first phase of RANGD includes:

- The 40-meter Thai National Radio Astronomical Telescope (TNRT),
- The 13-meter VGOS telescope (under collaboration with SHAO).

In particular, it devotes much attention to geodetic outputs from the facilities. Developments in both sciences alongside will push research works and innovations to a higher level and gain more benefits for nation and international collaborations. The Chiang Mai VGOS telescope aims to be a part of the IVS sessions, dedicated to the determination of the global parameters.

Recently, NARIT has begun building another VGOS telescope in southern Thailand. The goal is to gain more benefits for the domestic geodesy and geological studies from the approximately 1,300-kilometer baseline (Figure 1), while Thailand sits on two tectonic plates, Eurasia and Sunda.

2 VGOS Station in Songkhla, Thailand

2.1 Location

The Songkhla province is in southern Thailand at 7.15°N, 100.61°E. The site for the VGOS station is

1. National Astronomical Research Institute of Thailand (NARIT)
2. Yebes Observatory, Instituto Geográfico Nacional (IGN)

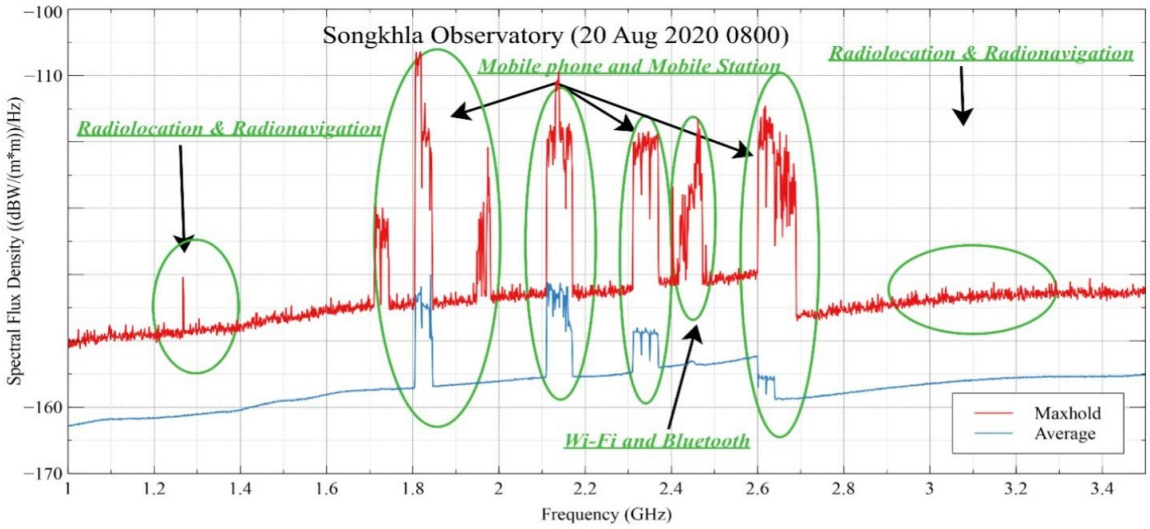

Fig. 2 Report of RFI measuring on site at Songkhla observatory.

at the NARIT Songkhla Regional Observatory. This location makes observations of these two stations in Thailand and can achieve almost the same UV coverage and observing sessions both in the Northern and Southern hemispheres by comparing $+41.5°$ and $-29°$. Results from the baseline determination will be a key to increasing the national geodetic network accuracy up to the millimeter level when combined with the GNSS CORS network and the national geoid model.

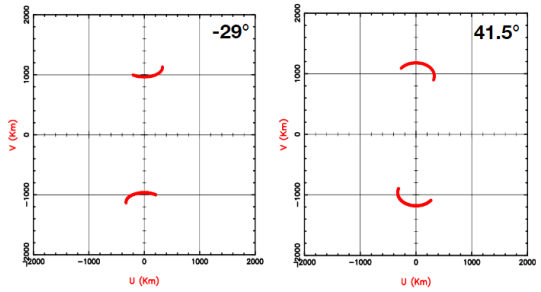

Fig. 3 UV coverage of Chiang Mai and Songkhla observations at $+41.5°$ and $-29°$ (Sukiyama, K.).

The radio frequency situation at Songkhla was measured and reported as an example in Figure 2. The results are considered for the design of the receiver system.

2.2 Receiver System

To perform VGOS observations, the receiver is expected to perform at 30 K over the whole band between 2 and 14 GHz. Songkhla will be equipped with the wideband receiver designed by Yebes Observatory, IGN, Spain.

The block diagram in Figure 4 shows details of the frontend system, being developed under collaboration and consultation with the Yebes group. The cryogenic dewar is composed of the QuadRidge Flared Horn (QRFH). The receiver is cooled using a two-stage cryostat (15 and 50 K). The frame labeled as number 1 is under development at YEBES.

The parts listed as number 2 will be supplied by NARIT and shipped to be assembled and tested on-site. The Antenna Cal Unit (Number 3) is being developed at NARIT.

From the construction site plan, the backend room will be located in a separate building, approximately 60 meters from the receiver room. The radio frequency (RF) signals will be sent from the telescopes via optical fibers so that RF-over-fiber (RFoF) transmitters and receivers (Parts number 4) are required. The dual linear polarizations are split into a low (2.0–6.0 GHz) and a high-frequency part (3.6–14.0 GHz). The corresponding RFoF receivers are located in the control room, close to the backends.

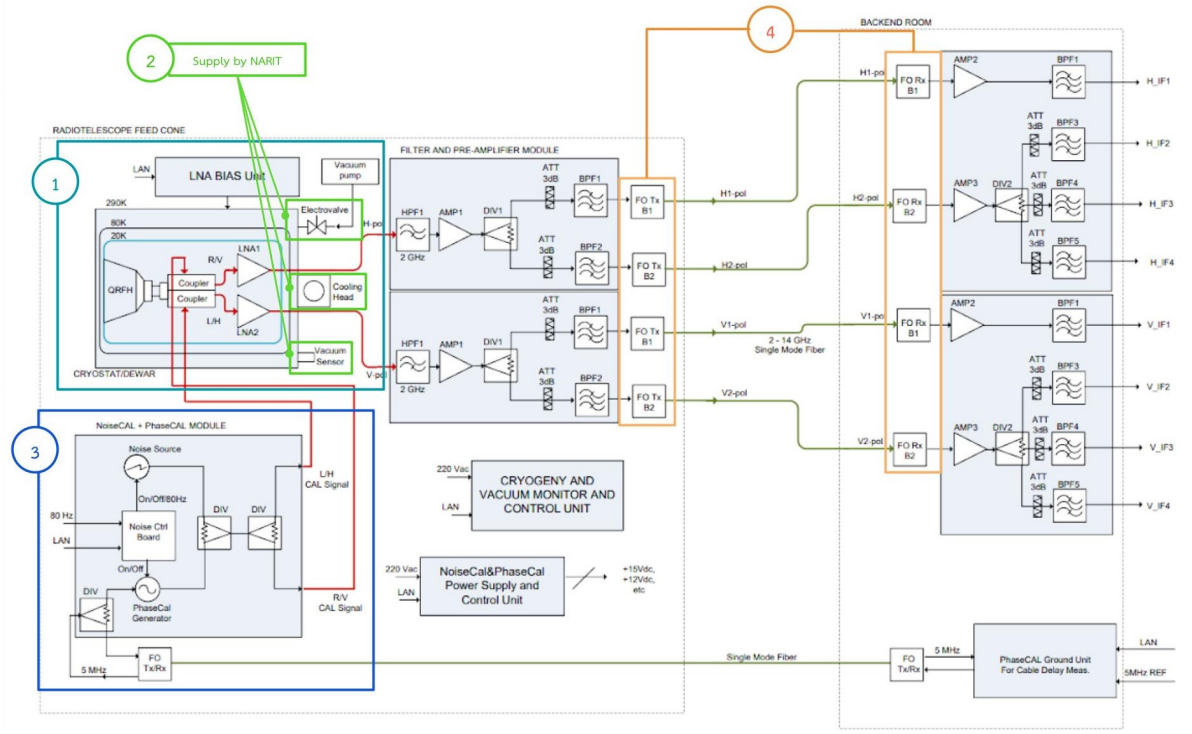

Fig. 4 The frontend block diagram developed at Yebes Observatory.

3 Summary

According to aforementioned details and other relevant components, the specifications of the Songkhla station can be summarized as in Table 1.

Table 1 Station specifications.

Antenna diameter	13 meter
Antenna type	Ring-focus
Slew speed	12°/s
Feed	QRHF
Frequency	2–14 GHz
Receiver temperature	$\leq$ 30 K
Backend unit	DBBC3-8L8H
Data recorder	Mark 6

The digital backend (DBBC3) and the VLBI storage system (Mark 6) were purchased and have arrived at NARIT, the RFoF modules included. The team is now focusing on the integration of the DBBC3 and Mark 6 controls into the VLBI Field System.

In Table 2, the estimated project timeline is presented. According to the plan, parts of the telescope will be delivered to the site in September 2023. The installation will take approximately 115 days until the first movement, and then the receiver system will be installed in February 2024. The commissioning of VGOS Songkhla station is expected to be by mid-2024.

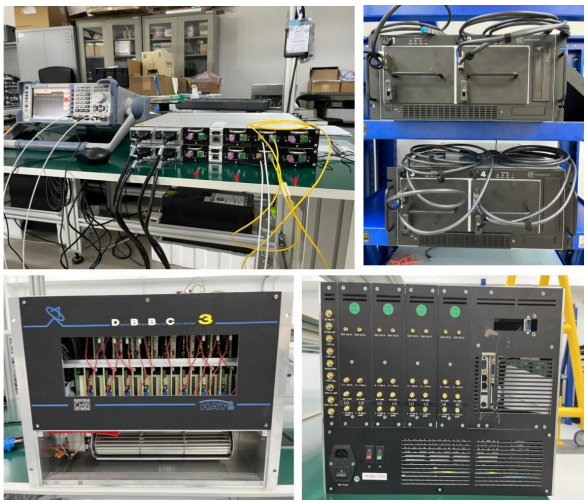

Fig. 5 Parts that are at NARIT: RFoF, Mark 6, and DBBC3-8L8H.

Table 2 VGOS Songkhla timeline.

Time schedule	Activity
October 2021	Telescope design phase
July 2022	Telescope manufacturing
December 2022	Site Preparation
January 2023	Tower construction
September 2023	Telescope on site installation
February 2024	Telescope commissioning
March 2024	Receiver system installation
August 2024	Station commissioning

References

1. Lopez Perez A, de Vicente P, Lopez Fernandez J A, et al., "Instrumentation Developments for VGOS at IGN Yebes Observatory." In: R. Haas, S. Garcia-Espada, J. A. Lopez Fernandez (eds.): Proc. 24th EVGA Working Meeting, pp. 22–26, 2019.

Status of the Ishioka VLBI Station for the Past Two Years

Saho Matsumoto, Tomokazu Nakakuki, Toru Yutsudo, Haruka Ueshiba, Yu Takagi, Kyonosuke Hayashi, Katsuhiro Mori, Yudai Sato, Tomokazu Kobayashi

Abstract The Ishioka 13-m VLBI telescope has participated in IVS sessions since 2015. From 2020 through 2021, it could not be involved in the scheduled sessions for several months because of system troubles. This report describes the process of the troubleshooting and our efforts to prevent the recurrence of these problems.

Keywords Ishioka, Troubleshooting

1 Introduction

The Ishioka VLBI observing station (hereafter "Ishioka", Figure 1) participates in IVS observing all year round. Ishioka is one of the VGOS stations and is participating in both the VGOS and S/X sessions by changing its receiver. In the past few years, we had experienced some troubles. In 2020 and 2021, we could not avoid stopping observing for several months because of a problem with the driving system for the elevation drive. In addition, in early 2020, a strong noise occurred in V-polarization with the VGOS receiver, and Ishioka was not able to provide the complete observational data until the problem was fixed in March 2022. We report the overview of these problems, the process of troubleshooting, and our efforts to avoid having the same problems occur again.

Geospatial Information Authority of Japan

Fig. 1 Ishioka VLBI observing station.

2 Overview of Troubles and Troubleshooting

2.1 Motor Trouble in 2020

In June 2020, the telescope emergently stopped frequently, only for elevation (EL) driving around EL 60 degrees during observing because of errors caused by the motor for the elevation drive. We suspended the observing. First, a problem with the software was suspected, but there was no problem with it. Next, the hardware was investigated. It was found that the torque value for one of the motors for elevation driving had a vibration where the telescope points to EL 60 degrees (Figure 2), and the teeth of a gear rim were worn to around 1 mm in thickness where the teeth engage when the telescope points to EL 60 degrees. Therefore, it was revealed that the vibration generated by the worn teeth of the gear rim caused the motor over-torque, and the telescope emergently stopped. The manufacturer

assumed that lack of lubricant on the gear teeth had made the gear teeth worn. (However, it has not been made clear why only one side of the gear was worn even though there are two gear rims for elevation driving and they were maintained in the same way.) After the threshold of the torque limiter was raised, the error has not occurred. To prevent the teeth from being whittled down more, the surface of the worn gear teeth was polished by a specialist, and the contact surface of the teeth was changed by software. Ishioka resumed observing at the end of November 2020. It means that the operation was interrupted for five months.

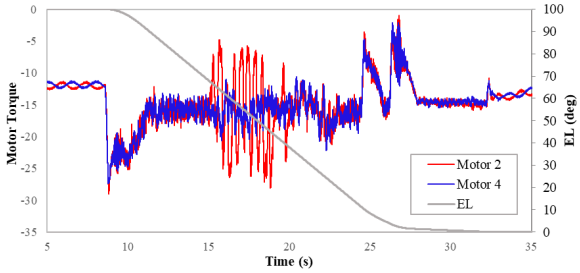

Fig. 2 Torque value of the motors monitored by ACU. The red and blue lines show the torque of Motors 2 and 4, respectively. The gray line shows the EL angle. Motor 2 shows the abnormal vibration around the EL angle of 60 degrees.

2.2 Motor Trouble in 2021

In May 2021, trouble with another motor for the elevation drive happened, and the telescope stopped frequently, only for EL driving at various EL degrees during observing. This time, a servomotor amplifier error occurred, and the cause was suspected to be a failure of the encoder, encoder cable, control board, or electric contact. Swapping the control board and the cable for the encoder and installing a new control board were conducted, but the error was not resolved. Once the motor was dismantled and reassembled by the manufacturer, the error never happened again. Thus, the error seemed to have been caused by a contact failure of the motor encoder. While we were investigating, we participated in observing as much as possible with a slow slew speed (EL 3 deg/sec). As the telescope stopped frequently in spite of the slow speed, it was necessary to monitor the telescope during observing. We restarted observing with a normal slew speed (EL 6 deg/sec) in November 2021, so it took more than five months to return to observing completely.

2.3 Noise in V-polarization with the VGOS Receiver

Noise had occurred in V-polarization with the VGOS receiver since January 2020, and Ishioka had not been able to provide fine observational data (Figure 3). From the investigation, it was made clear that the LNA for V-polarization on the VGOS receiver was broken and caused the noise. After replacing the LNA, the problem was resolved, and we were able to detect clear fringes with a fringe test between Onsala and Ishioka in March 2022. Ishioka has participated in VGOS observing in good condition starting from VO2083 on March 24th.

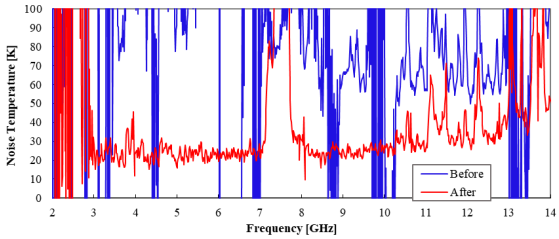

Fig. 3 Noise temperature before (blue) and after (red) replacing the LNA.

3 Our Efforts to Prevent the Same Trouble

To prevent recurrence of the same trouble, we reconsidered how to maintain the telescope. In the case of the motor trouble in 2020, the reason for the worn teeth of the gear was assumed to be a lack of lubricant on the gear rim. To avoid this, the frequency of the lubrication was increased by two times by changing the setting of the auto lubrication system. In addition, to spread the oil on all of the gear teeth, we shuttled the telescope in the EL direction between 0 and 100 degrees before and after each observing session. Furthermore, we increased the frequency of the regular maintenance by the manufacturer's Japanese agency (from once a year to twice a year). In addition to the regular maintenance,

we conducted maintenance focused on the gear and motor. Specifically, we check the motor torque and the rotation speed frequently if there is something wrong with the motor, and the agency also analyzes the data once a month. In addition, the agency checks the gear teeth directly when the driving degree total for elevation reaches a certain count (every 90,000 degrees at the moment). Since the trouble in 2021, we have begun to make efforts to achieve redundancy for parts of the observing instruments and modules for the telescope driving system. One of the reasons it had taken time to solve the problem was taking time to purchase the necessary parts of the telescope to replace them. Being under the spread of coronavirus was suggested as one of the causes. Storing the spare parts helps us to investigate the cause of troubles promptly. Because GSI operates only one telescope, the unavailability of Ishioka has a large impact on its contributions as one of the IVS stations. As time goes by from the construction of the telescope, however, a further increase of trouble is anticipated. It is important to build up resilience to avoid interrupting observing for a long time when problems occur.

4 Conclusions

Ishioka was not able to participate in IVS sessions for several months because of two troubles with the telescope driving system in 2020 and 2021. The first one was caused by the worn teeth of a gear rim, and we enhanced the inspection to check the status of the telescope. The second trouble was caused by the contact failure of the motor encoder. In addition, from 2020, Ishioka data taken with the VGOS receiver in V-polarization contained noise. The noise was solved by replacing the LNA on the receiver. We have built up redundancy of the instruments to prevent prolonging down periods.

Acknowledgments

We appreciate the IVS participants for their understanding and cooperation with our irregular observing during the time that we had problems with the telescope.

IVS Seamless Auxiliary Data Archive (SADA) and EVN Monitor

A. Neidhardt[1], Ch. Plötz[2], M. Verkouter[3], A. Keimpema[3], S. Weston[4]

Abstract Continuous data in real-time offer a tremendous benefit. Operators get detailed information about system status and quality. External partners and companies can retrieve historic values for intervals of events and failure situations. Correlation and analysis can integrate highly-sampled correction parameters. These advantages were the drivers of an IVS Seamless Auxiliary Data Archive at Wettzell as well as the EVN Monitor at JIVE. The EVN Monitor has received funding from the European Union's Horizon 2020 research and innovation programme under grant agreement No. 730884. This paper shows the current status, possibilities for participating, and first results. A video with the presentation can be found here: https://youtube/wJM11NePz3o

Keywords Auxiliary data, Database, IVS Service, ZABBIX

1 Introduction

The IVS Seamless Auxiliary Data Archive (SADA) and also the EVN Monitor are databases accessible from the Internet. The open-source network monitoring suite ZABBIX is used for these central services [4]. SADA is located at the Wettzell observatory, Germany at the address "https://vlbisysmon.evlbi.wettzell.de/zabbix/". The EVN Monitor is located at JIVE ERIC, The Netherlands at the address "https://evn-monitor.jive.de". Users need a username and password for login. There is a general IVS guest, respectively an EVN guest, user login for data downloads. Information about how to download data can be requested from the main author of this article. Using these accounts, data can be presented dynamically via web pages or downloaded as text files for further processing. A Python script "ZabbixAPI" is published for that purpose [1].

All data in the archive directly come from the observatories. Antennas and sites can continuously inject supplementary data sets (such as meteorology and clock offsets) with a minimum sampling rate of one second. There is a special encrypted SSH mechanism to upload data sets. There is no requirement to install additional software at the location of the observatory. Senders just call a program "zabbix_sender" with according arguments containing the data sets on the central database server.

There are different levels of data sets from elementary values to extended value templates for controlling purposes. The basic data set each antenna should support is:

- clock offsets "dotmon" (microseconds)
- air temperature (centigrade)
- humidity (percentage)
- air pressure (hectopascals)
- wind speed (kilometers per hour), if available
- wind direction (degree), if available

An overview of the services is shown in Figure 1. The following sections demonstrate use cases where SADA was used.

1. Technical University of Munich, Geodetic Observatory Wettzell, Germany
2. Federal Agency for Cartography and Geodesy, Geodetic Observatory Wettzell, Germany
3. Joint Institute for VLBI ERIC, The Netherlands
4. Auckland University of Technology, New Zealand

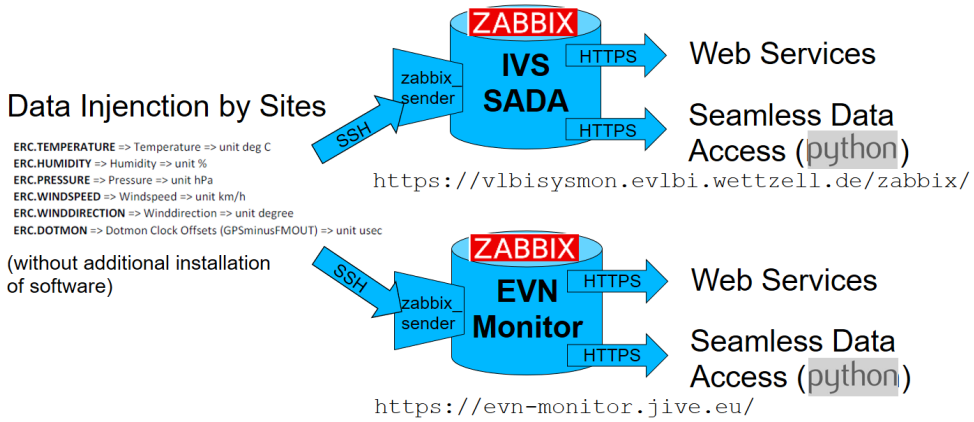

Fig. 1 Overview of the services for seamless auxiliary data.

2 Use Case: Troubleshooting

Extended data sets enable a detailed system overview. This can help to find causes in cases of error situations, missing results, system changes, or quality issues. This is even possible with the reduced number of data of a basic support described before.

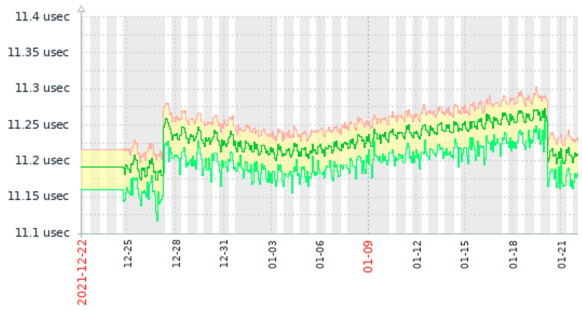

Fig. 2 Sample of continuous clock offsets showing some jumps.

For example, clock jumps or instabilities can be detected even when no VLBI session is in operation, using continuous clock offsets (see Figure 2). This improves narrowing down when the issue occurred. With the established system of VLBI observations, a change can only be recognized from session to session. A more precise definition of the point in time is impossible if it started outside of a session. A precise point in time is often essential for the search for the cause.

Another sample can be given with pointing effects due to wind gusts. Thunderstorms become more and more a serious problem in times of climate changes.

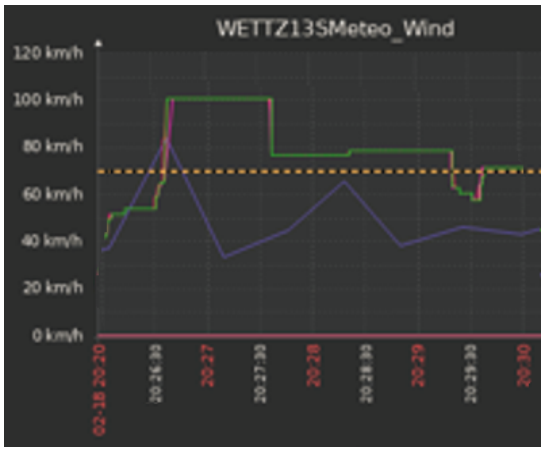

Fig. 3 Sample of continuous wind speeds showing some gusts.

They appear immediately and show some strong gusts leading to pointing instabilities or wind stows (see Figure 3). Cross-checks during correlation and analysis can help to determine effects, as seen for antenna WETTZ13S during the correlation of session “vt2049” at the Haystack correlator.

3 Use Case: Quality Improvement

Huge improvements can be detected using continuous data sets from IVS SADA for clock determination. Clock offsets (GPS minus formatter/DBBC output) are usually just available in log files exactly for the time of a session. One value is always stored per scan because the value is requested as part of the post-observation

procedure (“postob”). But, for example, legacy Intensive sessions to derive UT1-UTC just have about 18 scans, which leads to 18 clock values for this hour. A sample calculation of drifts and trends of the clock offset using IVS SADA and log file data for the session “i22074wz” clearly shows that this number of values is not enough to derive the real drift and trends.

Using SADA data, it is possible to individually select the time interval of data sets. Clock offsets in this database have a sampling rate of one value per minute leading to 1,440 values per day. Therefore, a 24-hour interval can be selected, so that the Intensive is exactly in the middle. This provides a clear statement about the behavior of the clock in relation to the time of the observation.

This can be demonstrated with Intensive session “i22074wz” lasting one hour (the Wettzell antenna uses a Symmetricom SyncServer S250 as a GPS receiver, a DBBC2/FILA10G, and a T4Science EFOS36 as a maser). A comparison between linear trend lines over one hour with values from the log file and from SADA shows huge differences (see Figure 4). Using a larger interval of six hours around the observation session shows that this linear trend shows a similar slope such as calculated before with the SADA data, which gives a better estimation of the clock behavior. It is also visible that polynomial trends show a very similar behavior for this period of time. Using only linear or polynomial long-term trends over one day reduces the accuracy again because they don’t represent the daily trends. Piecewise linear functions work better here.

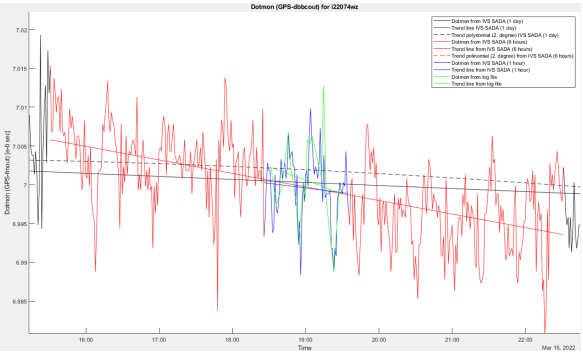

Fig. 4 Analysis of clock offsets for i22074wz.

This demonstration is slightly different for Intensive sessions with VGOS. Due to the short observation times, scans for 68 sources are recorded per hour. Therefore, the number of “dotmon” values is comparable to the number of values from SADA. Trend lines are very comparable here (such as calculated for “v22074ws”; the WETTZ13S antenna uses a Microsemi SyncServer S650 as a GNSS receiver, a DBBC2/FILA10G, and a T4Science EFOS60 as a maser; see Figure 5). A slight improvement might be given if a larger interval around the pure observation is taken from SADA. But this requires further investigations as also different hardware is used, showing different daily trends.

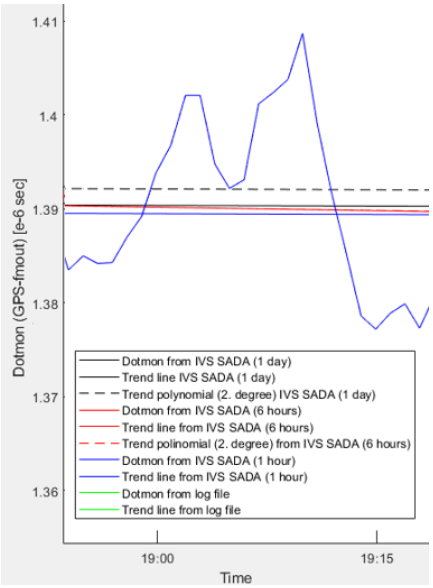

Fig. 5 Excerpt from the graph of clock offsets for v22074ws.

4 Use Case: External Support

Data of the IVS SADA also offer additional potential. Additional events and phenomena can be detected, having higher sampled recordings. A good demonstration was possible using meteorological pressure data for a time period which included the Hunga-Tonga–Hunga-Ha’apai Event [2]. An underwater volcano eruption produced one of the largest phreatomagmatic events ever measured on January 15, 2022, at 04:14 UT. It also sent out a series of waves around the globe, for example also a huge barometric pressure wave propagating in the atmosphere. While regular

recordings in log files, such as from an AOV session, just detected the event, SADA data could be used to clearly see the different arrival times of this wave at different locations (see Figure 6). Therefore, it was possible to exactly derive the running time of the wave between different sites. For example, it required 27 minutes and 39 seconds for the distance of 523 kilometers between Medicina and Wettzell. This leads to a speed of 1,135 km/h which is similar to a number published by the Royal Meteorological Society in London [3].

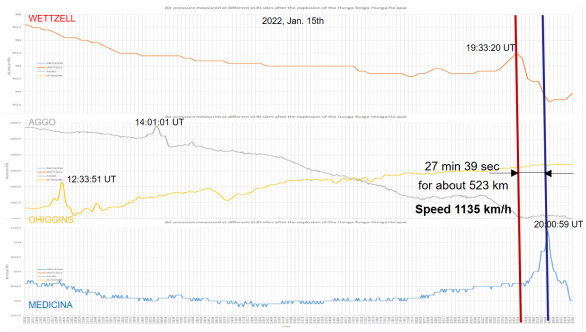

Fig. 6 The Hunga-Tonga–Hunga-Ha'apai Event as a barometric pressure wave in the SADA data.

5 Summary

There are first nice demonstrations showing the benefit of higher-sampled, continuous, seamless, auxiliary data. Besides operational aspects at the locations of the sites where these data are already successfully in use, centralized databases offer also new possibilities for improving products, as shown. Nevertheless, this requires additional investigations and also discussions concerning which data are necessary and what are the requirements for the recording.

Acknowledgements

The EVN Monitor has received funding from the European Union's Horizon 2020 research and innovation programme under grant agreement No. 730884. We also want to thank people from antenna sites who tested and continuously use the sending of data, especially Medicina for the early and continuous support.

References

1. A. Neidhardt, S. Weston, "Data Unlimited – The IVS Seamless Auxiliary Data Archive at the Wettzell observatory", In R. Haas, editor, Proceedings of the 25th European VLBI Group for Geodesy and Astrometry Working Meeting, Chalmers, ISBN: 978-91-88041-41-8, pages 142–146, 2021
2. A. Neidhardt, "Hunga-Tonga Hunga-Ha'apai Event", In D. Behrend, K. Armstrong, H. Hase, and H. Johnson, editors, IVS NEWSLETTER, NASA GSFC, ISSUE 62, pages 9–10, 2022
3. G. Harrison, "Pressure anomalies from the January 2022 Hunga Tonga-Hunga Ha'apai eruption", Royal Meteorological Society, https://rmets.onlinelibrary.wiley.com/doi/10.1002/wea.4170?af=R, 2022
4. ZABBIX webpage, https://www.zabbix.com/, Download 2022-06-30

Modernization of the Subreflector Surface of the RT-32 Radio Telescopes

Sergey Serzhanov[1], Andrey Shamov[1], Valery Olifirov[1]

Abstract In order to improve the accuracy of VLBI observations in the high-frequency bands, the subreflector surface of the Quasar network RT-32 radio telescopes was upgraded. This paper presents a description of the design, installation, and alignment of new panels. This project was implemented in 2020–2021.

Keywords Radio telescopes, subreflector, photogrammetry

1 Introduction

The reflective antenna system of the RT-32 radio telescopes consists of:

- a main quasi-parabolic mirror (diameter of 32 m, focal distance of 11.4 m) and
- a secondary mirror (subreflector). It has the form of a modified hyperboloid with one plane of symmetry and is not an axisymmetric body.

The subreflector surface is composed of nine panels: eight petals and one central panel. The central panel of the old design was molded out of an aluminum sheet and was attached to the other eight panels. Adjustments of the central panel were not possible. The RMS of the old central panel is about 1 mm, and the entire subreflector RMS is 0.73 mm. In 2013, the central panels on all three subreflectors were replaced with new ones made out of solid aluminum. The new panels were produced by milling and were attached with their own fasteners, which allowed them to be adjusted. As a result, the RMS of the new central panels was approximately 0.13 mm, and for the entire subreflector it became 0.62 mm approximately.

To improve the RMS of the subreflector surface further, it was decided to replace the eight petal panels with more accurate ones. This work was carried out in 2020.

2 The Design of New Panels and its Advantages

The old panels were molded out of an aluminum sheet (2 mm thickness) and fixed to the primary frames with rivets. The primary frame of the panel was made of rivets and interconnected U-shaped aluminum channels. The thickness of the entire panel is 200 mm. The panels are fastened to the subreflector's spatial truss frame with firmly fixed pins. This type of fastening allows adjusting of the position of the panels vertically only. The primary structure of the subreflector is the same as it was, so, the position and number of attachment points remains the same. The panel scheme is also preserved. The new panel consists of several molded aluminum sheets fixed to a primary frame. The primary frame is made of aluminum angle bars with cutouts. A polyurethane sealant is used to connect the primary frame of the panel to the reflective surface sheet. This design of the frame and its attachment allows the shape of the reflective sheet to be completely repeated and avoids stresses in it. The total thickness of each panel is about 100 mm. It is not possible to mount this type of panel on old studs. The fastening height of the old panels is 30–40 mm from the base, and the fastening height of the new ones is 140–150 mm. The increased

1. The Institute of Applied Astronomy of the Russian Academy of Sciences

Fig. 1 The old panel and its fasteners.

distance could increase the loads on the studs and lead to the displacement of the panels due to gravity or other factors (wind, snow). Therefore, a new type of fastener was developed. It provides a wide range of panel adjustment and firm fastening. Panels are fixed with an M10 threaded stud (Figure 2, right drawing, position 2) to the bracket (position 4), which is welded to the platform on the spatial truss frame (position 6). Elongated holes for fastening are made in the brackets and panels. They are perpendicular to each other, which allows panels to move in two planes. Adjustment in the third plane (height) is carried out along the threaded stud. The primary structures of the panel and the bracket are not strictly parallel. To compensate for this factor, on the side of the bracket, the stud is fastened with spherical washers. The design of the panel structure and fasteners was carried out jointly with Vertex Antennentechnik GmbH.

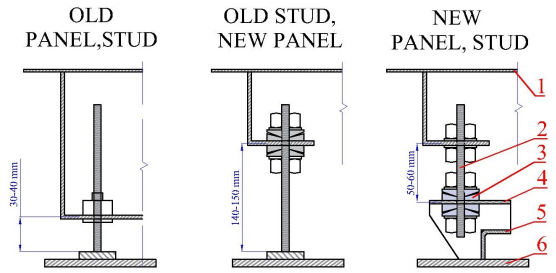

Fig. 2 Panel fixing scheme: 1–panel's surface, 2-–M10 threaded stud, 3—spherical washers, 4—bracket, 5—adapter, 6—platform on the subreflector truss.

3 Installation of New Panels

In parallel with the development of panels, the installation plan was developed. The dismantling of the entire subreflector assembly was not an option, because that could have led to the strong imbalance of the antenna reflective system. Load from an imbalanced antenna reflective system is transmitted through the elevation drives and the oscillating platform and is able to damage the azimuth bearing. In addition, the process of dismantling the entire subreflector assembly is very laborious and dangerous. As a result, it was decided to replace the panels one by one in the antenna elevation position of 90°. To do this, it was necessary to erect scaffolding around the over-mirror cabin. Scaffolding is needed to provide a comfortable working space of the same area as the subreflector, roughly. Then the final calculation of the entire structure weight was made. The weights of the installation sites, equipment, and workers located on them were taken into account. The result is about two tons. This is much lower than the calculated snow load (about 45 tons). This design is suitable for mounting and has no significant impact on the supporting structures of the radio telescope.

The main load-bearing pillars were arranged in the shape of two octagons. The outer octagon rested on the service platform around the over-mirror cabin, and the inner one (rotated 22.5° relative to the outer one) rested on the edge of the upper platform of the over-mirror cabin. Both octagons were connected by a system of beams. The resulting spatial truss structure was ten meters high and five meters in diameter. All the compo-

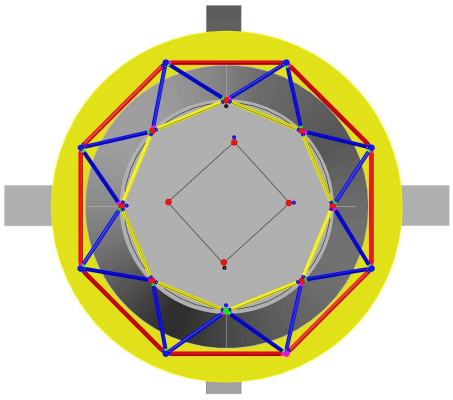

Fig. 3 Scaffolding scheme. Top view: red–outer octagon, yellow–inner octagon, blue-–beams.

nents of the scaffolding assembly were lifted through the hatches inside the over-mirror cabin by electric hoist. But the size of the hatches was insufficient to pass the subreflector panels through them. Hoisting the panels over the edge of the main reflective surface was also not possible. So, it was decided to remove two panels in the fourth row of the main reflective surface. An electric crane was installed above this place, and the panels of the subreflector were lifted through this opening. The replacing of the panels was carried out

Fig. 4 Scaffolding installation process.

step by step. The old panel was removed along with the old studs. Then, an adapter for a new bracket was pre-fixed to the sites. Studs and brackets were attached to the new panel, and after that it was installed in its place. Brackets with studs were installed in the pre-design positions and pre-fixed by welding. Then the panel was removed from the studs, and the final fixation of the adapters and brackets was made. Welds were cleaned and primed. Then, the new panel was returned to its

Fig. 5 Panel replacement process (one panel left to replace).

place, and it was preliminarily adjusted in relation to the neighboring panels. After that, the subreflector was rotated, and the procedure was repeated with the next panel. This method made it possible to install the panels quite accurately and quickly. At the same time, the original shape of the subreflector was preserved quite accurately.

4 Geodetic Control Procedures

Before installing the panels in place, it was necessary to make sure that they meet the characteristics specified in the design documentation and quality certificates. Input control measurements of the new panels were carried out in a closed thermostatic room. The measurements were made with high-precision geodetic equipment (AT-401 Leica absolute tracker) using the contact method. As a result, it was found that the RMS of the new panels' reflective surfaces lies between 0.21 and 0.23 mm, which satisfies the requirements of the technical specifications (to be no more than 0.25 mm).

Then, it was necessary to measure the geometry of the original subreflector surface to understand how the geometry of the reflective surface changed after the upgrade. The measurements were carried out with high-precision geodetic equipment (TDRA 6000 Leica tacheometer) using the step-by-step scanning method, which provides uniform coverage of the entire reflective surface with measuring points. This work was carried out at night when fluctuations in air temperature had not exceeded 2°C.

The successive replacement of the subreflector's panels allows formation of a new reflective surface which closely repeats the geometry of the original one.

For the final formation of the required geometry, the panels were adjusted. To do this, deviations of the actual form from the theoretical model were determined. Based on the obtained measurement results, recommendations were prepared for panel position corrections. After the panels were adjusted, the measurement of the reflective surface was again performed. If, according to the measurement results, the obtained surface shape did not correspond to the specified accuracy, then the cycle of the above steps was repeated. Thus, after three to five stages of adjustment, the best RMS value was achieved. During the next year after the completion of the panel replacement, control measurements were made by the photogrammetric method. The measurements were carried out with high-precision geodetic equipment (Aicon DPA Industrial coordinate mea-

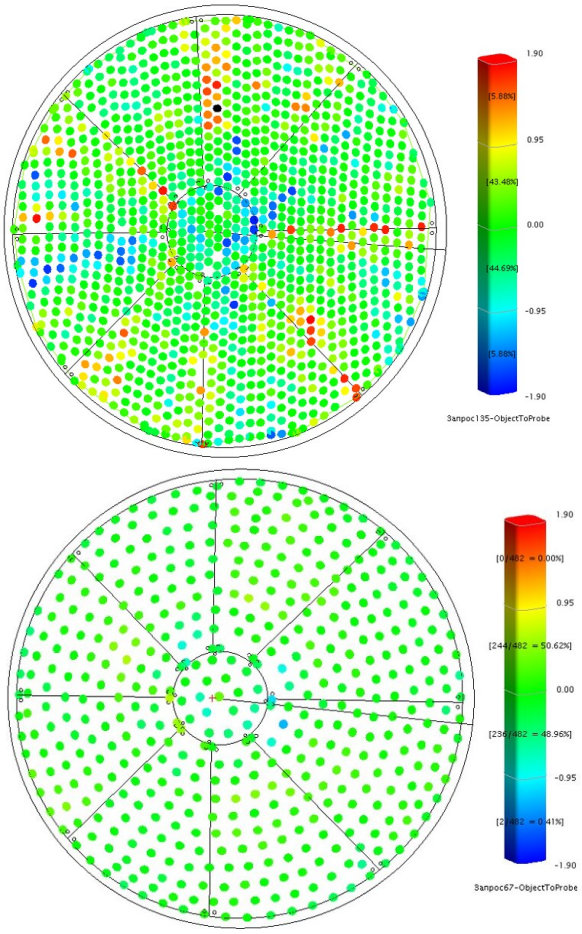

Fig. 6 Cartograms of deviations from the theoretical model before (top) and after (bottom) modernization on the example of a subreflector at the Badary observatory.

suring system). This method combines the advantages of the contact method (measurement accuracy) and the step-by-step scanning method (speed of obtaining the result).

As before, these works were carried out at night, when the fluctuations in air temperature did not exceed 2°C.

Table 1 RMS subreflector surface before and after modernization.

Observatory	Before 2	After 3	Improvement
Svetloe	0,61 mm	0,34 mm	1,79
Zelenchuk	0,63 mm	0,38 mm	1,66
Badary	0,61 mm	0,31 mm	1,97

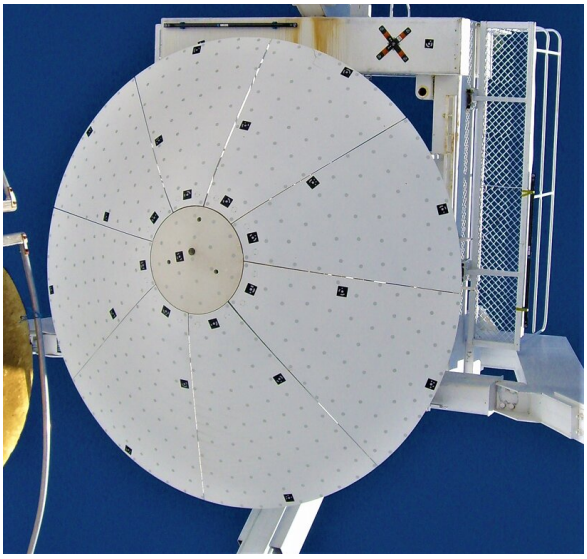

Fig. 7 New panels with photogrammetric marks.

5 Conclusions

As a result of the work carried out on its modernization, it was possible to almost double the geometric parameters of the RT-32 subreflector surface in all observatories of the IAA RAS. During the design and preparation of these works, complex engineering tasks were set and successfully solved. Among other things, with the development of more advanced geodetic control systems, it becomes possible to more accurately control the spatial position of the panels of the secondary and primary parts of the RT-32 reflective system.

An Agile Method to Detect Deformations of the VLBI Dish

Ulla Kallio, Joona Eskelinen, Jyri Näränen, Markku Poutanen

Abstract Gravity and temperature variations deform the radio telescope dish and structure during VLBI measurements, thus affecting the reference point determination. Full determination of the deformations is time-consuming and requires a dedicated campaign to investigate the form of the full paraboloid surface of the VLBI antenna dish. In this paper we investigate a more agile method using spherical prisms attached to the dish structure and a robot tachymeter. We tested the method at the Metsähovi Geodetic Research Station's VGOS antenna and measured the angles and distances to the points in the telescope and dish structure in different antenna elevation positions. The distances between the points were calculated and projected in each elevation position to the Cartesian system, axes of which are the pointing direction, the elevation axis direction, and the third one orthogonal to those. The projected distances were then analyzed. In our experiment we detect mm-level changes at different dish elevation positions. The method could be used to complement the full determinations, even during VLBI-sessions.

Keywords Gravitational deformations, VLBI telescope

1 Introduction

Temperature variations and gravity among other environmental parameters deform the telescope dish. Laser-scanning is currently the main method of getting information on the dish surface and the changes in focal length (e.g., [1]). Organizing or preparing a laser-scanning campaign is laborious. There is a risk of damaging the structure or the equipment, while the cost-benefit ratio might be low. A relevant option is to use close-range photogrammetry. Another problem is how and where the instrument should be placed. From ground level, the dish surface is not visible at higher elevation positions. One solution is to use drones (e.g., [2]).

Terrestrial measurements have been long used in the determination of the reference point (RP) of the telescope. The targets or prisms were measured in different antenna angle positions and the coordinates of RP estimated [3]. Sarti et al. [4] used tachymeter measurements with the laser-scanning and finite element model successfully also for modeling the signal path variation and gravitational deformations.

Developing an agile method to detect deformations is ongoing. The method could be used between the more complete deformation measurements. The agile method should be quick, to not allow unknown environmental parameters to change during the measurements. There should be no need for extra preparations and no need to touch the telescope. The measurements and processing should be automatic.

In this paper, we present the first results of tachymetric measurements for detecting changes in the distances between the points in the structure of the telescope.

2 Measurements

Angles and distances were measured to spherical prisms, attached to the dish structure, with a Leica

Finnish Geospatial Research Institute

Fig. 1 Measurements with Leica TS50 robot tachymeter.

TS50 robot tachymeter (Figure 1). The azimuth of the VLBI telescope was kept fixed to the angle optimal for the prism incident angle. The measurements were connected to the local pillar network (Figure 2). The same prisms were observed in 19 elevation positions. The left and right sides of the telescope were measured separately by rotating the telescope around the azimuth axis about 180°. The measurement session

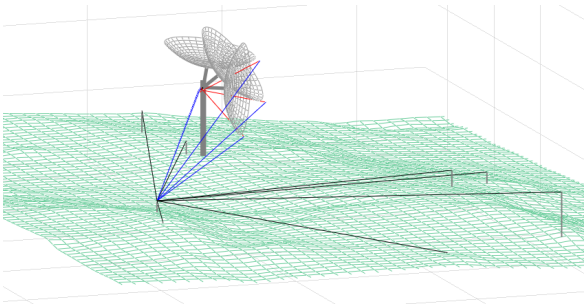

Fig. 2 Measurements: black lines are for instrument orientation, blue ones are for the prisms on the structure of telescope, and red lines are the vectors between the points to monitor.

was automated. The movement of the VLBI telescope was controlled with an in-house MATLAB routine using predefined azimuth and elevation angles, as well as elapsed time values for moving to the new position. The tachymeter measurements were synchronized with VLBI movements and controlled with another in-house software. The predefined approximate prism coordinates were used for quick automatic aiming and measurements. The whole measurement session took about 20 minutes.

3 Data Processing

The first velocity correction and scale and additive constant corrections were applied to slope distances. The angles were aligned to refer to the ellipsoid normal using the geoid model. The horizontal orientation came from the local pillar network, which is aligned to ITRF2014. The coordinates for each prism point were calculated.

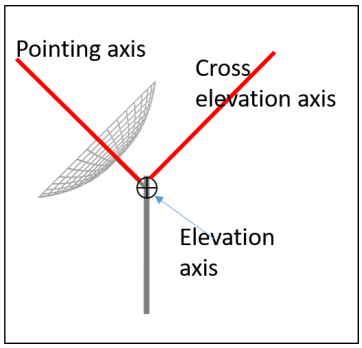

Fig. 3 Axis system where the monitored distances were projected.

4 Analysis

The distances between the determined prism points were calculated, and the coordinate differences were transformed into the Cartesian coordinate system of the telescope. Both of the tracked prism points rotate around the elevation axis, which was estimated by fitting the two circles with a common axis. The pointing axis was then calculated as a cross product of an estimated azimuth axis and elevation axis. The cross elevation axis was then orthogonal to the elevation axis and the pointing axis (Figure 3).

The azimuth axis or the pointing axis cannot be estimated from the collected data, so an estimated azimuth axis from previous reference point monitoring was used. The axis directions form the base of the coordinate system of the telescope. The vectors between the prism points are then transformed to that base and stan-

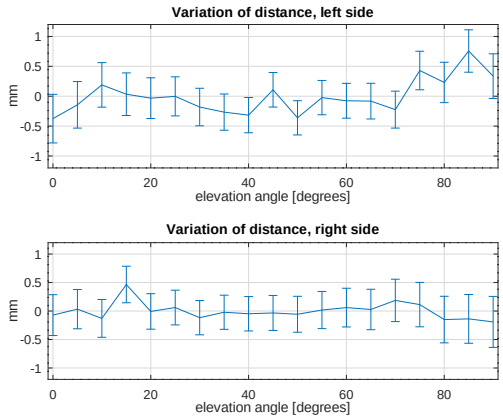

Fig. 4 Variation of the monitored inter-prism distances. The averages of the distances were 8.8544 for the left side and 9.6234 for the right side.

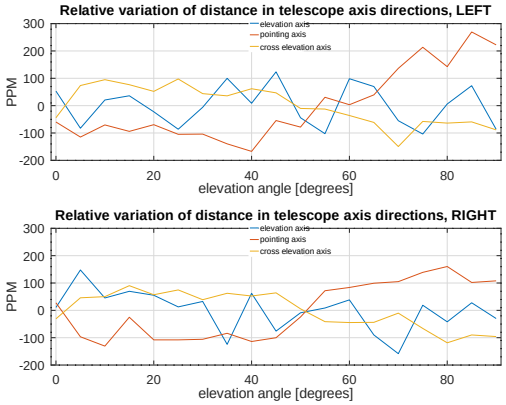

Fig. 5 Variation of inter-prism distances projected to the telescope axis system.

dardized by dividing them by the corresponding component and multiplying the result by 10^{-6} to obtain a PPM value (Figure 5).

5 Results

The results of the variation of the distance (Figure 4) and the PPM values (Figure 5) of each component in the telescope base are presented as a function of the elevation angle of the VLBI telescope. In the pointing direction, the distance increases when the elevation increases. The diameter of the dish seems to decrease in the cross elevation direction when the elevation angle increases. We are not able to see the deformation in the elevation axis direction.

6 Conclusions

The experiment was successful, showing the potential of the method. We also noticed several places which can be developed in the future. More prisms and simultaneous observations with two tachymeters from the left and right sides will give us more geometrical information, especially in the elevation axis direction. The prism points need to be carefully chosen to allow determination of the most relevant distances for the analysis of the dish deformation (or other purposes). This method is applicable also to other sites, and most importantly, it can be used during the normal operation of a telescope.

Acknowledgements

The 18SIB01 GeoMetre project has received funding from the EMPIR program, co-financed by the Participating States and from the European Union's Horizon 2020 research and innovation program. MP Acknowledges the Academy of Finland grant 315722.

References

1. C. Holst, A. Nothnagel, R. Haas, and H. Kuhlmann. Investigating the gravitational stability of a radio telescope's reference point using a terrestrial laser scanner: Case study at the Onsala Space Observatory 20-m radio telescope. *ISPRS Journal of Photogrammetry and Remote Sensing*, 149:67–76, 2019.
2. M. Lösler, R. Haas, C. Eschelbach, and A. Greiwe. Gravitational deformation of ring-focus antennas for VGOS: first investigations at the Onsala twin telescopes project. *Journal of Geodesy*, 93(10):2069–2087, 2019.
3. U. Kallio, M. Lösler, S. Bergstrand, R. Haas, and C. Eschelbach. Automated Simultaneous Local Ties With GNSS and Robot Tacheometer. In *IVS 2016 General Meeting Proceedings*, edited by D. Behrend, K. Baver, and K. Armstrong, NASA/CP-2016-219016, pp. 154–158, 2016.
4. P. Sarti, C. Abbondanza, and L. Vittuari. Gravity-dependent signal path variation in a large VLBI telescope modelled with a combination of surveying methods. *Journal of Geodesy*, 83(11):1115, 2009.

Development of Wideband Antennas

Hideki Ujihara

Abstract Wideband antennas are developing a next generation radiometer and wideband feed horns for upgrading of conventional Cassegrain antennas. This next generation radiometer uses a 16–64 GHz feed horn for observating water vapor spectra (22-GHz band), water drops in clouds (30-GHz band), oxygen (50-GHz band), and VLBI. Wideband feed horns for upgrading radio telescopes are designed for 1.5–15.5 GHz with a narrow beam of 15 degrees in the subtended angle of the sub-reflector.

Keywords Wideband, VLBI, radiometer

1 Introduction

Wideband feeds and OMTs developed for Gala-V have simple structure that can be easily arranged for higher frequency. Thus, the next generation radiometer has been developed with 16–64-GHz wideband feeds. The feed can be used with parabola or Cassegrain optics, because the beam width of the feed is easily changed to fit the optics. Further, it has been explored to extend the bandwidth with a narrower beam to other Cassegrain antennas in a simulation study. These activities are reported here.

Kyoto University

2 Next Generation Radiometer

Water vapor measurement experiments were done by the BBM of the K-Band multimode horn for the VSOP-2 satellite set on the 3.7-m antenna of NICT Okinawa in 2019. But the development was slowed down by COVID-19. The OMT and feed horns for 16–64 GHz were developed in 2020 and tested at Kyoto University in 2021. And now, 900 mm Cassegrain for a portable radiometer with high resolution is being developed at Kyoto University. The main mirror is a spun aluminum parabola dish, that is the same technique to make MARBLE dishes, but the surface is more accurate for higher frequcency. The mirror is supported by CFRP pipes and is easy to assemble and disassemble for the transportation through the stairs and doors of buildings. This system can be also used for VLBI in K/Q band or receiving satellite signals. In 2022, water vapor measurement experiments will be done at NICT Kashima, and VLBI experiments will be done with the Mizusawa 10-m dish at NAOJ.

3 Wideband Feed

Wideband feed horns for 1.5–15.5 GHz with a narrow beam have been developed in simulations. Based on the original designs of the IGUANA feed, it will be the coaxial feed. Using the third model of the IGUANA feed for Kashima 34-m, a 2.2–22 GHz test feed will be made.

4 Wideband OMT

The OMT of the radiometer delivers one linear polarization to the LNA for 16–34 GHz, and the other to the LNA for 26–62 GHz. They were tested at room temperature with wideband horns at Kyoto University. The LNA will be cooled by a stirling cooler; thus their bandwidth cannot cover the whole band. The first design of the OMT used TSA in the waveguide to make a thin ridge. The second design will be a quad-ridged waveguide, because factories in Japan are now in normal operation. These quad-ridged waveguide OMTs can have a sharp cut-off frequency to suppress RFIs in the same way as the Gala-V system.

5 Conclusions

Development schedules were delayed by COVID-19, but various wideband feeds and OMTs have been developed (Figure 1) and are waiting for experiments. Results will be presented at the next General Meeting.

Fig. 1 Developed wideband feed and OMT for next generation radiometer at NICT Kashima.

Acknowledgements

Development of the next generation radiometer and the wideband VLBI receiver system are supported by JSPS Kakenhi Grant Number 18H03828 and 21H04524. Development of the 1.5–15.5 GHz feed horn is supported by a powerful computer at the Max Plank Institute. Feeds were measured in METLAB of Kyoto University, and OMTs were measured at the NICT ICT device laboratory.

References

1. H. Ujihara, “Development of wideband feed for Kashima 34m Antenna,” Radio Sci., vol. 52, doi:10.1002/2016RS006071
2. H. Ujihara, K. Takefuji, M. Sekido, R. Ichikawa, “Development of Wideband Antennas,” International Symposium on Advancing Geodesy in a Changing World, pp. 25–28, Springer, Cham, https://doi.org/10.1007/1345_2018_41
3. M. Sekido, et al, “An Overview of the Japanese GALA-V Wideband VLBI System,” IVS 2016 General Meeting Proceedings, New Horizons with VGOS Edited by Dirk Behrend, Karen D. Baver, and Kyla L. Armstrong, NASA/CP-2016-219016, 25–33
4. W. Petrachenko, A. Niell, B. Corey, D. Behrend, H. Schuh, J. Wresnik, “VLBI2010: next generation VLBI system for Geodesy and Astrometry, Geodesy for Planet Earth,” Proceedings of the 2009 IAG Symposium. Springer, Buenos Aires, pp. 999–1006, ISBN 978-3-642-20337-4. doi:10.1007/978-3-642-20338-1.
5. T. Kondo and K. Takefuji K.(2016), “An algorithm of wideband bandwidth synthesis for geodetic VLBI,” Radio Sci., vol. 51, doi:10.1002/2016RS006070
6. The SKA Project, https://www.skatelescope.org
7. M. Pizzocaro, M. Sekido, K. Takefuji, H. Ujihara, et al. “Intercontinental comparison of optical atomic clocks through very long baseline interferometry,” Nature Physics, Oct. 2020, vol.17, pp.223-227(2021). DOI: https://doi.org/10.1038/s41567-020-01038-6
8. Hideki Ujihara, “Development of wideband feed with sharp cut-off frequency OMT for RFI”, ECMWF RFI2022 conference paper, https://doi.org/10.46620/RFI22-015

From BRAND to DBBC4

Gino Tuccari[1,2], Walter Alef[2], Helge Rottmann[2], Sven Dornbush[2], Armin Felke[2], Alan Roy[2], Michael Wunderlich[2]

Abstract The BRAND project is now overlapping with the DBBC4 project. This is due to the fact that a number of technological solutions already developed and still under development for BRAND are being applied to the DBBC4 front-end. The current status of the BRAND project with its latest achievements will be presented, together with an overview of the new DBBC4 project, which started this year. The DBBC4 is expected to provide new state-of-the-art functionalities for VLBI astronomy, geodesy, and space science.

Keywords Backend, DBBC, Artificial Intelligence

1 Introduction

Since the first implementation, the DBBC systems have pursued original and non-existent solutions. Such uniqueness, due to the adoption of innovative solutions and the best available technologies, has made it possible to develop and establish state-of-the-art solutions. The success of the operation is evidenced by the fact that the European VLBI network EVN adopted for over a decade DBBC systems as the standard back-end of the network, and numerous radio telescopes of the VLBI IVS (International VLBI Service) geodetic network use these systems on a regular basis. The implementation of the third DBBC3 generation is now used for the observations of the Event network Horizon Telescope, is used in the VGOS geodetic network, and is going to be adopted by the EVN for the modernization of the network, which is currently mainly equipped with second generation DBBC2 systems. The different versions DBBC1, DBBC2, FILA10G, and DBBC3 are today in use around the world in more than one hundred units.

Developments in the DBBC family recently have included the BRAND (BRoad-bAND) digital receiver covering the 1.5–15.5 GHz band, now in the final stages of development, and the design of the new DBBC4 digital front-end and back-end system, which has recently been launched with absolutely innovative elements for the characteristics and methods adopted, which allow it to be operated with wide reception bands up to 256 GHz and a product ‘data rate’ up to 4 Tbps.

The graph in Figure 1 shows in logarithmic scale the comparison between the various systems of the family, from which it is possible to highlight the growth in performance, together with some views of some specimens.

2 General Architecture

The new system, in order to maintain compatibility with the previous versions of DBBC systems, has an architecture which can allow an upgrade from previous versions. Such a possibility is guaranteed by the physical structure of the system and the organization of the various parts.

In terms of functionality, anyway, there are important differences, due to the extremely higher performance offered by the new system. Here is described the general architecture with the main parts and the novel functionalities which will be part of the system.

1. INAF Istituto di Radioastronomia, Bologna, Italy
2. Max-Planck-Institut für Radioastronomie, Bonn, Germany

DBBC Family Evolution (Table)

	DBBC1 (2004)	DBBC2 (2009)	DBBC2010 (2010)	DBBC3 (2014)	BRAND (2020)	DBBC4 (2024)
Max Input Bandwidth (MHz)	512	4096	8192	32768	57600	256000
Max Output Data rate (Mbps)	1024	8192	16384	131072	460800	4000000

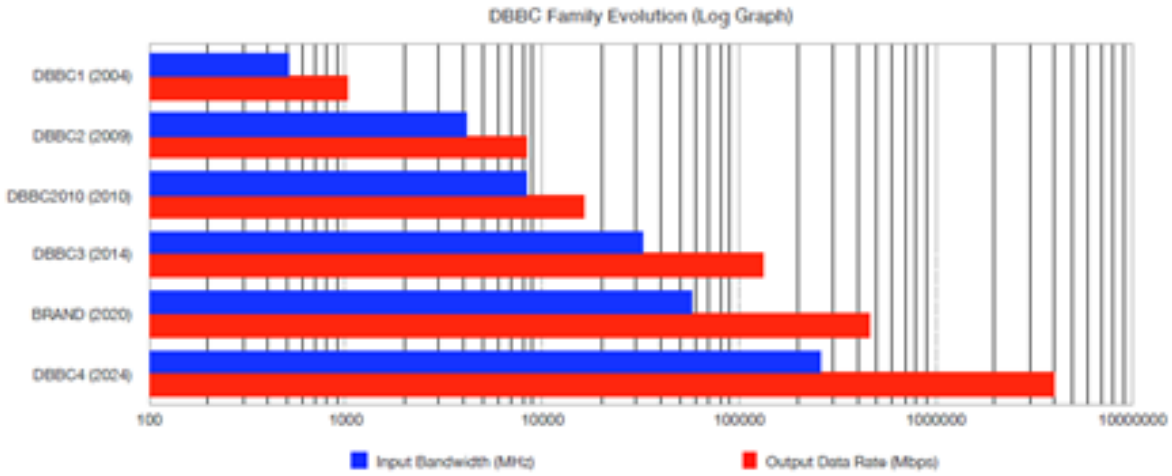

Fig. 1 DBBC family evolution performances.

The main difference which can be considered relevant in the DBBC4 is its nature of 'widespread system'. This means the traditional method for building a digital back-end for radio astronomy was to separate in very different physical positions the analog part of the receiver with respect to the digital part, including the transaction pin and the sampler. This concept was revised in the BRAND EVN project, where the realization of the very wide bandwidth digital front-end (called 'DI-FR-END'), was positioned close to the traditional analog front-end. This solution, even if it presents challenging implementations in terms of RFI shielding, allows superior performance in terms of phase stability, higher dynamic range, and robust and simple methods to transfer the pure sampled or digital preprocessed data to the back-end area, where it is still convenient to maintain a good part of the equipment for RFI shielding purposes.

The DBBC4 is mainly planning to adopt such a distribution between the digital front- and back-end, even if the possibility of performing such entire functionality in the back-end area is maintained. This in particular can be useful when traditional existing receivers are already routed to this area, or when very high frequency (sub-millimeter) receivers are used, then including frequency conversions in the antenna focal area. In order to accomodate such solutions a dedicated module is provided.

The 'widespread system' is not considered only for the digital front-end but includes other possible 'dislocated' elements in support of the more advanced functionalities the DBBC4 offers. These elements are sensors which collaborate with the DBBC4 main unit to provide information in support of new functionalities. Some of those will be defined later in this document, while still a larger number will be defined during the period of development and even at a later stage even with the DBBC4 well operative in the field.

In order to describe the system, it is useful to start from the planned maximum capabilities for its main features:

- Input bandwidth up to: 8 x 28 GHz = 224 GHz aggregate in digital front- or back-end

plus 8 x 4 GHz = 32 GHz aggregate in ancillary digital front

total full aggregate = 256 GHz

- Output data rate up to: 1 Tbps @ 2-bit, 2 Tbps @ 4-bit, 4 Tbps @ 8-bit

- Modes: DSC (full band for data transfer), OCT (wide bands defined in the input band)

- New functionalities: Burst-mode, AI-mode, Net-to-Memory/Disk capability.

The general architecture shown in the picture below is pretty simple and recalls the previous DBBC versions but presents also new elements. Here are the main components:

- 100GCoMo module, analog conditioning element
- ADCore4 module, A/D converter, and digital data processor
- FILA100G, data storage, and standard network interface
- A-EYE, AI deep neural network controller
- DiFrEnd28, digital 28 GHz front-end
- DiFrEnd4, digital 4 GHz front-end
- CONE-x, a number of different elements with dedicated functionalities to operate with the A-EYE Controller
- ROD-y, a number of different elements with dedicated functionalities to operate with the A-EYE Controller.

The signal coming from the analog front-end as usual is required to be conditioned to be adapted before being converted into digital format. For such a purpose, the 100GCoMo module was adopted to perform the functionality of optimizing the amplitude, measuring the total power in pre-determined ranges inside the input band, and applying ad hoc filters, when required. The output signal from the 100GCoMo is directly forwarded to the analog input of the ADCore4.

Alternatively to the analog input, the signal coming from the analog part of the receiver can be digitized by the digital front-end with 28 GHz bandwidth DiFrEnd28 and inserted into the system through the digital input. While the 28 GHz band is an alternative to the analog input version, the 4 GHz bandwidth input can enter the system in digital format only using the DiFrEnd4.

The ADCore4 is the central element of the system and is able to perform the double functionality, analog to digital conversion and digital data processing. As mentioned, the signal can be inserted in both modes, digital or analog for the high band (28 GHz) or only digital for the low band (4 GHz). After conversion, or after the digital data acquisition, the functionality required by the observation to be performed is applied. The modes are DSC, OCT, and DDC, as already well known from the previous versions of DBBC even if relevant differences can be applied, still maintaining compatibility with the existing modes. More details are described in the section describing the ADCore4.

The data with the final bandwidth and data rate, ready to be transferred for correlation or to be recorded, is sent to the FILA100G for the final aggregate format in single or multi-stream, depending on the output data rate. Before the composition of the final format, it is possible to store an amount of data useful for the burst mode functionality. An additional possibility is offered by the data storage on external SSD disks. The direct connection net to PCI-e offers the possibility of skipping any intermedia data transfer with great advantage for the writing data rate.

Particular attention is to be dedicated to the novelty in the DBBC family systems offered by the DBBC4. The Artificial Intelligence controller, called A-Eye, represents a great potentiality in a number of functionalities to which it can be dedicated. This part presents a great potentiality in both single dish observations and VLBI activities. In order to operate in real time the controller can make use of a number of additional elements, named Cone and Rod. The first type is supporting functionalities of preprocessing more complex than the second, which is simply forwarding the required information to the mixed hardware-software deep neural network in order to perform the planned functionality. The A-Eye controller can then interact with the elements mentioned above in both directions to perform the required functionality. More details are described in the dedicated section of this document.

3 100GCoMo

When an analog receiver is coupled with the DBBC4 receiver it is required to adapt the signal with the analog to digital converter. The last component can have different requirements depending on the type adopted. In the DBBC4 we plan to have more components in order to satisfy different types of observations. The bandwidth considered is 28 GHz (class H), but there are plans to consider even wider bands. More details later.

The 100GCoMo is a module having the requirements: power level control in AGC and manual, plus total power measurement in defined frequency ranges. A dedicated section could be added on request for ad hoc band definition/blanking which can also be software controlled. Due to the high frequency range in-

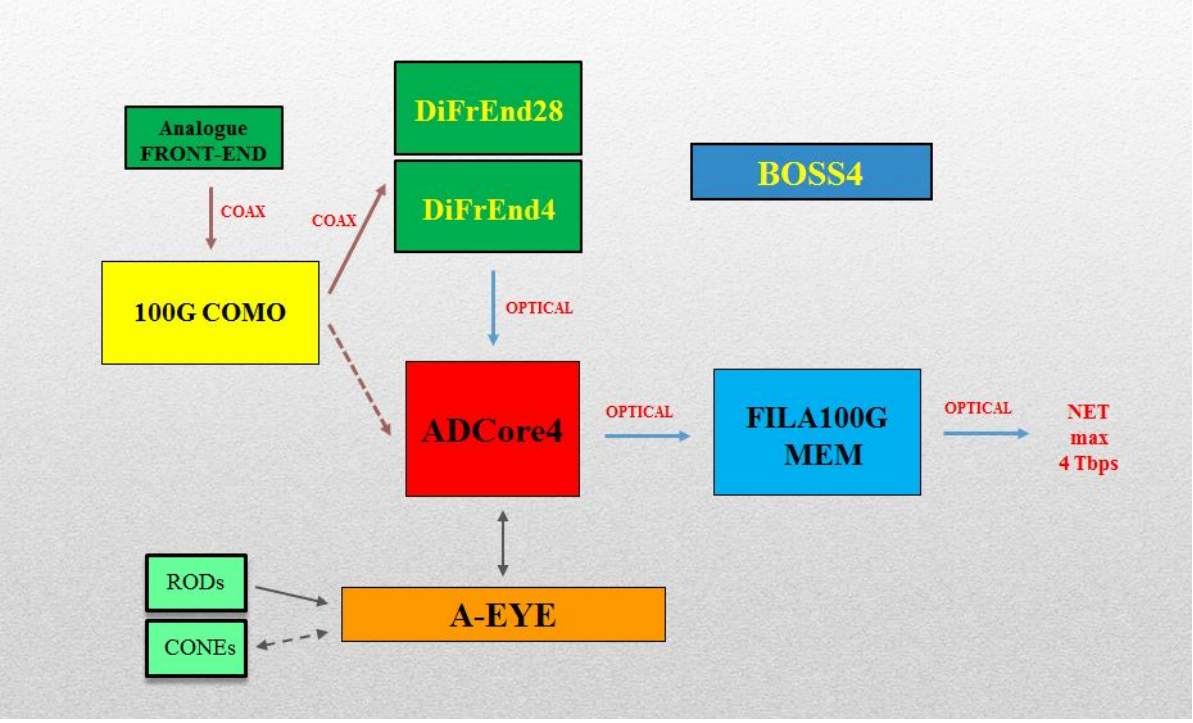

Fig. 2 DBBC4 architecture.

volved, a high class of components can be adopted to match the highest standards, and, for such a reason, the module will be customizable.

An additional novelty will be the introduction of wide band noise generators operating in different bands. This will simplify also the testing operations of the synchronous total power detector.

Communication to the general controller is realized using a serial connection with the option to be optical. This is required when the module is to be integrated into the analog section of the receiver and the digital front-end is adopted.

4 ADCore4

The module ADCore4 is a key element in the DBBC4 and again, similarly to the previous versions in the DBBC family, includes the functionality of the analog to digital conversion and data processing, but with state-of-the-art components and then capabilities.

The flexibility in defining the functionality is, as also in the DBBC4, an important element, and then a number of different options can be selected in order to optimize performance and requirements. Those include:

- ADC bandwidth, in the beginning with the possibility of 28 GHz and 4 GHz;

- Input in analog or digital format; in particular the 28 GHz sampler has both options, while the 4 GHz has only the digital format; when the digital front-end is adopted, the functionality of the 100GCoMo needs to be integrated into the analog front-end;

- More types of processing high-end FPGAs having the same pin-out; this allows adapting the complexity of the device to the process to be realized. The use of a socket to connect the FPGA device to the PCB board will be allowed.

The concept of a stack present in the previous DBBC version is still present but revised in order to optimize the length of the connections and improve the cooling. It could be divided into the functional elements: ADB4 Piggy-back unit, ADB4 Power unit, ADB4 Communication and Monitoring unit, CORE4 Main board, CORE4 Power unit, CORE4 Communication and Monitoring unit, IO4 Transceiver

unit, IO4 Transceiver Power unit, and IO4 Transceiver Communication and Monitoring unit.

The three main units ADB4, CORE4, and IO4 dialogue between each other, and all of them have two channels of communication with the control computer and the A-EYE controller.

The functionality is straightforward: the ADB4 unit required here when the data are inserted into the system in analog format is sampling what is conditioned by the 100GCoMo, and then the digital format of it is transferred to the CORE4 using an aggregate channel of serial lines. When the digital front-ends DiFrEnd28 and DiFrEnd4 are adopted, the information enters the system from the IO4 and is transferred to the CORE4. The required functionality between DSC, OCT, and DDC is then processed and available to the output channels of the IO4 in order to be sent out to the correlator/recorder or to the FILA100GMEM.

5 FILA100GMEM

This unit is useful for additional functionalities but could be skipped in case of modes which do not require them. The main additions involve:

- Memory banks for burst mode observations
- Direct writing of the received packets on SSD NVMe (PCIe mode) disk modules.

The schematic functionality with the main parts is made by the elements:

- Packetizer receiver
- Packetizer controller
- Packetizer transmitter
- Packetizer Communication and Monitoring unit.

The flow of data coming from the ADCore4 is received by the FILA100GMEM module, where the data are selected for a number of functionalities, which include reordering of channels, burst mode, and data storage. Additionally most of the functionalities present in the previous versions of the DBBC family packetized (FILA10G) are maintained.

The module can allocate a variable number of SSD NVMe units, expandable in memory capability as required by the burst mode duty cycle/number of channels/data rate. More FILA100GMEM modules can be used in parallel in order to improve the memory capability or the number of channels to be used in burst mode or to be recorded.

6 A-EYE Controller

Artificial Intelligence functionality meets the VLBI technology. The A-EYE module is a controller making use of artificial intelligence methods to perform a number of functionalities useful for the single dish and interferometric observations.

It will make use mainly of pre-trained networks, ready to be used for a number of functionalities which can include: RFI recognition and mitigation, extraction of non-statistical-noise signals, recognition of human-like extraterrestrial emissions, and other similar or different types of application.

The AI controller adopted for such functionality is a multi-CPU FPGA device optimized for this type of application. The general development working flow consists of a session dedicated to select and pre-train a suitable DNN (deep neural network) configuration with additional training dedicated to the specific purpose to be satisfied. This configuration is then synthesized in a hardware DNN with mixed software dedicated implementation. The entire synthesized solution is running in the above mentioned programmable device which is able to interact with the other units in the DBBC4 in order to drive specific functionalities in the different components of the system.

In order to be able to perform such operations the A-EYE controller can interact with supporter satellite elements, and by now, two of them have been identified: ROD and CONE. The ROD element is able to provide to the A-EYE elementary information, such as temperature, total power, or other physical parameters. The CONE acts like an edge processor, to provide already elaborated information, such as FFT ready data, visual decoded data, sequence recognition, and similar preprocessed elements useful for the AI functionality.

As additional functionality, the possibility of training the DNN in piggy-back mode during ordinary system operation will be implemented, to permit ad hoc network generalization.

Using the Multifunctional Digital Backend System on Radio Telescopes of Svetloe Observatory

Evgeny Nosov, Dmitry Marshalov, Leonid Fedotov, Yuri Bondarenko, Ismail Rahimov

Abstract The RT-32 and RT-13 VLBI radio telescopes of the Quasar network use various equipment for radio interferometric, radiometric, and spectral observations. The Data Acquisition Systems (DAS) currently used for Very Long Baseline Interferometry (VLBI) on the RT-32 telescopes at the Svetloe, Zelenchukskaya, and Badary observatories are narrow-band and do not fully meet modern requirements for the frequency bands of the recorded signals. The broadband DAS used on the RT-13 telescopes at the Badary and Zelenchukskaya observatories do not have sufficient functionality necessary to meet modern VGOS requirements. To solve these problems, the Institute of Applied Astronomy of the Russian Academy of Sciences (IAA RAS) has developed a Multifunctional Digital BackEnd system (MDBE) capable of replacing all the variety of DAS and other output devices used on the RT-13 and RT-32 radio telescopes.

Keywords Digital backend, Data Processing

1 MDBE Hardware Design

The task of a radio telescope backend is to capture the signals from receivers, make required processing with them depending on the type of observation being performed, and send the result to the recording system. The MDBE can contain up to 12 channels, or Digital Signal Processing (DSP) units, implementing this task with all output of the receiver. Each DSP unit contains a 10-bit analog-to-digital converter (ADC) digitizing the signal from the receiver, Field Programmable Gate Arrays (FPGAs) processing the digitized signal, and optical transceivers transmitting the output data to the recorder (Figure 1).

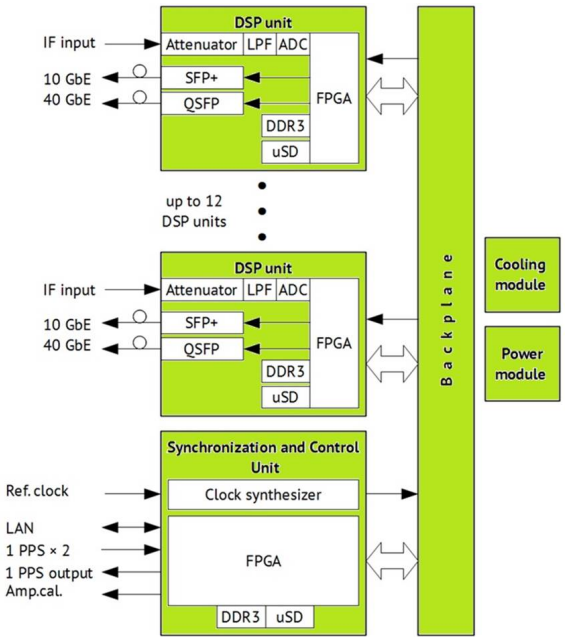

Fig. 1 MDBE Structure: DSP – digital signal processing unit, LPF – low-pass filter, ADC – analog-to-digital converter, IF – intermediate frequency signal, FPGA – field-programmable gate array, QSFP and SFP+ – quad and enhanced small form-factor pluggable optical transmitters, 1PPS – one pulse per second signal, LAN – local area network, Amp. cal. – amplitude calibration control signal, DDR3 – double-data-rate synchronous dynamic random access memory, and μSD – micro SD flash card.

The ADC works with a sample rate of 4096 MHz and 2 GHz input bandwidth. This allows the direct digitization of signals of the intermediate frequency (IF)

Institute of Applied Astronomy RAS

range coming from the receivers, which is either 100–1000 MHz for the RT-32 receiving system [1] or 1–2 GHz for the Tri-band [2] and ultra-wideband [3] receivers of the RT-13. The last modification of the ultra-wideband receiver has eight channels with an IF range from 50 MHz to 2 GHz. By using the MDBE, this allows observing in four bands located in a range from 3 to 16 GHz with a total recorded bandwidth of 8 GHz in each polarization, which gives a total data rate of 64 Gbps. The signal level of the DSP unit input can noticeably differ depending on the receiver type, the observing band, and the amount of radio-frequency interference (RFI) in the band. To prevent ADC saturation, the DSP unit contains a small analog frontend with a digital attenuator tuned in the range from 0 to 31.75 dB with a 0.25 dB step. The frontend also includes a low-pass filter to prevent aliasing from the second Nyquist zone. The FPGA captures the data stream from the ADC and performs signal processing, having onboard more than 400 thousands of flip-flops, 200 thousands of look-up tables, 900 DSP blocks, and an embedded dual-core ARM processor to implement all required DSP functions. By using embedded transceivers and SFP+ or QSFP modules, the output data are transmitted through fiber lines to the Recording and Data Buffering System [4]. One SFP+ module supports a 10 GbE link; that is enough for typical VLBI applications, using 2-bit quantization of output data. In case of need, an additional 40 GbE QSFP module allows transferring of the raw ADC data stream that can be used to implement even more sophisticated DSP algorithms in an external board or accelerator card. The DSP unit is implemented as the 14-layer printed circuit board (PCB), covered by a heat sink for heat removal and shielding noisy and sensitive parts of the circuit (Figure 2, shown without a heat sink).

Fig. 2 The DSP unit shown with the heat sink removed.

All DSP units are connected with the Synchronization and Control Unit (SCU) over a backplane. The SCU, based on the same FPGA as the one in DSP units, receives control commands through a 10/100/1000 Ethernet interface, either optical or copper, and communicates with all DSP units through dedicated 256 Mbps duplex links. The FPGA firmware of the SCU and DSP units can be loaded from the onboard microSD card or remotely over the network. Thanks to this, the developers can create perfectly tailored firmware for each observation mode and switch between them in seconds.

For clocking for all FPGAs and ADCs of the MDBE, the SCU contains a mezzanine module of a clock synthesizer that generates required signals. It accepts a 5, 10, or 100 MHz signal as a reference clock, normally from an H-maser. The generated clocks are distributed to all DSP units through aligned traces over highly stable clock distributors, located on the backplane. The resulting clock jitter measured from ADC clock input lies at the level of 250 femtoseconds and practically does not affect the signal-to-noise ratio of the digitized signals. Special care has been taken in the clock synthesizer design to ensure that the phases of generated clocks remain constant after resynchronization or a power reset. By this we keep constant the ADC clock phase that defines the position of sampling points in time and thus directly impacts the MDBE group delay. To indicate the first signal sample in a second, the SCU generates a special 1PPS (one pulse per second) signal and distributes it over all DSP units. The internal 1PPS signal can be synchronized by 1PPS coming from the observatory clock, and the delay between them is constantly measured.

To support continuous amplitude calibration, the SCU generates a control signal to switch on and off the calibration noise generator in the receiver. The frequency of the control signal can be set in a range from 2 Hz to 2 kHz. The SCU has identical PCB size and stackup, but the board is located in a covered cassette with a wider front panel to fit all required connectors (Figure 3).

The MDBE was originally designed to be installed inside the elevation cabin of the radio telescope, which simplifies the connection with the receivers and eliminates instabilities caused by transmission of sensitive analog signals over long coaxial or fiber lines through moving parts of the antenna's cable loops. The MDBE is based on a 19″ 3U Europac PRO chassis (Figure 4).

The chassis can fit one SCU and up to 12 DSP units that are inserted into the backplane along aluminum

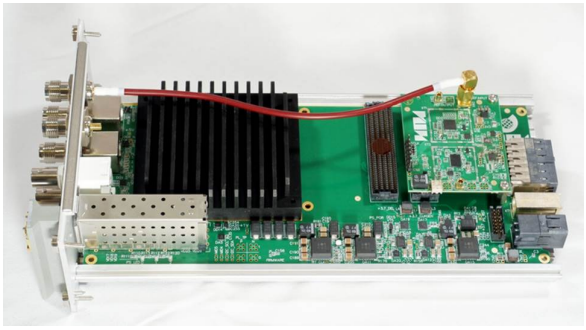

Fig. 3 MDBE Synchronization and Control Unit without a cover.

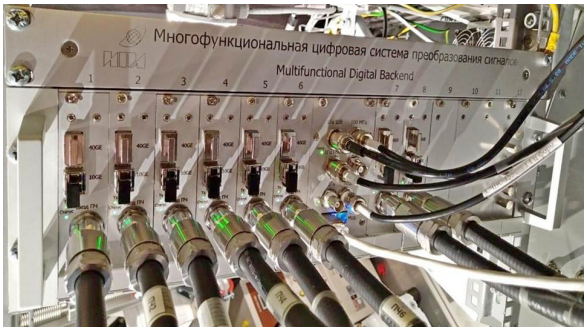

Fig. 4 The MDBE installed in the RT-13 radio telescope in the Svetloe observatory.

guide rails from the front side. Usage of the backplane and the guide rails makes the maintenance simple, as any unit can be easily replaced in a minute. To provide an adequate cooling of the system, there is a cooling module of 1U height, located above the main case. The module contains three regulated fans that are controlled by the SCU using a specialized three channel fan controller. All synchronization and control signals from the SCU pass to the DSP units through a backplane board. The SCU communicates with the DSP units through dedicated lines in the LVDS standard with a 256 Mbps data rate. The backplane includes distributors for the ADC and the FPGA clock signals, the 1PPS signal, and the ADC calibration signal.

2 MDBE Firmware Design

The data samples coming from the ADC have to be securely entered into the FPGA in correct order and without any glitches. The data samples come over four buses, and each consists of 10 data bits, an overrange flag, and an accompanying clock signal. The data rate of the coming samples is 1,024 MSPS per bus, which cannot be directly triggered by common FPGA resources because of operating frequency limits. To reduce the frequency the embedded deserializers are used, which convert input serial bit streams to a number of parallel streams with a respectively lower frequency, 256 MHz in our case. That gives totally 16 parallel samples of data on the output of the deserializer block, which further come to the downconverter block, where the main processing is performed. The block of downconverters cuts the interesting parts of the spectrum from the input band, shifts them to baseband, and filters them to form the required bandwidth. There is separate firmware created to implement either one 1,024 MHz channel or one 512 MHz channel or up to sixteen 32 MHz channels. The observations in wideband mode usually do not require fine frequency tuning in the backend, because the receiving system can tune frequencies with at least a 400 kHz step. In 1,024-MHz-bandwidth mode, the MDBE allows a choice between the ranges 0–1,024 MHz or 1,024–2,048 MHz. In 512-MHz-bandwidth mode the channel can be set anywhere in a range from 0 to 2,048 MHz with a 128 MHz step. For narrowband modes fine frequency tuning is required. The firmware supports a 10 kHz tuning step, which provides compatibility with legacy backends. The quantizer performs “requantization” of the samples from the downconverters to 2 bits, using the root mean square value of the signal as a threshold. The quantized samples come to the output stage that packs them into VDIF packets, forms Ethernet frames with the required upper-level headers (IP, UDP) and sends the resulting frames to the SFP+ transceiver. The output stage currently supports up to an 8,192 Mbps data rate through a single 10 GbE link. The VDIF formatter packs the input data stream into packets of the required size with a 32-byte header. The payload length can be set up to 8,192 bytes, which still fits to Jumbo frame limitations while simplifying recording of the data stream by reducing the number of packets per second. The Signal Analysis Functions combine several auxiliary blocks that are not directly involved in the signal path but are used to obtain various useful information about the signal. The overrange counter uses a special overrange bit of the ADC output buses to calculate the percentage of the ADC overflows. The ADC calibrator calculates the degree of discrepancy

between the samples received from the first and other ADC cores. The power meter is used to calculate the power of the samples received from the ADC. The PCAL extractor clears PCAL tones of noise, making them available for further analysis. The data exchange within the system is performed by a specially designed Control Link protocol, which is implemented in the FPGA. The communication protocol includes in each message a compact header containing the clock word, payload length, and message type. The integrity of the messages is monitored using a CRC32 checksum. The Direct Memory Access (DMA) controller provides a fast link between the Control Link and the allocated DDR3 memory area, allowing the processor to interrupt only when a message has been fully received and placed in memory or fully transferred from memory and sent. The control functions are implemented using the processing system based on an ARM Cortex-A9 processor. The program, written in C, performs the following functions:

- regularly reading onboard sensors and estimating the system health based on the values;
- setting the parameters implemented in the FPGA blocks and reading the required data from them;
- taking part in synchronization procedures;
- executing outside commands coming from the SCU itself or forwarded by the SCU from a remote host;
- receiving from the SCU new firmware and loading it;
- controlling internal registers of the SFP, the QSFP, and the ADC;
- other minor functions.

Currently the following VLBI modes are implemented in the DSP MDBE: Wideband 1024 MHz, Wideband 512 MHz, and VGOS mode with up to 16 channels with bandwidths of 32, 16, 8, 4, 2, and 0.5 MHz. The narrowband mode allows compatibility with "legacy" backends and allows the MDBE to be used to upgrade the RT-32 antenna. In addition, the MDBE firmware for single-dish modes for spectrometric observations [5] and radiometric observations with RFI rejection in the frequency domain is currently under active development. A more detailed description of the software and hardware implementation of the MDBE system can be found in [6]. The following are the main features.

3 Experimental Use of the MDBE

To test the compatibility of the MDBE with standard broadband systems, an experimental session of VLBI observations, r4121c, was conducted on April 30, 2020 based on Svetloe-Zelenchukskaya-Badary with the recording of signals in the 512 MHz wideband in the S and X frequency bands. As the result of processing the signals on the RASFX correlator, correlation responses with a signal-to-noise ratio (SNR) from 52.7 to 299 in the X-band and from 31.5 to 131.1 in the S-band were obtained for all sources (Figure 5). The values obtained are in good agreement with those predicted by theory.

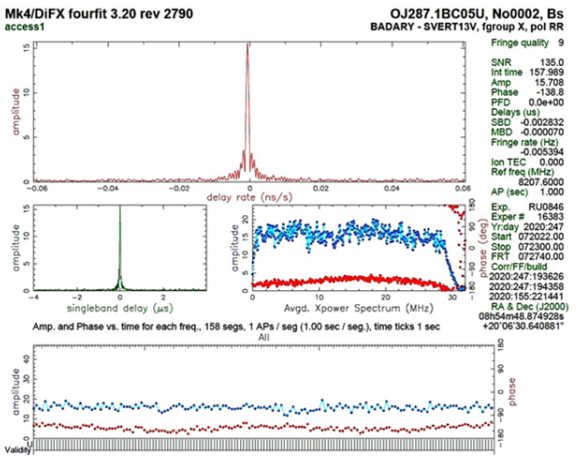

Fig. 5 An example of the correlation response from the OJ287 source in channel No. 9 during observations on the Svetloe–Badary radio interferometer using a narrow-band DAS and the MDBE.

The MDBE operation on the RT-13 radio telescope in the Svetloe observatory was checked during the international VLBI observing session R1972 of the IVS network on November 9, 2020. The IVS network operated with the standard geodesic frequencies set in the S- and X-bands and a sample of 16 frequency channels with 8 MHz width for each. For all 384 scans of observations in which the RT-13 radio telescope with MDBE participated, correlation responses with all foreign radio telescopes participating in the observations were registered.

In 2021 several experiments of radar observations of the Moon were carried out in the Svetloe Observatory. These experiments involved the 35-meter antenna

(DSA 3) to transmit and the RT-13 radio telescope to receive echoes from the Moon. The echo was recorded using the MDBE with 2-bit quantization in two separate channels in left and right circular polarizations. The system operated in the VGOS mode with 32 MHz bandwidth and 1,336 MHz in the IF band. The observation data were transmitted via high-speed optical communication lines from the observatory to the server of the IAA RAS Data Processing Center in St. Petersburg. As a result the power spectra of the echo signal reflected from the lunar crater "Archimedes" in left and right circular polarizations (Figure 6) and a radar image of the Moon at 4.2 cm wavelength [7] were obtained.

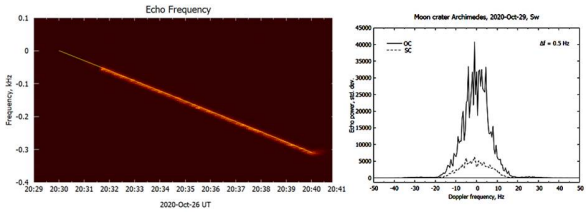

Fig. 6 Spectrogram and echo power spectra of the Moon obtained with the MDBE.

In December 2020, the MDBE was put into operation on the RT-13 radio telescope at the Svetloe Observatory. As part of the RT-13 equipment, the MDBE participated in all regular VLBI observations to determine UT1-UTC. From December 2020 more than 1,000 sessions of VLBI observations under the "R" program in the S- and X-bands, as well as more than 250 sessions under the "X" program in the S/X/Ka bands, were conducted with the MDBE's participation.

4 Conclusions

Experimental operation of this system at the Svetloe Observatory has shown that, in terms of its parameters and characteristics, the MDBE surpasses the DAS and the existing backends previously used on the radio telescopes of the Quasar VLBI Network. The MDBE provides signal conversion for both broadband and narrowband registration during VLBI observations, making it possible to conduct radar observations of the Moon. The use of the MDBE will allow in the future abandonment of separate recording systems for radiometric and spectral observations. The MDBE provides observations in various modes without replacing equipment and allows improvement of the obtained results.

Table 1 Basic parameters of the MDBE.

Number of DSP units	Up to 12
ADC sample rate	4096 MSPS
Input bandwidth	2 GHz
Full scale input power	0 dBm (1 GHz sine wave, open attenuator)
DSP unit output	10 GbE SFP+ module, 40 GbE QSFP module
DSP unit core chip	FPGA: 900 multipliers, 400K flip-flops, embedded ARM Cortex-A9 processor
Memory	512 MB (DDR3), microSD card
Control interface	10/100/1000 Ethernet, fiber or copper
Debug interface	USB-JTAG and USB-UART bridge
Input synch. signals	5, 10 or 100 MHz, 2 × 1PPS
Weight	15 kg (eight channel version)
Size	48 × 35 × 18 cm (L × W × H)
Power supply	220 VAC, 440 W

References

1. A.V. Ipatov, N.E. Kol'tsov, A.V. Krokhalev, A Radiometric System for the РТФ-32 Radio Telescope. *Instrum. Exp. Tech.*, 48, doi:10.1007/s10786-005-0084-0, pages 482–490, 2005.
2. V. Chernov, A. Evstigneev, O. Evstigneeva, D. Ivanov, A. Ipatov, I. Ipatova, E. Khvostov, A. Lavrov, V. Mardyshkin, I. Pozdnyakov, Y. Vekshin, M. Zotov, The S/X/Ka Receiving System for Radio Telescope RT-13 of the 'Quasar' VLBI Network. *IAA RAS Trans.*, 41, pages 79–84, 2017.
3. A. Evstigneev, O. Evstigneeva, E. Khvostov, A. Lavrov, V. Mardyshkin, I. Pozdnyakov, The Ultra-Wideband Receiver System for RT-13 Radio Telescope IAA RAS 'Quasar' Network. *IAA RAS Trans.*, 41, pages 49–52, 2017.
4. I.A. Bezrukov, A.I. Salnikov, V.A. Yakovlev, A.V. Vylegzhanin, A Data Buffering and Transmission System: A Study of the Performance of a Disk Subsystem. *Instrum. Exp. Tech.*, 61, doi:10.1134/S0020441218040164, pages 467–472, 2018.
5. S.A. Grenkov, N.E. Kol'tsov, A Backend System for Registering Narrowband Cosmic Radio Emissions., *Instrum. Exp. Tech.*, 63, doi:10.1134/S0020441220040041, pages 561–566, 2020.
6. E. Nosov, D. Marshalov, L. Fedotov, Y. Sheynman, Multifunctional Digital Backend for Quasar VLBI network. *Journal of Instrumentation*, V.16, doi:10.1088/1748-0221/16/05/p05003, P05003, 2021.
7. Yu.S. Bondarenko, D.A. Marshalov, S. Makarchuk, Radar images of the Moon at 4.2-cm wavelength, *53rd Lunar and Planetary Science Conference*, 2131, 2022.

Session 2

Observations, Operation and Correlation

IVS IAG SUOMEN AKATEMIA

NLS FINNISH GEOSPATIAL RESEARCH INSTITUTE FGI

Current Status of the EU-VGOS Project

Ezequiel Albentosa[1], Walter Alef[2], Simone Bernhart[3,14,2], Johannes Böhm[4], Ruben Bolaño González[5], Yoon K. Choi[3,14,2], Thomas Gansmoe[5], Susana García Espada[5], Cristina García Miró[6], Anastasiia Girdiuk[7], Javier González García[6], Silje A. Groøslie Wennesland[5], Jakob F. Gruber[4], Rüdiger Haas[8], Roger Hammargren[8], Robert Heinkelmann[9], Frédéric Jaron[4,2], Niko Kareinen[10], Ann-Silje Kirkvik[5], Hana Krásná[4], Elena Martinez[6], Iván Martí-Vidal[1], Axel Meldahl[5], Alexey Melnikov, Sadegh Modiri[7], Alexander Neidhardt[11], Axel Nothnagel[4], Olivia Panzenböck[4], Victor Pérez[12], Leonid Petrov[13], Christian Plötz[14], Helge Rottmann[2], Tuomas Savolainen[15,16,2], Matthias Schartner[17], Torben Schüler[14], Harald Schuh[9,18], Benedikt Soja[17], Eskil Varenius[8], Pablo de Vicente[6], Jan Wagner[2], Ming H. Xu[15,16], Nataliya Zubko[10] (The EU-VGOS Collaboration), Mark Kettenis[19], Saho Matsumoto[20], Richard Porcas[2], Des Small[19], Marjolein Verkouter[19] (External Collaborators)

1. Dpt. Astronomia i Astrofísica, Unversitat de València, C/Dr. Moliner 50, E-46100 Burjassot, Valencia, Spain
2. Max-Planck-Institut für Radioastronomie, Auf dem Hügel 69, 53121, Bonn, Germany
3. Reichert GmbH, Hittorfstr. 26, 53129 Bonn, Germany
4. Department of Geodesy and Geoinformation, Technische Universität Wien (TU Wien), Wiedner Hauptstraße 8-10, 1040, Vienna, Austria, e-mail: Frederic.Jaron@tuwien.ac.at
5. Geodetic Institute, Norwegian Mapping Authority, Hønefoss, Norway
6. Observatorio de Yebes (IGN), Apartado 148, E-19180 Yebes, Spain
7. Federal Agency for Cartography and Geodesy (BKG), Section G 1 - General Issues, Combination of Space Techniques, Richard-Strauss-Allee 11, 60598 Frankfurt am Main, Germany
8. Department of Space, Earth and Environment, Chalmers University of Technology, Onsala Space Observatory, SE-439 92, Onsala, Sweden
9. Helmholtz Centre Potsdam, GFZ German Research Centre for Geosciences, Telegrafenberg, D-14473 Potsdam, Germany
10. Finnish Geospatial Research Institute, Department of Geodesy and Geodynamics, National Land Survey of Finland, Vuorimiehentie 5, 02150 Espoo, Finland
11. Geodetic Observatory Wettzell, Technical University of Munich, FESG, Sackenrieder Str. 25, 93444 Bad Kötzting, Germany
12. Observatorio Astronómico Nacional de España, Madrid, Spain
13. NASA Goddard Space Flight Center, Greenbelt, MD 20771, USA
14. Geodetic Observatory Wettzell, Federal Agency for Cartography and Geodesy (BKG), Sackenrieder Str. 25, 93444 Bad Kötzting, Germany
15. Aalto University Metsähovi Radio Observatory, Metsähovintie 114, 02540, Kylmälä, Finland
16. Aalto University Department of Electronics and Nanoengineering, PL 15500, 00076, Aalto, Finland
17. ETH Zürich, Robert-Gnehm-Weg 15, 8093, Zürich, Switzerland
18. Technische Universität Berlin, Institute of Geodesy and Geoinformation Science, Berlin, Germany
19. Joint Institute for VLBI ERIC (JIVE), Oude Hoogeveensedijk 4, 7991 PD Dwingeloo, The Netherlands
20. Geospatial Information Authority of Japan, 1 Kitasato, Tsukuba, Japan

Abstract The EU-VGOS project began in 2018 with the aim of using the VGOS infrastructure in Europe to investigate methods for VGOS data processing. The project is now structured into Working Groups dealing with operations (stations), e-transfer, correlation and post-processing, and analysis. This is a report on the status of the project.

Keywords VGOS, Operations, E-transfer, Correlation, Analysis

1 Introduction

The EU-VGOS project began in 2018 with the aim of determining the optimal methods for VGOS data processing [1]. It is currently a collaboration of about 40 individuals working at different institutes, mainly in Europe but elsewhere around the world.

The structure of the EU-VGOS project is shown in Figure 1. Besides the project management team, there are four Working Groups (WGs) focusing on different steps of the VLBI processing chain. WG Operations coordinates procedures at the VLBI stations and improves the availability of calibration data. WG E-Transfer develops e-transfer tools and carries out performance tests. WG Correlation covers topics related to the transformation of raw observational data into databases for further analysis, with a focus on novel calibration and fringe-fitting methods. WG Analysis analyzes VGOSDBs resulting from EU-VGOS

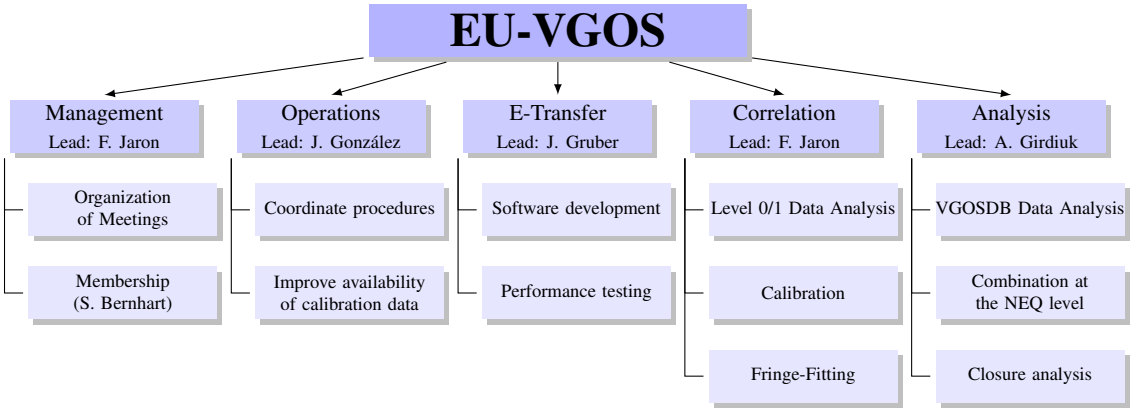

Fig. 1 Structure of the EU-VGOS project.

sessions and also looks into the combination at the normal equation level and closure analysis.

2 WG Operations

The locations of the EU-VGOS antennas are shown as filled circles in Figure 2. Five stations are VGOS-ready, four stations are going to be ready soon. The stations that are ready now are the twin telescopes in Onsala (one of them is currently under maintenance), Wettzell South (Wettzell North will also be ready this year), Yebes, and Ishioka (Japan). Details about the EU-VGOS stations are given in Tables 1 and 2.

3 WG E-Transfer

One important task of this WG is the development and testing of e-transfer tools. Currently there are four options for e-transfer: 1) `jive5ab` + `m5copy`; 2) the newly developed e-transfer daemon/client `etc/etd`; 3) it is possible to combine `etc/etd` with `m5copy`; 4) `tsunami`. Transfer speeds may depend on the data being transmitted. For instance, there can be a large overhead for the transfer of relatively small files. This WG carries out network performance tests under various conditions. Other active investigations currently include the MTU 9000 capability for global e-shipping routes, TCP/UDP benchmarking with different TCP congestion algorithm choices (e.g., Google BBR), and e-shipping limitations due to a particular file system and ethernet topology properties. The duration that it takes to transfer the data from the stations to the correlators is still a bottleneck to be resolved for continuous VGOS operations. For a global VGOS session, data transfer can take up to one month. Reasons for this delay include data rates that are in practice below theoretical values, but also logistical issues can delay the transfer. A subject of this WG is to address these issues. The locations of all institutes that correlate EU-VGOS data are shown in Figure 2 as filled squares, with their network speed in Gb/s.

4 WG Correlation

The scope of this WG is any data processing that is necessary or possible in order to transform raw observational (level 0) VLBI data into databases for further analysis (level 2). The different processing steps are shown in Figure 3. We receive level 0 data from the stations, mainly via e-transfer. Some stations provide the data with frequency bands split into separate files, known as *multi-file* data. Before, these had to be merged prior to correlation (using the tool `vmux`). Multi-file correlation (`DiFX`: multiple datastreams per station) and can now avoid this time consuming step.

We correlate the data using DiFX version 2.5.4, resulting from discussions within our WG. It collected a loose set of post-2.5.3 source code patches and certain DiFX-2.6 features into a consistent DiFX release. Key changes for VGOS: support for multi-file; fixes to phase cal tone extraction; Mk4 and FITS-IDI converter support/fixes for multi-file phase cal data; sup-

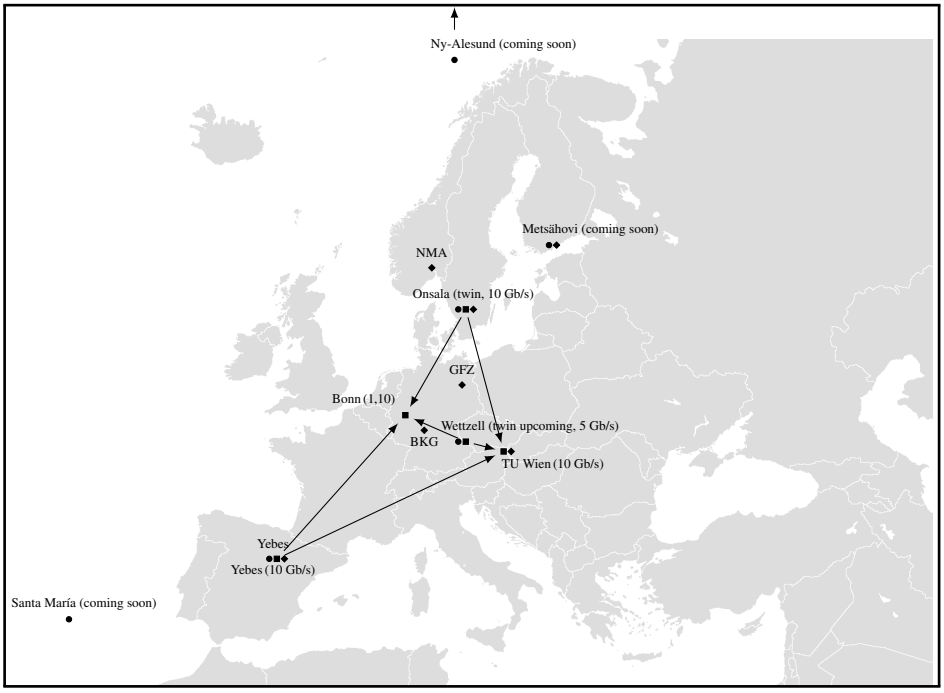

Fig. 2 Map showing the location of infrastructure related to the EU-VGOS project. Approximate antenna positions are indicated by filled circles, Correlation Centers are indicated by filled squares, and Analysis Centers are shown as filled diamonds. Where there are multiple activities at the same site, the corresponding symbols are shown next to each other. Ishioka also participates in the project from Japan, although its position is out of the map bounds.

Table 1 Details about the stations that are part of the EU-VGOS network.

Site	Backend	Recorder	Injection	80 Hz cap	Phase-cal	Cable-cal
Ready						
Ishioka	ADS3000+	K5VSI	Pre-LNA	No	5 MHz	Cable
Onsala East	DBBC3	Flexbuff	Pre-LNA	Yes	5 MHz	CDMS
Onsala West	DBBC3	Flexbuff	Pre-LNA	Yes	5 MHz	CDMS
Wettzell South	DBBC2 / DBBC3	Mark6 / Flexbuff	Post-LNA	No[1]	5 MHz	Cable
Yebes	RDBE-G	Mark6	Pre-LNA	Yes	10 MHz	CDMS
Coming soon						
Metsahövi	DBBC3	Flexbuff	Pre-LNA	Yes	10 MHz	CDMS
Ny-Ålesund	DBBC3	Flexbuff	Pre-LNA	Yes	10 MHz	CDMS
Santa María	Waiting for DBBC3	Mark6	Pre-LNA	Yes	10 MHz	CDMS
Wettzell North	DBBC3	Mark6 / Flexbuff	Post-LNA	No	5 MHz	Cable

All stations are equipped with a noise diode for amplitude calibration.
[1] 80-Hz noise diode is possible with the DBBC3, only power splitters pending to be ready.

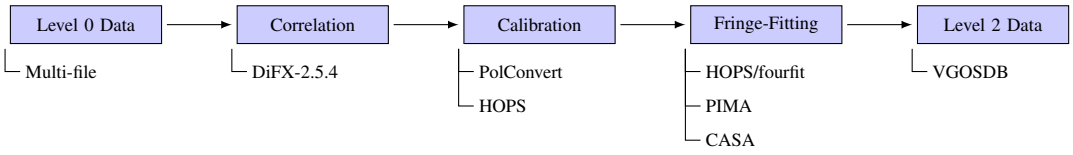

Fig. 3 Data processing steps of the WG Correlation.

Table 2 Details about the stations that are part of the EU-VGOS network (continuation of Table 1).

Site	Sessions observed	Data format	Current status
Ishioka	7	Singlethread-Multifile (4 datastreams/scan)	Ready
Onsala East	38	Singlethread-Multifile	Ready
Onsala West	28	Singlethread-Multifile (8 datastreams/scan)	Maintenance, DBBC3 in Bonn for cooling upgrade
Wettzell South	37	Multithread (needs vmux'ing[2])	Ready[3]
Yebes	37	Multithread (needs vmux'ing[2])	Ready
Metsähovi	0	-	Not ready, switch to VGOS operations in 2023
Ny-Ålesund	0	Singlethread-Multifile (planned)	Not ready, Field System integration pending
Santa María	0	Multithread (needs vmux'ing[2])	Not ready
Wettzell North	0	Multithread (needs vmux'ing[2])	Not ready, switch to VGOS operations in 2022

[2] Vmux operation converts multithread data into singlethread (typically for VGOS: $4 \times 16 \rightarrow 1 \times 64$). This operation takes approximately as long as the recording itself (!).
[3] Observing with DBBC2 systems

port for H/V linear polarization labels; a new HOPS software version; fixed DiFX native support for Mark 6 recorders.

After correlation, to combine the linear polarization products to Stokes *I* for fringe-fitting, complex cross-polarization bandpass calibration is necessary. We currently investigate two methods: the algorithm implemented in PolConvert [2], and the HOPS VGOS pipeline [3]. After that we use fourfit for Stokes *I* fringe-fitting, but we also consider the future use of other software packages. We export databases in the form of VGOSDB for further analysis.

One of our goals is to enable true Stokes *I* fringe-fitting, as opposed to pseudo Stokes *I*, implemented in the HOPS pipeline. This is achieved by performing a full complex cross-polarization gain calibration, i.e., making use of both amplitude and phase of the cross gains. HOPS only takes into account the phases. For this reason we expect an increase in data quality from true Stokes *I*. In addition to calibration, PolConvert converts the data from linear to circular polarization, which is more convenient for fringe-fitting.

Total group delays resulting from fringe-fitting polconverted data are plotted against the results from pseudo Stokes *I* in the left panel of the upper row of Figure 4. The results from both methods are consistent. The one-sigma uncertainties, shown in the middle panel, are also consistent, except for some larger differences, mainly occurring at large uncertainties. Also the signal-to-noise ratio, shown in the right panel, is very similar over a range from 0 to 4,000. The bottom row shows group delay differences as a function of time per baseline. In conclusion, the results from both methods are consistent, and the differences seem to be mostly noise-limited, but there are also hints for some systematic trends. The constant offset of the group delays is absorbed by the clock model in the final geodetic analysis and is not a matter of concern.

Table 3 Analysis Centers of the EU-VGOS project.

Institute	AC	Software
Finnish Geospatial Research Institute	FGI	VieVS
German Federal Agency for Cartography and Geodesy	BKG	Calc/Solve
German Research Centre for Geosciences	GFZ	PORT
Metsähovi Radio Observatory	MRO	Calc/Solve
Norwegian Mapping Authority	NMA	WHERE
Onsala Observatory	OSO	C5++, ASCOT
TU Wien	VIE	VieVS
Yebes Observatory	YBS	VieVS

5 WG Analysis

The main goal of this WG is to investigate how the different calibration and fringe-fitting methods affect the geodetic solutions. At the moment several Analysis Centers (ACs, Figure 2) process the available data based on their specific expertise. Most of the ACs have gained their experience by being member of the IVS Community. The others are organized newly at the observatories to follow their own project goals, which are aligned with the EU-VGOS project. Some Analysis Centers develop their own software: VieVS at TU Wien, PORT at GFZ, ASCOT at OSO, and WHERE at NMA; the others use existing ones as listed in Ta-

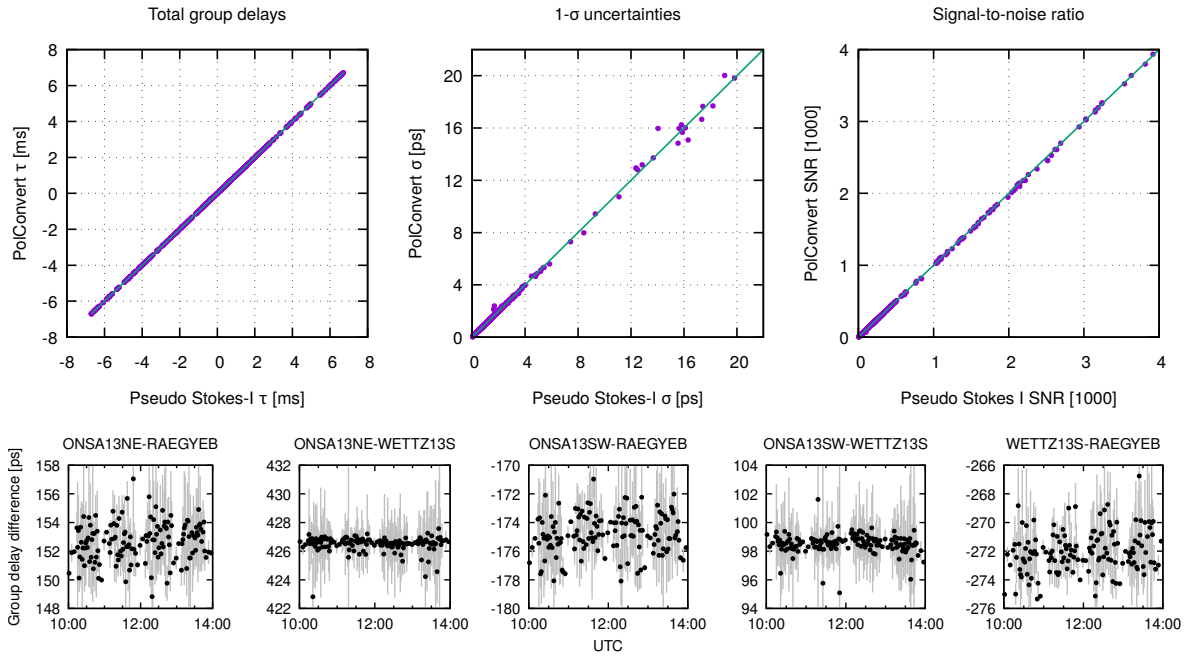

Fig. 4 Comparison of pseudo Stokes *I* and PolConvert on the observable level.

ble 3. All Analysis Centers use nuSolve as the first analysis step for interactive data reprocessing. Every VLBI analysis software is built to be as independent as possible. For this reason, the necessary a priori corrections and their own delay models are employed instead of the pre-computed model by nuSolve. That implies also an implementation of the solution parametrization such as selection of the reference clock, clock model, tropospheric model and station positions, source coordinates, and EOP.

6 Conclusions and Outlook

The EU-VGOS collaboration continues to investigate processing methods for VGOS data. We are currently planning new observations with the aim of improving calibration and to quantify the impact of calibration methods on the geodetic analysis results.

Acknowledgements

We thank Alan Roy from MPIfR for reading the manuscript and for providing very useful feedback. The computational results presented were achieved in part using the Vienna Scientific Cluster (VSC). This research was funded in part by the Austrian Science Fund (FWF) [P31625].

References

1. Alef W., Anderson J. M., Bernhart S., de Vicente P., González García J., Haas R., La Porta L., et al., 2019, *The EUropean-VGOS Project*, Proceedings of the 24th European VLBI Group for Geodesy and Astrometry Working Meeting, 17-19 March 2019, Las Palmas de Gran Canaria, Spain, Eds. R. Haas, S. Garcia-Espada, and J. A. López Fernández, ISBN: 978-84-416-5634-5, pp. 107-111
2. Martí-Vidal I., Roy A., Conway J., Zensus A. J., 2016, *Calibration of mixed-polarization interferometric observations. Tools for the reduction of interferometric data from elements with linear and circular polarization receivers*, A&A, 587, A143. doi:10.1051/0004-6361/201526063
3. Niell A., Barrett J., Burns A., Cappallo R., Corey B., Derome M., Eckert C., et al., 2018, *Demonstration of a Broadband Very Long Baseline Interferometer System: A New Instrument for High-Precision Space Geodesy*, RaSc, 53, 1269. doi:10.1029/2018RS006617

The Australian VGOS Observing Program

Ahmad Jaradat[1], Lucia McCallum[1], Jamie McCallum[1], Tiege McCarthy[1]

Abstract The AuScope VLBI array is entering the VGOS era: the Hobart 12-m and Katherine 12-m stations have already been upgraded with VGOS systems and Yarragadee will follow soon. However, due to some technical differences, the AuScope stations have not routinely joined the IVS VGOS sessions yet. The AUV observing program is a series of VGOS sessions with fortnightly cadence, aiming eventually at achieving mm precision. The scheduling is being continuously enhanced; for example, session duration was adjusted to 12 hours on a single baseline to optimize for results versus total data volume. Additionally, source behavior is a concern, and we have already identified several unsuitable sources due to bad performance in higher frequency bands (10–12 GHz). These sessions have been used to provide feedback about baseline sensitivity across frequency bands, identify RFI, and adjust the channels distribution accordingly. This paper presents the progress of the AuScope VLBI array's transition toward the VGOS era.

Keywords VGOS, Observing, Scheduling, Correlation, Manual phasecal

1 Introduction

The year 2011 saw the establishment of the AuScope Very Long Baseline Interferometry (VLBI) array, operated by the University of Tasmania (UTAS). The AuScope VLBI array consists of three stations: Hobart (Hb), Katherine (Ke), and Yarragadee (Yg). These stations are fast slewing (5°/s in azimuth and 1.25°/s in elevation), and small telescopes (12 m) to serve the next generation of VLBI, known as the VLBI Global Observing System (VGOS) [Petrachenko et al., 2009]. This new observing system is distinguished by a larger number of observations, a wider spanned bandwidth, and a higher data rate. VLBI, with other space-geodetic techniques, is utilized to achieve the Geodetic Global Observing System (GGOS) reference frame which aims for an accuracy of 1 mm and 0.1 mm/y stability [Plag et al., 2009]. The GGOS reference frame became essential to observe and monitor the Earth and its processes properly. Initially the AuScope VLBI array was commissioned with S/X receivers and participated in the International VLBI Service for Geodesy and Astrometry (IVS) [Nothnagel et al., 2017] experiments regularly such as the rapid-turnaround (R1, R4) sessions. Hb and Ke moved to VGOS in 2017 and 2019, respectively; however, they have not routinely observed in VGOS mode. In 2021, the Australian VGOS observing program (AUV) was initiated by carrying out a series of VGOS experiments on the baseline Hb-Ke aiming for mm precision and determine the optimal way of reaching this goal.

2 Scheduling

AUV operates at a frequency range of 3–13.5 GHz. In this range, neither the system equivalent flux density (SEFD) of the stations nor the fluxes of the sources are well known. VieSched++ [Schartner and Böhm, 2019] is used to schedule the AUV sessions. Fortnightly ca-

1. University of Tasmania, Private Bag 37, Hobart 7001, Australia

Table 1: Summary of the carried out AUV sessions.

Session	Status	Scan length	Comments
auv001	Failed	60 s	Power outage
auv002	Correlated	60 s	
auv003	Correlated	60 s	
auv004	Correlated	60 s	New frequency setup
auv005	Correlated	45 s	phasecal off
auv006	Correlated	45 s	
auv007	Failed	45 s	Ke cryo failure
auv008	Correlated	45 s	
auv009	Observed	30 s	
auv010	Observed	30 s	New frequency setup
auv011	Observed	30 s	New frequency setup
auv012	Observed	20 s	

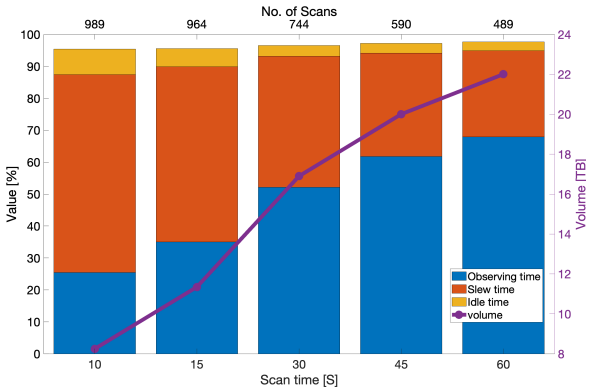

Fig. 1: The relationship between number of scans, slewing time, and the recorded data volume for a 12-h session, with 6-Gbps recording rate, on the baseline Hb-Ke. The left y-axis shows the percentage values of the bar plot. The right y-axis is the data volume in Terabyte (TB) corresponding with the line plot. The upper x-axis presents the number of scans corresponding with scan time in the lower x-axis.

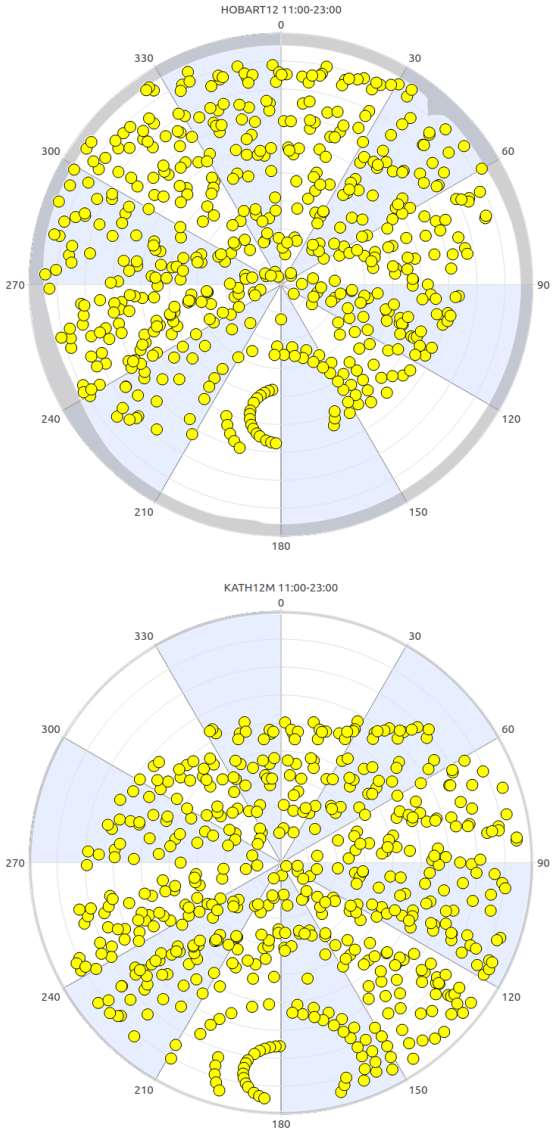

Fig. 2: Sky plot for Hb and Ke during the 12-hour auv008 session. This session has a total of 552 scans and 79 radio sources.

dence, 12 hours duration, 0.8 Jy minimum source flux density, and fixed scan length are the primary scheduling parameters for AUV. The initial scan length was set to 60 seconds and then gradually reduced. Decreasing the scan length is beneficial in two ways: firstly, it increases the number of scans per session, and secondly, the total recorded data volume is reduced. As illustrated in Figure 1, the number of scans increases with decreasing the scan length, as expected. Moreover, the data volume is decreased because the station spends more time slewing between the scans rather than on source time. This is particularly a good point given that data volume is one of the main VGOS limitations. For instance, data recorded in a 24-hour session with 15-s scan length is approximately equal to the recorded data volume in a 12-hour session with 60-s scan length. Figure 2 shows an example of the sky plot for a 12-hour session. This session observed 79 different radio sources with 552 scans and 45-s scan length.

Furthermore, the scheduler is forced to include a calibration scan for a very bright source every two

hours with double the scan time of the regular scans. These calibration scans are used later in the correlation and post processing.

3 Observing Mode

Both stations are equipped with a QRFH receiver covering 2.2–14 GHz frequency range. The signal sent via fiber optic to the control room to be band-pass filtered into three bands and input into DBBC3 [Tuccari et al., 2018] for down conversion and sampling. The data recorded using jive5ab[1] onto a Flexbuff machine in VDIF format, with six threads and two-bit sampling.

Each input band to the DBBC3 generates eight channels (using DDC mode with v124 firmware), see Figure 3. DBBC3 at Hb has four bands (32 channels) with 32-MHz bandwidth, whereas DBBC3 at Ke has only three bands (24 channels) with 32-MHz bandwidth as well. For now, the AUV observing mode is using three bands (24 channels), 32-MHz bandwidth, linear dual polarization (X and Y), and 2-bit sampling, which leads to a 6 Gbps recording rate. These bands have a simultaneous 4-GHz input bandwidth with frequency ranges 3–7 GHz, 6–10 GHz, and 9.5–13.5 GHz. The baseband channels can be selected freely within the band.

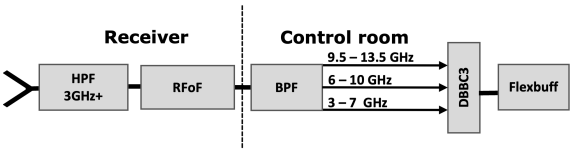

Fig. 3: AUV signal chain.

Exploiting the flexibility of the DBBC3, the frequency setup has changed several times to avoid Radio Frequency Interference (RFI) and to optimize the lag delay function by minimizing the side lobes and the width of the main lobe. Figure 4 presents a comparison between the IVS-VO frequency setup (32 channels) and the latest frequency setup used in AUV (24 channels). The IVS-VO mode has a very high side lobe (90% of the main lobe) where the AUV setup has a very low side lobe (59% of the main lobe) and narrower main lobe (10% narrower). The differential ionospheric (dTEC) estimation function shows a similar improvement with respect to sidelobe performance.

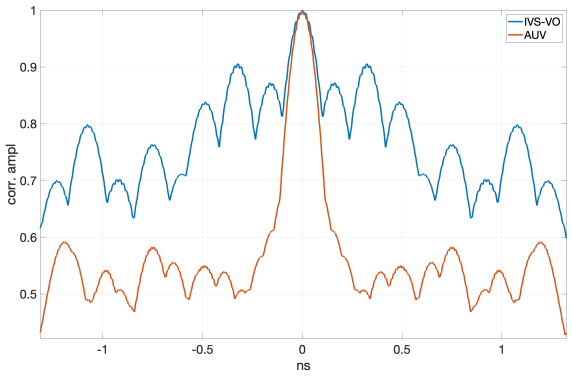

Fig. 4: Comparison between IVS-VO frequency setup and AUV in terms of the lag resolution function. The blue line using the IVS-VO frequency setup (32 channels) and the orange line using the AUV frequency setup (24 channels).

4 Correlation and Fringe-fitting

The data are shipped from Ke to Hb to be correlated at UTAS using DiFX [Deller et al., 2011]. Fringe-fitting is done using HOPS fourfit [MIT/Haystack, 2020] with manual phasecal using a high signal-to-noise ratio (SNR) calibrator scan as mentioned earlier. Manual phasecal (`pc_mode manual`) is used because the phase cal tones were too strong at low frequencies prior to a modification of the phase cal circuit and lead to saturation effects. This affects the sensitivity at lower channels. The phasecal tone generator was fixed at Hb only after auv005, allowing Hb to participate in IVS-VO sessions. However, it has not been fixed at Ke yet.

5 Results

At this stage, the main result we concern about is the baseline sensitivity. Since system temperature (T_{sys})

[1] `https://github.com/jive-vlbi/`

measurements were not available at the time because the noise calibration unit is not working properly at either station, only the baseline sensitivity is considered. Figure 5 illustrates a comparison between different sessions using the relative baseline sensitivity, which was produced by normalizing and averaging the SNRs of all scans per session.

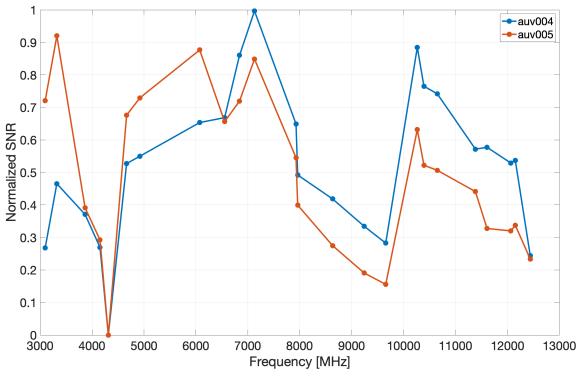

(a) Relative baseline sensitivity for auv004 (phasecal on) and auv005 (phasecal off).

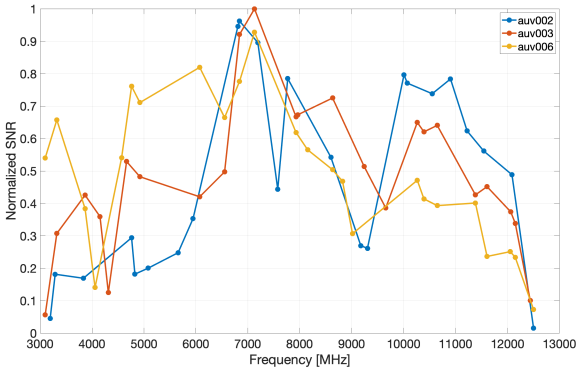

(b) Relative baseline sensitivity for auv002, auv003, and auv006. Each session has different frequency setups to avoid RFIs.

Fig. 5: Relative baseline sensitivity for several AUV sessions with different frequency setups.

For instance, Figure 5a depicts the relative baseline sensitivity of two sessions with the same frequency setup (auv004 and auv005), where the phasecal generator was either on or off. The relative baseline sensitivity is higher at the lower channels in auv005 compared with auv004 after switching off the phasecal unit, even with auv005's shorter scan time, which should theoretically yield a higher SNR.

Moreover, the baselines relative sensitivity is used to avoid the RFIs as in Figure 5b, which presents three different sessions with different frequency setups, each one encountered a different RFI. RFI is detected at 7.6 GHz, 4.3 GHz, and 4.1 GHz in auv002, auv003, and auv006, respectively.

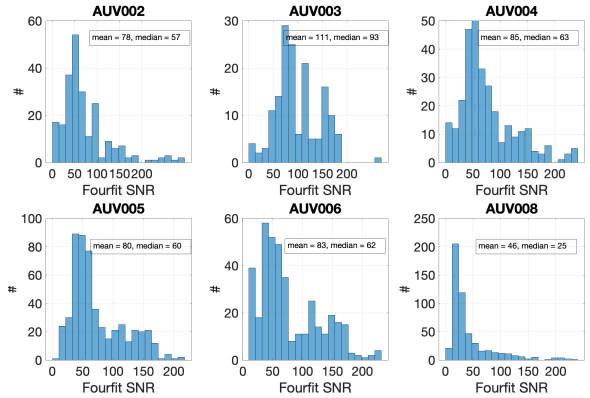

Fig. 6: Histogram of the fourfit SNR for all correlated sessions. The mean and median SNR for each session is shown as well. Values above 200 are excluded for clarity.

Figure 6 presents the distribution of the scans' SNR per session. Even with reducing the scan time from 60 s to 45 s as seen in auv006, the SNR is still high and allows to reduce the scan time even more except for auv008, which appears to have a sensitivity issue during the session.

6 Conclusions and Outlook

AUV is a series of experimental sessions to establish a VGOS observing routine within the AuScope VLBI array and improve stations sensitivity. Currently, AUV is carried out with a biweekly cadence on the baseline Hb-Ke. AUV is planned, scheduled, correlated, fringe-fitted, and analyzed at UTAS. Fixed scan time scheduling is used. After an initial 60 s scan duration, this has been gradually decreased down to 20 s in the latest session. Moreover, different frequency setups have been used to optimize the delay resolution function and avoid RFIs.

Additionally, the noise and phasecal units were repaired at Hb. The noise calibration unit enables T_{sys} measurement to get the SEFD as well as the sources flux density at the observing frequencies (3–13.5 GHz). These two values are fundamental for SNR based scheduling, which is one of the AUV goals. Finally, geodetic analysis for the AUV sessions is on the agenda and the main precision metric is the baseline length repeatability.

References

[Deller et al., 2011] Deller, A., Brisken, W., Phillips, C., Morgan, J., Alef, W., Cappallo, R., Middelberg, E., Romney, J., Rottmann, H., Tingay, S., et al. (2011). Difx-2: a more flexible, efficient, robust, and powerful software correlator. *Publications of the Astronomical Society of the Pacific*, 123(901):275.

[MIT/Haystack, 2020] MIT/Haystack (2020). Haystack observatory postprocessing system (hops). *https://www.haystack.mit.edu/haystack-observatory-postprocessing-system-hops/*. Accessed: 2022-06-30.

[Nothnagel et al., 2017] Nothnagel, A., Artz, T., Behrend, D., and Malkin, Z. (2017). International vlbi service for geodesy and astrometry. *Journal of Geodesy*, 91(7):711–721.

[Petrachenko et al., 2009] Petrachenko, B., Niell, A., Behrend, D., Corey, B., Boehm, J., Charlot, P., Collioud, A., Gipson, J., Haas, R., Hobiger, T., Koyama, Y., Macmillan, D., Malkin, Z., Nilsson, T., Pany, A., Tuccari, G., Whitney, A., and Wresnik, J. (2009). Design aspects of the vlbi2010 system. page pp 56.

[Plag et al., 2009] Plag, H.-P., Rothacher, M., Pearlman, M., Neilan, R., and Ma, C. (2009). The global geodetic observing system. In *Advances in Geosciences: Volume 13: Solid Earth (SE)*, pages 105–127. World Scientific.

[Schartner and Böhm, 2019] Schartner, M. and Böhm, J. (2019). Viesched++: a new vlbi scheduling software for geodesy and astrometry. *Publications of the Astronomical Society of the Pacific*, 131(1002):084501.

[Tuccari et al., 2018] Tuccari, G., Alef, W., Dornbusch, S., Wunderlich, M., Roy, A., Wagner, J., Haas, R., and Johansson, K. (2018). Dbbc3 the new wide-band backend for vlbi. In *Proceedings of the 14th European VLBI Network Symposium & Users Meeting (EVN 2018)*, pages 8–11.

The Yebes Observatory and the Future VLBI Correlator for the RAEGE Network

J. González, C. García-Miró, E. Martínez, J.A. López-Pérez, P. de Vicente

Abstract This paper describes the geodetic VLBI activities carried out at the Yebes Observatory and gives an update about the status of the RAEGE project. The design of a VLBI correlator for the RAEGE network has just started based on the experience gained with a prototype that is installed on site. The development of the correlator is part of the YNART project, co-funded with ERDF 2014–2020 funds, granted by the former Spanish Ministry of Economy, Industry, and Competitiveness.

Keywords Radio astronomy, space geodesy, global astrometry, VLBI technique, software correlator

1 Yebes Observatory and the RAEGE Project

The Yebes Observatory is a Spanish singular scientific and technical infrastructure, the only one located in the Castilla–La Mancha autonomous region, dedicated to astronomy and astrophysics and the study of the Earth through space-geodetic techniques. The observatory is strategically placed on the European tectonic plate, in the center of the Iberian Peninsula, 80 km from Madrid. Our 40-m diameter antenna, the only fully Spanish radio telescope, is a world reference in chemical studies of the interstellar medium [1, 2, 3, 4], and it participates in astronomical, geodetic, and global astrometric VLBI observations in collaboration with the main networks (e.g., EVN, GMVA, IVS). The RAEGE 13.2-m diameter VGOS-type antenna participates regularly in the VGOS and EU-VGOS observing programs and in other R&D campaigns. Apart from VLBI, the GNSS space-geodesy technique is also present at the observatory—in addition to a gravimetry laboratory, a local tie network, a time and frequency system, and other facilities. Thanks to the Spanish-Portuguese RAEGE Project (Atlantic Network of Geodynamical and Space Stations) and the European Regional Development Fund (ERDF), the observatory will soon become the first fundamental geodetic station in Spain, with the forthcoming addition of a Satellite Laser Ranging station. When completed, the RAEGE network (Figure 1) will consist of four fundamental geodetic stations located on the Azores Islands (two sites), Canary Islands (one site), and Yebes (one site), each equipped with a 13.2-m radio telescope with VGOS specifications, gravimeters, and at least one permanent GNSS station. All

Fig. 1 The RAEGE network, comprised of four sites from the Azores Islands (two sites) to the Canary Islands to Yebes Observatory on the Iberian Peninsula, will study in detail the interaction between the North American, the Eurasian, and the African tectonic plates.

Yebes Observatory, Instituto Geográfico Nacional (Spain)

these will be complemented with the Satellite Laser Ranging station at the Yebes site [5]. For the RAEGE network to operate autonomously, the YNART project (Infrastructures for updating the radio telescopes at Yebes Observatory) is providing a scalable and flexible software VLBI correlator.

2 Yebes Core Site Update

Currently there is a busy agenda at Yebes Observatory devoted to the development, testing, and installation of completing the VGOS-type receivers designed entirely by our engineers. A total of three broadband 2–14 GHz receivers will be completed by the end of 2022, for observatories such as Matera, HartRAO, and NARIT, and both Yebes and Santa María VGOS receivers will be upgraded according to [6].

The triband receiver currently installed at Santa María (Azores) will be replaced by the upgraded VGOS one by the end of 2022, and the triband receiver installed in Ny-Ålesund Observatory (NMA) will be replaced by the upgraded VGOS NMA1 receiver sometime during 2023 (the upgraded NMA2 VGOS receiver was installed in late 2021).

Additionally, a new phase calibration module [7] and superconducting filters are under development to improve geodetic receiver performance and avoid radio frequency interferences.

With the addition of the Satellite Laser Ranging station, the YLARA station (Figure 2), the Yebes core site will soon become the first Spanish fundamental geodetic station, with more than three space-geodetic techniques co-located at the same site: VLBI, GNSS, and SLR, together with a gravimetry pavilion and a local tie network of geodetic vertices.

The YLARA SLR station will allow ranging measurements of satellites equipped with retro-reflectors, located at distances ranging from 200 to 42,000 km, and space awareness applications. It will use a pulsed solid state laser on a biaxial telescope with alt-azimuth mount. The SLR civil works for the dome building were already initiated, with solid state laser and detector package commissioning activities to be performed soon at IWF facilities in Graz, Austria.

Fig. 2 Illustration of future YLARA Satellite Laser Ranging station at Yebes Observatory (design by Felipe A. Paredes, Yebes Observatory).

3 Future RAEGE VLBI Correlator

The RAEGE correlator is meant to be used for astronomical and geodetic applications of the RAEGE network. Designed to be an efficient correlator for a four-station network, its main specifications are the following:

- DiFX software correlator [8] running on an HPC.
- Correlator components: four computing nodes with 32 cores per node. Mass-storage with more than 1.5 PB managed under a BeeGFS distributed file system. The connection to the Internet is realized with a 100-Gbps line to the Spanish Research and Education network (RedIris), while Infiniband is the technology chosen to interconnect the nodes in the HPC to reduce latency.
- The initial design is sized to support a minimum of four stations, but it is scalable to support the correlation of larger networks such as EU-VGOS or VGOS.
- Integration of PolConvert [9] and TEC corrections to support antennas with linear and circular polarizations.

- HOPS [10] post-processing pipeline for geodetic applications.
- Flexible to support different VDIF data formats and easily upgradable.
- Support 'peta' level rates of floating point operations per second (PFLOPS).
- Support a minimum of four stations with a 32-Gbps data rate per station, observing two days per week.
- Appropriate thermal conditioning of the correlator room.

A 20-month service contract was awarded to the Spanish company QUASAR SCIENCE RESOURCES S.L., with the responsibility to perform a technological study, COTS selection and design of the correlator (in Phase 1), installation (in Phase 2), and commissioning and early operations (in Phase 3), with the schedule detailed in Figure 3.

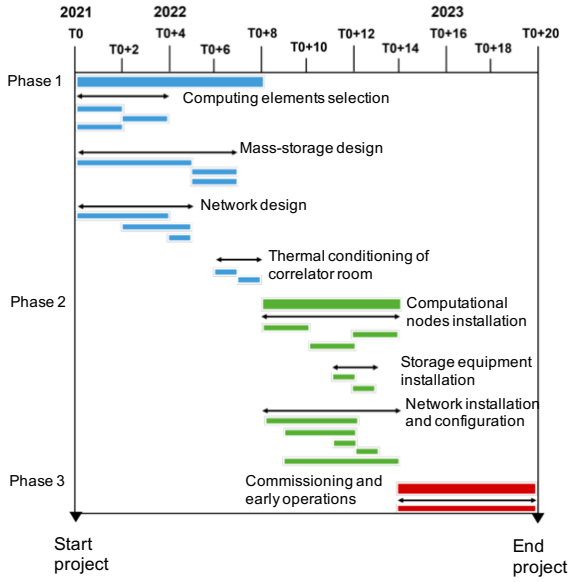

Fig. 3 RAEGE VLBI correlator project schedule.

Prototyping activities for the correlator were already initiated in Yebes, with the assembly of a VLBI DiFX software correlator [8] running on a distributed cluster with a 10 GE private network. This prototype is currently supporting ongoing correlation of EU-VGOS experiments and other local projects.

Additional prototyping activities carried out in the observatory compared CPU versus GPU performance in calculating Fast Fourier Transforms (FFT). The testbed used CUDA to export DiFX routines to parallelized GPU computing. Real VGOS data was applied to the modified DiFX version. It was found that the GPU performance is better than the CPU for increasing the number of points per vector (Figure 4, [11]).

There is a parallel effort at Yebes Observatory to develop a calibration server that contributes with an improved calibration for VGOS telescopes in the network with linear and circular polarizations and to correct for extended source structure.

4 Conclusions

The outcomes of the YNART project will contribute to position Yebes Observatory as the first fundamental geodetic station in Spain, by means of providing a versatile software correlator that supports the different scientific applications of the RAEGE network and that contributes to the correlation efforts of the VGOS and EU-VGOS projects.

Acknowledgements

The YNART project has been funded by the former Spanish Ministry of the Economy, Industry and Competitiveness and by the European Regional Development Fund (ERDF 2014–2020).

References

1. J. Cernicharo et al., "A Sensitive Line Survey of TMC-1: the Chemical Complexity of a Cold Dark Cloud", 2021 International Symposium on Molecular Spectroscopy (Virtual): June 21–25, 2021. Talk TJ05, 2021.
2. J. Cernicharo et al., "Discovery of C_5H^+ and detection of C_3H^+ in TMC-1 with the QUIJOTE line survey", In Astronomy & Astrophysics, Volume 657, id.L16, 5 pp., 2022.
3. V. M. Rivilla et al., "Discovery in space of ethanolamine, the simplest phospholipid head group", In Proceedings of the National Academy of Sciences, Volume 118, Issue 22, article id.e2101314118, 2021.
4. V. M. Rivilla et al., "Precursors of the RNA World in Space: Detection of (Z)-1,2-ethenediol in the Interstellar Medium, a Key Intermediate in Sugar Formation", In The Astrophysical Journal Letters, Volume 929, Issue 1, id.L11, 9 pp., 2022.

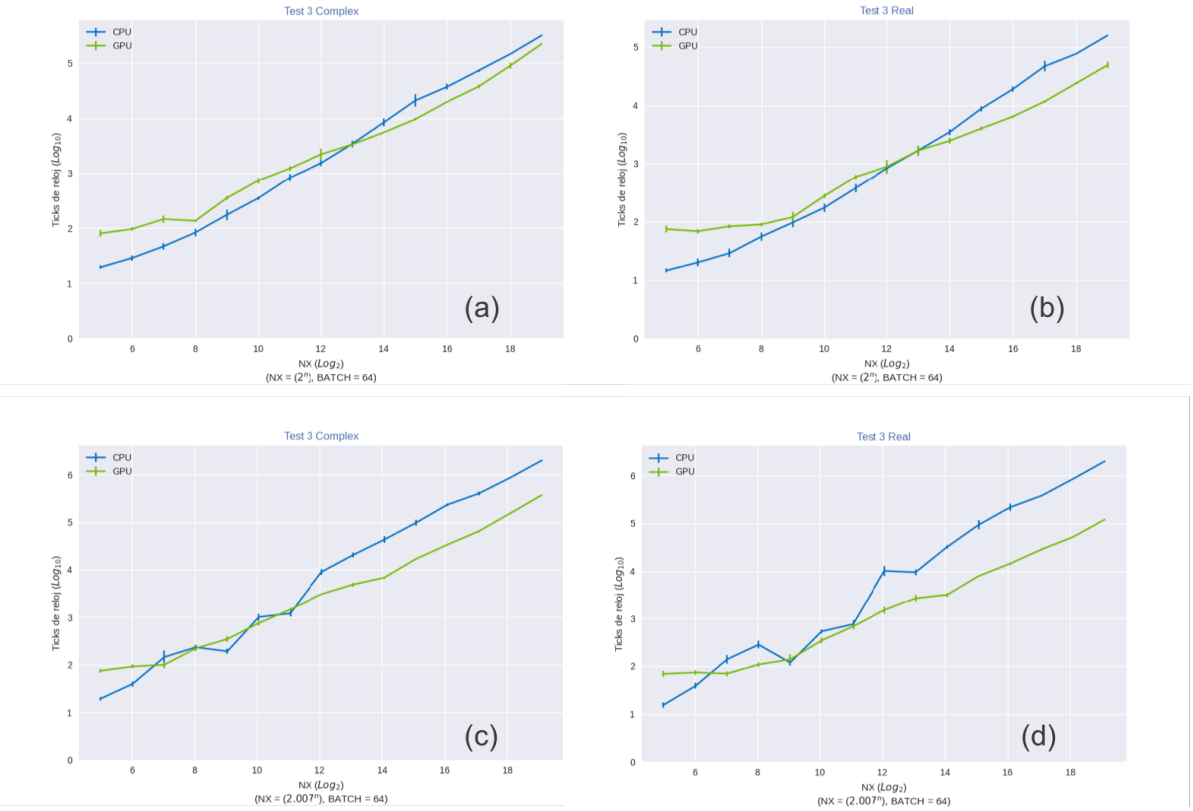

Fig. 4 FFT performance (tick clocks) comparison between a CPU Intel IPP (blue) and a GPU (green) increasing the number of points per vector (NX) for a complex (a,c) and a real (b,d) input and power of 2 number of points (a,b) or not (c,d).

5. J.A. López-Pérez et al., "The current status of RAEGE", 25th EVGA meeting, March 15–18, 2021.
6. J.A. López-Pérez et al., "Description of RAEGE Yebes VGOS receiver upgrades", 12th IVS GM Proceedings, this volume, March 28th – April 1st, 2022.
7. P. García-Carreño et al., "New Cable Delay Measurement System for VGOS Stations", Sensors, vol. 22, n.º 6, 2022, doi: 10.3390/s22062308.
8. A. T. Deller et al., "DiFX-2: A More Flexible, Efficient, Robust, and Powerful Software Correlator", In Publications of the Astronomical Society of the Pacific, Volume 123, Issue 901, pp. 275, 2011.
9. I. Martí-Vidal, A. Mus, M. Janssen, P. de Vicente, J. González, "Polarization calibration techniques for the new-generation VLBI", In Astronomy & Astrophysics, Volume 646, id.A52, 10 pp., 2021.
10. J. Barret, R. Capallo et al. "VGOS Data Processing Manual", Tenth IVS Technical Operations Workshop, Haystack Observatory, Westford, MA, USA, 2019.
11. C. Golvano, M. Prieto, J. González, "GPU acceleration of a DiFX correlator for radio astronomy", graduate degree project in Computer Science Engineering, Alcala University, 2021.

Australian VLBI Correlation Center

Tiege McCarthy[1], Jamie McCallum[1], Lucia McCallum[1], Oleg Titov[2]

Abstract We outline the progress and current plan for development of an Australian VLBI Correlation Center operated by the University of Tasmania. This center will fill the gap in Australian VLBI capabilities and initially focus on the correlation of geodetic VLBI data from Australia and the Asia-Pacific region, with the ultimate goal of becoming recognized by the IVS as an international VLBI Correlation Center. The center will be designed from the ground up with the data volumes of VGOS in mind and aims to address the current lack of Correlation Centers that are equipped to handle the routine correlation of VGOS sessions. We aim to transition from a local correlation cluster to an HPC environment, allowing us to overcome data I/O issues that are inherent to the high data rates of VGOS. This center will allow for better utilization of the Australian VLBI network, increasing cadence of observations with shorter turnaround times on processing.

Keywords Correlation, VLBI, VGOS

1 Introduction

In order to realize the goals of the VLBI Global Observing System (VGOS), data logistics and processing need to be considered and scaled up accordingly. High experiment cadence combined with higher data rates, resulting in larger data volumes, will push existing infrastructure beyond its limits. The ability to access and read data rapidly is a critical component of the data correlation process, and the greater than an order of magnitude increase in data rate for VGOS experiments is going to provide a significant challenge in the future.

The IVS Infrastructure Development Plan 2030 [1] identifies the need for more Correlation Centers as we move into the VGOS era. In partnership with Geoscience Australia, the University of Tasmania (UTAS) is establishing an Australian VLBI Correlation Center which aims to provide the missing piece of Australian geodetic VLBI capabilities. Development of expertise, documentation, and facilities will move us from our current ad-hoc correlation support to a consistent routine correlation service for the Asia-Pacific region and ultimately the IVS as a whole.

In this paper we outline our existing correlation facilities and workload, along with our plans for this future Australian VLBI Correlation Center.

2 Current UTAS VLBI Infrastructure

UTAS operates a geodetic VLBI array situated across Australia, with two antennas located at the Mount Pleasant Observatory (Hb and Ho) in southern Tasmania, one station in Katherine (Ke, Northern Territory) and one station in Yarragadee (Yg, Western Australia). The remote stations in Katherine and Yarragadee currently have poor network connections and therefore require experiment data to be shipped on disksets to Mount Pleasant Observatory for processing. Planned upgrades to the network connections for the remote stations will hopefully remove the need for the shipping of disksets in the not-too-distant future.

1. School of Natural Sciences, The University of Tasmania, Private Bag 37, Hobart, Australia
2. Geoscience Australia, PO Box 378, Canberra, Australia

2.1 Current Correlation Responsibilities

Currently UTAS is responsible for the correlation of the following sessions:

- Approximately two mixed-mode (legacy S/X stations combined with VGOS stations in a pseudo-S/X observing mode) sessions, rotating fortnightly between the AUA and AUM code sessions. These sessions are typically 24-hour experiments with 4–6 stations total.
- A weekly southern Intensive mixed-mode session with two-station short turnaround processing followed by a later three-station processing.
- VGOS test sessions between the VGOS-equipped Hobart 12-m and Katherine 12-m stations
- Occasional Asia-Oceania VLBI sessions. Approximately three times per year.

Our current correlation facilities are able to handle this existing workload; however, we currently do not have much room to expand our responsibilities. The establishment of this Australian Correlation Center will allow us to push our capabilties and provide a correlation service to a wider audience.

2.2 Mount Pleasant Correlation Cluster

Correlation at Mount Pleasant Observatory utilizes a small correlation cluster, along with Flexbuff data recording/storage machines. Disksets from remote stations are loaded into these machines so that they can be accessed alongside the locally recorded data. Each of the Flexbuff machines is connected to the observatory network switch with a 10-Gbps line.

The cluster itself is comprised of ten machines, that each have 20 available cores and 64 GB of memory. The machines from the cluster, similarly to the Flexbuff machines, are each connected with a 10-Gbps link to the network switch. Correlation is set up and performed on this cluster, with the subsequent fringe data sent to another local machine for fringe-fitting and post-processing before the vgosDB database is generated and distributed to the Analysis Centers. The correlation data and fringe-fitting data is then subsequently archived on a Research Data Storage Initiative (RDSI) node.

A typical five-station, 24-hour AUA session, with 9-Gbps total data rate when recording (the pseudo-S/X mode for VGOS stations is 3-Gbps data rate, legacy S/X is 1 Gbps), results in approximately 60 TB of data. We can currently correlate these sessions at approximately real time (24–30 hours). Comparing these numbers to a typical five-station VGOS session however, we are looking at five times higher data rates and data volumes, which will push this facility out of being able to comfortably perform routine correlation services.

3 Discussion of Solutions

The geographic location of UTAS (on the island state of Tasmania, off the southern coast of the Australian mainland), combined with existing telescope infrastructure and our increasing requirements provide a unique challenge when determining what the best course of action is for establishing this Correlation Center. The current solutions we are investigating include a substantial upgrade to our current in-house correlation setup or moving toward high performance computing (HPC) solutions.

3.1 Upgrade Existing Correlation Facilities

Upgrades to our existing correlation infrastructure can be made in three main ways:

1. Processing power;
2. Data input/output;
3. Data storage.

Processing power is a relatively cheap and easy to upgrade; however, it is unlikely to provide a significant upgrade to correlator performance until our correlation workloads move toward much higher station count experiments. When looking at core count versus correlation time for a fixed number of stations, in all cases we see great scaling with increasing core count up to a break point where we hit extreme diminishing returns (see Figure 1 for a three-station example using some southern Intensive data).

Data input/output on the other hand is where we believe the biggest improvements can be made; however, this is still an area we are actively investigating.

Additionally, when compared to upgrading processing power, data I/O improvements are much more expensive and difficult to implement into our existing correlation cluster.

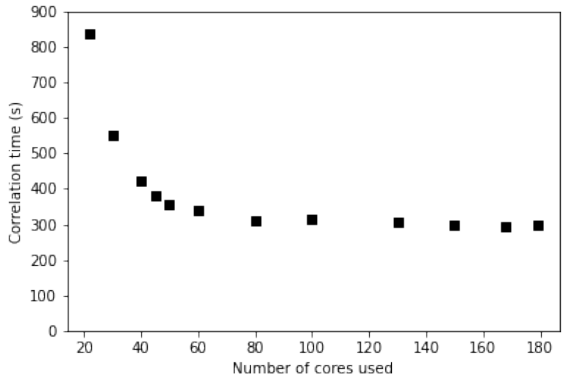

Fig. 1 Correlation time versus core count scaling for our current Mount Pleasant Observatory correlation cluster, using ten scans (580 seconds) of a three-station mixed-mode southern Intensive session.

Another problem with upgrading our current facility is that we are still limited by our network link across Bass Strait, the body of water between Tasmania and mainland Australia. Currently we share a 10-Gbps link across to the mainland with many other research facilities in Tasmania—meaning e-transfer data rates to our current facility is somewhat variable. This bottleneck may become even more pronounced, as our remote stations get upgraded with fiber connections and e-transferring data from these sites becomes standard practice.

3.2 Move to HPC Solution

We have access to two different HPC facilities as part of this project: (1) the UTAS run Tasmanian Partnership for Advanced Computing (TPAC) *kunanyi* HPC in Tasmania and (2) the National Computational Infrastructure (NCI) *Gadi* HPC in the Australian Capital Territory.

3.2.1 *kunanyi*

The TPAC *kunanyi* HPC has 6,720 cores distributed across 240 nodes with 128 GB of memory available on each node. The HPC has 1 PB of scratch storage, PBS job scheduling, and high-data rate (InfiniBand) connectivity between the nodes. This hardware should completely satisfy all performance and I/O needs for the foreseeable future.

However, moving to an HPC does not solve the issues of data transport and logistics, and getting large volumes of data onto *kunanyi* is a currently unsolved challenge. Data physically shipped to UTAS will still need to be moved onto the HPC. Theoretically, the Mount Pleasant Observatory is connected to *kunanyi* via a 10-Gbps link; however, current transfer testing has been hitting a 1-Gbps limit, which we hope will be rectified in the near future. One benefit of this HPC being local is the potential for a local data ingest station, where we can load Flexbuff disk sets directly into accessible storage on site. The feasibility of this is currently being investigated. On the other hand, the HPC being local means we suffer from the same reliance on our shared 10-Gbps link to mainland Australia.

3.2.2 *Gadi*

NCI's *Gadi* has 3,074 nodes each with 48 cores (147,552 total), 192 GB of memory, and similar to *kunanyi* high-data rate (InfiniBand) inter-node connectivity. It uses PBS job scheduling and will more than satisfy our processing and data I/O needs. Access to *Gadi* is provided through our partnership with Geoscience Australia, which are a major collaborator with NCI.

Again, similar to *kunanyi*, data logistics will also be an issue for *Gadi*. Currently, despite our 10-Gbps line to the mainland, our typical realistic transfer rate onto *Gadi* is between 2–3 Gbps. This makes shipping multiple stations worth of data to Hobart then subsequently transferring onto *Gadi* not feasible, even transferring VGOS data for just the Hobart 12-m will take 48 hours for a 24-hour VGOS session. However, we do have the possibility for a data-relay station at the Canberra Geoscience Australia (GA) headquarters, which we can ship data to from the remote stations and then transfer from GA onto Gadi at approximately 10 Gbps. This would alleviate the issue of 'double transferring'

and significantly cut down transfer times. This relay station would only be necessary as a stopgap solution until fiber connections to our remote stations are online in the next couple of years.

Gadi as a mainland based solution is very attractive moving forward and will scale better with future infrastructure upgrades. It also removes the Bass Strait network connection as a potential bottleneck, as we will only need to transfer data from one VGOS station across it (Hb) rather than potentially multiple remote stations.

3.3 Distributing Correlation across Infrastructure

Because moving the data around is our limiting factor for all solutions, potentially distributing our correlation jobs around all the potential solutions makes the most sense, especially for the short term while we are limited by physically shipping data. Depending on the experiment, data can be shipped to various locations—multiple large correlation jobs can be distributed to different correlation hardware, while our local cluster continues to handle smaller jobs or legacy/mixed-mode correlation.

While this solution doesn't drastically decrease processing latency, it could provide quite high overall throughput of the center. Additionally, as connectivity increases to our remote stations, we can be even more flexible with how we distribute correlation workloads.

A distributed correlation solution such as this carries with it the primary downside of drastically increased bookkeeping required to keep on top of the data logistics.

4 Summary

We aim to establish an Australian VLBI Correlation Center that will provide VGOS capable correlation services to the Asia-Pacific Region and the IVS as a whole. We outline our current existing correlation infrastructure and correlation workload, along with the three primary solutions we are investigating to provide suitable hardware moving forward. From our initial investigation, the two HPC solutions appear to be the most promising, with our existing cluster remaining for small projects.

We also discuss ways to navigate the current limiting factor of data transfer from remote stations by distributing our correlation workload across multiple facilities in order to increase total correlation throughput.

Acknowledgements

This work is funded by Geoscience Australia as part of the Positioning Australia project.

References

1. A. Nothnagel, J. Anderson, D. Behrend, et al., "IVS Infrastructure Development Plan 2030." In: International VLBI Service for Geodesy and Astrometry 2019+2020 Biennial Report, edited by D. Behrend, K. L. Armstrong, and K. D. Baver, NASA/TP-20210021389, pp. 3–11, 2021.

Bonn Correlator Status

Yoon Kyung Choi[1,2,3], Simone Bernhart[1,2,3] Walter Alef[3], Helge Rottmann[3], Torben Schüler[2], Jan Wagner[3]

Abstract We report on the status of the Bonn Correlation Center, focusing on geodesy. As well as technical aspects of the cluster and its performance, we introduce our duties as one of the IVS correlators and recent progress.

Keywords VLBI correlation, DiFX, VGOS

1 Introduction

The Bonn Correlation Center is operated jointly by the Max Planck Institute for Radio Astronomy (MPIfR) in Bonn and the Federal Agency for Cartography and Geodesy (Bundesamt für Kartographie und Geodäsie, BKG) in Frankfurt. The MPIfR hosts the correlator facility and shares the costs of the cluster, most of the staff, and the internet connectivity with the BKG. Since January 2017, the personnel responsible for the correlation of geodetic sessions are employed by the BKG via a private contractor, the Reichert GmbH.

2 Correlator Capabilities

The Distributed FX software correlator (Deller et al., 2011) in various versions is available at the Bonn correlator. For geodetic production we currently use DiFX-2.6.3 for S/X Legacy sessions, and we use DiFX-2.5.4 for VGOS observations.

The correlator runs on a high-performance computing (HPC) cluster, which was renewed in 2015 to match both VGOS and mm-VLBI requirements. It consists of 1) 68 nodes with 20 compute cores each, for a total of 1,360 cores, 2) three head nodes that allow execution of several correlations in parallel, 3) 2.5 PB disk space in RAID units, combined in a BeeGFS parallel cluster file system, 4) 14 Mark 5 playback units, and 5) 11 Mark 6 playback units, each with four bays.

The raw data are recorded at the stations either on modules (Mark 5 or Mark 6) or on storage servers, usually referred to as Flexbuffs. For geodetic experiments, the data are mostly e-transferred to the HPC cluster that is connected to the Internet through a 10-Gbit commercial line or a 1 Gbit line, part of the German Research Network (Deutsches Forschungsnetz – DFN). Various data formats have been already correlated in Bonn: Mark IV, Mk5, DVP, and various versions of VDIF. The correlated data (SWIN files) can be exported to FITS and HOPS (Mark IV) formats. For post-processing, the following software packages are available: AIPS, CASA, PIMA, and HOPS (Haystack Observatory Postprocessing System), the last of which is the standard tool for geodesy. The correlator outputs and other important files (e.g., VEX and v2d files) are backed up daily on the HPC cluster. The final products are archived on the MPIfR archive server, where they will be kept for at least ten years. The EXPAD and COMEDIA tools are used for bookkeeping of experiments and corresponding media correlated in Bonn. They are the frontends to a local database that records all relevant information such as the observation date, participating stations, modules, and status of the experiment.

1. Reichert GmbH
2. Bundesamt für Kartographie und Geodäsie
3. Max-Planck-Institut für Radioastronomie

3 Activities in Bonn

3.1 IVS Correlation

Our duties include the correlation of the weekly INT3 and R1 series, as well as OHIG and T2 sessions for the IVS S/X sessions and VGOS 24-hour sessions. In 2021 we correlated 43 INT3 (one-hour, weekly on Monday) sessions, 52 R1 (24-hour, weekly) sessions, seven T2 (24-hour, bimonthly) sessions, six OHIG (24-hour, bimonthly) sessions, and eight VGOS (24-hour) sessions (with ten sessions planned in 2022).

3.2 EU-VGOS

In March 2018, on the initiative of W. Alef of the Bonn Correlation Center, a collaboration with the three European stations of Wettzell, Onsala, and Yebes, equipped with both standard S/X and VGOS systems, was launched to carry out a VGOS proof-of-concept study. The aim of the project is to verify the processing chain for VGOS experiments end-to-end, from the scheduling to the geodetic analysis of the derived observables. The total number of sessions planned to date was 41 (three aborted/canceled). Twenty-four sessions were processed in Bonn: nine of the ten schedules in 2018 (one was aborted, mostly two stations only), 14 of the 16 scheduled in 2019 (two were aborted/canceled), and one of the 15 scheduled in 2020. Other sessions in 2020 were correlated in Vienna or Yebes, and ev0034 was processed in Russia. There were no observations in 2021, but we plan to restart observations this year. Correlated sessions have partly been post-processed in single band and pseudo Stokes I mode, the latter based on the Haystack VGOS post-processing chain. Some sessions were also used to test the polarization conversion for VGOS data based on the PolConvert software for VGOS developed by I. Marti-Vidal (Marti-Vidal et al. 2015).

3.3 DiFX-2.5.4

In addition to our EU-VGOS correlations, we started correlating 24-hour IVS VGOS sessions in 2021. Each correlator has its own local patches and different versions of DiFX to correlate and difx2mark4 to convert the data. In August 2021, in order to regain a cross-site consistent DiFX-2.5 installation for VGOS correlation, as opposed to the local patches at correlator sites, Jan Wagner gathered necessary patches and backported certain features from mainline DiFX-2.6, and together with Haystack-provided HOPS 3.22, released DiFX version 2.5.4 to the DiFX community.

3.4 Multi-Datastream Correlation

Recorded bands are spread across several files, and previously these VGOS data had to be vmux-ed to "merge" them for single-datastream correlation under DiFX-2.5.3. This occupied disk space doubly and needed extra time/work. In Bonn we carry out DiFX multi-datastream correlation, possible under DiFX-2.5.4 and 2.6.3 using multi-datastream configuration. Onsala (Oe/Ow) and Ishioka now observe with multi-files and e-transfer their files without prior "merging".

3.5 10 Gbps Upgrade

Previously, we used two 1 Gbps NREN (DFN) links (BONN, RZBONN Servers). In October 2021, we upgraded to a commercial 10 Gbps link (NetCologne) for e-VLBI and replaced the "BONN" server. " RZBONN" is still working. Transfer protocols that we use are JIVE jive5ab/m5copy and JIVE e-transfer etc/etd[1]. After the upgrade, the transfer speed is much faster than before. For example, in the case of Onsala VGOS data, a transfer (of 23 TB) takes two days instead of two weeks.

[1] https://github.com/jive-vlbi/etransfer

References

1. A. T. Deller, W. F. Brisken, C. J. Phillips, J. Morgan, W. Alef, R. Cappallo, E. Middelberg, J. D. Romney, H. Rottmann, S. J. Tingay, R. Wayth, “DiFX-2: A More Flexible, Efficient, Robust, and Powerful Software Correlator”, PASP, 2011, 123, 275–287.
2. I. Marti-Vidal, A. Roy, W. Alef, J. Conway, M. Lindqvist, A. J. Zensus, “Solving the polarization problem in ALMA-VLBI observations”, in Proceedings of the 12th European VLBI Network Symposium and Users Meeting, Cagliari, Italy, 2014, ID: 034 M.

VLBI Correlator Wettzell – A New IVS Component

C. Plötz[1], W. Probst[1], R. Wildenauer[1], B. Fischalek[1], A. Neidhardt[2], M. Seegerer[1], M. Schönberger[1], T. Schüler[1]

Abstract The Geodetic Observatory Wettzell (GOW) in Germany was enhanced with a VLBI correlation facility. An initial DiFX-based correlator was operated between 2016 and 2020 for the evaluation of local VLBI baseline measurements between the three VLBI radio telescopes of the GOW (Wz, Wn, and Ws). In December 2021, a high performance cluster (HPC) based DiFX VLBI correlator replaced obsolete small hardware, which also enabled the necessary performance for handling VGOS observations. Additional correlation duties came along with serving the local VLBI observation program in Wettzell and a small VLBI network with BKG radio telescopes located in Argentina (AGGO) and O'Higgins (Antarctica). Since late 2021, the VLBI correlator at Wettzell has been acknowledged as an official IVS correlation component in order to contribute to the IVS correlation resources. A special focus is on serving a timely ΔUT1 estimation with dedicated legacy S/X Intensive sessions between Wettzell and AGGO and with a newly established IVS VGOS Intensive observation program between Wettzell and MacDonald Observatory (MGO). Automation is an important aspect from provisioning the IT infrastructure towards an automatized correlation workflow, in particular the Intensive sessions. The new VLBI correlation facility has a close integration into the Geodetic Observatory Wettzell and its infrastructure as a geodetic fundamental station, as well as the other IVS components at Wettzell, namely the Operation Center (OC DACH) and the three VLBI network stations. These components are a valuable addition to the worldwide geodetic VLBI infrastructure.

Keywords VLBI correlator, DiFX, VGOS Intensive

1 Introduction

The Geodetic Observatory Wettzell contributes since 1983 with the 20-m radio telescope as network station to the international VLBI community. Over the years, several other components were added. The German Antarctic Receiving Station (GARS) O'Higgins in Antarctica was established in 1991. Since 2002, the 6-m radio telescope TIGO (Transportable Integrated Geodetic Observatory) in Chile was in operation before moving to Argentina in 2016. It was since named Argentinian German Geodetic Observatory (AGGO). In 2013, the VGOS twin radio telescopes, Wettzell-South and Wettzell-North, extended the geodetic infrastructure at the GOW. All of these network stations take part in a broad range of VLBI observation programs (e.g., R1, R4, T2, VGOS, and various Intensive programs). The IVS VLBI Operation Center DACH (Deutschland: BKG, Austria: TU Wien, Confoederatio Helvetica: ETH Zürich) began operations in November 2019. In September 2020, the IVS Seamless Auxiliary Data Archive (SADA) was initiated at Wettzell. The latest addition is the establishment of the IVS VLBI correlator Wettzell (WETZ) in September 2021.

(1) Bundesamt für Kartographie und Geodäsie (BKG), Geodätisches Observatorium Wettzell, Sackenrieder Str. 25, D-93444 Bad Kötzting, Germany

(2) Technische Universität München (TUM), Geodätisches Observatorium Wettzell, Sackenrieder Str. 25, D-93444 Bad Kötzting, Germany

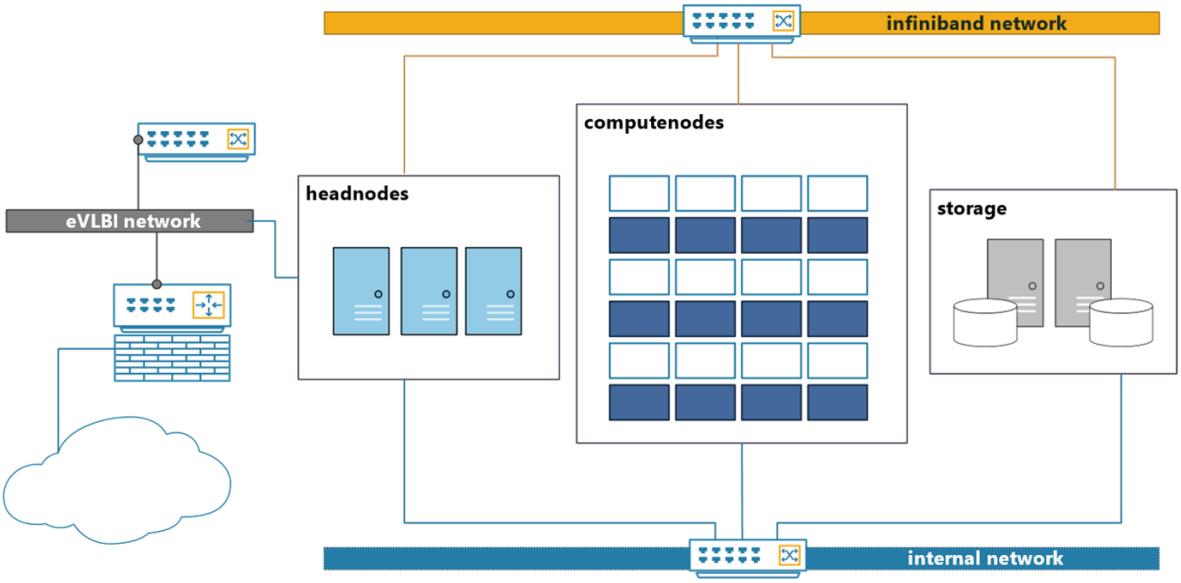

Fig. 1 Wettzell VLBI correlator: Hardware block diagram.

2 VLBI Correlator Wettzell – Hardware and Software Overview

The hardware topology was specified as a High-Performance Cluster (HPC) configuration. There are three head nodes (one of them acts for data transfers) and 24 compute nodes available. The data is transported with an Infiniband bus and a corresponding switch interconnects all related hardware units. The HPC-cluster storage capacity is currently at 834 TB. A dual-UPS protects against power failures. The nominal usable internet data rate is 4 Gbps for up- and download of VLBI raw data.

The software installation consists of Linux CentOS 7 as operating system for the HPC cluster. Ansible is the software tool for provisioning, configuration management, and application deployment. DiFX is used as a software correlator application [Deller et al., 2011] and the Haystack Observatory Postprocessing System (HOPS) is installed for the subsequent fringe-fitting process. In order to manage different users and configurations for all correlation duties, a SLURM (Simple Linux Utility for Resource Management) workload manager for batch processing was introduced at the HPC cluster. Two basic configuration sets are currently in use. One for VGOS (DiFX version 2.5.4, hops 3.23) and another for legacy S/X (DiFX 2.6.3, hops 3.23).

3 Current IVS Correlation Program

A milestone towards an official IVS VLBI correlator component was the start of VLBI short baseline observations at the GOW in 2016 [Phogat et al., 2019]. Since 2018, a domestic Intensive VLBI session program with AGGO and Wettzell was established [Plötz et al., 2019]. Furthermore, in this context, a few dedicated VLBI sessions between Wettzell, AGGO, and O'Higgins were conducted. In 2019, the small initial correlator hardware needed to be replaced and a new correlator hardware was installed at the end of December 2020.

Currently, a VGOS Intensive observation program is assigned to the Wettzell correlator. The IVS VGOS Intensive series S22 between McDonald (Mg), located in Texas/US, and Wettzell (Ws) in Wettzell/Germany is observed on Tuesdays at 19:45 UT and the duration is one hour. After the S22 had finished a short calibration session (S2A), which takes normally ten minutes, is appended. The purpose is to collect further insight in correlation, source characterization, and slewing characteristics of the involved radio telescopes.

The VGOS Intensive series started on December 7, 2021 with the first session. As of the time of writing, there were 12 sessions correlated and their analysis showed that the S22 VGOS Intensive series performed well. For example, let's consider the VGOS In-

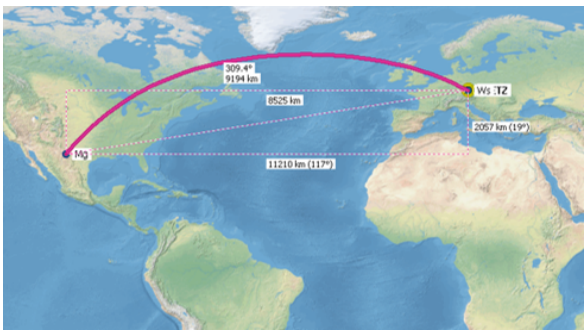

Fig. 2 VGOS Intensive baseline: McDonald (Mg) to Wettzell (Ws).

tensive session S22053. The formal error value of 4 µs for ΔUT1 is within the expectation. In one hour, 91 scans were observed and no losses occurred during correlation. The analysis showed few outliers (3.2 %). The standard deviation of the group delays is at a level of 12 mm and comparable to other VGOS Intensive sessions.

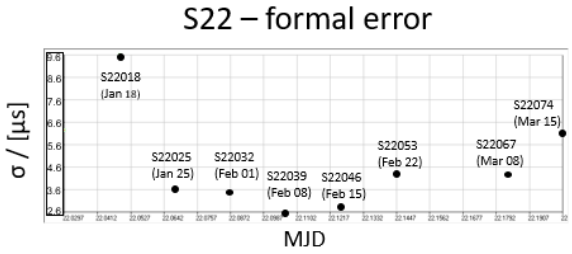

Fig. 3 Formal errors of the first S22 VGOS Intensive sessions.

The current in-house observation program with the legacy S/X Intensive program was conducted with the radio telescopes of Wettzell and AGGO. Typical session durations were two hours to correlate. At Wettzell, the short baseline VLBI observations between the 20-m radio telescope Wettzell and both twin radio telescopes were also VLBI sessions handled at the VLBI correlator Wettzell.

4 Conclusions

The VLBI correlator Wettzell started regular operations in December 2021 as an official IVS component. Currently, the S22 and S2a IVS sessions are assigned to the Wettzell VLBI correlator. A focus is on the development of an automatic VGOS Intensive correlation workflow as the next step. The configuration and setup management of the HPC-based VLBI correlator is based on the common and well-established software tool-chains of Ansible and SLURM. The general design of the VLBI correlator hardware enables scalability as it will be needed in the future. An advantage of the close integration into the infrastructure of the Geodetic Observatory Wettzell is that the recorded raw data of the Wettzell network station are instantaneously obtainable and do not use internet network resources, when the session is correlated at Wettzell. This gives an advantage towards a closer real-time workflow. Quality monitoring procedures were established and the supervising of them is an ongoing task that will lead to improving the VLBI processing chain. This means, for example, that continuous station monitoring checks many system parameters and reports if any value is out of an expected range. The VLBI correlation resources are available for more sessions to correlate. It is intended to upgrade the internet bandwidth up to 10 Gbps and the correlator storage capacity might be enhanced up to 2 PT.

References

[Deller et al., 2011] A. T. Deller, W. F. Brisken, C. J. Phillips, J. Morgan,W. Alef, R. Cappallo, E. Middelberg, J. D. Romney, H. Rottmann, S. J. Tingay & R. Wayth. “DiFX-2: A More Flexible, Efficient, Robust, and Powerful Software Correlator.” PASP, 123, 275–287, 2011.

[Plötz et al., 2019] C. Plötz, T. Schüler, H. Hase, L. La Porta, M. Schartner, J. Böhm, S. Bernhart, C. Brunini, F. Salguero, J. Vera, A. Müskens, G. Kronschnabl, W. Schwarz, A. Phogat, A. Neidhardt, M. Brandl, “INT9 – ΔUT1 Determination Between the Geodetic Observatories AGGO and Wettzell.” In: R. Haas, S. Garcia-Espada, and J. A. López Fernández (eds.), Proceedings of the 24th European VLBI Group for Geodesy and Astrometry Working Meeting, pp. 124–128, 2019. doi: 10.7419/162.08.2019.

[Phogat et al., 2019] A. Phogat, C. Plötz, T. Schüler, H. Hase, G. Kronschnabl, A. Neidhardt, J. Kodet, U. Schreiber, W. Alef, H. Rottmann, L. La Porta, S. Bernhart, “Implementation and First Results of the Local Wettzell VLBI Correlator GOWL.” In: K. L. Armstrong, K. D. Baver, and D. Behrend (eds.), IVS 2018 General Meeting Proceedings “Global Geodesy and the Role of VGOS – Fundamental to Sustainable Development”, pp. 102–106, NASA/CP-2019-219039, 2019.

Monitoring Source Flux Density and Antenna Sensitivity with Improved Feedback for the AUSTRAL VLBI Sessions

Lim Chin Chuan[1], Lucia McCallum[1], Jamie McCallum[1], Guifré Molera Calvés[1]

Abstract Very Long Baseline Interferometry (VLBI) is a unique technique for measuring the Earth's orientation for deriving precise reference frames that allow accurate positioning of objects on the Earth and in the sky. Although it has a long history, VLBI in the Southern Hemisphere is not as old as in the Northern Hemisphere, with significantly fewer telescopes and observations. Therefore, VLBI observations and results from the Southern Hemisphere are crucial to the global community to prevent inaccuracies in the derived global reference frames. As one of the main contributors from the south, the Australian AuScope VLBI array strives to achieve better results through improved source flux density and antenna sensitivity monitoring with more automation. We investigated an improved approach to monitoring the performance of VLBI sessions and are implementing it in the Australian mixed-mode sessions using the dynamic observing program (Dynob). This work is an overview of the implementation of Dynob with emphasis on automated feedback, which allows quick and continuous session improvements.

Keywords VLBI, Dynamic observing, Dynamic feedback

1 Introduction

The VLBI telescopes at Hobart, Katherine, and Yarragadee, which are owned by the University of Tasmania (UTAS) in Australia, have been dedicated to VLBI observations globally and locally since 2011. A VLBI observation is the recording of radio signals of specific frequency ranges from distant quasars using two or more radio telescopes. As we now prepare to enter the next generation of VLBI observing, known as the VLBI Global Observing System [VGOS, 5], UTAS has explored the possibility of a more efficient and improved way of observing. For operational efficiency, UTAS has initiated the 'dynamic observing' research aiming to reduce the labor and cost for continuous observing [4]. This original study focused on short-notice automated scheduling, which is beneficial for utilizing antennas and potentially improving a schedule when some antennas fail to participate in the observation [3]. While inheriting the original goals, the research on dynamic observing, now called Dynob, has been extended to improve the observing efficiency and results of the VLBI mixed-mode observing using automated feedback.

On the global scale, the observing efficiency is only about 80% in terms of the used-to-scheduled ratio, averaged from the analysis reports of the first half-year of 2021 for the participating stations. There can be various reasons that reduce the efficiency, and one of those is the mismatch of the predicted and actual source flux density and antenna sensitivity. The a priori source flux density and antenna sensitivity are essential parameters in VLBI scheduling to calculate the integration time for observations based on a minimum target signal-to-noise ratio (SNR). Conventionally, the antenna sensitivity is characterized by the system equivalent flux density (SEFD), a measurement of the combined system temperature proportional to the total power received at the receiver (Tsys). The antenna SEFD is usually measured once after each major upgrade, such as a receiver change. The SEFD value, in theory, should not vary significantly at daily intervals due to a cooling

1. University of Tasmania

or ambient temperature control mechanism at the telescopes. However, the telescope sensitivity may fluctuate in reality, due to recording backend and hardware issues that are not immediately obvious, in the form of temperature, which especially has a detrimental effect on the AuScope VGOS stations.

The source flux density used for planning the geodetic VLBI observations is estimated after every 24-hour session based on the global average. This procedure has been sufficient for the legacy S/X sessions with a 100% error factor for the target SNR used at the planning stage. Although adequate, this approach is not ideal as it compromises the possibility for more observations within the 24-hour session window and does not reliably solve the observing efficiency issue. Here is where Dynob comes into play, by continuously monitoring antenna sensitivity and source flux density based on a scan-by-scan technique, wherein a 'scan' is when two or more telescopes observe the same source simultaneously. The details for the scan-by-scan performance monitoring approach can be found in [2]. We demonstrate this approach using the AUSTRAL VLBI sessions observed by the Australian network with contributions from Warkworth and Hartebeesthoek, utilizing better feedback from the Dynob program.

2 Dynamic Observing

The AuScope dynamic observing has evolved from an automated scheduling and observing technique [4] to the core of the feedback system in the new mixed-mode observing at the University of Tasmania (UTAS) [1]. The development of Dynob extends the original concept of the AuScope dynamic observing into automating the entire VLBI operation from scheduling to correlation, with an additional mechanism to monitor the performance of telescopes in near real-time, providing constant feedback for improvement. Dynob is also the tool that centralizes and controls all the VLBI operational procedures optimized for the practices at UTAS. The first application of the expanded Dynob project was the establishment of a one scan per week, less-than-60-second per scan 'fringe check' series for the diagnosis of the program while providing quick feedback on the antenna performance. Although fringe checking usually involves only one scan, the entire observing and processing process still applies. The Dynob program has now replaced the manual operation procedure at UTAS, allowing the operator and observers to perform a fringe check with multiple AuScope VLBI telescopes by clicking a button. About 90 fringe check sessions have been run using Dynob in parallel with its development, observing various sources.

The general Dynob process is illustrated in Figure 1, with more information given in [1]. The Dynob process starts by creating the schedule files and passing them to the observing computer, and then it triggers the loading of the schedule and the start of observing according to the scheduled time. It can automatically proceed with the data transfer and correlation when the observation ends before finally generating a visible plot showing the scan quality. Each component can be manually started or interrupted and resumed again with the automation. The complete automation of this process applies to the fringe check sessions because they involve only the AuScope telescopes, and the size of data is relatively small so that transferring over the Internet is feasible. For the 24-hour sessions, each station would need a super-fast connection to the correlator and the data recorded on the FlexBuff system to achieve the same. A few near real-time fringe checking tests for 24-hour sessions were conducted with collaboration from Hartebeesthoek to stream the data to Hobart after every scan. The automation works for the weekly fringe check sessions, but real-time transferring of the S/X data recorded in the AUSTRAL mode [6] takes about seven hours for every six hours of observations from Hartebeesthoek. For the data recorded using Mark5B at Yarragadee, Dynob automatically extracts about 12

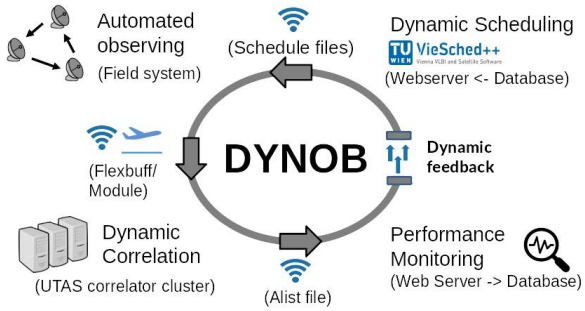

Fig. 1 Dynob is the tool that automates and connects each component of the VLBI operation. Near real-time performance is feedback to improve the schedule quality.

seconds of the data at the interval between each scan before sending it to avoid interruption of recordings. By default, the near real-time fringe checks run once every three hours on bright sources only with source flux densities above 2 Jy.

The evolution of the dynamic observing concept into Dynob was driven by the need for a stable telescope calibration with a better, faster, and continuous approximation of the antenna SEFDs and source flux densities to achieve good observed-to-expected SNRs, i.e., closer to 1. This improvement can allow the SNR error factor placed during the scheduling process to be reduced from more than 100% to a lower value to yield more observations and better station coordinate repeatabilities. The minimum SNR needed for the post-processing is 7, but the usual target SNR used is 20, whereas [2] shows that the optimum range is around 10 — 13. The error factor is in place for many reasons, but all serve the purpose of reducing the number of observations lost due to a low SNR. The automated feedback system of Dynob consistently monitors the source flux density and antenna sensitivity and improves the schedule so that the predicted SNRs are much closer to those observed.

3 Improved Feedback

The modern scheduling technique of a VLBI session typically involves telling the software scheduler how sensitive the telescopes are and how bright the sources are. The scheduler then recursively calculates and assigns an integration time to a scan to achieve the target SNR based on these inputs until the individual scans make up the typical 24-hour session. To attain a good observed-to-expected SNR agreement at all baselines, the predicted sensitivity of all stations should be as accurate as possible, given that the source flux density prediction is precise. The SNR performance of a 24-hour session is seen clearly through the feedback of Dynob, as illustrated in Figure 2 using two radio sources visible to the AUSTRAL network at the opposite time.

Starting from the X-band, the first information, marked as ‘1’, shows that the SNR ratio for source 1741-038 was generally around 1 for the Hb-Yg baseline, whereas the source 0454-234 had higher than predicted flux density. The digital sampler at

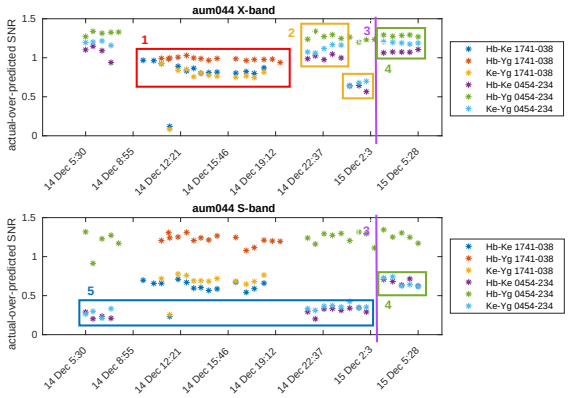

Fig. 2 Illustration of the performance feedback for AUM044 conducted on 14 December 2021. Only the 12-meter Australian telescopes at Hobart (Hb), Katherine (Ke), and Yarragadee (Yg) are shown.

Katherine was unstable during the session. As a result, the sensitivity of the station dropped, as marked by the box with the number ‘2’, compared to the first box. This effect caused the SNR ratio of all its baselines to degrade by about 50%. A reconfiguration of the digital sampler at time ‘3’ solved the problem. As shown in the S-band, there was basically non-detection for source 1741-038 before the reconfiguration, which was the larger part of the session. One more thing to note is that the sensitivity of Ke at the S-band was significantly lower than predicted for this session. With the feedback loop, we can quickly alert the operator to check the system and fix any issues or schedule the next session with an SEFD value closer to reality. Figure 3 shows the more desired performance feedback in AUM045, conducted in January 2022.

This session used the source flux densities monitored by the AUSTRAL session three months before the session and the same antenna SEFDs as AUM044. As we see in the X-band, the SNR ratio for all baselines converged around 1, which means that the predictions of the source flux densities for the two sources and the sensitivities for all telescopes were accurate. In contrast with the existing approach to monitoring the antenna SEFD and the source flux density, which is based on the session’s average (session-wise), we use a “selective scans” (scan-wise) method [2]. The reason for a new approach is that the session-wise re-estimation cannot reliably indicate the source flux density and the antenna sensitivity. As seen from Figure 2, the poorly performed observations can make up most of a session

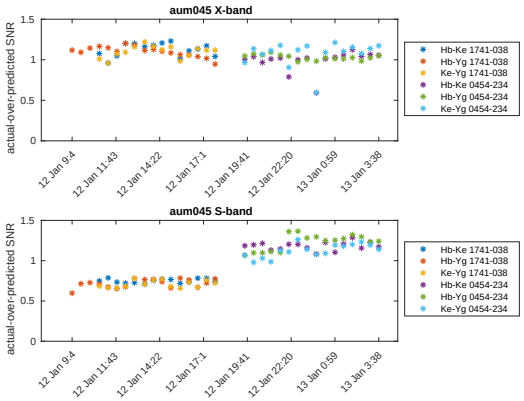

Fig. 3 Illustration of the performance feedback for AUM045 conducted on 12 January 2022. Only the 12-meter Australian telescopes at Hobart (Hb), Katherine (Ke), and Yarragadee (Yg) are shown.

and should be removed during the re-estimation process.

An important aspect of the scan-wise method is selecting only the well-observed radio sources with stable flux densities as the reference, which we can determine via the Dynob feedback mechanism through constant monitoring. Figure 4 shows a source used as the reference in [2]: 0454-234, versus a more stable source: 0458-020, relative to the Australian network within the last half of the year 2021.

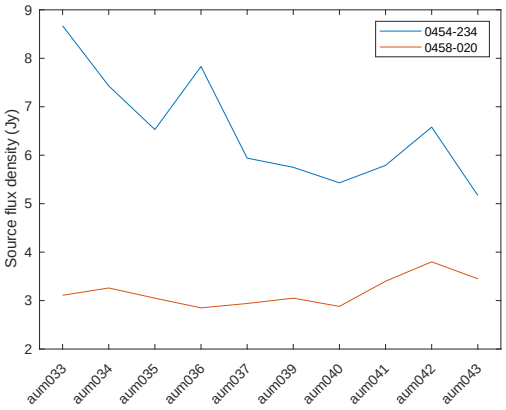

Fig. 4 Comparison of source flux density for sources 0454-234 and 0458-020 monitored by the AUSTRAL station network. The latter source appears to be more stable and could be a better candidate as a reference source.

The variability of the source flux density is often inconsistent, which means a regular update of the reference source is also needed. An arbitrary half-a-year window might be sufficient to determine the rate and degree of changes. This process of monitoring the antenna SEFD and the source flux density and updating reference sources can be more efficient through automated feedback. Using a set of more stable reference sources could potentially solve the less accurately predicted source flux densities, such as in the S-band for the source 1741-038 in Figure 3.

The processing time of a 24-hour AUSTRAL session from observing to analysis takes about three months without Dynob, including the data transfer from other stations to Hobart. Even the highest priority sessions within the International VLBI Service for Geodesy and Astrometry (IVS) would take three to four weeks. In the continuous observing era where data start to accumulate, Dynob will play a critical role in monitoring the source flux density and antenna sensitivity, keeping these pieces of information the most up-to-date, thereby maintaining the quality and efficiency of observations.

4 Results

This section compares the median SNR performance for 12 AUA sessions (once a month) and 18 AUM sessions (once or twice a month) in 2021. The AUM series has a better observed-to-predicted SNR ratio in the X-band than the AUA series and about the same performance in the S-band (Figure 5). All AUM sessions used the Dynob-monitored antenna SEFDs for the scheduling, but the source flux densities were from the general catalog of SKED. The reason was due to the modelling approach and feedback mechanism for the source flux density still under research and development.

From Figure 5, we see that the issues with the telescopes around 11 April and 22 September are more apparent for the AUM as the SNR ratio became unusually low, although it impacted both the AUA and AUM sessions. A plunge in the actual-to-predicted SNR ratio for the AUA and AUM is usually a DBBC3 (digital sampler) issue, as the DBBC3s at Katherine and Hobart were still in the commissioning phase. Nevertheless, the median ratios for the AUA data points are 0.7 and 0.9 in the X- and S-band, respectively, compared to 1.0 and 1.1 for the AUM.

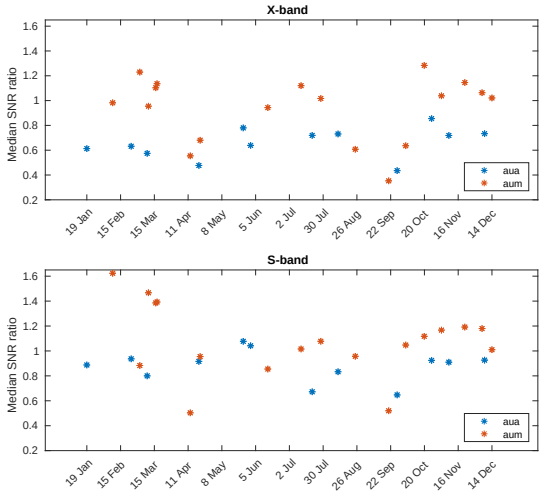

Fig. 5 Median SNR for 12 AUA and 18 AUM sessions in 2021. The AUM performed significantly better than the AUA in the X-band while having a similar performance in the S-band.

5 Future Work

The Dynob program is functioning as intended, and all AUM sessions in 2022 have implemented it from scheduling until performance monitoring. Automation for the reference source list updates will be a future functionality for Dynob. Using Dynob on a larger station network and its application at other operating centers will need further research. The current work is a fully functioning prototype optimized for the AUSTRAL sessions, which serves as the proof of concept for dynamic observing in a continuous observing era.

6 Conclusion

The AuScope dynamic observing program (Dynob) is a tool that automates the entire VLBI observation procedure from scheduling to correlation, with a feedback mechanism to monitor the SNR performance of the session. Dynob implements the new scan-wise monitoring approach, which allows the continuous monitoring of the antenna SEFD and source flux density through its dynamic feedback to improve the prediction of SNR for subsequent schedules. Results show an improvement of the actual-to-predicted SNR ratio in the X-band for the 2021 AUM sessions, which used the antenna SEFD monitored by Dynob, compared to the conventionally scheduled AUA sessions. Dynob's feedback mechanism can detect stable radio sources through the time series resulting from consistent monitoring, which will be the candidates for the reference sources for future performance monitoring.

References

[1] L. Chin Chuan, L. McCallum, J. McCallum, G. Molera Calvés, and T. McCarthy. Improving the effciency of the AuScope VLBI observations through dynamic observing. In *Proceedings of the 25th European VLBI Group for Geodesy and Astrometry Working Meeting*, pages 95–99, 2021.

[2] L. Chin Chuan, L. McCallum, J. McCallum, G. Molera Calvés, and T. McCarthy. New source flux density and antenna sensitivity monitoring in AUSTRAL VLBI sessions for improved feedback and results. *PREPRINT (Version 1) available at Research Square*, doi:10.21203/rs.3.rs-1655703/v1, in review.

[3] E. Iles, L. McCallum, J. Lovell, and J McCallum. Automated and dynamic scheduling for geodetic VLBI–A simulation study for AuScope and global networks. *Advances in Space Research*, 61(3), 962–973, 2018.

[4] J. Lovell, L. Plank, J. McCallum, S. Shabala, and D. Mayer. Prototyping automation and dynamic observing with the AuScope array. In *International VLBI Service for Geodesy and Astrometry 2016 General Meeting Proceedings*, pages 92–95, 2016.

[5] W. Petrachenko, D. Behrend, H. Hase, C. Ma, A. Niell, H. Schuh and A. Whitney. The VLBI2010 global observing system (VGOS). In *EGU General Assembly Conference Abstracts*, 2013

[6] L. Plank, J. Lovell, J. McCallum, D. Mayer, C. Reynolds, J. Quick, S. Weston, O. Titov, S. Shabala, J. Böhm and others. The AUSTRAL VLBI observing program. *Journal of Geodesy*, 91(7), 803–817, 2017.

Improving IVS Communication through a VLBI Communications Center

M. Bérubé[1], J. Gipson[1], J. Lovell[1], D. Lakins[2]

Abstract Since 2000, the International VLBI community has greatly invested in developing new hardware and software to improve data precision, processing, and latency. There is also a significant effort in automating observations and processes. Unfortunately, one element that has not been improved is how the different VLBI components, Operation Centers, stations, correlators, and analysts are communicating. The current VLBI communication system was developed 25 years ago and relies mainly on emails, archiving system, and the dedicated people monitoring the information relevant to them. This is not a suitable communication system for operational VLBI.
To improve the actual system, the GSFC group at NASA has developed a VLBI Communications Center (VCC) and tools for near real-time, machine-to-machine, two-way communication between IVS components. The VCC is a web service supported by a database and a message broker using formatted information designed for access by computers. The database keeps up-to-date data on schedules, catalogs and all relevant information on various IVS components (e.g., station's availability, latest SEFDs). The message broker is used to inform any IVS components that some data/information at the VCC are relevant for them. The VCC knows who acknowledges the message and uploaded the schedule, allowing full traceability of data/information exchanges. This paper will show the limitations of the current communication system, describe the various components of the VCC, and how it could improve the communication and data exchange between IVS components. The tests done with the VCC hosted by NASA will also be presented.

Keywords IVS, VLBI, VCC

1. NVI, Inc./NASA Goddard Space Flight Center, 7257 Hanover Parkway, Suite D, Greenbelt, MD 20770, USA
2. NASA Goddard Space Flight Center, Greenbelt, MD 20771, USA

1 Introduction

Many IVS components have automated their processes but still need human interactions when communicating with other IVS groups. IVS components are exchanging information through email exploders and Data Centers. Many delays are built into processes to account for uncertainties in data synchronization and communication exchanges.

Because of IT security issues, it is not possible for IVS components to open their IT infrastructure to other groups to facilitate data exchange. To bypass this issue, a central dedicated server, the VLBI Communications Center (VCC), was developed to provide near real-time, machine-to-machine, two-way communication system between all IVS components.

2 Current Method of Communication

The current communication method was developed 25 years ago around IVS mail exploders, archiving systems, and web pages.

The IVS mail exploders are sending hundreds of emails every week to registered members on different issues. People need to spend time reading these emails to evaluate their relevance and extract valuable infor-

mation. Unless people reply to these emails, there is no easy way to know if messages have reached the target audience. Some applications were developed to extract valuable information regarding master schedules and station operational data with limited success. These emails are written for people and are not following a standard format that could be easily read by software.

The IVS Data Centers are mainly archiving systems for safekeeping of the IVS data files. Because of their operational and synchronization rules, it may take minutes to hours before a submitted file is available at all Data Centers. This synchronization issue may create situations where different versions of a file reside on the Data Centers at the same time. The way files are retrieved from Data Centers, it is not possible to know who has downloaded specific files and when.

This is not an operational system for rapid exchange of information and traceability. Some delays are required to ensure the specific IVS components have received the information and retrieve the needed data files. For example, schedules must be submitted seven days in advance to avoid problems inherent in this communication method. Schedules are rarely modified if stations cannot observe as expected to avoid the use of different schedules.

3 Proposed VLBI Communications Center

The VCC was designed for removing uncertaintains in IVS data exchange and communications and supporting automation. The main characteristics of the system are:

- Fully automated;
- Machine-to-machine data exchange;
- Near real-time, two-way communication; and
- Traceability of data/information exchange.

The VCC has three essential components needed to support all its functionalities:

1. Database 
2. Web Service (API) 
3. Message Broker 

3.1 Database

The main purpose of the database is keeping the latest information on sessions, catalogs, station performances (SEFDs), and availability (maintenance) for more efficient scheduling. All transactions, messages, and events at the VCC are kept in the database for traceability. For example, we may need to know who has downloaded or uploaded files and when to ensure that everyone has the same version of a schedule.

All VCC users must be registered and have access to specific functionalities. The database keeps credentials on each user along with its roles and responsibilities. For example, only the Operation Center identified in the master schedule could upload the schedule for a session.

The database is populated and queried using the Web Service.

3.2 Web Service

The VCC Web Service is an application programming interface (API) that conforms to the constraints of REST architectural style. The users provide or retrieve data through http requests (get, post, put, or delete) using specific JavaScript Object Notation (JSON) data exchange format. Users provide credentials using Jason Web Token (JWT) included in the header of the http requests. The API is validating all users and ensure the request is valid for this user. The API provide credentials to access the message broker. After answering a request, the API analyzes who should know about this and informs specific users through the message broker.

3.3 Message Broker

The VCC is a near real-time, two-way communication system but cannot connect to other servers to deliver messages. The VCC uses a message broker dispatching structured messages using specific rules. Messages are routed to one or more queues that store information until a user acknowledges having received them. Appropriate routing rules are dynamically created so the users are receiving only messages relevant to them.

Each IVS component has its specific queue or inbox. Users need to connect to the message broker to retrieve messages in their inbox.

4 VCC Data Flow

To show how the VCC could deliver information in near real-time, Figures 1 to 5 illustrate the process of uploading a schedule and making sure every station has it. This approach could greatly reduce the submission time for schedules.

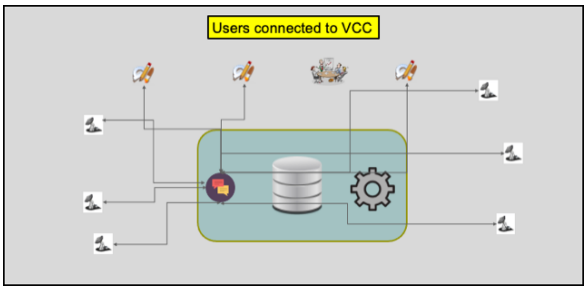

Fig. 1 Users connected to VCC. The VCC is not pushing any messages to external servers, so users must be connected to their private inbox to receive messages.

The Operation Center (OC) needs to generate a new schedule at pre-defined time prior to the start of a session. The OC could query the VCC to have the latest information on station performance and availability. After generating the new schedule, the OC uploads it to the VCC API (Figure 2).

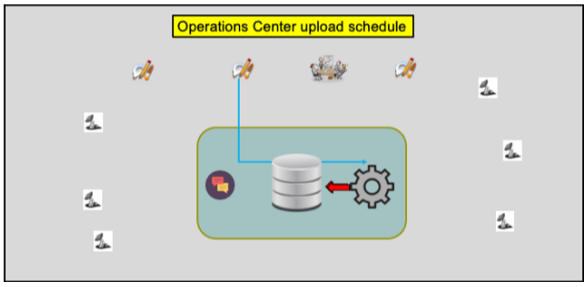

Fig. 2 Operation Center submits new schedule. First, the API validates that the OC is resposible for this session. After uploading the file, the VCC logs the process in the Database and informs the OC of success.

At any time, the API could be used to retrieve the status of a session. The returned information includes the time the last schedule was uploaded and when the stations downloaded it.

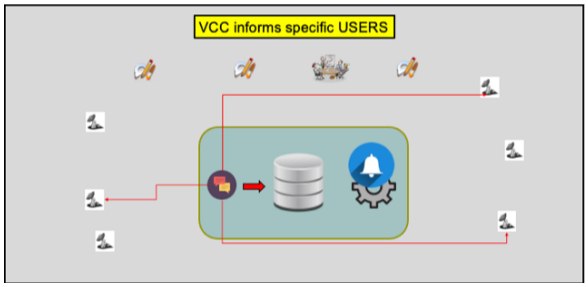

Fig. 3 VCC informs specific users. The API generates a message and dispatching rules to inform specific users through the message broker. If registered, Correlators and Analysis Centers would receive the message.

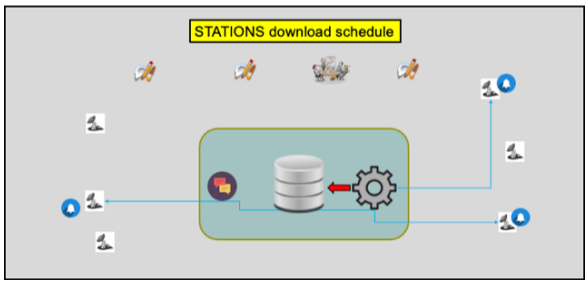

Fig. 4 Stations download schedule. On receiving the message, stations download the schedule file from the VCC and could drugd it. The VCC is recording who downloaded the file and when.

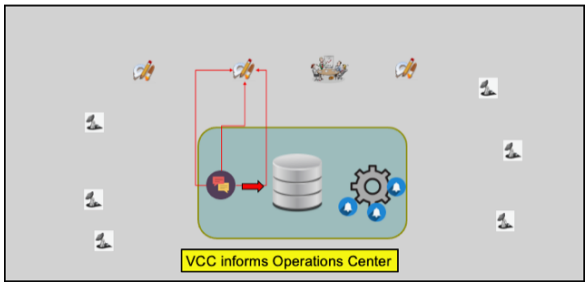

Fig. 5 VCC informs Operation Center.

This process took few seconds with the maximum delay coming from stations downloading the schedule. If something is wrong, a new schedule could be safely uploaded ensuring that all stations are using the same version.

5 Proof of Concept

To demonstrate how IVS components could communicate and exchange information through a VLBI Communications Center, we developed a first version of the VCC server and client applications for Coordinating Center, Operation Centers, and Network Stations.

A limited number of messages were created for the first demo.

A Dashboard application (Figure 6) was developed to show the exchange of information between the different IVS components. The Dashboard uses the API to get the latest status of a session and stations. It also connects to the message broker to receive any message related to the session. This tool could be used by any IVS component to check on session status.

5.1 VLBI Communications Center

- Linux server (Ubuntu)
- MariaDB
- Web Service
  - Python using FastAPI
  - Data exchange using JSON
  - Trigger most events for informing IVS component
- Message broker
  - RabbitMQ
  - Message structure has been defined
  - Dispatching rules have been defined

5.2 VCC Client Applications

- Coordinating Center
  - Create/update sessions
  - Maintain catalogs (database)
- Operation Center
  - Retrieve data (network availability, performence, catalogs) for generating schedule
  - Submit schedule (skd, vex, txt) files
- Network Station
  - Message listener
    - sessions have changed (get session information from API)
    - new schedule (download schedule, drudg)
  - Message publisher to inform IVS of station status (e.g., scan, source, problems)
  - Data uploader for SEFDs or logs
- Dashboard
  - Session viewer that could be used by any IVS group. See Figure 6.

The first demo was simulating a four-station schedule lasting ten minutes with a problem at one of the stations. The station application was not running at existing stations but on different servers than the VCC. Using the VCC message broker, one of the stations informed IVS that it could not participate due to power outage at the site. The Operation Center uploaded a new schedule that was downloaded by all participating stations in few seconds. The Dashboard showed when stations downloaded the new schedule and started observing. It also displayed the antennas downtime and recording status (e.g., scan, source) during simulated observation. During the demo, two Dashboards were running at the same time at different locations showing that VCC configuration is automatically adapting the rules for dispatching messages to all interested users.

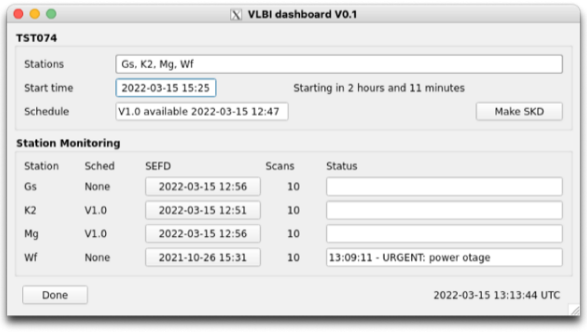

Fig. 6 VLBI Dashboard.

6 Conclusions

The actual IVS communication method needs to be improved to remove uncertainties, reduce delays in information exchange, and facilitate automation. The VCC has shown that it is possible to have a near real-time, machine-to-machine, two-way communication system between IVS components without compromising IT security.

The actual VCC is near operational mode, but we still need to define/add more messages and functionalities to cover most of the IVS activities. The VCC has a very flexible design and can easily accept more tasks as needs increase.

A Python package and applications were developed to help the different IVS components to access the VCC to submit or retrieve information.

The VCC is intended for IVS users with specific roles and restrictions. To limit access to IVS users only, the latest VCC is accessed through SSH tunnel and users need to submit a public SSH key. For extra security, some information between users and VCC API are encrypted using the SSH keys and Jason Web Token (JWT).

Documentation for accessing VCC API and Message Broker will be developed for Python and non-Python users.

Towards Automating Operations of SGP VGOS Stations

Jim Lovell[1], Darryl Lakins[2]

Abstract The NASA Space Geodesy Project (SGP) aims at establishing a network of up to ten VGOS stations in the next several years. The goal is to have the network controlled and monitored from the Space Geodesy Network Operations Center (SGNOC) with the local operations teams focused on safety, maintenance, and the technical aspects of operations. To attain this high level of automation, a set of use scenarios and requirements were defined for the Next-Generation Field System (NGFS). The initial steps on the road to the NGFS and automated operations were made with additions to the current Field System (FS). *Fesh2* is an automated schedule file management module that checks the IVS data repositories for current master and session schedule files, downloads updated versions, and prepares stations for observing. In addition, work was done on an SGP Automation module that will take over local operator hands-on FS tasks before, during, and after an observing session. In this paper we describe the new modules as well as future steps.

Keywords Software, Observations, Operations, Scheduling, Correlation

1 Introduction

A core component of VLBI systems is the software responsible for handling site operations and at most IVS stations this is the NASA Field System. Development of the current Field System began over 40 years ago and it is currently in use at over 30 sites worldwide. It is an essential component of the IVS network and is also widely used for astronomical VLBI. With the advent of VGOS, the number of stations in the NASA Space Geodesy Project (SGP) network increases with up to ten planned, as well as new broadband feeds and receivers, digital back ends and high bandwidth networks. It was determined that a systematic approach is required to design a new system based on this extensive experience with the Field System. The Next Generation Field System (NGFS) will be built, so it can support VGOS stations, can be effectively maintained, is adaptable to future technological developments, and is capable of a high level of automation.

The NASA vision is for a Space Geodesy Network Operations Center (SGNOC) to coordinate operations of all geodetic techniques supported by the SGP, including VLBI (Figure 1). The SGNOC may not need to be confined to a single location but could be virtualized, capable of running in a follow-the-sun mode. Ultimately, in a "post-integrated operational network", a lights-out mode is envisaged where operation is fully automated and site on-call personnel are only required to resolve safety-related anomalies, respond to emergencies, or manage occasional hands-on tasks such as maintenance. The NGFS will handle communication with the SGNOC

In preparation for development of the NGFS we have examined future usage scenarios and, with the assistance of the IVS community, documented the software requirements necessary to achieve them. Usage scenarios encompass operations; station calibration (e.g., pointing, amplitude calibration, phase and cable-delay measurement); equipment and proce-

(1) NVI, Inc./NASA Goddard Space Flight Center, 7257 Hanover Parkway, Suite D, Greenbelt, MD 20770, USA
(2) NASA Goddard Space Flight Center, Greenbelt, MD 20771, USA

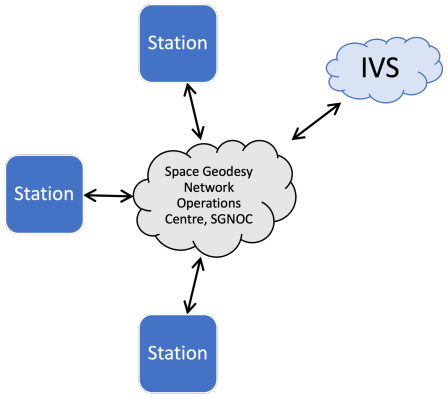

Fig. 1 The Space Geodesy Network Operations Center (SGNOC) provides coordination of station activities and a conduit to the IVS for schedules, logs, status reports, etc.

dure testing; antenna mechanical performance testing and monitoring; system sensitivity and stability tests; fringe checking; and maintenance tasks.

Work on a development strategy is now underway with coding and testing to follow in the coming few years.

In the meantime, we are developing some of the techniques required for automation using the existing Field System and a test VLBI Communications Centre (VCC), analogous to the VLBI component of a future SGNOC [1]. The new software will be tested and eventually deployed at the SGP stations, producing information on how well automation works in practice, which will help speed up development of and transition to the NGFS.

This work has started with two initial station-based software applications: *fesh2* and *SGPAutomate*. In the following sections we describe these, their current status, availability, and future work.

2 Fesh2

Fesh2, a progression of *fesh*, which is available as part of the Field System, is a Python package that provides automated schedule file preparation.

Fesh2 runs in a terminal window and regularly checks IVS schedule servers for new or updated versions of master and schedule files for the specified station. A check for the latest version of the master file(s) is done first, but skipped if the time since the last check is less than a specified amount. Similarly, checks on schedule files are only done if the time since the last check exceeds a specified duration. If new or updated schedules are found, they are optionally processed with *drudg* to produce `snp`, `prc`, and `lst` files. By default, once the files have been checked, *fesh2* will provide a summary and then go into a wait state before carrying out another check. *Fesh2* can also be run once for a single check or status report and not go into a wait state. *Fesh2* can also be run in a mode that gives a continually updating status report but does not process any files. Multiple instances can be run simultaneously. If *drudg* output `snp` or `prc` files have been modified at the station and a new schedule becomes available, *fesh2* will download the file but not overwrite *drudg* output, but it will warn the user.

Fesh2 can be run as a foreground application or as a service in the background. It is compatible with Python version 3.5 and above. Figure 2 shows the *fesh2* user interface. Is this case the AuScope station at Katherine is being managed. Both the 24-hour and Intensive master files are being monitored and any schedule for this station within the following 14 days is being monitored and processed.

2.1 Availability

At time of writing (June 2022), *fesh2* is being prepared for release and will be made available via the NVI repository on GitHub [2].

2.2 *From* fesh2 *to* fesh3

While *fesh2* communicates with the existing IVS file servers to monitor and maintain schedule files, *fesh3* will adopt an approach much closer to the NGFS model. *Fesh3* will maintain a communications link with a test VCC server, receiving push notifications of schedule changes (which is more efficient than regular polling from the station to IVS servers) and providing feedback to the VCC of schedule status at the station.

Fesh3 is currently at a proof-of-concept stage and, given its dependancy on a test VCC server, will initially be tested and deployed at SGP stations only. However,

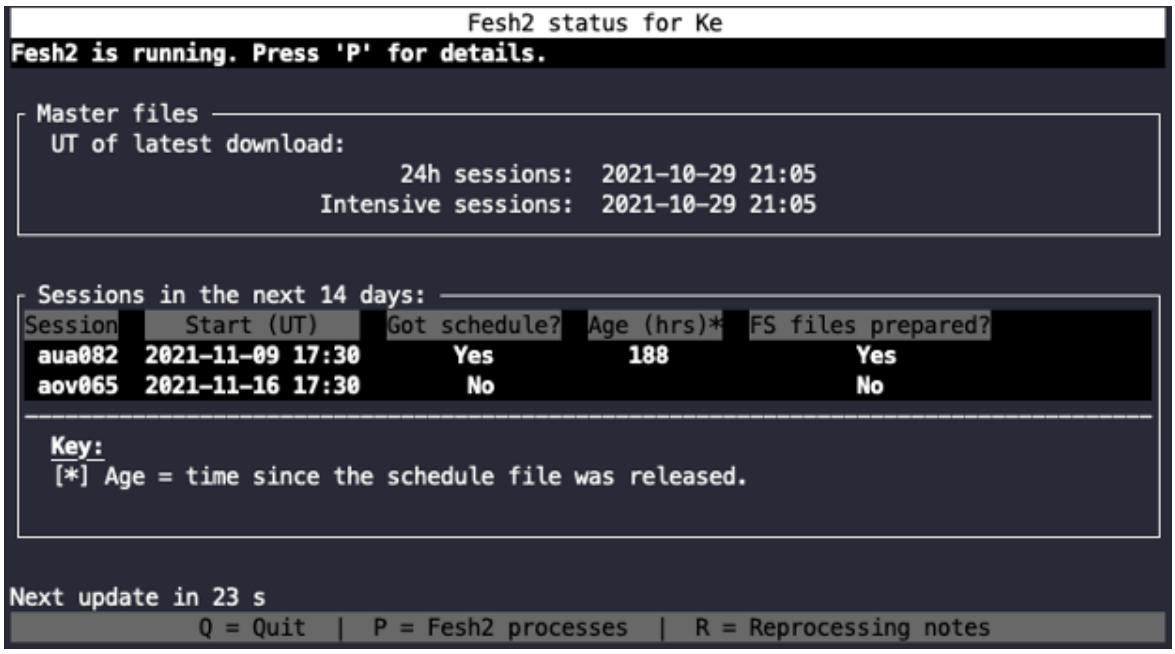

Fig. 2 The *fesh2* user interface, in this case for AuScope Katherine station. It shows the status of the latest master files downloaded, then a list of sessions over the following two weeks and their schedule status. In the case of aua082, the schedule file has been downloaded and the necessary Field System files produced with *drudg*. The schedule for aov065 is yet to be released but *fesh2* is regularly polling the IVS file servers and will download and process it once available.

it is hoped that the work on *fesh3* will inform NGFS development.

3 SGP Automation Software

At present, many of the session tasks carried out at the stations are done by hand via Field System commands which are time consuming and sometimes error prone. The *SGPAutomate* software is intended to provide automation of as many tasks as possible to allow local operations teams to focus on safety, maintenance, and the technical aspect of operations. Like *fesh3*, *SGPAutomate* is written in Python and is compatible with version 3.5 and above.

3.1 Code Structure

SGPAutomate interacts with the Field System server (`fsserver`) and is modular at the level of distinct operational tasks, which can be grouped to suit any defined scenario. For example, a typical IVS session consists of four *sequences* of tasks: pre-session checks, start of session tasks, in-session checks and monitoring, and post session tasks. Each task within each *sequence* is implemented in a separate module as defined in the software and can be used once or in multiple groupings as desired. Listing 1 shows part of the *SGPAutomate* configuration file that defines each *sequence* and the tasks to be carried out in each. Pre-session tasks start with a Network Time Protocol (NTP) check, `CheckNTP` (line 11), which checks that the computer time is synchronized with the NTP server. This is followed by opening a log file, checking hardware, and then carrying out a range of other system checks. The second *sequence* (line 21 onward) contains tasks that are carried out at the start of an experiment. It can be seen here that individual tasks can be re-used. In this case, `CheckNTP` is repeated. There is also a facility to continuously repeat a sequence, which may be desirable for regular system checks during a session. This may be configured by setting the `repeating` variable and specifying a time gap between repeats with `repeat_gap_min`.

```
[sequences]
    # Arrays contain a list of tasks (given above) in the order they should be executed for a a
    # specific activity. For example, the PreSession sequence contains all tasks to be carried out
    # before a sesion starts
    [sequences.PreSession]
        name = "Pre-session"
        description = "Procedures to be carried out before the session."
        repeating = false
        repeat_gap_min = 0
        tasks = [
            "CheckNTP", "StartFSLogFile",
            "CheckRDBE", "CheckMark6",
            "CheckMCI", "MountMark6",
            "CheckTiming",
            "InitializePointing",
            "SetModeAtten", "CheckRDBEs",
            "CheckPointing",
            "TestRecording"
        ]

    [sequences.StartExperiment]
        name = "Session start"
        description = "Procedures to be carried out at the start of the session."
        repeating = false
        repeat_gap_min = 0
        tasks = [
            "CheckNTP",
            "StartMulticastLogging",
            "SendReadyMessage", "StartSched",
            "SendStartMessage"
        ]
```

Listing 1 A section of a *SGPAutomate* configuration file defining procedure sequences which each consist of several tasks. See the text for a more detailed description.

The software will run each task in order and process output to decide if it was completed successfully or not. It will issue warning messages if there are problems and pause the sequence to allow for operator intervention if the task is unsuccessful.

SGPAutomate has a graphical user interface (GUI) and a limited text-based interface. Figure 3 shows an annotated screenshot of the current (unfinished) GUI. It consists of a status summary at the top followed by a tabbed section, one for each of the defined sequences. Each task is listed with the following features:

- The task can be selected for execution or not;
- A link is provided to documentation that describes the task;
- The user can choose to be prompted or not before continuing after the task;
- The task status (pending, done, or unsuccessful);
- If the task has been run, a link to the relevant part of the log is given; and
- It is possible to run each task individually when a sequence is not underway using the `[run]` button.

Typically a user will select a sequence, confirm the tasks to be carried out, and then press the `[Go]` button to commence. For tasks that cannot be fully automated (e.g., mounting a Mark-6 module) *SGPAutomate* will pause the sequence and notify the operator that manual intervention is required.

Lastly, the GUI shows a log of interaction with the Field System server which can be filtered to search for events of interest.

To assist stations wishing to add new tasks, *SGPAutomate* includes commented template Python code and accompanying documentation as a guide.

3.2 Next Steps

Work is continuing to implement as many tasks as possible. At the moment the focus is on tasks required to support a geodetic session, but the software could be easily expanded for other activities such as end-to-end system checks, pointing or SEFD calibration observations, or other maintenance tasks.

It is planned to add VCC communications to *SGPAutomate* in the future so that the station can automatically provide live status information to the operations center and bypassing (for example) the need to send ready, start, and stop emails.

It is hoped that, once the software has reached a higher level of maturity and has undergone testing, a version may be released more widely to accompany the Field System as an optional addition.

4 Conclusions

Fesh2, *Fesh3*, and *SGPAutomate* are placed outside the main FS distribution so they can be developed and maintained on a different timescale. However, attention should be made to the FS compatibility as commands and responses, which *SGPAutomate* uses, may change with new releases.

It should also be noted that similar developments are occurring elsewhere (e.g., [3, 4]) and there may be opportunities for coordination of efforts.

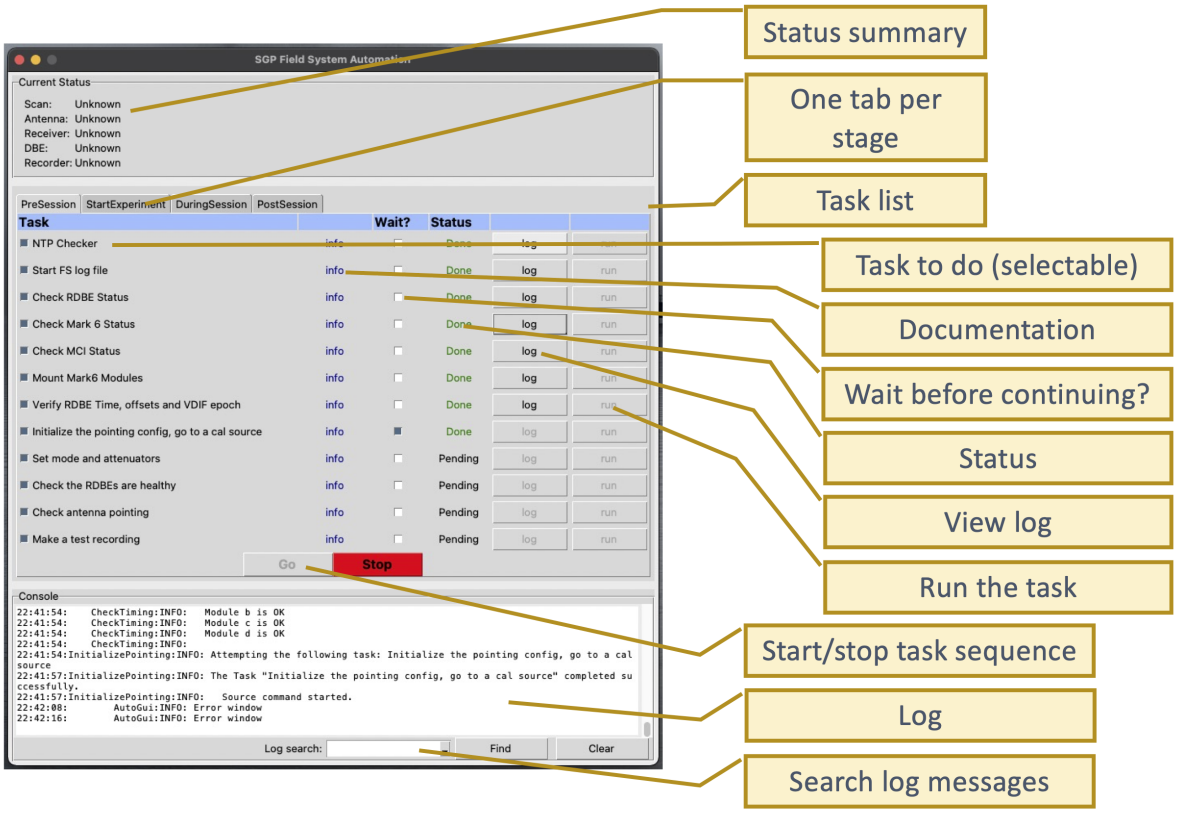

Fig. 3 A development version of the graphical user interface for the *SGPAutomation* software. See the main text for a description.

References

1. M. Berube, J. Gipson, J. Lovell and D. Lakins 2022, "Improving IVS communication through a VLBI Operating Center", these proceedings
2. NVI Inc GitHub web page https://github.com/nvi-inc
3. A. Neidhardt et al. 2019, "The Smart Observatory for Autonomous and Remote Observations", In Armstrong, Baver, and Behrend, editors, IVS 2018 General Meeting proceedings, https://ivscc.gsfc.nasa.gov/publications/gm2018
4. A. Neidhardt 2019a , "A New Generation of Wettzell's Remote Access to the NASA Field System using Web-based Techniques", In Armstrong, Baver, and Behrend, editors, IVS 2018 General Meeting proceedings, https://ivscc.gsfc.nasa.gov/publications/gm2018
5. A. Neidhardt 2019b, "Install and configure the monitoring of EVN Jumping JIVE and IVS Seamless Auxiliary Data (operation, diagnostic, and analysis data)" https://www.haystack.mit.edu/workshop/TOW2019/files/Seminars/Neidhardt_Sem1.pdf

Alternative Frequency Setups for VGOS

Hayo Hase[1]

Abstract In the search for an appropriate frequency setup for VGOS observations, arguments from three different perspectives are discussed: (1) radio regulation, (2) smart selection of the frequency sequence using the Golomb ruler, and (3) consistency requirements for the ICRF.

Keywords VGOS, frequency setup

1 Introduction

During decades, legacy geodetic VLBI observations with dualband S/X receivers have been made using the same frequency configuration. The advantage is a consistent time series of radio sources for the ICRF as well as consistent time series of station positions for the ITRF. There is no need to question it. The VGOS observation system introduces broadband receivers extending the frequency range from the S/X-bands to the range of 2–14 GHz, the number of observation channels from 14 to 32, and the bandwidth of each channel from 16 to 32 MHz. This opens up the question of: **Where to put the VGOS observation channels?** For the attempt to answer we consider three perspectives:

1. an allocated or available spectrum,
2. optimizing the precision analyzing with the group delay resolution function,
3. consistency with the ICRF.

1. Bundesamt für Kartographie und Geodäsie

2 Allocated or Available Spectrum

The ITU Radio Regulations allocate spectral bands to PRIMARY and secondary services. Bands are allocated for up to six different services in the VGOS range of 2–14 GHz (Figure 1). There are no “not-allocated” bands for VGOS exclusively available.

In Figure 1 the orange-red rectangles mark allocations to MOBILE telecommunication while the green fields are related to FIXED broadcast services, both of which are a major threat for radio quietness at radio telescope sites. The allocated bandwidths for the Radio Astronomy Service (RAS) are marked with red and sum up to 250.9 MHz (Table 1). The minimum accumulated bandwidth requirement of VGOS is 1,024 MHz instead. VGOS has to tolerate any other active service according to the radio regulations and receives a certain protection only in bands assigned to the Radio Astronomy Service (RAS).

Another strategy to achieve protection for the observation bands of VGOS would be for the IVS to come up with a fixed frequency setup of 32 channels, which should be then protected by footnotes in the radio regulations. A fixed frequency setup would be adequate for the long-term time series for the ICRF and UT1 but would give away the possibility of escaping in a flexible manner from increasing RFI. Emissions from outside of the VGOS channel bands might still interfere and be detrimental to the VGOS observations, though.

As a matter of fact VGOS is a *global* network, but radio regulations are introduced by *national* authorities, although mostly according to the agreements reached by the World Radio Conferences. The introduction of 5G in the 3.6 GHz bands shows different allocations between nations. This makes it even harder to maintain a common VGOS frequency setup for the

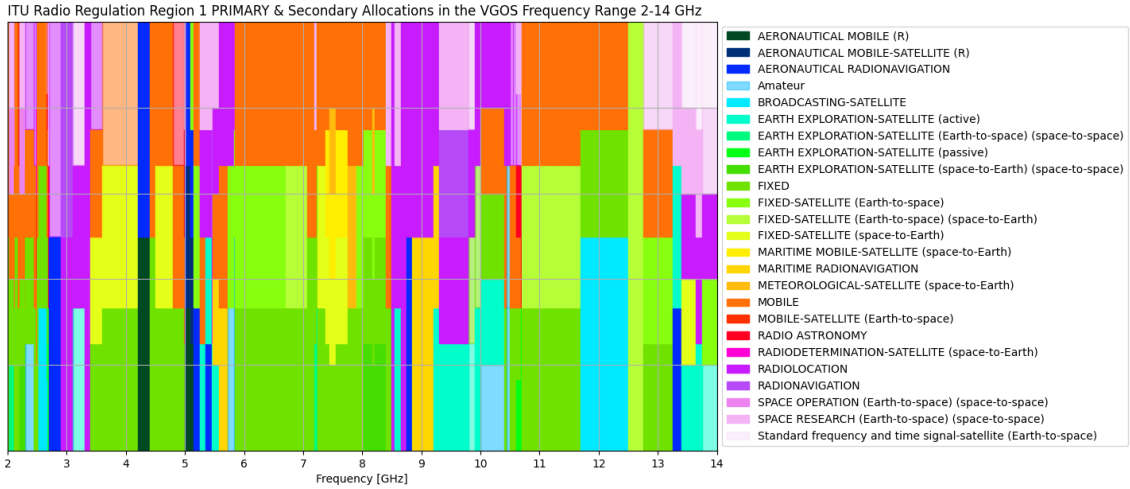

Fig. 1 Frequency allocation in the range of 2–14 GHz in ITU Region 1 (Europe-Africa). (There exist only small differences with respect to Regions 2 and 3.) Free frequency bands for VGOS are not available.

global VGOS network as we encounter different RFI situations among the VGOS countries.

This situation suggests for ideal VGOS sites to be located in a radio-quiet-zone (RQZ) or at least in a coordination zone in which conflicts of interest can be regulated by the authorities.

Table 1 Spectral bands in the VGOS range of 2–14 GHz allocated to the Radio Astronomy Service with different levels of protection. VGOS requires at least 1,024 MHz of bandwidth to reach its goals. [ITU-R Radio Regulations]

Frequency [MHz]	Bandwidth	Allocation, Footnote
2655 – 2670	15	secondary, No. 5.149, 5.208B
2670 – 2690	20	secondary, No. 5.149, 5.208B
2690 – 2700	10	PRIMARY, No. 5.340, 5.413, 5.20B
3260 – 3270	7	No. 5.149
3332 – 3339	7	No. 5.149
3345.8 – 3352.5	6.7	No. 5.149
4825 – 4835	10	secondary, No. 5.149
4950 – 4990	40	secondary, No. 5.149
4990 – 5000	10	PRIMARY, No. 5.149, 5.402, 5.443B
6650.0 – 6675.2	25.2	No. 5.149, 5.458A
10600 – 10680	80	PRIMARY, No. 5.149
10680 – 10700	20	PRIMARY, No. 5.340
total:	**250.9**	**RAS bandwidth in 2-14 GHz**

3 Optimizing the Precision Analyzing with the Group Delay Resolution Function

The VGOS concept was developed in order to overcome limitations in the time resolution of the S/X measurements and to improve the radio telescope infrastructure by a network of more homogeneous instruments (Table 2). One leverage for increasing the accuracy is to increase the observation bandwidth. This includes observing a wider spectrum and observations up to Ku-band (up to 14 GHz). Observing with 32 channels (instead of 14) with 32 MHz bandwidth (instead of 16) promises much more information per time unit, and hence the duration of scans can be shortened. More observations per time interval enable a denser atmosphere sampling. The higher temporal resolution resolves frequency dependent source positions (source structure).

Table 2 Time resolution is inversely proportional to the observed bandwidth.

	spanned bandwidth	resolution
full potential VGOS	2.0 ... 14.0 GHz = 12.0 GHz	83 ps
VGOS-480, VGOS-992	3.0 ... 10.7 GHz = 7.7 GHz	130 ps
legacy X-band	8.213 ... 8.933 GHz = 0.720 GHz	1388 ps

Table 3 lists the known (legacy S/X from R1 sessions, VGOS-480 as a benchmark setup, and VGOS-992) and some alternative frequency setups (G8-1-2, G22+10, and G22) which were developed by [1].

Table 3 Three known and three alternative frequency setups for geodetic VLBI. The legacy S/X setup is typical for the R1 sessions. VGOS-480 is the VGOS benchmark setup. and VGOS-992 covers a wider bandwidth for each block of eight channels compared to VGOS-480. The alternative setup G8-1-2 contains the application of the Golomb ruler of the order 8 for the spacing where the two upper channels are downshifted to match the available block bandwidth of 992 MHz (to be comparable with VGOS-992) but extended to Ku-band. G22 uses the Golomb ruler of the order 22 using only 22 channels, with G22+10 adding ten channels to G22 in a least redundant way in order to make use of the hardware available.

leg. S/X	VGOS-480	VGOS-992	G8-1-2	G22+10	G22
2225.99	3000.4	3000.4	3000.4	2576.4	2576.4
2245.99	3032.4	3032.4	3032.4	2608.4	2608.4
2265.99	3064.4	3064.4	3128.4	2864.4	2864.4
2295.99	3192.4	3288.4	3288.4	3024.4	3024.4
2345.99	3288.4	3576.4	3480.4	3632.4	
2365.99	3352.4	3768.4	3704.4	3952.4	3952.4
	3416.4	3896.4	3896.4	4176.4	
	3448.4	3960.4	3960.4	4496.4	
8212.99	5240.4	5240.4	5304.4	4816.4	4816.4
8252.99	5272.4	5272.4	5336.4	5968.4	5968.4
8352.99	5304.4	5368.4	5432.4	6480.4	6480.4
8512.99	5432.4	5528.4	5592.4	6544.4	6544.4
8732.99	5528.4	5816.4	5784.4	6672.4	6672.4
8852.99	5592.4	6008.4	6008.4	7664.4	7664.4
8912.99	5656.4	6136.4	6200.4	8304.4	8304.4
8932.99	5688.4	6200.4	6264.4	8592.4	
	6360.4	6360.4	7864.4	8912.4	
	6392.4	6392.4	7896.4	8976.4	
	6424.4	6488.4	7992.4	9104.4	9104.4
	6552.4	6648.4	8152.4	9392.4	
	6648.4	6936.4	8344.4	9712.4	9712.4
	6712.4	7128.4	8568.4	10672.4	10672.4
	6776.4	7256.4	8760.4	10992.4	10992.4
	6808.4	7320.4	8824.4	11216.4	11216.4
	10200.4	10200.4	12888.4	11632.4	
	10232.4	10232.4	12920.4	11888.4	11888.4
	10264.4	10328.4	13016.4	12656.4	
	10392.4	10488.4	13176.4	13136.4	13136.4
	10488.4	10776.4	13368.4	13488.4	13488.4
	10552.4	10968.4	13592.4	13712.4	
	10616.4	11096.4	13784.4	13872.4	13872.4
	10648.4	11160.4	13484.4	13968.4	13968.4

The comparison of the cross power spectrum of VGOS-480 vs. VGOS-992 shows that a wider block bandwidth results in a better side peak suppression. When the spanned bandwidth is extended to Ku-band (G8-1-2) a further improvement can be reached (Figure 2). The enhancement of the block bandwidth from 480 MHz (left) to 992 MHz (right) reduces the number of high side peaks. It shows that the selection of the frequency sequence has an impact on the easiness of determining correctly the main peak in the correlation process.

This analysis shows that the high performance of VGOS can be optimized further by smart frequency selection. It seems that the best performance can be achieved by applying the Golomb ruler to the frequency sequences. In this comparison the sequence G22 performs best in terms of minimum main peak width, and G22+10 performs best in side peak suppression (Figure 3). Both differ marginally but are significantly better than VGOS-480 or VGOS-992, both not using Ku-band (Figure 4)! G22 allows saving of resources, as with fewer channels/less data, an equivalent result can be achieved. In summary, the VGOS accuracy can be improved by an adequate frequency selection. Optimization trials are worth the effort before a new sequence will be frozen for decades in order to provide consistency over time!

4 Consistency with ICRF

We know that ICRF reference sources are mostly Active Galactic Nuclei (AGN) and expose some frequency dependencies of their cores plus a time variable position. With the increased resolution from VGOS, this source structure is an issue to be resolved in the analysis. This reveals the question: To which radio frequency do the ICRF sources refer?

The ICRF3 publication reads: *"The new frame, referred to as ICRF3, is based on nearly 40 years of data acquired by very long baseline interferometry at the standard geodetic and astrometric radio frequencies (8.4 and 2.3 GHz), supplemented with data collected at higher radio frequencies (24 GHz and dual-frequency 32 and 8.4 GHz) over the past 15 years."* [A&A 644, A159 (2020)] This implies that the group delay is referred to that frequency of "8.4 GHz". No statement could be found about how the data is linked to that specific radio frequency. Hence it seems to be just a label. Note that the average X-band frequency of the R1 observation sequence as listed in Table 3 is 8.60349 GHz, instead of 8.4 GHz! It appears that, due to non-resolved

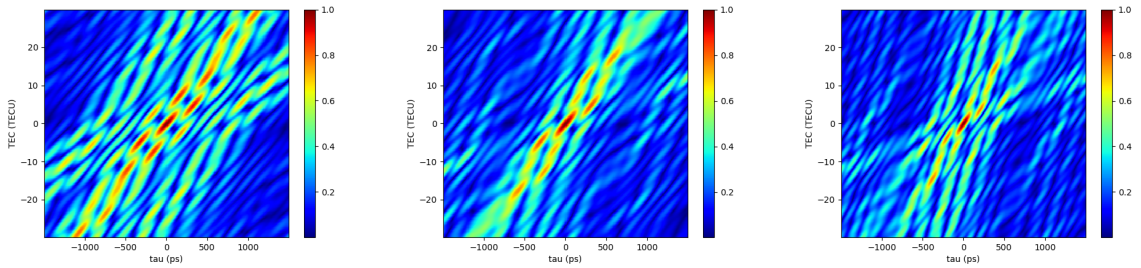

Fig. 2 Cross power spectrum of VGOS-480 (left) vs. VGOS-992 (middle) vs. G8-1-2 (right). The color code shows the level of correlation (0..1) between group delay (TAU) and total electron content units (TECU) of a given frequency sequence. In this bird perspective the red spots mark correlation peaks. The searched for main peak is centered.
VGOS-992 vs. VGOS480: Wider block bandwidth results in better side peak suppression (fewer red spots).
G8-1-2 vs. VGOS-992: Inclusion of the Ku-band increases time resolution and reduces the main correlation peak width.

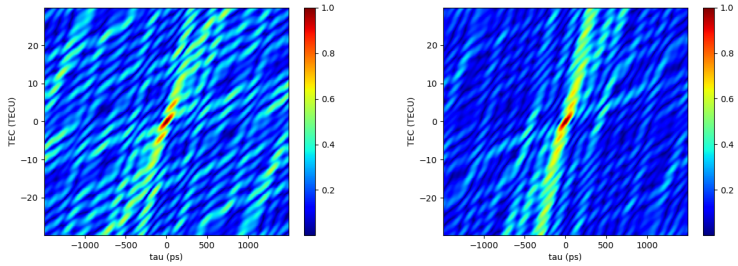

Fig. 3 Cross power spectrum of G22 (left) vs. G22+10 (right). The rigorous application of the Golomb ruler of the order 22 covering the frequency range from 2.5 to 14 GHz achieves with only 22 channels an even better result than G8-1-2. Adding ten more observation channels with a least redundant approach in the linear combinations among the channel frequencies reduces side peaks further but does not change much the overall performance.

sources in the legacy S/X data bases, the subject of a precise *reference frequency* had not been an issue.

This triggers a number of new questions:

1. What is the ICRF "reference frequency" in a VGOS sequence?
2. Do we introduce four source positions for each frequency block group delay (e.g., VGOS-480/992, G8-1-2)?
3. Or do we use one super group delay combined from the four block group delays?
4. Do we use only one group delay over a wider spectrum using the average frequency as reference (e.g., G22/+10)?
5. Do we need to select frequencies with respect to maintaining consistency with the former ICRF?

Figure 5 shows the distribution of the discussed observation channels (Table 1) with their center frequency of all channels. The closest center frequency to "8.4 GHz" is the G22+10 sequence.

5 Conclusions

Three perspectives on the frequency selection for VGOS can be summarized:

1. All radio bands are allocated, mostly to active services which potentially interfere with intended VGOS observations. Radio Quiet Zones (RQZ) for VGOS sites are desirable, and at least coordination zones should be established.
2. Currently used VGOS sequences can be improved by alternative sequences making use of the Golomb ruler. Reduction from 32 to 22 channels is then possible and would save resources.
3. The future VGOS sequence will define a new CRF as source structure is resolved. The adequate frequency selection could preserve consistency with legacy ICRFs.

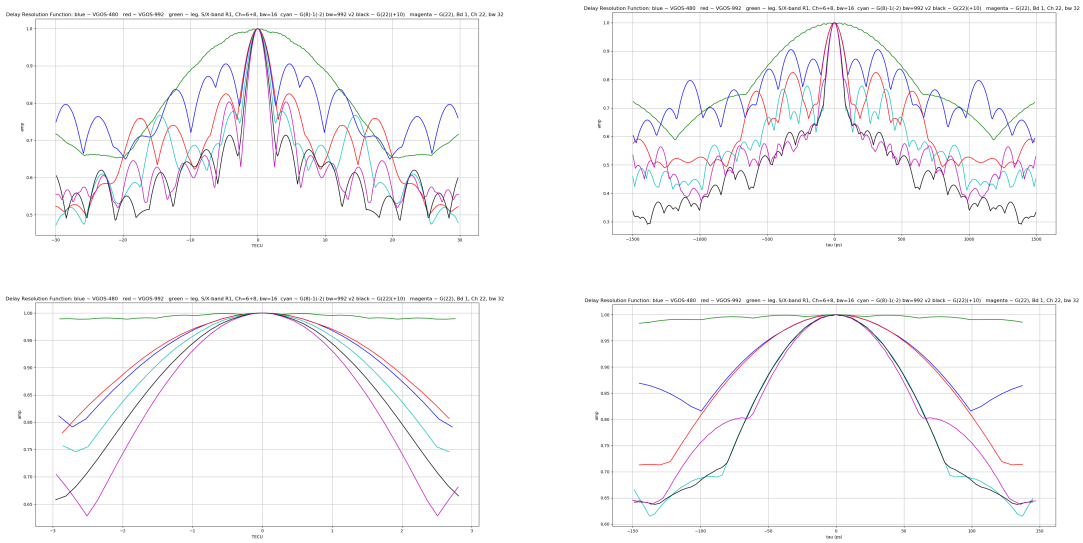

Fig. 4 Superposition plots of the cross power spectrum of the presented frequency sequences as side views to the power spectrum, along TECU (left) and TAU (right). The main peak is 10x amplified in the lower figures. The best performance is shown by G22 (magenta) and G22+10 (black).

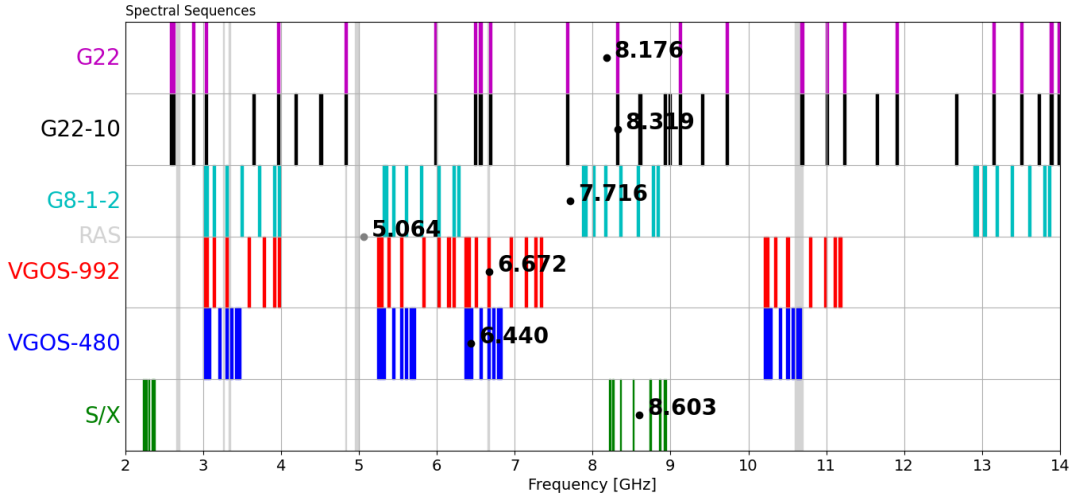

Fig. 5 Channel distribution in the range of 2–14 GHz with their respective center frequencies for different frequency sequences. The selection of channels may be of importance for consistency of the ICRF when it is to be tied to the legacy observations. (RAS bands of Table 1 are in grey.)

Acknowledgements

The plots in Figures 2, 3, and 4 were created with the delfun1.py script from Bill Petrachenko.

References

1. H. Hase, “On the Frequency Selection for Geodetic VLBI”, unpublished paper for IVS-VTC, July 8, 2021.

VGOS Technology R&D Sessions

B. Petrachenko[1], M. Schartner[2], M. Xu[3,4]

Abstract A series of VGOS technology R&D sessions has been undertaken. In total, seven 24-hour sessions were scheduled along with associated 1-hour tests. The primary goal is to significantly increase the number of observations per session at each station. In the VGOS R&D series so far, the number of observations per session has more than doubled when compared to current operational VGOS sessions. Other related priorities include: 1) to optimize high rate schedules both for geodesy and for imaging; 2) to develop and test processes to determine and apply source structure corrections; and 3) to evaluate and test improved frequency sequences. Sources were analyzed to produce closure images, maps, models, and preliminary corrections.

Keywords VGOS, Technology, VTC, R&D

1 Introduction

In early 2021 the IVS Observing Program Committee (OPC) informed the VGOS Technical Committee (VTC) that resources had been allocated for a series of VGOS technology R&D sessions. Within this mandate, a series of seven 24-hour VGOS R&D sessions were undertaken along with associated 1-hour tests. The main purpose of the sessions is to demonstrate operational readiness for "high rate observing," in other words, to move towards the VLBI2010 target [2] of, on average, one scan every 30 seconds at each station. Other related priorities include: 1) to optimize high rate schedules both for geodesy and for imaging; 2) to develop and test processes to determine and apply source structure corrections; and 3) to evaluate and test improved frequency sequences.

1. Natural Resources Canada (retired), Canada
2. Institute of Geodesy and Photogrammetry, ETH Zürich, Robert-Gnehm-Weg 15, CH-8093 Zurich, Switzerland
3. Aalto University Metsähovi Radio Observatory, Metsähovintie 114, FI-02540 Kylmälä, Finland
4. Aalto University Department of Electronics and Nanoengineering, PL15500, FI-00076 Aalto, Finland

2 The Sessions

A total of seven 24-hour VGOS R&D sessions and six 1-hour tests were placed in the Master Schedule. These are summarized in Table 1.

Table 1 VGOS R&D sessions.

Observing date	Session code	Duration (hours)	Integrations (seconds)	Frequency sequence
2021-07-29	VR2101	24	7–20	Standard
2021-10-15	V1288A	0.5	60	New
2021-10-15	V1288B	0.5	60	New
2022-01-20	VR2201	24	7–20	Standard
2022-02-18	VT2049	1	7–20	V1288A
2022-03-17	VR2202	24	7–20	V1288A
2022-03-18	VT2077	1	5–18	Standard
2022-05-19	VR2203	24	7–20	Standard
2022-07-21	VR2204	24	5–18	Standard
2022-07-22	VT2203	1	120	New
2022-09-15	VR2205	24	7–20	Standard
2022-09-16	VT2259	1	120	New
2022-11-09	VR2206	24	7–20	New
2022-11-10	VT2314	1	?	?

3 Frequency Sequence Development

The current operational VGOS frequency sequence was developed in support of the GGAO–Westford proof of concept sessions. Now, after several years, the VGOS network has expanded and RFI problems have become more ubiquitous. A review of the frequency sequence has been undertaken.

Two basic tendencies are required of a good frequency sequence: 1) that the SNR for fringe detection is as low as possible; and 2) that delay precision is as high as possible. In general, delay precision improves as channel separation increases and fringe detection improves as channel distribution becomes more even.

These tendencies are tempered by hardware constraints. To ensure network compatibility, a system with four 512-MHz bands across 3 to 10.7 GHz (the same as for the proof-of-concept system) will be considered the benchmark.

In addition, other factors must be considered, e.g., the loss of channels due to narrow-band RFI, the loss of whole regions of the spectrum due to broadband RFI, non-linear behavior of the system, and non-linear behavior caused by source structure.

In the design process used here, it is assumed that band-A and band-D will be placed as near as possible to the extremes of the 3 to 10.7 GHz frequency range. This is to ensure adequate delay precision. To study the detectability aspect of the sequences, the probability of a missed phase connection is then calculated at every possible pair of band-B and band-C frequencies as they are moved, in 32-MHz steps, throughout the intervening spectral region.

In Figure 1, log_{10} of the best (i.e., lowest) 8,000 probabilities are plotted assuming an SNR of 10 in each band. At this SNR, it can be seen that there is a wide range of sequences that perform well, e.g., for sequences in the blue and green regions the probability of error is less than 1 part in 10^5. The existence of these somewhat broad regions means that, at least to some extent, frequencies can be adjusted to avoid broadband RFI.

The best performing sequence (located at f=[3,000.4; 4,472.4; 6,584.4; 10,200.4] MHz) has been tested in two 1-hour sessions, V1288A, VT2049, and in one 24-hour session, VR2202. In the sessions correlated so far, no serious RFI issues were detected although not all stations were included in the tests. Detailed RFI analysis at each station will be required for a more definitive and robust sequence definition.

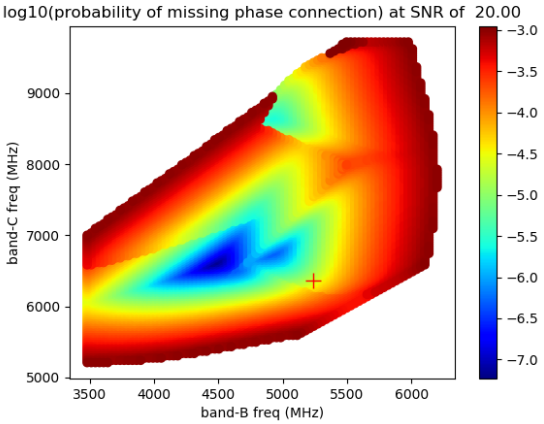

Fig. 1 Log_{10} of the probability of a phase connection error at SNR=20. The + symbol represents the position of the current VGOS sequence.

Intuitively, it is expected that sequences will perform reasonably well even if a small number of channels are lost. With the current VGOS mode using 8-Gbps recording, 50% of each band is occupied, which provides significant redundancy. This was verified numerically for pairs of channels (Figure 2). The red trace represents the Delay Resolution Function (DRF) for the V1288A sequence, while each green trace represents the DRF for the same sequence but with the loss of two channels. All possible combinations of channel pairs were considered. In addition to the loss of about 3% SNR (which is not reflected in the figure), the DRFs are distorted somewhat but not enough to significantly degrade fringe detection.

Finally, the impact of nonlinear phase is considered in a numerical study. The phase of a single VGOS band is offset and this is repeated in sequence for each of the four bands. In all cases, the phase offset produces a noticeable shift of the main peak of the DRF (which manifests as an unwanted delay bias). However, for band-B or band-C, the delay bias is also accompanied by a significant distortion of the DRF which greatly increases the probability of a sub-ambiguity error. For the sequence used in V1288A and a phase offset of 45°, the height of the highest sidelobe is nearly as high as the main peak (Figure 3). This emphasizes the importance of careful calibration of the system phase and the danger of using sources with excessive structure.

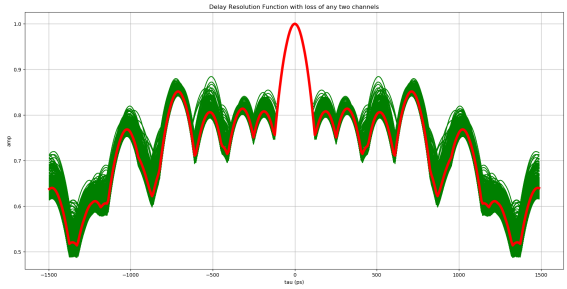

Fig. 2 DRFs of the V1288A sequence. Green traces assume the loss of arbitrary pairs of channels. Horizontal grid lines are separated by 10% of the central peak and vertical grid lines are separated by 500 ps.

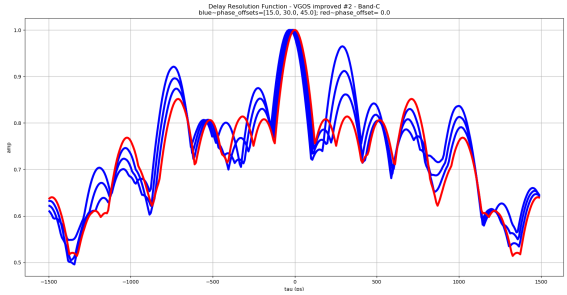

Fig. 3 DRFs of the V1288a sequence. Blue traces represent DRFs for phase offsets of 15°, 30°, and 45° at band-C. The red trace is for no phase offset. Horizontal grid lines are separated by 10% of the central peak and vertical grid lines are separated by 500 ps.

4 Scheduling

The VGOS R&D sessions are scheduled using VieSched++ [3] with the session designed individually.

The main focus of the R&D sessions is to increase the observing rate, i.e., the number of observations per session at each station. This is accomplished primarily through the following scheduling-related strategies:

- Two (instead of one) record modules are used at the Mark-6 stations. This ensures that data can be recorded in real-time without waiting for a record buffer to flush. The resulting saving is significant given that, with the current VGOS single module mode, the "buffer flush" is equal in duration to the data record time.
- The accuracy of the antenna slew models was confirmed; if necessary they were improved. This ensures that the scheduling software accurately predicts on-source arrival time so that antennas are neither needlessly waiting for observations to begin nor arriving too late. The Onsala case was particularly interesting where it was discovered that slew rate can change depending on antenna pointing angle and slew direction.
- Field system procedures (preob and midob) were streamlined, removing unnecessary and time-consuming checks. As a result, the preob time was reduced from four seconds to two seconds.
- Signal-to-Noise (SNR)-based scheduling, similar to that developed for some early EU-VGOS sessions [1], was used. With this approach, the integration time is adjusted, within limits, to achieve a specified SNR. For the R&D sessions, the integration time limits were either from 7 seconds to 20 seconds or from 5 seconds to 18 seconds (see Table 1 for details). This is in contrast to operational VGOS sessions where fixed 30-s integrations are used. SNR calculations require accurate system SEFDs and source fluxes. Since source fluxes are not available at the VGOS band frequencies, S/X flux densities were inter-/extrapolated to VGOS frequencies assuming a power-law spectral index. For VR2203, the first VGOS-based band-ABCD source flux density catalog, derived from previous VGOS sessions, was tested. Also, the R&D SNRs were typically too low for good calibration. As a result, calibration scans were inserted into the schedules. The cadence was either every hour or every two hours and the duration was either 60 seconds or 120 seconds (see Table 2 for details).

Table 2 VGOS R&D scheduling statistics. Columns: session name, number of stations, number of observations, number of scans, and number of sources.

Session code	#sta	#obs	#scans	#src	Cal. scans # | duration	Source catalog
VR2101	7	25,619	3,397	94	24 | 120 s	S/X-based
VR2201	9	36,644	4,352	176	12 | 60 s	S/X-based
VR2202	9	37,701	3,707	141	12 | 60 s	S/X-based
VR2203	8	26,840	4,295	90	24 | 60 s	VGOS ABCD

Each R&D session has its own targets and strategies, e.g.:

- VR2101 is the first VGOS R&D session to use SNR-based scheduling. Additionally, the schedul-

ing algorithm tried to include only sources that are observed in at least ten scans. This was done utilizing iterative source selection as discussed in [3].

- VR2201 set the minimum and target number of scans per source to ten and 22, respectively, to put even more emphasis on a better distribution of scans among sources. Based on the target number of scans and the network source visibility, a minimum time between two scans to the same source was calculated. This was done for each source. [Note that fillin-modes and other scheduling algorithms could still cause some sources to be observed more frequently.] As a result, the number of scheduled sources was increased to 176, with an average number of scans per source of 24.8 ± 7.8. Additionally, for the first time, a southern-hemisphere station, HOBART12, was included in tagalong mode. To ensure good inclusion, the tagalong mode was improved by a second round of fillin-mode scans, the so-called fillin-mode a posteriori. As a result, HOBART12 was scheduled in over 1,000 scans despite its remote location and tagalong status. Finally, VR2201 included one pair of radio sources scheduled 27 times in phase-referencing mode.
- VR2202 put slightly less emphasis on the distribution of scans among sources in favor of improving good short-term station sky coverage. This was done to enable a better estimation of high-frequency tropospheric disturbances. To achieve this, the Monte-Carlo simulation approach was adjusted to include high-frequency troposphere estimates. Additionally, the station-dependent sky coverage optimization parameters were utilized to account for the different antenna slew rates and sky visibilities.
- VR2203 used, for the first time, a VGOS frequency source flux density catalog for the calculation of the SNR-based integration times. In addition, the minimum time between two scans to the same source was lowered to 20 minutes to obtain more scans per source.

5 Source Structure and Modeling

For VGOS, the first image processing task is to fit Gaussian components based on closure phases and closure amplitudes. This can be divided into three steps. First, isotropic total variation regularization is applied, which favors the smoothness of the flux density distribution to solve the ill-posed problem in imaging, to obtain a map of flux densities on any predefined pixels [4]. The process can be called closure imaging [5]. Secondly, we use these "closure" maps to self-calibrate visibilities. Finally, the Gaussian components are fitted from these self-calibrated visibilities.

The second task is to determine the total flux densities of the maps if there is amplitude calibration information available for a fraction of the antennas but not necessarily for all the antennas. This is necessary because the amplitudes were not calibrated based on the SEFD and antenna gain curves, leading to the closure maps missing a correct scale of the total flux densities. Even though this scale itself does not affect the derived corrections for source structure, it is important to determine the correct total flux density for an image so that we can predict SNR in scheduling.

Aligning the images over frequency is the third task. The information of the phase center is lost in imaging due to difficulties in calibrating the visibility phases; note that this is a common problem in VLBI imaging rather than a unique issue for the closure imaging. To derive coherent visibility phases, like that of a point source, by correcting structure phases based on the four-band maps, the phase centers of these four maps must be accurately linked with each other [6].

The imaging results for VGOS R&D session VR2101 are publicly available[1], where we report the statistics of closure imaging, maps, and models of Gaussian components, and the preliminary results of the model corrections. Table 3 summarizes the imaging results. Out of the 28 imaged sources, only eight sources do not have a second bright component ($> 30\%$ to the peak) at any of the four bands.

For VGOS R&D session VR2201, we have imaged 106 sources. The Gaussian components can be determined for 103 sources, a demonstration of a significant improvement in the imaging capability. This session allows for many of the low-declination sources to be imaged, as shown in Figure 4 for source 0748+126.

The on-going work includes the second and the third tasks of the imaging process, and challenges can be foreseen in particular for the image alignment. A common issue is that parts of the jet components may

[1] `http://www.metsahovi.fi/~xum2/me/vr2101/`

Table 3 Number of the Gaussian components and the flux density ratio of the second bright component to the peak component based on the observations from VGOS R&D session VR2101.

Source	3.3 GHz		5.5 GHz		6.6 GHz		10.5 GHz	
	$N_{\rm cmp}$	$R_{\rm flux}$	$N_{\rm cmp}$	$R_{\rm flux}$	$N_{\rm cmp}$	$R_{\rm flux}$	$N_{\rm cmp}$	$R_{\rm flux}$
0016+731	2	0.93	3	0.38	3	0.38	3	0.34
0059+581	2	0.08	2	0.80	2	0.98	2	0.73
0133+476	2	0.14	2	0.19	2	0.17	2	0.11
0202+319	2	0.32	2	0.16	2	0.15	2	0.86
0235+164	1	—	1	—	1	—	2	0.01
0529+483	2	0.08	3	0.81	3	0.94	3	0.03
0552+398	1	—	2	0.65	2	0.81	2	0.87
0613+570	1	—	2	0.58	2	0.10	2	0.14
0716+714	2	0.12	2	0.13	2	0.17	2	0.15
0748+126	3	0.45	3	0.41	3	0.22	2	0.13
0805+410	2	0.05	2	0.07	2	0.13	2	0.09
0955+476	2	0.20	2	0.12	2	0.11	2	0.03
1144+402	2	0.59	2	0.62	2	0.54	2	0.13
1156+295	2	0.11	2	0.08	2	0.08	2	0.04
1606+106	3	0.82	3	0.45	3	0.50	3	0.35
1749+096	2	0.23	2	0.58	2	0.06	2	0.21
1751+288	2	0.07	2	0.05	1	—	1	—
1803+784	3	0.45	2	0.28	4	0.35	3	0.30
1849+670	3	0.11	2	0.12	2	0.09	2	0.35
2000+472	2	0.62	2	0.12	2	0.66	3	0.81
2059+034	2	0.08	2	0.18	2	0.18	2	0.06
2113+293	2	0.09	2	0.29	2	0.11	2	0.39
2215+150	1	—	1	—	1	—	2	0.46
2229+695	2	0.52	3	0.28	3	0.20	3	0.28
NRAO150	3	0.50	1	—	1	—	2	0.64
OJ287	3	0.82	3	0.63	5	0.96	3	0.68
3C371	2	0.40	3	0.86	3	0.65	3	0.40
3C418	3	0.42	3	0.53	2	0.50	3	0.44

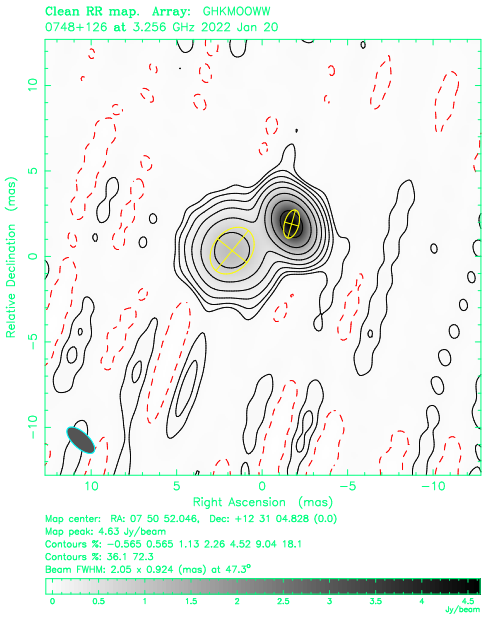

Fig. 4 VGOS image of source 0748+126 at 3.3 GHz from R&D session VR2201 (January 20, 2022). The Gaussian components are shown as the yellow ellipses.

contribute to the modeled core and change its position. Due to the large difference in the angular resolutions across the four bands, the "core" position will move towards the jet by a different offset at each of the four bands. The differences in the u,v coverage of a given source from session to session can also affect the stability of the image alignment over time.

References

1. F. Jaron, S. Bernhart, J. Böhm, J. González Gracía, J. Gruber, Y.K. Choi, I. Martí-Vidal, M. Schartner, B. Soja, J. Wagner, E. Varenius, H. Verkouter, on behalf of the EU-VGOS collaboration, "EU-VGOS activities in Vienna," Proceedings of the 25th European VLBI Group for Geodesy and Astrometry Working Meeting, 2021, ISBN: 978-91-88041-41-8
2. B. Petrachenko, A. Niell, D. Behrend, B. Corey, J. Böhm, P. Charlot, A. Collioud, J. Gipson, R. Haas, T. Hobiger, Y. Koyama, D. MacMillan, Z. Malkin, T. Nilsson, A. Pany, G. Tuccari, A. Whitney, J. Wresnik, "Design aspects of the VLBI2010 system," Progress report of the IVS VLBI2010 Committee, NASA/TM-2009-214180, 2009. https://ivscc.gsfc.nasa.gov/publications/misc/TM-2009-214180.pdf
3. M. Schartner and J. Böhm, "VieSched++: A New VLBI Scheduling Software for Geodesy and Astrometry," Publications of the Astronomical Society of the Pacific, vol. 131, no. 1002. IOP Publishing, p. 084501, Jun. 18, 2019. doi: 10.1088/1538-3873/ab1820.
4. Xu M. H., Savolainen T., Zubko N., Poutanen M., Lunz S., Schuh H., Wang G. L., "Imaging VGOS Observations and Investigating Source Structure Effects," 2021, Journal of Geophysical Research (Solid Earth), 126, e21238. doi:10.1029/2020JB021238
5. Chael, A. A., Johnson, M. D., Bouman, K. L., Blackburn, L. L., Akiyama, K., and Narayan, R., "Interferometric Imaging Directly with Closure Phases and Closure Amplitudes," The Astrophysical Journal, vol. 857, no. 1, 2018. doi:10.3847/1538-4357/aab6a8
6. Xu M. H., Savolainen T., Anderson J. M., Kareinen N., Zubko N., Lunz S., Schuh H., "Impacts of the image alignment over frequency for VLBI Global Observing System," A&A, 663 A83 (2022), doi: https://doi.org/10.1051/0004-6361/202140840

Obtaining Local-Tie Vectors from Short-Baseline Interferometry

R. Handirk[1], E. Varenius[1], T. Nilsson[2], R. Haas[1]

Abstract With the VLBI Global Observing System (VGOS) being the next step in the development of geodetic VLBI, it is necessary to connect the new VGOS network to the existing legacy S/X telescopes. At the Onsala Space Observatory (OSO), this is being done by short-baseline interferometry between the VGOS Onsala twin telescopes ONSA13SW and ONSA13NE and the legacy antenna ONSALA60.

The main aim of these sessions, referred to as ONTIE, is to obtain local-tie vectors between these three OSO telescopes that all take part in regular geodetic VLBI observations. Each ONTIE session is about 24 h long, during which all three telescopes observe simultaneously the same sources at X-band. A total of 37 ONTIE sessions have been observed since April 2019. In November 2021, the ONTIE sessions were for the first time observed with alternative observation frequency setups in order to mitigate the influence of known RFI. Additionally, scheduling was done—also for the first time—with *VieSched++* instead of *sked*.

Interesting findings of the ONTIE sessions include unexpected offsets in the results of group and phase delays, jumps in the coordinates of the twin telescopes, and apparent yearly trends that might be an artifact of unmodeled thermal expansion of the telescopes that is left in the data.

Future ONTIE sessions are envisioned to happen on a regular basis and could, as a by-product, also serve as quasar flux-monitoring sessions by investigation of the recorded system temperatures during observation.

This paper summarizes the current status and results of the ONTIE sessions.

Keywords Onsala twin telescopes, OTT, ONSALA60, VGOS, legacy S/X, local ties

1 Introduction

The three antennas ONSALA60 (On), ONSA13NE (Oe), and ONSA13SW (Ow) at the Onsala Space Observatory (OSO) are regularly used for short-baseline interferometry measurements. These dedicated measurements are referred to as ONTIE sessions and have been carried out since April 2019. This kind of session is important for determining local ties for the International Terrestrial Reference Frame (ITRF) between the legacy S/X telescopes and the new generation VLBI Global Observing System (VGOS) telescopes.

Since April 2019 we carried out 37 ONTIE sessions. Throughout these, we used six different frequency setups, and we used two different software packages to schedule the experiments. The databases of the first 25 sessions (until 2020-11-13) have already been published by [1].

In Section 2 we present the setup of the 12 new sessions in 2021 and 2022. Section 3 is dedicated to the data of 30 ONTIE sessions and the discussion of the results. Section 4 gives a short look at the further scope.

1. Department of Space, Earth, and Environment, Onsala Space Observatory, Chalmers University of Technology, 439 92 Onsala, Sweden
2. Lantmäteriet – The Swedish Mapping, Cadastral, and Land Registration Authority, Lantmäterigatan 2C, 801 82 Gävle, Sweden

2 Experiment Setup and Methods

On is a legacy S/X antenna of 20-m diameter, recording right-handed circular polarized signals. Both Oe and Ow are part of the new VGOS telescope generation and are commonly referred to as the Onsala twin telescopes. They have a diameter of 13.2 m and record linearly polarized signals (horizontal and vertical). All three telescopes share the ability to observe in X-band; ONTIE sessions make use of the 8–9 GHz frequency range. The baseline between the twin telescopes Oe and Ow is about 75 m long, and their distance to On is about 470 m and 550 m, respectively (cf. Figure 1).

All sessions were scheduled with *sked* [2], except for the three latest ones in November 2021 (on1323, on1324, and on1325), which were scheduled with *VieSched++* [3]. We chose the radio sources for the ONTIE sessions from the list which currently serves as the radio source catalog for the IVS operational VGOS series (VO). In addition to the individual horizon mask of each telescope, we set a cut-off angle of 5°. The session length was always 23 h or 24 h, with a minimum duration of 30 s per scan. The last three sessions (November 2021) are an exception as the minimum scan length was reduced to 10 s. Figure 2 shows an exemplary sky plot of observed sources during a 24 h ONTIE session.

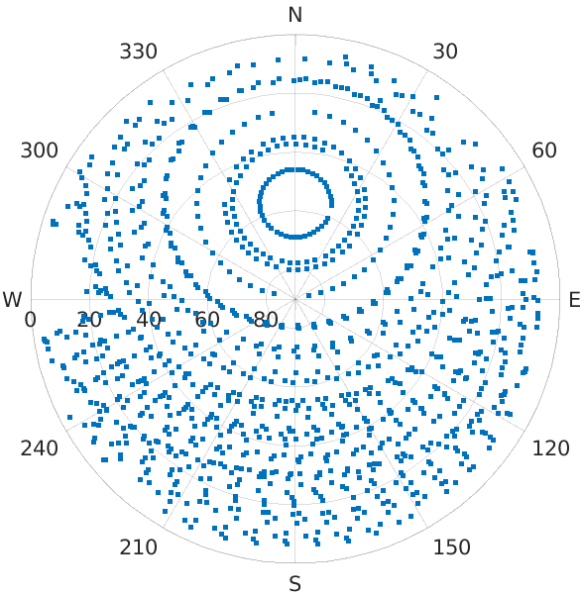

Fig. 2 Sky plot of the 23-h ONTIE session on1325 (2021-11-21) for ONSALA60, including 55 sources to which 1,133 scans were observed.

Fig. 1 The telescopes On, Oe, and Ow at the Onsala Space Observatory.

We observed on eight channels with 32 MHz bandwidth each, and the frequency setup for the new sessions presented here corresponds to configuration C. For the latest three sessions in November 2021, three different setups were used (see Table 1). These configurations D–F aim at avoiding local Radio Frequency Interference (RFI) and are based on short-term local RFI measurements. RFI is one of the biggest issues in VLBI, as strong artificial signals impede the observation of the much weaker astronomical signals and can even damage the receivers. Concerning the choice of observation frequencies, in particular for the new VGOS network or global campaigns designed for specific purposes, the schedulers clearly benefit from knowing the local RFI situation at each station.

The RFI recordings at OSO were carried out with a spectrum analyzer in max-hold mode, i.e., the maximum occurring power per frequency during the recording time will be stored. This allows very strong RFI to be seen immediately; however, it does not reveal for how long a particular RFI signal was actually present. Figure 3 shows the recorded RFI data as a blue curve: the larger the power, the stronger the RFI. We therefore

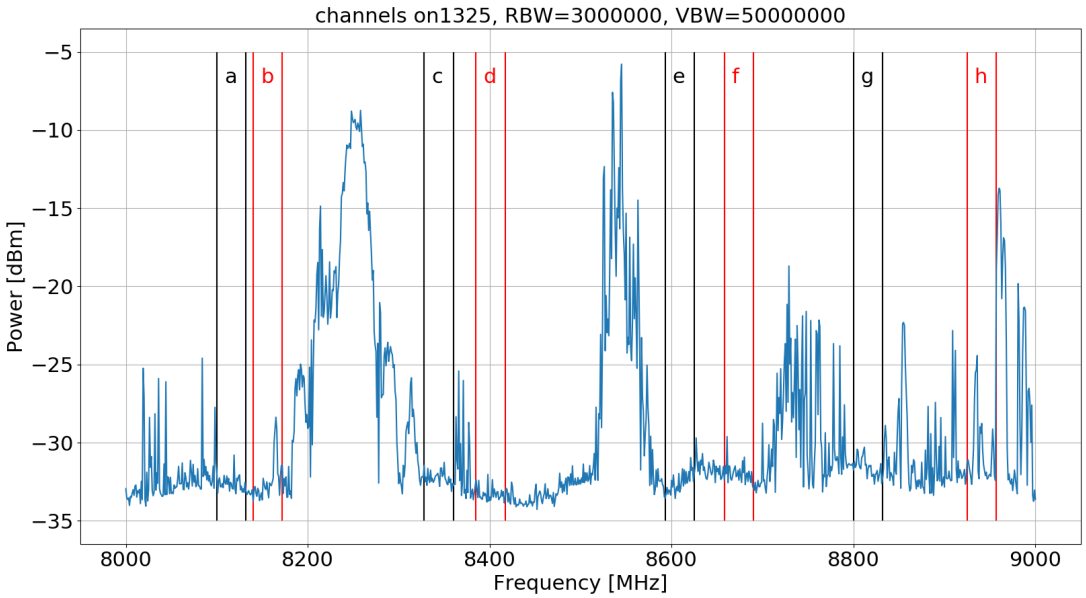

Fig. 3 Fourfit channels a–h used during session on1325 (2021-11-21) in order to mitigate RFI influence (blue). This corresponds to configuration F in Table 1. The channels are alternately represented in black and red in order to make them more perceptible.

Table 1 List of frequency configurations in addition to [1], denoting the lower edge of each correlated BBC channel with the bandwidth 32 MHz. Frequencies given in MHz.

Fourfit channel	Conf. C	Conf. D on1323	Conf. E on1324	Conf. F on1325
a	8,244.99	8,099.99	8,099.99	8,099.99
b	8,284.99	8,139.99	8,139.99	8,139.99
c	8,384.99	8,384.99	8,384.99	8,327.99
d	8,544.99	8,544.99	8,456.99	8,384.99
e	8,764.99	8,764.99	8,799.99	8,592.99
f	8,884.99	8,884.99	8,884.99	8,657.99
g	8,924.99	8,924.99	8,924.99	8,799.99
h	8,964.99	8,964.99	8,964.99	8,924.99

aim to place our channels where the least interference occurs.

Configurations D–F were chosen on the basis of these RFI data and the technical limitations of the recording system. These technical limitations are the reason why the fourfit channel d could not be moved up to a higher frequency and why there is no third channel in the range of 8300–8500 MHz. The fourfit channels a–h displayed as well in Figure 3 represent the setup for the session on1325/configuration F, for which all channels were shifted compared to the setup which had been regarded as the standard setup until then (configuration C as in [1], also listed in Table 1 here).

The correlation of the new ONTIE session data was done with DiFX, the fringe fitting with HOPS, and the analysis with ASCoT, following the same strategy applied by [1]. In particular, we used DiFX version 2.5.4 and HOPS version 3.23 to correlate and fringe fit on1323, on1324, and on1325.

3 Results

In this paper, we exclude all sessions where a phase calibration signal for On was not available, i. e. we focus on a total of 30 sessions.

Figures 4 and 5 show the phase and group delay results obtained from the ONTIE sessions, with 3σ uncertainties. The coordinates of Oe and Ow were solved relative to On; displayed are the differences in the East, North, and Up components w. r. t. the a priori coordinates. Coordinate solutions for Oe are displayed as blue circles and for Ow as yellow squares. The bars indicate the respective 3σ uncertainties. The black dashed vertical lines mark the installation (2020-05-19) and dismount (2021-03-02) of a focal finder (FF) on Oe.

The focal finder was installed in order to determine the optimal position of the receiver. Due to Covid-19 related restrictions the FF stayed on Oe much longer

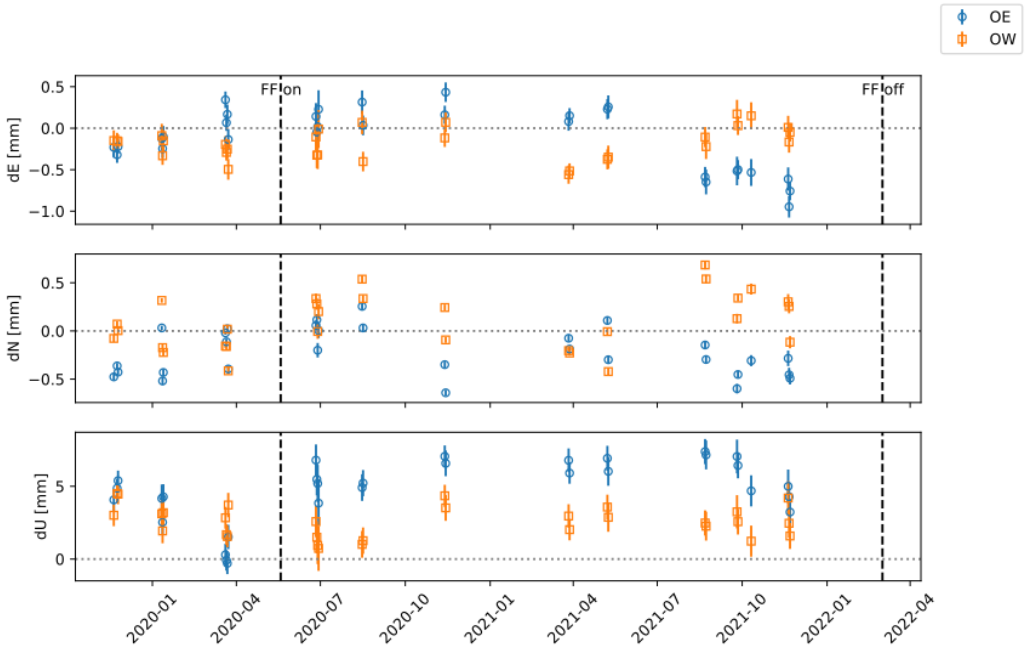

Fig. 4 Phase delay results obtained from ONTIE sessions for the coordinate solution differences w. r. t. the a priori coordinates, displayed separately for dE, dN, and dU versus the respective date of each session. Sessions without phase cal for On are excluded. Blue circles are used for Oe; yellow squares are used for Ow. Bars indicate the respective 3σ uncertainties. Dashed vertical lines mark the mount and dismount of the focal finder (FF) on Oe.

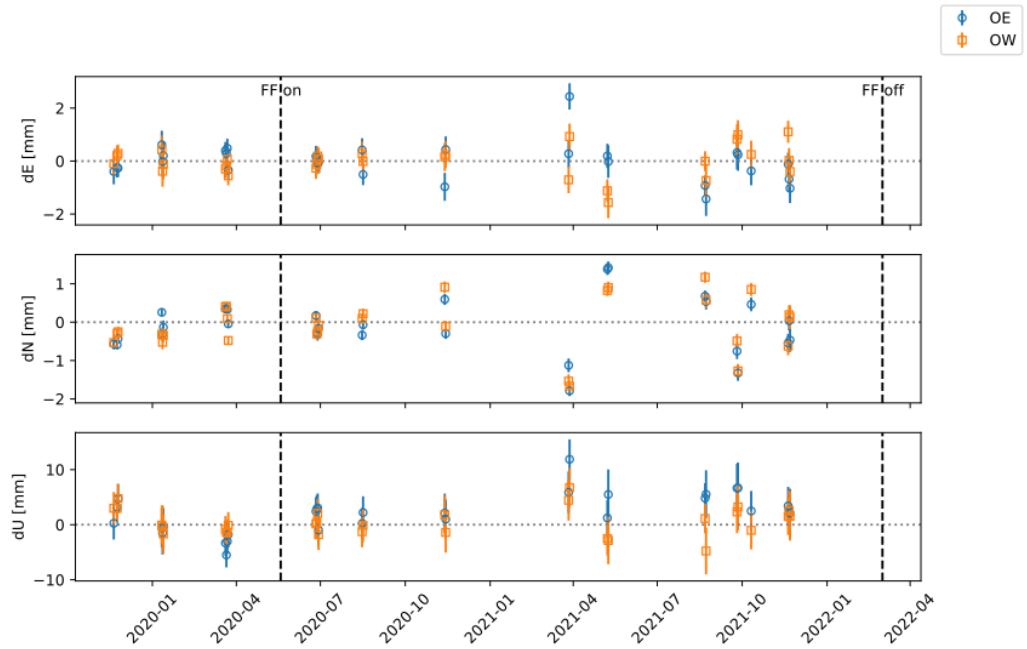

Fig. 5 Group delay results obtained from ONTIE sessions for the coordinate solution differences w. r. t. the a priori coordinates, displayed separately for dE, dN, and dU versus the respective date of each session. Sessions without phase cal for On are excluded. Blue circles are used for Oe; yellow squares are used for Ow. Bars indicate the respective 3σ uncertainties. Dashed vertical lines mark the mount and dismount of the focal finder (FF) on Oe.

than originally intended. After the installation of the FF on Oe, we observe an offset of roughly 4 mm between the phase delay coordinate solutions for Oe and Ow in the Up component (cf. Figure 4). An investigation of the FF following its dismount revealed that a movable component within the FF might have led to an unintended elevation-dependent effect on the observations.

Comparing the Up component solutions from phase delays and group delays (Figures 4 and 5), we observe another offset of about 3 mm between those two solutions, which seems to be of a systematic nature. This has already been noted by [1]. However, it is not yet clear what causes this offset, and it needs further investigation.

Looking at the Up components from both phase and group delay analysis, we further note a signature that could be a seasonal variation. This could be related to unmodeled thermal expansion of the telescope towers. Investigation of the tower height data and the models of all telescopes within ASCoT is currently ongoing, possibly aided by a higher repetition rate of the ONTIE experiments.

4 Ongoing Research and Further Scope

Ongoing research around the ONTIE sessions includes the search for the optimal frequency setup in order to mitigate the influence of local RFI. As a first approach, RFI has been recorded on different weekdays and at different times of the day, while Oe was running in a standard IVS VGOS session, as well as while positioning it at zero degrees elevation pointing to the north. This position is considered to be best in protecting the receiver from RFI, especially ship radar. As mentioned before, we recorded RFI in max-hold, which does not display how long a particular RFI signal lasted. We therefore aim for scan-wise RFI measurements during future experiments, so that we know their time stamp and also possibly direction.

More ONTIE sessions after the dismount of the FF on Oe will be performed and analyzed to test the hypothesis of its assumed elevation-dependent influence on the measurements. Also, experiments with the FF installed on Ow are planned, in order to investigate the expected impact of the FF.

Our further scope, besides having more and regular ONTIE sessions, includes a revision of the source list that is currently being used for scheduling and an investigation into if the position results from ONTIE experiments agree with independent classical local measurements.

Moreover, we also intend to continue using the recorded T_{sys} data for flux monitoring of the observed sources. Because this data is automatically recorded during each experiment, it is already available to us. A first analysis of these data has been carried out by [4], which revealed, i. a., significant long-term variability for some frequently used sources in IVS sessions.

References

1. Varenius E, Haas R, and Nilsson T (2021) Short-baseline interferometry local-tie experiments at the Onsala Space Observatory. *Journal of Geodesy* 95, doi:10.1007//s00190-021-01509-5.
2. Gipson J (2018) Sked VLBI Scheduling Software User Manual. Web document https://ivscc.gsfc.nasa.gov/IVS_AC/sked_cat/SkedManual_v2018October12.pdf
3. Schartner M (2021) VieSched++ VieVS VLBI Scheduling Software. Web document https://github.com/TUW-VieVS/VieSchedpp
4. Varenius E, Maio F, Le Bail K, and Haas R (2022). Broad band flux-density monitoring of radio quasars with the Onsala twin telescopes. Submitted to *Experimental Astronomy*.

Quality Assessment of the Mizusawa Software and GPU Correlators

Takaaki Jike, Tomoaki Oyama, Aya Yamauchi

Abstract Mizusawa has multiple software correlation systems. These currently operating correlation processing systems have several variations in CPU and GPU. Data evaluation was performed to verify the consistency and reliability of the correlation data obtained from these individual correlation processing systems. From these test results, it was found that the differences in the number of CPU cores and the number of FFT points changes the magnitude of the additional error to the correlation data. The magnitude of this additional error was six to 19 times that of the noise artificially added during the correlation processing.

Keywords additional error, number of cores, FFT points

1 Introduction

We recognize that next-generation astronomy, geodesy, and space-time measurements target parameter estimation accuracy at less than 1 mm, 1 microarcsecond, attosecond levels of clock tempo, and 1 micro Jy. At the ninth IVS General Meeting, we reported the results of the delay measurement and geodetic parameter estimation with theoretical white noise delay error of 2 picoseconds root-mean-square (rms) [1]. However, the post-fit residual rms was more than 15 picoseconds, and therefore, it is acknowledged that noisy or systematic compound errors were added during the observation and analysis processes. Guaranteeing required accuracy in the complex of focus, receiving, transfer, digitizing, recording, and correlation is a necessary task to reduce the magnitude of the post-fit residual rms and to achieve the target accuracy. As an investment in the expected goal, we inspected the delay estimation accuracy guaranteed by the current Mizusawa Software Correlator specification. The purpose of this research is to accumulate effective inspection techniques for investigating the performance of next-generation electromagnetic wave-based space-time measurement techniques.

Mizusawa VLBI Observatory, National Astronomical Observatory of Japan

2 Status Parameters of the Mizusawa Software and GPU Correlators

In Mizusawa, two FX-type correlators are implemented; one is the Software Correlator (MSC), and the other is the GPU Correlator (MGC). The MSC is under regular operation, and multiple PC units are available depending on the application. These operating PCs are built with multiple CPUs, motherboards, and operating systems. The engine of correlation processing, called "gico3", is developed by NICT and is installed with optimization according to the number of CPU cores. The MGC is newly developed as the high-end model of the MSC and is now in the test phase. The correlation engine, called "kfxcom", is developed by NAOJ and ©KIMSOFT, and parallel processing is executed by multiple cores arranged inside the GPU, achieving a higher processing speed.

In this study, we estimated the delay from the same observation data using multiple correlators with different specifications and correlation processing modes, and we examined the difference in the additional error

corresponding to each correlator and the change of the correlation mode. Table 1 shows the types and specifications of correlators used for validation. Even if the CPUs have the same number of cores, the CPU and motherboard type are different in each PC.

Table 1 Specifications of the MSC and MGC used for verification.

Correlator PC Name	IP25	IP90	IP114	IP76	IP61
Core type	CPU				GPU
Number of cores	6			8	4352
FFT math library	FFTW332				
Matrix math library	avx2	avx	avx2	avx512	none
Operation engine	gico3-2.6.8				kfxcom-2.0

3 Correlation Data Set

The observation data used in the correlation test is shown in Table 2. Several correlation processes with different settings were performed using common data. The parameters changed during the correlation test are the number of FFT points and the type of PCs, substantially the number of cores. Hereafter, each correlation processing name will be *IPaaa-bbbk* according to this setting, where *IPaaa* is the correlator name and *bbb* is the number of FFT kilo-points. For example, in the case of 512-point FFT correlation processing using PC "IP90", the processing mode is named *IP90-0.5k*.

4 Estimating the Reference Additional Error Scale

In the correlation processing by gico3, white noise error where the size falls within a certain distribution is artificially added at the time of FFT processing. Figure 1 shows the difference between the first cross-correlation coefficient and the other nine correlation coefficients when the same 40 seconds of data is correlated ten times in *IP90-0.5k* mode. This short correlation process is named *IP90-0.5k40*. Moreover, kfxcom does not have such a noise addition function. This is a comparison of the absolute values of the normalized correlation coefficients represented as a single precision complex number. The individual coefficients are obtained from the integral of the time of one second and bandwidth of 2 MHz. Most of the scatter is within $\pm 2 \times 10^{-5}$. It is considered that the magnitude of scattering when converted to this fringe function decreases to $1/102.4$ in the integrated value for 40 seconds. Based on this result, the delay estimates are compared between *IP90-0.5k* and *IP25-0.5k*, and the results are shown in Figure 2. When the absolutes of the delay differences are arranged along the theoretical white noise error, a proportional line can be drawn at the edge of the delay difference distribution. The delay differences are scattered between the proportional line and the y_0 line. We speculate that the reason for this scattering is the noise added during the FFT processing. When performing a fringe peak search with a three-point quadratic function fitting, even when noise of the same magnitude is added, the smaller the signal-to-noise ratio is, the larger the deviation of the estimated position of the fringe peak becomes. Figure 3 explains this property as an image.

Table 2 Specification of correlated data.

Observation	r19336k, VERA K-band Geodesy
Epoch of Data	2019y 336doy 0h - 12h
Network Stations	VERA (Vm, Vr, Vo, and Vs)
Format	1024 Msps - 2 bit - 1 stream
Recording	OCTADISK 2048 Mbps
Accumulation Frequency	1 Hz
Correlation Output Form	CODA FS / FITS-IDI

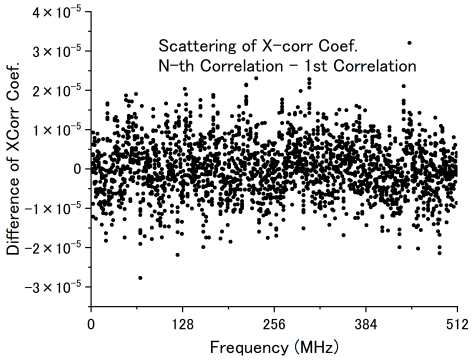

Fig. 1 Reproducibility of the cross-correlation coefficient.

To get evidence to support this speculation, delay estimations were attempted by adding fluctuations of $\pm 2 \times 10^{-7}$ to the quadratic fringe function of *IP90-*

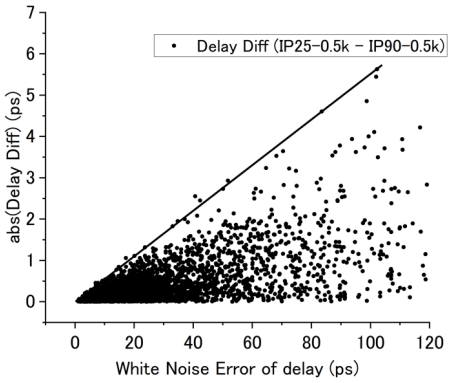

Fig. 2 Distribution of delay differences between *IP25-0.5k* and *IP90-0.5k*.

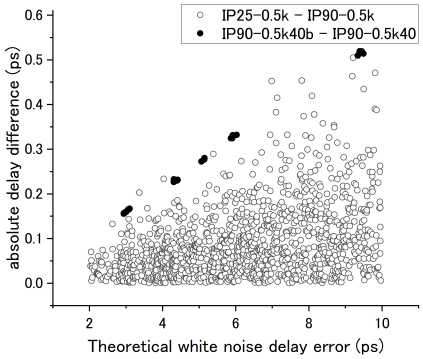

Fig. 4 Estimating the delay deviation with artificial noise added to the fringe.

0.5k40. The name of this process is *IP90-0.5k40b*. Figure 4 is shown by superimposing the delay difference between *IP90-0.5k40* and *IP90-0.5k40b* on the distribution of the delay difference between *IP25-0.5k* and *IP90-0.5k*. The delay differences between *IP90-0.5k40b* and *IP90-0.5k40* is distributed on a proportional straight line along the edge of the distribution of the delay differences between *IP25-0.5k* and *IP90-0.5k*. This is consistent with the case that the maximum fluctuation of the fringe function value is expected to be $\pm 2 \times 10^{-7}$ when the additional error integrated for 40 seconds contributes to the fringe function. Therefore, it was stipulated that the distribution of the delay difference was due to the additional error, and the effect of the additional error was estimated to be 52 femtoseconds/picosecond in terms of the proportionality coefficient. From now on, this additional error will be used as a reference scale. In addition, differences in the CPU model, motherboard, FFT math library, and matrix math library seem to have little effect on the uncertainty of delay estimation.

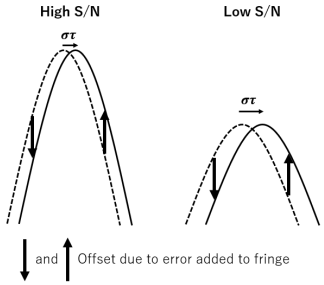

Fig. 3 Relationship between signal-to-noise ratio and deviation of the estimated fringe peak position for the same additional noise.

5 Differences in Correlation Processing Modes and Their Impact on Additional Errors

In order to confirm that the magnitude of the additional error differs depending on the mode of the correlation processing, the correlation processing was performed in several different modes, and the rate of additional error was estimated from the delay difference between multiple modes. These results are listed in Table 3. The rate of additional error is represented by a proportional coefficient along the edge of the delay difference distribution as in Figure 2.

Because the results in the table are for confirming the tendency of additional errors to occur, more systematic testing is required to estimate the characteristics and causes of additional errors. However, the number of cores of the correlator and the FFT score of the correlation processing have the following characteristics regarding the additional error:

1) When the number of FFT points is the same and the number of cores is the same, the additional error is dominated by the artificial noise added during the FFT of the correlation processing.

Table 3 Relation of correlation mode and rate of additional error.

Mode1 - Mode2	Rate of Additional Error (ps/ps)
EQ. Number of Cores. and EQ. FFT Points	
IP25-0.5k - IP90-0.5k	0.052
IP114-0.5k - IP90-0.5k	0.052
IP114-2k - IP90-2k	0.053
EQ. Number of Cores and NE. FFT Points	
IP61-4k - IP61-2k	0.316
IP61-2k - IP61-1k	0.412
IP61-4k - IP61-1k	0.441
IP76-4k - IP76-2k	0.346
IP76-2k - IP76-1k	0.540
IP76-4k - IP76-1k	0.556
IP76-1k - IP76-0.5k	0.778
IP76-2k - IP76-0.5k	0.801
IP90-2k - IP90-0.5k	0.803
NE. Number of Cores and EQ. FFT Points	
IP76-2k - IP61-2k	0.360
IP90-2k - IP61-2k	0.459
IP76-2k - IP90-2k	0.486
IP76-1k - IP61-1k	0.495
IP76-0.5k - IP90-0.5k	0.977
NE. Number of Cores and NE. FFT Points	
IP76-1k - IP90-2k	0.634
IP76-2k - IP90-0.5k	0.795
IP76-1k - IP90-0.5k	0.834
IP76-0.5k - IP90-2k	0.857

2) When the number of FFT points and the number of cores are changed, the magnitude of the additional error increases from six to 19 times the reference additional error scale.

3) As the ratio of FFT points between processes increases, so does the ratio of magnitude of additional error.

4) The difference in the number of FFT points affects the increase in the additional error, and the rate of increase in the additional error is larger in the MSC than in the MGC.

It is considered that the additional errors that change due to the difference in these correlation modes form a complex generated in the process of various operations. One of the components in this complex appears to be noise-like errors in the frequency and time domains. However, the characteristics and causes of this error are insufficiently identified; rather, it may be a complex of errors with systematic characteristics such that the magnitude of noise changes depending on the number of FFTs and cores. Another main part of the complex is presumed to be the accumulation error from fringe rate mis-tracking. The larger the FFT segment, the longer the time length of data used for one FFT process. At this time, uncorrected frequency fluctuations are accumulated. This error is systematic and can be seen in the geodetic solution as shown in Figure 5, which shows the relationship between the UT1-TAI solution and the number of FFT points. The solutions of UT1-TAI step according to the number of FFT points. The MGC also is represented as steps in the solutions, but the size of the steps is smaller than with the MSC.

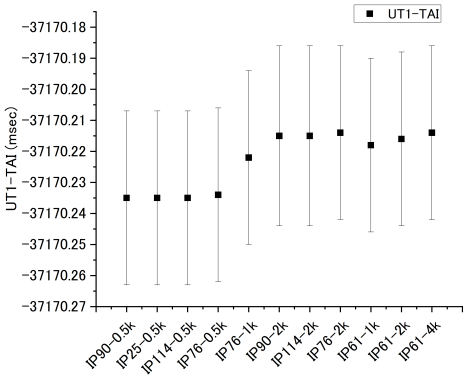

Fig. 5 Relationship of the number of FFT points and step-like differences of UT1-TAI solutions.

6 Characteristics of Additional Error in the Time Domain

The characteristics of the additional error in the time domain were investigated using the MGC. The specifications of the observations are the same as those of Table 2 except that the radio source “3C454.3” was tracked continuously for three hours. Delays were estimated every 32 seconds from each of the correlation processes with FFT points changed to 1k, 2k, and 4k. The statistical parameters of the delay difference compared between 1k and 2k and between 1k and 4k are shown in Table 4. Figure 6 shows the distribution of delay differences used to estimate the statistics in Table 4.

The displacement of the delay difference distribution over time is considered to be the cumulative error

Table 4 Time domain statistics of delay difference distributions obtained from the same observation, the same MGC (IP61), and different FFT points.

Diff. of FFT points	*2k-1k*	*4k-1k*
Baseline: Vm-Vr		
average displacement rate of distribution (ps/hr)	0.199	0.328
rms of scatter (ps)	0.271	0.277
average delay error (ps)	1.875	1.875
Baseline: Vm-Vo		
average displacement rate of distribution (ps/hr)	0.524	0.815
rms of scatter (ps)	0.331	0.349
average delay error (ps)	2.169	2.169
Baseline: Vr-Vo		
average displacement rate of distribution (ps/hr)	0.542	0.758
rms of scatter (ps)	0.435	0.464
average delay error (ps)	2.870	2.869
Baseline: Vo-Vs		
average displacement rate of distribution (ps/hr)	-0.184	-0.312
rms of scatter (ps)	0.622	0.695
average delay error (ps)	4.168	4.168

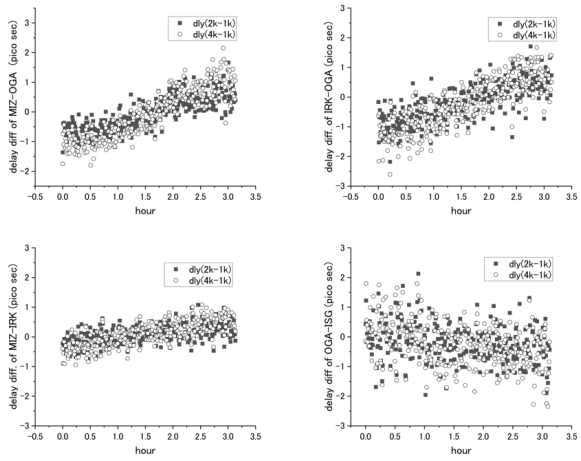

Fig. 6 Distribution of the delay difference of each baseline in the time domain.

caused by fringe rate mis-tracking due to the change in the number of FFT points. There is a difference of 120 to 290 femtoseconds/hour in the displacement rate between *2k-1k* and *4k-1k*. On the other hand, the magnitude of the delay difference scattering is six to 73 femtoseconds between *4k-1k* and *2k-1k*, and the dependence on the FFT point ratio is small, but it can be confirmed. Therefore, it is considered that the cumulative error of the fringe rate mis-tracking is the dominant additional error that depends on the change in the number of FFT points, and the cause of this scattering error is expected to be the bit-real conversion and its correction and operational errors that occur during the FFT and integration process.

7 Conclusions and Outlook

The following is a summary of this report.

The core engine "gico3" of the Mizusawa Software Correlator is equipped with a noise addition function during FFT. Expressing the magnitude of this noise as an additional error in delay estimation, the increment rate is 52 femtoseconds/picosecond as a proportional coefficient to the theoretical white noise error of delay. This additional error is treated here as a reference additional error scale.

The noise addition function implemented in the MSC gives $\pm 2 \times 10^{-5}$ fluctuation to the complex visibility obtained from 512-point FFT correlation processing.

When the correlation processing was performed by changing the number of arithmetic cores of the CPU and GPU and the number of FFT points, the magnitude of the additional error increased from six to 19 times the reference scale.

One of the components constituting this additional error is the cumulative error due to the fringe rate mistracking linked to the number of FFT points. This error indicates a step-like indeterminacy in which the geodetic estimation parameters are linked to the number of FFT points. In order to reduce this error, it is desirable to develop a new method of fringe stopping, such as improving the accuracy of high-order term tracking of the delay before the FFT. The other component is noise-like errors that may occur during the various processes of the correlator. This may be solved by improving the computational precision of the correlator and improving the signal reproducibility by increasing the number of layers of bits.

References

1. T. Jike, "VERA Geodetic VLBI with a Newly Developed High-speed Sampler and Recorder", In D. Behrend, K. D. Baver, and K. L. Armstrong, editors, *IVS 2016 General Meeting Proceedings*, NASA/CP-2016-219016, pp. 159–162, 2016.

Optimal Signal Averaging Time in VLBI Sessions

Yuriy Vekshin, Voytsekh Ken, Sergei Kurdubov

Abstract We propose a technique for determining an optimal averaging time of source signals in VLBI, taking into account signal delay instability in the radio telescope's equipment. Delay instability is determined by calculating fringe parameters over a continuous one-hour source tracking session. Optimal signal averaging time (which provides minimum error of delay measuring) is determined by calculating the Allan deviation. The delay measurement error increases at a longer averaging time due to delay instability. Source signal averaging time is determined in such a way that the delay's calculated standard deviation is not less than the radio telescope equipment's delay instability Allan deviation. The results of measuring delay instability of the RT-13 radio telescopes of the Quasar VLBI Network in the S-, X-, and Ka-bands were applied to R-X sessions postprocessing. Some previous sessions were recalculated by changing the scheduled source signal averaging time to an optimal one for more intensive sources. The comparison of the UT1-UTC determination and its formal errors obtained with scheduled averaging time and optimal averaging time is presented.

Keywords radio interferometer, VLBI, tri-band receiver, correlator, signal-to-noise ratio, group delay, delay stability, Universal Time

Institute of Applied Astronomy of the Russian Academy of Sciences (IAA RAS)

1 Introduction

The accuracy of Universal Time determination is greatly dependent on the group delay measurement accuracy of the radio interferometer. The measurement error of fringe delay depends on signal delay instability in radio telescope equipment [1]. It should be measured and taken into account when scheduling source scan times in VLBI-sessions.

The signal-to-noise ratio (*SNR*) of the radio interferometer at the correlator output is determined by the source flux F_s, system equivalent flux density (*SEFD*) of radio telescopes, quantization efficiency η, bandwidth Δf, and averaging time τ_a [2].

$$SNR = \frac{\eta \cdot F_s}{\sqrt{SEFD_1 \cdot SEFD_2}} \sqrt{2 \cdot \Delta f \cdot \tau_a}. \qquad (1)$$

Theoretical fringe delay error σ_{tSNR} depends only on SNR and bandwidth Δf [2].

$$\sigma_{tSNR} = \frac{\sqrt{12}}{2\pi \cdot \Delta f \cdot SNR}. \qquad (2)$$

Real fringe delay error σ_t depends on signal delay instability in radio telescope equipment σ_{tEq}, including receivers, acquisition systems, synchronization systems, etc.

$$\sigma_t = \sqrt{\sigma_{tSNR}^2 + \sigma_{tEq}^2}. \qquad (3)$$

2 Measurement Technique

To obtain signal delay instability, we have carried out a continuous one-hour tracking session of the cos-

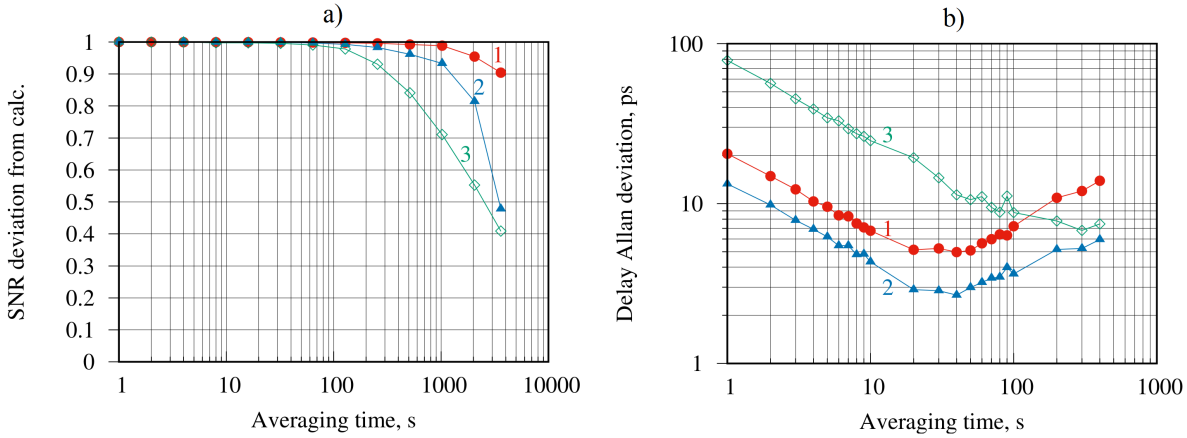

Fig. 1 a) Signal-to-noise ratio deviation from the calculated one; b) Delay Allan deviation for one-hour 3C454.3 tracking: 1–S-band, 2–X-band, 3–Ka-band.

mic source 3C454.3 by the RT-13 radio telescopes [3] at Badary, Zelenchukskaya, and Svetloe. Triband receivers with the S- (2.2–2.6 GHz), X- (7.0–9.5 GHz), and Ka- (28–34 GHz) bands [4] Broadband Acquisition System (Δf=512 MHz, 2 bit quantization) [5] were used. Signal-to-noise ratios and group delays at 1 s averaging time (3,600 points) were obtained by the RASFX correlator [6, 7]. The total geometric delays were calculated, ionospheric delays were taken into account, and NGS files were generated, which were further processed by the "Quasar" software [8]. O-C files were obtained, containing the differences between the observed and calculated delays.

The signal-to-noise ratio at the correlator output was then calculated at different averaging times (Figure 1, a). It was found that the SNR decreases by 10% from the value calculated by (1) at one hour for S-band, 1400 s for X-band, and 350 s for Ka-band due to frequency standards instability.

Then we have the calculated delay Allan deviation, and we found that delay instability appears at shorter time intervals (Figure 1, b). The Allan deviation decreases like white noise, proportional to the square root of the averaging time according to (1, 2) up to 20 s averaging time in the S- and X-bands and up to 200 s averaging time in Ka-band. It is an optimal averaging time, at which the minimum delay Allan deviation value is achieved. Radio telescope equipment instability prevails at longer averaging times. The minimum delay deviation is 5 ps in S-band, 3 ps in X-band, and 7 ps in Ka-band. White noise in Ka-band is greater than in the S/X-bands due to the lower signal-to-noise ratio, so the averaging time to reach the radio telescope equipment delay instability is longer. The first theoretical term of delay error (3) is the straight line on the Allan deviation plot in a log-log scale (Figure 1, b), and this line moves parallel along the y-axis depending on the source flux F_s according to (1) and (2). The second practical term of delay error (3) is the radio telescope equipment delay instability and is source independent. The intersection of these two terms gives the optimal averaging time for the source signal. So, each source has its own optimal averaging time. We propose to choose the averaging time of a source signal when scheduling VLBI-sessions in such a way that the delay's calculated standard deviation is not less than the radio telescope equipment's delay instability Allan deviation. A further increase in averaging time will give an increase in the delay measurement error (Figure 1, b).

3 Practical Application

We have tested this technique on the R-X sessions in the S/X/Ka-bands. As scheduled, the session lasts one hour and contains 22 scans with an averaging time of 120 s. The signal-to-noise ratio was measured for all sources, and the delay error was calculated by (2) in the S-, X-, and Ka-bands (Table 1).

The calculated delay error in X-band for some Intensive sources (1156+295, 1546+027, and NRAO150) is less than the real delay instability of 3 ps and, con-

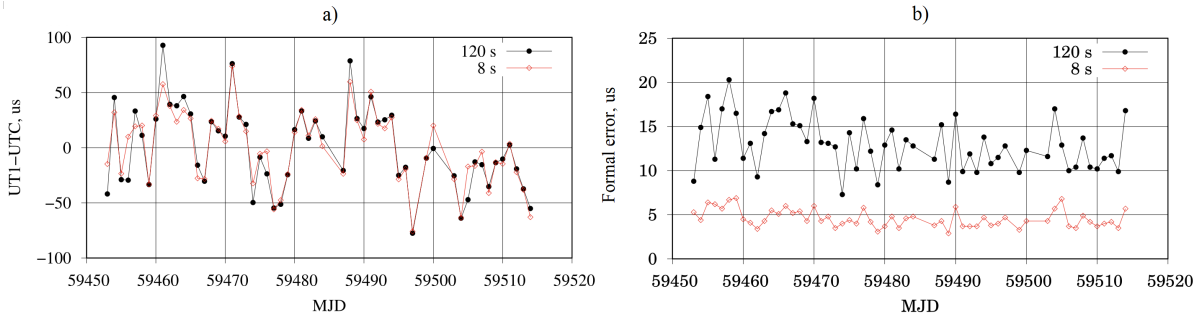

Fig. 2 X/S-band combination results: a) UT1-UTC differences with respect to the IERS finals series; b) formal errors (UT1-UTC).

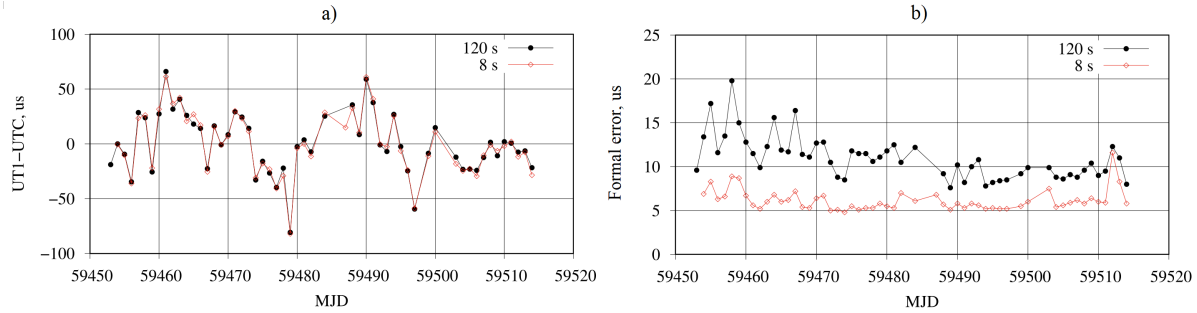

Fig. 3 Ka/X-band combination results: a) UT1-UTC differences with respect to the IERS finals series; b) formal errors (UT1-UTC).

Table 1 Measured SNR and calculated delay standard deviation in R-X sessions.

Source	Number of obs.	SNR (meas.)			σ_{tSNR}, ps (calc.)		
		S	X	Ka	S	X	Ka
1717+178	1	136	184	33	7.9	5.8	32.4
0642+449	1	122	198	41	8.8	5.4	26.3
1156+295	2	61	628	260	17.7	**1.7**	4.1
1642+690	1	122	165	18	8.8	6.5	61.0
1546+027	6	363	861	98	3.0	**1.3**	11.0
NRAO150	2	93	644	185	11.6	**1.7**	5.8
OK290	2	62	211	35	17.4	5.1	30.3
0716+714	6	85	201	36	12.6	5.4	29.8
0805+410	1	58	244	21	18.5	4.4	51.1

sequently, is not achieved in practice. So, the averaging time has been reduced for these Intensive sources. 120 s scans were cut into slices, and then all were processed.

The R-X sessions from a two month period (27.08.2021–27.10.2021) were processed with different averaging times for selected sources. The averaging times varied from 120 s to 8 s. UT1-UTC differences with respect to the IERS finals series and its formal errors were obtained by "Quasar" software [8] for X/S-band and Ka/X-band combinations. The second band is used to eliminate ionospheric delay. The formal error is the root mean square of residual errors after solving a system of equations by the least squares method.

UT1-UTC series and formal errors for the 120 s and 8 s averaging times are presented in Figure 2 for the X/S combination and in Figure 3 for the Ka/X combination. The standard deviations of the (UT1-UTC) series $\sigma_{UT1-UTC}$ and mean formal errors were calculated and are presented in Table 2.

Table 2 Standard deviations of (UT1-UTC) series residuals from IERS finals and its formal errors, in microseconds.

Aver. time, s	X/S-bands		Ka/X-bands	
	$\sigma_{UT1-UTC}$	Form. error	$\sigma_{UT1-UTC}$	Form. error
120	36.6	13.0	27. 2	11.0
60	35.1	10.6	27.4	9.5
30	34.5	8.1	27.3	8.0
15	33.7	5.9	27.4	6.8
8	32.4	4.6	27.7	6.1

Reducing the averaging time from 120 s to 8 s has led to reducing the standard deviation of the UT series by 4 μs and the formal error by 8 μs for the X/S com-

bination. Errors have decreased for the 8 s averaging time because white noise in the delay Allan deviation plot prevails over this interval for X-band (see plot 2 in Figure 1, b), and delay instability does not affect the measurement result; at longer averaging times, delay instability prevails. For Ka/X, the combination formal error has decreased by 5 μs at the 8 s averaging time. The standard deviation of the (UT1-UTC) series in Ka-band is almost independent on the averaging time from 120 s to 8 s, because there is white noise on the delay Allan deviation plot in Ka-band over these time intervals (see plot 3 in Figure 1, b). The standard deviation of UT1 corrections in regular two-hour R sessions in the S/X-bands with different scan times from 16 s to 60 s is about 20 μs.

4 Conclusions

The radio telescope's equipment delay instability should be taken into account in addition to the signal-to-noise ratio when scheduling VLBI-sessions. Long continuous source tracking and Allan deviation calculation should be used to obtain the delay instability of the radio interferometer. The optimal source signal averaging time is determined by the minimum of the delay Allan deviation plot in such a way that the delay's calculated standard deviation is not less than the radio telescope equipment's delay instability Allan deviation. Reducing the averaging time (cutting scans into slices) for Intensive sources leads to a decrease in UT determination errors, because instability does not affect the delay error at short time intervals. A change in scheduling, providing reduction of source scan times and an increase in the number of sources, should lead to a greater decrease in UT determination errors.

Acknowledgements

We are grateful to Alexey Melnikov, Svetlana Mironova, and Igor Surkis for their assistance and discussion of the results.

References

1. Y. Vekshin, V. Ken, V. Chernov, A. Evstigneev, E. Khvostov, M. Zotov. Analysis of VLBI Interferometer Characteristics Using Zero-baseline Lab Prototype and RASFX Correlator. *Proceedings of Science*, vol. 344, 142, 2019. doi:10.22323/1.344.0142.
2. A. R. Thompson, J. M. Moran, G. W. Swenson Jr. *Interferometry and Synthesis in Radio Astronomy*. Springer, 2017. doi:10.1007/978-3-319-44431-4.
3. D. Ivanov, A. Ipatov, D. Marshalov et.al. Russian New Generation VLBI Network. *IVS 2022 General Meeting Proceedings*, 2022, this volume.
4. A. A. Evstigneev, V. K. Chernov, O. Eu. Evstigneeva, I. A. Ipatova, Eu. Yu. Khvostov, A. P. Lavrov, I. A. Pozdnyakov, Yu. V. Vekshin, M. B. Zotov. RT-13 VLBI receivers. *Transactions of IAA RAS*, vol. 55, pp. 36–40, 2020. doi:10.32876/ApplAstron.55.36-40.
5. E. Nosov, D. Marshalov, A. Melnikov. Operating Experience with the Broadband Acquisition System on the RT-13 Radio Telescopes. *IVS 2016 General Meeting Proceedings "New Horizons with VGOS"*, edited by D. Behrend, K. Baver, and K. Armstrong, NASA/CP–2016–219016, pp. 53-57, 2016.
6. I. F. Surkis, V. F. Zimovsky, V. O. Ken et al. *Instrum Exp Tech*, 61, pp. 772-779, 2018. doi:10.1134/S0020441218060131.
7. V. O. Ken. Overview of RASFX: IAA RAS VLBI software correlator. *Transactions of IAA RAS*, vol. 55, pp. 41–44, 2020. doi:10.32876/ApplAstron.55.41-44.
8. S. L. Kurdubov, V. S. Gubanov. Main results of the global adjustment of VLBI observations. *Astron. Lett.*, 37 (4), pp. 267–275, 2011. doi:10.1134/S1063773711010063.

IVS Data Center at BKG

Anastasiia Girdiuk, Markus Goltz, Daniela Thaller

Abstract Three primary IVS Data Centers cooperate closely together to establish and maintain common data processing procedures. Our aim is to support as similar as possible data handling at each IVS Data Center. The workflow of the data acceptance is maintained to resemble one at another IVS Data Center, so that each Data Center ensures data acceptance, storage, availability of the data and compatibility with the other Data Centers. We present here the current procedures of the data acceptance at BKG and our future plans to extend the data center infrastructure. The Data Center storage capacity covers the foreseen requirements to store vgosDb files intuitively based on the data rate increase in the last year. We are interested also in the extension of the currently accepted IVS Data Center structure to additionally store the correlated data; however, the expected storage capacities need to be better defined and properly advocated. The approval process is expected to be considerable as well. While this work is in progress, the BKG Data Center uses its available capacities to serve as an exchange server for the projects of relatively small disk space demands: TPWLO and EU-VGOS. The structure of the projects repeats the IVS Data Center structure to facilitate the exchange internally. Also, it means that it would be possible to make the internal project available on the official Data Center once this is decided. The projects are maintained with restricted access, which allows us to learn the new routines to handle the data acquisition. The restricted access to our server with File Transfer Protocol (FTP) over Secure Socket Layer (SSL) is planned to be in place for all of our users according to the requirements of our internal IT Infrastructure and EU regulations on Data Security.

Federal Agency for Cartography and Geodesy (BKG)

Keywords VLBI Data, IVS Data Center, Software

1 Data Center Summary

The IVS Data Center at BKG works together with the representatives of CDDIS and OPAR to maintain the data center duties. The availability and accessibility of all data at any time, as well as the ability to upload the VLBI data, are provided to the users. At this moment the BKG Data Center is accessible for data downloading or listing via FTP-SSL and HTTPS as user "anonymous." The data uploading is supported by FTP-SSL connection and personal user accounts. The unprotected FTP access had to be discontinued due to security reasons. The login with the personal user account is arranged to replace the ivsincoming-user uploading procedure. We register the connections between 1 and 6 MB/sec for data uploading and 2 and 7 MB/sec for data downloading. Considering the data size the connectivity satisfies the regular data demand. The updated information about the access to the BKG Data Center can be seen on our Web page: https://ivs.bkg.bund.de/.

Data acceptance is managed uniquely among the three IVS Data Centers by means of the validation procedures. As follows, all kinds of VLBI data have to adhere to the naming convention [3] as of August 2, 2021. The validation procedures are employed at BKG and OPAR by the ingest script developed by the CDDIS group [2]. In the data acceptance workflow each received file is checked with an antivirus program; this step takes the longest time in the data handling scheme as a rule. The virus-marked files are quarantined, while the passed files are forwarded to the ingest script as it is seen in Figure 1. The received data which fail the

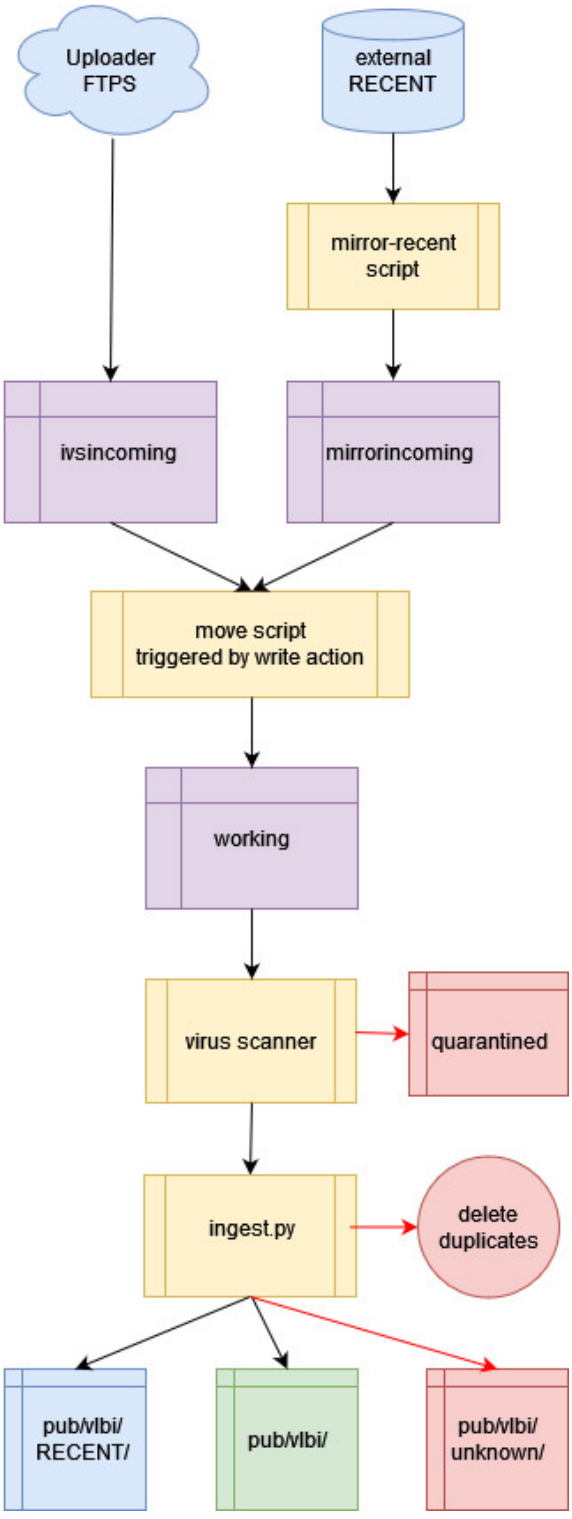

Fig. 1 The workflow of the Data Center.

validation after an attempt to ingest them at our data center can be found under the directory called "UNKNOWN." The possibility of seeing the failed data in "UNKNOWN" is kept at the BKG Data Center for historical reasons. Meanwhile it is considered useful in the transitional period to accommodate the naming convention. The legitimate VLBI data, which has passed the validation by ingest script successfully, is placed in the appropriate directory (green box in Figure 1) according to the data type as specified in the so-called data definition file (DDF, [2]) also empowered by the ingest script. Additionally, the ingest script checks if the same data are already present in the data center. As follows, the duplicated files are dropped. The most recent data are considered the data which were received in the last 14 days. These data are copied to the "RECENT" directory. The data availability is secured by mirroring the data provided under this directory "RECENT" at the other data centers. Further, an entire data center is to be mirrored on a regular basis. The BKG Data Center structure is listed in Table 1, where additionally the vgosDb files from correlators at Bonn, GSI, Shanghai, UTAS, and Wien are collected. The USNO group was delivering vgosDb files, which were stored under vgosdb_usno. Since 2022 the corresponding vgosDb files are uploaded to the Data Center directly. The files are placed according to their type under ivsdata/vgosdb. Besides, vgosdb_bkg contains the vgosDb data processed by the BKG Analysis group.

The data acceptance workflow, along with the current BKG Data Center, was established on the new machine. It allowed for internal data ingest verification. All data from the old server was uploaded to the new one, which resulted in a significant amount of unrecognized data from the validation procedures and DDFs. The largest part of the unrecognized data is the historical tropospheric products. The Data Center Working Group has decided that these tropospheric products are recognized to be not an IVS product any longer, because the data are available at the GNSS data centers and the IVS Components have no interest in them. These products are not defined as IVS data (see [3]); thus, these data are not available at the BKG Data Center. The other large portion of the products was recognized to have been created for non-IVS sessions. The smaller parts of the unrecognized historical data have some minor differences in the name pattern. There are probably a few data types for which DDFs need to be created. The status of the different cases of the unrec-

ognized data is the subject for discussions of the Data Center Working Group.

Table 1 The structure tree of the IVS Data Center at BKG.

Level 1	Level 2	Description
ivscontrol/		IVS DC control files
ivsdata/		VLBI data files
	vgosdb/	VLBI data in vgosDb format
	vgosdb_bkg/	vgosDb processed by BKG AC
		vgosDb prepared by:
	vgosdb_bonn/	Bonn Correlator
	vgosdb_gsi/	GSI Correlator
	vgosdb_shao/	Shanghai Correlator
	vgosdb_utas/	UTAS Correlator
	vgosdb_wien/	Wien Correlator
	vgosdb_usno/	submitted by the USNO group
	db/	mk3db data storage
	ngs/	NGS-cards data storage
	aux/	session supplementary data
	swin/	SWIN files
ivsdocuments/		IVS DC documents
ivsformat/		master-format
ivsproducts/		analysis products
	crf/	source coordinate
	trf/	station position
	eops/	24h EOP time series
	eopi/	Intensive EOP time series
	daily_sinex/	SINEX of 24 h sessions
	int_sinex/	SINEX of Intensives
	trop/	tropospheric products
gsfc/		software-related input data
	ancilliary/	minimal set of a priori data*
	sked/	frequency catalog (SKED)
RECENT/		all data of the last two weeks

* in the file format in use by nuSolve and Calc/Solve.

2 Data Center: Main Area

The VLBI data takes about 700 GB at the moment, while the main area of the Data Center has altogether 7 TB. Besides, disk space of 20 TB is assigned to the SWIN files. The Shanghai correlator is uploading the SWIN files to us directly. The rest of the SWIN data are to be acquired from CDDIS.

Along with the main area of the Data Center, the vgosDb files from different correlators are collected as shown in Table 1. We mirror twice per hour the public data storage referred to the VLBI data at the Bonn, GSI, Wien, and UTAS Correlators. At this moment the Shanghai and USNO Correlators are delivering vgosDb files to our Data Center. Here, it is worthwhile to note that we register and allow with respect to the ingest script procedures a replacement of the vgosDb files at any Data Center. Let us follow the analysis chain. First of all, the correlator that is responsible for a session uploads its vgosDb file set, in which at least the correlator version 1 of the wrapper file is provided. Next, the Analysis Center (AC) that is responsible for this session according to the master file uploads the analyzed vgosDb file set, in which the version from the correlator is retained. This version of the vgosDb file set is recognized as official and final, unless new correlation or fringe fitting is prepared. If the correlator uploads a version of a vgosDb file set which is already present at a Data Center, the vgosDb file set gets replaced. At this point it makes no difference whether an AC or a correlator has uploaded the vgosDb file set; the newer version with respect to the stored digital fingerprints of the file (md5sum and shasum verify file integrity) will be chosen to be placed in the Data Center. This version from the correlator, however, does not include either the previous correlation version or the corresponding analysis version. Thus, the responsible AC will upload only the analysis of the last available version of the vgosDb file set to the Data Center.

The analyzed vgosDb files of the ACs other than the responsible one are not available within the vgosDb file set. That is why the BKG Analysis Center provides its own analysis version of the vgosDb files at our Data Center under ivsdata/vgosdb_bkg.

3 Data Center: Additional Activities

Considering the VLBI data increase, we have disk space left to provide our service for the projects demanding a relatively small disk space. At this moment we work with the European VGOS (EU-VGOS, [1]) and the Test of the continuous Piece-Wise Linear Offset parameterization (TPWLO, [4]) projects. The disk space and IVS-like storage environment with protected data access are provided. The chosen login authorization has been seen to complicate the procedure; thus, a simple login sharing routine was enabled for the IVS uploading accounts. The IVS compatible data structure is initialized so that the data can be accepted with the same procedures as if they were submitted to the main area of the Data Center. As an end effect, the

Table 2 SINEX files are to be received from five IVS ACs under the TPWLO project.

Institution	IVS AC
Federal Agency for Cartography and Geodesy BKG	BKG
Vienna University of Technology TU Wien	VIE
Onsala Space Observatory OSO	OSO
Norwegian Mapping Authority NMA	NMA
German Geodetic Research Institute DGFI	DGF

project data could be forwarded to the main area of the Data Center and accepted straightforwardly. That means that the same ingest script with validation procedures and DDFs operates on the incoming data, where the database is extended to accept the project-assigned solution names and research groups which do not have an Analysis Center affiliated with IVS.

The TPWLO project, in which some of the IVS ACs participate (see Table 2), requires only the acceptance of SINEX files. The EU-VGOS project shares the SINEX files as well. Besides, the vgosDb files of the sessions observed under the EU-VGOS project are made available for the project members (see Table 3). The EU-VGOS main project goal [1], which is to test the impact of the different calibration and fringe-fitting methods for the geodetic solutions, sets an additional challenge for the Data Center procedures by requiring the possibility of sharing with the project members more than one correlation version per session.

Table 3 Under the EU-VGOS project the vgosDb files are provided by the correlators at Bonn and TU Wien. And SINEX files are to be received from eight ACs and institutions.

Institution	IVS AC
Federal Agency for Cartography and Geodesy BKG	BKG
Vienna University of Technology TU Wien	VIE
German Research Centre for Geosciences GFZ	GFZ
Onsala Space Observatory OSO	OSO
Metsähovi Radio Observatory (MRO*)	–
Yebes Observatory (YBS*)	–
Norwegian Mapping Authority NMA	NMA
Finnish Geospatial Research Institute (FGI*)	–

* affiliations given for recognition at the Data Center.

4 Outlook

The BKG Data Center takes an active part in the joint activity of the IVS Data Center components. We have established our workflow with the ingest script and validation procedures. We support data acceptance and data redundancy by collecting vgosDb files from the correlators and providing BKG Analysis group results. Besides, the BKG Data Center's entire data set was processed with the ingest script; thus a considerable amount of data was declined by the validation procedures and DDFs. The validation workflow was adjusted in agreement with the Data Center Working Group. Further verification of the remaining unrecognized data is planned in line with a similar CDDIS activity.

The BKG Data Center is working to follow the EU regulations and provide users with convenient access. As follows, the HTTPS is expected to be crafted for uploading as well. The data completeness is to be checked by mirroring the entirety of CDDIS and OPAR at least once a day. On one hand, we apply our best efforts to follow the IVS recommendations about the availability of the SWIN files. On the other hand, the acquisition of new space is limited to the defined requirements, the definition of which is reviewed regularly (currently: a disk space increase of 5 TB during two years) and set in connection with the actual user demand.

Meanwhile available disk space is given to the VLBI-related projects. Compliance with the demands of these projects benefits our operations on a smaller scale than an entire IVS Data Center. In particular, experience with the personalized access has facilitated the adjustment of the setup of the IVS accounts. These projects are valuable for further development.

References

1. F. Jaron et al., Current Status of the EU-VGOS Project, IVS General Meeting Proceedings, 2022, this volume.
2. D. Behrend, M. Bérubé, J. Gipson, A. Girdiuk, M. Goltz, T. Yates, P. Michael, C. Barache, Data Ingest at the IVS Data Centers, Presented at: IVS 2022 General Meeting, 2022.
3. D. Behrend, Data Center file conventions, https://ivscc.gsfc.nasa.gov/products-data/DataCenter_File_Conventions.pdf, 2021.
4. A. Nothnagel, S. Böhm, R. Dach, A. Girdiuk, M. Glomsda, H. Hellmers, A-S. Kirkvik, T. Nilsson, D. Thaller, First results of Earth rotation parameter estimation with piece-wise linear offsets, IVS General Meeting Proceedings, 2022, this volume.
5. T. Yates, J. Woo, N. Pollack, J. Ash, J. Roark, S. Blevins, P. Michael, VLBI Data Ingest Improvements at NASA CDDIS, IVS General Meeting Proceedings, 2022, this volume.

VLBI Data Ingest Improvements at NASA CDDIS

Taylor Yates[1], Justine Woo[1], Nathan Pollack[1], Jennifer Ash[2], James Roark[2], Sandra Blevins[1], Patrick Michael[3]

Abstract NASA's Crustal Dynamics Data Information System (CDDIS) and the International Very Long Baseline Interferometry (VLBI) Service for Geodesy and Astrometry (IVS) have been collaborating for several years to identify and rectify issues including data and derived product collection completeness and availability. The issues identified include inconsistent quality assurance (QA) across Data Centers, fringe visibilities missing in the archive, latency in resolving data submission issues, and a reliance upon on-premises servers to provide these datasets to the community. In 2021, several improvements to address these issues were made. A new QA architecture has been introduced that utilizes common standards (Data Description Files, DDFs) provided by the IVS. This centralization of QA standards has proven to be vital in improving archive quality and consistency across multiple data centers. SWIN data files contain raw output from the Distributed FX (DiFX) software correlator (Level 1 data) in the Swinburne format [SWIN]. These files are large, compressed directories of the fringe visibilities. Adding SWIN files to the CDDIS archive increases their visibility and use in the community. Additional software has been written that informs data providers when an uploaded file is not recognized, greatly reducing the response time for any anomalies. Cloud deployment of the CDDIS archive will increase data usability via the option to use data in place; therefore, steps are being taken to deploy CDDIS VLBI datasets to be available on Amazon Web Services (AWS) without disrupting active use of the data by the community.

1. Science Systems and Applications, Inc.
2. Adnet Systems, Inc.
3. NASA Goddard Space Flight Center

Keywords VLBI, CDDIS, SWIN, DDF, Archive

1 New QA Architecture

The CDDIS ingest processing software now includes new quality analysis (QA) utilizing Data Description Files (DDFs) provided by the IVS which are common to all Data Centers and are source controlled using Git. Unique DDFs for each dataset specify the following:

- Filename scheme
- File destination in the directory
- Product ID for metadata uses
- Data type
- Content type
- Data format
- Validation procedure
- Magic
- Compression type

The CDDIS ingest processing software uses these DDFs as shown in Figure 1.

IVS centralization and control of DDF parameters improves uniformity among the Data Centers by formalizing the requirements for file acceptance and placement.

2 SWIN Data

SWIN Files are compressed directories of observational fringe visibility data in the DiFX format. These are very large (as large as 500 GB per file) and see significant benefit from storage in a centralized archive.

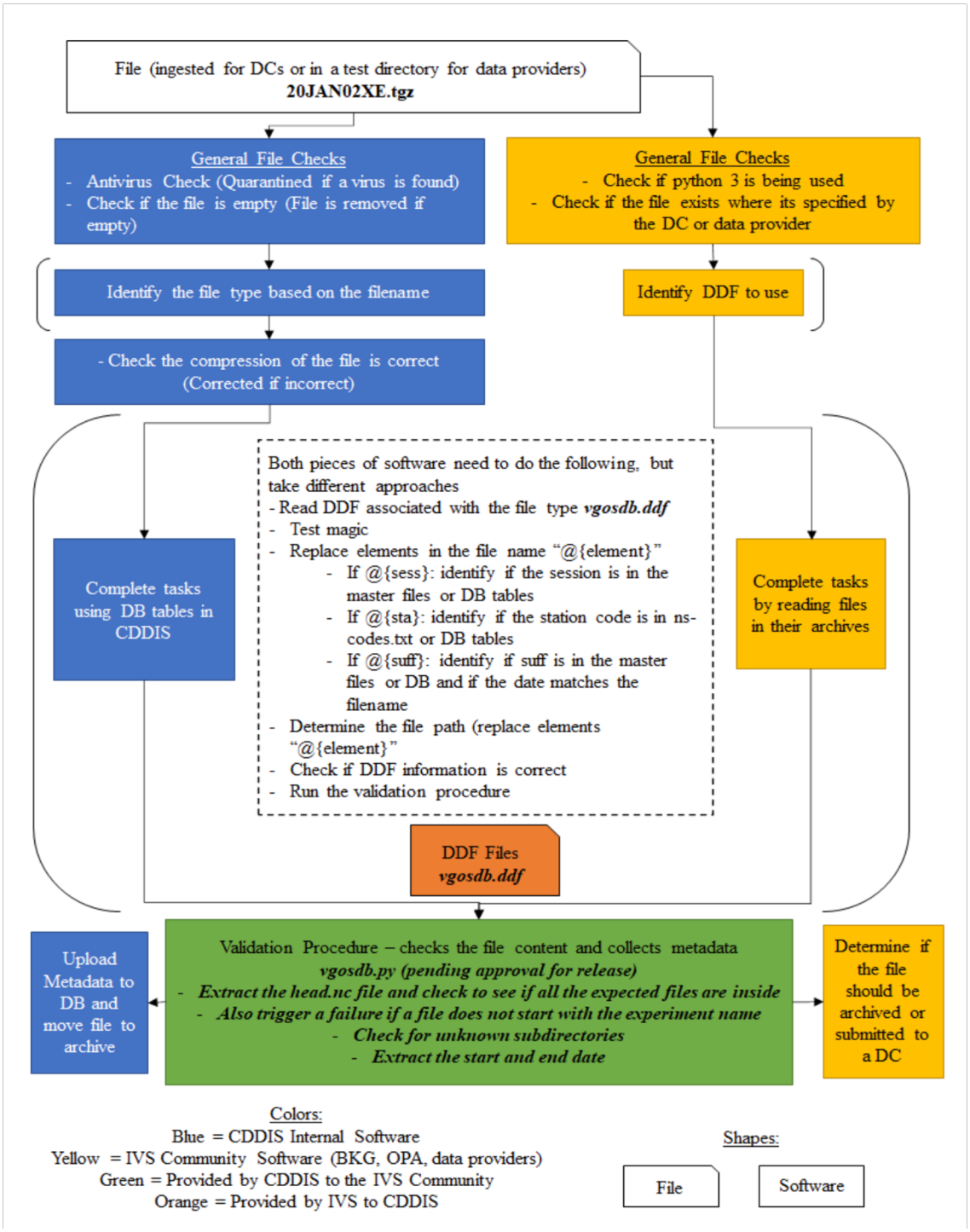

Fig. 1 CDDIS VLBI QC Overview

SWIN dataset acceptance began in early 2021. During CY21, 2.7 TB of 2021 SWIN data were accepted. Additionally, during this time 3.7 TB of backlog SWIN data from 2017–2020 were accepted into the archive.

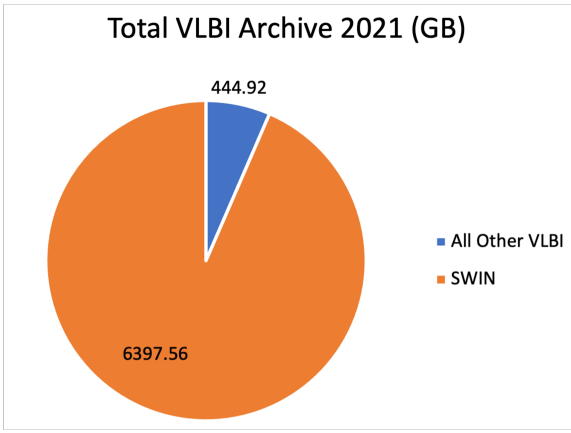

Fig. 2 CDDIS VLBI 2021 archive size.

The introduction of the SWIN dataset increases the CDDIS VLBI archive size by an order of magnitude. In addition, the SWIN dataset itself is expected to grow as more correlators upload SWIN data to the CDDIS archive. This is shown in Figure 3 with data from 2021 and the projection for 2022.

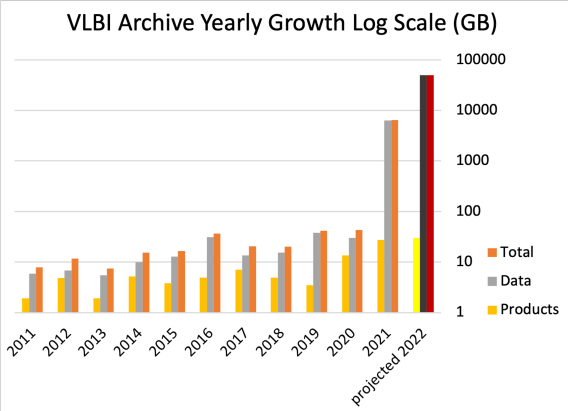

Fig. 3 CDDIS VLBI yearly volume growth.

This growth brings novel challenges to the CDDIS File Ingest System. To resolve these challenges, SWIN uploads use a separate upload web app, ingest script, and partition for archived data. Despite these differences in upload and storage, SWIN availability for users is identical to other VLBI datasets as shown in Figure 4.

The CDDIS SWIN archive is available for public consumption at the URL in Figure 5.

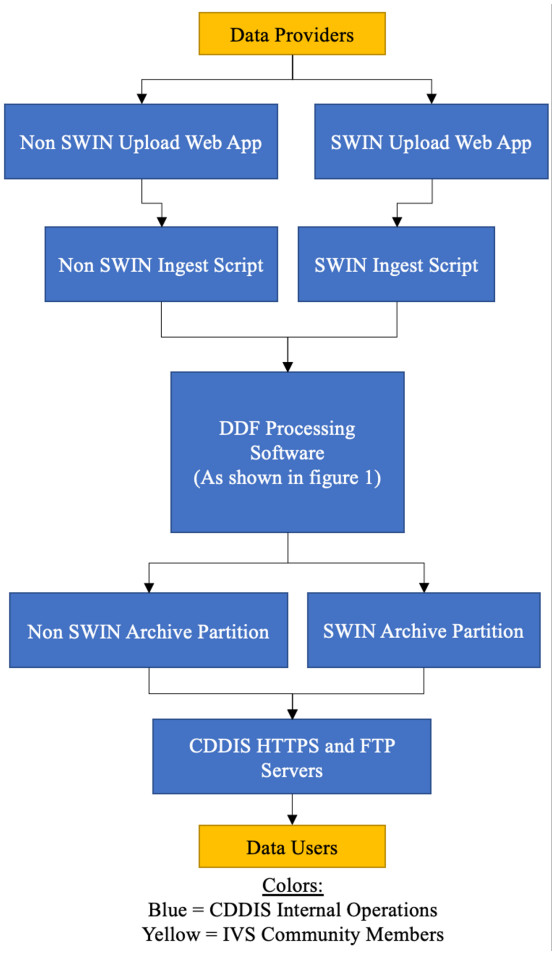

Fig. 4 CDDIS Ingest/QC/Archive architecture.

Fig. 5 CDDIS SWIN archive HTTPS QR code.

3 Unknown File Error Handling

Files received by CDDIS undergo QA tests to confirm the filetype. Any file that cannot be identified by the QC software is flagged as an 'Unknown File.'

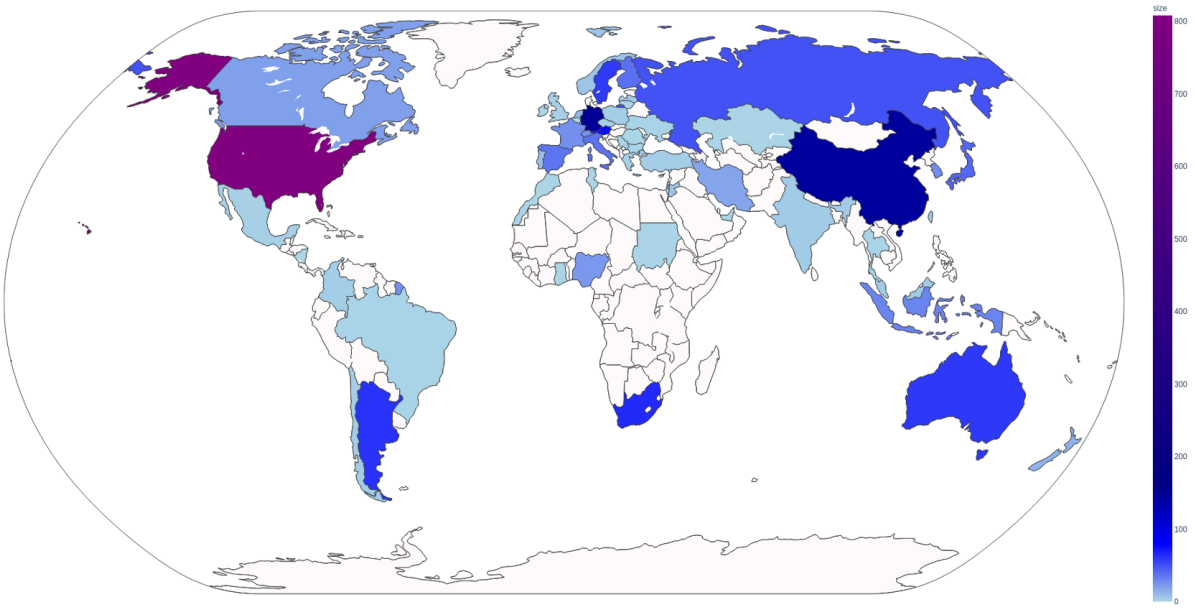

Fig. 6 CDDIS 2021 VLBI unique users.

This can be a point of frustration for uploaders when the file is not available in the archive. To remedy this, software has been introduced to alert providers via email when a file is flagged as unknown.

4 Planned Cloud Deployment

In partnership with other Data Centers in NASA's Earth Science Data and Information System (ESDIS) Project, CDDIS is planning to transition from the current on-premises archive to a cloud-based system, NASA's Earthdata Cloud (EDC).

With data located in AWS S3 buckets, users can choose to either download the data or use it in place. This option bypasses the current requirement to download data from the CDDIS archive to a local machine for use. Unnecessary downloads represent a waste of bandwidth and storage space. Removing the requirement to download data before use will greatly increase the future availability of large VLBI datasets for analysis. With the global userbase that CDDIS services (shown in Figure 6), this would be a significant benefit for the community.

References

1. C. Noll, The Crustal Dynamics Data Information System: A resource to support scientific analysis using space geodesy, Advances in Space Research, Volume 45, Issue 12, 11 June 2010, Pages 1421–1440, ISSN 0273-1177, DOI:10.1016/j.asr.2010.01.018.
2. Deller, A., Tingay, Steven, & Bailes, M.. (2007). DiFX: A Software Correlator for Very Long Baseline Interferometry Using Multiprocessor Computing Environments. Publications of The Astronomical Society of The Pacific, Vol. 119, Issue 853, pp. 318–336, DOI:10.1086/513572.

Session 3

Data Structures, Scheduling and Analysis Strategies

Automatic Processing of INT Sessions with nuSolve

Sergei Bolotin, Karen Baver, Mario Bérubé, John Gipson

Abstract IVS INT sessions are conducted to determine the change in Earth rotation, which is measured as a correction to Universal Time, or dUT1. This correction varies unpredictably with time. Because dUT1 is used in precise navigation, particularly GNSS, rapid turnaround is very important. The elapsed time from observation to obtained results can be shortened using automatic data processing at the analysis stage. To develop an application for this analysis, we used the script mode of the VLBI data processing software nuSolve. In this script mode, nuSolve reads commands from a script file and executes them. The script engine is implemented by the Qt library and supports the ECMAScript (standardized Java script) programming language.

A user of the script mode has access to the same functionality of nuSolve as a user of the GUI mode. In this paper we discuss the application of the script for the automatic processing of INT sessions. We conducted a comparison of results from the script execution with manual data analysis for all INT S/X and VGOS sessions performed during the last five years. For 50% of the sessions the automatic script gives a solution that is identical to the one obtained by an operator. For 75% of the sessions, the difference of the dUT1 estimation between the two types of solutions is less than 5 microsec. We discuss the anomalies of INT sessions that cause significant differences between automatic and operator solutions.

Keywords VLBI, data analysis, automatization, software

NVI, Inc., NASA GSFC Code 61A, 8800 Greenbelt Road, Greenbelt, Maryland 20771, USA

1 Introduction

One of the practical goals of the geodetic Very Long Baseline Interferometry (VLBI) technique is the determination of the change in Earth rotation. These variations are caused by interactions of Earth, ocean, and atmosphere and cannot be predicted. Using VLBI observations it is possible to obtain this unmodeled change of Earth rotation, which is measured as a correction to Universal Time, or dUT1. A special type of VLBI observations, an INT session, is organized to estimate dUT1 only. The International VLBI Service for Geodesy and Astrometry (IVS) [Nothnagel et al., 2017] INT sessions are planned to last one hour (though a VLBA part of the IVS-IN1 network was scheduled to run two hours). Because dUT1 is used in precise navigation, particularly GNSS, rapid turnaround is very important.

At NASA GSFC, we developed software that automates operations of downloading files with VLBI observations, performes necessary calculations and calibrations, and prepares a new VLBI session ready for processing by an analyst. When the analyst has processed the session, the software obtains a solution and submits the results to the IVS Data Centers for further use.

The procedure of session analysis is performed manually by an analyst with the nuSolve software [Bolotin et al., 2014]. During the initial processing of a session the following steps should be made: resolving of group delay ambiguities; elimination of outliers; checking for presence of clock break effects; and evaluation of ionosphere corrections among others. This is an important part of the geodetic VLBI data flow.

To reduce the latency from observations to obtained results we developed an application for automatic analysis using the script mode of the VLBI data processing software nuSolve. In this script mode, nuSolve reads commands from a script file and executes them. A script is a plain ASCII file that nuSolve reads and executes line by line. The script engine is implemented by Qt library and supports the ECMAScript (standardized Java script) programming language. nuSolve exports its types, objects, and functions to make them accessible to the script engine. That makes it possible for a user to have access to the same functionality of nuSolve as available in GUI mode. In a script a user can read a session, change models and parameterization, obtain a solution, create a report on an obtained solution, store a new version of the session, and so on.

The script mode appeared in nuSolve in 2018, in version 0.6.0 of the software distribution. Since then it has been used by NASA GSFC and other VLBI Analysis Centers for data processing, investigations, and testing the software.

2 Automatization of Data Analysis

Initially, when the script mode appeared in nuSolve, the script `pia4INT.js` was created and included in the distribution. The purpose of this script was to demonstrate how routine operations performed by an analyst can be conducted in script mode. Script `autoINT.js` is derived from script `pia4INT.js` and basically performs the same operations. Additional functionality and the ability to adjust the configuration is added to this script. The new script also checks for some known problems of INT sessions, e.g., unusable data at very short baselines if a notch filter was not applied during correlation.

The script `autoINT.js` performs the following procedures:

- Read a database in vgosDb format [Gipson, 2012]. If the version is greater than 3, reset all editing.
- Check for known anomalies and set up a clock reference station.
- Set parameters for estimation: clock offsets and rates only. Get a single band delay solution for S-band.
- Check group delay ambiguities in S-band. Get a solution and check outliers.
- Check group delay ambiguities in X-band. Get a solution and check outliers.
- Evaluate ionosphere corrections.
- Set parameters for estimation: clocks, zenith delays, and baseline vector(s) or dUT1.
- Perform a reweighting/outlier processing loop.
- Obtain a final solution.
- Save a report in spool file format.
- If it was specified by the user, save a new version of the database.

The script processes one database at a time. A spool file and additional output are stored in predefined directories.

To compare results of the script for automatic analysis with a solution obtained by an analyst, a simplified script was derived from the `autoINT.js` script. This script reads a database, sets up parameters in the same way as it is done by the `autoINT.js` script, and obtains a final solution with the editing stored in the database. Then, a spool file and similar additional output are stored. A solution obtained with this script serves as a reference solution.

To compare the two versions of editings, the following values of a final solution were collated:

- Number of potentially usable and processed observations.
- WRMS of the solution.
- Estimation of dUT1: a posteriori value, an adjustment and its standard deviation.

For a given INT session, if these six values of automatic and operator solutions are the same, then both solutions are equal.

3 Data

To test the `autoINT.js` script we analyzed 2,494 INT sessions observed from January 2017 until July 2022 (S/X, VGOS, and mixed mode). That includes the IVS-IN1, IVS-IN2, IVS-IN3, VGOS-INT, VG, and SI series. 19 stations from 15 sites participated in the observations: GGAO12M, HART15M, HOBART12, ISHIOKA, KASHIM34, KOKEE, KOKEE12M, MACGO12M, MK-VLBA, NYALE13S, NYALES20, ONSA13SW, PIETOWN, SESHAN25, SVETLOE, WESTFORD, WETTZ13N, WETTZ13S, and WETTZELL. Two of the stations have tested new

equipment with bogus station names: NYALDBBC, WETTDBBC, and WETTVDIF. The observations were correlated at the seven correlators: BONN (Max Planck Institute for Radio Astronomy, Bonn, Germany), GSI (Geospatial Information Authority of Japan, Tsukuba, Japan), HAYS (MIT Haystack Observatory, Westford, Massachusetts), OSO (Onsala Space Observatory, Onsala, Sweden), UTAS (University of Tasmania, Hobart, Australia), WASH (U.S. Naval Observatory, Washington, DC), and WETZ (Geodetic Observatory Wettzell, Wettzell, Germany). According to IVS procedures, different series of INT sessions are processed by different IVS Analysis Centers and then submitted to the IVS Data Centers.

Most of the INT sessions are single baseline sessions, although some of the sessions have more than one baseline. A single baseline S/X INT session collects 20 to 40 observations. Due to unpredicted problems during the observations some data can get lost and the length of a session could decrease. For the processed set of INT sessions, the shortest one has 20 minutes of observations.

The single baseline VGOS INT sessions usually have 40 to 80 observations in an interval of 60 minutes. In two VGOS sessions, VGOS-T2049 (22FEB18VG) and VGOS-T2077 (22MAR18VG), all available VGOS stations participated in observations collecting more than a thousand observations. The INT sessions (like any other geodetic VLBI sessions) could have different problems (clock breaks, non-detection, etc.) that makes it impossible to process them at all. For example, session IN121-102 (database 21APR12XU) has a total of 20 observations, and only four of them have a quality code greater than zero (i.e., the rest of data are non-detections).

4 Analysis

To compare the automatic and human solutions we used results of session processing that were performed at the Goddard VLBI Analysis Center. Auxiliary software tools were developed to extract data from the two sets of solutions and to compare them. The comparison showed that for 1,259 out of the 2,494 sessions the automatic script gives a solution that is identical to the one obtained by an operator.

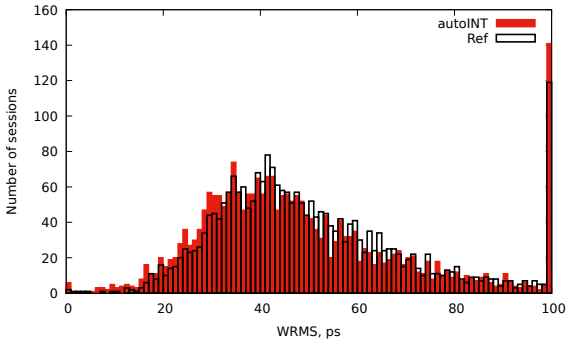

Fig. 1 Histogram of WRMS for the automatic (filled, red bars) and the reference (empty bars) solutions.

Figure 1 shows distributions of the number of sessions as a function of WRMS for the two sets of the solutions. The bars with zero WRMS display the number of sessions that have an insufficient number of usable observations for the least-squares estimation (fewer than six observations for a one-baseline session). The bars with WRMS 100 ps and more correspond to sessions that have severe problems (like clock breaks, subambiguities, problems with phase calibration, etc.). The bars of the reference solution with WRMS 0 ps and 100 ps shows the number of problematic INT sessions in the five-year period (not including sessions for which databases were not created or were not preprocessed by an operator). The corresponding bars of the automatic solutions are bigger; the difference of the numbers of sessions with the reference solution shows how many sessions the `autoINT.js` script was not able to process. The automatic script was not able to obtain a solution for a total of 26 INT sessions; these sessions have to be processed manually.

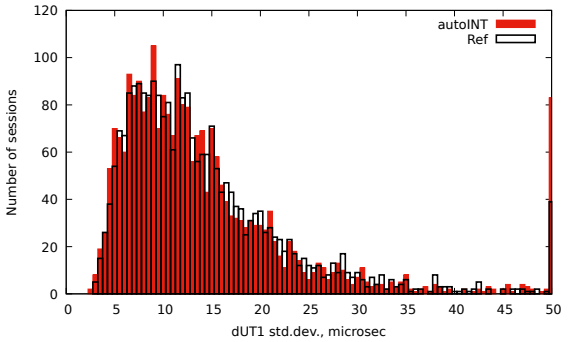

Fig. 2 Histogram of dUT1 standard deviations for the automatic (filled, red bars) and the reference (empty bars) solutions.

Distributions of the number of sessions as a function of the standard deviations of dUT1 estimation for both sets of solutions are shown in Figure 2. As one can see, most of the INT sessions have standard deviations of UT1 that are in a range of 5 to 15 microseconds. The rightmost bar represents sessions with standard deviations for UT1 of 50 microseconds or more. The difference of numbers of sessions for automatic and reference solutions for these bars is 44 sessions.

Figure 3 shows distributions of the number of sessions as a function of the difference of dUT1 estimation for the two sets of the solutions. The central bar that is representing 1,189 sessions is removed from the figure to make other bars visible. For 1,905 sessions, or 76%, the difference of the dUT1 estimation between the two types of solution is less than 5 microseconds. The range of dUT1 differences was chosen to be -50 to 50 microseconds. 89 sessions do not fall in this range, which indicates that they, perhaps, need to be processed manually too. However, checking these sessions showed that the relatively large difference in the estimated dUT1 parameter is caused by deselecting (or including) one or a few observations in the automatic solution that was/were not present (or deselected) in the reference solution. When a number of observations used in a solution is small (e.g., ten observations and six estimated parameters), adding or removing one observation can change results drastically.

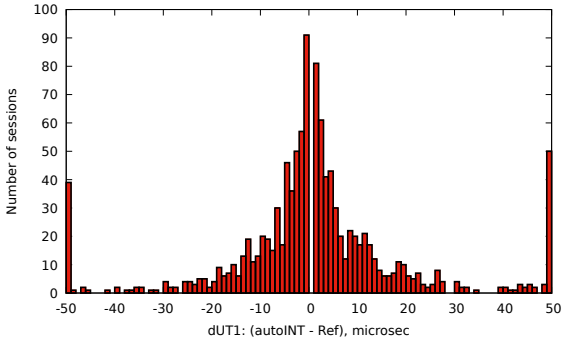

Fig. 3 Histogram of the difference of dUT1 estimation between automatic and reference solutions.

A histogram of scaled differences of dUT1 estimations (i.e., the differences divided by the standard deviations of dUT1 estimation) between the two sets of the solutions is represented in Figure 4. A total of 2,180 sessions, or 87%, have scaled differences of dUT1 estimation that are in the range of -1 to 1.

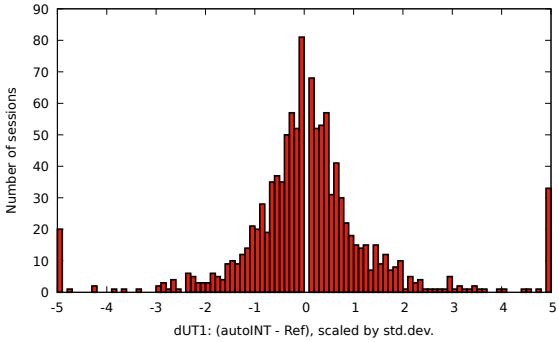

Fig. 4 Histogram of scaled by standard deviation difference of dUT1 estimation between automatic and reference solutions.

Analysis of the INT sessions that have different automatic and reference solutions showed that for most of these sessions the difference between the two solutions is caused by a very small number of analyzed observations. Having 10–20 good observations is not enough to determine outliers.

For VGOS INT sessions (which usually have more observations than the S/X sessions), a comparison of the differences between the automatic and reference solutions showed that for 138 (or 46%) of a total of 298 sessions the solutions are equal.

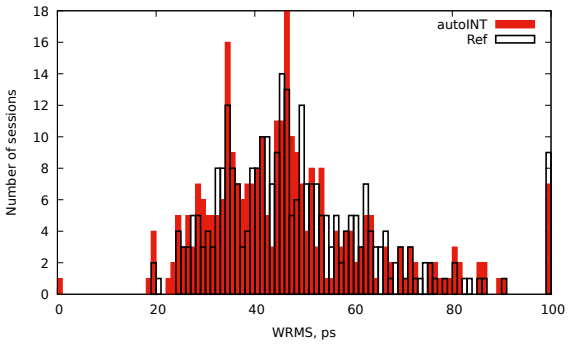

Fig. 5 Histograms of WRMS for the automatic (filled, red bars) and the reference (empty bars) solutions for VGOS INT sessions only.

Figure 5 shows histograms of WRMS for VGOS sessions for the automatic and the reference solutions. The script was unable to process only one of the VGOS sessions, VGOS-21349 (21DEC15VI), with nine us-

able observations. For the rest of the VGOS sessions the results of the automatic analysis and an operator solution are close.

Histograms of distributions of standard deviations of dUT1 estimations are shown in Figure 6. For VGOS INT sessions most of the sessions have standard deviations of UT1 that are in the range of 3 to 10 microseconds. For 250 (84%) of the VGOS INT sessions the difference of the dUT1 estimation between two types of solution is less than 5 microseconds. And 264 sessions, or 88%, have scaled differences of dUT1 estimation that are in the range of -1 to 1.

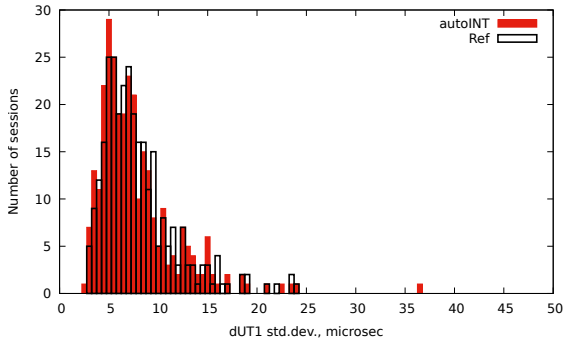

Fig. 6 Histograms of dUT1 standard deviations for the automatic (filled, red bars) and the reference (empty bars) solutions for VGOS INT sessions only.

It should be noted that work on the script `autoINT.js` is not finished. The functionality of the script can be improved; for example, there are many sessions produced by the GSI correlator where the single band delays are non-usable (e.g., IN322-059 (22FEB28XK)). Because the script starts its analysis from processing the single band delays, these sessions will fail in automatic analysis. Using the group delays and the delay rates instead of the single band delays could solve this problem.

5 Conclusions

The automatic script is capable of processing INT sessions. For 2,494 INT sessions collected over five-and-a-half years, the script has failed to process 44 sessions. The scaled differences of dUT1 estimations between the automatic and the reference solutions for 87% of INT sessions are in the range of -1 to 1.

Special treatment of outliers is required when a session with a small number of observations is processed.

The script is part of the nuSolve distribution. The work on the script is continuing. We plan to update the script and continue to include the modified versions in the future nuSolve releases.

References

[Bolotin et al., 2014] S. Bolotin, K. Baver, J.M. Gipson, D. Gordon and D. MacMillan. *The VLBI data analysis software νSolve: development progress and plans for the future*. In: D. Behrend, K.D. Baver, and K. Armstrong, editors, *IVS 2014 General Meeting Proceedings*, ISBN 978-7-03-042974-2, Science Press, Beijing, China, pages 253–257, 2014.

[Gipson, 2012] J.M. Gipson *IVS Working Group 4: VLBI Data Structures* In D. Behrend, and K.D. Baver, editors, *IVS 2012 General Meeting Proceedings*, NASA/CP-2012-217504, NASA GSFC, Maryland, pages 212–221, 2012.

[Nothnagel et al., 2017] A. Nothnagel, T. Artz, D. Behrend, Z. Malkin, Journal of Geodesy 91(7), 711 (2017). DOI 10.1007/s00190-016-0950-5.

The Application of the Rapid Data Observations of The Quasar VLBI Network in Order to Improve the Accuracy of the Universal Time Prediction

Marina Gribanova, Elena Skurikhina

Abstract The main purpose of this work is to test various ways of using "QUASAR" VLBI observation data to improve the accuracy of the UT1-UTC prediction. A brief overview of the theoretical foundations of the method used—local approximation, IAA Universal Time series description, and testing procedure—is included in the paper. Our tests' results show that the most accurate and prompt prediction for the entire length is obtained by replacement of the past few points of the reference series with values according to the R program. The study is more important from a practical point for rapid data analysis.

Keywords The Quasar VLBI Network, local approximation, prediction, Universal Time, rapid data

1 Introduction

The VLBI Stations of the "QUASAR" network (VGOS 13.2-m antennas SVERT13V, BADRT13V, and ZELRT13V, and Legacy antennas "Svetloe", "Badary", and "Zelenchukskaya") [1] perform rapid observations to determine Universal Time several times a day. This UT1-UTC series is available more quickly than the IERS finals data [2] are updated. Therefore, it is advisable to use them to solve the problem of operative analysis, in our case, for short-term prediction of Universal Time. It is important for users who perform operative processing of the space geodesy data. The first two points of the forecast are especially essential, because they are used in the Lagrange interpolation for four points in the data's reductions.

Institute of Applied Astronomy of the Russian Academy of Sciences

2 The Local Approximation Technique

The Local Approximation technique (LA) [3] is used as the prediction method in this work. The method was tested and proven to be high quality in the short-term prediction of Universal Time in our previous work [4]. The main idea of the LA is to divide the area into several local subareas, build an approximating model (we chose a linear function in our case), estimate the parameters of these models separately in each area using the least squares method, and then build a forecast based on the calculated parameters. We use an iterative, few-steps-ahead method for the LA technique in this work. The example of the UT1-UTC prediction for the 2021 year is shown in Figure 1; the comparison (using the root mean square (RMS)) with the IERS prediction and the method currently used in the IAA RAS is presented in Table 1.

3 IAA RAS Universal Time Series

We used two IAA Universal Time series from 2021 for our tests. The first series "iaa-R.eopi" was obtained in the IAA RAS from two-hour observations for the R program: on a network of three 13.2-m VGOS VLBI antennas located in the "Svetloe", "Badary", and "Zelenchukskaya" observatories. Observations were held four times a day. The second series "iaa-RI.eopi" was obtained from daily one-hour sessions of VLBI

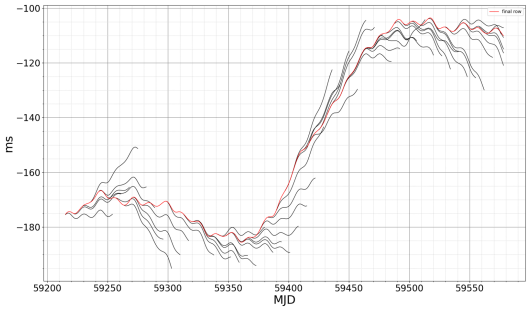

Fig. 1 "finals.data" for 2021 (red) and the LA forecast of up to 40 days with seven days step (black) for UT1-UTC.

Table 1 Example of accuracy of the UT1-UTC different predictions for several years, ms.

Years	Method	Days				
		1	5	10	20	40
2019	LA	0,08	0,45	1,25	3,49	10,09
	IAA RAS	0,41	2,35	3,52	5,60	9,12
	IERS	0,09	0,26	0,61	2,11	6,51
2018	LA	0,08	0,58	1,69	4,92	10,45
	IAA RAS	0,46	1,27	2,51	4,67	8,47
	IERS	0,08	0,20	0,54	2,34	5,10
2017	LA	0,20	0,55	1,29	3,04	6,04
	IAA RAS	0,38	1,02	1,85	3,15	6,74
	IERS	0,08	0,20	0,63	1,92	5,60
2016	LA	0,16	0,72	1,98	5,44	14,16
	IAA RAS	0,50	1,14	2,18	4,19	7,44
	IERS	0,12	0,22	0,67	1,99	4,50

observations for the RI program: on 32-m antennas of the "QUASAR" complex. The Zelenchukskaya-Badary baseline is mainly used, and if necessary, one of the stations can be replaced by the Svetloe station. E-vlbi technology is used for data transfer. The RAS-FX correlator developed at the IAA RAS ([5]) is used for the data correlation. Secondary data processing is performed with the QUASAR software package ([6]), also developed at the IAA RAS. The latency of the IAA dUT1 results is about six hours.

4 Testing Procedure

We used the rapid IERS EOP series "finals.data" as a reference series for the prediction and two IAA RAS Universal Time series "iaa-R.eopi" and "iaa-RI.eopi" for our experiments. In the first part of the tests, the last few points of the reference series "finals.data" were replaced by the points from the rapid series "iaa-R.eopi" and "iaa-RI.eopi". In the second experiment, the first one or two points of the constructed forecast were replaced by these values from the corresponding time series. We try to simulate the real situation with this way, when the "finals.data" series is still unavailable. The epochs of the IAA dUT1 time series do not correspond to the midnight epoch, so the UT1-UTC values were interpolated by splines of order 1 to midnight epochs for the comparison with the "finals.data". The comparison between each version of the LA prediction and the final series "finals.data" was performed. The RMS and the mean absolute error (MAE) of the difference prediction series and the final series were chosen as criteria for estimating the accuracy of the prediction. We used the first order iterative method with the reference interval of three years for the LA prediction. The test results are shown below. The statistics are given for 2021.01.01–2021.12.31. The number of last points replaced for the first test is four, and the number of first ones for the second experiment is one. The table shows the RMS and the MAE for each forecast version. We use the following designations: the "LA" is the ordinary version of the prediction with no IAA RAS data; "`Refer_repl`" is the prediction with the replacement of the last few points of the reference series, and "`Pred_repl`" is for the replacement of the first points of the constructed forecast. Also Figure 2 shows the concept of our tests.

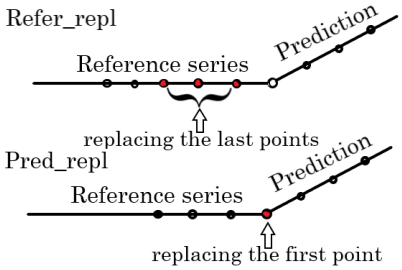

Fig. 2 Illustration of two test versions.

5 Results

As we can see from Table 2, using the IAA RAS rapid data improved the results in all kinds of the tests in

Table 2 Accuracy of the UT1-UTC prediction for 2021, ms.

Years	Method	Days								
		1	2	3	4	5	10	15	20	40
RMS										
	LA	0,12	0,20	0,32	0,48	0,66	1,84	3,34	5,01	12,56
R	Refer_repl	0,06	0,14	0,26	0,41	0,58	1,74	3,24	4,86	11,99
	Pred_repl	0,02	–	–	–	–	–	–	–	–
RI	Refer_repl	0,15	0,28	0,45	0,64	0,85	2,08	3,56	5,23	12,64
	Pred_repl	0,07	–	–	–	–	–	–	–	–
MAE										
	LA	0,09	0,17	0,28	0,40	0,56	1,60	2,85	4,38	10,62
R	Refer_repl	0,04	0,11	0,21	0,33	0,46	1,43	2,72	4,17	9,89
	Pred_repl	0,08	–	–	–	–	–	–	–	–
RI	Refer_repl	0,11	0,22	0,36	0,51	0,68	1,71	2,97	4,31	10,18
	Pred_repl	0,05	–	–	–	–	–	–	–	–

comparison with the LA method. The more precise results for the entire length of the prediction are obtained from the replacement of the last few points of the reference series with iaa-R.eopi values. Using the rapid series for the first point instead of the forecast shows obvious good results, so it's an important advantage to have constantly updated operative observations.

References

1. D. Ivanov, A. Ipatov, D. Marshalov, and G. Ilin, "Quasar" VLBI Network Stations Report, In D. Behrend, K. Armstrong, and K. Baver, editors, *International VLBI Service for Geodesy and Astrometry 2019+2020 Biennial Report*, NASA/TP-20210021389, pages 100–104, 2021.
2. International Earth Rotation and Reference Systems Service. URL: https://www.iers.org/
3. A. Loskutov, D. Zhuravlev and O. Kotlyarov, "Applications of a local approximation technique for forecasting of economic indicators", Physics Faculty, Moscow State University after M. V. Lomonosov, 2003.
4. M. Gribanova and E. Skurikhina, "Prediction of Earth rotation parameters using local approximation techniques", *Transactions of IAA RAS*, Iss. 54, pages 11—20, 2020.
5. I. Surkis, V. Ken et al., "The RASFX VGOS GPU based software correlator", *Transactions of IAA RAS*, Iss. 41, pages 123-–126, 2017.
6. S. Kurdubov. "QUASAR software in IAA EOP service: Global Solution and Daily SINEX", In J. Boehm, A. Pany and H. Schuh, editors, *Proceedings of the 18th European VLBI for Geodesy and Astrometry Working Meeting*, pages 79-–82, 2007.

Impact of the Source Selection and Scheduling Optimization on the Estimation of UT1-UTC in VLBI Intensive Sessions

L. Kern[1], M. Schartner[2], J. Böhm[1], S. Böhm[1], A. Nothnagel[1], B. Soja[2]

Abstract With the help of Very Long Baseline Interferometry (VLBI), it is possible to determine a large number of parameters, including station and source coordinates as well as the Earth orientation parameters (EOP). Due to the limitation of observations of one-hour single baseline sessions, so-called *Intensive* sessions, only a few parameters such as clock offsets and zenith wet delays per station can be estimated in addition to the parameter of primary interest, which is the difference between UT1 (Universal Time 1) and UTC (Coordinated Universal Time).

Thus, the remaining parameters, including station and source coordinates, as well as EOP, are fixed to their a priori values, making the precision of the UT1-UTC estimate dependent on the accuracy of the a priori values used in the estimation process. Additionally, due to the daily rotation of the Earth and the revolution around the Sun, the source visibility and selection changes continuously, resulting in variations of the estimates of interest over time. Furthermore, the scheduling optimization process itself also has an impact on the results obtained by real observations or simulations. In this study, we show the variations of UT1-UTC estimates due to varying source selection and scheduling optimization strategies throughout the investigation period of one year using the simulation results of [7].

Keywords VLBI, Intensives, simulation, UT1-UTC

1. TU Wien
2. ETH Zürich

1 Introduction

The purpose of Very Long Baseline Interferometry (VLBI) observations includes the realization of the International Terrestrial Reference Frame (ITRF) [1] and the International Celestial Reference Frame (ICRF) [6]. Furthermore, it is possible to estimate the complete set of Earth orientation parameters (EOP) with VLBI [8]. So-called *Intensive* sessions, or shortly *Intensives*, are one-hour VLBI sessions between mostly two to three stations and are observed daily with the main goal of deriving the difference between UT1 (Universal Time 1) and UTC (Coordinated Universal Time) with a short latency. Due to the highly restricted number of observations, only a few parameters can be derived in addition to the main parameter of interest, namely zenith wet delays per station and a linear function for the clock differences. Thus, each of the remaining EOP, station, and source coordinates is fixed to its a priori value. As a result, the precision of the UT1-UTC estimate from *Intensives* is not only dependent on the baseline geometry (see [10]) but also on the accuracy of the a priori values used in the estimation process (see [7]). Furthermore, the overall scheduling process, including the source selection as well as the optimization strategies, influences VLBI observables. Based on our previous study [7], where we analyzed the impact of erroneous a priori information on the UT1-UTC estimate from *Intensives*, we are now taking a closer look at the differences in the UT1-UTC estimates themselves. By comparing the monthly estimates, the impact of the source visibility can be assessed, while the variations within one month represent the impact due to the scheduling process.

2 Data

The data were taken from our previous study [7], where we generated a 10 × 10 degree grid of artificial VGOS telescopes, which were assumed to have the same properties as the WETTZ13S telescope. In the course of the study, all possible baselines between so-called reference stations located at the reference meridian at zero degrees and any other artificial station were investigated, leading to almost 3,000 investigated baselines. In Figure 1 the gray dots represent the artificial antennas, and the red star highlights a reference station at 50 degrees latitude. For demonstration purposes, four random baselines are displayed using different colors.

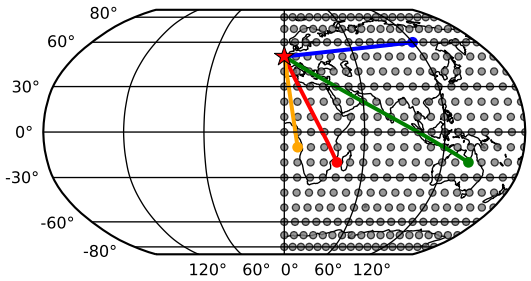

Fig. 1 Experiment setup. All single baselines between the reference station (red star) and any other station (gray dot) are investigated. For demonstration purposes, four random baselines are displayed.

Highly optimized schedules per baseline and month were generated with the help of VieSched++ [11] over the investigation period of one year using different optimization strategies. In this respect, the weight factors for sky-coverage, scan duration, and low elevation observations as well as the corner switching cadences within the *Intensive* scheduling algorithm [10] are varied. Hence, per session, almost 100 schedules were created and simulated. In addition, a compact list of 125 suitable sources was used to mitigate the impact of varying source selection within the different schedules. However, as concluded in [7] and as can be seen in more detail in Section 3, changes in the source selection and thus scheduling results between the different months are still visible.

In this previous study, out of the 96 schedules per session, only the best performing schedule was selected for further processing, where we investigated the difference (ΔUT1) in the simulated UT1-UTC value of an unaltered evaluation, where no errors were introduced in the a priori information, and several modified evaluations. For this purpose, the remaining EOP, including the x_p- and y_p-components of polar motion and the dX- and dY-components of the nutation offsets, were taken from the IERS Rapid Service and Prediction Center (finals2000A.daily). The topocentric station coordinates of the second station of each baseline were compromised with an error of 162 µas or 5 mm. For more details on the impact of errors in the a priori information on the UT1-UTC determination with *Intensive* sessions, see [7].

Due to the high scatter of the monthly ΔUT1 values of some baselines, we found that the scheduling process itself, including the source visibility and selection as well as the optimization strategies, can have a significant impact on the precision of the estimates on the order of tenths of µs. In this additional study, we now want to analyze the results of all generated schedules per session created within the study [7] and show the variations of ΔUT1 per a priori error source within the 96 generated schedules and throughout the investigation period of one year.

3 Analysis

In the following Figures 2, 3, 4 and 5, the distribution of the ΔUT1 values of the different evaluations of all 96 generated schedules per month are displayed for four representative baselines. Comparing the monthly solutions makes it possible to quantify the impact of source visibility, while the distribution within one month represents scheduling-related impacts. The lines connect the medians of the monthly sessions to demonstrate the variations between the monthly sessions. The filled area represents the upper and lower quartiles of the 96 individual ΔUT1 estimates, while the whiskers show the total range of the estimates. Among the selected baselines are the northern INT1 baseline between Wz (Wettzell, Germany) and Is (Ishioka, Japan) (blue), the southern baseline between Ht (Hartrao, South Africa) and Hb (Hobart, Tasmania) (green), the INT9 baseline between Ag (Aggo, Argentina) and Wz (orange) with a midpoint close to the equatorial plane, and a north-south oriented baseline which is close to being parallel to the Earth's rotation vector between Wz and Ht (pur-

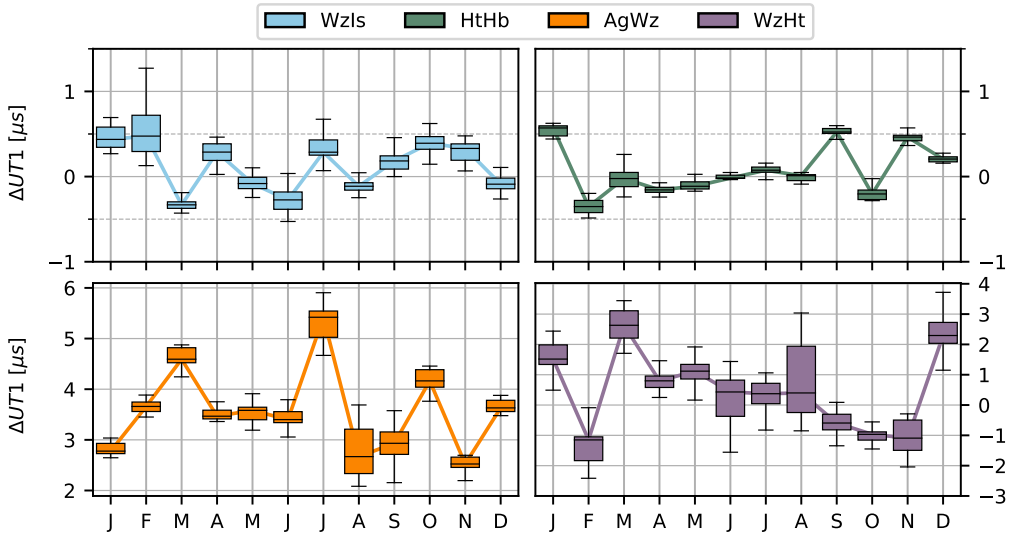

Fig. 2 Effects on ΔUT1 by errors in the up–down direction of the a priori station coordinates.

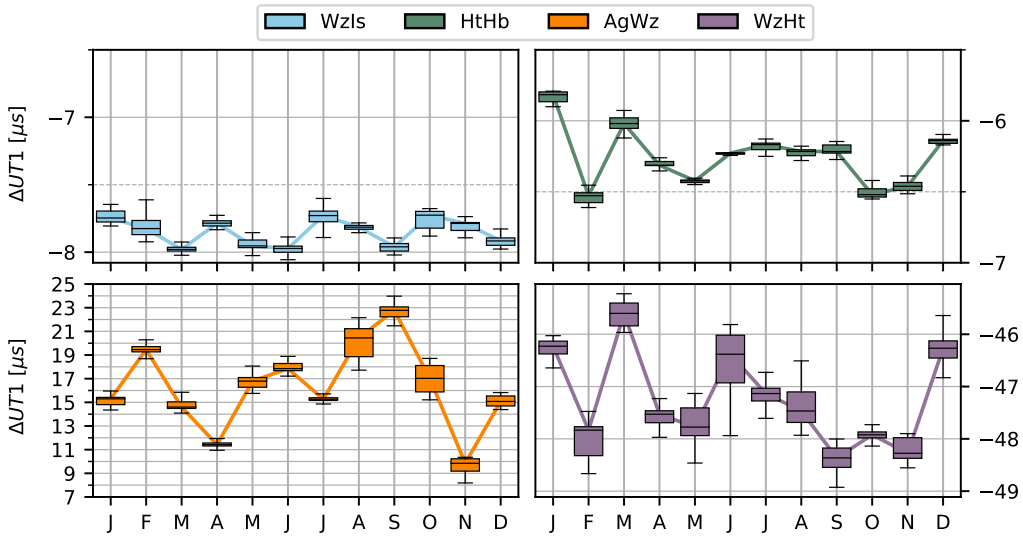

Fig. 3 Effects on ΔUT1 by errors in the east–west direction of the a priori station coordinates.

ple). Except for the last baseline WzHt, all baselines are observed on a regular basis in *Intensive* sessions.

In Figure 2, an error of 5 mm was introduced in the up-component of the topocentric coordinates of the corresponding second station. In the case of the WzIs and HtHb baselines, the ΔUT1 values of about zero µs represent the high resistance against this a priori error. Furthermore, the overall scatter (standard deviation of all ΔUT1 biases) is rather low for both baselines ($\sigma = 0.3$ µs), just as the variations within the individual sessions. In contrast, the differences in the UT1-UTC values for the AgWz and WzHt baselines are higher, and the standard deviations of all values are 0.8 and 1.4 µs. Moreover, the session-wise scatter is much higher, as noted by the different (larger) y-axis limits.

Figure 3 depicts the results of an evaluation with a modified east-component, which overall has a higher impact on the results compared to an error in up-direction. However, the baselines WzIs and HtHb are again more consistent throughout the year ($\sigma = 0.1$ / 0.2 µs), although a clear bias due to the altered a priori coordinates is present, and within one session. In comparison, the individual plots of AgWz

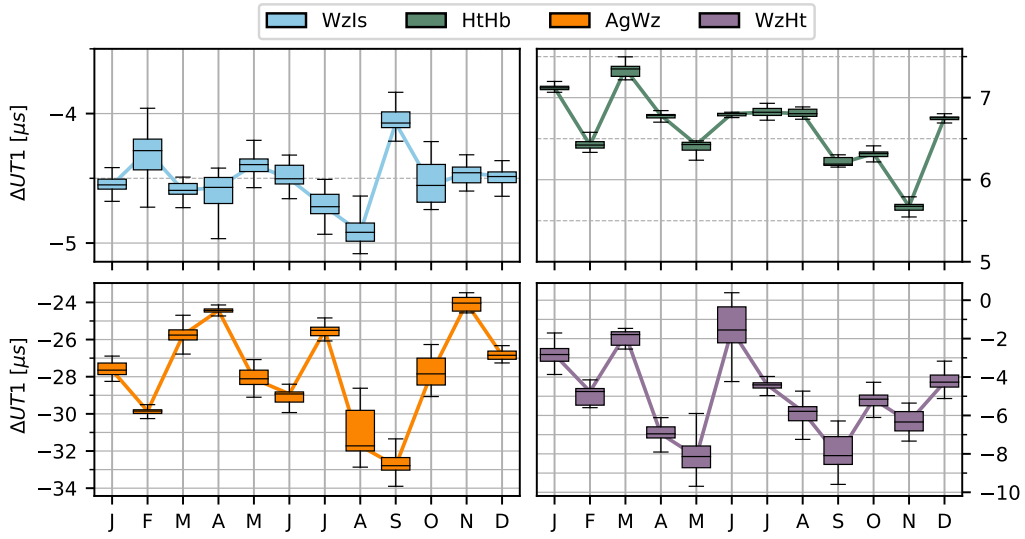

Fig. 4 Effects on ΔUT1 by errors in the north–south direction of the a priori station coordinates.

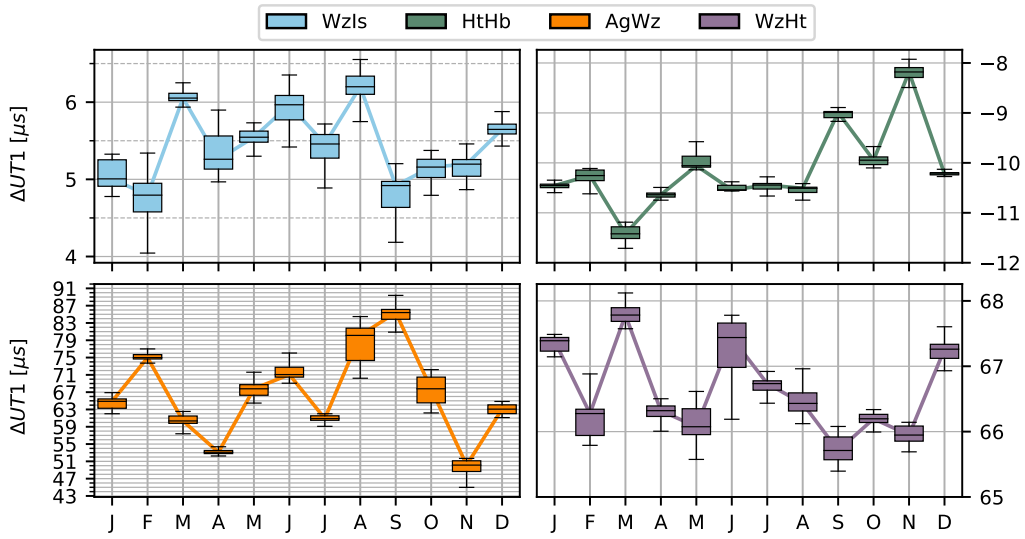

Fig. 5 Effects on ΔUT1 by errors in the x_p- and the y_p-components of the a priori polar motion information.

and WzHt (σ = 3.6 / 0.9 µs) depict how sensitive these baselines are against changes in the source selection.

Comparable results can be obtained if an error is introduced in the north-component (see Figure 4) with standard deviations of 0.2 (WzIs), 0.4 (HtHb), 2.6 (AgWz), and 2.2 (WzHt) µs.

In all cases with erroneous a priori station coordinates, the scatter between the individual months is greater than the scatter within one month. Therefore, one can conclude that the impact of source visibility is greater than the impact of scheduling.

Lastly, errors in the x_p- and y_p-components of the a priori polar motion information strongly affect the AgWz baseline, resulting in a standard deviation of 10 µs and ΔUT1 values of approximately 67 µs (see Figure 5). The other three baselines seem to be more resistant against changes in the source selection with standard deviations of 0.5 (WzIs), 0.8 (HtHb), and 0.7 (WzHt) µs.

4 Conclusions

Intensives are strongly influenced by the baseline geometry, errors in the a priori information, source visibility, and the scheduling process. While the baseline geometry and errors in a priori information were already studied in [10] and [7] respectively, this study reveals that the source visibility seems to have a larger impact compared to changes in the scheduling optimization. As can be seen from this study as well as in [7], some baselines (baselines with a midpoint close to the equatorial plane, e.g., INT9) are more affected than others (long east–west oriented baselines). This can be partly explained by the fact that baselines that exhibit a large scatter in the UT1-UTC estimates are also declared as not optimal for this determination due to their geometry or, more precisely, due to the restricted right ascension angles of observed sources [10]. Lastly, the examined southern baseline did not perform much worse than the northern baseline although fewer good sources are available in the southern hemisphere [6, 9]. More information on the performance of real southern *Intensives* can be found in [5].

References

1. Altamimi Z, et al. (2016) ITRF2014: A new release of the International Terrestrial Reference Frame modeling nonlinear station motions. Journal of Geophysical Research: Solid Earth 121(8):6109–6131. https://doi.org/10.1002/2016JB013098
2. Böhm J, Schuh H (2007) Forecasting Data of the Troposphere Used for IVS Intensive Sessions. In: Proceedings of the 18th European VLBI for Geodesy and Astronomy working meeting, Vienna, 12-13 April 2007, pp 153–157.
3. Böhm J, et al. (2010) Asymmetric tropospheric delays from numerical weather models for UT1 determination from VLBI Intensive sessions on the baseline Wettzell-Tsukuba. Journal of Geodesy 84:319–325. https://doi.org/10.1007/s00190-010-0370-x
4. Böhm J, et al. (2018) Vienna VLBI and Satellite Software (VieVS) for Geodesy and Astrometry. Publications of the Astronomical Society of the Pacific 130(986):044,503. https://doi.org/10.1088/1538-3873/aaa22b
5. Böhm S, et al. (2022) Probing a southern hemisphere VLBI intensive baseline configuration for UT1 determination. Earth, Planets and Space (accepted for publ.).
6. Charlot P, et al. (2020) The third realization of the International Celestial Reference Frame by very long baseline interferometry. Astronomy & Astrophysics. https://doi.org/10.1051/0004-6361/202038368
7. Kern L, et al. (2022) On the importance of accurate pole and station coordinates for VLBI Intensive baselines. Journal of Geodesy. submitted to Journal of Geodesy.
8. Petit G, Luzum B (2010) IERS Conventions 2010. IERS Technical Note 36.
9. Plank L, et al. (2015) Challenges for geodetic VLBI in the southern hemisphere. Advances in Space Research 56(2):304–313. https://doi.org/10.1016/j.asr.2015.04.022
10. Schartner M, et al. (2021) Optimal VLBI baseline geometry for UT1-UTC Intensive observations. Journal of Geodesy 95(75). https://doi.org/10.1007/s00190-021-01530-8
11. Schartner M, Böhm J (2019) VieSched++: A New VLBI Scheduling Software for Geodesy and Astrometry. Publications of the Astronomical Society of the Pacific 131(1002):084,501. https://doi.org/10.1088/1538-3873/ab1820
12. Schartner M, et al. (2020) Optimal antenna locations of the VLBI Global Observing System for the estimation of Earth orientation parameters. Earth, Planets and Space 72(1):87. https://doi.org/10.1186/s40623-020-01214-1

Quality Assessment of UT1-UTC (dUT1) Estimates Using VGOS Observations

Dhiman Mondal[1], Pedro Elosegui[1], John Barrett[1], Brian Corey[1], Arthur Niell[1], Chester Ruszczyk[1], Mike Titus[1], John Gipson[2]

Abstract Currently a network of up to nine next-generation VLBI, or VGOS, stations observes 24-hour-long sessions once every two weeks, and two VGOS stations in Hawaii and Germany observe one-hour-long sessions, known as Intensives, five days a week. Similar sessions are conducted with the predecessor S/X legacy system, with a network of up to 15 stations observing 24-hour sessions twice a week and the same pair of stations as for VGOS observing one-hour Intensives every day. The goal of the Intensives is to measure dUT1 precisely in a more timely manner than possible for the 24-hour sessions, which have broader scientific goals. Individual VGOS observations are more precise than S/X observations (Niell et al., 2018). Therefore, the precision and accuracy of the dUT1 estimates from VGOS have the potential to be better than that from S/X.

In this paper, we investigate the level of agreement of dUT1 measurements obtained from both one-hour- and 24-hour-long VGOS sessions with dUT1 obtained from simultaneous S/X legacy sessions and with external dUT1 series from IERS and USNO. We find that the median formal error of the dUT1 is a factor of two smaller for VGOS Intensives than for the S/X Intensives, but similar for VGOS and S/X 24-hour sessions. The VGOS-derived dUT1 series is in good agreement with the S/X-derived dUT1, which is an indication that VGOS and S/X reference frames are in good agreement. Comparisons with external EOP series show that both VGOS and S/X-derived dUT1 are in good agreement with the USNO series for both 24-hour and one-hour sessions. The scatters of the differences of VGOS-derived dUT1 with S/X-derived dUT1 and other external dUT1 series are not consistent with the estimated VGOS formal errors which suggests that a significant amount of unmodeled noise is present in the VGOS observations.

Keywords UT1-UTC, dUT1, VGOS, Geodetic VLBI

1 Introduction

The VLBI Global Observing System (VGOS) is a broadband geodetic VLBI system made up of small, fast, sensitive antennas capable of observing radio sources with a faster cadence than the predecessor S/X legacy system. VLBI is the only space-geodetic technique, among four, that observes distant quasars. VLBI is therefore capable of realizing a Celestial Reference Frame (CRF) and solving for all five earth orientation parameters: UT1-UTC, two polar motion parameters, and two nutation parameters. Among the space-geodetic techniques, VLBI is the only one that provides UT1-UTC, the diurnal earth rotation phase, otherwise known as dUT1. A significant portion of this quantity can be modeled and predicted using different geophysical phenomena. However, some variations cannot be modeled and need to be observed with high precision.

At present, the S/X legacy VLBI network is providing dUT1 via the so-called Intensive sessions (INT1), which run every day for 1 hour using a single baseline between Kokee Park, Hawaii, and Wettzell, Germany (Figure 1). This network also observes 24-hour sessions (R1/R4) twice a week with 7–14 stations. The newer VGOS network of nine stations has demon-

1. MIT Haystack Observatory, MA, USA
2. NVI Inc./NASA GSFC, MD, USA

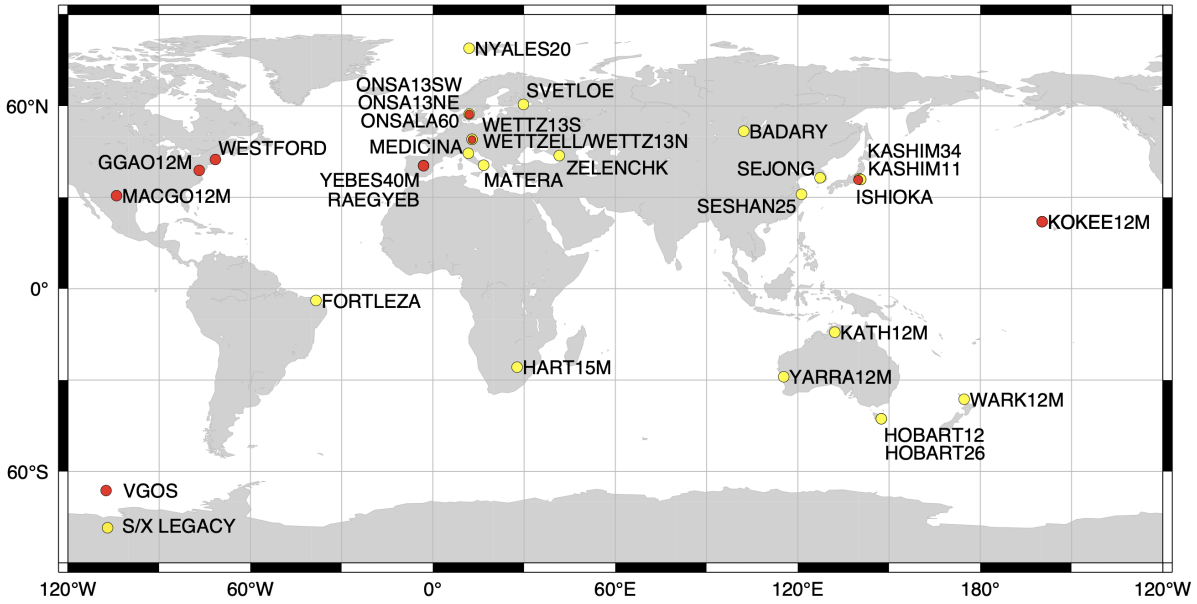

Fig. 1 Location of VGOS (red circles) and S/X legacy (yellow circles) VLBI stations.

strated theoretical observation uncertainties that are a factor of ten smaller than from S/X legacy systems (Niell et al., 2018). Therefore, the dUT1 parameters from VGOS observations could be more accurate and precise than that from S/X legacy.

High precision UT1-UTC is critical for many applications, such as satellite orbit determination, spacecraft navigation, astronomical observations, and other geophysical studies. In this paper, we explore the quality of dUT1 measurements obtained from VGOS observations and compare them with dUT1 measurements obtained from S/X legacy observations, as well as with external dUT1 from IERS and USNO.

2 Data

We utilized both one-hour-long Intensive and 24-hour-long VGOS and S/X legacy sessions observed between 2019 and 2021. The Intensive sessions, both VGOS and S/X, have the observations from only two stations and thus from a single baseline. The regular 24-hour sessions contain multiple baselines among the stations observing a source simultaneously. S/X legacy stations observed both one-hour Intensive and 24-hour regular sessions more frequently than the VGOS network. Therefore, we used only the S/X sessions that overlapped the day of a VGOS session and estimated the dUT1 parameter at the common integer day boundary. In total, we have used the Intensive sessions for 85 days and the 24-hour regular sessions for 65 days. All VGOS and S/X sessions are publicly available on the CDDIS server (https://cddis.nasa.gov/archive/vlbi/ivsdata/).

3 Analysis

We processed the VLBI observables from all sessions using the VieVS geodetic software package (Böhm et al., 2009) to obtain dUT1 estimates, along with other parameters of geodetic interest, as described next. Given that the Intensive and regular VLBI sessions have different observing lengths and station network configurations, the analysis strategies are different. The 24-hour sessions were observed with seven or more stations; therefore, site positions, source positions, clocks parameters, atmospheric parameters, and EOPs can all be estimated. In contrast, the one-hour Intensive sessions do not contain enough

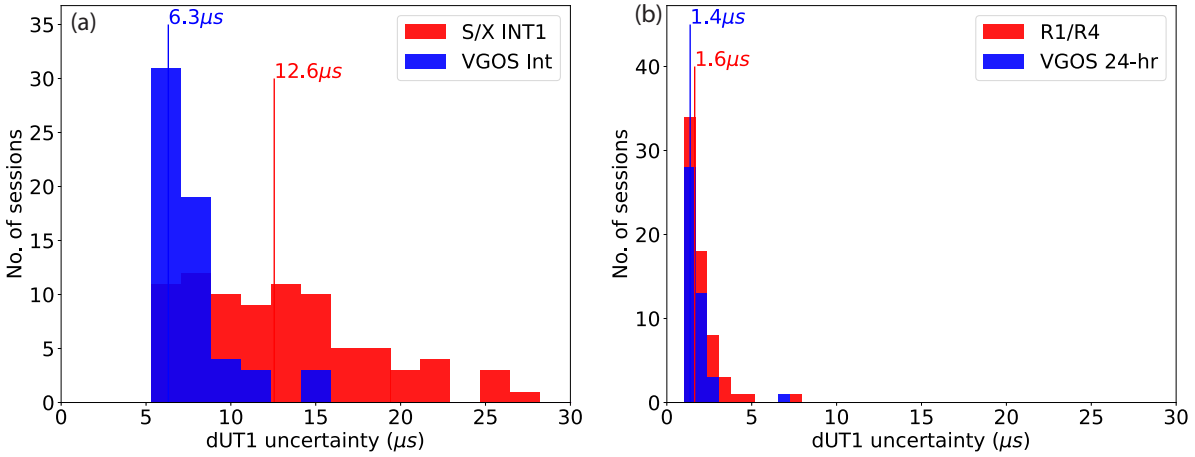

Fig. 2 Histogram of the dUT1 uncertainties (formal errors) estimated for (a) one-hour Intensive sessions and (b) 24-hour-long sessions from VGOS and S/X legacy observations. The vertical lines and the numbers represent the median of the formal error from all sessions.

observations to estimate all the parameters. Therefore, only one clock offset at one station, atmospheric wet delay at both stations, and one dUT1 parameter are estimated. The site positions, source positions, polar motion, and nutation parameters remained fixed in the solution. We have used ITRF2014-equivalent site positions of the VLBI stations. For the 24-hour sessions, we first generated the normal equations and then stacked the normal equations to solve for the EOPs using a common set of stations as a reference frame datum. For the one-hour Intensive sessions, we compared the dUT1 values estimated independently for each session. Comparisons were made among the dUT1 series from four sources: values obtained from VGOS observations, values obtained from S/X legacy observations, and external EOP series from the IERS 14C04 and USNO Final series. We used the weighted mean (bias) and weighted standard deviations (scatter) as the metrics to describe the agreement and scatter between two series.

4 Comparison of Formal Error

We compared the formal errors estimated from the VGOS and S/X 24-hour and one-hour sessions. The formal error is the uncertainty of the dUT1 parameter estimated from a re-weighted solution in which extra noise was added in quadrature to each observation to account for mismodeling and to make the chi-square per degree of freedom, χ^2/dof, equal to one (Equation 1).

$$\sigma_j^2 = \sigma_{j,meas}^2 + \sigma_{j,noise}^2 \quad (1)$$

Here, $\sigma_{j,meas}^2$ is the group delay variance for each observation and $\sigma_{j,noise}^2$ is the constant additive noise variance.

The median formal error of 6.3 μs for the VGOS Intensives is a factor of two smaller than the median error of 12.6 μs for the S/X legacy Intensives (Figure 2a). The smaller error for VGOS dUT1 is due mainly to the lower group delay uncertainties and increased number of observations in VGOS sessions, given that the baseline geometry is identical for both S/X and VGOS Intensives. The mean number of observations in a VGOS Intensive is typically twice the mean number in an S/X Intensive. The group delay uncertainties for VGOS are also approximately ten times smaller than for S/X; for example, the median group delay uncertainties in VGOS and S/X legacy sessions observed on 19 October 2021 were 1.3 ps and 11.1 ps, respectively.

In the 24-hour regular sessions, the median formal errors from VGOS and S/X are comparable (Figure 2b), 1.4 and 1.6 μs, respectively. The similarity in the formal errors likely reflects differences in the geographical distributions of the networks. If the networks were similar, one would expect the dUT1 for-

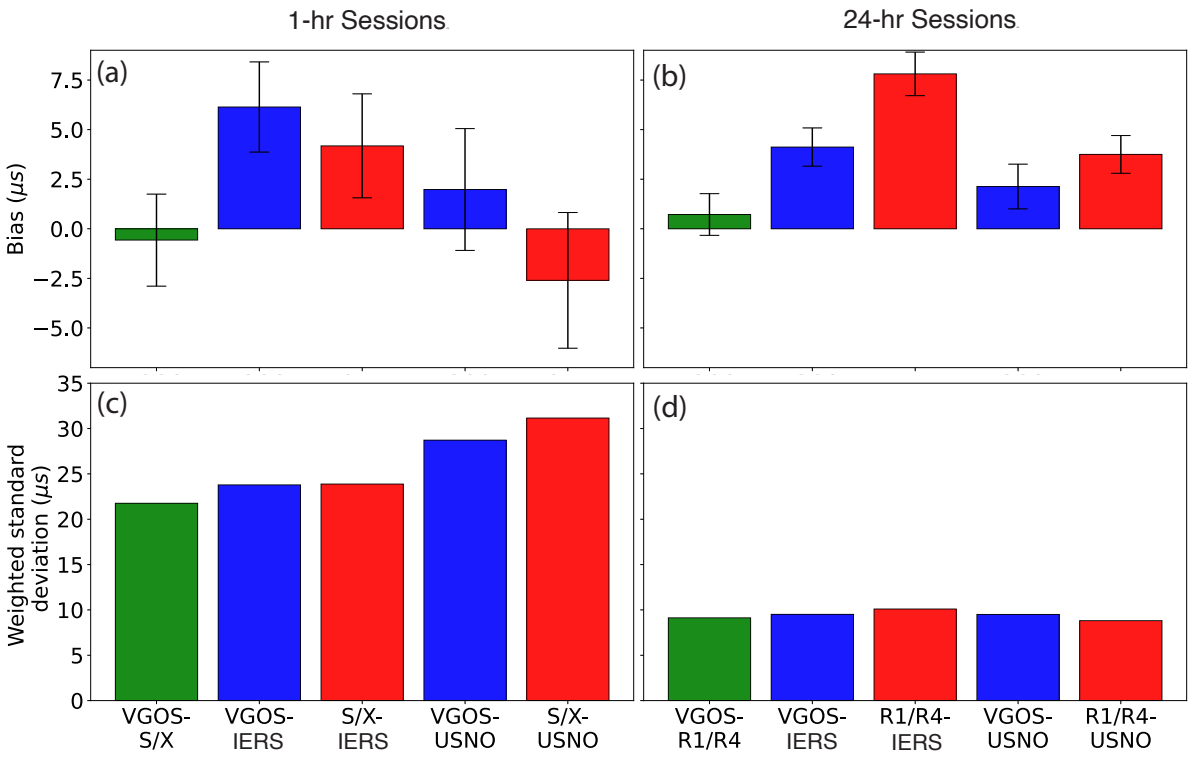

Fig. 3 Weighted mean bias (a and b) and weighted standard deviation (c and d) of the difference of VGOS and S/X dUT1 with respect to each other and with respect to other external EOP series for one-hour Intensive (left column) and 24-hour (right column) sessions.

mal errors to be significantly smaller for VGOS than for S/X, as was observed for the one-baseline Intensives. The VGOS network has 7–9 stations mostly distributed over the northern hemisphere, whereas the S/X legacy network has more than nine stations distributed over both hemispheres. Thus, the S/X legacy network may have provided better geometric strength for measuring dUT1 than the VGOS network.

The formal errors for the Intensive sessions are larger than for the 24-hour sessions for both VGOS and S/X legacy networks, primarily because of the smaller number of observations in Intensive sessions. This difference in the number of observations is due both to the difference in session duration and to the greater number of baselines in 24-hour sessions.

5 VGOS Comparison with Other EOP Series

We have compared the bias and scatter of the differences of dUT1 values estimated from VGOS observations with dUT1 values estimated from S/X observations, and with the dUT1 values from other Combination Centers. The Combination-Center dUT1 series include the solutions from S/X observations but not from VGOS observations; therefore, the VGOS-derived dUT1 values are independent of all of the other dUT1 series.

For the Intensive observations, the VGOS-derived dUT1 series is in the best agreement with S/X-derived dUT1; the bias of the difference between two series is -0.6 ± 2.3 μs (Figure 3a). Both VGOS and S/X have negligible bias to the USNO series. Both series agree better with USNO than with IERS dUT1. The scatter of the VGOS series is smaller when compared with S/X than with IERS and USNO (Figure 3c).

For the 24-hour-long sessions, the VGOS-derived dUT1 series is also in good agreement with S/X derived dUT1 series (Figure 3b). The bias between two series is 0.7 ± 1.0 µs. In general, the VGOS-derived dUT1 agrees better with IERS and USNO dUT1 series than does S/X. The scatters of the VGOS-derived dUT1 series with S/X and other external EOP series are similar (Figure 3d).

The scatter (standard deviation) of the Intensive-derived dUT1 is larger than the dUT1 estimated from the 24-hour sessions. This is partly because the dUT1 derived from the Intensive sessions absorbs the error from the parameters that remained fixed in the solution, such as the terrestrial and celestial reference frames, polar motion, and nutation. It is possible to estimate these additional parameters in the analysis of the 24-hour-long sessions because of the availability of more observations. However, the primary reason the 24-hour sessions have smaller dUT1 uncertainties, and thus scatter, is because those sessions have a larger number of antennas and a better network geometry, as well as many more observations.

6 Conclusions

Our comparison shows that the formal errors of the dUT1 estimates are a factor of two smaller for the VGOS Intensives than for the S/X Intensives, but is similar for the VGOS and S/X 24-hour sessions. VGOS-derived dUT1 estimates, from both 24-hour and one-hour Intensive, agree better with USNO Final EOP series than with IERS. The best agreement is seen with the simultaneous S/X sessions. The small bias between the VGOS and S/X dUT1 estimates suggests that the reference frames for the two networks are in good agreement.

The VGOS dUT1 scatters relative to IERS, USNO Final, and S/X series are similar, though larger for Intensives than for the 24-hour sessions, as one would expect. The large scatter is not consistent with the smaller formal error for both the VGOS and S/X dUT1 results, which suggests that there is significant unmodeled noise present in the solutions. For example, the observed scatter of the dUT1 differences between VGOS and S/X Intensives is about 21.7 µs; however, one would expect the scatter to be about 14.0 µs, given that the median formal errors of VGOS and S/X Intensives are 6.3 and 12.6 µs, respectively. Therefore, about 16.5 µs of additional noise is present. Similarly, the VGOS minus S/X 24-hr series contains about 8.8 µs of unmodeled noise.

Acknowledgments

The authors would like to thank all the individuals who make the geodetic VLBI endeavor possible. The work by MIT Haystack Observatory was supported under NASA contract 80GSFC20C0078. The work by NVI, Inc. was supported under NASA contract NNG17HS00C.

References

Böhm, J., Spicakova, H., Plank, L., Teke, K., Pany, A., Wresnik, J., Englich, S., Nilsson, T., Schuh, H., Hobiger, T., Ichikawa, R., Koyama, Y., Gotoh, T., Kubooka, T., and Otsubo, T. (2009). Plans for the Vienna VLBI Software VieVS.

Niell, A., Barrett, J., Burns, A., Cappallo, R., Corey, B., Derome, M., Eckert, C., Elosegui, P., McWhirter, R., Poirier, M., Rajagopalan, G., Rogers, A., Ruszczyk, C., SooHoo, J., Titus, M., Whitney, A., Behrend, D., Bolotin, S., Gipson, J., Gordon, D., Himwich, E., and Petrachenko, B. (2018). Demonstration of a Broadband Very Long Baseline Interferometer System: A New Instrument for High-Precision Space Geodesy. *Radio Science*, 53(10):1269–1291.

Evaluation of KOKEE12M-WETTZ13S VGOS Intensives

John Gipson[1], Karen Baver[1], Sergei Bolotin[1], Frank Lemoine[2], Pedro Elosegui[3], Chester Ruszczyk[3], Dhiman Mondal[3], Andrew Sargent[4], Phillip Haftings[4], Chris Coughlin[5], Christian Plötz[6], Torben Schüler[6], Alexander Neidhardt[7]

Abstract The KOKEE12M-WETTZ13S (K2-Ws) VGOS Intensive series began on January 4, 2021. This series observed simultaneously with the INT01 S/X Intensives involving KOKEE-WETTZELL (Kk-Wz). Initially, the K2-Ws sessions ran roughly once a week. By the end of 2021 the cadence increased to 5/week. On January 31, 2022, the scheduling parameters were changed to increase the number of scans. Hence we divide the K2-Ws series into 'Old' and 'New.' In this note we evaluate the performance of these sessions using the Calc/Solve analysis software. We compare the UT1 estimates from the K2-Ws VGOS Intensives with several other UT1 series: 1) The simultaneous Ks-Wz INT01 S/X Intensives; 2) The R1 and R4 series; 3) An EOP series produced by JPL. We demonstrate that both VGOS Intensive series are better than the S/X series, and that 'New' is better than 'Old.' For example, if we take the difference of the UT1 estimates from the R1 and R4 and the Intensives and compute the RMS, we find 25.3 μs (S/X) and 22.8 μs (Old) and 16.7 μs (New). The RMS is higher than that predicted based on the formal errors of the estimates, which indicates there is unmodeled error.

Keywords UT1-UTC, dUT1, VGOS, Geodetic VLBI

1. NVI, Inc.
2. NASA Goddard Space Flight Center
3. MIT Haystack Observatory
4. United States Naval Observatory
5. Peraton
6. Bundesamt für Kartographie und Geodäsie
7. Technische Universität München

1 Introduction and History

In 2020 our institutions coordinated a series of Intensive VGOS sessions using different stations including various combinations of KOKEE12M, MACGO12M, GGAO12M, WESTFORD, and WETTZ13S. This was done to demonstrate the feasibility of these sessions and to gain experience in all aspects of the data flow. These initial sessions were scheduled at Goddard, correlated at Haystack, and analyzed at Goddard.

Based on the success of these sessions, we proposed a regular series of VGOS Intensives using the KOKEE12M-WETTZ13S (K2-Ws) baseline to run simultaneously with the KOKEE-WETTZELL INT01 sessions. The ultimate goal was to include the estimated UT1 from the VGOS Intensives in operational IVS products. These sessions began on January 4, 2021. Initially, these sessions ran roughly once a week but as we gained experience the cadence was increased to 5/week by the end of 2021. The schedules continued to be made and analyzed by Goddard. However, the responsibility for correlation was taken over by the Washington Correlator.

This data set is particularly interesting, because the standard INT01 series uses the co-located KOKEE-WETTZELL baseline (Kk-Wz). This allows us to directly compare the UT1 estimates from the two sets of Intensives. Initially these VGOS Intensives were scheduled similarly with the same limits on scan length as the Kk-Wz scheduled by USNO, with a minimum and maximum scan length of 40 s and 200 s. The SNR target per band was 20, somewhat higher than USNO targets of 20 and 15 for X- and S-band. In part this was done to be conservative, since we had no experience with how these sessions would perform. The K2-Ws Intensives differed from the Kk-Wz Intensives in that

we inserted three 120-s calibrator scans. Subsequently the scan length parameters were changed to 20 s and 60 s, and the SNR target reduced to 15. This was based on simulation studies which showed that this would result in an increased number of observations and better formal errors with no adverse effects. Because of the change in scheduling parameters, we divide these into two sets: K2-Ws Old and K2-Ws New.

Some considerations that went into changing the parameters is given by Baver et al. [1]. The new scheduling parameters were first used on January 31, 2022 and have been used in the subsequent K2-Ws Intensives.

In this brief note we evaluate the performance of the K2-Ws VGOS Intensives using Calc/Solve. For a related analysis using *VieVs*, see Mondal et al. [2].

We make the following comparisons which are described in more detail in the appropriate sections:

1. We compare the UT1 estimates from the simultaneous S/X and VGOS Intensive sessions. This gives us a measure of the consistency of the sessions.
2. We compare the UT1 estimates from S/X Intensives and the two VGOS series with UT1 estimates from the R1 and R4 series. This allows us to evaluate the performance of the different Intensive series.
3. We compare the UT1 estimates from S/X Intensives and the two VGOS series with an EOP series produced by JPL.

In these comparisons we take the difference in UT1 estimates and calculate the RMS as a proxy for precision. We also compare the measured RMS with the predicted values based on the formal errors. We demonstrate that there is still substantial unmodeled error.

All the VGOS Intensives were scheduled by Karen Baver of NVI using the *sked* scheduling software. Karen Baver and Sergei Bolotin were responsible for the initial analysis of the VGOS and S/X Intensives, as well as the R1 and R4 sessions, using *nuSolve*. Station support at Kokee Park for both the S/X and VGOS Intensives was provided Chris Coughlin of Peraton. Institutional and station support at Wettzell was provided by Christian Plötz and Torben Schüler of BKG and Alexander Neidhardt of TU Munich. Andrew Sargent and Phillip Haftings of USNO correlated the sessions. Pedro Elosegui, Chester Ruszczyk, and Dhiman Mondal of MIT Haystack Observatory provided technical assistance. John Gipson is responsible for the analysis in this paper.

2 Intensive Data Sets

We considered three different Intensive data sets from 2021 through 2022-6-30:

1. S/X Standard: Kk-Wz S/X Intensives scheduled by USNO. For the sake of uniformity, we exclude S/X Intensives with more than two stations, or Intensives that use other stations.
2. K2-Ws Old: Scheduled using old scheduling parameters. MinScan 40, MaxScan 200, and SNR 20.
3. K2-Ws New: Scheduled using new scheduling parameters. Minscan 20, MaxScan 60, and SNR 15.

We used the standard Goddard processing methodology for Intensives on all of three series. *nuSolve* was used to do initial data editing and ambiguity resolution. In the final analysis, where we estimate UT1 using *Solve*, the reference frame was fixed to a TRF and CRF derived from all available 24-hour S/X and VGOS sessions through 2021-12-31; the USNO finals was used for the a priori EOP; we used VMF3 for the a priori atmosphere and mapping functions, and modeled atmosphere loading. In addition to estimating a UT1 offset, we estimated wet zenith delay offsets at the Kokee and Wettzell antennas and a second order clock at Wettzell. The zenith delay offsets were constant for each session. We did not estimate gradients. The data was reweighted on a session-by-session basis by adding in a constant amount of noise to each observation in an Root Sum Square sense until $\chi^2 \sim 1$.

Figures 1 and 2 display the number of observations and the Formal Error (FE) session-by-session.

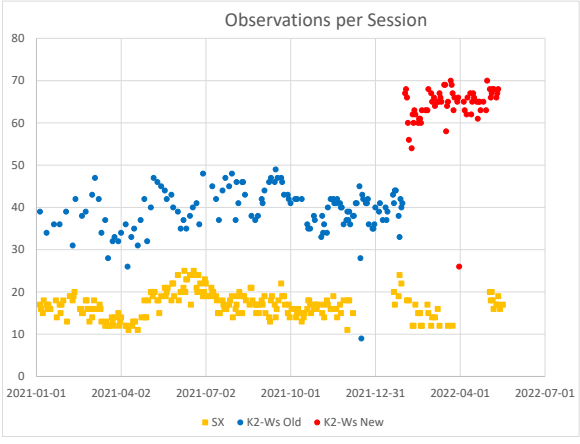

Fig. 1 Observations per session.

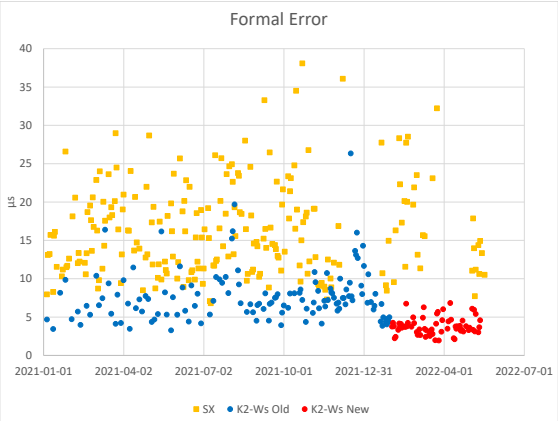

Fig. 2 Formal Errors of S/X and VGOS Intensives. Note the clear reduction in formal error with the K2-Ws New VGOS.

Table 1 summarizes some statistical characteristics of these series. In this and subsequent tables, to minimize the effect of bad data in calculating numerical results, we exclude sessions with fewer than ten observations, or a formal error greater than 40 µs. These sessions would probably not be used in operational analysis. The K2-Ws Old sessions have more than twice the number of observations as the S/X sessions, and the formal error (FE) is roughly half that of the S/X sessions. The reduction in FE is due to two factors: an increase in the number of observations, and a reduction in the uncertainty of each observation. The K2-Ws New series has roughly 60% more observations than K2-Ws Old, and the median formal errors are 33% smaller. Based on these results we would expect the K2-Ws Old series to be better than the S/X series, and the K2-Ws New series to better yet.

Table 1 Characteristics of Data Sets.

Data Set	Span	# Sess	Med # Obs	Med FE (µs)
S/X Standard	2021-01-04 to 2022-06-30	207	18	18.3
K2-Ws Old	2021-01-04 to 2022-01-28	120	40	9.5
K2-Ws New	2021-01-31 to 2022-06-30	74	65	6.4

3 Consistency between S/X and VGOS Intensives

In this section we study the consistency of the S/X and VGOS Intensives. For each day that we have both an S/X and VGOS Intensives we compute the difference between the S/X and VGOS estimates of UT1. As mentioned previously, for the S/X Intensives we only use the two station Kk-Wz Intensives. This comparison is particularly clean because of the following:

1. Since the S/X and VGOS antennas co-located, geophysical effects will be common and hence will disappear when we compute the difference.
2. Because the sessions are scheduled to run simultaneously with the same duration, there is no need to extrapolate the UT1 estimates.

Figure 3 displays the difference in UT1 estimates between the S/X and VGOS Intensives. Large gaps in the plot are due to instrumental problems at one of the stations. Since the S/X and VGOS sessions are assumed independent, the error in the estimated UT1 is uncorrelated, and hence the error in the UT1 difference is the RSS of the FE errors of each estimate. Visually there is a clear reduction in scatter for the New strategy: the agreement between S/X and VGOS is improved. Since there is no systematic change in the S/X observing, this implies that the New strategy with more observations is more accurate.

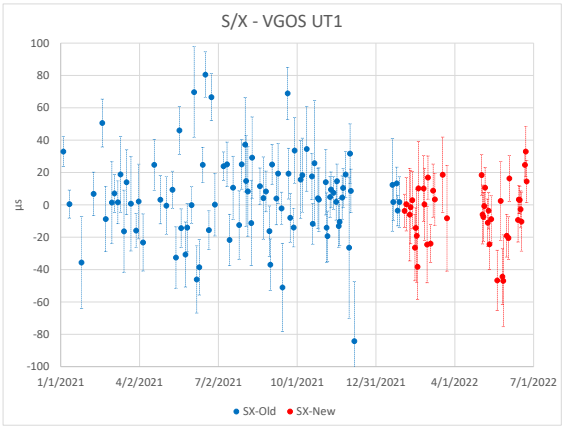

Fig. 3 Difference between S/X and VGOS UT1 estimates.

Table 2 presents the same results in tabular form. The third column computes the average difference between the two series, the fourth the RMS of the difference. The last column gives median formal error of the difference. The K2-Ws New series agrees more closely with the S/X than the K2-Ws Old series. The difference between the RMS and the median FE is a measure of

the unmodeled error. For the K2-Ws Old series the difference is much larger than for K2-Ws New.

Table 2 Difference (μs) between S/X and VGOS estimates.

Data Set	# Session	Avg. Dif.	RMS	Median FE
K2-Ws Old	108	+3.4	25.0	19.4
K2-Ws New	43	−5.3	18.7	18.2

4 Comparison with R1 and R4 Sessions

In this section we compare the UT1 estimates from the Intensives with R1 and R4 ('Rapid') sessions. The Rapid sessions observe for 24 hours, use a large network (typically 10–14 stations), and have on the order of 10,000 observations instead of the 20–60 in the Intensives. Because of this, the formal error for UT1 is much less than for the Intensives, typically ~ 2 μs. We also expect a reduction in systematic errors since some station-dependent errors will average out. Although there is some variation because of holidays and maintenance schedules, the Rapids typically start on Monday (R1) and Thursday (R4). The INT01 series observe every week day. Figure 4 displays the temporal relationship between the Intensive and Rapid schedules for the first week of 2021. The start and end of each session is indicated on the horizontal axis. The vertical axis has no meaning, and the different heights are used to distinguish the Intensive from the Rapid sessions.

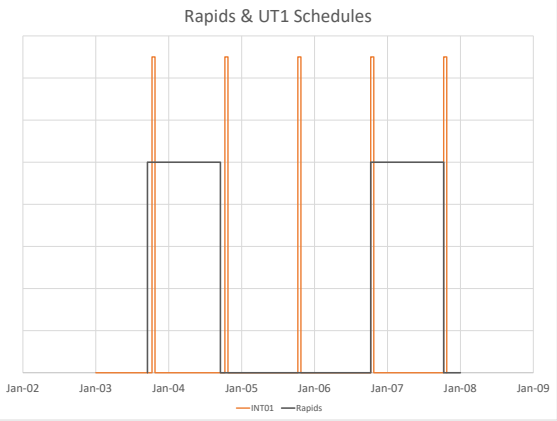

Fig. 4 Rapids and INT01 during the first week of 2021.

The comparison of the UT1 estimates is complicated by the following:

1. The Rapid networks vary from session to session.
2. The time span is different.
3. The epoch of UT1 estimate is different.

The last problem can be addressed, because, in contrast with the Intensives, the Rapids estimate both a UT1 offset and a rate. This allows us to extrapolate the UT1 estimate to the epoch of the Intensives. This extrapolation introduces additional error, both because of the uncertainty in the estimates of the offset and rate, and also because of the stochastic nature of UT1. Assuming we knew the offset and rate perfectly, the expected error in extrapolation grows like 35 μs $T^{3/2}$, where T is measured in days. To limit extrapolation error, we only consider Rapids which are within ∼0.5 days of the Intensive, which leads to an extrapolation error of ∼10 μs. As illustrated in Figure 4, this accounts for 80% of the Intensives.

Table 3 summarizes the results. The last column gives the expected FE of the difference and includes the effect of extrapolation error. Both of the VGOS series agree more closely with the Rapid series than does the S/X, and the New agrees more closely than the Old. Figure 5 presents the same data in graphical form. For clarity we offset the S/X results by 100 μs.

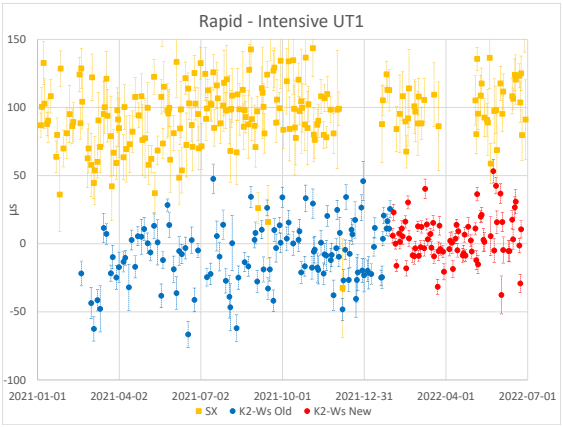

Fig. 5 Difference between Rapid and Intensive estimates of UT1. S/X results offset by 100 μs.

Table 3 Difference (μs) between Rapid and Intensive UT1.

Data Set	# Session	Avg. Dif.	RMS	Median FE
S/X	207	−4.6	25.3	22.4
K2-Ws Old	120	−7.6	22.8	15.3
K2-Ws New	74	+4.1	16.7	14.2

5 Comparison with JPL EOP series

In this section we compare the S/X and VGOS Intensives with a JPL EOP series. This is an external series that combines EOP from VLBI and GNSS, and other information such as atmospheric angular momentum. Because UT1 estimates from S/X VLBI data are one of the inputs, the JPL series is not totally independent of S/X VLBI data. It is independent of VGOS UT1 estimates. We use linear extrapolation of the JPL series to get the UT1 at the epoch of the Intensives. Since we are uncertain of how to handle the errors in the extrapolation, we do not calculate the expected formal error.

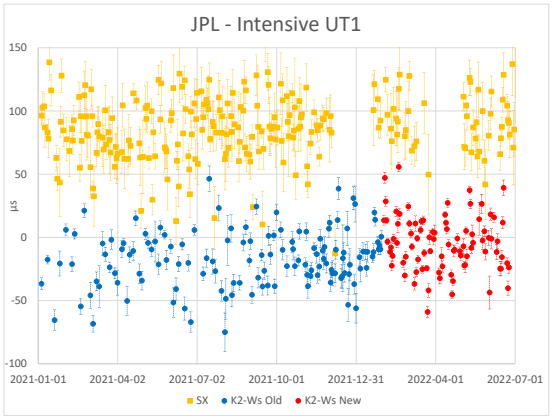

Fig. 6 Difference between JPL and Intensive estimates of UT1. S/X results offset by 100 μs

Table 4 Difference (μs) between JPL EOP and Intensive UT1.

Data Set	# Session	Avg. Dif.	RMS
S/X	248	−12.9	26.6
K2-Ws Old	134	−16.6	22.1
K2-Ws New	87	−4.5	21.6

The pattern is similar to what we have seen before. The VGOS scatter is less than the S/X scatter, and the scatter of K2-Ws New is smaller than K2-Ws Old. However the difference between the New and the Old case is not as large as previously. We attribute this to noise in the JPL time series.

6 Conclusions

In this note we have studied UT1 estimates from three different Intensive series: the standard S/X series using Kk-Wz and two VGOS series using K2-Ws. We have shown that the S/X and VGOS UT1 estimates are consistent and that the K2-Ws New agrees more closely with the S/X then the K2-Ws Old, 18.7 μs vs 25.0 μs. We see similar results when we compare the UT1 estimates from the Intensives with those from the Rapid sessions. The RMS of the differences are: S/X (25.3 μs), K2-Ws Old (22.8 μs), and K2-Ws New (16.7 μs). We also compared the S/X and VGOS estimates of UT1 with the JPL time series. The conclusions are similar to above, although the difference between the Old and New schedules is not as pronounced.

Our overall conclusion is that the K2-Ws VGOS Intensive UT1 estimates are better than the Kk-Ws S/X Intensive estimates and that the K2-Ws New series, with more scans, is substantially better. The UT1 estimates from the VGOS estimates are ready to be used in operational IVS products.

Acknowledgements

The authors would like to thank all of the individuals who are involved with geodetic VLBI infrastructure. The work by NVI, Inc. was supported under NASA contract NNG17HS00C. The work by MIT Haystack Observatory was supported by NASA contract 80GSFC20C0078.

References

1. Baver, K., Gipson, J., Lemoine, F. “The First Year of KOKEE12M-WETTZ13S VGOS Intensive Scheduling: Status and Efforts Towards Improvement”, this volume.
2. Mondal, D., Elosegui, P., Barrett, J., Corey, B., Niell, A., Ruszcyk, C., Titus, M, Gipson, J., “Quality assessement of UT1-UTC (dUT1) estimates using VGOS observations”, this volume.

The First Year of KOKEE12M-WETTZ13S VGOS Intensive Scheduling: Status and Efforts Towards Improvement

Karen Baver[1], John Gipson[1], Frank Lemoine[2]

Abstract The KOKEE12M-WETTZ13S (K2-Ws) VGOS Intensive series began on January 4, 2021. Evaluation of the first year of schedules has shown that the series is performing reasonably well, but the schedules could be improved. For example, the number of scheduled scans in a typical K2-Ws session is approximately half those of the first few MACGO12M-WETTZ13S Intensive sessions, and scheduling fewer scans negatively impacts UT1 results. Also, preliminary analysis of the K2-Ws scans' scheduled and achieved SNRs and their ratios shows examples where the achieved SNRs are either too high, indicating long scans that could have been replaced by a greater number of shorter scans, or too low, indicating a lack of robustness that could lead to scan loss. In this paper, we discuss the areas of concern and the status of efforts to make improvements in these areas.

Keywords VGOS, Intensives, scheduling

1 Introduction

The International VLBI Service for Geodesy and Astrometry (IVS) observes several series of one-hour single baseline ("Intensive") sessions that provide rapid UT1-TAI estimates. One of these series is the "V-series" (e.g., V21004), in which the WETTZ13S (Ws) and the KOKEE12M (K2) VGOS antennas observe. This series began on January 4, 2021. Scheduling of the K2-Ws series is done by the Sked program, mainly through automated scheduling. Manual scheduling is used as a supplement to insert three calibrator scans at least 15 minutes apart at times when Sked has automatically selected the target calibrator source or a source at a similar right ascension and declination, if possible. Manual scheduling is used as needed for other reasons, such as adding scans when Sked's automated mode fails.

Scheduled scan (observation) lengths are very important in an Intensive session due to the session's short duration. Scheduled scan lengths determine the number of scheduled scans and, in turn, the maximum number of achieved scans. This metric then directly affects the session's UT1 formal error, which decreases as 1 over the square root of the number of scans. With only one hour of observing time in an Intensive session, the number of potential scans in an Intensive session is limited; so it is important to keep the scheduled scans short to increase the number of scheduled scans. But scans must also continue for enough time to achieve a minimum SNR that will enable the scan to be correlated and included in the final set of a session's data. This is especially important in a one-hour session, in which the loss of a source and its scans will remove a greater percentage of the data. So the scheduled scan lengths must be balanced between being short enough to provide many scheduled scans but long enough that the scans will be successful.

Three aspects of scheduling significantly affect the scheduled scan lengths. The greatest impact comes from the values of the minimum and maximum permitted scan lengths. During 2021 these values were set to 40 seconds and 200 seconds, respectively. The values were a carryover from the S/X INT01 schedules, and they were retained in the 2020 V-series schedules,

1. NVI, Inc.
2. Goddard Space Flight Center

which included three additional antennas whose baselines sometimes needed longer scan lengths. The minimum and maximum scan lengths should have been reduced when the 2021 K2-Ws series began, but, due to an oversight, the reduction was not made. The oversight was realized during comparison of the K2-Ws series to the first MACGO12M-WETTZ13S (Mg-Ws) VGOS Intensives. The Mg-Ws series was initiated in December 2021 by NASA GSFC, Geodetic Observatory Wettzell, and ETH Zurich as a research program to test improvements to Intensive scheduling using the VieVS software and to commission a "backup" VGOS baseline for UT1 determination whenever the K2-Ws baseline might be unavailable. The first Mg-Ws sessions averaged 60 to 65 scans per hour, roughly 50% more than in the 2021 K2-Ws series. This motivated us to look for ways to increase the scan count for the K2-Ws series. The smaller K2-Ws scan counts were traced to the excessively large minimum and maximum scan lengths, and plans were quickly made to reduce the minimum and maximum scan lengths to values that would generate more scans but make sure that the scans would be strong enough to be correlated.

The other two factors that affect a scan's scheduled length are the system equivalent flux densities (SEFDs) of the antennas in the scan and the flux density (flux) of the source being observed. The SEFDS and flux used to a schedule a scan contribute to the scan's scheduled length according to the following equation [2]:

$$ScanLength = \left(\frac{SNR}{\eta \times F}\right)^2 \times \frac{SEFD_1 \times SEFD_2}{SR \times NC} \quad (1)$$

where SNR is the scan's target SNR, η is the degradation in SNR due to digital sampling multiplied by a constant that corrects approximations made during correlation, F is the flux density of the source being observed, $SEFD_1$ and $SEFD_2$ are the SEFDs of the two observing antennas, SR is the sampling (recording) rate (double the bandwidth (per channel)), and NC is the number of channels (the total number of tracks recorded (excluding fan-out)) [2]. When the schedule is observed, the scan length from Equation 1 and the actual SEFDs and fluxes at the time of the scan then provide a scan's achieved SNR according to the following inversion of the first equation [2]:

$$SNR = \frac{\eta \times F \times \sqrt{SR \times NC \times ScanLength}}{\sqrt{SEFD_1 \times SEFD_2}} \quad (2)$$

If the achieved SNR from Equation 2 is less than 7, the scan will not be correlated, reducing the session's final scan count. So, it is important to use antenna SEFDs and source fluxes during scheduling that will provide good scan lengths that during observing will generate high enough SNRs so that the scans will be correlated.

But a complicating factor is that a schedule is expected to be submitted to the IVS seven days before the schedule is observed, and the SEFDs and fluxes can change greatly during that time. Therefore, the antenna SEFDS used in the 2021 K2-Ws scheduling were calculated for each schedule based on the averages of SEFDs from Ws and K2 ready, start, and stop messages (when available). SEFD averages from the past day, week, two weeks, and month were considered. Source fluxes were updated approximately once per week, based on four to six weeks of the most recent R1 and R4 data. This provided some averaging of the source fluxes. But it should be noted that the flux information at the time of scheduling was out-of-date because it generally takes two to three weeks for a correlator to receive and correlate the data from an R1 or R4 session.

Feedback about the accuracy of the SEFDs and the fluxes used in scheduling comes from looking at the SNRs from the observed sessions and also at the ratios of the observed to the scheduled SNRs. Preliminary analysis of these metrics in the 2021 K2-WS schedules shows examples in which the ratios are either too high, indicating long scans that could have been replaced by a greater number of shorter scans, or too low, indicating a lack of robustness that could lead to scan loss. This indicates a need to look more closely at the determination of the antenna SEFDs and source fluxes for use in scheduling.

This paper discusses the areas of concern and the status of efforts to make improvements in these areas. Section 2 discusses efforts that have already been made to reduce the minimum and maximum scheduled scan lengths. These efforts are assessed by comparing six weeks of sessions scheduled with the new schedule configuration to six weeks of sessions scheduled with the original configuration. Section 3 provides a preliminary assessment of the antenna SEFDs and source fluxes used for scheduling during 2021 using all of the

2021 data. It then briefly discusses initial future plans. Section 4 presents conclusions.

2 Minimum and Maximum Scheduled Scan Lengths

In December 2021, we noticed that the number of scans in the 2021 K2-Ws sessions were approximately half those of the initial MACGO12M-WETTZ13S (Mg-Ws) sessions. We identified the cause as the fact that the Mg-Ws schedules had short scans that lasted mostly 30 to 48 seconds with a few 120 second scans of calibrator sources. In contrast, the K2-Ws schedules had scans ranging from 40 to 200 seconds. Steps were quickly taken to run simulations to determine new, reduced minimum and maximum scan lengths that would generate more scans in the K2-Ws schedules but not weaken the scans enough that they would not be correlated. Several combinations of shorter minimum and maximum scan lengths were tested. A 20/60 second minimum/maximum scan length combination was promising, but the combination generated some short schedules in Sked's automated mode due to a reduction of the list of sources that could be observed. Reducing the target SNRs from 20 to 15 did not help. But the configuration with 20/60 second minimum/maximum scan lengths and target SNRs of 15 provided the most scans and the best UT1 formal errors as discussed in [1]. Short schedules can be finished manually; so, on January 31, 2022, testing of the new schedule configuration began in the daily K2-Ws sessions.

The remainder of this section evaluates the effects of the new scheduling configuration. Source availability has a large impact on one-hour sessions. So, this section compares the first six weeks of the new-style sessions (January 31 to March 15 in 2022) to old-style sessions from the corresponding six weeks in 2021 to ensure that the two session sets observed the same areas of the sky. Due to a change in scheduling frequency, there are 12 old-style sessions and 29 new-style sessions.

Figure 1 (left) shows that the new schedule configuration increases the number of scheduled scans. The scan counts range between 60 and 70, which is closer to the Mg-Ws scan counts. But Figure 1 (right) shows that the new configuration also increases the average number of scheduled scans per source. This increase could have a mixed effect. On the one hand, having more scans per source decreases robustness because if a source is observed more times, its scans will make up a greater percentage of the schedule, and therefore the loss of the source will have a greater impact on the session. On the other hand, there is some concern within the IVS that if a source is observed only once in a session, the source's scan might not connect well within the session's solution. The GSFC Analysis Center has not investigated this possibility, but we consider it as a minor factor when generating the K2-Ws schedules. Figure 2 shows that the new schedule configuration reduces the average number of sources observed once in a session from eight in the old-style sessions to 3.5. On the other hand, the new-style sessions have more sources with four scans per session, significantly more sources with five or six scans per session, and a few sources with seven scans per session, in contrast to the old-style sessions, which have no sources with seven scans. So the new configuration has a mixed effect on the number of scans per source in a session, and this effect should be studied further.

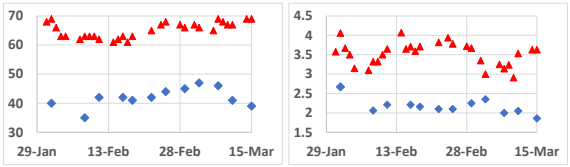

Fig. 1 Old-style (2021) sessions (blue diamonds) vs. new-style (2022) sessions (red triangles): number of scheduled scans (left) and number of scheduled scans per source (right).

Finally, observation loss as measured by the individual scans' observed SNRs and the sessions' average observed-to-scheduled SNR ratios are considered. In its first six weeks, the new schedule configuration did not hurt the individual observed SNRs. In fact, the SNRs slightly improved. Only 0.2% (3) of the new-style schedules' scans failed, in contrast to 1.2% (5) of the scans made with the old schedule configuration during the six weeks in 2021. The SNR ratios averaged over a session also show no problems. There is no obvious difference between the old-style and new-style average ratios, as shown in Figure 3, and the average of each session type's average ratios is 1.1.

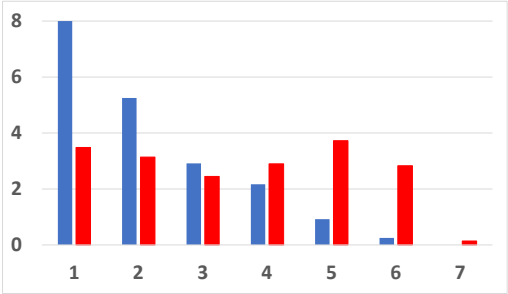

Fig. 2 Average number of sources per session (y-axis) that were scheduled N times in the session (x-axis). E.g., on average, 0.9 sources were scheduled five times in the old-style sessions, and 3.7 sources were scheduled five times in the new-style sessions. Old-style (2021) values are represented by the blue (left) bar in each pair, and new-style (2022) values are represented by the red (right) bar in each pair.

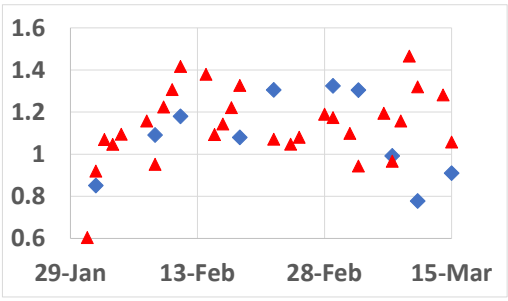

Fig. 3 Observed-to-scheduled SNR ratios averaged over all scans in a session: old-style (2021) (blue diamonds) vs. new-style (2022) (red triangles).

3 Antenna SEFDs and Source Fluxes

The observed SNRs and the ratio of the observed SNRs to the scheduled SNRs provide feedback about the antenna SEFDs and source fluxes used for scheduling. The observed SNRs from the entire set of 2021 (old-style) K2-Ws sessions indicate that the antenna SEFDs and the source fluxes used for scheduling were reasonable. 4,816 (97.8%) of the 4,925 scans in 2021 had an SNR of at least 7 and were successfully correlated. Where scans failed, the failures seemed to be generally unrelated to the schedule. Only four (0.1%) of the scans seemed to be related to the schedule (specifically to the source fluxes used), although we admit that the causes of the failures of 16 (0.3%) of the scans are not known.

But the averages of each session's observed-to-scheduled SNR ratios indicate some problems. Figure 4 plots the ratios of the observed-to-scheduled SNRs (averaged over all scans in a session) for all of the sessions in 2021. Lower averages show an overestimation of antenna and source strength (that is, an underestimation of SEFDs and an overestimation of fluxes) that could lead to scan loss. Higher averages show an underestimation of strength (an overestimation of SEFDs and an underestimation of fluxes) that kept additional scans from being scheduled. We think that it is best to have SNR ratios between 0.9 and 1.1. It should be noted that the ratios have been cut in half because observed SNRs are based on four bands while scheduled SNRs are based on one band.

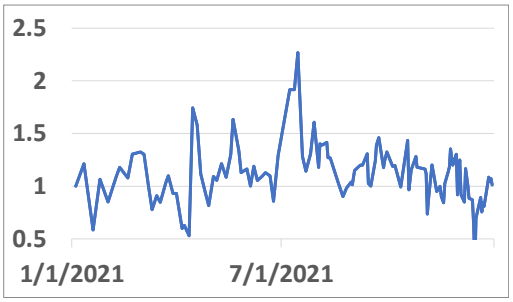

Fig. 4 Ratios of the observed-to-scheduled SNRs (averaged over all scans in a session) for all sessions in 2021.

Antenna SEFDs have a large impact on scheduling because they affect every scan and because the scheduled scan lengths vary as the product of each scan's two SEFDs, as shown in Equation 1 above. Unfortunately, SEFD measurements are currently only available through an antenna's ready, start, and stop messages, and antenna operators do not always have time to measure their antennas' SEFDs. Also, sometimes strong sources are not visible at an antenna, and the operators cannot take an SEFD measurement. During 2021, SEFD measurements were only available for both the WETTZ13S antenna and the KOKEE12M antenna on 79 of the 182 days on which a schedule was written and/or observed. On 73 of the days, SEFDs were only available for one antenna, and on 30 days, SEFDS were not available for either antenna. So it is currently hard to determine the SEFDs at the time of scheduling or to use the SEFDs at the time of observing to assess the accuracy of the SEFDs used during

scheduling. The GSFC Analysis Center is discussing ways to obtain SEFD measurements more frequently.

The source fluxes only affect individual sources; so it will be easier to determine their quality and, if necessary, correct how they are generated once the systematic impacts of the antenna SEFDs are known and, as necessary, corrected. But preliminary analysis yields two insights. Figure 5 plots the observed-to-scheduled SNR ratios of the 4,925 successful scans in 2021 vs. the declinations of the sources observed in the scans. First, the SNR ratios greater than 4 come from underestimated fluxes of two sources in two catalog versions. This indicates that the worst underestimations came from a transient condition. Second, all 130 scans with source declinations less than or equal to 17.16° have SNR ratios less than 1. This behavior is not seen in the S/X KOKEE-WETTZELL Intensive sessions, so it might be due to the small data set. But this behavior should be watched to see if it continues.

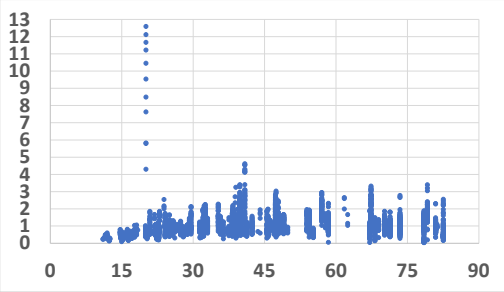

Fig. 5 Ratios of the individual scans' observed-to-scheduled SNRs in the 2021 sessions vs. the declinations in degrees of the sources that were observed in the scans.

4 Conclusions

Scheduled scan lengths are important in scheduling one-hour Intensive sessions. Three factors that contribute to the scan lengths are the minimum and maximum scan lengths allowed during scheduling and the antenna SEFDs and the source fluxes used during scheduling.

The 2021 K2-Ws schedules had minimum and maximum scan lengths that were too high (40 and 200 seconds, respectively). Starting with the January 31, 2022 schedule, the minimum and maximum scan lengths were reduced to 20 and 60 seconds, respectively, and the target SNRs were reduced from 20 to 15 to avoid excluding too many sources due to the reduction of the maximum permitted scan length. The new schedule configuration has improved the number of scheduled scans in a session without harming the session's observed SNRs or the average ratios of the session's observed-to-scheduled SNRs. But more scans are now scheduled per source during a session, which can have a mixed effect on the session.

The 2021 K2-Ws scans generally achieved good SNRs after correlation. But the observed-to-scheduled SNR ratios averaged over a session are sometimes too low or too high, indicating a need to look more closely at the antenna SEFDs and the source fluxes used during scheduling. Individual scans' observed to scheduled SNR ratios with values greater than 4 come from only two source fluxes in two catalogs, indicating a transient issue. Antenna SEFDs are not always available; so determination of the SEFDs to be used during scheduling, as well as the assessment of the SEFDs used during scheduling, can be difficult. The GSFC Analysis Center is discussing ways to improve SEFD determination for scheduling. Once this is accomplished, it will be easier to assess the quality of the source flux values generated by the GSFC Analysis Center and to determine how to improve them, if necessary.

Acknowledgments

We thank the KOKEE12M and WETTZ13S operators for providing SEFD measurements whenever possible. We also thank Andy Sargent (Washington Correlator) for providing information about the correlation of the K2-Ws sessions.

References

1. J. Gipson, K. Baver, S. Bolotin, F. Lemoine, P. Elosegui, C. Ruszczyk, D. Mondal, A. Sargent, P. Haftings, S. Hardin, C. Coughlin, C. Plötz, A. Neidhardt, T. Schüler, "Evaluation of the KOKEE12M-WETTZ13S VGOS Intensives with Calc/Solve", this volume.
2. J. Gipson, Sked manual, 2018-Oct-12 version, pages 180 and 181.

Comparison of Simultaneous VGOS and Legacy VLBI Sessions

Matthias Glomsda[1], Manuela Seitz[1], Detlef Angermann[1]

Abstract The VLBI Global Observing System (VGOS) represents the next-generation VLBI system, which consists of a growing network of small and fast-slewing radio antennas performing broadband observations. It has been developed to increase the accuracy and precision of VLBI measurements and the geodetic parameters that can be obtained from analyzing the latter. Ultimately, VGOS is expected to approach the accuracy goals of the Global Geodetic Observing System (GGOS) of the International Association of Geodesy (IAG), which are 1 mm for a terrestrial reference frame (TRF) and 1 mm/decade for its long-term stability. Next to the enlarged bandwidth, these goals shall be achieved by the greater number of observations per unit time with VGOS and the resulting higher temporal resolution for the tropospheric parameters. After first experimental VGOS observations in 2014 and initial global measurement efforts during the Continuous VLBI Campaign in 2017 (CONT17), an operational series of bi-weekly VGOS sessions (denoted by 'VG') has become available in the meantime. Starting in early 2019, this series now has a length of about three years, and the current number of sessions is about twice as large as the number of sessions used for the ITRS 2020 realization. Furthermore, the 'VG' sessions have been scheduled to accompany the legacy VLBI rapid turnaround sessions. Hence, these data provide the opportunity to juxtapose the results of the new VGOS broadband to the legacy S/X-band observations, even though the VGOS antenna networks are rather small and still suffer from an unsatisfactory global distribution. In this presentation, we will compare the parameters (i.e., station coordinates, Earth Orientation Parameters, and radio source positions) that we computed with our DGFI Orbit and Geodetic parameter estimation Software (DOGS) for all available 'VG' sessions between 2019 and 2021 to their respective counterparts in the rapid turnaround sessions. In particular, we will investigate the implied local ties between co-located VGOS and legacy antennas, as well as potential systematic offsets in radio source positions observed at the different frequencies. This might provide valuable information on how to combine the new VGOS with the legacy S/X network.

Keywords VGOS, VLBI analysis, EOP

1 Introduction

The next generation of Very Long Baseline Interferometry (VLBI) is represented by the VLBI Global Observing System (VGOS; Petrachenko et al., 2009). By the end of 2021, it consisted of nine operational radio antennas, which simultaneously observe four bands in a frequency range between 3 and 11 GHz instead of the distinct legacy S (about 2 GHz) and X (about 8 GHz) bands. These VGOS antennas are usually smaller, stiffer, and faster-slewing than the legacy antennas. This makes them less sensitive to gravitational deformation, and it allows for more observations per unit time. With the latter, a higher resolution of parameters describing the atmospheric refraction of the radio signal becomes possible. Furthermore, the VLBI observable, i.e., the signal delay between each of the two antennas forming a baseline,

1. Deutsches Geodätisches Forschungsinstitut der Technischen Universität München

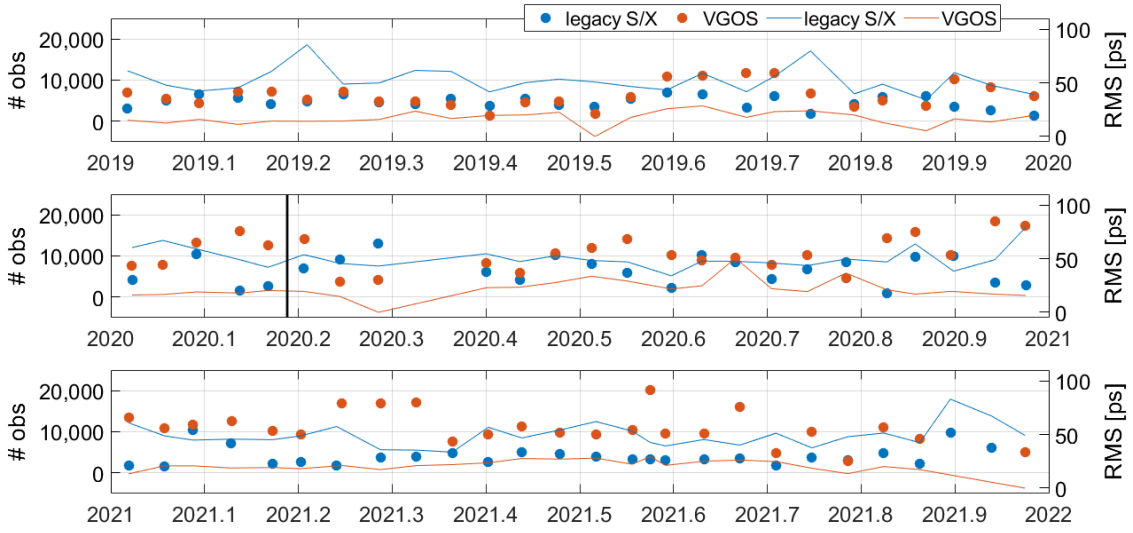

Fig. 1 Number of observations (dots, left Y-axis) and RMS of post-fit residuals (lines, right Y-axis) for both legacy S/X (blue) and simultaneous VGOS (red) sessions between 2019 and 2021. The black vertical line represents the approximate barrier between sessions used (before) and not used (after) for the ITRF2020.

is supposed to be more accurate and more precise with VGOS.

The history of VGOS observations is rather short yet. However, between 2019 and 2021, about 75 VGOS sessions have been performed and correlated (i.e., twice a month), which finally enables the analysis of a firm set of data. For comparison, these sessions have each been scheduled to overlap with a legacy rapid turnaround session. The starting epochs of both the VGOS and the simultaneous legacy sessions are shown on the X-axis of Figure 1. On the left Y-axis, the number of observations per session is depicted. The right Y-axis represents the root mean square (RMS) error of the observation residuals in a least-squares fit of geodetic parameters to these observations (compare below). From the figure, one can see that, for the VGOS sessions, the number of observations is generally larger, although the number of participating stations per session is at most nine for VGOS, while there are about 10–12 stations involved in the legacy rapid turnaround sessions. As mentioned before, this is a result of the faster-slewing VGOS antennas. Since the latter also provide more precise observations, the RMS of post-fit residuals is generally smaller (average across sessions: 18.8 ps) than for the legacy observations (50.3 ps).

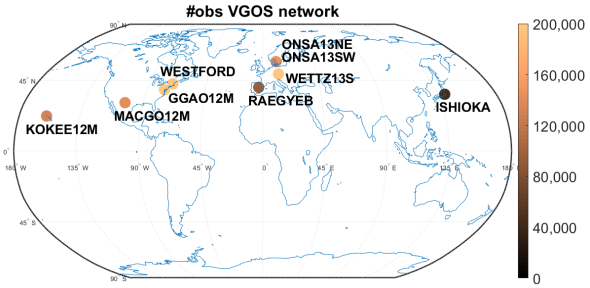

Fig. 2 The operational VGOS station network at the end of 2021. The color code indicates the number of observations per station across all sessions between 2019 and 2021.

The operational VGOS station network as of December 2021 is shown in Figure 2. It is restricted to the Northern hemisphere.

2 Analysis Setup

To compare their geodetic results, we analyzed the simultaneous VGOS and legacy S/X sessions with our DGFI Orbit and Geodetic parameter estimation Software (DOGS; Gerstl et al., 2000). For each session, we estimated constant station positions at midnight, the

full set of Earth orientation parameters (EOP, terrestrial pole offsets and drifts, UT1-UTC and LOD, and celestial pole offsets) at the session's mid epoch, and constant radio source coordinates at epoch 2015.0 (the reference epoch of the Third International Celestial Reference Frame, ICRF3; Charlot et al., 2020). As auxiliary parameters, we also included piece-wise linear tropospheric zenith and gradient delays, as well as clock correction terms (quadratic plus piece-wise linear offsets). The corresponding observation and normal equations were set up with DOGS-RI (Radio Interferometry), while we added the datum constraints and inverted the final normal matrix with DOGS-CS (Combination & Solution).

The geophysical models used are basically the same as those applied in our DGFI-TUM Analysis Center solution 'dgf2020a' for the International VLBI Service for Geodesy and Astrometry (IVS). For the VGOS sessions, however, we increased the resolution for the tropospheric zenith (1h to 0.25h) and gradient delays (6h to 1h) to exploit the larger number of observations per unit time. Although the VGOS observations refer to broadband, and radio source positions potentially change with frequency (e.g., Petrachenko et al., 2009), we had to apply the same a priori source coordinates as for the legacy observations (ICRF3 S/X), because there is no broadband frame yet.

The major difference w.r.t. 'dgf2020a' is the a priori station positions. Because the previous International Terrestrial Reference Frame (ITRF2014; Altamimi et al., 2016) does not contain the coordinates of the VGOS stations, we used a preliminary realization of the International Terrestrial Reference System (ITRS) 2020 for VLBI stations that we computed at DGFI-TUM. It will be called 'DTRF2020VP' in the following, and it is based on the official IVS input to the ITRS 2020 realization (Hellmers et al., 2021). DTRF2020VP combines the VGOS and legacy networks by EOP, local ties, mixed-mode sessions, ONTIE sessions (Varenius et al., 2021), three antennas that participated in both networks (ISHIOKA, RAEGYEB, and WESTFORD), and the velocities of co-located VGOS and legacy antennas.

Finally, the geodetic datum was constrained as follows: there are a no-net-rotation (NNR) condition w.r.t. the defining sources of ICRF3 S/X, as well as both no-net-translation (NNT) and NNR conditions w.r.t. stable stations in DTRF2020VP. In particular, the VGOS stations ISHIOKA, MACGO12M, and WETTZ13S are not among the datum stations, as they had large transformation residuals.

3 Comparison of Geodetic Parameters

3.1 EOP w.r.t. IERS 14 C04

The common benchmark for estimated EOP is the 14 C04 series (Bizouard et al., 2019) of the International Earth Rotation and Reference Systems Service (IERS). We interpolated the estimated EOP from the simultaneous VGOS and legacy sessions to common epochs and computed the differences w.r.t. the C04 series for each observation mode. Table 1 lists the weighted means as well as the weighted root-mean-square (WRMS) values of these differences.

Table 1 Statistics of the differences between the IERS 14 C04 series and the EOP estimated for the simultaneous VGOS and legacy sessions between 2019 and 2021.

EOP	unit	wmean legacy	wmean VGOS	WRMS legacy	WRMS VGOS
x-pol	[µas]	−3.2	−192.9	107.4	266.1
x-pol rate	[µas/d]	18.3	9.0	215.1	297.8
y-pol	[µas]	−36.8	−112.4	115.5	255.7
y-pol rate	[µas/d]	−14.7	116.3	222.7	285.0
UT1-UTC	[µs]	9.0	5.1	10.9	13.8
LOD	[µs/d]	2.1	6.4	16.2	14.6
DXCIP	[µas]	−8.7	−1.7	109.7	454.1
DYCIP	[µas]	−9.1	104.2	109.6	443.9

We obtain significant offsets between C04 and the VGOS EOP for polar motion (except for the x-pol rate) and the Y component of the celestial pole offsets. The size of these offsets depends on the choice of VGOS datum stations, i.e., it changes if all VGOS stations are used for the NNT and NNR conditions (not shown here). Possible reasons are the Northern hemisphere bias of the VGOS station network or residual rotations between the VGOS and legacy networks in our a priori TRF, DTRF2020VP. The WRMS values for the terrestrial and celestial pole parameters are also significantly larger for the VGOS sessions. For UT1-UTC and its reverse-signed rate (length-of-day, LOD) on the other hand, there are neither offsets nor increased WRMS values, which is in line with the East-West distribution of VGOS baselines.

3.2 Formal Errors

Because the measurement precision of VGOS is better than for the legacy S/X observations, one would expect the formal errors of the estimated parameters to decrease for the VGOS sessions. While this is the case for the station coordinates (see Figure 3), we could not confirm this for the EOP or the source coordinates yet. This may again be related to the imperfect VGOS station distribution.

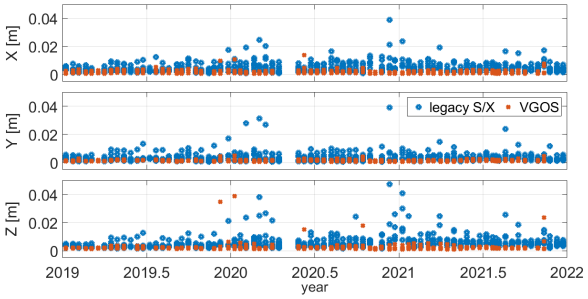

Fig. 3 Formal errors (Y-axis) for all station coordinates in the simultaneous VGOS (red) and legacy (blue) sessions. The X-axis refers to the parameter epoch, which is the same for all coordinates within the same session.

3.3 Co-location Velocities

There are four sites with co-located VGOS and legacy antennas: Kokee Park, Hawaii; Onsala, Sweden (with two VGOS antennas); Wettzell, Germany; and Yebes, Spain. In the DTRF2020VP, the a priori velocities of the co-located antennas are basically equal, because they have been constrained accordingly. However, if we estimate the velocities from the a posteriori positions for each distinct antenna, we sometimes obtain quite different velocities for the co-located VGOS and legacy antennas. For example, Figure 4 shows the X-coordinates of the co-located stations KOKEE12M (VGOS) and KOKEE (legacy S/X). In this case, the fitted a posteriori velocities differ by almost 7 mm/yr.

Generally, a discrepancy can be expected, because the used time series are rather short (three years), and there are different numbers of sessions related to the VGOS and the legacy antennas. For KOKEE12M, however, there is another effect: there is a bunch of

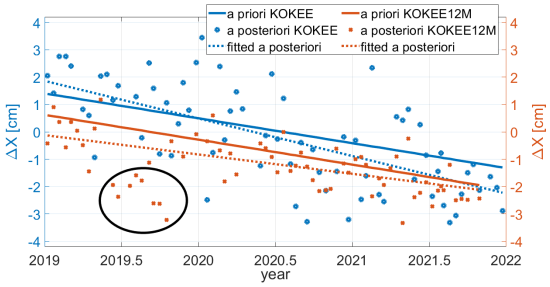

Fig. 4 A priori and estimated x-coordinates of the co-located antennas KOKEE (legacy, blue, $-5,543,837.84$ m $+ \Delta X$) and KOKEE12M (VGOS, red, $-5,543,831.75$ m $+ \Delta X$) at Kokee Park. In the VGOS sessions within the black ellipse, ISHIOKA was not part of the VGOS network.

VGOS sessions (indicated by the black ellipse) with quite different a posteriori coordinates compared to the other ones. In these sessions, ISHIOKA was not part of the VGOS station network. From Figure 2, we learn that the network volume is much smaller without the remote station ISHIOKA, and the sky coverage at KOKEE12M is much worse, too. If we exclude these inferior sessions from the velocity fit, the fitted value for KOKEE12M's x-coordinate only differs by 0.13 mm/yr from its (DTRF2020VP) a priori value.

3.4 Local Ties

We computed 'cross-session local ties' for all epochs t with both a VGOS and a legacy S/X session containing a co-location site, and we compared them to the official local ties LT_i:

$$\left[S_i^{VGOS}(t) - S_i^{legacy}(t)\right] - LT_i\,, \qquad (1)$$

with S_i $(i = x,y,z)$ representing the estimated station coordinates per session. This measure is quite noisy, because we compute the differences between two random variables. However, systematic differences might indicate discrepancies between the co-located antennas or problems with the official local ties. In Figure 5, the cross-session local ties of Equation (1) have been transformed to the local North, East, and Up coordinate system, and we actually observe some systematic behavior: the cross-session local ties are almost exclusively larger than the official local ties for both the Up direction at Yebes and the East direction at Kokee Park.

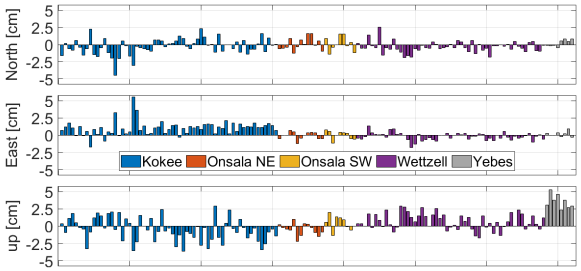

Fig. 5 The 'cross-session local ties' of Equation (1) at the co-location sites rotated from the Cartesian to the local coordinate system.

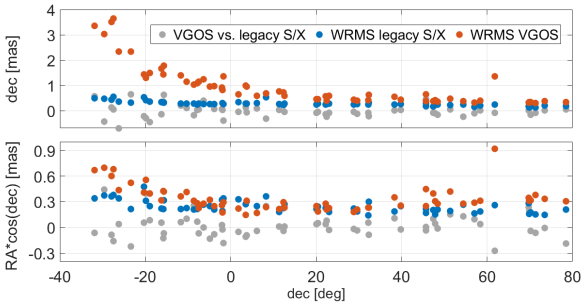

Fig. 6 The differences (grey) between the constant declinations (top) and right ascensions (bottom) as fitted for each common source (X-axis) from VGOS and legacy S/X sessions. For comparison, also the WRMS values for both VGOS (red) and legacy (blue) sessions are given, representing the scatter of estimated source coordinates around their fitted coordinate.

For Wettzell, the distribution of these ties does not look completely random, either.

4 Source Coordinates

VGOS measurements cover a broader frequency range than the legacy S/X observations. Because source positions are frequency and time dependent, we might expect to estimate systematically different source coordinates from the two observation modes. There are 203 sources which have been observed in both VGOS and legacy S/X sessions. Out of these, 58 are contained in at least 20 sessions for both modes. We fitted constant coordinates at epoch 2015.0 to the estimated source coordinates of the VGOS and legacy S/X sessions, respectively. Figure 6 shows that the fitted coordinates actually deviate, but the differences are generally smaller than the scatter of the estimated coordinates itself (which is generally larger for VGOS, especially for negative declinations due to missing Southern hemisphere stations). Hence, we are not able to distinguish VGOS and legacy S/X source positions yet.

5 Conclusion

The geodetic parameters estimated from VGOS observations are already promising. However, there still are discrepancies w.r.t. the legacy S/X observations, which might mainly be attributable to the inferior station distribution of the VGOS network. Hence, the expected improvements in terms of accuracy and precision are not fully realized yet.

References

Altamimi Z., Rebischung P., Metivier L., and Collilieux X. (2016): ITRF2014: A new release of the International Terrestrial Reference Frame modeling nonlinear station motions. *J. Geophys. Res. Solid Earth*, Vol. 121 (8), pp. 6109-6131.

Bizouard C., Lambert S., Gattano C., Becker O., and Richard J.Y. (2019): The IERS EOP 14C04 solution for Earth orientation parameters consistent with ITRF 2014. *J. Geod.*, Vol. 93, pp. 621-633.

Charlot P., Jacobs C.S., et al. (2020): The third realization of the International Celestial Reference Frame by very long baseline interferometry. *A&A*, 644.

Gerstl M., Kelm R., Müller H., and Ehrnsperger W. (2000): DOGS-CS – Kombination und Lösung großer Gleichungssysteme. *Int. Rep.*, DGFI-TUM.

Hellmers H., Modiri S., Bachmann S., Thaller D., Bloßfeld M., Seitz M., Gipson J. (2021): Combined IVS contribution to the ITRF2020. *Proceedings of the 25th EVGA Working Meeting*, pp. 61–65.

Petrachenko B., Niell A., et al. (2009): Design aspects of the VLBI2010 system. Progress report of the VLBI2010 committee. *NASA/TM-2009-214180*.

Varenius E., Haas R., and Nilsson T. (2021): Short-baseline interferometry local-tie experiments at the Onsala Space Observatory. *J. Geod.*, Vol. 95 (54).

The Current and Future Performance of VGOS

Tobias Nilsson[1], Rüdiger Haas[2], Eskil Varenius[2]

Abstract In this work we investigate the performance of the 24-hour VGOS sessions observed in 2019–2021. We look at the station positions and the Earth Orientation parameters (EOP), and we compare them with the results from the legacy S/X VLBI sessions as well as with simulations. We find that the station position repeatabilities obtained from the VGOS sessions are significantly better than what is obtained from the legacy S/X VLBI sessions. However, the EOP from the VGOS sessions are less accurate than those from the legacy S/X sessions, a consequence of the low number and poor global coverage of the currently operational VGOS stations.

1 Introduction

The VLBI Global Observing System (VGOS) is the new geodetic VLBI system currently being deployed [1]. By using small, fast-moving antennas and broadband observations, the aim is to obtain millimeter-level accuracy for the station coordinates, which is about one order of magnitude better than what is achieved by the current legacy (S/X) geodetic VLBI system. Since the beginning of 2020, operational 24-hour VGOS sessions are observed every second week (every week since the beginning of 2022). Additionally, there were VGOS test sessions observed every second week in 2019. In 2021, there were nine stations (at eight different locations) participating in the VGOS sessions, see Figure 1.

1. Lantmäteriet - The Swedish mapping, cadastral and land registration authorityt, Gävle, Sweden
2. Chalmers University of Technology, Göteborg, Sweden

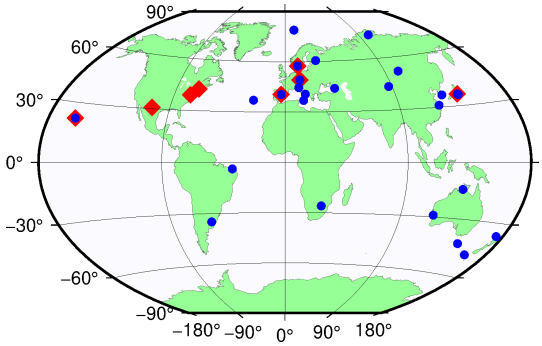

Fig. 1 The VGOS (red diamonds) and legacy (blue dots) networks as of 2021.

With three years of VGOS observations now being available, it is interesting to evaluate the results. In this work we look at the obtained precision of the estimated station coordinates and Earth Orientation parameters (EOP).

2 Data Analysis

The data were analyzed with the ASCOT software [2]. The modeling basically followed the guidelines for the IVS analysis for ITRF2020. The coordinates of the ICRF3 [3] defining radio sources were fixed to their a priori values, the other radio source coordinates were estimated. Offsets were estimated for each EOP, as well as rates for polar motion and UT1-UTC. The tropospheric zenith total delays were estimated with a 20-minute temporal resolution and the tropospheric gradients with a 2-hour temporal resolution. Two solutions were calculated: one where the station coordinates were estimated and one where the station coor-

dinates were fixed to the results of a global solution. The latter solution were used for the EOP results, in order to get as good EOP as possible.

We analyzed all 24-hour VGOS sessions that were observed in 2019–2021, a total of 76 sessions. For comparison, we also analyzed the standard legacy S/X sessions (IVS-R1 and IVS-R4) observed simultaneously with the VGOS sessions. These were analyzed using the same parameterization as for the VGOS sessions.

3 Simulations

To get a feeling for what accuracy we could expect from the current VGOS sessions, simulations were performed. We made simulations for all the VGOS sessions in 2019–2021, based on their real schedules. The simulations were done using the method presented in [4]. Station dependent refractivity structure constants, C_n^2, were estimated using GNSS data. The clocks were assumed to have an Allan standard deviation of 10^{-14} @ 50 min, and the observation noise was assumed to be white with a standard deviation of 5 ps. For each session, we performed 1,000 simulation runs in order to obtain good statistics.

The station position repeatabilities obtained from the simulations are presented in Figure 2. The repeatability for the vertical coordinate is about 3 mm, while it is 1 mm for the horizontal components. For the stations KOKEE12M (Hawaii, USA) and ISHIOKA (Japan) the repeatabilities for the horizontal components are a bit worse, around 2 mm. This is probably because those stations are located far from other stations; thus it is not possible to achieve a good sky coverage.

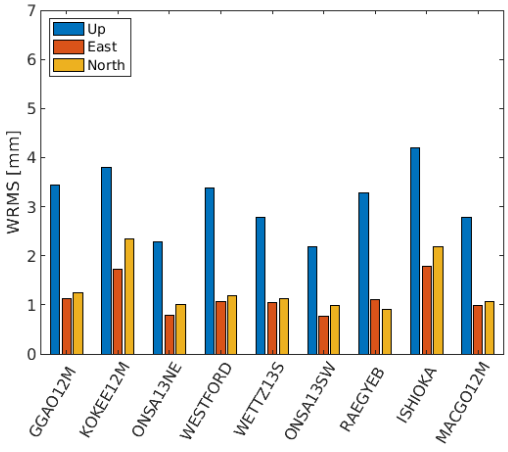

Fig. 2 Station position repeatability obtained from simulations of the VGOS sessions.

4 Results

Figure 3 shows the station position repeatbilities obtained from the analysis of the VGOS sessions 2019–2021. In general, the repeatability is about 3–4 mm for

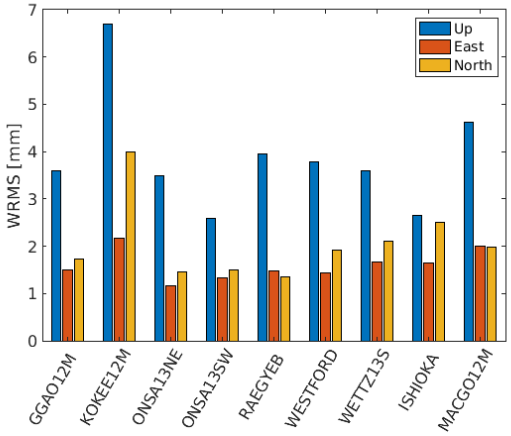

Fig. 3 Station position repeatability of VGOS stations obtained from analysis of the VGOS sessions.

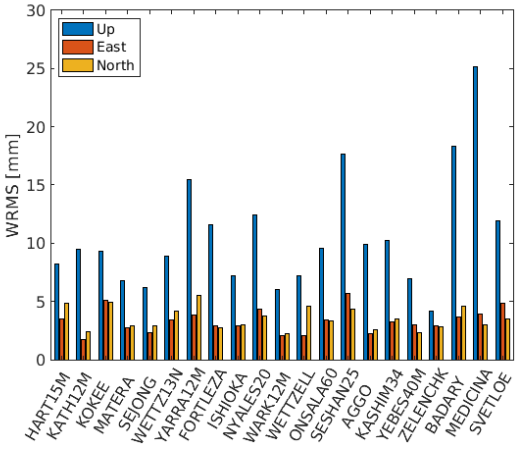

Fig. 4 Station position repeatability obtained for legacy S/X VLBI stations obtained from analysis of IVS-R1 and R4 sessions.

the vertical component and 1.5–2 mm for the horizontal components, i.e., similar or slightly worse than what was obtained in the simulations. The exception is the station KOKEE12M, where the repeatability is about 7 mm for the vertical coordinate. For comparison, the station position repeatabilities for the legacy stations, obtained from analysis of the IVS-R1 and IVS-R4 sessions 2019–2021, are shown in Figure 4. We can clearly see that these are about three times worse than what was obtained from the VGOS sessions.

To evaluate the EOP, we compared the EOP estimates from the VGOS sessions, as well as the IVS-R1 and IVS-R4 legacy sessions, with the EOP estimates from GNSS. The GNSS solution was used for the CODE IGS Analysis Center final solution [5]. Figure 5 shows the Weighted Mean (WM) and Weighted Root-Mean-Square (WRMS) differences between the EOP estimated by VLBI (VGOS or S/X legacy) and GNSS. We can see that the WRMS differences are smaller for legacy than for VGOS, especially for x-pole and the polar motion rates. The reason for this is that

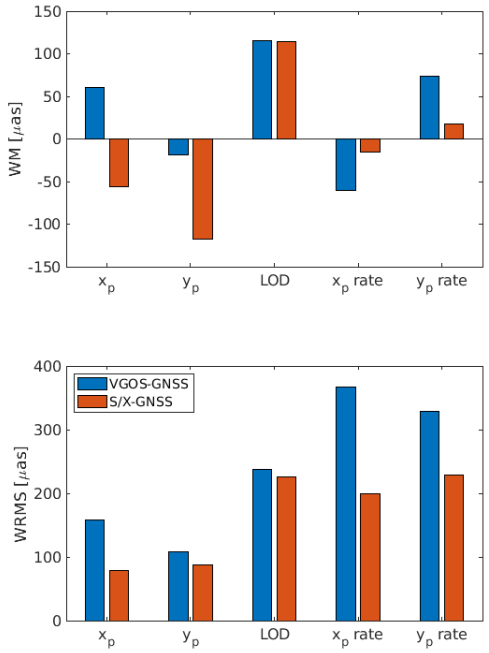

Fig. 5 Weighted Mean (WM) and Weighted Root-Mean-Square (WRMS) difference between the EOP estimated from VLBI (VGOS and legacy S/X) and from GNSS.

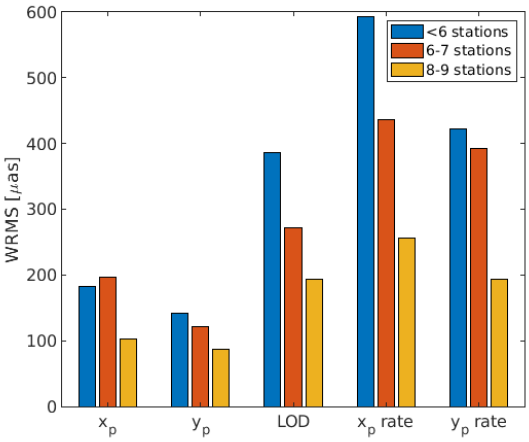

Fig. 6 Weighted Root-Mean-Square (WRMS) difference between the EOP estimated from VLBI and from GNSS for VGOS sessions with different number of stations; less than 6 (blue), 6–7 (red), and 8–9 (yellow).

the current VGOS network is not optimal for estimation of EOP, with all the stations being located in the northern hemisphere. The legacy S/X stations have a better global distribution (see Figure 1).

Another reason could be that the current VGOS network contains a relatively small number of stations. In most VGOS sessions only 6–7 stations participated, in some even less, while the networks used in the legacy S/X IVS-R1 and IVS-R4 sessions currently often contain ten or more stations. To investigate the impact of the number of stations, we divided the VGOS stations into three groups depending on the number of participating stations: five or less (17 Sessions), six or seven stations (44 sessions), and eight or nine stations (16 sessions). The WRMS differences relative to GNSS of the EOP were calculated for each group. The results are shown in Figure 6. It can clearly be seen that the WRMS differences get smaller as the number of stations increase. For the group with eight or nine stations, the WRMS values are similar to what is obtained with the legacy S/X VLBI system.

5 Future VGOS Performance

The current VGOS sessions are not yet living up to the full potential of the VGOS system. First, there are presently only a few stations operational and their

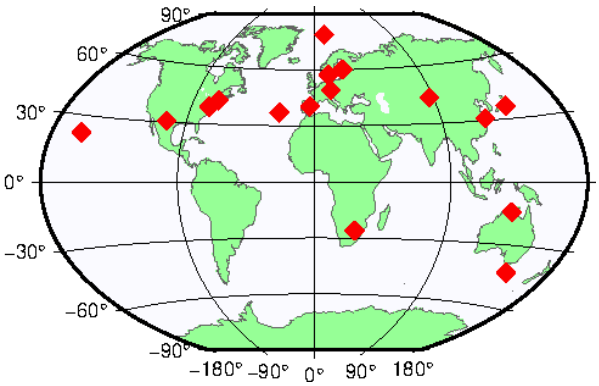

Fig. 7 A potential future network of VGOS stations.

global distribution is far from optimal. Secondly, the current VGOS schedules are generated with a conservative minimum scan length of 30 s, while it is in principle possible to have scan lengths as short as 5–10 s with VGOS. Thus, there is room for improvements in the future. To investigate how this can affect the results, we performed simulations using a 17-station network including all stations likely to become operational in the next couple of years, see Figure 7. A schedule for this network was generated using the VieSched++ software [6], without imposing any constraints on the minimum scan length. Simulated observations were generated for this schedule and analyzed with the ASCOT software.

The station position repeatabilities obtained from these simulations can be seen in Figure 8. We can see

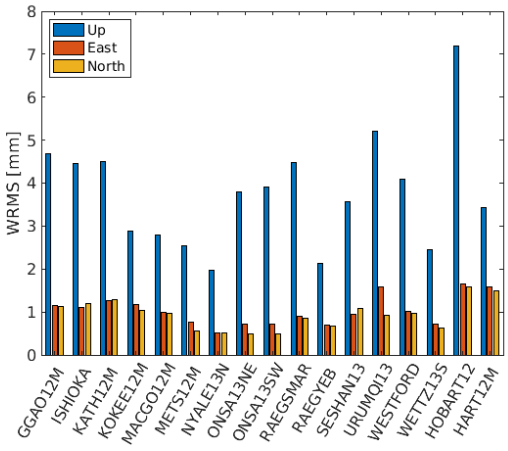

Fig. 8 Station position repeatabilities obtained from the simulations using the VGOS network in Figure 7.

that the performance is varying between the stations. The best stations achieve about 1.5 mm in the vertical and 0.5 mm in the horizontal directions. Others have repeatabilities of around 3 mm in the vertical and 1 mm in the horizontal directions, i.e., similar to what was achieved with the current VGOS network (see Section 3). The worst performing station is HOBART12, Australia. This station had the lowest number of observations in the generated schedule (7,423 observations, compared to the average of 17,012 observations). The reason for this is probably because the station location is a bit remote, as well as the antenna is of the slower VGOS type (6°/s in azimuth, while the fast VGOS antennas do 12°/s).

6 Discussion and Conclusions

The station coordinate repeatabilities obtained with VGOS is clearly better then what is achieved with the legacy VLBI system (in the IVS-R1 and IVS-R4 sessions). However, the goal of 1 mm accuracy is not yet reached. One reason for this is the conservative scheduling of the VGOS sessions, with minimum scan length of 30 s. Another reason could be the few number of stations and their poor global distribution, making it difficult to get a good sky coverage at some stations. As more stations join in and the scheduling allows for shorter scans, we can expect improvements.

The station KOKEE12M gives significantly worse repeatabilities than the other stations. This could indicate some kind of problem at this station. However, part of the reason for the poor performance is probably because it has a remote location in the current VGOS network, thus it is not possible to generate a schedule with a good sky coverage for this station. This is particularly the case when ISHIOKA is not participating, what is still the case for many VGOS sessions.

For the EOP, the current VGOS sessions generally obtain worse results than the legacy ones. The reason for this is the low number of VGOS stations and, most importantly, the poor global station distribution. All stations are located at latitudes between 22.1°N (KOKEE12M) and 57.4°N (ONSA13NE and ONSA13SW in Sweden). For EOP, it is known that a good global distribution of stations is crucial. Hence, as more VGOS stations join in, especially ones in the

southern hemisphere, we can expect the EOP results to improve significantly.

References

1. B. Petrachenko, A. Niell, D. Behrend, B. Corey, J. Böhm, P. Charlot, A. Collioud, J. Gipson, R. Haas, T. Hobiger, Y. Koyama, D. MacMillan, Z. Malkin, T. Nilsson, A. Pany, G. Tuccari, A. Whitney, and J. Wresnik. "Design aspects of the VLBI2010 system". In D. Behrend and K. Baver (eds.), International VLBI Service for Gerodesy and Astrometry 2008 Annual Report, NASA Technical Publications, NASA/TP2009-214183, 2009.
2. T. Artz, S. Halsig, A. Iddink, and A. Nothnagel, "ivg::ASCOT: Development of a New VLBI Software Package", In D. Behrend, and K. D. Baver, and K. L. Armstrong, editors, IVS 2016 General Meeting Proceedings "New Horizons with VGOS", NASA/CP-2016-219016, pp. 217–221, 2016.
3. P. Charlot, C. S. Jacobs, D. Gordon, S. Lambert, A. de Witt, J. Böhm, A. L. Fey, R. Heinkelmann, E. Skurikhina, O. Titov, E. F. Arias, S. Bolotin, G. Bourda, C. Ma, Z. Malkin, A. Nothnagel, D. Mayer, D. S. MacMillan, T. Nilsson, and R. Gaume, "The third realization of the International Celestial Reference Frame by very long baseline interferometry." A&A, vol. 644, A159, 2020. doi:10.1051/0004-6361/202038368
4. T. Nilsson and R. Haas, "Impact of atmospheric turbulence on geodetic very long baseline interferometry", J. Geophys. Res., vol. 115, B03407, 2010, doi:10.1029/2009JB006579
5. R. Dach, S. Schaer, D. Arnold, M. Kalarus, L. Prange, P. Stebler, A. Villiger, and A. Jaeggi. "CODE final product series for the IGS", Published by Astronomical Institute, University of Bern, 2020, URL:http://www.aiub.unibe.ch/download/CODE; doi:10.7892/boris.75876.4.
6. M. Schartner and J. Böhm. "VieSched++: A New VLBI Scheduling Software for Geodesy and Astrometry", Publ. Astr. Soc. Pacific, 131:084501, 2019, doi:10.1088/1538-3873/ab1820

Analysis of VGOS Sessions: Evaluation of Performance with Different Software

Esther Azcue[1], Víctor Puente[1], Mariana Moreira[2], Elena Martínez-Sánchez[3]

Abstract VGOS (VLBI Global Observing System) is the new generation of the VLBI system. It has been developed since 2005, and it is based on the so-called broadband delay that uses four or more frequency bands. High data rate observations are taken by fast-slewing antennas, smaller than those used in the current legacy S/X infrastructure. These improvements in instrumentation are aimed at obtaining more accurate geodetic products. In order to test the analysis of these new data, the historical VGOS sessions have been analyzed with different software. Difficulties in the current processing and similarities with the S/X generation processing are studied. Results in terms of the accuracy in EOP (Earth Orientation Parameter) estimation and coordinate repeatability are also discussed in this contribution.

Keywords Analysis, Geodesy, GGOS, VGOS, VLBI

1 Introduction

The Global Geodetic Observing System (GGOS) is the contribution of Geodesy to the scientific and non-scientific community providing geodetic observations, data, and products for monitoring the Earth system and global change research. Among these products are the reference frames required for all location-dependent observations. These frames are defined using several Space-Geodetic techniques, among them VLBI, GNSS, SLR, and DORIS.

With modern instrumentation and analytical techniques, Geodesy is now capable of detecting time variations ranging from large and secular scales to very small and transient deformations with increasing spatial and temporal resolution, high accuracy, and decreasing latency. An example of this modernization is the new generation VLBI system VGOS (VLBI Global Observing System, [8]). It has been developed since 2005, and it is based on the so-called broadband delay that uses four or more frequency bands. High data rate observations are taken by fast-slewing antennas, smaller than those used in the current legacy S/X infrastructure.

In order to test the analysis of these new data, the historical VGOS sessions were analyzed with different software. Difficulties in the current processing and similarities with the S/X generation processing are studied. Results in terms of the accuracy in EOP (Earth Orientation Parameter) estimation and coordinate repeatability are also discussed in this contribution.

2 The RAEGE Project

The co-location of the different space geodetic techniques is key in the definition of reference systems, as they allow the integration of the individual networks of each technique into a single system. Additionally, they provide an idea of the quality and precision of the systems themselves, thanks to the validation of the results between techniques. This is realized by worldwide dis-

1. National Geographic Institute of Spain, Madrid, Spain
2. Estação RAEGE de Santa Maria, Associação RAEGE Açores, Santa Maria - Azores, Portugal — Atlantic International Research Centre, Terceira – Azores, Portugal
3. Yebes Observatory, National Geographic Institute of Spain, Yebes, Spain

tributed Fundamental Space Geodetic Stations, some of which are GGOS Core Sites.

RAEGE (Atlantic Network of Geodynamic and Space Stations) is a project resulting from the cooperation between the National Geographic Institute of Spain (IGN) and the Government of Azores. It is a unique project at a geodetic and geodynamic level. It is devoted to the combination of geodetic techniques in four stations: two in Spain (Yebes and Gran Canaria) and two in Azores (Flores and Santa Maria). They will be Fundamental Space Geodetic Stations, being classified as GGOS core sites.

The RAEGE project focuses not only on the instrumentation and on operating the observing and the stations but also on developing analysis capabilities that allow RAEGE observatories to explode the geodetic observations. A VLBI analysis group, in the frame of RAEGE, was established. The group consists of collaborators from the IGN and the observatories of Yebes and Santa Maria. Among the objectives of this group are the promotion of the VLBI analysis activities in the RAEGE project, expansion of its research activities, obtaining opportunities to participate in other international projects and/or interact with other groups, and testing and improving the capacity of processing VGOS data. Several research activities are currently being developed by the RAEGE Data Analysis Group; among them are multi-technique analysis with special focus on VGOS data processing and GNSS, station performance and statistics, and the study of the gravitational deformation of the antennas.

3 Analysis of VGOS Sessions and Test Cases

Two software sets are used in the analysis group for VLBI analysis: VieVS software, [5], from the Technical University of Vienna and Where, [10], from the Norwegian Mapping Authority. The use of different software strengthens the group skills and allows the comparison and validation of results. Beyond the routine processing of the IGN as an IVS Analysis Center (AC) and works carried out in the processing of R1/R4 sessions, CONT campaigns and Intensive sessions, [2] [14], the group is starting into the processing of VGOS data. The goal is testing the capabilities for this new type of data and identifying the differences and best setting for its optimal processing.

The main differences found between VGOS and legacy analysis are the selection of the reference coordinates and velocities and the outlier removal criterion. The selection of the reference coordinates and velocities is important because some of these stations have not enough history for defining reliable velocities. In some sessions very few stations participate, and datum definition is limited. Each software avoids this difficulty in different ways: VieVS uses its self coordinates and velocities, VieTRF, and Where fixes the coordinates due to the lack of reference stations for imposing the datum. Moreover in VGOS sessions there are more observations, and maybe more outliers can be removed due to quality parameters than in legacy sessions. For testing this, an additional test case, being strict with the removal of outliers, in processing with VieVS is considered. Hence different test cases are distinguished to evaluate the influence of these assumptions on the final estimated parameters. Test cases are shown in Table 1.

Table 1 Test case configuration.

Solution	Software	CRD ref	Vel ref	Outlier removal
RAEG #1	VieVS	VieTRF	VieTRF	Standard
RAEG #2	VieVS	VieTRF	VieTRF	Strict
RAEG #3	VieVS	VieTRF	GNSS ITRF14	Standard
RAEG #4	Where	Fixed to a priori values		Strict
RAEG #5	Where	VieTRF	VieTRF	Strict
RAEG #6	Where	VieTRF	GNSS ITRF14	Strict

The use of nearby GNSS stations' velocities is considered in test cases 3 and 6 to test if there are significant differences with the use of these velocities. There are some differences between GNSS velocities (using the ITRF2014 as reference, [1]) and the ones used in VLBI analysis that can reach the mm level per year (Table 2). All VGOS stations analyzed are co-located with a GNSS station that has a long data history (at least more than the VGOS antenna). Moreover most of these GNSS stations have participated in the ITRF2014, except for the ISHI GNSS station close to the ISHIOKA VGOS antenna, and reliable velocities are known. Due to proximity, if the GNSS station is stable and there is no deformation due to monument use, its velocity represents also the VLBI antenna velocity.

The performance of each software for processing VGOS sessions has been evaluated. Seventy-six VGOS sessions published from January 2019 to December

Table 2 VGOS antenna list and co-located GNSS antennas with GNSS vel (ITRF14) – VLBI vel (VieTRF) differences in X, Y, and Z coordinates in mm/yr.

VLBI antenna	GNSS antenna	X diff	Y diff	Z diff
WESTFORD	WES2	0.1	−0.2	0.0
WETTZ13S	WTZR	0.5	−0.1	0.3
GGAO12M	GODZ	−0.5	1.1	−0.7
KOKEE12M	KOKB	0.2	0.2	0.1
MACGO12M	MDO1	0.2	−0.2	−1.7
ONSA13NE	ONSA	0.1	−0.1	0.0
ONSA13SW	ONSA	0.1	−0.1	0.0
RAEGYEB	YEBE	−0.4	0.0	−0.5
ISHIOKA	ISHI	–	–	–

2021 were analyzed. Three were not processed by any software. Some problems in the Where software for processing sessions with an extremely small number of stations were observed. The number of observations processed in the VGOS sessions is notably larger than in R1/R4 sessions during the time span. A different criterion for removing outliers was tested, being less or more lax removing observations.

As the volume of the network correlates with the expected EOP accuracy, the theoretical volume of each network was computed for R1/R4 sessions and VGOS. The volume was computed as the volume of tetrahedrons defined by a Delaunay triangulation, following [11], for VGOS networks and also for R1/R4 session networks. The mean values of network volumes are 230.62 Mm^3 for R1/R4 sessions and 13.38 Mm^3 for VGOS sessions. There is an important difference in the order of magnitude between both networks that would be fixed with the addition of more VGOS stations and a better geographical distribution.

4 Results

4.1 Earth Orientation Parameters

EOPs from different test cases with respect to the EOP 14 C04 series (IAU2000, [3]) are analyzed in terms of Weighted Mean (WM) and Weighted Root Mean Square (WRMS) errors. The solutions from additional Analysis Centers that processed VGOS sessions have been included to compare the results. These Analysis Centers are BKG, GFZ, and OPA. These solutions rely on the standard VLBI analysis configuration; in particular, the IERS Conventions 2010 [9], the VMF1 mapping function [4] and ITRF2014 [1] and ICRF3. The only point to be highlighted is that VieVS does not estimate derivatives of the EOP because it uses a parametrization based on continuous piecewise linear offsets. The software used and the number of sessions processed are shown in Table 3.

Table 3 Processing compared and software used.

Solution	Software	# sessions
RAEG #1	VieVS	73
RAEG #2	VieVS	73
RAEG #3	VieVS	73
RAEG #4	Where	69
RAEG #5	Where	69
RAEG #6	Where	69
BKG	Calc/Solve	76
GFZ	Port	76
OPA	Calc/Solve	76

Results are shown in Table 6. Differences in the WM of RAEGE processing were detected with respect to other Analysis Centers. In the polar motion components, the WM is significantly smaller than the results of the other ACs, except for the test case RAEG #4 (fixing the station coordinates and not estimating them). Adopting a relaxed or strict criterion for removing outliers has not significantly affected the results. The use of GNSS velocities produces variations in EOPs (most notably in pole coordinates with tens of micro arc seconds in some cases).

4.2 Site Coordinate Repeatabilities

Site coordinate repeatabilities in mm were computed. Results are shown in Table 4. As expected, the solution fixing coordinates (grey in the table) have almost zero repeatabilities, where the non zero values of WESTFORD, RAEGYEB, and ISHIOKA are due to taking those stations' coordinates and velocities from vtrf2017d, while the rest of the stations are fixed to their static a priori coordinates. A similar order of magnitude with both software sets was obtained. Comparing the three VieVS tests, there are no significant variations in the results. Comparing the Where processing, slight differences in the GNSS solution are appreciated.

Table 4 Mean site coordinate repeatabilities in mm. N, E, U components.

Solution	# coord estimated	Global repeatabilities in mm N	E	U
RAEG #1	469	13.63	21.3	5.03
RAEG #2	471	13.53	21.31	4.9
RAEG #3	471	13.7	22.25	4.74
RAEG #4	453	4.22	6.5	1.11
RAEG #5	453	14.83	23.23	6.96
RAEG #6	453	15.84	24.04	8.16

Table 5 VLBI vs. GNSS troposphere ZTD.

VLBI	GNSS	Δ(G−V) height (m)	Δ(G−V) trop. tie (mm)	ZTD diff (m) Mean	STD
WESTFORD	WES2	−1.8	−0.6	+3.2	70.1
WETT13S	471	−6.5	−1.9	+1.7	10.0
GGAO12M	471	−4.0	−1.3	−1.9	17.7
KOKEE12M	453	−1.1	−0.3	−3.3	13.2
MACGO12M	453	114.5	+28.1	−1.7	14.4
ONSA13NE	453	−6.6	−2.1	+0.9	11.6

4.3 Troposphere Parameters

VLBI estimation of the troposphere zenith total delay with respect to a reference GNSS solution in co-located antennas was analyzed. VLBI ZTD were extracted from the VieVS standard processing, which were estimated using a sampling interval of 30 minutes. The GNSS solution was retrieved from the Center for Orbit Determination in Europe (CODE) products, [6]. In this solution, troposphere delays are estimated every two hours using double differences in a globally distributed network. For the correction of the troposphere tie due to the height difference between the co-located antennas, meteorological data derived from the GPT3 model [7] over the period 2019–2022 were used, and then a mean value of the troposphere tie for this period was computed. For the computation of the height difference, the eccentricity of the GNSS antenna was also considered. The list of stations analyzed is shown in Table 5, together with the height difference between the VLBI and the GNSS antennas and the troposphere tie. The ZTD differences in terms of mean and standard deviation are also shown in Table 5. Values of a few millimeters for the mean of the differences and values larger than 10 mm for the standard deviation were obtained. These values are significantly larger than those obtained in other studies for R1/R4 sessions, [14], with values around 7 mm in the standard deviation. Large outliers in the VLBI solution at Westford, degrading significantly the standard deviation of the differences, were also found.

5 Conclusions

We have seen that the main differences between R1/R4 and VGOS analysis are the selection of reference coordinates and velocities and the possibility of being more strict or lax in the outlier removal. Evaluating the performance of the software in VGOS processing, we have been able to process 96% of the published sessions successfully with VieVS and 90% with the Where software, finding some problems in sessions with very few stations. Moreover a much smaller volume of the VGOS network than the R1/R4 network was noted. In the future, more VGOS stations and a better geographical distribution could fix this difference.

The EOP analysis shows that in comparison with other AC solutions of VGOS processing published in the IVS, significantly smaller differences with respect to IERS C04 EOP have been achieved in the RAEGE processing, with the exception of the test case without site coordinate estimation. To adopt a lax or strict outlier removal criterion has not affected significantly the solution (the X component of the polar motion (PM) is the most sensitive). The use of GNSS velocities, as a priori data, produces significant variations in the WM of the EOP: larger variations in the X component of the PM were observed. Differences with respect to IERS seem to be minimized in the X component of the PM and enlarged in the Y component, but the results are not conclusive enough.

The coordinate repeatability analysis shows that in VieVS, the use of different a priori coordinates plus velocities or a different outlier removal criterion does not affect significantly the coordinates' repeatabilities. In Where, the a priori coordinates and velocities define the estimation or non-estimation of the coordinates during the processing. The use of GNSS velocities affects the results (maximum differences of $\sim$1.2 mm in the UP component and being the worst repeatabilities in all components). A similar order of magnitude with both software sets was obtained.

The troposphere analysis shows that the mean and the STD of the ZTD differences are significantly larger than in the R1/R4 sessions.

Table 6 Weighted Mean (WM) and Weighted Root Mean Square (WRMS) differences between solutions and the IERS long term EOP, EOP 14 C04 (IAU2000A).

Solution	XPO (μas)		YPO (μas)		UTC (μs)		NUTX (μas)		NUTY (μas)		XPOR (μas)		YPOR (μas)		LOD (μs)	
	WM	WRMS	WM	WRMS	WM	WRMS	WM	WRMS	WM	WRMS	WM	WRMS	WM	WRMS	WM	WRMS
RAEG #1	-102.78	599.46	57.82	579.26	-24.49	291.95	-11.30	321.24	-19.41	242.73						
RAEG #2	-128.10	607.96	54.27	575.63	-24.40	290.70	-1.65	253.66	-17.24	234.80						
RAEG #3	4.15	613.19	-267.62	554.07	-27.92	289.93	-18.82	319.21	-21.05	235.78						
RAEG #4	-4896.71	3173.60	-3399.11	1803.25	204.24	247.61	18.41	2318.72	-385.63	2017.64	168.35	2311.04	600.79	1738.84	13.58	101.40
RAEG #5	-92.39	584.73	-115.50	550.90	30.21	221.98	-15.50	358.38	-229.47	520.14	-227.07	1096.35	399.22	1270.89	-4.81	71.97
RAEG #6	-38.42	633.76	-128.46	536.93	36.35	224.04	-14.19	358.69	-229.37	520.31	-225.49	1095.43	399.08	1271.01	-4.81	71.98
BKG	1672.01	674.30	-1728.70	616.76	92.08	318.356	-13805.01	27290.20	-5973.76	19645.68	-233.03	1208.72	91.05	1286.22	-2.54	73.32
GFZ	-1568.96	2020.78	-803.26	545.27	-29.98	383.59	-8.49	328.92	-79.95	340.84	71.29	1290.35	-151.80	1030.35	-7.79	74.93
OPA	-461.98	7541.69	26392.77	28751.17	366.79	696.98	-8948.15	21523.83	-3527.34	15945.37	-221.17	1288.60	386.97	1399.537	5.2	63.47

References

1. Altamimi Z., Rebischung P., Metivier L., Collilieux X. ITRF2014: A new release of the International Terrestrial Reference Frame modeling nonlinear station motions. Journal of Geophysical Research: Solid Earth https://doi.org/10.1002/2016JB013098
2. Azcue E. et al. Initial VLBI Data Analyses at the National Geographic Institute of Spain. IVS 2018 General Meeting Proceedings, pp. 233–236.
3. Bizouard C., Lambert S., Gattano C. et al. (2019) The IERS EOP 14 C04 solution for Earth orientation parameters consistent with ITRF 2014., In J. Geod 93(5):621-633, https://doi.org/10.1007/s00190-018-1186-3
4. Böhm, J., Werl, B., Schuh, H. (2006) Troposphere mapping functions for GPS and very long baseline interferometry from European Centre for medium-range weather forecasts operational analysis data. J Geophys Res 111(B02):406.https://doi.org/10.1029/2005JB003629.
5. Böhm J., Böhm S., Boisits J., Girdiuk A., Gruber J., Hellerschmied A., Krásná H., Landskron D., Madzak M., Mayer D., McCallum J., McCallum L., Schartner M., Teke K. Vienna VLBI and Satellite Software (VieVS) for Geodesy and Astrometry. Astronomical Society of the Pacific, Vol. 130(986), 044503 (2018). doi: 10.1088/1538-3873/aaa22b
6. Rolf, D., Schaer, S., Arnold, D., Kalarus, M. S., Prange, L., Stebler, P., Villiger, A., Jäggi, A. (2020). CODE final product series for the IGS. By Astronomical Institute, University of Bern. URL: http://www.aiub.unibe.ch/download/CODE; DOI: 10.7892/boris.75876.4.
7. Landskron D., Böhm J. VMF3/GPT3: Refined discrete and empirical troposphere mapping functions. J. Geod. 2017;92:349–360. doi: 10.1007/s00190-017-1066-2
8. Hase, H., Behrend, D., Ma, C., Petrachenko, B., Schuh, H., Whitney, A. The Emerging VGOS Network of the IVS. In Proceedings of the IVS 2012 General Meeting, Madrid, Spain, 4–9 March 2012; pp. 8–12.
9. Petit, G., Luzum, B. Conventions IERS (2010) (eds) IERS TechnicalNote 36. Verlag des Bundesamts für Kartographie und Geodäsie, Frankfurt.
10. Kirkvik A-S., Hjelle G.A., Dahnn M., Fausk I., Mysen E. Where - A new software for geodetic analysis. 23th EVGA Working Meeting and 18th IVS Analysis Workshop, 2017.
11. Malkin Z. On comparison of the Earth orientation parameters obtained from different VLBI networks and observing programs. J Geod 83, 547–556 (2009). doi:10.1007/s00190-008-0265-2
12. Nothnagel A., Artz T., Behrend D., Malkin Z. International VLBI Service for Geodesy and Astrometry – Delivering high-quality products and embarking on observations of the next generation, Journal of Geodesy, Vol. 91(7), pp. 711–721, (2017).
13. Poutanen M., Rózsa S. The Geodesist's Handbook 2020. J Geod 94, 109 (2020). https://doi.org/10.1007/s00190-020-01434-z
14. Puente V, Azcue E, Gomez-Espada Y, Garcia-Espada S. Comparison of common VLBI and GNSS estimates in CONT17 campaign. J Geod 95, 120 (2021). doi:10.1007/s00190-021-01565-x

Determining Favorable Locations for VGOS Establishment in India

Sujata Dhar[1,2], Susanne Glaser[1], Robert Heinkelmann[1], Harald Schuh[1,3], Nagarajan Balasubramanian[2], Onkar Dikshit[2]

Abstract To support the ambitious goals of the Global Geodetic Observing System (GGOS), more antennas are required to achieve the uniform global distribution of the VLBI network. Many countries are joining the VLBI Global Observing System (VGOS) network with their proposed stations. India is one such country that is planning to establish this state-of-the-art technology for national and global needs. Thus, extensive simulation studies were performed on 42 potential locations to assess the performance of different regions of India. Optimized scheduling, Monte-Carlo simulations and analysis were carried out to examine the impact on the estimated geodetic parameters from the addition of an Indian VGOS antenna to the reference network. As the performance from the simulation study depends on the considered reference network, four different reference networks are considered for this assessment. The simulation assumes ideal situations, but in reality the VGOS observations depend on the practical conditions on site. Thus, environmental variables, such as extreme weather events, that might affect the performance of VGOS are also incorporated with a weighted scoring model for investigating the performance of different regions in India. This comprehensive study will help to indicate the favorable locations in India with high performance potential for VGOS.

Keywords VGOS, India, scheduling, simulations, environmental variables, favorable locations

1. GFZ German Research Centre for Geosciences, Potsdam, Germany
2. Indian Institute of Technology Kanpur, Uttar Pradesh, India
3. Technische Universität Berlin, Berlin, Germany

1 Introduction

Very Long Baseline Interferometry (VLBI) actively contributes to deriving the International Terrestrial Reference Frame (ITRF), and the International Celestial Reference Frame (ICRF) is solely derived from it. Apart from that, it's the only technique to determine the complete set of Earth Orientation Parameters (EOP) that are used for the transformation between the terrestrial and celestial reference frames. VLBI with its indispensable accuracy will support most demanding commercial, military, and scientific applications of a country. Thus, India will benefit enormously by establishing VLBI, specially the space applications sector. VLBI will help to serve the national scientific community well by creating opportunities for global collaboration and by developing strong economic and scientific spheres. Co-location of VLBI with the other existing space geodetic techniques in India, especially the CORS network, will strengthen the link between the national frame and the ITRF.

Thus, investigating the optimal performance of VGOS in different parts of India was significant for a comprehensive understanding of the region. The effect of an added antenna on the precision of geodetic parameters was examined from the simulation study. Different locations experience different environmental conditions that may impact the ideal operation of VLBI assumed in the simulation study. Also, maintaining the long history of VLBI data provided by these locations is essential for reference frame stability, and hence, the vulnerability of the considered locations from different regions of India was also incorporated along with the latter. This practical and thorough analysis of VGOS performance was used to determine favorable

locations for the establishment of an antenna in the Indian subcontinent.

2 Methodology

In this study, the reference network for the simulation is a global network of VGOS stations which are either currently operative or are working on the installation of a VGOS signal chain, as depicted in the status of the projected VGOS network of IVS. To this, an antenna was added one-by-one from the prospective VGOS locations in India, called the study locations. 42 study locations were chosen to cover the whole Indian subcontinent. The setup of the reference network and study locations is shown in Figure 1. Because the expected precision of the derived geodetic parameters from the addition of an antenna depends on the reference network geometry to which it was added, four cases of different reference network geometries were considered in the study.

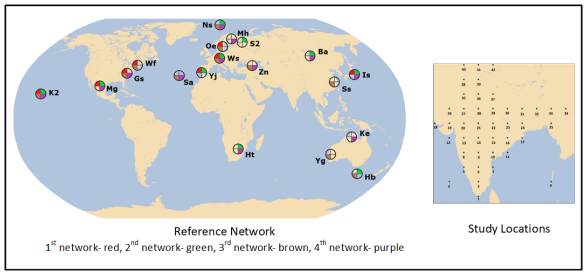

Fig. 1 Reference network stations and study locations. All VGOS stations are shown by their IVS code names, except VGOS at Seshan (Ss), Badary (Ba), Zelenchukskaya (Zn), and Svetloe (S2).

First of all, scheduling was carried out by optimized weighting of the scheduling parameters in each of the four cases. These weights were decided from the best schedule obtained from the multi-scheduling. Then, a Monte-Carlo simulation strategy was adopted with input parameters of 4 ps of white noise per baseline observation, $1\text{x}10^{-14}$s @ 50 min of Allen Standard Deviation (ASD) for modelling clock drifts, and tropospheric delay with a structure constant (Cn) value of $1.80\text{x}10^{-7}$ $\text{m}^{-1/3}$. Then, analysis of the estimated geodetic parameters was performed by comparing the precision of the estimates determined from just the reference network and that from the reference network with an added VGOS antenna at the study location. VieSched++ was used to perform scheduling, simulations, and analysis. In this study, the mean formal error was used as the measure of precision for the simulation study carried out to examine the impact on geodetic parameters from the addition of an Indian VGOS antenna. The estimated geodetic parameters studied in this study are station coordinates and EOP, i.e. X and Y coordinates of Polar Motion (PM), the difference between universal time and coordinated universal time (dUT1), and X and Y coordinates of Celestial Pole Offsets (CPO).

Now, the investigation of the impact of possible problematic environmental events on the study locations was divided into two criteria—"operationality" and vulnerability. The operationality examined those probable environmental events that decrease the quantity of observations by frequent halts in the antenna operation and degrade the observation quality by increasing the noise in some cases, while the vulnerability dealt with the probability of any natural calamity causing destruction to the VLBI establishment at the study location. To incorporate these environmental effects of the study locations, a weighted scoring model was used. These models are the summation of weighted scores of the multiple criteria that are to be taken into account, and they are a great aid for decision making. In this, the weights are assigned based on the importance of the considered criteria, and scores are based on the impact. The following weighted scoring model was considered to determine the final scores of the study locations.

$$score_{final} = (0.4 \times score_{opr}) + (0.6 \times score_{vul})$$

0.4 and 0.6 are the respective weights of operationality and vulnerability. The weight of vulnerability is set a bit more as the considered environmental variables in this criterion can potentially cause irreversible damage to VLBI. The $score_{opr}$ was determined by calculating the annual occurrence of extreme weather events such as thunderstorms, dust/sand storms, snowfall, rainfall (> 10 mm), and hail storms on the study locations using data provided by the Indian Meteorological Department (IMD). For incorporating the effect of strong winds on study locations, the wind hazard map of the IMD was assessed. The weightage of meteorological weather events and strong winds were

Table 1 Interpretation of scores used in the weighted scoring model for incorporating environmental variables.

Scores	Operationality	Vulnerability
3	Susceptible to frequent periods of inoperation and more chances of getting noisy data	High risk of complete destruction
2	Lesser halts in operation and some chances of getting noisy data	Moderate risk of destruction
1	Very-low or no halts and no chance of getting noisy data	Low chances or no risk of destruction

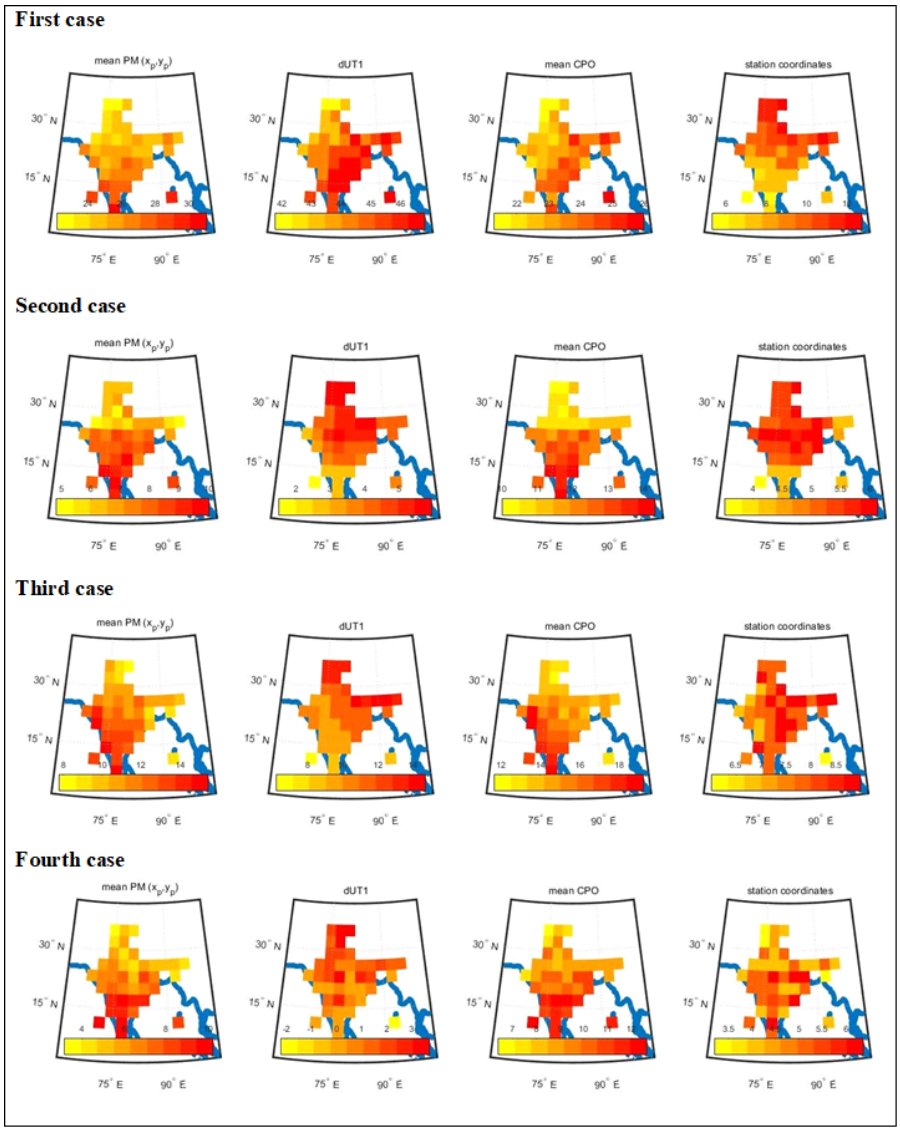

Fig. 2 The expected improvement percentage in the precision of the estimated geodetic parameters from the simulation study.

kept the same for calculating the $score_{opr}$. For calculating the $score_{vul}$, common natural calamities such as earthquakes, floods, cyclones, and landslides, were considered, and their weights were based on their occurrence probability in India, i.e. 0.05, 0.52, 0.31, and 0.11 respectively. The occurrence frequency and impact of stated extreme events on different regions were taken from the Vulnerability Atlas of India (published

by the IMD). Then, the study locations were categorized into one of the three categories of Excellent, Good, and Poor, based on the normal distribution of their $score_{final}$ values.

3 Results

The results from the simulation study are shown in Figure 2. The improvement percentage in the expected precision of a geodetic parameter is depicted by individual color blocks plotted over the study location. The geodetic parameters that are shown are the mean of PM coordinates (mean PM), dUT1, mean of CPO coordinates (mean CPO), and station coordinates. The mean PM and mean CPO were plotted, as the values of their X and Y coordinates were similar. Further, it wouldn't ever happen that just a single study location from a region would show optimal performance, but the group of study locations from a region will display homogeneous performance. Thus, the performance of different regions in India are discussed in the results of the study.

In the first case of a network with eight reference stations, the expected improvement obtained is the maximum of all the considered cases in this study. The reason for this is the relatively smaller number of reference stations in this case and, too, that they are clustered in America and Europe. This is also the reason for the southern study locations performing better than other regions in India, for the polar motion and CPO estimates of this case. For dUT1, the eastern study locations show smaller precision. This is due to the long east-west baseline extensions that can be formed with the reference stations for better sensitivity to dUT1. The expected improvement in the station coordinates is larger for the north and northeastern regions by a factor of $\sim$2.8.

Although the reference stations are distributed better in the second network than in the previous one, most of them are in the northern hemisphere above 22 degrees. Thus, the southern and central study locations show maximum improvement in PM and CPO in the second case. The northern study locations show maximum improvement in estimated dUT1 by $\sim$4 relative to other Indian regions. The estimated station coordinates don't show substantial variation in precision among the study locations, but still the northern regions perform better in the second case.

The number of reference stations in the third network is just one more than that in the second network. But, the expected improvement shown is much more than in the latter network. The reference network is almost similar in both cases, except that one of the southern hemisphere reference stations (HART15M) does not participate. This might be the reason for the increased improvement in the precision shown by the addition of an Indian antenna in this case over the previous case. The southern antennas in India show smaller precision in the polar motion and CPO estimates. The northeastern, and then northern study locations show maximum improvement in dUT1. There is no visible trend observed in the study locations for the expected precision of station coordinates, but the northern and northeastern regions perform well.

In the fourth network more reference stations, mostly situated around India, are considered in the reference network. Thus, the expected improvement is the minimum of all the cases. But the trend of southern and some central study locations portraying maximum improvement in polar motion and CPO is persistent in this case too. The VGOS antennas from the northern study locations show maximum improvement in derived dUT1. The precision of station coordinates is improved by the addition of Indian VGOS stations, but no clear regions of maxima can be observed in India for this case.

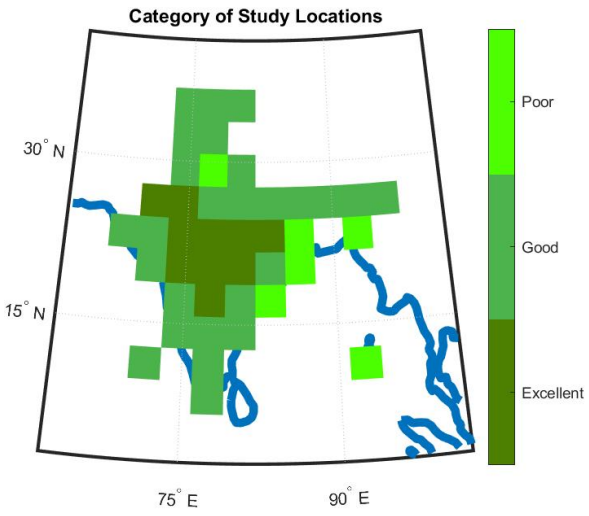

Fig. 3 The different categories assigned to study locations based on the impact of environmental variables on VGOS.

The impact of the disturbing environmental variables in the Indian locations can be visualized from Figure 3. It shows that the eastern coastal regions and some northern locations at the foothills of the Himalayas are the poor choice for VGOS, although most of the Indian locations provide suitable environmental conditions for VGOS.

4 Conclusions

The selection of favorable locations for optimal performance of VGOS is a complex problem which involves many variables. Apart from the precision of estimated geodetic paramaters, the decision for a proposed VGOS location will depend on other factors such as staff availability, vicinity to supporting supplies, geological conditions, RFI, power availability, broadband internet accessibility, funding, and other requirements. But, these factors are highly variable and difficult to quantify, and hence they were not investigated in this study. To make the expected performance of the potential locations more practical, the impact of environmental variables was investigated in this study along with the precision of geodetic parameters, such as EOP and station coordinates. The scheduling of the considered sessions was optimized to make it realistic. The examination of the four cases considered in this study interprets that the southern and central regions of India improve the polar motion and CPO estimates by a factor of 1.4 to 3.3 and 1.2 to 2 respectively, depending on the reference network geometry, while the VGOS antennas from the northern and northeastern regions show the best precision of dUT1 estimates by a factor of 1.1 to 4. The station coordinates are improved by a factor of 1.5 to 2.4, without any specific region showing the best precision in all of the cases. This makes it clear that the optimal location for a new VGOS establishment in India will depend on the geodetic parameter of interest. The study also indicates that a VGOS antenna established at any Indian location will improve most of the geodetic parameter estimates, and the difference in the precision does not vary substantially among the study locations. Further, the impact of the examined environmental factors depicts that the Indian plateau regions are excellent choices for optimal VGOS performance.

Acknowledgements

I acknowledge the DAAD: German Academic Exchange Service for providing financial support enabling my research stay in GFZ Potsdam, Germany.

References

1. Schuh, H., & Schmitz-Hubsch, H. (2000). Short Period Variations in Earth Rotation as seen by VLBI. Surveys in Geophysics, 21, 499-520.
2. Pany, A., Böhm, J., MacMillan, D., Schuh, H., Nilsson, T., & Wresnik, J. (2011). Monte Carlo simulations of the impact of troposphere, clock and measurement errors on the repeatability of VLBI positions. Journal of Geodesy, 85(1), 39-50.
3. Petrachenko, W. T., Niell, A. E., Corey, B. E., Behrend, D., Schuh, H., & Wresnik, J. (2012). VLBI2010: Next Generation VLBI System for Geodesy and Astrometry. In Geodesy for Planet Earth, 999-1005.
4. Glaser, S., Ampatzidis, D., König, R., Nilsson, T., Heinkelmann, R., Flechtner, F., & Schuh, H. (2016). Simulation of VLBI Observations to Determine a Global TRF for GGOS. In International Symposium on Earth and Environmental Sciences for Future Generations, pp. 3-9.
5. Schartner, M., & Böhm, J. (2019). VieSched++: A New VLBI Scheduling Software for Geodesy and Astrometry. Publications of the Astronomical Society of the Pacific, 131(1002).
6. Vulnerability Atlas of India. (2019). (third edition). Building Materials and Technology Promotion Council (BMTPC), Ministry of Housing and Urban Affairs, Government of India.
7. Schartner, M., & Bohm, J. (2020). Optimizing schedules for the VLBI global observing system. Journal of Geodesy, 94.
8. Behrend, D. (2021). Realization Status of VGOS Infrastructure Buildout. 11th IVS Technical Operations Workshop, virtual.

Digital Object Identifiers for the IVS

Glenda Coetzer[1,2], Yu Takagi[3], Kirsten Elger[4]

Abstract One of the goals of the International VLBI Service for Geodesy and Astrometry (IVS) is to provide data and products to support geodetic, geophysical and astrometric research, and operational activities (IVS, 2022). The IVS is committed to supporting scientific discovery through good data management. To enhance data visibility and sharing, IVS data and products need to adhere to the FAIR (Findable, Accessible, Interoperable and Reusable) data principles. In support of FAIR data, the IVS Directing Board agreed on the use of persistent identifiers, *i.e.*, Digital Object Identifiers (DOIs), for permanently identifying its data and products. We provide feedback of an exploratory study that is being conducted to establish best practices for attributing DOIs to IVS data and products.

Keywords DOI, research data management, research data repository

1 Introduction

Research institutions and scientists are evaluated on the scientific output (*i.e.* scholarly literature and citation numbers) they produce (Bordelon, Grothkopf, and Meakins, 2018). Compared to other scientific disciplines, geodesy researchers appear to be producing less "countable scientific output". This is because geodesy researchers are much more involved in operational aspects of institutions, data creation, and provision (Elger *et al*., 2020). It is imperative to establish structured and well-documented mechanisms for geodesy data, products, software, equipment/instruments, stations, and networks, which can assure discovery, retrieval, and citation of data used in scientific publication, and to give recognition to individuals, institutions and funders for the creation and storage of data (Bordelon, Grothkopf, and Meakins, 2018; Elger *et al*., 2020).

1. South African Radio Astronomy Observatory
2. University of Pretoria, South Africa
3. Geospatial Information Authority of Japan
4. GFZ German Research Centre for Geosciences

2 Digital Object Identifiers

Four years after the implementation of Digital Object Identifiers (DOIs) for unambiguously identifying and linking to online articles, the first DOI for digital datasets was registered in 2004. Originally developed with the purpose of providing permanent access to static datasets referred to in scholarly literature, DOIs are increasingly being used for dynamic datasets, collections of datasets, and networks (e.g. time series from observational networks) (Elger *et al*., 2020). Persistent identifiers, such as DOIs, are ideal tools for providing citable and traceable references to various types of sources (e.g. data, software, samples, equipment), and importantly, it is a means towards rewarding the originators of the data. DOI-referenced and cited datasets comply with the FAIR data principles of Wilkinson *et al*. (2016).

DOI-referenced and cited datasets are (Elger, 2021a):

- **Findable** on the Internet, in repositories, databases, etc. (e.g., CDDIS and UNAVCO)
- **Accessible** via the DOI link (e.g., https://doi.org/10.prefix/suffix)

- **Interoperable** with applications or workflows
- **Reusable** – resolve to DOI landing page, containing standardized metadata and documentation.

Fig. 1 FAIR data principles (Wilkinson *et al.*, 2016).

DOI-referenced and cited datasets are also:

- Machine readable,
- Exchangeable – standardized metadata enhance data discovery via Online Public Access Catalogues (OPACs),
- Trackable in scholarly literature, and
- Used for acknowledging and rewarding institutions and researchers.

3 Initial Questions Regarding DOIs for IVS

- What type of data and products do the IVS have (i.e., data classification)?
- Who is already using DOIs and for which data, products, etc.?
- How is the scientific community using IVS data and products?
- Where do we find best practices for citable data and products?
- What about unstandardized metadata and the many schemes available?
- Should DOI-related metadata be included in existing standards, or should it remain separate and complementary to existing standards?
- Who will be responsible for minting DOIs for the IVS (licensing, etc.)?
- What about granularity of data and products? Should DOIs be assigned for instruments, stations, and networks of the IVS community?

The scientific community's response to the question of granularity of data and data products and whether DOIs should be assigned for instruments, stations, and networks of the IVS is summarized in Figure 2.

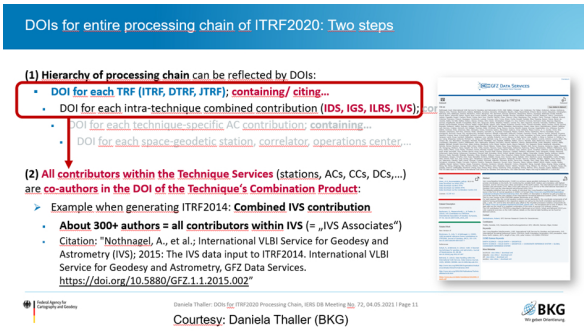

Fig. 2 Hierarchy of a processing chain reflected by DOIs (Thaller, 2021).

4 IVS Components, Data and Products

An inventory of IVS components, data, and products was conducted. This step is crucial for the DOI attribution process. It was ascertained that the IVS consists of various components as depicted in Figure 3 and that both static and dynamic data are generated by these IVS components. Products are derived from the data.

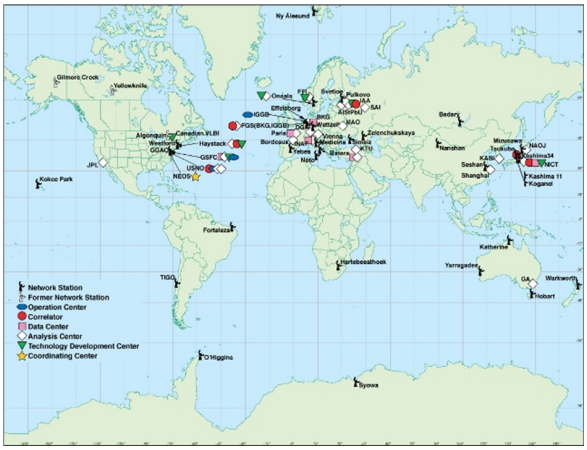

Fig. 3 IVS components (IVS, 2022).

4.1 IVS Data (Static and Dynamic)

- DB: Database files, binary fields in vgosDB format (e.g. ivsdata/vgosdb_bonn/)
- NGS: NGS card files, ASCII files in NGS card format (ivsdata/ngs/)
- SWIN: SWIN files, binary files of fringe visibilities in DIFX SWIN format (ivsdata/swin)
- AUX: Auxiliary files, ASCII files including schedules, notes and session log files (ivsdata/aux/)

4.2 IVS Products

- EOP-I: Intensive EOP series (ivsproducts/eopi/)
- EOP-S: Session EOP series (ivsproducts/eops/)
- TRF: Terrestrial Reference Frame (ivsproducts/trf/)
- CRF: Celestial Reference Frame (ivsproducts/crf/)
- DSNI: Daily UT1 solutions (ivsproducts/int_sinex/)
- DSNX: Daily EOP + station coordinates solutions (ivsproducts/daily_sinex/)
- TROP: Tropospheric parameters (ivsproducts/trop/)
- BASELINE: Time series of baseline lengths (available only on BKG/DGFI Combination Center Web site)
- VTRF: Station positions and velocities results from accumulated station coordinates, from combined normal equations of any 24-hour session (BKG/DGFI Combination Center)

5 Use Cases

To determine what other communities are doing regarding DOI minting, use cases were reviewed.

5.1 The Global Geodetic Observing System (GGOS) Working Group on DOIs for Geodetic Datasets

This Working Group (WG) was established in 2019 by the International Association of Geodesy's (IAG) GGOS and is chaired by Dr. Kirsten Elger (GFZ, Potsdam). Objectives of the GGOS WG are to (Elger, 2021a):

- address challenges and identify opportunities for improved coordination for the use of DOIs within the geodetic community,
- explore DOI minting and citation practices from other communities,
- establish best practices,
- advocate for consistent implementation of DOIs across the IAG and the geodetic community,
- explore geodetic metadata – standards, e.g. GeodesyML, as well as other DOI related discovery metadata, and
- explore the inclusion of Persistent Identifiers (PIDs), e.g., Open Researcher and Contributor Identifiers (ORCIDs) and Research Organization Registry (ROR).

5.2 NASA Earth Science Data and Information System (ESDIS)

This project started investigating the assignment of DOIs to data products in 2010 (Wanchoo, James, and Ramapriyan, 2017). Objectives of ESDIS are as follows:

- developing processes, guidelines, and models for creating and assigning DOIs
- capturing of product metadata
- establishing an automated system for assignment of DOIs

5.3 International Federation of Digital Seismograph Networks (FDSN)

This organization developed the concept of network DOIs used for citation purposes. The FDSN is responsible for (Clark, Evans and Strollo, 2014):

- providing DOI services, which include DOI mapping, minting and management services,
- promoting the use of DOIs by all networks using FDSN-assigned network codes,
- recommending metadata fields based on the DataCite model,

- providing citation examples for 'self-minted' DOIs and 'FDSN-minted' DOIs, and
- hosting the FDSN-minted DOI landing page (http://www.fdsn.org/networks/detail/);
  Other network operators who mint DOIs are responsible for their own landing pages (e.g., http://geofon.gfzpotsdam.de/doi/network/GE).

6 Metadata

An identifier, such as a DOI, is of no value without some related metadata describing what is being identified. DataCite is a leading organization devoted to promoting better access to research data. DataCite's metadata scheme is one of a number of metadata schemes available to the public. The FDSN community strongly encourages the use of DataCite's metadata model.

Metadata concepts to be considered by the IVS:

- DataCite DOI metadata scheme, ISO 19115 metadata standard
- Mandatory and discovery properties for metadata (see Figure 4)
- GeodesyML and PIDs (e.g., ROR, ORCID, FundRef, etc.)
- Controlled vocabularies
- Suffix-naming conventions and namespacing for next-consecutive-integer DOI naming that is meaningful and machine-readable
- Machine-readable embedded metadata (e.g., using <meta> tags in landing pages)

7 Citation

To counter the stigma that geodesy researchers produce less countable scientific output, it is recommended that landing pages of networks, institutions, etc. include a *'Cite this Dataset'* which should feature a pre-generated reference (see Figure 5) that users can copy-paste (Elger, 2021a). Thus, citing the resource/data is easy and guaranteed to include the DOI (Elger, 2021b).

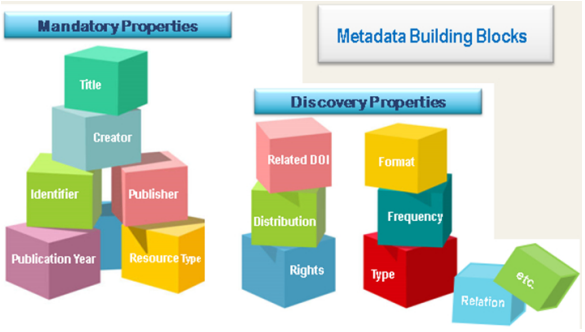

Fig. 4 Metadata properties (Bordelon, Grothkopf and Meakins, 2018).

Food for thought ...

- Citing all sources of data is good scientific practice and required by the *CC BY 4.0 Licence*.
- Citation of final products should include existing DOIs related to these products.
- DOIs of related work need to be cited (see Elger, (2021b) for INTERMAGNET Global Magnetic Observatory use case).

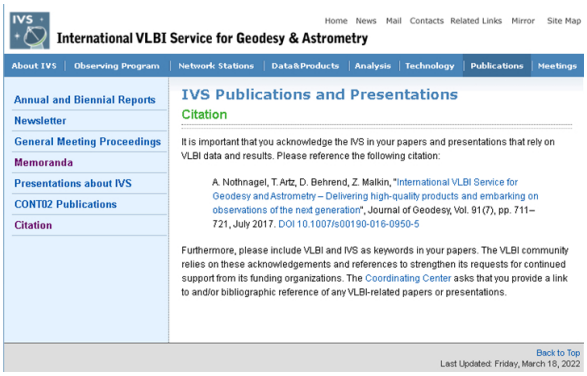

Fig. 5 Example of a pre-generated citation of a paper (IVS, 2022).

8 Conclusions

To adhere to the FAIR data principles, it is essential to attribute DOIs to IVS data and products. DOIs provide a structured and well-documented mechanism which enhances citability and scientific recognition. Cur-

rently, community-agreed methods for assigning DOIs and the application of a uniform metadata standard are lacking. Going forward, several questions need answering first. Community agreement is required to address issues such as: responsibility for minting of IVS DOIs (agency, client, etc.), metadata standards, homogenized approaches on completing metadata (with practical examples), and citation formats. Also required is the provision of DOI services (e.g. seismology community use case) allowing data users to enquire if an IVS dataset is associated with a DOI (harvest DOIs and associated metadata) and whether there are any restrictions/embargoes and licences. Knowledge gained from the GGOS WG on DOIs for Geodetic Datasets can be put to good use in our endeavor to attribute DOIs to IVS data and products.

Acknowledgments

We thank Dirk Behrend and Axel Nothnagel for sharing their insights and knowledge with us. We wish to also thank Kirsten Elger and the GGOS WG on DOIs for Geodetic Datasets for the work they are doing and from whom much of the information presented in this poster originates.

References

1. Bordelon, C., Grothkopf, U. and Meakins, S. 2018. First light for DOIs at ESO. Library and Information Services in Astronomy VIII. European Physical Journal Web of Conferences. EDP Science.
2. Clark, A., Evans, P.L. and Strollo, A. 2014. FDSN recommendations for seismic network DOIs and related FDSN services. https://www.fdsn.org/pdf/V1.0-21Jul2014-DOIFDSN.pdf
3. Elger, K. 2021a. News from the GGOS DOI Working Group. GGOS Days 2021. October 11–13, 2021. https://ggos.org/event/ggos-days-2021/
4. Elger, K. 2021b. DOI minting and citation strategies for complex/hierarchical geodetic products: example GNSS products. GGOS WG Meeting presentation.
5. Elger, K., Coetzer, G., Botha, R. and GGOS DOI Working Group. 2020. Why do geodetic data need DOIs? First ideas of the GGOS DOI Working Group. EGU General Assembly 2020. https://doi.org/10.5194/egusphere-egu2020-17861
6. IVS. 2022. IVS Organizations: Components. https://ivscc.gsfc.nasa.gov/about/org/components/index.html
7. Thaller, D. 2021. DOIs for ITRF2020 processing chain. IERS DB Meeting, 72. 4 May 2021.
8. Wanchoo, L., James, N. and Ramapriyan, H.K. 2017. NASA EOSDIS Data Identifiers: approach and system. *Data Science Journal*, 16:15, 1–11.
9. Wilkinson, M.D. et al. 2016. The FAIR guiding principles for scientific data management and stewardship. *Sci Data*, 3:160018. https://doi.org/10.1038/sdata.2016.18

Exploring Source Structure with the Bordeaux VLBI Image Database

Comparing Jet Directions with Optical-Radio Offset Vectors

Arnaud Collioud[1], Patrick Charlot[1], Sébastien Lambert[2]

Abstract The Bordeaux VLBI Image Database provides to the international VLBI community almost 8,000 VLBI images of radio sources at S and X band and some others at K and Q band. Such images are of interest for astrometric and astrophysical applications, such as the determination of the VLBI jet direction. We developed a fully automatic method to extract this direction from any VLBI image, which we then applied to all BVID images, resulting in the production of 9,215 jet directions for 1,221 sources. Comparing the mean jet directions over all epochs at X band to the Gaia EDR3 (optical) − ICRF3 S/X (radio) offset vector directions indicates that the offset vector is aligned within 30° of the jet direction in roughly half of the sources, thereby confirming previous studies.

Keywords VLBI, Database, Imaging, Source Structure, Jet Direction, ICRF, Gaia

1 Introduction

Since 2008, the Bordeaux VLBI Image Database (BVID)[1] has made VLBI images of radio reference frame sources available to the international VLBI community [1, 2]. The vast majority of these images have been produced from RDV (Research & Development VLBA) or VLBA experiments. The BVID currently contains around 7,900 such images at S and X band (2.3 and 8.6 GHz), along with some at K and Q band (22 and 43 GHz), and associated data about source structure (compactness and structure index information), which are of interest for astrometric and astrophysical applications. Those images cover a period of time of more than 20 years and are available for a total of about 1,500 different sources.

Most of the sources show non-point-like structures on VLBI scales and often exhibit jets. The directions of these jets may be of interest for astrophysical studies, but also for astrometric scheduling purposes where one tries to mitigate the effect of source structure by avoiding observations with projected VLBI baselines aligned onto the jet directions. Section 2 presents a new method that we developed to automatically determine the jet direction from a VLBI map. In Section 3, we discuss the results derived when applying this method to the BVID images and the potential applications of such results. One of these is the study of the relation between the jet directions and the directions of the offset vectors revealed by comparing the Gaia Early Data Release 3 (EDR3) and S/X-band ICRF3 positions. This application is further investigated in Section 4.

2 Method to Determine Jet Direction

We developed a fully automatic pipeline to determine the jet direction from any VLBI map. The algorithm can be decomposed into several successive steps which are described below and also illustrated by Figure 1 (upper- and lower-left panels):

1. Read the source model (i.e., the CLEAN components) and some additional information from the image (map and beam size, residual map RMS

1. Laboratoire d'Astrophysique de Bordeaux, Université de Bordeaux, CNRS, France
2. SYRTE, Observatoire de Paris, Université PSL, Sorbonne Université, CNRS, France

[1] Available at https://bvid.astrophy.u-bordeaux.fr

noise). Our method does not require model-fitting of the source, a task which can be time-consuming and user-dependent when manually done.
2. Split the image plane into 10-degree azimuthal bins and sum the flux of the individual components in each bin to obtain the distribution of the flux with respect to the direction.
3. Compute the mean and the standard deviation of this flux distribution.
4. Repeat step 3 when considering the model components located outside an increasing radius (starting from the center of the map). The procedure stops when a certain flux cut-off is reached.
5. Compute the global weighted mean direction and error from the mean directions determined at each radius. This global direction ranges from 0 to 180° (anti-clockwise) and from 0 to −180° (clockwise).

At the end of the procedure, we also plot the global direction (from step 5 above) overlaid on the VLBI map to visually check that it is consistent with the morphology of the source, in particular with any detected jet-like structure (see Figure 1, lower-right panel).

3 Application to BVID Images

We applied our pipeline to all the images available in the BVID database. Overall, we determined 9,215 jet directions for 1,221 sources with the distribution between frequencies indicated in Table 1 below.

Table 1 Number of jet directions for each frequency band.

Band	S	X	K	Q	Total
Frequency (GHz)	2.3	8.6	22.0	43.0	
N sources	1,145	1,145	274	132	1,221
N jet directions	3,905	3,975	1,068	267	9,215

Almost all sources have jet directions available at two or more frequency bands. Thus, it is of interest to compare the jet directions in the different bands. For example, Figure 2 displays the jet directions determined for the source OJ287 (0851+202) at the four bands. In this case, the directions are consistent (within the errors) between bands even if the maps result from data at different epochs (2020 for S and X band and 2002 for K and Q band). We plan to develop further this comparison between bands in a study to come.

In addition, we can also take advantage of the long time span of the BVID data to produce time series of the jet direction for each source at each frequency band. Studying those may reveal time variability, and even periodicity, that could possibly be tied to the physical properties of the source jet and/or its inner black hole. An example of such time series, again for the source OJ287, is shown in Figure 3. Overall, the jet direction exhibits no strong variation with time, but a long-term trend is seen at S and X band between 2007 and 2017. A systematic study of the time series is out of the scope of this work but is planned for the near future.

Finally, we computed for all sources and all bands the mean direction over all epochs (i.e., the temporal mean). Those directions will be used in the next section for comparison with the optical-radio offset vector orientations.

4 Comparison between Jet Directions and Optical-Radio Offset Vectors

Gaia is a space mission of the European Space Agency, launched in 2013, dedicated in particular to measure the positions, distances, and motions of several billions of objects in the sky. Especially, more than 1.5 million extragalactic sources are available in the Gaia EDR3 delivered on 3 December 2020 [3]. After cross-matching the EDR3 catalog (optical) with the ICRF3 catalog at S/X-band (radio), we obtained a list of 3,477 common sources. For each source in that list, we computed the optical-to-radio offset vector angle, illustrated in Figure 4, in the same way as for the comparison of the ICRF3 to Gaia DR2 catalogs in [5]. The distribution of the offset vector angles (Figure 5, left panel) shows a roughly uniform distribution, but with an excess at 0° and 180°, i.e., along the declination axis, which is likely due to observing network effects.

From the results of Section 3, we also computed the distribution of the BVID jet directions at X band, which is displayed in Figure 5 (right panel). As before, the jet direction distribution exhibits peaks at 0° and 180°, most probably also caused by network effects.

With this information, we are now able to compare the BVID jet direction at X band and the optical-radio offset vector angle source by source (see Figure 4). The distribution of the difference between these an-

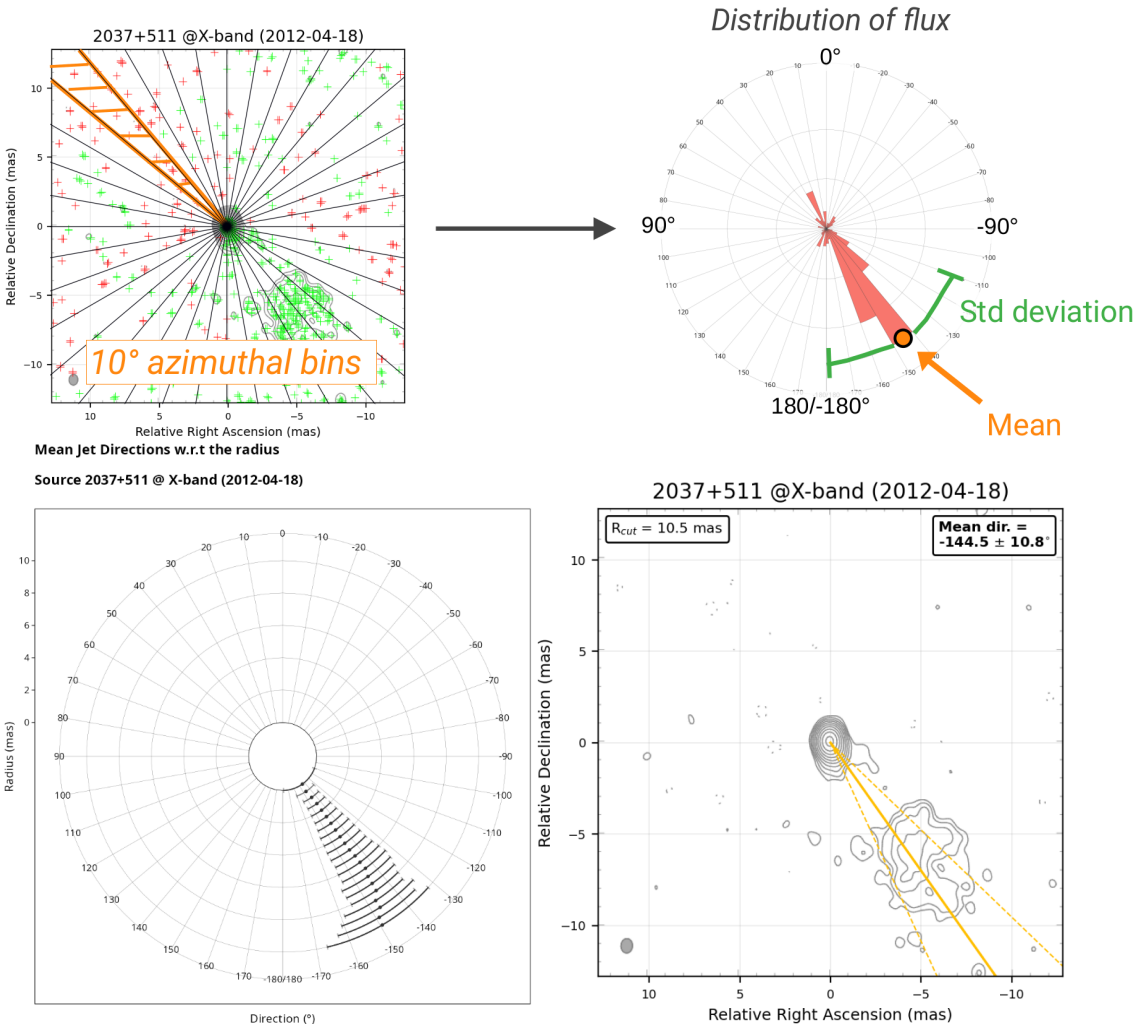

Fig. 1 Application of the jet-determination algorithm to the VLBI map of the source 2037+511 observed on 2012-04-18 at X band. (Top-left) View of the image plane sliced into 10-degree azimuthal bins. (Top-right) Azimuthal flux distribution after summing the flux of the components in each bin. The important values are the mean and standard deviation of this distribution. (Bottom-left) Plot of the individual mean directions and errors as a function of the increasing radius. (Bottom-right) Global mean direction ($-144.5 \pm 10.8°$) overlaid on the underlying jet-like structure.

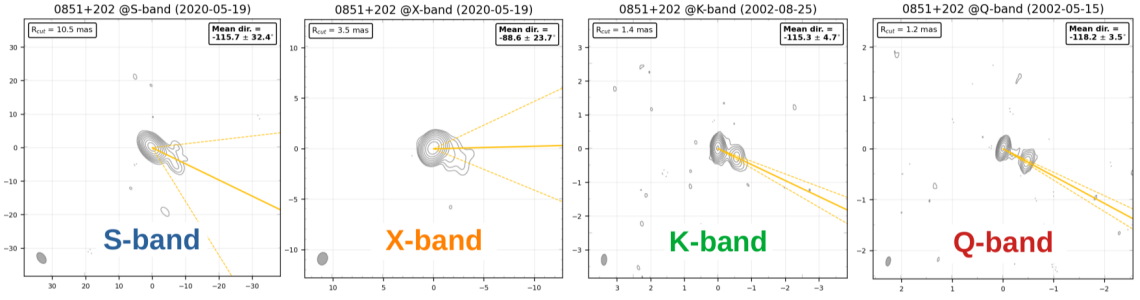

Fig. 2 Example of the jet directions computed from four images at S, X, K, and Q band of the source OJ287 (0851+202). The jet directions are found to be consistent within the error bars, although the maps are not from the same epoch.

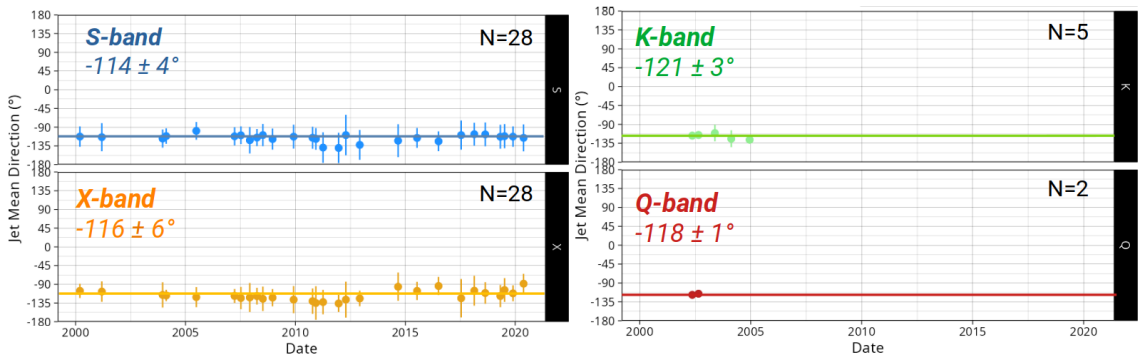

Fig. 3 Example of jet direction time series for the source OJ287 (0851+202) at S, X, K, and Q band. For each time series, the mean jet direction over all epochs and its error are computed. The mean jet directions are consistent at the four bands for this source.

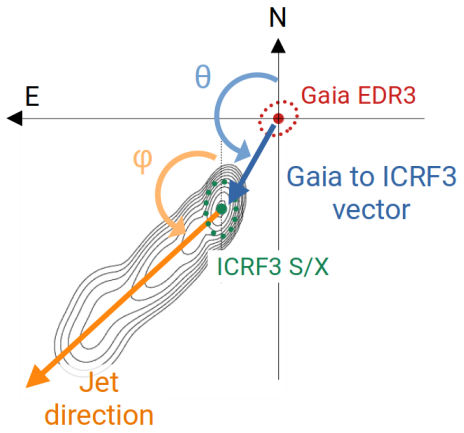

Fig. 4 Illustration of the comparison between the Gaia EDR3 and ICRF3 S/X-band positions, resulting in the optical-radio offset vector direction θ. This angle may be compared to the jet direction φ. It is assumed here that the ICRF3 position is located at the peak of the brightness distribution. The angle difference between θ and φ is small in this case, indicating that the jet and the optical-radio offset vector are almost aligned.

gles is plotted in Figure 6 (left panel) for the 865 common sources. From the plot shown, we deduce that the optical-radio offset vector predominantly aligns with the jet direction. This alignment is within a range of $\pm 30^\circ$ for almost half of the sample (393 sources), with 253 and 140 sources in the same and opposite direction, respectively.

This result confirms the conclusions from previous studies, which used other VLBI catalogs, other Gaia data releases, and/or other methods for computing the jet directions [4, 6, 7, 8, 9]. The specificity of the current work is that the VLBI positions and jet directions were obtained from data at the same frequency band.

To go further, we can study the impact of the normalized separation on the previous distribution (see Figure 6, right panel). The normalized separation N_{sep} is the angular separation between the Gaia EDR3 and ICRF3 positions, normalized by its formal uncertainty [5]. The higher the normalized separation, the more precise the Gaia-ICRF3 offset vector angle. For the sources with $N_{sep} < 2\sigma$, no particular alignment is found. The peak around 0° becomes slightly visible for $N_{sep} \sim 2\sigma$ and that around 180° for $N_{sep} \sim 3\sigma$. At the highest values of the normalized separation ($N_{sep} > 6\sigma$), all sources but a small portion (4%) show alignment between the jet directions and Gaia-ICRF3 offset vectors. By examining individual maps for this fraction of sources, we note that 75% of them show no jet or have a two-sided jet, which can thus lead to an incorrect determination of the jet direction. The remaining 25% are not yet understood and will have to be investigated in more detail.

5 Conclusion

We developed a fully automatic method to determine source jet directions directly from VLBI images. This method was successfully applied to all available BVID images at S, X, K, and Q band, resulting in the production of 9,215 jet directions for 1,221 sources. From these directions, we further computed the mean jet direction over all epochs for each source. Comparing the mean jet directions at X-band with the Gaia EDR3 (optical)-ICRF3 S/X-band (radio) offset vector directions confirms that the two directions are aligned within 30° in roughly half of the sources.

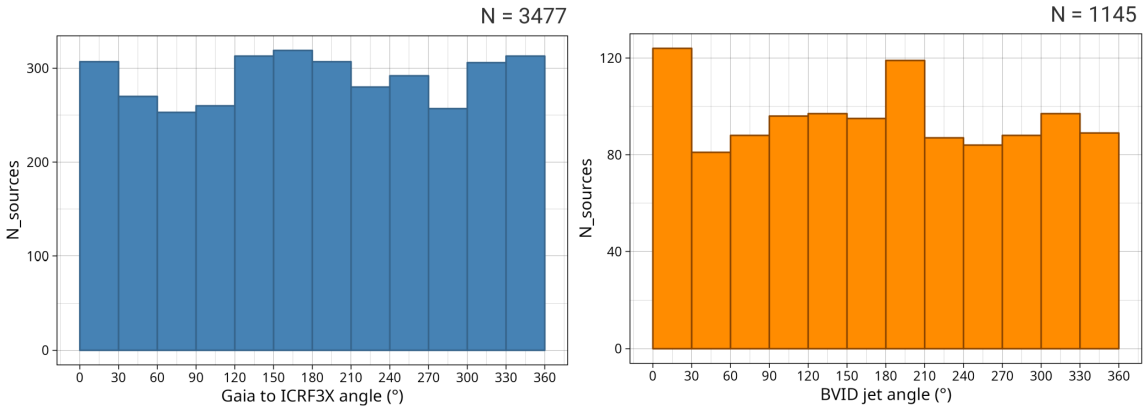

Fig. 5 Distributions of the Gaia EDR3 to ICRF3 S/X-band offset vector angles (left) and BVID jet directions at X-band (right).

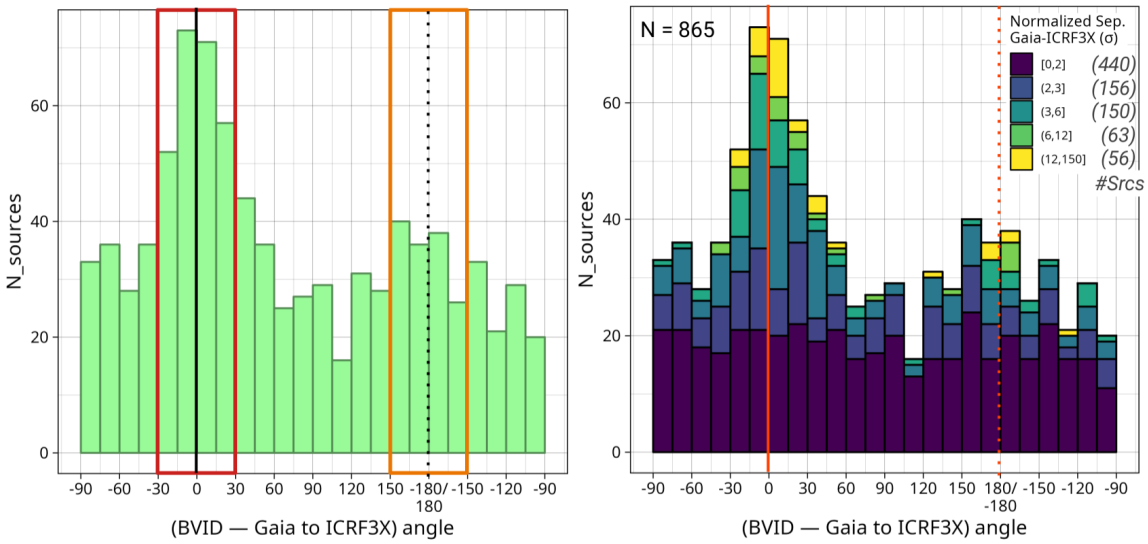

Fig. 6 (Left) Distribution of the differences (BVID − Gaia EDR3 to ICRF3 S/X-band offset vector directions). The optical-radio offset vectors are aligned within a range of ±30° (indicated by the colored rectangles) with the jet directions in 393 sources. (Right) The same distribution color-coded according to the normalized separation. The alignment is preferentially visible for the highest normalized separations.

Future prospects include studying the variability of the jet directions with time, comparing the jet directions between frequency bands, and comparing the Gaia EDR3-ICRF3 offset vector angles to the jet directions at K band.

References

1. A. Collioud, P. Charlot, Proceedings of the 19th EVGA Working Meeting, 24-25 March 2009, Bordeaux, France, Eds G. Bourda, P. Charlot and A. Collioud, pp. 19–22, 2009.
2. A. Collioud, P. Charlot, Proceedings of the 24th EVGA Working Meeting, 17-19 March 2019, Las Palmas de Gran Canaria, Spain, Eds R. Haas, S. Garcia-Espada, and J.A. López Fernández, pp. 219–223, 2019.
3. S.A. Klioner et al., A&A, forthcoming article, DOI: 10.1051/0004-6361/202243483, 2022.
4. S. Lambert et al., A&A, 651, A64, DOI: 10.1051/0004-6361/202140652, 2021.
5. P. Charlot et al., A&A, 644, A159, DOI: 10.1051/0004-6361/202038368, 2020.
6. Y. Kovalev, L. Petrov, A. Plavin, A&A, 598, L1, DOI: 10.1051/0004-6361/201630031, 2017.
7. A. Plavin, Y. Kovalev, L. Petrov, ApJ, 871, 143, DOI: 10.3847/1538-4357/aaf650, 2019.
8. L. Petrov, Y. Kovalev, A. Plavin, MNRAS, 482, 3023, DOI: 10.1093/mnras/sty2807, 2019.
9. Xu et al., A&A, 647, A189, DOI: 10.1051/0004-6361/202040168, 2021.

First Results of Project on Six-hourly EOP Piecewise Linear Offset Parameterization

A. Nothnagel[1], S. Böhm[1], R. Dach[2], M. Glomsda[3], H. Hellmers[4], A.-S. Kirkvik[5], T. Nilsson[6], A. Girdiuk[4], D. Thaller[4]

Abstract Continuous piecewise linear functions are a helpful way of parameterizing time series in least-squares adjustments employing a Gauss-Markov model. In this publication, we present the benefits for routine IVS Earth Orientation Parameter (EOP) estimation and show results of a project set up for demonstrating the feasibility of this approach. Before we start with that, we point out deficits of the current EOP estimation approach with 24-hour offsets and rates stemming from the mismatch of tabulated a priori EOP values at day boundaries and the two-calendar-day spanning of contemporary IVS observing sessions. In addition, the current EOP parameterization causes a mismatch of the IVS-derived EOPs labeled with "24 hours" with the daily EOPs derived from other space-geodetic techniques.

Keywords Earth Orientation Parameter estimation, continuous piecewise linear functions

1 Introduction

In routine Earth Orientation Parameter (EOP) estimation of the International VLBI Service for Geodesy and Astrometry (IVS) functional values at a reference epoch (commonly called offset) and the first time derivative (commonly called rate) are the parameters of interest for the two polar motion (PM) components x_p and y_p as well as for universal time represented as UT1-UTC. For the latter parameter, the rate reflects the length of day (LOD) which has the opposite sign for historical reasons. In terms of consistent handling of multiple solutions of different IVS Analysis Centers (ACs), the use of identical a priori values for every individual delay observation is a fundamental prerequisite.

The current procedure is that EOP tables of the International Earth Rotation and Reference Systems Service (IERS) are used: either the tables of the IERS Rapid Service and Predictions Center (usno_finals) or the IERS Series C04. Both contain time series of EOP at midnight epochs with daily resolution. These are then taken to interpolate the respective EOP components at the epoch of the delay observation either linearly, as spline functions, or with the Lagrange method. With the individual EOP at time of observation, the observed-minus-computed vector is corrected for the variability in Earth rotation. Furthermore, the set of EOP values at the session's reference epoch, normally the middle of the session, is calculated for the computation of the total unknown parameters composed of these a prioris and the adjustments.

The critical part is related to the EOP rates and their a prioris. What happens here is dependent on the EOP reference epoch of the session. Since most IVS observing sessions start around 18h00 UT, the EOP reference epoch is at around 06h00 UT and thus between the second and third midnight epoch used for interpolation (Figure 1). In most analysis software packages, the a priori EOP rate is then calculated with these second

1. Technische Universität Wien, Department für Geodäsie und Geoinformation, Wiedner Hauptstraße 8, 1040 Wien, Austria
2. University of Bern, Astronomical Institute, Switzerland
3. Deutsches Geodätisches Forschungsinstitut der Technischen Universität München (DGFI-TUM), Germany
4. Federal Agency for Cartography and Geodesy (BKG), Frankfurt a.M., Germany
5. Norwegian Mapping Authority (NMA), Kartverksveien 21, 3511 Hønefoss, Norway
6. Lantmäteriet – The Swedish mapping, cadastral and land registration authority, Lantmäterigatan 2C, 801 82 Gävle, Sweden

and third functional values (rate II) depending on the interpolation scheme. As is obvious from Figure 1, this rate does not represent the real EOP rate for the whole observing session but only that of the last 3/4 of the total session length. If the session lasts from 18h00 UT to 18h00 UT as in Figure 1, the correct a priori rate would be the one which is depicted as rate III. The effect on the total EOP estimate, i.e., a priori plus adjustment, may be small for polar motion rates, but may be significant for LOD.

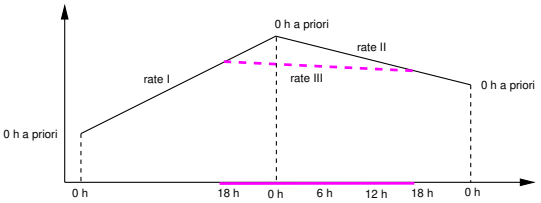

Fig. 1 Current scheme of EOP interpolations from IERS tables. In magenta, the correct rate representation for a generic observing session from 18h00 UT to 18h00 UT is depicted. Linear interpolation is chosen for a good interpretability of the graph, but the same applies also for any other interpolation scheme.

Another issue in this context is the documentation of the a priori rates in the SINEX files. Usually, there is no indication of what a priori rates are reported, so the parameter epoch transformation in the combination process at the IVS Combination Center is applied without distinction.

Furthermore, this kind of EOP parameterization results in estimates that are labeled as "24-hour EOPs," but the 24-hour interval is fully different from the 24-hour intervals for EOP estimation by the other space-geodetic techniques, which is usually attached to the standard day, i.e., covering 00h00 UT to 24h00 UT [7]. As a consequence, these EOPs cannot be reliably combined, although it is still done for the operational IERS EOP products.

To overcome these deficits in IVS operations and prepare for a higher time resolution of EOP in the VGOS era, we propose to establish routine EOP estimation with continuous piecewise linear functions (CPLF) at fixed intervals and epochs. CPLFs come along in two different representations: with rates, or with functional values at supporting points (Figure 2). In the first case, the estimated parameters are an offset or functional value f_0 at a reference epoch (e.g., at the start of the session) and a series of new rates r_i for consecutive intervals continuously linked together at the nodes. Mathematically equivalent is the estimation of a series of functional values f_i for the nodes.

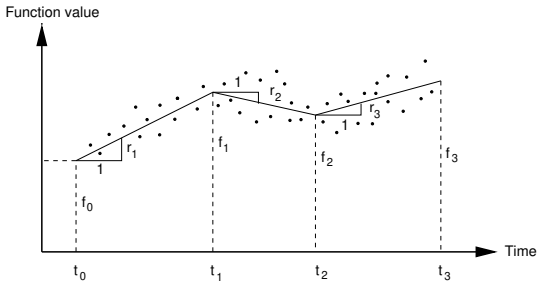

Fig. 2 Continuous piecewise linear function fit to generic observations (dots) either with an initial functional value f_0 and a series of rates r_i, or with a series of functional values f_i for the nodes.

Applying this scheme to EOP estimation for IVS EOP observing sessions allows to increase the time resolution easily, and permits the reporting of unambiguous a priori values of the nodes as interpolated from the tabulated IERS values at midnight epochs (Figure 3) in the SINEX files. Ideal is the choice of nodes at fixed integer hours including the midnight epoch, e.g., 18h00 UT, 00h00 UT, 06h00 UT, 12h00 UT, and 18h00 UT for six-hour intervals. In doing so, the resulting EOPs can easily and unambiguously be compared and combined with EOPs resulting from the other space-geodetic techniques.

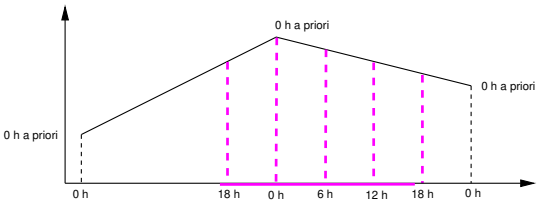

Fig. 3 Proposed scheme of EOP interpolations from IERS tables. In magenta, the nodes at six-hourly intervals (including 0h00 UT) for a generic observing session from 18h00 UT to 18h00 UT is depicted. Linear interpolation is chosen for a good interpretability of the graph, but the same applies also for any other interpolation scheme.

2 Experiment Setup

To demonstrate the validity of the concept, we performed a test by analyzing all 52 IVS-R1 sessions of

the year 2020 with six-hourly continuous piecewise linear offsets. The level 2 data analysis was carried out with the softwares ASCoT (OSO) [1], (Calc/Solve, not invertible), DOGS-RI (DGF) [6], Where (NMA) [5], and VieVS (VIE) [2], with the standard setup as used in the computations for the ITRF2020 submissions. Due to the observing periods of the R1 sessions from 17h00 to 17h00 UT, we estimated the Earth Rotation Parameters (ERP) at 12h00, 18h00, 0h00, 6h00, 12h00, and 18h00 UT, covering the observing session in its entirety. Since the first section (12h00 to 18h00 UT) merely contains observations of one hour (17h00 to 18h00 UT), the first parameter of each session is determined only very weakly. Therefore, we excluded these parameters in the subsequent interpretations.

In the simultaneous estimation of polar motion and celestial pole offsets (CPO), the higher the time resolution of polar motion, the more correlated the corresponding estimates are. Hence, we fixed the CPOs to the IAU2000A/2006 nutation model plus an empirical Free Core Nutation (FCN) model (Section 3). Furthermore, all sub-daily geophysical models were organized to be identical.

For our assessment, we also made use of combined time series produced by the IVS Combination Center at BKG in the same way as those for ITRF2020 [4]. The combination could be performed straight away with no major modifications of the combination software necessary. The combined time series then formed an additional ERP data set.

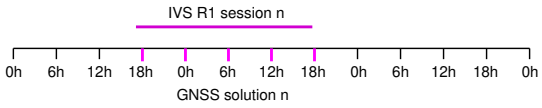

Fig. 4 Extraction scheme of GNSS results.

To allow for an external comparison, a special CODE Analysis Center GNSS solution [3] was computed with the same six-hourly resolution as for the VLBI solutions. For stability reasons, three-day arcs with 13 ERP epochs were chosen, where the terrestrial frame was estimated session-wise with No-Net-Rotation conditions w.r.t. IGSR3. This setup allowed the extraction of consistent ERP from a single three-day arc for epochs identical to the six VLBI session epochs (Figure 4).

3 Handling of Nutation

It is well known that the separation of polar motion and celestial pole offsets is only possible through the concept of a rotation axis. We need a full rotation of the Earth to decorrelate PM and CPOs sufficiently. VLBI observations at a single epoch alone will only have three rotational degrees of freedom and the normal equation system will be singular if we set up both PM and CPO parameters in this case. The more time of a day we cover with observations, the more the correlation coefficients between PM and CPOs will be reduced. In the opposite direction, we face higher and higher correlations when we introduce more and more continuous piecewise linear offsets (PWLO). This has an effect already for six-hour intervals, and therefore the estimation will require some constraints on the CPOs to detect genuine signals in the PWLOs for PM.

The standard procedure is to take the IERS 14C04 or a VLBI solution's CPOs and interpolate between adjacent epochs with some suitable interpolation scheme. However, the VLBI results for the CPOs, which are the basis for IERS 14C04 or usno_finals, are rather noisy by several tens of microarcseconds from session to session. On one hand, there is no nutation variability below two days by the IERS PM/CPO conventions. On the other hand, the main phenomenon which should dominate the CPO estimates is FCN, with variable amplitudes up to 0.3 mas and a more or less constant period of 430 days. Although there might be a retrograde resonance of Atmospheric Angular Momentum in the FCN band, time series analyses of the CPOs do not show unmodeled effects larger than 30 µas (Ferrándiz, priv. comm.). Any interpolation scheme for fixing the CPOs will thus only generate noise in the PM data.

Since FCN is the dominant variation in the CPOs, we fitted the parameters of a simple 430-day period sine/cosine function (plus rate and offset) to the VLBI data from 2019/07/01 to 2021/06/30 (Figure 5) to cover the year 2020 with some overlap and about two FCN periods. The quality of the fit should then just be assessed by the data in 2020. The residuals are still quite large which underscores that the accuracy of the VLBI CPO estimates is only about 80–100 µas. The model for any Modified Julian Day (MJD) epoch is

$$\text{comp [mas]} = A \cdot \sin(f \cdot t) + B \cdot \cos(f \cdot t) + C + D \cdot t \quad (1)$$

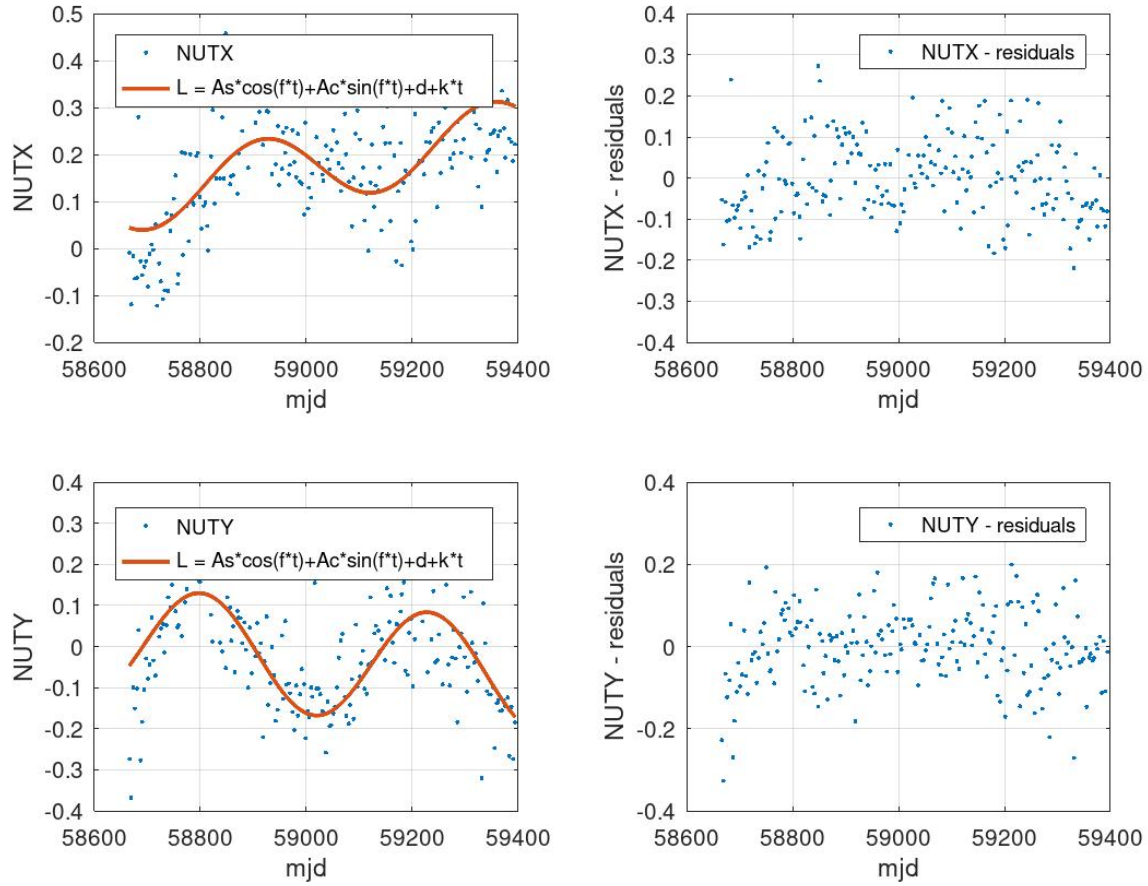

Fig. 5 Estimation of Free Core Nutation from dX/dY celestial pole offsets. Left: Observations with fit (L) in red. Right: Residuals of fit. All in mas.

with frequency $f = 2\pi/430$ and epoch $t = MJD - 58849.0$. The estimated coefficients for the X nutation component are $A = +0.06373$ mas, $B = +0.04188$ mas, $C = +0.14386$ mas, and $D = +0.00018$ mas/day. For the Y nutation component, they are $A = -0.08826$ mas, $B = +0.10496$ mas, $C = -0.01245$ mas, and $D = -0.00011$ mas/day. These were used to compute the fixed CPOs for each MJD, and the results are added to the IAU2000A/2006 nutation components in the VLBI analyses of all ACs.

4 Results

The first analysis step was a direct comparison of the estimates from the individual ACs, which revealed a few inconsistencies in modeling and general setup. After eliminating these, it turned out that 15 of the IVS R1 sessions had an insufficient number of telescopes participating, especially in the second half of 2020. Consequently, the number of observations per six-hour interval was rather small, leading to a larger than expected scatter in the ERP estimates. For the sake of easy implementation, a general threshold of a minimum number of stations of nine was introduced. At this stage, we did not test any other minimum criterion. This is foreseen for future steps of the project.

The scatter of the results of individual sessions and of individual Analysis Centers can best be depicted if an offset and a rate, as regularly estimated for each session in standard VLBI analyses, are subtracted from the PWLO estimates. With at least nine telescopes participating in every R1 session, the general variability of all individual VLBI solutions, their combination, and also the GNSS results is approximately ±500 µas for x pole (Figure 6); the y pole component is similar.

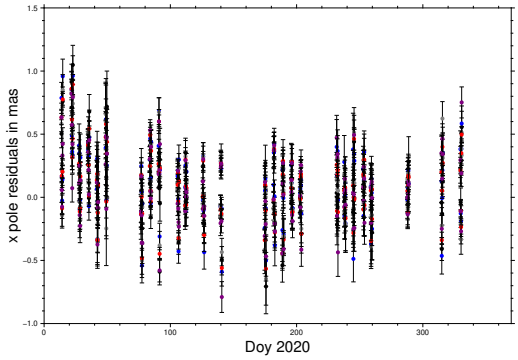

Fig. 6 x pole component variability in each session. Black = VIE, Light Blue = NMA, Gray = OSO, Dark Red = DGF, Blue = GNSS, Red = VLBI Combi.

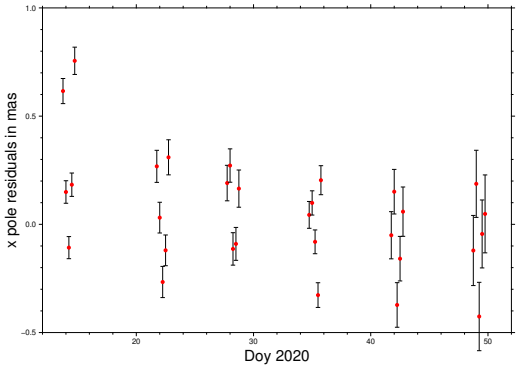

Fig. 8 x pole component differences of VLBI combination minus GNSS, enlarged for first six sessions of 2020.

In terms of agreement between VLBI and GNSS, the WRMS differences of all ACs are in the range of 250 to 300 µas, with the x_p component agreeing slightly better (Table 1).

Table 1 WRMS of VLBI minus GNSS in µas (n = number of epochs = 130); 20 µas bias subtracted in y_p.

	VIE	NMA	OSO	DGF	Combi
x_p	249	276	266	269	255
y_p	286	296	281	282	277

Since the VLBI combination nicely represents all VLBI contributions, in the next steps only the VLBI combination results and the GNSS results are compared for a better graphical visualization (Figure 7 and zoom of the first six sessions of 2020 in Figure 8).

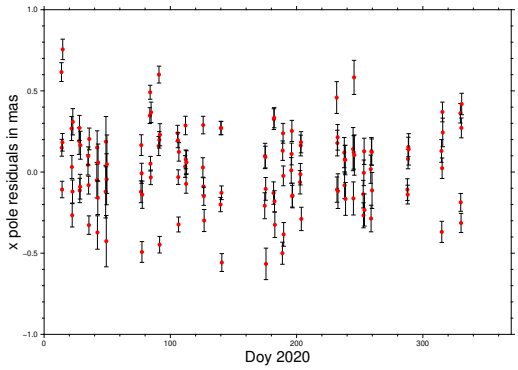

Fig. 7 x pole component differences of VLBI combination minus GNSS.

The plot of the differences of all sessions with nine or more telescopes (Figure 7) still looks rather arbitrary. Only when zooming in, some systematics show up. There seems to be an arc-like behavior with minima at or near the middle of the sessions. Since the differences between VLBI and GNSS should be random if both techniques produced correct results, the characteristics of the differences but also the results themselves need to be investigated further.

As a sideline of our investigations, we can also look at the differences of VLBI minus GNSS for the 0h UT epochs alone. In contrast to the routine VLBI–GNSS comparisons, no interpolation is needed for the VLBI results. However, the number of VLBI observations contributing to these parameters are naturally smaller in the PWLO case than for the operational offset and rate estimation from the full 24-hour sessions. Nevertheless, the results are rather promising (Table 2) since for the x_p component, they are about 20% smaller than the overall values (Table 1). Unfortunately, the differences of the y_p component are slightly larger. In any case, we can show that with the PWLO estimation the need for interpolations in VLBI–GNSS comparisons will disappear.

Table 2 WRMS of VLBI minus GNSS for the 0h UT epoch alone in µ (n = 26); no bias subtracted from y_p results.

	VIE	NMA	OSO	DGF	Combi
x_p	190	249	212	230	230
y_p	303	313	307	319	303

5 Accuracy Considerations

The formal errors of the individual VLBI analyses are in the range of 100 to 200 µas in all components. The combination produces formal errors in the range of 80 to 100 µas. Although the GNSS results are reported with formal errors of 7 to 10 µas, we know that we have to inflate them by a factor of about ten due to the neglect of correlations between subsequent carrier phase observations. The GNSS results can therefore be judged to be approximately of a similar quality as the VLBI combination results. The formal errors of the differences VLBI combi minus GNSS are then approximately 120 µas, while the differences of the individual VLBI ACs minus GNSS are at the level of about 170 µas. The scatter of the differences is thus by about 50% larger, as we see in the computed WRMS differences (Table 1).

6 Conclusions

In this paper we have demonstrated that estimating ERP with continuous piecewise linear functions with a temporal resolution higher than 24 hours can be realized easily by many VLBI ACs. This also applies to the combination process on the basis of normal equation systems. However, we also saw that robust networks with many observations per time interval are essential for this approach. The scatter of the differences between the VLBI and the GNSS results is still too large for a reliable interpretation of the results.

Nevertheless, the use of continuous piecewise linear functions with offset representation is the next step which the IVS analysis community has to go for a higher time resolution of the ERP results. In addition, this approach eliminates the deficit of incorrect handling of the a priori ERP rates when sessions extend across midnight epochs. Finally, unambiguous comparisons of ERP results from VLBI and other space geodetic techniques are possible without the need for interpolations, which regularly increase the noise level.

References

1. T. Artz, S. Halsig, A. Iddink, A. Nothnagel. ivg::ASCOT: Development of a New VLBI Software Package. In D. Behrend, K. D. Baver, and K. L. Armstrong, editors, *IVS 2016 General Meeting Proceedings: "New Horizons with VGOS"*, NASA/CP-2016-219016, 217–221, 2016.
2. J. Böhm, S. Böhm, J. Boisits, A. Girdiuk, J. Gruber, A.Hellerschmied, H. Krásná, D. Landskron, M. Madzak, D. Mayer, J. McCallum, L. McCallum, M. Schartner, K. Teke. Vienna VLBI and Satellite Software (VieVS) for Geodesy and Astrometry. *Publications of the Astronomical Society of the Pacific*, 130(986):044503, 2018 https://doi.org/https://doi.org/10.1088/1538-3873/aaa22b.
3. R. Dach, I. Selmke, A. Villiger, D. Arnold, L. Prange, S. Schaer, D. Sidorov, P. Stebler, A. Jäggi, U. Hugentobler. Review of recent GNSS modelling improvements based on CODEs Repro3 contribution. *Advances in Space Research*, 68:3, 1263–1280, 2021, https://doi.org/10.1016/j.asr.2021.04.046.
4. H. Hellmers, S. Modiri, S. Bachmann, D. Thaller, M. Blossfeld, M. Seitz, J. Gipson. Combined IVS contribution to the ITRF2020. *To appear in: IAG Symposia Series*, IAG Scientific Assembly 2021, 2022.
5. A.-S. Kirkvik, G.A. Hjelle, M. Dähnn, I. Fausk, E. Mysen. Where - A New Software for Geodetic Analysis. In R. Haas, S. García-Espada and J. A. L. Fernández, editors, *Proceedings of the 23rd European VLBI Group for Geodesy and Astrometry Working Meeting*, 248–252, 2017. doi:10.7419/162.08.2019.
6. Y. Kwak, M. Gerstl, M. Bloßfeld, D. Angermann, R. Schmid, M. Seitz. DOGS-RI: new VLBI analysis software at DGFI-TUM, *Proceedings of the 23rd European VLBI Group for Geodesy and Astrometry Working Meeting*, 212–215, 2017. doi:10.7419/162.08.2019.
7. D. Thaller, M. Krügel, M. Rothacher. Combining one year of homogeneously processed GPS, VLBI and SLR data. In: H. Drewes (ed), *Proceedings of the IAG Symposium on Geodetic Reference Frames GRF2006*, Munich, Germany. IAG Symposia, Vol. 134, Springer-Verlag, 17–22, 2006, doi: 10.1007/978-3-642-00860-3_3.

VieSched++

Recent Developments and Lessons Learned from Two Years of Fully Automated Scheduling

Matthias Schartner[1], Christian Plötz[2], Helene Wolf[3], Benedikt Soja[1]

Abstract VieSched++ is an open source VLBI scheduling and simulation software that is already operationally used worldwide. Within the IVS, over ten active observing programs are currently scheduled using VieSched++. This accumulates to over 400 sessions for the year 2022 alone. Within this work, the most recent developments of VieSched++ are summarized. Additionally, the quality of the derived schedules is investigated based on the INT2 and INT3 observing programs. Within these programs, the reported UT1-UTC formal errors could be reduced by up to 50 %. Finally, improvements in the robustness of the automated scheduling pipelines are discussed, as well as an outlook of future development plans of VieSched++ is provided.

Keywords Scheduling, VieSched++

1 Introduction

Scheduling is an integral part of every VLBI experiment. It directly determines the quality of the results by defining the observations that will be available for the analysis. Over the last decades almost all geodetic VLBI schedules were generated using the scheduling software *sked* [1], developed and maintained by the NASA Goddard Space Flight Center VLBI group. However, in the most recent years, the new scheduling software *VieSched++*[1] [3], developed at TU Wien and now maintained at ETH Zurich, has become more and more popular. As of today, VieSched++ is used to schedule the IVS observing programs AUA, AUM, CRD, CRF, INT2, INT3, OHG, T2, T2P, VGOS-B, VGOS-C, VGOS-R&D, VGOS-S, as well as other test sessions. This accumulates to a total of approximately 400 schedules that will be scheduled in the year 2022 alone. In order to enable the processing of this huge amount of sessions a fully automated VLBI scheduling pipeline was developed[2]. This pipeline is in operational use since 2020. As of June 2022, over 70 24-hour sessions and over 450 one-hour Intensives have been automatically, and successfully, scheduled and submitted to the IVS Data Centers.

Furthermore, VieSched++ is used for research and development purposes. In addition to classical R&D sessions, such as VGOS-R&D, VieSched++ is also used to test new algorithms, approaches, and capabilities. For example, a VLBI satellite scheduling module is currently being developed and studied at TU Wien.

Within this work, we give an overview of the most recent developments (Section 2), discuss the scheduling quality based on two selected observing programs, namely INT2 and INT3 (Section 3), and report on the status and lessons learned from the fully automated scheduling pipeline (Section 4). Finally, a short outlook regarding the future of VieSched++ is provided (Section 5).

1. ETH Zurich
2. Bundesamt für Kartographie und Geodäsie (BKG)
3. TU Wien

[1] https://github.com/TUW-VieVS/VieSchedpp

[2] https://github.com/TUW-VieVS/VieSchedpp_AUTO

2 Recent Developments

VieSched++ is still in active development, although the development speed of major new features has decreased over the last year to provide some form of stability, required to ensure a reliable operational use.

However, some major updates have still been released within the last year. For the VGOS-R&D session VR2202, the treatment of the sky-coverage objects has been extended. One major goal of VGOS is to greatly improve the sky coverage within short periods [2] for a more rapid determination of tropospheric turbulences. To properly account for different slew rates and visibility areas of VGOS stations, it is now possible to assign custom sky-coverage optimization parameters per sky-coverage object. The sky-coverage optimization parameters describe the saturation of the local sky as a function of the previously scheduled observations, azimuth, elevation, and time. Thereby, multiple stations, such as twin radio telescopes, can share the same sky-coverage object. During VLBI scheduling, one task is to find a good balance between the station sky coverage and the number of scans. The former requires having long slew distances between two consecutive scans, while the latter requires having short slew distances. In practice, this means that stations with a poor common visibility with the remaining network, or stations with slower slew rates, can use smaller saturation areas, leading to a worse distribution of scans over the local sky. In contrast, stations with high slew rates can be parameterized by using larger saturation areas, forcing longer slew angles and therefore a better distribution of scans.

Furthermore, several algorithms, such as the fillin-mode a posteriori, were improved. The motivation for these changes were, again, the VGOS-R&D sessions, in particular the better inclusion of the southern-hemisphere station HOBART12 (Tasmania) with the remaining VGOS network that only consists of northern-hemisphere stations. The imbalanced network geometry leads to a challenging situation to properly include HOBART12 with the remaining network, especially since HOBART12 is scheduled in tagalong mode, meaning that the schedule is first generated without considering HOBART12, while HOBART12 is later added to as many scans as possible. Normally, this leads to a poor inclusion and large idle times for HOBART12, because the remaining stations tend to observe mostly northern-hemisphere sources, which are not visible for HOBART12, especially since only three-station scans are scheduled in VGOS experiments. Figure 1 depicts the observable sky coverage of HOBART12 with the remaining VGOS stations. Only the blue areas would be observable based on the default algorithms.

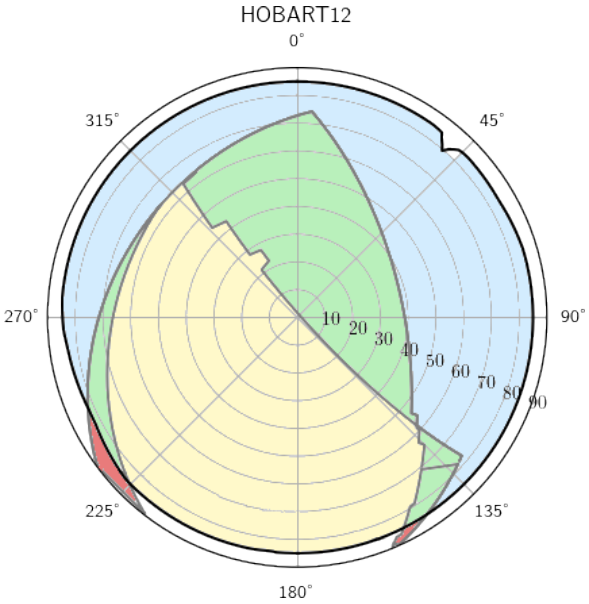

Fig. 1 Sky coverage of HOBART12. Blue: visible by 3+ stations. Green: visible by two stations. Yellow: only visible by HOBART12.

To overcome this issue, the fillin-mode a posteriori is used. After station HOBART12 is added to as many scans as possible using the tagalong mode, a new iteration of fillin-mode is started. Since it happens at the very end of the scheduling process, it is called fillin-mode a posteriori. This mode investigates the station idle times between all consecutive scans and schedules some additional scans in between, in case of available idle time. Within this mode, station HOBART12 is treated as a normal station. Furthermore, also two-station scans are allowed during this special fillin-mode and the restriction of minimum time between two scans to the same source is lowered as well. This leads to a significantly better inclusion of HOBART12 within the remaining network.

Among the improved features is also the previously mentioned satellite scheduling module. Within VieSched++, satellites are now treated similarly as any

other available source. Therefore, the full capability of the source-based parameterization can be utilized. This means that every satellite, or custom-defined group of satellites, can utilize its own set of scheduling parameters. This ensures the highest flexibility when scheduling satellite observations. Furthermore, a manual satellite scheduling graphical user interface (GUI) is available as well. Within this GUI, possible satellite scans can be hand-picked and adjusted freely. After the satellite scans are fixed, the remaining time is filled using classical observations of active galactic nuclei. However, it is to note that the satellite scheduling module is still in development and has been, so far, only used for simulation studies [7].

3 INT2 and INT3 Session Performance

To assess the quality of schedules generated with VieSched++, the INT2 and INT3 observing programs are studied. INT2 sessions are typically observed with a single baseline using a recording rate of 256 Mbps while INT3 sessions are multi-baseline Intensives involving up to five stations and using a recording rate of 1 Gbps [6]. Starting in 2019, INT3 sessions were scheduled using VieSched++ instead of sked and INT2 followed mid-2020. Figure 2 compares the performance of sessions generated with the two scheduling software packages between August 2016 and August 2021. The performance is expressed via the formal error of UT1-UTC. The top plot depicts the most observed INT2 baselines, while the bottom depicts the most frequently used INT3 networks. The bars in the background represent the number of corresponding sessions.

It can be seen that the INT2 performance of baseline IsWz was improved by 11 %, while the improvement is 32 % for baseline KkWz and 44 % for baseline MkWz.

For INT3, the five-station network was improved by 45 %, while the four-station network is improved by 25 %. Only the three-station network shows a degradation of the UT1-UTC precision of 12 %. However, on further inspection, it is revealed that the majority of three-station INT3 sessions were originally scheduled using a bigger network where some stations dropped out. This is indicated by the hatched areas in Figure 2.

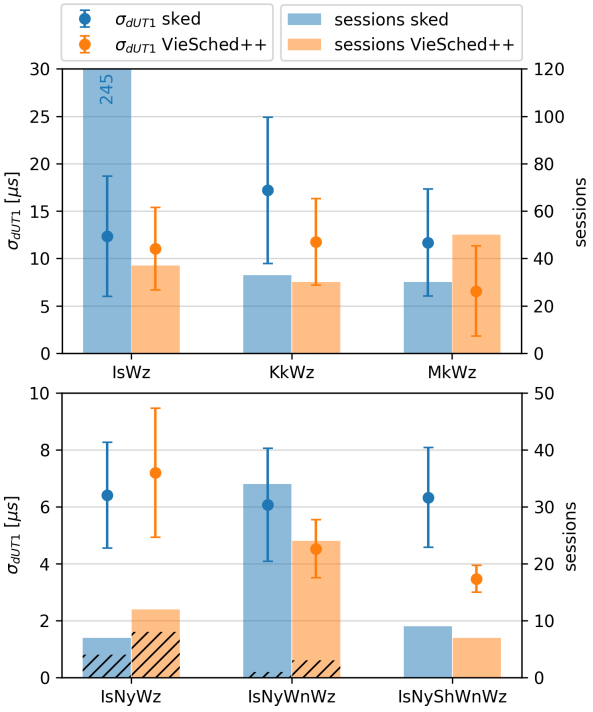

Fig. 2 Top: performance of INT2 sessions grouped by observed baseline. Bottom: performance of INT3 sessions grouped by the observing network. The dashed areas mark sessions that were originally scheduled with a larger network, but only analyzed using the listed stations.

Therefore, these sessions are not suitable for a scheduling comparison.

A more detailed investigation of the INT2 and INT3 session performance including a comparison of the scheduling approaches can be found in [6]. A discussion regarding the utilized VieSched++ Intensive scheduling approach is available in [5], Appendix A.

4 Automated Scheduling

The majority of the schedules created with VieSched++ are generated and distributed using a fully automated scheduling approach. The automated scheduling pipeline is based on a Python framework, which is executed daily. It downloads the most recent schedule master, as well as the scheduling catalogs, and generates the upcoming schedules using templates describing the scheduling approaches that should be taken. In general, several hundred different schedules

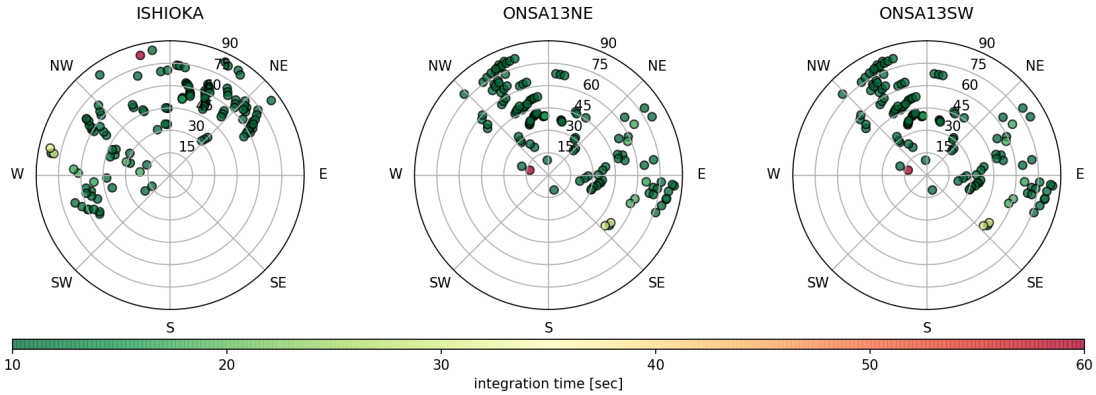

Fig. 3 Sky coverage as reported by the automated VLBI scheduling software for VGOS-B session B22176 (2022-06-25).

are generated per session. Every schedule is further simulated and analyzed one thousand times to assess the expected precision of the estimated geodetic and astrometric parameters. Based on the simulated results, the best performing schedule is selected and distributed. More information regarding the automated scheduling approach can be found in [4].

Within the last years, some major improvements regarding the robustness and quality control of the automated scheduling software were achieved.

First of all, the software does now perform daily checks if a station network has been changed since the submission of the schedule. In case of a network change, the corresponding personnel is notified via mail.

Furthermore, daily checks are conducted if the scheduled sessions are properly available at the IVS Data Centers. Therefore, it is more rigorously checked if the upload has been successful. In case of missing schedules, notifications are distributed via mail as well.

Finally, the quality control has been improved. This is done by a complete overhaul of the reports that are distributed via mail for every scheduled session. The reports do not only include the schedule files but also various statistics and comparisons of the scheduled session with previously scheduled sessions of the same observing program. The statistics are provided graphically. Furthermore, sky-coverage images are distributed, once by color-coding the observation duration per scan and once by color-coding the scan start time. Figure 3 depicts the sky coverage of session B22176 (VGOS-B) with color-coded observation duration. Together this provides a comprehensive but also very concise overview of the scheduling quality. Examples can be seen at the IVS Operation Center DACH webpage.

However, it is to note that some observing programs, such as CRDS and CRF were removed from the automated scheduling pipeline. This was mainly done since these sessions require a more detailed assessment of the observed sources. For every session, the source list is adapted based on previous sessions. Furthermore, special care has to be taken to include enough calibration scans and to also include some special sources. Since not all of these sources are properly defined within the sked catalogs, some further adjustments are needed. For example, the integration time is fixed for some sources with insufficient or missing flux density information. More research and development work is required to be able to automatically schedule CRDS and CRF sessions again.

It is to note that some R&D sessions are not scheduled using the automated approach.

5 Future Plans

In future, it is planned to further extend VieSched++.

First of all, it will be required to work towards defining a new set of scheduling catalogs. Currently, VieSched++ utilizes the sked catalogs. However, several key parameters, especially for VGOS, are not included in the current catalog files. This does not only include the VGOS observing mode definition but also (elevation-dependent) SEFD values for the VGOS frequencies, as well as new methods of defining source flux densities.

Next, it is planned to improve the simulation capabilities. Scheduling is only as good as the underlying simulations. Deficiencies in simulations will prevent the selection of the most optimal schedule. Therefore, improving simulations will be a key requirement to improve scheduling in the future. In particular, it is planned to provide custom tropospheric turbulence parameters per station, which should lead to more realistic simulations.

Another project includes the mitigation of spaceborn radio frequency interference (RFI) via dynamic masks. With the drastic increase of satellites emitting radio signals, it will be required to properly mask areas where satellites are present in order to not schedule observations in these directions.

6 Conclusion

Within the IVS, VieSched++ is operationally used for over ten active observing programs. In the year 2022, it is expected that the schedules of around 400 VLBI experiments of the IVS will be generated using VieSched++.

In this work, some of the more recent major developments are briefly introduced. This includes a more flexible definition of the sky-coverage objects, potentially leading to an improved sky coverage at the stations, an improvement of existing algorithms, as well as an improvement of the satellite scheduling module. While the improved sky-coverage definition has already been utilized in VGOS-R&D sessions, the satellite scheduling module has been, so far, only used for simulation studies.

Moreover, the quality of the operationally generated schedules was assessed by investigating the INT2 and INT3 session performance. Thereby, it was revealed that the formal errors of UT1-UTC were reduced by up to 50 %. More detailed investigations regarding the INT2 and INT3 session performance is available in [6].

Furthermore, a report regarding the automated scheduling pipeline [4] is presented. It is in operational use since 2020 and in total over 500 IVS session have already been scheduled fully automatically. Improvements in the automated scheduling pipeline aim to provide a more robust system. Therefore, additional checks are executed every day looking for changes in the scheduled station network after schedule submission and checking the availability of uploaded schedules. Furthermore, the reports that are distributed for every scheduled session were overhauled. The reports include valuable statistics and comparisons of the current schedule with past schedules of the same observing program, allowing for a quick evaluation of the scheduling quality.

Overall, it can be seen that VieSched++ is in a healthy state. It is still actively developed and maintained and the resulting schedules are of excellent quality, while mostly being generated fully automatically.

References

1. J. Gipson, “An introduction to Sked,” in: D. Behrend and K.D. Baver (eds) International VLBI Service for Geodesy and Astrometry 2010 General Meeting Proceedings, pp. 77–84, NASA/CP-2010-215864. https://ivscc.gsfc.nasa.gov/publications/gm2010/IVS-2010-General-Meeting-Proceedings.pdf
2. B. Petrachenko, A. Niell, D. Behrend, B. Corey, J. Böhm, P. Charlot, A. Collioud, J. Gipson, R. Haas, T. Hobiger, Y. Koyama, D. MacMillan, Z. Malkin, T. Nilsson, A. Pany, G. Tuccari, A. Whitney, J. Wresnik, “Design aspects of the VLBI2010 system,” Progress Report of the IVS VLBI2010 Committee, NASA/TM-2009-214180, 2009. https://ivscc.gsfc.nasa.gov/publications/misc/TM-2009-214180.pdf
3. M. Schartner and J. Böhm, “VieSched++: A New VLBI Scheduling Software for Geodesy and Astrometry,” Publications of the Astronomical Society of the Pacific, vol. 131, no. 1002. IOP Publishing, p. 084501, Jun. 18, 2019. doi: 10.1088/1538-3873/ab1820.
4. M. Schartner, C. Plötz, and B. Soja, “Automated VLBI scheduling using AI-based parameter optimization,” Journal of Geodesy, vol. 95, no. 5. Springer Science and Business Media LLC, Apr. 25, 2021. doi: 10.1007/s00190-021-01512-w.
5. M. Schartner, L. Kern, A. Nothnagel, J. Böhm, and B. Soja, “Optimal VLBI baseline geometry for UT1-UTC Intensive observations,” Journal of Geodesy, vol. 95, no. 7. Springer Science and Business Media LLC, Jun. 19, 2021. doi: 10.1007/s00190-021-01530-8.
6. M. Schartner, C. Plötz, and B. Soja, “Improvements and comparison of VLBI INT2 and INT3 session performance,” Journal of Geodesy, vol. 96, no. 4. Springer Science and Business Media LLC, Apr. 2022. doi: 10.1007/s00190-022-01621-0.
7. H. Wolf, J. Böhm, A. Nothnagel, U. Hugentobler, and M. Schartner, “Precision of Galileo satellite orbits obtained from simulated VLBI observations,” EGU General Assembly 2022, Vienna, Austria, 23–27 May 2022, EGU22-4834, https://doi.org/10.5194/egusphere-egu22-4834, 2022.

A Comparison of VieSched++ Simulations with Observed VLBI Sessions

Sara Hardin[1]

Abstract The scheduling software VieSched++ uses simulations to predict the formal errors for Earth Orientation Parameters (EOPs) in a variety of generated schedules as a means of selecting the best one. To determine how closely the simulations match real Very Long Baseline Interferometry (VLBI) observations, VieSched++ is used to simulate existing VLBI schedules and predict EOP formal errors. These predicted formal errors are then compared to the observed formal errors produced by the USNO Analysis Center for both one-hour and 24-hour geodetic VLBI sessions. Comparisons use the Pearson correlation coefficient (ρ) to determine the correlation between simulated and observed EOPs.

Keywords VLBI, Scheduling, Simulation

1 Introduction

Simulation can be a powerful tool for improving VLBI scheduling techniques. It allows for the optimization of individual schedules and helps inform observing strategies for future sessions types. However, using these predictions is only effective if the simulation results reflect actual observations.

VieSched++ [1] is VLBI scheduling software that generates multiple schedules (typically between ten and 1,000) with different parameters. The schedules are then simulated to obtain formal error predictions for EOPs. These predictions are used to find schedules with favorable formal errors, and to ultimately select a single schedule to use. Numerous VLBI sessions are already scheduled for the International VLBI Service for Geodesy and Astrometry (IVS) using VieSched++ with simulations; the DACH Operation Center uses it for the AUAs, CRDs, CRFs, INT2/3s, and more.

VieSched++ simulations are also used to study improvements to the design of VLBI sessions. They have been used to suggest new VLBI station locations [2] and the optimal geometry for geodetic sessions [3, 4].

1. U.S. Naval Observatory

2 Methodology

IVS VLBI S/X schedules are simulated with VieSched++ and are compared to the observed formal errors from the sessions.

The observed EOP formal errors are taken from usn2021c.eoxy and usn2021c.eopi, which are published by the USNO Analysis Center and are publicly available from the CDDIS, BKG, and OPAR Data Centers.

Table 1 Session summary.

Session Type	Date Range	# Sessions
1-hour Int. (I, Q)	2020-01-02 to 2022-03-10	720
24-hour sess. (R1, R4)	2020-01-02 to 2022-02-28	225

Predicted EOP formal errors are generated using existing IVS schedules. 113 IVS-R1 (R1928–R11040) and 112 R4 (R4927–R41039) schedules are used for 24-hour geodetic sessions. 486 IVS-INT1 (I20002–I22069) and 234 INT2/INT3 (Q20004–Q22066) schedules are used for the one-hour UT1-UTC Intensive sessions. These sessions are summarized in

Table 1. These schedules are input into VieSched++ with the *–sim* flag, along with the default simulation templates provided with VieSchedpp_AUTO. When simulated, all scheduled observations are considered to be successful when calculating the formal errors.

For fitting, all one-hour Intensive sessions are combined and all 24-hour sessions are combined. Any 1-sigma outliers for observed formal errors are rejected from fitting.

3 Results

IVS Intensive simulations and observations for UT1-UTC formal errors tend to agree fairly well, with a Pearson correlation coefficient of $\rho = 0.519$. The relationship between simulations and observations is linear aside from a large number of high formal errors in the observation data (Figure 1). A histogram of the ratios also demonstrates the large number of sessions with high formal errors from the observed data (Figure 2). Since one-hour sessions have a small number of scans and the simulations assume all scans are successful, any failed observations could cause formal errors to deviate from predictions.

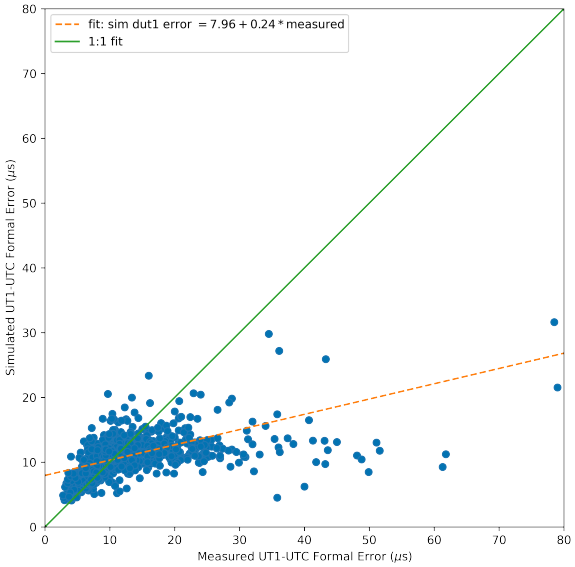

Fig. 1 Simulated UT1-UTC formal errors versus observed formal errors for IVS Intensive sessions (I, Q). The dashed orange line is the line of best fit, while the solid green line denotes a 1:1 fit.

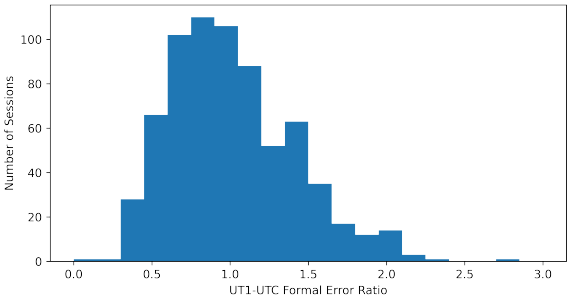

Fig. 2 Distribution of the ratio of simulated to observed UT1-UTC formal errors for IVS Intensive sessions.

IVS 24-hour simulations for most EOP formal errors also correlate well with observed formal errors. UT1-UTC, X Nutation, and Y Nutation all correlate strongly ($\rho = 0.630$, $\rho = 0.759$, and $\rho = 0.754$, respectively). There is more scatter in the relationship between simulated and observed errors for the X and Y pole coordinates ($\rho = 0.185$ and $\rho = 0.230$, respectively). These relationships are shown in Figures 3 and 4.

The results for both Intensive and 24-hour sessions are summarized in Table 2.

Table 2 Simulation statistics.

EOP	# Sessions Fit	Pearson Corr. Coeff. (ρ)
1-hour UT1-UTC	700	0.519
24-hour UT1-UTC	183	0.630
X-axis Polar Motion	195	0.185
Y-axis Polar Motion	194	0.230
X-axis Nutation	199	0.759
Y-axis Nutation	194	0.754

4 Conclusions

For IVS 24-hour sessions, VieSched++ is able to simulate the formal errors for UT1-UTC and nutation in a way that correlates well with the observed formal errors. The correlation for polar motion is much weaker.

For IVS one-hour Intensive sessions, VieSched++ is able to simulate UT1-UTC formal errors. Although most of the predictions correlate with observations, a subset of the observed formal errors tend to be much higher than predicted. This may be due to failed observations in sessions that have relatively few scans.

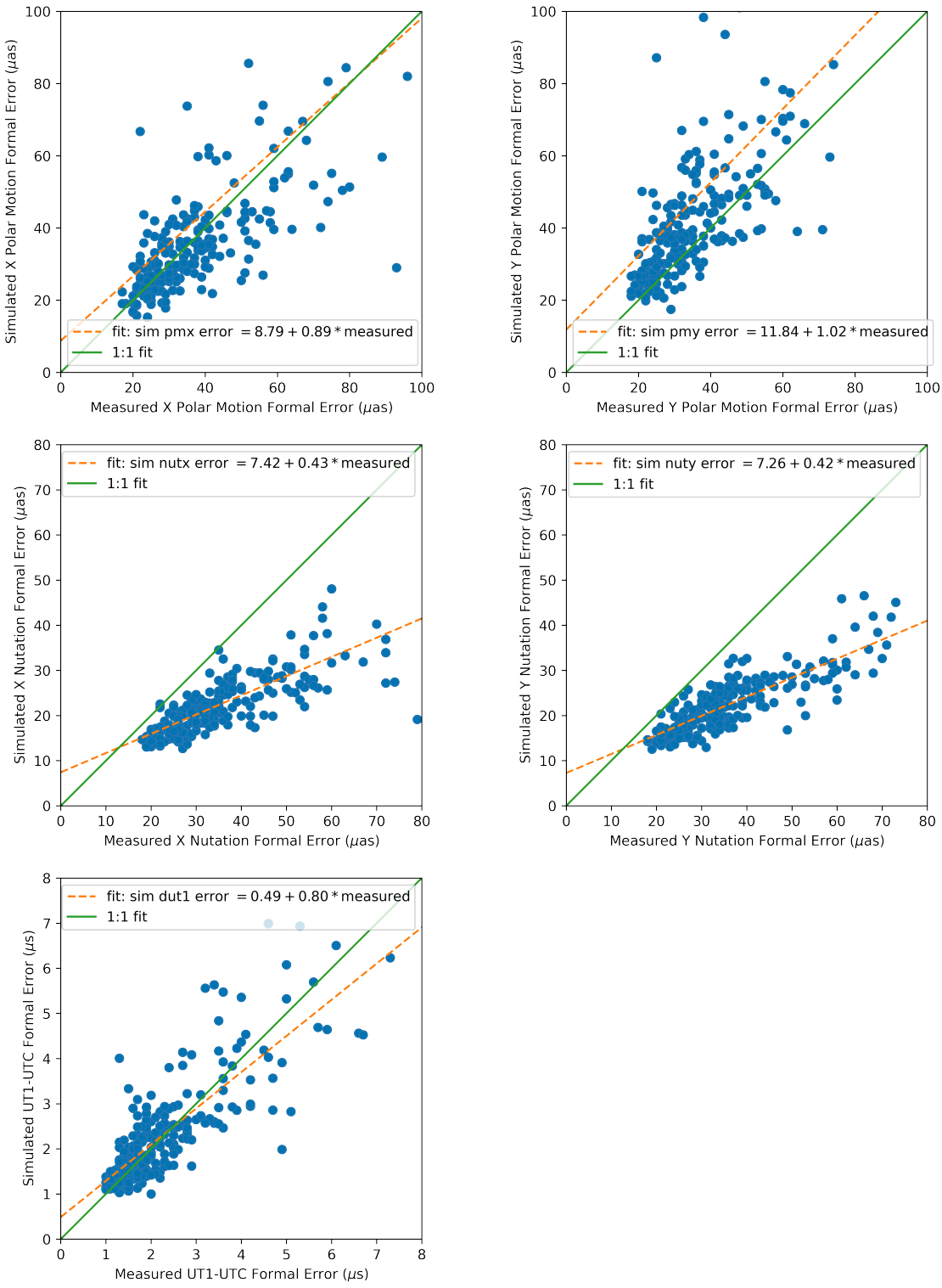

Fig. 3 Simulated EOP formal errors versus observed formal errors for IVS rapid sessions (R1, R4). The dashed orange line is the line of best fit, while the solid green line denotes a 1:1 fit.

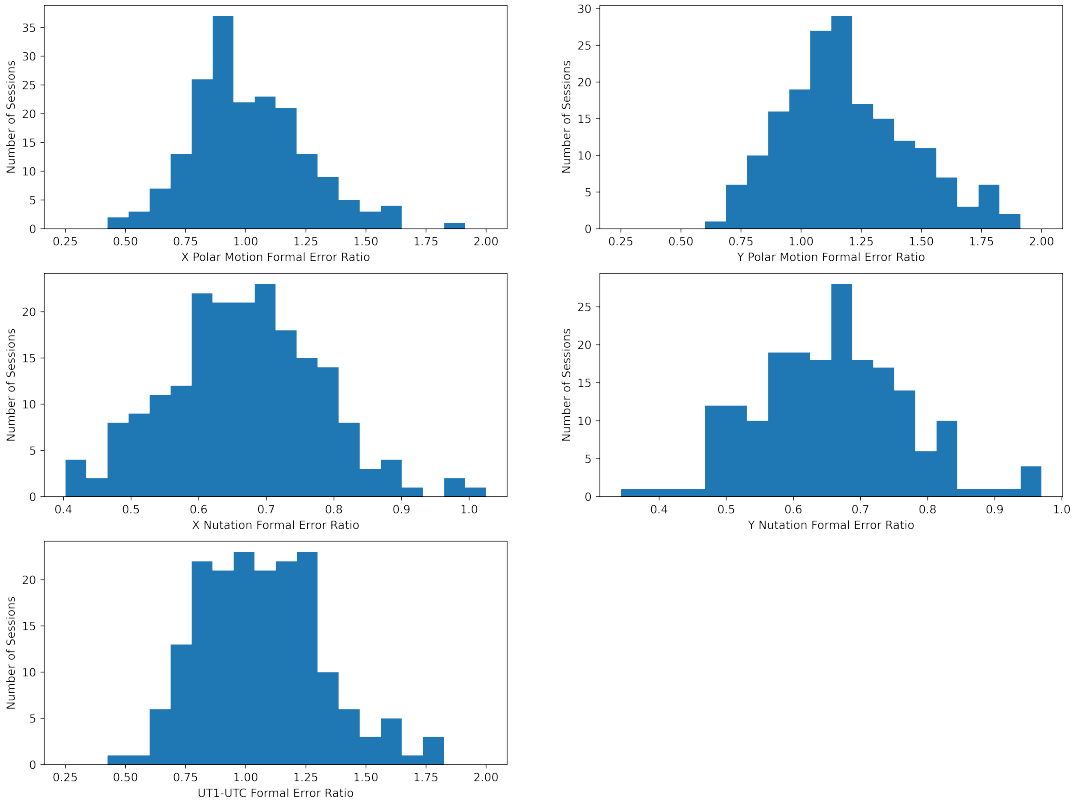

Fig. 4 Distribution of the ratio of simulated to observed EOP formal errors for IVS rapid sessions.

VGOS sessions were not compared because for VGOS sessions, no observed EOPs have been published yet. Possible avenues for future work include comparing VGOS sessions, investigating why polar motion is only weakly correlated, and examining other comparison methods (such as computing f statistics).

References

1. Schartner, M. and Böhm, J. (2019). VieSched++: A New VLBI Scheduling Software for Geodesy and Astrometry. PASP 131 084501.
2. Schartner, M. and Böhm, J. (2020). Optimizing schedules for the VLBI global observing system. J Geod 94, 12.
3. Kern, L. M. (2021). Simulation of VLBI intensive sessions for the estimation of UT1 [Diploma Thesis, Technische Universität Wien]. reposiTUm. https://doi.org/10.34726/hss.2021.92322
4. Schartner, M., Kern, L., Nothnagel, A., Böhm, J., Soja, B. (2021). Optimal VLBI baseline geometry for UT1-UTC Intensive observations. J Geod 95, 75.

Session 4

Interpretation of VLBI Results in Geophysics, Geodesy and Astrometry

IVS IAG SUOMEN AKATEMIA

NLS FINNISH GEOSPATIAL RESEARCH INSTITUTE FGI

ITRF2020 and the IVS Contribution

Zuheir Altamimi[1], Paul Rebischung[1], Xavier Collilieux[1,2], Laurent Métivier[1], Kristel Chanard[1]

Abstract The ITRF2020 is provided in the form of an augmented reference frame. In addition to station positions, velocities, and Earth Orientation Parameters (EOPs), parametric functions for both Post-Seismic Deformation (PSD) for stations subject to major earthquakes and seasonal (annual and semi-annual) signals expressed in the Satellite Laser Ranging (SLR) center-of-mass and the center-of-figure frames are also provided to the users. At the time of writing, a full article on ITRF2020 results is under preparation [1]. However, this paper provides an extended summary of ITRF2020, with a special focus on the IVS/VLBI contribution, in particular the level of the scale agreement of the four techniques as well as their variations and behavior over time.

Keywords VLBI, ITRF, ITRF2020

1 Extended Summary

The reader may refer to the full article on ITRF2020, which is under preparation by the same authors [1]. However, we provide here the main features of ITRF2020, focusing on the contribution of the International VLBI Service for Geodesy and Astrometry [2, 3]. The ITRF2020 is characterized by the following key points:

- The input data to the ITRF2020 are in the form of the time series of station positions and EOPs, provided by the four technique services of the International Association of Geodesy: weekly solutions for IDS/DORIS and ILRS/SLR, daily solutions for IGS/GNSS, and session-wise solutions for IVS/VLBI.
- 253 local tie vectors between GNSS and the three other technique reference points were used: 77 for VLBI, 53 for SLR, and 123 for DORIS. These tie vectors were actually used in the form of station coordinates provided in SINEX format with full variance-covariance information.
- An innovative and new analysis strategy was adopted for the ITRF2020 computation, that is, rigorously accumulating the full time series of the four techniques all together and adding local ties and co-motion constraints at co-location sites (equating station velocities and seasonal signals).
- The Post-Seismic Deformation (PSD) parametric models for sites subject to major earthquakes were refined using the ITRF2020 extended data. As an example, Figure 1 exhibits the trajectory of the VLBI station at Concepcion, Chile, before and after the 2010 mega earthquake where the PSD parametric model determined by IGS/GNSS data fits perfectly the VLBI station position time series.
- The number of the IVS/VLBI session-wise solutions included in the final ITRF2020 combination is 6,178, spanning in total 41 years of observations, involving 154 stations at 117 sites, with only 14 sites in the southern hemisphere. The majority (86%) includes a small number of stations, ranging between three to nine stations. 842 (13%) sessions involve ten to 19 stations; eight sessions have 20 stations, while one session exceptionally includes 31 stations. In addition to station positions, the solutions include the full set of EOPs.

1. IGN-IPGP, Université Paris Diderot UFR STEP / IPGP 35 rue Hélène Brion 75205 Paris Cedex 13, France
2. IGN-IPGP-ENSG, 6-8 Avenue Blaise Pascal, 77420 Champs-sur-Marne, France

- The scale of the ITRF2020 long-term frame is determined using internal constraints in such a way that there are zero scale and scale rate between ITRF2020 and the scale and scale rate averages of VLBI selected sessions up to 2013.75 and SLR weekly solutions covering the time-span 1997.7–2021.0, as depicted in Figure 2. This is the first time in ITRF history where the intrinsic SLR and VLBI scales agree at the level of 0.15 ppb at epoch 2015.0 (equivalent to 1 mm at the equator), with zero drift. The reasons for the scale offset before 1997.7 for SLR and the scale drift after 2013.75 for VLBI are unknown to the authors and are under investigation by the ILRS and IVS. The noisy and scattered scale before 1993.0 for SLR are due to the weak observation of the LAGEOS I satellite. Figure 2 (bottom panel) illustrates the IDS/DORIS and IGS/GNSS scale time series that exhibit significant offsets and drifts with respect to ITRF2020: $\simeq 1.4$ and $\simeq 0.7$ ppb at epoch 2015.0 and $\simeq 0.03$ and $\simeq 0.02$ ppb/yr for IDS/DORIS and IGS/GNSS, respectively.

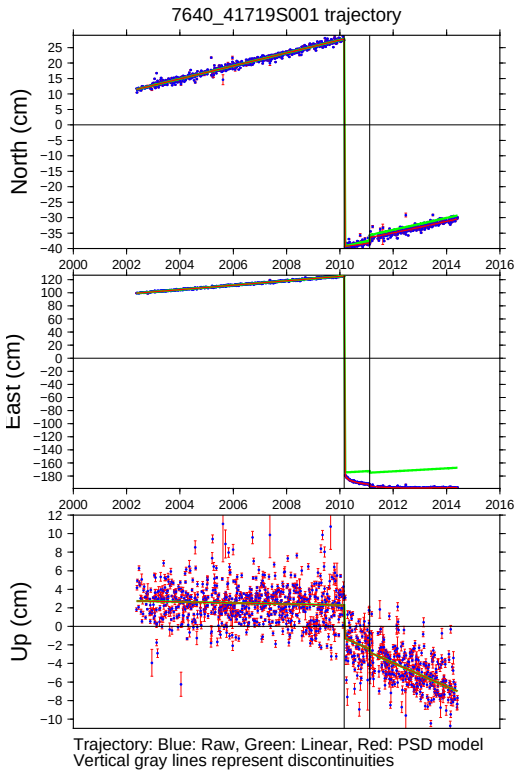

Fig. 1 Trajectory of TIGOCONC station in ITRF2020.

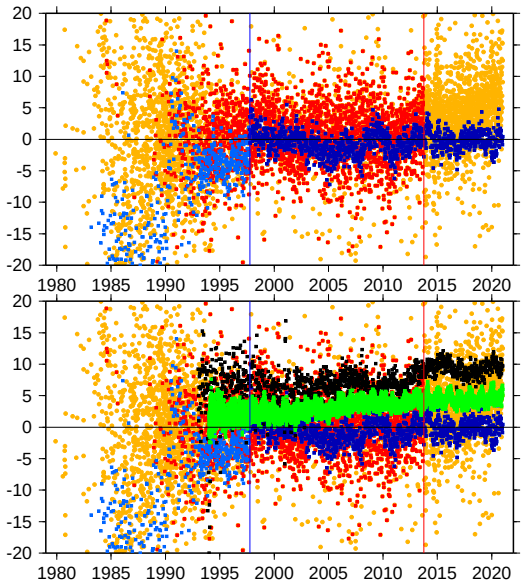

Fig. 2 SLR and VLBI scale time series with respect to ITRF2020 (top), adding DORIS and GNSS (bottom), in mm. Light blue and orange: all SLR and VLBI time series; dark blue and red: selected series whose average defines the ITRF2020 scale; black: DORIS; and green: GNSS.

Acknowledgements

The ITRF activities are funded by the Institut National de l'Information Géographique et Forestière (IGN), France, and partly by the Centre National d'Études Spatiales (CNES), under the TOSCA grant. We are indebted to all Analysis and Combination Centers of the Technique Services who constantly provide data for ITRF solutions which would not exist without their valuable contributions.

References

1. Z. Altamimi, P. Rebischung, X. Collilieux, L. Métivier, K. Chanard, ITRF2020: An augmented reference frame refining the modeling of nonlinear station motions, article under preparation, 2022.
2. Hellmers, H., Modiri, S., Bachmann, S., Thaller, D., Bloßfeld, M., Seitz, M., Gipson, J.: Combined IVS contribution to the ITRF2020, International Association of Geodesy Symposia series, 2022 (under review)
3. Nothnagel, A., T. Artz, D. Behrend and Z. Malkin, "International VLBI Service for Geodesy and Astrometry - Delivering high-quality products and embarking on observations of the next generation", Journal of Geodesy, Vol. 91(7), pp. 711–721, DOI 10.1007/s00190-016-0950-5, 2017.

Scale Evaluation of the ITRF2020 Solution

Hendrik Hellmers[1], Sadegh Modiri[1], Sabine Bachmann[1], Daniela Thaller[1], Mathis Bloßfeld[2], Manuela Seitz[2], John Gipson[3]

Abstract As the next official realization of the International Terrestrial Reference System, the ITRF2020 represents the successor of the currently used frame, ITRF2014. This global solution is based on an inter-technique combination of all four space geodetic techniques—VLBI, GNSS, SLR, and DORIS—and benefits from a variety of contributions from different international institutions. In this context, the Combination Center of the International VLBI Service for Geodesy and Astrometry (IVS)—operated by the Federal Agency for Cartography and Geodesy (BKG, Germany) in close cooperation with the Deutsches Geodätisches Forschungsinstitut (DGFI-TUM, Germany)—generates the final VLBI contribution to ITRF2020. Thereafter, an intra-technique combination is applied using the individual contributions of multiple Analysis Centers (ACs) with different software packages. For the contribution to the ITRF2020, sessions containing 24-hour VLBI observations from 1979 until the end of 2020 were processed by 11 ACs and submitted to the IVS Combination Center as session-wise SINEX files. These files contain datum-free normal equations with station coordinates, source positions, and full sets of Earth Orientation Parameters (EOP). To ensure consistency between all AC contributions, normal equation transformations to equal epochs and a priori values were carried out for every AC-specific normal equation system before stacking them in order to get the IVS combined solution. The resulting individual solutions, as well as the combination, are subject to further analysis concerning EOP and station coordinates as well as the scale and a VLBI-only Terrestrial Reference Frame (VTRF). This contribution focuses on detailed investigations concerning the scale of the IVS contribution and the global solution. In this paper, we compare the IVS contribution with the combined ITRF2014 and ITRF2020 solutions. In addition, detailed statements on the accuracy of ERP estimates are carried out. In this context, the individual solutions of the different Analysis Centers are compared and investigated concerning potential AC- and/or software-related systematics.

Keywords ITRF2020, IVS, Combination, Terrestrial Reference Frame, Helmert Transformation, Scale

1 Introduction

The International Terrestrial Reference Frame (ITRF), as the realization of the International Terrestrial Reference System (ITRS), is commonly used as the official global reference frame. It includes positions and velocities of globally distributed observing stations, qualifying the ITRF as a basis for scientific research and applications in geosciences. Common examples are climate change, global sea-level rise, and crustal deformations, e.g., due to earthquakes (Métivier et al., 2014).

For ensuring the high quality of the current ITRF, an update is computed every five to six years, considering up-to-date models, parameterizations, and data evaluation. Besides newly observed satellites, the utilization of new observing stations leads to a more dense

1. Federal Agency for Cartography and Geodesy (BKG), Department Geodesy, Frankfurt am Main, Germany
2. Deutsches Geodätisches Forschungsinstitut of the Technische Universität München (DGFI-TUM), Munich, Germany
3. NVI, Inc./NASA Goddard Space Flight Center, Greenbelt, Maryland

station network for improving the station geometry in some cases.

The upcoming ITRF2020 includes new general physical models for pole tides and high-frequency Earth rotation, as well as VLBI-specific models for galactic aberration and the gravitational deformation of the radio telescopes. The final ITRF2020 product—which replaces the current ITRF2014 (Altamimi et al., 2016)—is released by the ITRS Center of the International Earth Rotation and Reference Systems Service (IERS)[1]. The applied physical constants and mathematical models for data analysis are provided by the IERS 2010 Conventions (Petit G, Luzum B, 2010).

To benefit from the individual strengths of the different observation methods, the ITRF computation is based on an inter-technique combination of the four space-geodetic observation techniques, i.e. Global Navigation Satellite Systems (GNSS), Satellite Laser Ranging (SLR), Doppler Orbitography and Radiopositioning Integrated by Satellite (DORIS), and Very Long Baseline Interferometry (VLBI; Thaller, 2008). While the first three techniques are satellite-based and therefore deliver solutions realizing an Earth-centered reference system, VLBI is the only technique observing extragalactic objects (radio sources), which enables determination of the orientation of Earth in inertial space. Consequently, VLBI delivers the full set of Earth Orientation Parameters (EOP).

The Combination Center of the International VLBI Service for Geodesy and Astrometry (IVS; Nothnagel et al., 2017) is located at the Federal Agency for Cartography and Geodesy (BKG, Germany) and works in close cooperation with the Deutsches Geodätisches Forschungsinstitut of the TU München (DGFI-TUM, Germany; cf. Bachman et al., 2017). It realizes a combination of individual VLBI solutions from multiple IVS Analysis Centers (ACs) that represents the IVS contribution to the ITRF. This intra-technique combination is based on the level of normal equations (NEQs; Venebusch et al., 2007; Böckmann et al., 2010) and realized by utilizing the software DOGS-CS. Finally, the combined IVS contribution to the ITRF2020 is delivered as session-wise SINEX files (Bachmann et al., 2016).

This paper gives an overview of the IVS contribution to ITRF2020. Section 2 describes the data basis of the pre-analyzed VLBI contributions, and Section 3 summarizes the IVS combination procedure. Section 4 presents the evaluation of the contributions by the individual IVS ACs and the combined product. The scale w.r.t. the current ITRF2014 and the upcoming ITRF2020 is investigated and analyzed concerning offset and trend behavior. In addition, the impact of the weighting strategy of the different software packages on EOP estimation is investigated.

2 Contribution by IVS Analysis Centers

For the ITRF2020 contribution, the individual ACs deliver 24-hour session-wise VLBI re-processed data from 1979 until the end of 2020. The required SINEX format contains datum-free normal equations, including station coordinates, source positions, and EOP. The guidelines for the homogeneous analysis were provided by the IVS Analysis Coordinator[2]. The different ACs contributed to the IVS Combination Center almost 6,600 sessions that were subjected to several quality controls (numerical stability, completeness and format, and application of the required precession and nutation models) to ensure consistency. Within the combination process (Section 3) an outlier detection based on a *three-sigma range test* rejects contributions with low quality. Finally, 94.5% of the submitted sessions could be successfully combined. Table 1 summarizes the different ACs and the utilized software packages, respectively.

Table 1 Software packages used by the different IVS ACs.

AC	Name	Software
ASI	Italian Space Agency	CALC/SOLVE
BKG	Federal Agency for Cartography and Geodesy	CALC/SOLVE
DGFI-TUM	Deutsches Geodätisches Forschungsinstitut	DOGS-RI
GFZ	German Research Centre for Geosciences	PORT
GSF	Goddard Space Flight Center	CALC/SOLVE
IAA	Institute of Applied Astronomy	QUASAR
NMA	Norwegian Mapping Authority	Where
OPA	Observatoire de Paris	CALC/SOLVE
OSO	Onsala Space Observatory	ivg::ascot
USNO	United States Naval Observatory	CALC/SOLVE
VIE	Vienna University of Technology	VieVS

[1] https://itrf.ign.fr/en/solutions/ITRF2020

[2] https://ivscc.gsfc.nasa.gov/IVS_AC/IVS-AC_ITRF2020.html

The goal of the combination is to benefit from the diversity of contributions and improve the quality of estimated parameters compared to the individual solutions delivered from the ACs. In our case, 11 ACs submitted their re-processed solutions, and seven different software packages were utilized.

For ITRF2020, almost 92% of the combined sessions (i.e., 5,725) include the contributions of nine or more ACs. On the other hand, 122 submitted sessions include three to four ACs only and are mostly characterized by a poor configuration of small regional networks.

3 IVS Combination Process

The main goal of the intra-technique combination is the generation of precise and stable session solutions through the reduction of the analysis noise characterized by the individual data analysis and modelling. In addition, AC-specific systematics are identified and considered. Furthermore, the combination on the level of normal equations, as performed here, allows for a correct consideration of correlations between all (explicitly and implicitly) included parameters.

The actual procedure of the combination process comprises several steps which ensure consistency of the different contributions, an outlier detection for rejecting data with poor quality, and the setting of datum conditions for estimating station coordinates and EOP. Therefore, a session-wise transformation to equal epochs and a priori values is carried out. The reference epoch is the middle of the observation interval, and the TRF is defined by the latest IVS Quarterly solution (VTRF 2020/Q2), which represents an update of the reference frame ITRF2014.

For computing individual solutions, No-Net-Rotation (NNR) and No-Net-Translation (NNT) conditions w.r.t. the a priori reference frame are applied based on a subset of core stations. The source positions are fixed to ICRF3 and are eliminated from the equation system. In contrast, the full set of EOP is estimated as free parameters. The individual parameter estimates (station coordinates and EOP) are subject to an outlier detection (Rousseeuw et al., 2005; Bachmann et al., 2012). Finally, the combined solution consists of the accumulated and relatively weighted contributions from all ACs with stacked station coordinates and EOP. The individual weighting factors result from a variance component estimation (VCE) procedure respecting the global variance factor.

4 VLBI Evaluation Results

In order to assess the quality of the IVS product, evaluations of the resulting estimates were carried out. In this work, we focus on the scale determination of the combined product w.r.t. the ITRF2020 and—for obtaining information about changes to the current ITRF—the ITRF2014. Furthermore, it is shown how software-related systematics affect the applied weighting strategy.

The scale between the VLBI solutions and the ITRF2014/2020 is computed by session-wise seven-parameter Helmert-transformations using a predefined network of 155 globally distributed core stations with high accuracy. Characterized by an adequate number of observations over a time period of several years, uncertainties within the scale estimation due to the station network are assumed to be minimal.

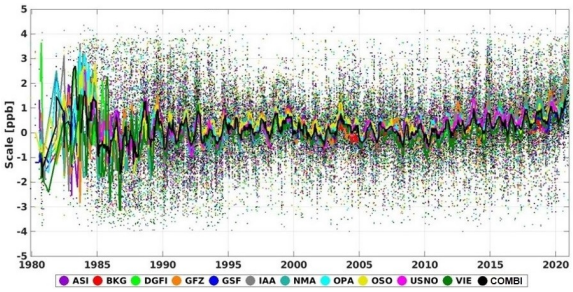

Fig. 1 The scale difference of individual solutions and the IVS combination w.r.t. ITRF2020.

Figure 1 shows the scale differences of the individual and the combined solutions w.r.t. ITRF2020. The dots illustrate the raw scale parameters for each session, and the continuous graphs result from applying a moving median filter of 90 days. The combination, in this case, mathematically describes a weighted mean of the individual solutions.

The first years are characterized by large variations at all solutions with a maximum value of ± 3 ppb at the 90-day median. This can be explained by the weak network configuration in the early years before 1990,

when only a fraction of the current VLBI station network was operating. However, after 1990, a nearly constant scatter is observed.

Furthermore, an annual oscillation becomes obvious over the whole time span due to non-tidal loading deformations. These are not corrected within the ITRF2020 contribution and are causing a seasonal signal within the scale. In addition, the time series are characterized by a significant drift after 2015, where the absolute scale differences w.r.t. ITRF2020 increased by a factor of four in comparison to the constant part of the time series. The reason for the drift is still not explained and is the subject of further research. Nevertheless, a good agreement on the scale estimates could be reached between all ACs, and—as expected—the combined solution appears in the middle of the individual estimates.

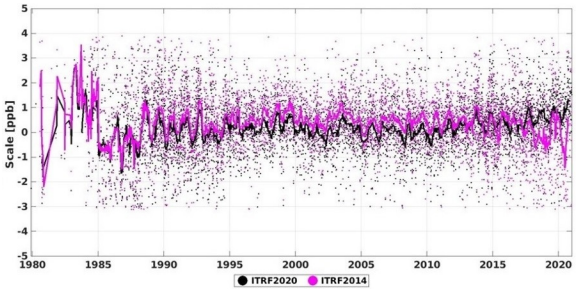

Fig. 2 The scale difference of the IVS combination w.r.t. ITRF2014 and ITRF2020.

Figure 2 shows the comparison of the scale difference between ITRF2014 and ITRF2020 w.r.t. the combined solution. After the initial uncertainty, both time series show a similar behavior until 2015. A divergence can be recognized for the last five years. Although the ITRF2020 scale shows an explicit drift, a reduction of the scatter could be reached compared to ITRF2014. This is a result of an extended data basis for the ITRF2020 contribution. Finally, a mean offset of 0.25 ppm and 0.40 ppm for the constant parts of ITRF2020 and ITRF2014, respectively, could be derived.

As supplements, Figure 3 and Figure 4 show the unweighted offsets and WRMS values of the scale for the individual and the combined solutions w.r.t. ITRF2014 and ITRF2020, respectively. In the first case, the WRMS values of all solutions are in the range of about 1.5 ppm. Thereby, the combination is

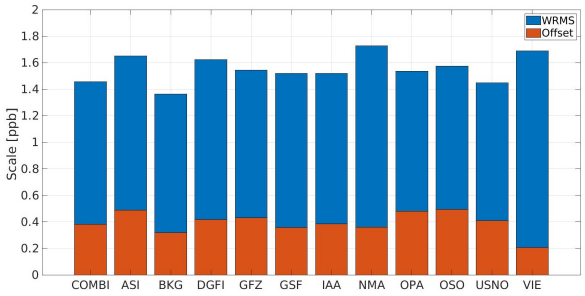

Fig. 3 Mean scale offsets of the individual and the combined solutions w.r.t. ITRF2014.

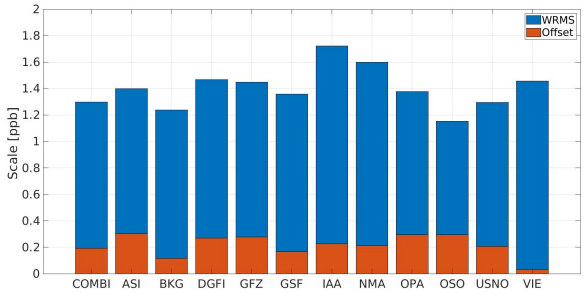

Fig. 4 Mean scale offsets of the individual and the combined solutions w.r.t. ITRF2020.

characterized by the highest accuracy compared to the individual solutions (only the BKG AC has a lower WRMS value because this AC delivered fewer SINEX files compared to other ACs, especially in the early years).

In comparison to that, the WRMS values of the ITRF2020 scales are in the range of 1.3 ppb and, hence, indicate a higher accuracy compared to the previous case. Except for the contributions of BKG and OSO, the combination reaches the highest accuracy level in comparison to the individual solutions. Moreover, the

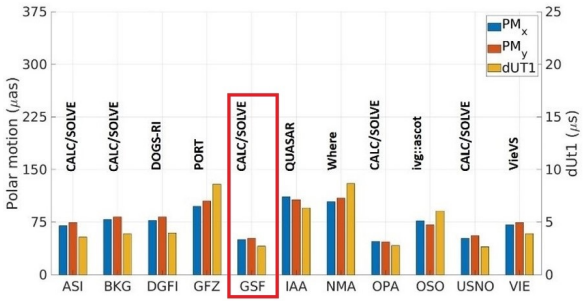

Fig. 5 WRMS of ERP estimation (AC minus Combination). Individual weights per AC are applied.

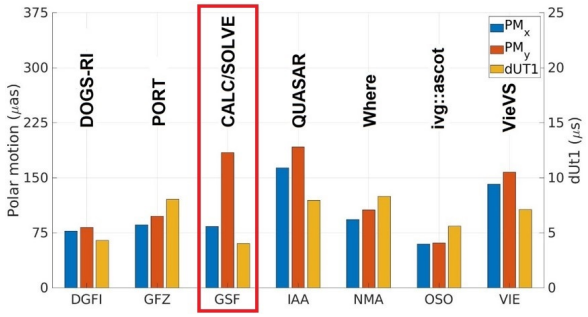

Fig. 6 WRMS of ERP estimation (AC minus Combination). Only one contribution per software.

scale offsets are almost in the range of 0.2 ppb. Consequently, the mean scale difference w.r.t. ITRF2014 could be reduced by about a factor of two.

In addition to the findings about the scale, we carried out a detailed investigation concerning software dependencies on the weighting strategy. Figure 5 shows the WRMS values of polar motion and dUT1 for all individual ACs w.r.t. the combined solution. The fact that five ACs utilize the CALC/SOLVE software package causes a strong dependency of the combination on these contributions. A higher accuracy level in comparison to the remaining ACs can be observed. The GSF solution is characterized by significantly smaller WRMS values for all three ERP components. Reducing the impact of CALC/SOLVE, a second combination type was calculated, using every software-specific contribution only once. Figure 6 shows the WRMS values of the remaining seven ACs. In this case, the GSF represents the CALC/SOLVE solution.

It becomes evident that the accuracy level for GSF decreases (especially for the polar motion), confirming that a significant impact on the number of software appearances exists. Applying an equally distributed utilization of the software packages leads to a more independent combination, which will be respected in further works. An adapted weighting strategy concerning software tools will be focused on.

5 Conclusion and Outlook

Detailed investigations about the scale of the IVS contribution to ITRF2020 were presented in this paper. The IVS Combination Center delivers a session-wise combination of the individual contributions of 11 Analysis Centers. For that, a combination on the level of normal equations is carried out, where EOP and station coordinates are stacked. The source positions are fixed to ICRF3 and are eliminated from the equation system. Based on a variance component estimation, individual weightings for each AC are determined for obtaining unbiased estimations, taking statistical information and correlations between the parameters into account. After applying NNT and NNR conditions, estimates of the full set of EOP and station coordinates are obtained.

Based on seven-parameter Helmert-transformations the scale differences between our IVS contribution and the ITRF2014/2020 are computed. It is evident that an improvement of the scatter for ITRF2020 scale could be reached. However, a significant trend within the last years of the time series can be observed. The behavior is not finally investigated and will be focused on in the future.

We performed a further investigation regarding the software-specific impact of the weighting strategy. It could be shown that the number of identical software packages affects the combination. The more identical software packages are included, the higher is the accuracy level of these contributions w.r.t. combination.

Further investigations will therefore focus on a reliable weighting strategy, taking multiple appearances of equal software tools into account.

References

Altamimi, Z., Rebischung, P., Métivier, L., & Collilieux, X. (2016). ITRF2014: A new release of the International Terrestrial Reference Frame modeling nonlinear station motions. Journal of geophysical research: solid earth, 121(8), 6109-6131. DOI 10.1002/2016JB013098

Bachmann, S., Lösler, M., Messerschmitt, L., Schmid, R., Bloßfeld, M., & Thaller, D. (2012). IVS combination center at BKG-Robust outlier detection and weighting strategies. International VLBI Service for Geodesy and Astrometry, 266–270.

Bachmann, S., Thaller, D., Roggenbuck, O., Lösler, M., & Messerschmitt, L. (2016). IVS contribution to ITRF2014. Journal of Geodesy, 90(7), 631-654. DOI 10.1007/s00190-016-0899-4

Bachmann, S., Messerschmitt, L., Schmid, R., Bloßfeld, M., & Thaller, D. (2017). BKG/DGFI-TUM Combination Center Biennial Report 2015+2016. In: Baver KD, Behrend D., Armstrong KL (Eds.) International VLBI Service for Geodesy and Astrometry 2015+2016 Biennial Report, 204-208, NASA/TP-2017-219021.

Böckmann, S., Artz, T., & Nothnagel, A. (2010). VLBI terrestrial reference frame contributions to ITRF2008. Journal of Geodesy, 84(3), 201-219. DOI 10.1007/s00190-009-0357-7

Luzum, B., & Petit, G. (2012). The IERS Conventions (2010): reference systems and new models. Proceedings of the International Astronomical Union, 10(H16), 227–228.

Métivier, L., Collilieux, X., Altamimi, Z., & Lercier, D. (2014). The ITRF and its scientific applications. Journées 2013 “Systèmes de référence spatio-temporels”, 3–6.

Nothnagel, A., Artz, T., Behrend, D., & Malkin, Z. (2017). International VLBI service for geodesy and astrometry. Journal of Geodesy, 91(7), 711–721. DOI 10.1007/s00190-016-0950-5

Rousseeuw, P. J., & Leroy, A. M. (2005). Robust regression and outlier detection. John wiley & sons. DOI 10.1002/0471725382

Thaller, D. (2008). Inter-technique combination based on homogeneous normal equation systems including station coordinates, Earth orientation and troposphere parameters (Doctoral dissertation, Technische Universität München).

Vennebusch, M., Böckmann, S., & Nothnagel, A. (2007). The contribution of very long baseline interferometry to ITRF2005. Journal of Geodesy, 81(6), 553–564. DOI 10.1007/s00190-006-0117-x

Changing from ITRF2014 to ITRF2020 in the Routine VLBI Analysis: First Investigations

Anastasiia Girdiuk, Gerald Engelhardt, Daniela Thaller, Dieter Ullrich

Abstract The IVS Analysis Center at BKG took part in the activity to build the next generation ITRF2020. Here we present the first results of the implementation of the preliminary release ITRF2020P in our routine analysis. The a priori station coordinates and velocities are updated as well as the PSD model coming along with ITRF2020P. The most prominent improvement is recognized for the new VGOS stations, which are particularly valuable for the different types of the VGOS sessions (IVS VGOS, mixed mode sessions, and local ONTIE observations) observed in the last few years. The advancement of the PSD model is validated at the affected stations. We consider the product of the Intensive session solution to verify the PSD model performance. The rest of the reductions are applied along with to the current bkg2020a solution. While we focus our study on the verification of the VGOS station positions, we also look into the EOP time series variations derived from the 24-hour session solution.

Keywords VLBI Analysis, ITRF2020, IVS products

1 Introduction

The most recent International Terrestrial Reference Frame ITRF2020 [12] was released after the 12th IVS General Meeting; thus the preliminary version of the ITRF2020P release was used in this paper. The final release is not expected to introduce any significant differences. The a priori station positions, as provided by ITRF, is one of the central reductions in the VLBI Analysis. Due to the lack of observations, the accurate a priori corrections of the new stations are crucial for the generation of reliable IVS products at the IVS Analysis Center. In this case, this work focuses on the station positions of the new VGOS antennas. In order to support an operational analysis the a priori station positions of VGOS antennas were obtained internally at BKG by means of the single technique VLBI solution. The actual operational bkg2020a time series is parameterized with respect to the ITRF2020 campaign requirements, where ITRF2014 [1] is applied as the a priori corrections for the station positions. The aforementioned internal VLBI solution is employed for the stations, which are not present in ITRF2014, such as VGOS stations. Here we compare the application of ITRF2020P by considering our two VLBI solutions, in which the only difference is the applied a priori station position corrections. Hereinafter, itrf2020p refers to the solutions, while ITRF2020P is the a priori model. The PSD model is utilized in the analysis procedures to be consistent with ITRF2020P. Its advance is verified in the station positions' variations. The Intensives session product is also used to validate the PSD model: the station positions in their parameterization are fixed to the a priori corrections, thus any offset would have to be related to the deficiencies of the a priori model.

2 Data and Analysis

The processed data of the operational 24-hour session solution bkg2020a can be found in the Data Center [7], where the corresponding daily SINEX files are provided for each processed session along with the EOP

Federal Agency for Cartography and Geodesy (BKG)

Fig. 1 The obtained distance variations of the VGOS stations are plotted as derived from two solutions: bkg2020a and itrf2020p. The ONTIE sessions are marked with "plus" sign and the other VGOS sessions with circles.

products in both formats (eops and eoxy). These products are updated every time the new session is available for the analysis. The operational EOP products of solution bkg2020a do not include the corresponding results of the VGOS sessions, even though the corresponding SINEX files are provided.

The itrf2020p solution is built for the exact same data set as bkg2020a and the same parameterization is applied. That means, in the case of the VGOS sessions, that all stations are evaluated with NNR/NNT uniform constraints defined by the sigma 0.1 mm. The source positions are estimated with the NNR uniform constraints defined by the sigma of 0.2 as applied to the ICRF3-SX defining sources, and by the sigma of 2 mas to all of them imposed on declination and right ascension, where ICRF3-SX is the a priori catalog [3]. The EOP time series are obtained once per session with respect to the Bulletin A [10], including modeling for the high-frequency part Desai&Sibois/Egbert [4] and precession-nutation variations IAU2006/2000 [8]. The corresponding constraints of 45 mas and 3 ms are applied to the estimates of the polar motion and dUT1 and 45 mas/day and 3 ms/day to the polar motion and LoD rates. The computed nutation is unconstrained. The clocks at each station are modeled as a quadratic spline at a one-hour interval with the rate constraint of 5^{-14}, with the exception of the referenced. The troposphere is adjusted by evaluating the wet part of the hourly zenith delay with the rate constraint of 50 ps/hour and gradients at the beginning and the end of the session as a linear spline, with an offset constraint of 0.5 mm and rate constraint of 2.0 mm/day.

The obtained station position variations from solutions bkg2020a and itrf2020p are plotted for the VGOS stations in Figure 1. Here the station position variations of the total values defined as the distance $\sqrt{x^2+y^2+z^2}$ are reduced by the common mean of the weighed average. The largest reductions are seen in the European stations, while the stations located in the USA do not show such irregularity and the station positions of ISHIOKA in Japan are affected slightly. The same station position variations obtained from ONTIE session solutions show very small differences between the two solutions (see the "plus" marks depicting ONTIE sessions on Figure 1). However, the ONTIE session solutions are different from bkg2020a. The station positions of ONSALA60 are fixed to the applied a priori model, the station positions of twin antennas are not

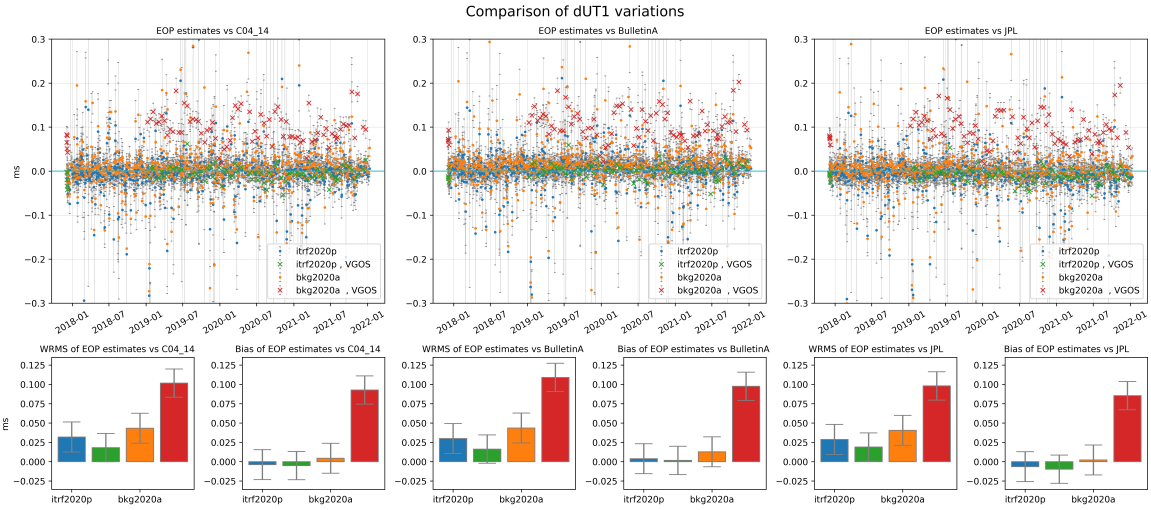

Fig. 2 The comparison of the dUT1 variations is plotted in the upper panel with respect to the three a priori EOP time series: C04 14, Bulletin A, and JPL. The lower panel contains pair plots of WRMS and bias corresponding to the a priori model above. Each of the solutions, bkg2020a and itrf2020p, is additionally divided to highlight the results derived from VGOS sessions in contrast to the S/X sessions.

constrained, and the atmospheric parameters are not estimated for ONSA13NE. This parameterization of the ONTIE sessions is along with the one suggested by the group in Onsala [9], who designed, conducted, and analyzed these sessions. These inaccuracies of the VGOS station positions propagate directly to the ERP time series evaluation, while LoD and celestial pole offsets seem to show a substantial resemblance. The effect is shown in Figure 2 for dUT1. The ERP time series estimates are compared against three a priori time series: C04 14 [2], Bulletin A, and JPL [11] (upper panel: left to right). The differences to the a priori corrections for the dUT1 variations are shifted by 0.1 ms on average, and for the two components of the polar motion the offsets are of about 1 and -2 mas correspondingly. The solution itrf2020p, however, shows the results from the VGOS sessions to be aligned with the results of the rest of the sessions. The WRMS and bias of the differences plotted in the upper panel are shown in the lower panel of the Figure 2. A sizable reduction in the WRMS and the bias is recognized where the new ITRF2020P is applied. The prominent offset in the ERP time series estimates is the reason why the EOP products are not populated with VGOS sessions in the operational solution version bkg2020a.

The same comparison is done in the Intensive sessions. An offset is detected in the results derived from the VGOS Intensives only as shown in Figure 3. The standard S/X Intensive sessions are unaffected: the regularly participating stations set is fixed and limited to the reliable stations—their coordinates are well-known as a rule. However, a considerable number of the Intensive sessions were observed at the Kashima and Tsukuba stations, where some severe discontinuities were detected. In the last two ITRF releases, the PSD model was applied to take into account the station position variations after these earthquakes. In the previous work [6] when we have considered the analysis of the BKG Intensives time series, it was shown that the PSD model is sufficient to take those effects into account. Before ITRF2014 was released, the station positions were derived from the 24-hour sessions observed at about the same time as the Intensives with Kashima and Tsukuba [5]. The implementation of the new PSD model provided with ITRF2020P shows a high consistency with the previous release.

3 Conclusions

The preliminary ITRF2020 version benefits from the inclusion of the VGOS sessions, namely the station position corrections that provide a better agreement with observations and the obtained EOP time series that are aligned with the results from the 24-hour S/X ses-

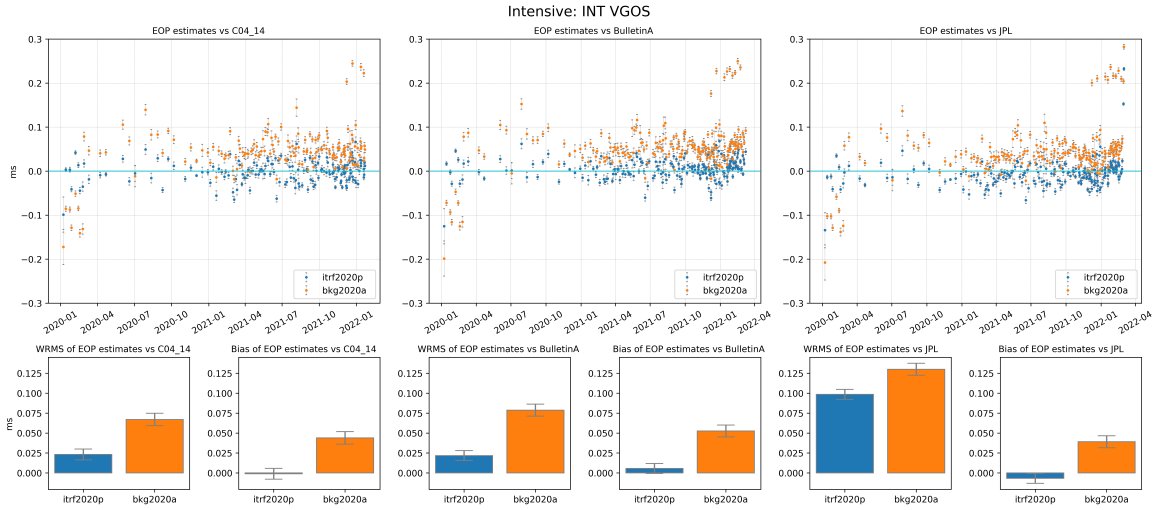

Fig. 3 The comparison of the dUT1 variations from the analysis of the different types of the VGOS Intensive sessions is plotted in the upper panel with respect to the three a priori EOP time series: C04 14, Bulletin A, and JPL. The lower panel contains pair plots of WRMS and bias corresponding to the a priori model above.

sions. Besides, the dUT1 estimates derived from the Intensive sessions observed on the new VGOS antennas are improved substantially, mainly because the station positions are fixed to the a priori values in the analysis. The new PSD model provided along with ITRF2020P seems to be very similar to the previous version. The dUT1 estimates derived from itrf2020p solutions show a very good agreement with the current solution bkg2020a, including sessions where Kashima and Tsukuba, for which PSD model is applied, participate. The southern mixed mode and all S/X Intensives reveal no impact of the a priori station position corrections in the obtained dUT1 variations. The comparison of the dUT1 with the three different a priori models indicates the high quality of the VGOS and mixed mode intensives, which is on the level with the operational INT1, INT2, and INT3 products. In the case of the southern Intensives, Onsala Intensives (data base code, dbc, VB), and MgWs Intensives (VJ) a bias might be seen due to the small number (8–9) of sessions.

References

1. Z. Altamimi, P. Rebischung, L. Metivier, and X. Collilieux, ITRF2014: A new release of the International Terrestrial Reference Frame modeling nonlinear station motions, J. Geophys. Res. Solid Earth, 121, doi:10.1002/2016JB013098, 2016.
2. C. Bizouard, S. Lambert, C. Gattano, et al. (2019) The IERS EOP 14C04 solution for Earth orientation parameters consistent with ITRF 2014, J Geod 93(5):621-633, https://doi.org/10.1007/s00190-018-1186-3, 2019.
3. P. Charlot, C. S. Jacobs, D. Gordon, S. Lambert, A. de Witt, J. Böhm, A. L. Fey, R. Heinkelmann, E. Skurikhina, O. Titov, E. F. Arias, S. Bolotin, G. Bourda, C. Ma, Z. Malkin, A. Nothnagel, D. Mayer, D. S. MacMillan, T. Nilsson and R. Gaume. The third realization of the International Celestial Reference Frame by very long baseline interferometry A&A, 644 A159, DOI: https://doi.org/10.1051/0004-6361/202038368, 2020.
4. Desai and Sibois, "Evaluating predicted diurnal and semidiurnaltidal variations in polar motion with GPS-based observations", J. Geophysical Research: Solid Earth, 121, pp. 5237–5256, doi:10.1002/2016JB013125, 2016.
5. G. Engelhardt, V. Thorandt, D. Ullrich. Refinement of the rapid UT1 estimation derived from Tsukuba VLBI measurements after the 2011 earthquake. In: D. Behrend, K. D. Baver, K. Armstrong, editors, *International VLBI Service for Geodesy and Astrometry 2016 General Meeting Proceedings*, NASA/CP-2016-219016, 225–228, 2016.
6. A. Girdiuk, D. Thaller, D. Ullrich, G. Engelhardt, R. Wojdziak, C. Plötz. Analysis of Intensive Sessions at BKG. In: R. Haas, S. García-Espada, J. A. López Fernández, editors, *Proceedings of the 24th European VLBI Group for Geodesy and Astrometry Working Meeting*, Centro Nacional de Información Geográfica (CNIG). 2019.
7. A. Nothnagel, T. Artz, D. Behrend, Z. Malkin, "International VLBI Service for Geodesy and Astrometry – Delivering high-quality products and embarking on observations of the next generation", *Journal of Geodesy*, Vol. 91(7), pp. 711–721, July 2017. DOI 10.1007/s00190-016-0950-5.
8. Petit, Gerard and Luzum, Brian, IERS Conventions (2010), IERS Technical Note 36, 2010.

9. E. Varenius, R. Haas, T. Nilsson, Short-baseline interferometry local-tie experiments at the Onsala Space Observatory, *Journal of Geodesy* 95, 54, https://doi.org/10.1007/s00190-021-01509-5, 2021.
10. https://www.iers.org/IERS/EN/Publications/Bulletins/bulletins.html
11. https://eop2-external.jpl.nasa.gov/
12. https://itrf.ign.fr/en/solutions/ITRF2020

Assessment of Parameters Describing the Signal Delay in the Neutral Atmosphere Derived from VGOS Observations

Rüdiger Haas[1], Jan Johansson[1], Gunnar Elgered[1], Periklis-Konstantinos Diamantidis[1], Tobias Nilsson[2]

Abstract We use the VGOS session VR2101 to assess parameters describing the signal delay in the neutral atmosphere. VGOS results are compared to corresponding results derived from co-located GNSS stations for all sites, and additionally to results from a ground-based microwave radiometer for the Onsala Space Observatory. For the first time all three independent techniques can be compared with the same high temporal resolution of 5 min. Zenith total delays from VGOS and GNSS reveal correlation coefficients larger than 0.9 for all but one of the participating sites. Corresponding offsets are between 1–8 mm and root mean square differences are between 4–14 mm. Horizontal gradients from VGOS and GNSS have correlation coefficients between 0.2–0.5 for the east components and 0.4–0.7 for the north components. Corresponding offsets are sub-millimeter, and root mean square differences are on the order of 0.5–2.2 mm. The comparisons for the Onsala site of VGOS and GNSS w.r.t. microwave radiometer show correlation coefficients larger than 0.96 for the zenith total delays with offsets on the order of 7–11 mm and root mean square differences of 9–12 mm. Horizontal gradients show correlation coefficients of about 0.2 for the east components and about 0.5 for the north components. The corresponding offsets are between 0.6–1.8 mm and the root mean square differences are 0.9–1.3 mm.

Keywords VGOS • GNSS • WVR • ZTD • gradients

1. Chalmers University of Technology
2. Lantmäteriet – The Swedish Mapping, Cadastral, and Land Registration Authority

1 Introduction

During the design phase of VGOS, one major restricting factor was identified to be turbulence that is affecting the signal delay in the neutral atmosphere (Nilsson and Haas, 2010). In order to address this aspect the VGOS design focuses on radio telescopes that can move fast in azimuth and elevation, so that many observations in many different local directions can be achieved (Petrachenko et al., 2009) during an experiment. This shall allow to sample the signal delay introduced by the atmosphere much better than with legacy S/X observations and thus lead to improvements for the estimated geodetic parameters. An assessment of the parameters describing the signal delay in the neutral atmosphere can be achieved by comparisons with results from independent co-located instrumentation, such as GNSS stations and ground-based microwave radiometers, often referred to as water vapor radiometers (WVR).

2 VGOS Observations

VGOS is still in its roll-out phase, and so far only eight sites routinely participate in operational VGOS sessions organized by the International VLBI Service for Geodesy and Astrometry (IVS). One of the sites, the Onsala Space Observatory (OSO), operates two VGOS stations, the Onsala twin telescopes (OTT) (Haas et al., 2019). The current VGOS operational network is a purely northern hemisphere network, see Figure 1. During 2019, 24-hour long VGOS test observations (VT) were organized by the IVS every second week. Beginning in 2020, 24-hour long VGOS operational

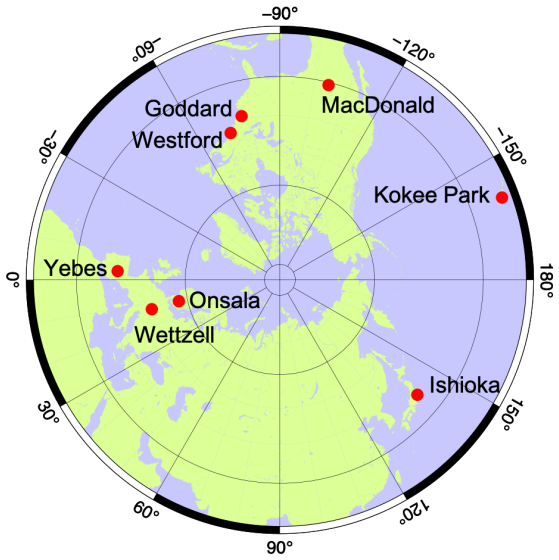

Fig. 1 The current operational VGOS network.

(VO) sessions were performed every second week. Since 2022, there is one VO session every week. The standard VGOS setup throughout 2019–2022 is to have scans of 30 s long, and the schedules are produced with the *sked* software (Gipson, 2010).

In addition to the VO series, the IVS also organizes 24-hour long so-called VGOS research-and-development (VR) sessions to investigate various aspects of the VGOS system, such as different frequency setups, different radio source catalogs, or shorter scan lengths. Such a VR session is of interest in this study.

3 The VGOS R&D Session VR2101

The VGOS R&D session VR2101 was observed on 29/30 July 2021 and involved seven VGOS stations at six sites: GGAO12M (Goddard, US), KOKEE12M (Kokee Park, US), MACGO12M (MacDonald, US), ONSA13SW (Onsala, SE), ONSA13NE (Onsala, SE), WESTFORD (Westford, US), and WETTZ13S (Wettzell, DE). All sites are equipped with co-located GNSS stations, often several ones, and at least OSO operates a WVR. As an example, Figure 2 presents the co-located instrumentation at OSO.

The VR2101 schedule was prepared with the software *VieSched++* (Schartner and Böhm, 2019) and re-

Fig. 2 Co-located instrumentation at the Onsala Space Observatory: The Onsala twin telescopes (left); ONSA and ONS1, two of the GNSS stations (middle); the microwave radiometer (right).

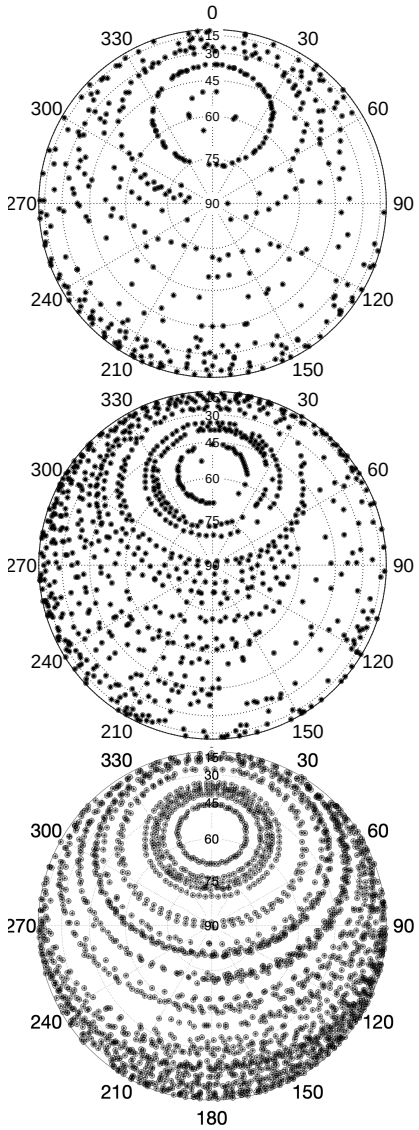

Fig. 3 Local sky coverage at the Onsala Space Observatory for R11101 (top), VO1203 (middle), and VR2101 (bottom).

sulted in 3,397 scans with a total of 23,040 observations. The goal of the session was to observe with short scan length in order to achieve as many observations as possible in different directions so that the local sky at the participating stations could be sampled densely.

To provide some insight into the sky coverage aspect, we can compare the sky coverage at OSO obtained for VR2101 to a standard R1 session and an operational VO session. OSO regularly contributes to R1 sessions with its 20-m diameter telescope ONSALA60. The legacy S/X session R11101 was observed in August 2021 involving seven stations and had 1,638 total scans with an average scan length of 75 s. During this session ONSALA60 participated in 436 scans. The session VO1203, observed in July 2021, involved seven VGOS stations. The total number of scans was 1,265 with an average scan length of 30 s. During this session, each of the OTT participated in 856 scans, i.e., two times more than during a standard R1 session. The session VR2101 involved seven VGOS stations and had in total 3,397 scans with an average scan length of 11 s. Each of the OTT participated in 2,436 scans, i.e., three times more than during a standard VO session. Figure 3 illustrates the distribution of observations in these different sessions.

4 Data Analysis

We analyzed the VGOS database of VR2101 with the *ASCOT* software (Artz et al., 2016) using a least-squares analysis. The analysis strategy followed the recommendations for the IVS ITRF2020 analysis (Gipson, 2020). A minimum elevation cutoff of 5^o was used and the VMF3 mapping functions (Landskron and Böhm, 2018) were applied. Zenith hydrostatic delays (ZHD) were modeled using the locally observed pressure as recorded in the VLBI logfiles. Zenith wet delays (ZWD) corrections and horizontal gradients (GRAD) were estimated with a 5-minute temporal resolution using loose constraints. Zenith total delays (ZTD) were calculated by adding the a priori ZHD and estimated ZWD.

Data recorded with the co-located GNSS stations at all sites (except Westford where no GNSS data were available) were analyzed with the GipsyX software (Bertiger et al., 2020). The analysis used multi-GNSS data with the precise point positioning (PPP) approach (Zumberge et al., 1997). A minimum elevation cutoff of 7^o was used and the VMF3 mapping functions (Landskron and Böhm, 2018) were applied. ZHD were modeled using standard pressure values, while ZWD corrections and GRAD were estimated with a 5-minute temporal resolution using loose constraints. Again, ZTD were calculated by adding the a priori ZHD and estimated ZWD.

The data of the WVR at OSO were analyzed with an in-house software. A sky-mapping analysis with an elevation cutoff of 25^o was performed using unconstrained least-squares analysis (Elgered et al., 2019). ZWD and GRAD parameters were estimated with a 5-minute temporal resolution.

The WVR is not sensitive to the hydrostatic delay, i.e., the derived parameters are pure ZWD and wet horizontal gradients. There are various ways to compare WVR-derived atmospheric parameters to those derived from VLBI and GNSS. For this study we chose to compare ZTD and total horizontal gradients. To do so, we added ZHD based on the locally recorded pressure data at Onsala to the ZWD from the WVR analysis and added VMF3-referred horizontal hydrostatic gradients (VMF data server, 2022) based on ERA-Interim numerical weather model data to the WVR-derived gradients.

For comparsion purposes, we referred all ZTD values to the same reference height, which we chose to be the GNSS reference point at each station. We applied corresponding height corrections (Rothacher et al., 2011), since the reference points of the different techniques are usually at different heights, see Figure 4. For the GRAD parameters, no further corrections were needed, except the one described above for the WVR.

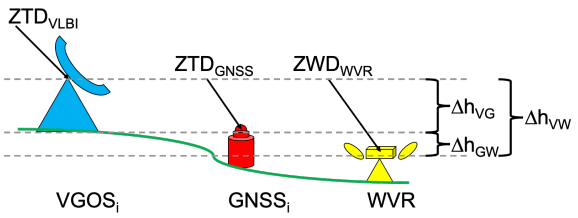

Fig. 4 Sketch showing a co-location site with three different instruments and the heights of their respective reference points. In order to meaningfully compare atmospheric parameters, corresponding height corrections need to be applied.

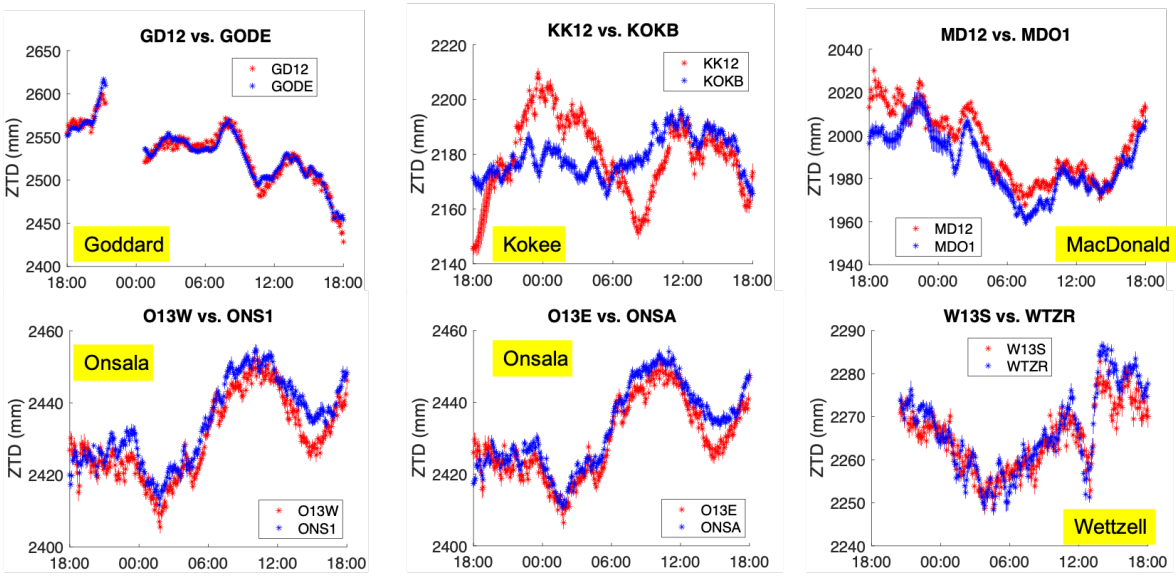

Fig. 5 Time series of ZTD with a 5-minute temporal resolution from VGOS (red) and GNSS (blue), respectively, for the six sites participating in VR2101 that had both techniques operating.

5 Results

Figure 5 presents comparisons for all six sites participating in VR2101 where both VGOS and GNSS data were available. ZTD from VGOS and GNSS are shown in red and blue, respectively. For most sites the red and blue curves show a high degree correlation with similarity even for short-term signatures. The exception is Kokee Park, where the GNSS results show less variability than the VGOS results. Statistical information on correlation coefficients, biases and weighted root-mean-scatter are provided in Table 1 for both ZTD and GRAD. Table 2 focuses on ZTD and GRAD derived from the co-located equipment at OSO including both twin telescopes (O13E, O13W), two GNSS stations (ONSA, ONS1), and the WVR.

While the correlation coefficients for ZTD are all larger than 0.91 (except for Kokee Park), the correlations for the gradient components are smaller and do not exceed 0.71. The correlation coefficients are generally smaller for the east than for the north gradients, which is unusual and contradicts previous studies, e.g., Ning and Elgered (2021). Furthermore, the presence of gradients varies significantly with time, and a 24-hour-long experiment is not a representative data set in order to draw general conclusions.

Table 1 Comparison of VGOS and GNSS: ZTD, east (GRE) and north (GRN) gradient components: ρ – correlation coefficient, δ – offset VGOS-GNSS (mm), $\Re$ – RMS difference (mm).

	ZTD			GRE			GRN		
Station	ρ	δ	$\Re$	ρ	δ	$\Re$	ρ	δ	$\Re$
GGAO12M	0.97	−0.8	7.5	0.54	0.0	1.2	0.62	0.7	1.6
KOKEE12M	0.33	0.2	13.4	0.32	−0.1	1.7	0.40	0.7	2.2
MACGO12M	0.93	7.7	9.6	0.25	0.0	1.1	0.37	−0.2	1.2
ONSA13NE	0.96	−3.2	4.6	0.20	−0.2	0.6	0.63	0.0	0.5
ONSA13SW	0.96	−2.6	4.1	0.22	−0.1	0.6	0.59	0.0	0.5
WETTZ13S	0.91	−1.6	4.5	0.45	0.1	0.6	0.71	−0.1	0.7

Table 2 Comparison of ZTD, east (GRE) and north (GRN) gradient components at the Onsala Space Observatory, from both OTT (O13W, O13E), two GNSS stations (ONSA, ONS1), as well as the microwave radiometer (WVR): ρ – correlation coefficient, δ – offset (mm), $\Re$ – RMS difference (mm).

	ZTD			GRE			GRN		
Stations	ρ	δ	$\Re$	ρ	δ	$\Re$	ρ	δ	$\Re$
O13E - O13W	0.99	−0.6	0.9	0.94	−0.0	0.2	0.96	0.0	0.2
ONSA - ONS1	0.99	−1.9	2.6	0.70	0.0	0.4	0.70	0.0	0.5
O13E - ONSA	0.96	−3.2	4.6	0.20	−0.2	0.6	0.63	0.0	0.5
O13E - ONS1	0.95	−4.5	5.8	0.22	−0.2	0.6	0.66	0.0	0.6
O13W - ONSA	0.96	−2.6	4.1	0.22	−0.1	0.6	0.60	0.0	0.5
O13W - ONS1	0.95	−4.0	5.3	0.11	−0.1	0.6	0.63	0.0	0.6
O13E - WVR	0.96	−11.1	12.2	0.26	−0.1	1.1	0.51	−0.1	0.7
O13W - WVR	0.96	−10.5	11.6	0.29	−0.8	1.1	0.50	−0.1	0.6
ONSA - WVR	0.97	−7.5	8.8	0.21	−0.6	1.0	0.47	−0.1	0.7
ONS1 - WVR	0.96	−5.6	7.4	0.16	−0.6	1.1	0.53	−0.1	0.7

6 Conclusions and Outlook

To our knowledge, for the first time, parameters describing the signal delay in the neutral atmosphere derived from the independent co-located techniques VLBI, GNSS, and WVR could be compared with an identical temporal resolution of 5 min. This high temporal resolution for VLBI was possible thanks to VR2101, with a large number of scans. High correlations, above 0.9, are achieved for the ZTD. The correlations for the horizontal gradients are lower and do not exceed 0.5 and 0.7 for the east and north components, respectively. Offsets and RMS differences are in the sub-millimeter to millimeter range. Further VGOS R&D sessions (VR sessions) are needed to understand the level of disagreement and its reasons.

References

Artz T, Halsig S, Iddink A, Nothnagel A (2016) ivg::ascot: Development of a new vlbi software package. In: D. Behrend, K. D. Baver, K. L. Armstrong(eds) *IVS 2016 General Meeting Proceedings*, **NASA/CP-2016-219016**, 217–221, https://ivscc.gsfc.nasa.gov/publications/gm2016/045_artz_etal.pdf

Bertiger W, Bar-Sever Y E, Dorsey A, Haines B, Harvey N, Hemberger D, Heflin M, Lu W, Miller M, Moore A W, Murphy D, Ries P, Romans L, Sibois A, Sibthorpe A, Szilagyi B, Vallisneri M, Willis P (2002) GipsyX/RTGx, a new tool set for space geodetic operations and research. *Advances in Space Research*, 66(3), 469–489, doi:10.1016/j.asr.2020.04.015

Elgered G, Ning T, Forkman P, Haas R (2019) On the information content in linear horizontal delay gradients estimated from space geodesy observations, *Atmosospheric Measurement Techniques*, 12, 3805–3823, doi:10.5194/amt-12-3805-2019

Gipson J (2018) Sked VLBI Scheduling Software User Manual. Web document https://ivscc.gsfc.nasa.gov/IVS_AC/sked_cat/SkedManual_v2018October12.pdf

Gipson J (2020) IVS Checklist for ITRF2020. https://ivscc.gsfc.nasa.gov/IVS_AC/ITRF2020/ITRF2020_checklist_v2020Jan13.pdf

Haas R, Casey S, Conway J, Elgered G, Hammargren R, Helldner L, Johansson K-Å, Kylenfall U, Lerner M, Pettersson L, Wennerbäck L (2019) Status of the Onsala twin telescopes – two years after the inauguration. In: R. Haas, S. Garcia-Espada, J. A. Lopez Fernandez (eds) *Proc. 24th European VLBI for Geodesy and Astrometry (EVGA) working meeting*, ISBN: 978-84-416-5634-5, 5–9.

Landskron D, Böhm J (2018) VMF3/GPT3: refined discrete and empirical troposphere mapping functions. *Journal of Geodesy*, 92, 349–360, doi:10.1007/s00190-017-1066-2

Nilsson T, Haas R (2010) Impact of atmospheric turbulence on geodetic very long baseline interferometry. *Journal of Geophysical Research: Solid Earth* 115(B3), doi:10.1029/2009JB006579

Ning T, Elgered G (2021) High-temporal-resolution wet delay gradients estimated from multi-GNSS and microwave radiometer observations. *Atmosospheric Measurement Techniques*, 14, 5593–5605, doi:10.5194/amt-14-5593-2021

Petrachenko B, Niell A, Behrend D, Corey B, Böhm J, Charlot P, Collioud A, Gipson J, Haas R, Hobiger T, Koyama Y, MacMillan D, Malkin Z, Nilsson T, Pany A, Tuccari G, Whitney A, Wresnik J (2009) Design aspects of the VLBI2010 system. **NASA/TM-2009-214180**

Rothacher M, Angermann D, Artz T, Bosch W, Drewes H, Gerstl M, Kelm R, König D, König R, Meisel B, Müller H, Nothnagel A, Panafidina N, Richter B, Rudenko S, Schwegmann W, Seitz M, Steigenberger P, Tesmer S, Tesmer V, Thaller D (2011) GGOS-D: homogeneous reprocessing and rigorous combination of space geodetic observations. *Jour. of Geodesy*, 85(10):679–705, doi:10.1007/s0019 0-011-0475-x

Schartner M, Böhm J (2019) VieSched++: A New VLBI Scheduling Software for Geodesy and Astrometry. *Publications of the Astronomical Society of the Pacific*, 131:084501, doi:10.1088/1538-3873/ab1820

re3data.org: VMF Data Server; editing status 2020-12-14; re3data.org - Registry of Research Data Repositories, doi:10.17616/R3RD2H

Zumberge J F, Heflin M, B Jefferson D C, Watkins M M, Webb F H (1997) Precise Point Positioning for the efficient and robust analysis of GPS data from large networks. *Journal of Geophysical Research*, 102(B3), 5005–5017, doi:10.1029/96JB03860

A New Wiggle in the Wobble?
Uncovering Periodic Signals in Intensive Series

Christopher Dieck, Megan Johnson

Abstract Evaluating the residual series generated by differencing the values of UT1−UTC from an Intensive provides valuable information for use in assessing the quality of the Intensive series. Ideally, the residuals have a mean of zero, with some random noise. Applying a non-parametric Nadaraya-Watson kernel regression to the residuals of the MK-VLBA:PIETOWN VLBA Intensive series, with respect to multiple reference series, revealed that there is a statistically significant periodic deviation from the ideal. Additionally, a discontinuity in the series is seen and causally attributed to the 2018 Hawai'i earthquake through evaluation of the co-located GNSS receivers at both stations. Applying the same regression analysis to the KOKEE:WETTZELL IVS Intensive series suggests that the same periodic signal in the residuals may be present, just with a smaller amplitude. Analysis of the sensitivity of UT1−UTC to shifts in station position for both baselines likely explains the difference in amplitude; the value of UT1−UTC determined at KOKEE:WETTZELL is approximately four times less sensitive to station position shifts than that measured with MK-VLBA:PIETOWN. Though the MK-VLBA:PIETOWN UT1−UTC discontinuity is determined to be the result of a change in the MK-VLBA station position, there is no periodic change in the position of the co-located GNSS receivers that accounts for the periodicity noted in the UT1−UTC residual series. Therefore, either a heretofore unidentified mechanism is at play, a known mechanism is not being modeled in the estimation process, or there are errors in the applied models.

United States Naval Observatory

Keywords UT1, Intensive, VLBA

1 Introduction

Regular monitoring of the Earth's rotation phase is important to the maintenance of numerous systems at the foundation of modern society (e.g., GNSS). VLBI is unique among space geodetic techniques in its ability to directly measure this parameter, expressed as UT1−UTC. In any series of short duration, single-baseline VLBI sessions ("Intensives") must provide consistent and stable measurements of UT1−UTC as a function of time so that there is confidence in any one measurement from the series.

Both the relatively small number of observations in and the geometry of Intensives limit the parameters that can be estimated from these sessions. Thus, models must be used to construct the equations from which the estimates of UT1−UTC are made. There can be errors in those models, and investigations have shown that these errors propagate into errors in the measurement of UT1−UTC (e.g., Nothnagel and Schnell, 2008). One such model is the model of the position of the stations during the observation of the Intensive session.

In this work we explore the UT1−UTC values from the Intensive series observed on the baseline formed by the Maunakea (MK-VLBA; Mk) and Pie Town (PIETOWN; Pt) stations of the Very Long Baseline Array (VLBA). They exhibit a periodicity in their residuals to a reference series of Earth Orientation parameters (EOPs) and an isolated discontinuity in May, 2018. Section 2 describes the VLBI and GNSS data we use to investigate the hypothesis that station position shifts are the cause of both the discontinuity and the peri-

odicity in the residuals. The analysis of the magnitude of the discontinuity and station displacement, as well as the calculation of the sensitivity of the measure of UT1−UTC on the Mk-Pt baseline to shifts in the participating stations, is performed in Section 3, with a discussion of the mixed results and necessary future work in Section 4.

2 Data

2.1 Maunakea-Pietown VLBA Intensives

From late 2011 through April 2021, the United States Naval Observatory (USNO) observed single-baseline Intensive sessions between the MK-VLBA and PIETOWN stations of the Very Long Baseline Array (Geiger et al, 2019). As a regular part of reviewing the data from the series, the values of UT1−UTC are differenced with one of three reference series: `latest_midnight.eop` from the NASA Jet Propulsion Lab, `eopc04_IAU2000.62-now` from the Paris Observatory, or `finals2000A.all` from the USNO, which is used in this work. While reviewing the resulting residual series in mid-2018, USNO staff identified a discontinuity which was preliminarily associated with the magnitude 6.9 Hawai'i earthquake that occurred on May 4, 2018 (Dieck et al, 2019). The discontinuity could be corrected for in the USNO VLBI Analysis Center global solution after several 24-hour VLBI sessions that included the MK-VLBA station were observed following the earthquake. The last global solution that contained the discontinuity was `usn2019c`. This analysis of the Mk-Pt series thus utilizes the UT1−UTC values from that solution, and includes data from November 14, 2015 (when the Mk-Pt series resumed after major maintenance at MK-VLBA) to January 28, 2020 (the end of the `usn2019c` Intensive series).

2.2 Co-located GNSS Stations

To facilitate the testing of the hypothesis that a shift of the MK-VLBA station is responsible for the discontinuity of UT1−UTC residuals, we make use of the fact that both the MK-VLBA and PIETOWN stations have co-located GNSS receivers, labelled MKEA and PIE1, respectively. MKEA is 87.772 m from MK-VLBA, and PIE1 is 61.795 m from PIETOWN. Being so close ($<$ 90 m) to each other at each site, we make the assumption that the VLBI and GNSS stations are subject to the same geologic processes and thus position changes recorded by the GNSS station apply directly to the VLBI station as well. Position information from both MKEA and PIE1 is processed by the International GNSS Service (IGS), and this work uses the station position history for each site from the third reprocessing campaign of the IGS, referred to as 'repro3'.

Occasionally, the antenna or receiver of a GNSS station is repaired or replaced. According to the station logs, MKEA has a consistent setup from February 23, 2016 through September 23, 2018, and PIE1 has a consistent setup from June 30, 2017 through October 1, 2018. Thus, the time period when both stations have consistent setups that span the occurrence of the earthquake is June 30, 2017 through September 23, 2018.

3 Analysis

3.1 Application of the Nadaraya-Watson Estimator

Given the inherent scatter in the residual values, we employ the Nadaraya-Watson estimator (NWE; Nadaraya 1964; Watson 1964) to smooth the residuals. This facilitates the determination of the magnitude of the UT1−UTC discontinuity in the Mk-Pt residuals. The NWE returns an estimated value of a regression function m at a given point, x, calculated as the weighted average of a sample $\{(X_i, Y_i)\}_{i=1}^{N}$. The total weights are determined by the product of the inverse square of the sample values' formal errors, σ_{Y_i}, and the kernel, applied here as a Gaussian. The width of the Gaussian is set by the bandwidth parameter, the value of which is tuned by leave-one-out cross validation (see Feigelson & Babu, 2012).

By splitting the Mk-Pt UT1−UTC residuals at the moment of the earthquake (MJD = 58242.940) and applying the NWE to the two segments independently, we can calculate the difference in estimated UT1−UTC from before and after the earthquake. Prior to applying the NWE smoothing, the first order polynomial fit

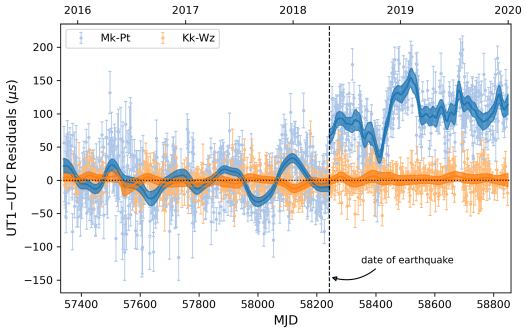

Fig. 1 The residuals of the Mk-Pt Intensives with respect to the USNO reference series, in light blue, and, for reference, the residuals of the Kk-Wz Intensives, in light orange. The date of the Hawai'i earthquake is denoted by the vertical dashed line. Both series of residuals have had large outliers removed and a first order polynomial fit and subtracted. For the Mk-Pt series, the polynomial was fit to the data prior to the earthquake and applied to the entire series. For each series, the regression functions calculated by the Nadaraya-Watson estimator are shown in the corresponding dark color with 3σ confidence bands in the shaded region. The Mk-Pt regression was applied in two parts, one before and one after the earthquake, to show the discontinuity and enable the magnitude of it to be calculated.

to the first segment is subtracted from both segments to remove any systematic offset from the series. The result of this process, shown in Figure 1, leads to the estimate of the magnitude of the UT1−UTC discontinuity of

$$\Delta(UT1-UTC)_{MK-VLBA} = 75.7 \pm 4.6 \text{ µs}. \quad (1)$$

As can be seen in the GNSS station position time series shown in Figure 2, there is no break at the time of the earthquake at the PIE1 station, but there is one at the MKEA station. The same method to determine the discontinuity in a time series at the time of the earthquake is applied to all three axes of the MKEA station, while each axis of the PIE1 data is smoothed as one segment. The resulting MKEA station displacement estimates are reported in Table 1.

3.2 UT1−UTC Sensitivity to Station Position Change

To see if the observed station position shift at the MKEA site can explain the discontinuity seen in the Mk-Pt UT1−UTC residuals, we need to calculate how sensitive the UT1−UTC value is to changes in the a priori positions of the MK-VLBA and PIETOWN stations. By using real data but with altered a priori positions when estimating the value of UT1−UTC and comparing it to a control value where nothing was altered, we can directly calculate the sensitivity value for a given station of a particular baseline. Of course, this is the opposite of what is hypothesized to have occurred in the Mk-Pt series. There, the a priori MK-VLBA position did actually change, but the value used in the model did not. The consequence of this is that the simulated effect is equal in magnitude but opposite in sign from the real effect. The results of this calculation, performed on all Mk-Pt sessions from 2020, are shown in Table 2. Also shown in the table, by way of comparison, are the results of the same sensitivity analysis performed on the KOKEE:WETTZELL (Kk-Wz) Intensive sessions from 2020. The sensitivity value is the mean of the ∼200 individual measurements, and the uncertainty is the sample standard deviation of those measurements.

Table 1 The estimated station displacements in each orthogonal axis of the MKEA GNSS station and the corresponding contribution to the expected shift in UT1−UTC based on the sensitivities reported in Table 2. The total magnitude of the station shift and the total expected shift in the VLBI measurement of UT1−UTC from the station displacement due to the earthquake are shown in the last row.

Axis	Displacement	Δ(UT1−UTC) Contribution
X	1.6 ± 1.2 mm	−0.8 ± 1.0 µs
Y	−7.4 ± 0.6 mm	24.4 ± 3.0 µs
Z	−9.9 ± 0.5 mm	43.6 ± 5.0 µs
Total	12.5 ± 1.4 mm	67.2 ± 5.9 µs

Table 2 The sensitivity of UT1−UTC to changes in station position for the stations of the MK-VLBA:PIETOWN Intensive baseline and for the stations of the KOKEE:WETTZELL Intensive baseline. Units are µs/mm. As expected, the sensitivities of the two stations of the same baseline are the same magnitude but of opposite sign. Note also the low magnitude and standard deviation of the sensitivities of the stations in the longer baseline compared to the stations in the shorter baseline.

Coord	Mk	Pt	Kk	Wz
X	−0.5 ± 0.47	0.5 ± 0.47	0.4 ± 0.06	−0.4 ± 0.06
Y	−3.3 ± 0.31	3.3 ± 0.31	−1.3 ± 0.09	1.3 ± 0.09
Z	−4.4 ± 0.45	4.4 ± 0.45	−0.1 ± 0.12	0.1 ± 0.12

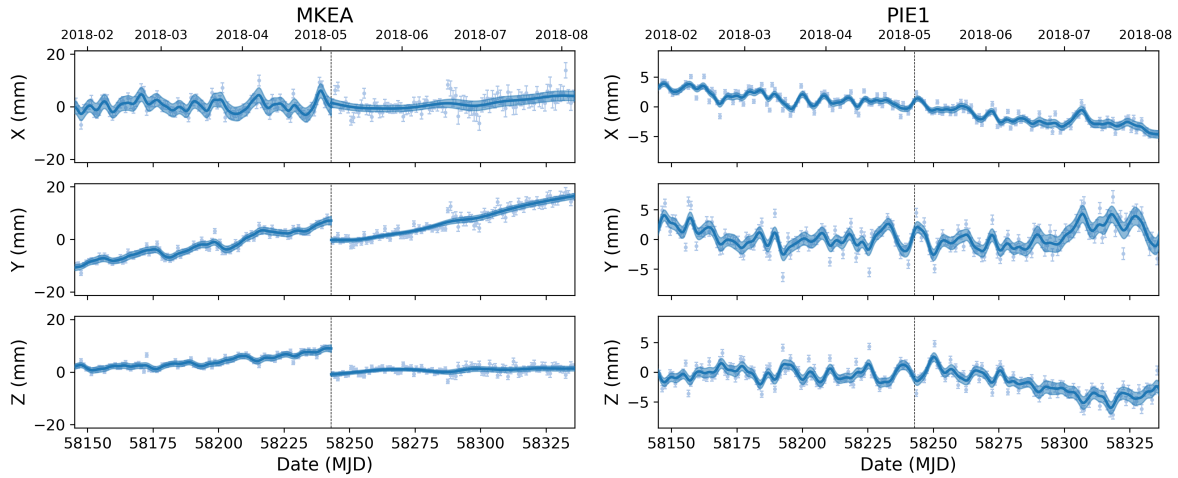

Fig. 2 The time series of the X, Y, and Z positions of the MKEA and PIE1 GNSS stations from the IGS repro3 data set. Values are from roughly three months before and after the Hawai'i earthquake marked by the vertical dashed line. Values relative to an arbitrary zero point are shown. The regression function calculated by the Nadaraya-Watson estimator is shown in the solid blue line, with the shaded blue regions denoting the 3σ confidence bands. No position shift is evident in the PIE1 data, so the regression is applied in one part over all the data, while there is a break evident at the time of the earthquake in the MKEA data. Thus, the regression for MKEA is applied in two parts. The vertical scales between the two stations are different, which enhances the apparent variability of the PIE1 series relative to the MKEA series.

With the MKEA station displacements reported in Table 1 and the sensitivities reported in Table 2, we calculate the expected shift in UT1−UTC due to the shift in the MKEA station as the total derivative of UT1−UTC with respect to the three coordinate axes

$$d(UT1-UTC) = \sum_{i=1}^{3} \frac{\partial UT1-UTC}{\partial x_i}\, dx_i. \quad (2)$$

This can be restated as

$$\Delta(UT1-UTC)_{station} = S_X \Delta X + S_Y \Delta Y + S_Z \Delta Z \quad (3)$$

where the S_A are the UT1−UTC sensitivities and the ΔA are the station shifts in each orthogonal coordinate. Evaluating Equation 3 we find that

$$\Delta(UT1-UTC)_{MKEA} = 67.2 \pm 5.9 \text{ µs}. \quad (4)$$

The error propagation calculation assumes uncorrelated Gaussian uncertainties because the sensitivities and the GNSS-measured station displacements are determined independently.

The difference between the estimated UT1−UTC discontinuity from Equation 1 and the expected shift in UT1−UTC from Equation 4 is 8.5 ± 7.5 µs, or 1.1 σ. The two values are statistically consistent. So, the change in position of the MKEA station, translated to a change in position of the MK-VLBA station, that happened at the same time as the UT1−UTC discontinuity explains why the jump occurred. Can the same effect account for the observed periodicity in the Mk-Pt UT1−UTC residuals?

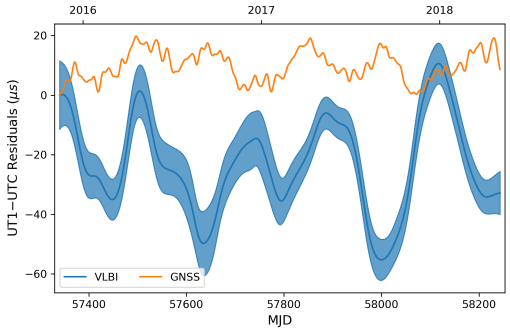

Fig. 3 Comparison of the observed UT1−UTC residuals from the Mk-Pt VLBI Intensive series (in blue) with the expected shift of the observed UT1−UTC value as calculated from the position shifts of the MKEA and PIE1 GNSS stations and the sensitivities of the co-located VLBA stations to those changes (in orange). Both curves are changed since a common starting date. This shows that the two are not closely related, and thus the changes in the station position alone are not sufficient to explain the periodicity in the Mk-Pt UT1−UTC residuals.

Using only data from before the earthquake, we extend the effective shift calculation to both MKEA and PIE1 and then add them together. Setting a common zero point for both the Mk-Pt UT1−UTC residuals and the expected effective shift calculation, we produce the two lines shown in Figure 3. No correlation statistics are necessary to see that the two curves do not correspond, either in amplitude or in phase. Thus, changes in the station positions are not sufficient to explain the periodicity in the UT1−UTC residuals, even with higher UT1−UTC sensitivities to such changes on the Mk-Pt baseline versus the Kk-Wz baseline.

4 Discussion and Conclusion

The analysis of Section 3.1 clearly shows that there is a periodic signal, with a period of roughly half of a year, in the Mk-Pt UT1−UTC residuals. It is present for residuals calculated from each of the three reference series (not shown here), and it is potentially present in the Kk-Wz residuals as well. This signal contributes to the systematic error of the measurement series and is not captured in the formal error. If subsequently used in combination, such a series would be too heavily weighted if only the formal errors were taken into account. It would also drive the predicted values of UT1−UTC away from the truth, most notably at the extrema of the periodic signal. There is no apparent reason why this effect would be limited to baselines of the VLBA, and there are indications the signal is present in other baselines. Therefore, it seems prudent to move forward under the assumption that this is affecting all Intensive baselines, though with varying severity seemingly dependent on the baseline length and geometry.

As the requirements on the precision and accuracy of UT1−UTC tighten moving into the future, the source of this signal needs to be better understood. From this work, it is not clear what causes the periodicity in the residuals. Though the station displacement due to the earthquake as recorded by the MKEA receiver is shown to be able to explain the UT1−UTC discontinuity in the Mk-Pt VLBA Intensive series, GNSS station position evolution does not explain the periodicity in the residuals. Therefore, one or more of the applied models used to establish the a prioris for the estimation of UT1−UTC with Intensives contains an error, a known contributor to variations in the output of the estimate is not being included in the estimation at all, or there is a mechanism that is not yet understood or identified that is causing this behavior. Further investigation to identify and correct this missing information must be undertaken.

Acknowledgements

The authors acknowledge use of the Very Long Baseline Array under the USNO's time allocation. This work supports USNO's ongoing research into the celestial reference frame and geodesy. The VLBA is an instrument of the National Radio Astronomy Observatory which is a facility of the National Science Foundation operated under cooperative agreement by Associated Universities, Inc.

References

1. Christopher Dieck, Maria Davis, Megan Johnson, John Gipson, Sharyl Byram, and Dan MacMillan. Intensive Sessions with the Mauna Kea VLBA Station. In R. Haas, S. Garcia-Espada, and J. A. López Fernández, editors, *Proceedings of the 24th European VLBI Group for Geodesy and Astrometry Working Meeting*, pages 152–156, 2019.
2. Eric D. Feigelson and G. Jogesh Babu. *Modern Statistical Methods for Astronomy*, Cambridge University Press, 2012.
3. Nicole Geiger, Alan Fey, Christopher Dieck, and Megan Johnson. Intensifying the Intensives with the VLBA. In K. L. Armstrong, K. D. Baver, and D. Behrend, editors, *International VLBI Service for Geodesy and Astrometry 2018 General Meeting Proceedings*, NASA/CP–2019-219039, pages 219–222, 2019.
4. E. A. Nadaraya. On Estimating Regression. *Theory of Probability & Its Applications*, 9(1), doi:10.1137/1109020, 141–142, 1964.
5. Axel Nothnagel and Dorothee Schnell. The impact of errors in polar motion and nutation on UT1 determinations from VLBI Intensive observations. *Journal of Geodesy*, 82(12), 863–869, 2008.
6. Geoffrey S. Watson. Smooth Regression Analysis. *Sankhyā: The Indian Journal of Statistics, Series A*, 26(4), 359–372, 1964.

On the Prospects of Explaining and Modeling with Higher Accuracy the Precession-nutation from VLBI Solutions

José M. Ferrándiz[1], Santiago Belda[1], Sadegh Modiri[2], Maria Karbon[1], Robert Heinkelmann[3], Alberto Escapa[1], Harald Schuh[3,4]

Abstract We show the extent of the variance of CPO time series solutions from VLBI that can be reduced by adding suitable corrections to the precession model, and provide information concerning nutations.

Keywords VLBI, CPO, precession, standard models

1 Introduction

According to the IERS Conventions (2010) [1] the rotation relating to the terrestrial and celestial geocentric reference frames is characterized by five angles named the Earth orientation parameters (EOP). Among them, the deviations of the actual celestial intermediate pole (CIP) with respect to its location according to the conventional a priori precession-nutation model IAU2000A/2006 are the celestial pole offsets (CPO), usually expressed as the pair dX and dY. For decades, accurate enough CPO solutions can be only derived from Very Long Baseline Interferometry (VLBI) observations. Therefore, most of the actual CPO values directly inferred from observations comes from the analysis of the 24-hour-long VLBI R1 and R4 sessions, performed twice a week. Each IVS operational Analysis Center (AC) routinely computes solutions for the EOP on a session-wise basis with a latency of a few weeks, which is higher for the combined solutions derived by the IVS Combination Centers. In turn, the IERS Earth Orientation Center produces and releases a series of daily EOP, the CPO pair being time–densified by applying sophisticated algorithms.

Whatever the analysis procedure is, the obtaining of CPO solutions from VLBI data is impossible without using some a priori model for the location of the CIP, given the magnitude of its motion. The scatter of the CPO time series indicates how good the a priori is and would vanish if the latter was perfect. But this is not the case and it is known that the precession-nutation theories suffer from inaccuracies, inconsistencies, and have outdated components—and they are not the only EOP affected by issues (Ferrándiz et al., 2021 [2]). A prompt improvement of the Earth rotation theories and models was encouraged by Resolution 5 of the IAG (International Association of Geodesy) in 2019 and then by Resolution B2 of the IAU (International Astronomical Union) in 2021. The IAU/IAG Joint Working Group on Improving Theories and Models of the Earth's Rotation (JWG ITMER) is contributing to the implementation of the said resolutions. Matters related to the improvement of the current precession-nutation models are prioritized, according to the recommendations of the 2019 International Earth Rotation Service/Global Geodetic Observing System Unified Analysis Workshop. A replacement of the whole theories in force seems unfeasible at the short-term, because of its too high effectiveness-cost ratio; however, their improvement by supplementing each one with suitable corrections seems possible.

In this contribution we use a sample of single AC and combined CPO solutions, paying attention to the unexplained variance of those CPO time

1. University of Alicante VLBI Analysis Centre, Department of Applied Mathematics, Alicante, Spain
2. Federal Agency for Cartography and Geodesy (BKG), Section G 1, 60598 Frankfurt am Main, Germany
3. Helmholtz Centre Potsdam, GFZ German Research Centre for Geosciences, D-14473 Potsdam, Germany
4. Technische Universität Berlin, Institute of Geodesy and Geoinformation Science, Berlin, Germany

series—expressed as weighted root mean square (WRMS)—and present results on to which extent it could be reduced at short term by using suitable sets of corrections to the current conventional models. We focus mainly on the precession model, which may be improved quite easily and keeping its theoretical framework.

2 Precession

The IAU2006 precession model consists of the two components of the P03 theory (Capitaine et al., 2003 [3]), namely the precession of the equator and that of the ecliptic. Two main new features introduced by P03 are using 5-degree polynomials to model the two former components and considering the Earth's dynamical ellipticity H not as a constant like up to then, but as a linear function of time, taking into account the Earth's J_2 rate inferred at that time from the satellite laser ranging (SLR) observations available since 1976.

In the last years, different authors have brought to light some issues related to the two former features:

- Accuracy of the precession polynomials when testing them with the observations available so far;
- Inconsistencies between IAU2006 and the IAU2000 nutation model, where H is constant;
- Other issues arising from the J_2 time-variation actually inferred from observations versus the simplified model used in P03.

2.1 Linear Detrending

Regarding the first subject, the far dominant components of precession are the linear terms. The adopted values of the precession rates and offsets (at the initial date J2000.0) need some updating, according to all the analyses published in the last years (e.g., Belda et al. 2017 [4], Nurul et al. 2020 [5], Zhu et al. 2021 [6]). The magnitudes of the biases of the former parameters are small compared to the overall uncertainties, but statistically significant.

Therefore, a main objective is to estimate optimal values for them in an attempt to derive corrections that may reach a wide agreement and be applied as standards. We address that problem using exclusive VLBI observations. As a common requirement, all the results showed next are based on solutions that cover the period 1984–2021, have over 4,000 points, and provide CPO in terms of dX and dY. That interval was chosen because it spans two full cycles of the lunar node and we considered that convenient for analyzing nutations despite the poorer accuracy of the observations till the early 1990s; moreover, some experiments performed with the time interval starting in 1990 supported this idea.

This criterion led to select four recent solutions from single ACs, namely those identified with labels bkg2020a, gsf2020a, opa2020a, and usn2021c; and five quarterly combined solutions, namely bkg20q2, dgfi20q2, gsfc20q2, ivs20q2X, and ivs19q4X. The ivs19 series ends earlier, but we preferred to keep it because its trend was closer to those of other combined solutions than to that of ivs20. Data were downloaded from CDDIS or BKG data sites[1].

We first show the results of performing a simple linear detrending to each solution, for the period 1984–2021. The results for the single AC ones are displayed in the upper part of Table 1, whose columns display the offsets and rates, the formal uncertainties of these parameters as provided by the fit software, the number of points and the WRMS of raw and detrended data, as well as the WRMS improvement percentage. The WRMS decrease is evident at first glance in most cases; the lowest value is obtained by the usn2021 series (in bold), followed by gsf2020.

Results for the combined solutions appear in the lower part of Table 1. It can be noticed that the lowest WRMS for dY corresponds to ivs20q2 and is 146 μas, whereas for dX it happens to appear for ivs19q4 with 153 μas vs. 168 μas for ivs20q2. These distinguished labels and WRMS are in bold. A quick look to both tables is enough to reveal that combined solutions provide lower WRMS than single AC ones.

The rates of each CPO from the former solutions are gathered in Figure 1 for easier viewing and comparison. Each individual trend is displayed as a point surrounded by its 95% confidence interval (CI). Besides, we plot the medians of each group of trends as vertical lines, as well as the mean extended to all the solutions. For the comparison sake, a vertical dotted line displays the trends extracted similarly from IERS14C04.

[1] `https://cddis.nasa.gov/` or `ftp://ivs.bkg.bund.de`

Table 1: Reduction of WRMS by simple linear detrending in the period 1984–2021 of four selected recent IVS individual and combined quarterly solutions. Offsets are in J2000.0; units μas, years.

CPO	solutions	Offset [μas]	trend [μas/y]	σ offset	σ trend	No. obs.	WRMS raw	WRMS detrend	WRMS % gain		Offset [μas]	trend [μas/y]	σ offset	σ trend	WRMS raw	WRMS detrend	WRMS % gain
dX	bkg2020a	44.65	6.253	4.03	0.287	5989	214.6	172.6	19.6	dY	-14.39	1.649	4.10	0.292	176.1	175.6	0.3
	gsf2020a	22.38	6.058	3.66	0.262	6431	196.0	166.1	15.2		-88.69	2.285	3.84	0.274	184.5	172.8	6.4
	opa2021a	-28.26	4.797	4.34	0.308	7027	211.1	205.8	2.5		-129.62	3.177	4.23	0.304	223.1	201.1	9.8
	usn2021c	16.64	5.402	3.73	0.272	5613	183.4	**160.8**			-82.22	1.907	3.89	0.283	176.6	**165.2**	6.5
	MEANS	13.85	5.628						12.4		-78.73	2.255					5.7
dX	bkg20q2	2.18	4.691	4.1	0.329	4209	177.8	167.3	5.9	dY	-84.03	2.328	4.36	0.347	186.2	174.9	6.0
	dgfi20q2	-1.46	4.653	4.4	0.343	4034	172.6	162.4	5.9		-85.88	2.804	4.66	0.36	179.0	168.8	5.7
	gsfc20q2	19.95	3.101	4.03	0.313	4229	176.9 1	67.6	5.3		-90.42	2.435	4.29	0.332	190.8	177.8	6.8
	ivs20q2X	-27.55	10.029	4.89	0.351	4266	205.0	168.0	18.1		-93.94	3.061	4.36	0.309	158.2	**145.9**	7.8
	ivs19q4X	16.37	5.147	4.38	0.337	4215	173.1	**152.9**	11.74		-83.56	0.277	4.66	0.357	174.0	**159.3**	8.4

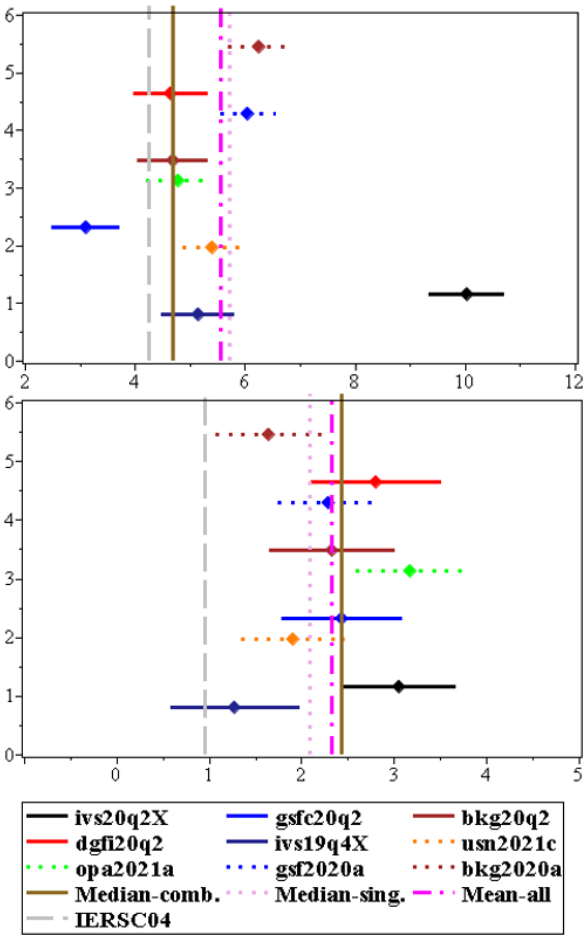

Fig. 1: CPO rates of individual and combined solutions (1984–2021) with CI 95% in μas: upper plot dX, lower plot dY.

Taking into account the former results and considerations, we think that the unexplained variance of the CPO may be reduced at short term in a noticeable but easy way by undertaking a few potential simple actions, e.g.:

- Determine, agree, and apply corrections to the dX and dY trends. Using the means of a sample of VLBI solutions or simply the trends of the IVS reference solution may be a rough first choice to start estimation and validation; for instance, reference initial values may be:
  - dX trend correction about 5.524 to 5.628 mas/yr
  - dY trend correction about 2.255 to 2.381 mas/yr
- Get more insight into the causes of the offsets—it might take longer

2.2 Inaccuracy Derived from Inconsistencies among IAU2006, IAU2000, and the Actual Variation of the Dynamical Ellipticity

The first of the last two issues cited at the beginning of this section arises from the fact that IAU2006 assumes a constant J_2 rate unlike IAU2000, which considers this precession parameter as a constant; moreover, both theories adopted different values for the obliquity and the "precession constant", i.e., the longitude rate proportional to the constant components of H (or J_2). These inconsistencies may be compensated by applying a few corrections to the nutation model derived by Escapa et

al. (2017) [7]

$$\begin{aligned} \mathrm{dX} =& (-6.2 + 15.4\,t)\,\sin\Omega - (0.6 + 0.6\,t^2)\,\cos\Omega \\ & + 1.4\,t\,\sin(2F - 2D + 2\Omega), \\ \mathrm{dY} =& (0.8 - 25.4\,t)\,\cos\Omega - (0.8 + 0.3\,t^2)\,\sin\Omega \\ & - (0.3 + 1.8\,t)\,\cos(2F - 2D + 2\Omega). \end{aligned}$$

The former corrections have small magnitude but contain secular–mixed terms whose amplitude grows with time and thus become more relevant as time gets away from the initial date J2000.0. For that reason, when the topic was discussed prior to the IAU 2018 General Assembly, it was decided that applying them was not urgent then and may be delayed until the time of adopting corrections of a higher magnitude.

The situation is worse when the actual J_2 time-variation is considered instead of the linear variation adopted by IAU2006, which was inferred from the Earth's oblateness trend of -3.001×10^{-8}/yr observed formerly. It is equivalent to a rate of $H_1 = H_0\,(-2.7719 \times 10^{-8})$/yr , H_0 being the reference dynamical ellipticity. The actual J_2 values were taken from the long-term solution provided by the Center for Space Research of The University of Texas at Austin (Cheng et al. 2013 [8]), shown in black in Figure 2, which also displays the linear model assumed by IAU2006 as a red line. However, the trend started to change sign in 1997, and has reversed along the last 20 years. At present, the observed $J_2 = -C_{20}$ evolution is better represented by a second-degree polynomial, depicted in blue in Figure 2 (see e.g., Marchenko & Lopushanskyi 2018 [9], Chao & Chung 2020 [10]).

By straightforward integration of the equations of motion, it is immediate that the linear H trend assumed in IAU2006 contributes a quadratic term to the precession polynomial in longitude, whereas a quadratic term of the fit contributes a cubic parabola to it. The effect of the observed H variations is more difficult to compute and thus the procedure cannot be detailed here; let us say that we used numerical methods under the Hamiltonian formalism. The longitude variations resulting from the observed values, expressed as dX, are shown in black in Figure 3 together with the foresaid quadratic and cubic components of dX, in red and blue respectively. It is clear that the cubic model for correcting the dX precession gives results closer to the actual dX variations computed numerically than the quadratic model currently in force.

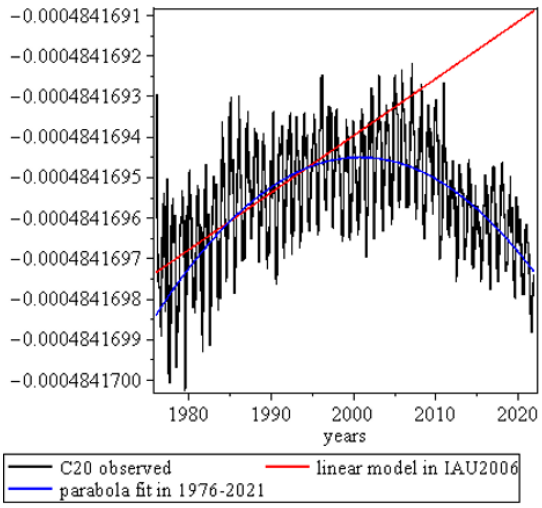

Fig. 2: C20 from CSR long-term series, observed (black), IAU2006 linear model (red), and fitted parabola (blue), 1976–2021.

Let us notice that such a quadratic component was not provided explicitly in P03 (Capitaine et al. 2003 [3]) and thus we would have to recompute it and then subtract it before applying the cubic correcting term if a second-degree polynomial would be adopted as the basic simple model for the H change.

Considering the H modeling related issues, we may think of different actions for easily improving the precession model at short term, like the following:

- Leave the theory as it is (no action) or update the value of the H linear trend;
- Replace the linear trend of H by a quadratic fit, a model closer to reality;
- Return to an *old-style* model with constant H.

3 Additional Comments and Conclusions

As for the forced nutation models, a first conclusion from practically all the analyses published in the last years is that the amplitudes of the main nutation components need also some updating (Belda et al. 2017 [4], Nurul et al. 2020 [5], Zhu et al. 2021 [6]). The WRMS may be reduced significantly (e.g., Ferrándiz et al. 2022 [11]).

The implementation of an agreed, suitable set of semi-empirical corrections to the precession and forced

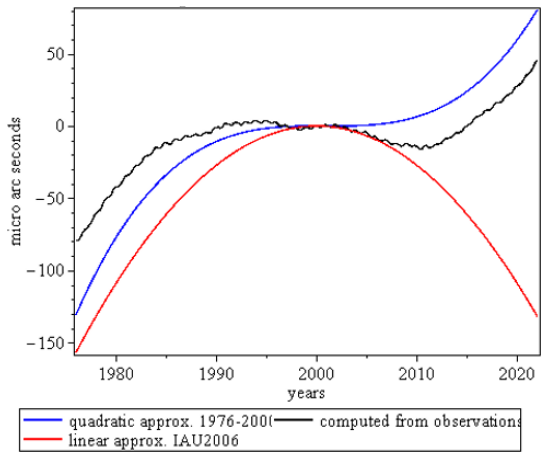

Fig. 3: dX variations from the observed J_2 (black), the IAU2006 linear approximation (red), and the parabolic fit (blue), 1979–2022.

nutation models IAU2006 and IAU2000 may not take long and bring the WRMS of each CPO to the vicinity of 120 µas for combined IVS solutions, or 140–150 µas for single analysis center solutions, respectively. Let us recall that significant further improvement of accuracy may be gained by using supplemental FCN models.

Acknowledgements

The UA authors were supported partially by Generalitat Valenciana (PROMETEO/2021/030, SEJIGENT/2021/001), the Spanish Ministerio de Ciencia e Innovación (MCIN/AEI/10.13039/501100011033/, PID2020-119383GB-I00), and the European Union-NextGenerationEU (ZAMBRANO 21-04).

References

1. G. Petit, B. Luzum (eds), "IERS Conventions (2010)", IERS TN 36, Verlag des Bundesamts für Kartographie und Geodäsie, Frankfurt am Main, http://www.iers.org/TN36/, 2010.
2. J.M. Ferrándiz, R.S. Gross, A. Escapa, J. Getino, A. Brzezinski, R. Heinkelmann, "Report of the IAU/IAG Joint Working Group on Theory of Earth Rotation and Validation", International Association of Geodesy Symposia, No. 152, https://doi.org/10.1007/1345_2020_103, 2021.
3. N. Capitaine, P.T. Wallace, J. Chapront, "Expressions for IAU 2000 precession quantities", Astron. Astrophys. 412, 567, https://doi.org/10.1051/0004-6361:20031539, 2003.
4. S. Belda, R. Heinkelmann, J.M. Ferrándiz, M. Karbon, T. Nilsson and H. Schuh, "An Improved Empirical Harmonic Model of the Celestial Intermediate Pole Offsets from a Global VLBI Solution", Astronomical Journal 154, 166, https://doi.org/10.3847/1538-3881/aa8869, 2017.
5. I. Nurul Huda, S. Lambert, C. Bizouard and Y. Ziegler, "Nutation terms adjustment to VLBI and implication for the Earth rotation resonance parameters", Geophys. J. Int. 220, 759, https://doi.org/10.1093/gji/ggz468, 2020.
6. P. Zhu, S.A. Triana, J. Rekier, A. Trinh and V. Dehant, "Quantification of corrections for the main lunisolar nutation components and analysis of the free core nutation from VLBI-observed nutation residuals", J. Geod. 95, 57, https://doi.org/10.1007/s00190-021-01513-9, 2021.
7. A. Escapa, J. Getino, Ferrándiz J.M., and T. Baenas, "Dynamical adjustments in IAU 2000A nutation series arising from IAU 2006 precession", Astron. Astrophys. 604, A92, https://doi.org/10.1029/2020JB019421, 2017.
8. M. Cheng, B. D. Tapley, and J. C. Ries, "Deceleration in the Earth's oblateness", J. Geophys. Res. 118, 740, https://doi.org/10.1002/jgrb.50058, 2013.
9. A.N. Marchenko, A.N. Lopushanskyi , "Change in the Zonal Harmonic Coefficient C_{20}, Earth's Polar Flattening, and Dynamical Ellipticity from SLR Data", Geodynamics 2, 5, https://doi.org/10.23939/jgd2018.02.005, 2018.
10. B.F. Chao, Y. Yu and C.H. Chung "Variation of Earth's oblateness J_2 on interannual to decadal timescales", J. Geophys. Res.: Solid Earth 125, https://doi.org/10.1029/2020JB019421, 2020.
11. J.M. Ferrándiz, S. Belda, M.A. Juárez et al., "Accuracy of proposed corrections to the current precession-nutation models: A first assessment", EGU22-4031, https://doi.org/10.5194/egusphere-egu22-4031, 2022.

Current CRF Status at X/S and K Bands

David Gordon[1], Alet de Witt[2], Christopher S. Jacobs[3]

Abstract We present the status of the X/S- and K-band celestial reference frames four years after ICRF3 was generated. The reference frames now have ∼20% more sources at X/S-band and ∼25% more sources at K-band. Median scaled uncertainties for the original ICRF3 sources have improved by ∼25% at X/S-band and by ∼37–40% at K-band.

Keywords ICRF3, X/S band, K band, astrometry

1 Introduction

ICRF3 [1] was approved by the International Astronomical Union in August 2018 and became the official IAU celestial reference frame in January 2019. ICRF3 contains catalogs of precise positions of compact extragalactic radio sources at three radio frequencies—a primary catalog of 4,536 sources at X/S-band (8.6/2.3 GHz) and secondary catalogs of 824 sources at K-band (24 GHz) and 678 sources at X/Ka-band (8.4/32 GHz). However, observations to maintain and expand the ICRF have continued at all three bands during the four years since ICRF3 was finalized. In the next sections we present the curent CRF status at X/S- and K-bands.

1. US Naval Observatory
2. South African Radio Astronomy Observatory
3. NASA Jet Propulsion Laboratory, California Institute of Technology

2 The CRF at X/S band

The X/S CRF catalog currently contains 5,442 sources, some 20% more than ICRF3. Most of the additional sources (∼750) were added in monthly 2 Gb/s astrometry sessions on the Very Long Baseline Array (VLBA) and in bi-monthly RDV sessions (VLBA plus several IVS stations) at 512 Mb/s. Approximately half of these additional sources are within 7° of the ecliptic, observed in an effort to provide more sources for future spacecraft navigation. IVS sessions have added another ∼150 more sources, mainly in AOV and AUA sessions. The distribution of these 5,442 sources is shown in Figure 1. The source distribution clearly favors northern hemisphere observations, showing a sudden drop in source density south of $\sim -45^\circ$ declination, the practical limit of the VLBA. Due to a scarcity of large southern hemisphere antennas available for X/S VLBI astrometry/geodesy, this assymetry cannot currently be remedied.

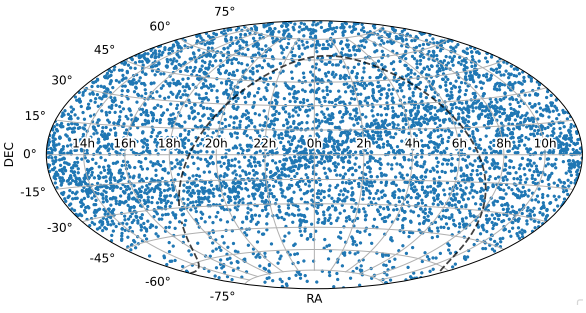

Fig. 1 Distribution of the 5,442 sources in the current X/S-band CRF catalog. The dotted line shows the galactic plane.

3 The CRF at K band

The K-band CRF catalog now contains 1,035 sources, some 211, or 25% more than the ICRF3-K catalog. Most of these (183) were added in monthly K-band VLBA astrometry sessions, at 2 Gb/s before November 2019 and at 4 Gb/s after. Southern hemisphere observations on the HARTRAO–HOBART26 baseline have also added an additional 28 sources south of $-46°$ declination. And 206 of the sources were observed on both the VLBA and HARTRAO–HOBART26 networks, helping to tie the two networks together. The distribution of K-band sources is shown in Figure 2. Unlike at X/S-band, the K-band sources are much more evenly distributed over the sky, although source positions are much less precise in the far south.

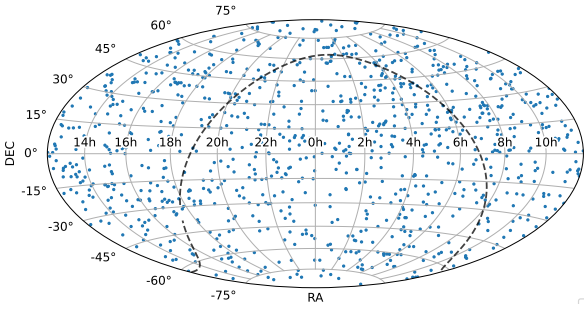

Fig. 2 Distribution of the 1,035 sources in the current K-band CRF catalog. The dotted line shows the galactic plane.

4 Precision Improvements

With four additional years of observations, the median scaled Right Ascension/Declination errors for the 4,536 ICRF3-SX sources has improved from 127|218 µas to 95|161 µas, or by ∼25%. And for the 824 ICRF3-K sources, it has gone from 73|134 µas to 46|80 µas, improving by ∼37|40%. In Table 1 we intercompare K and X/S precision for common sources. For the original ICRF3 sources, K-band was ∼15|53% less precise than X/S. The current K-band, with an additional ∼200 sources in common, is slightly more precise in RA than the original ICRF3-SX, but slightly less precise than the current X/S. The K-band ICRF3 noise floor was 30 µas in RA and 50 µas in Dec, a result of the shorter north-south extent of the VLBA compared to its east-west extent; so Declination uncertainties are always greater for K-band. Even so, K-band has the potential to surpass X/S-band in precision over the next few years.

Table 1 K vs. X/S median scaled RA/Dec errors for common sources.

# Sources	ICRF3-K	ICRF3-XS
793	72.0/132.6 µas	62.6/86.8 µas
# Sources	Current K	ICRF3-XS
999	48.2/82.7 µas	51.8/67.9 µas
# Sources	Current K	Current XS
1014	48.4/83.2 µas	46.9/60.3 µas

Acknowledgements

The authors gratefully acknowledge use of the Very Long Baseline Array since 2017 under the US Naval Observatory's time allocation. This work supports USNO's ongoing research into the celestial reference frame and geodesy. The VLBA is operated by the National Radio Astronomy Observatory, a facility of the National Science Foundation and operated under cooperative agreement by Associated Universities, Inc. This research was partly supported by the South African Radio Astronomy Observatory (SARAO,) a facility of the National Research Foundation (NRF) of South Africa. Part of this research was carried out at the Jet Propulsion Laboratory, California Institute of Technology, under a contract with the National Aeronautics and Space Administration (80NM0018D0004).

References

1. Charlot, P., Jacobs, C.S., Gordon, D., Lambert, S., de Witt, A., Bohm, J., Fey, A.L., Heinkelmann, R., Skurikhina, E., Titov, O., Arias, E.F., Bolotin, S., Bourda, G., Ma, C., Malkin, Z., Nothnagel, A., Mayer, D., MacMillan, D.S., Nilsson, T., and Gaume, R., 2020, Astronomy and Astrophysics, 644, A159. [doi 10.1051/0004-6361/202038368]

Three Years of ICRF3 Source Positions

Phil Cigan[1,2], David Gordon[1], Megan Johnson[1]

Abstract Precise astronomical reference frames are extremely important for a wide variety of applications, including astronomical observations and navigation, to name a few. ICRF3 is the third realization of the International Celestial Reference Frame, created from the combined international efforts of nearly 40 years of VLBI radio observations of thousands of quasars. In the time since ICRF3 was adopted by the International Astronomical Union on January 1, 2019, many additional astrometric and geodetic observations have been carried out, allowing for a regular cadence of global solutions which estimate updated earth orientation parameters as well as celestial reference frame source positions. In this paper we will examine the shifts in the radio positions of ICRF3 sources over the past three years, derived from VLBI global solutions.

Keywords ICRF, source positions

1 Introduction

Very Long Baseline Interferometry (VLBI) is a powerful technique that allows us to attain extremely precise astrometric positions of celestial sources. However, this also requires precise knowledge of the positions of the antennae used for the observations. When many 'stationary' reference sources are observed from numerous locations across the globe, over long periods of time, we can solve for both in a global solution. Through meticulous efforts, long-term observation series can be combined to make quality celestial reference frames, which are important for a wide variety of applications. Radio-derived celestial reference frames have been constructed for many years using data at X and S bands, and the current international standard is ICRF3 [1], shown in Figure 1. The sources observed to construct the ICRF are quasars, which are believed to be accreting supermassive black holes in the nuclei of galaxies, commonly known as Active Galactic Nuclei (AGN).

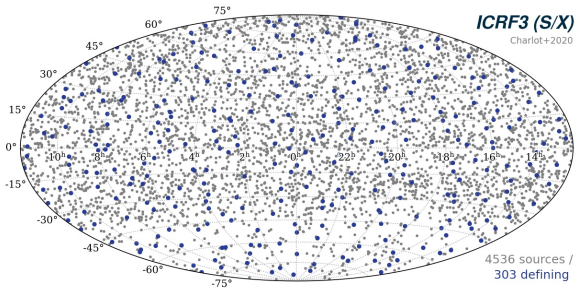

Fig. 1 ICRF3 at S/X bands, consisting of 4536 sources, of which 303 are defining sources [1].

There are numerous aspects to consider with regards to selecting quality reference frame sources. Isotropy and widespread coverage of sources on the sky is important for ensuring proper density, and targets should appear as point-like as possible so as to avoid confusion when observing their positions. Furthermore, sources should ideally be stable in terms of both their position and brightness. However, the AGN typically observed in astrometric and geodetic style sessions are real astrophysical objects, and so by their nature will have various deficiencies in those regards. There is often extended emission to contend with, which can depend on a source's proximity and

1. United States Naval Observatory
2. George Mason University

observing frequency, and the brightness of the various components in these physical systems can naturally vary depending on the local conditions and activity around the black hole and galaxy center. The following is a brief discussion of variations in the measured positions of reference frame sources, as compared to their ICRF3 values.

2 Data

In this work, we consider individual observing session measurements over time, as well as successive combined global solution position estimates made between 2018 and 2022. The positions are estimated from the USNO X/S TRF+CRF global solutions[1]. All of the data presented herein are differences in source position from the official ICRF3 values. When considering the distributions of positions, we look at both the full set of ICRF sources as well as those of just the defining sources from which the reference frame is made rigid.

Figure 2 shows an example of a time series of the R.A. and Dec. coordinates across observing sessions, for source 0107-610. The individual points show relatively large scatter paired with uncertainties on the order of 1 mas; however, with a large number of observations, the weighted root mean square (wrms) of the position differences for a source can be an order of magnitude smaller or better. Defining source positions are generally fairly stable over time, but many do still show signs of variability.

3 Analysis

The variability among individual observing sessions can help assess quality as a reference frame source, with an important caveat that they can also affected by local conditions at the time of the observations. It can be useful to inspect the time series of measured coordinates such as in Figure 2 for signs of variation, as dispersion of values and outliers are obvious. The wrms also gives a simple quantitative measure of variability over time.

[1] Available at https://crf.usno.navy.mil/vlbi-analysis-center

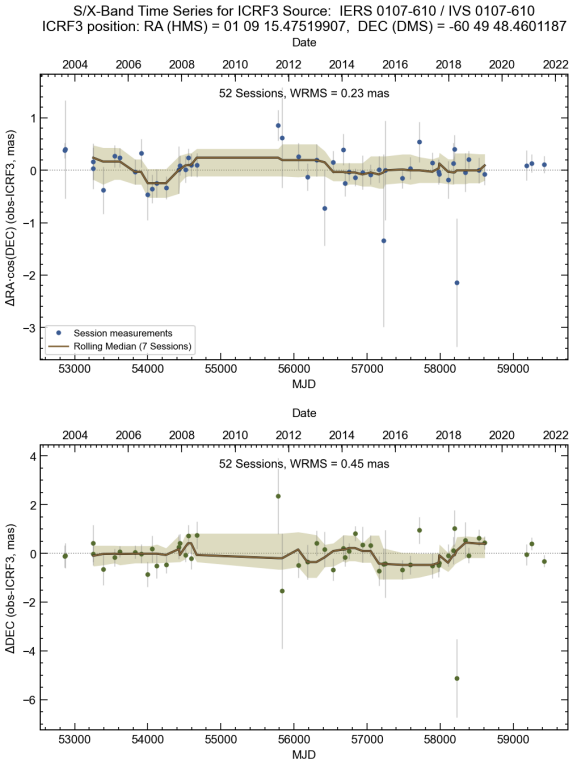

Fig. 2 Time series of astrometric measurements of right ascension and declination: difference from ICRF3 coordinates for source 0107-610.

It is also instructive to inspect the plotted sky position (R.A. vs. Dec.) over time, for trends, changes in precision/accuracy over time, drifts, discontinuities, and other apparent motion in the sky. Variation over time can be quite striking for some sources when animated over time. Static plots from two sources with apparent motion over timescales of years are shown in Figure 3, one general ICRF3 source (left) and one defining source (right). Even some defining sources show notable trends over the total timescales of these VLBI observation series.

The uncertainties of global solution position estimates are often an order of magnitude (or better) smaller than individual session uncertainties, because they derive from the combination of numerous observations over many years. Figure 4 shows a quantitative visualization of the largest difference from the ICRF3 position in the global solution (usn2021c in this case), as the minimum threshold of $N_{sessions}$ is increased. For ICRF3 sources with at least $\sim$ 35 observed sessions, the largest offsets are all $<$ 1 mas. For ICRF3 defin-

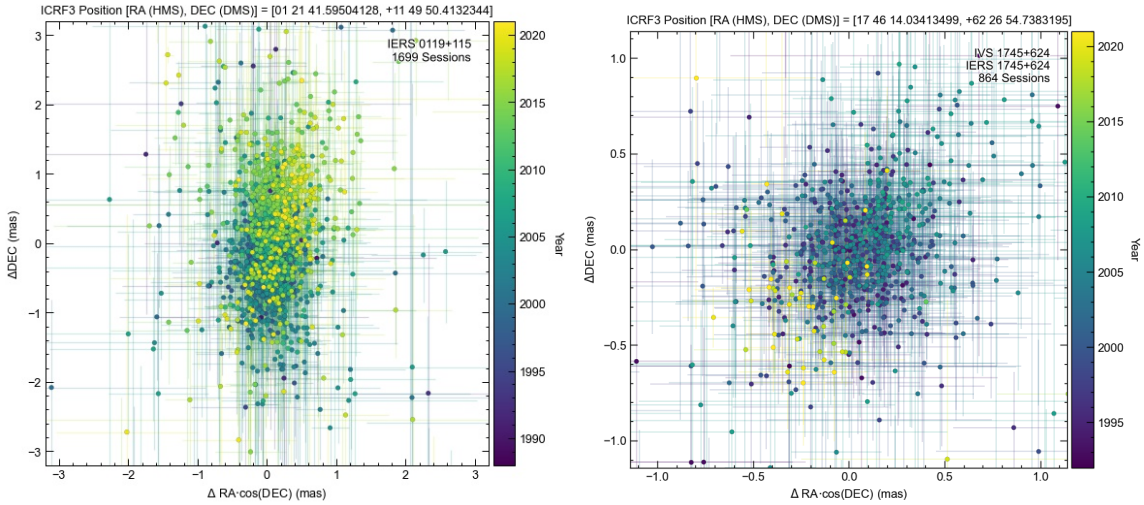

Fig. 3 Sky plot of session observation differences from ICRF3 positions for two sources. The data are color-coded by date of the observations. While there is a fairly large amount of scatter among individual data points, the center of mass of the points clearly shifts over time. This is not only true of general ICRF sources; the source on the right is a defining source.

ing sources, the largest offset drops below 0.5 mas at a threshold of $>$ 25 sessions. This highlights the fact that almost all sources with large offsets have few ($\sim$ 10–20) observing sessions.

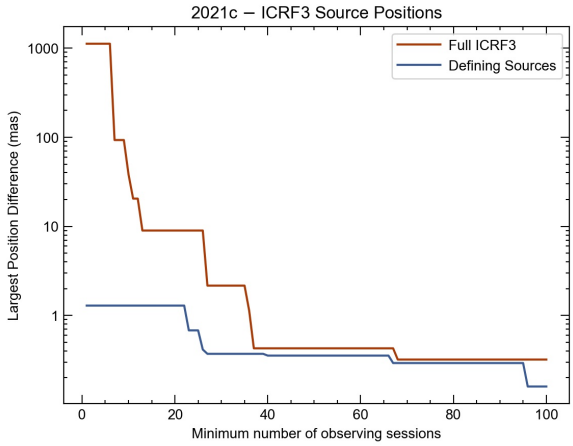

Fig. 4 Largest difference from the ICRF3 position in solution usn2021c, as a function of the minimum threshold of observing sessions. As the threshold for observing sessions increases, the largest difference decreases. Above $\sim$ 35 observations, the largest differences from ICRF3 positions are $<$ 1 mas.

Animations of global solution positions over time also contain a variety of useful information. Figure 5 shows a static frame of the positions of sources on the sky, determined from the usn2021c global solution and showing only sources with $>$ 10 observations. The arrows denote the direction and magnitude of the offset from ICRF3. The colorscale and size of the dots denote the number of observed sessions, highlighting again the impact that the number of observations has on the differences from the reference positions.

The distributions of the position differences are also useful for characterizing the data. Figure 6 shows histograms of the differences from the ICRF3 position (separately for R.A., Dec., and total), for the usn2021c global solution. Distributions are roughly log-normal with a small number of outliers (again, primarily due to a low number of observed sessions). The distributions gradually show an improvement in differences from ICRF3 over time with successive global solutions.

Table 1 lists some extremes from the usn2021c global solution: sources with the largest differences from ICRF3, as well as sources with the smallest differences. Lists are given both for general ICRF3 sources as well as defining sources. Again, the largest offsets are generally seen for sources with few observations; for the general source list the largest differences can be tens of mas or more, but for the defining sources the largest offset is $\sim$ 1 mas. The smallest offsets are on the order of $\sim$ 1–3 microarcsec. The majority of sources in the usn2021c solution are generally well-constrained—91% of the full ICRF source list shows offsets of $<$ 1 mas, and 26% have offsets of

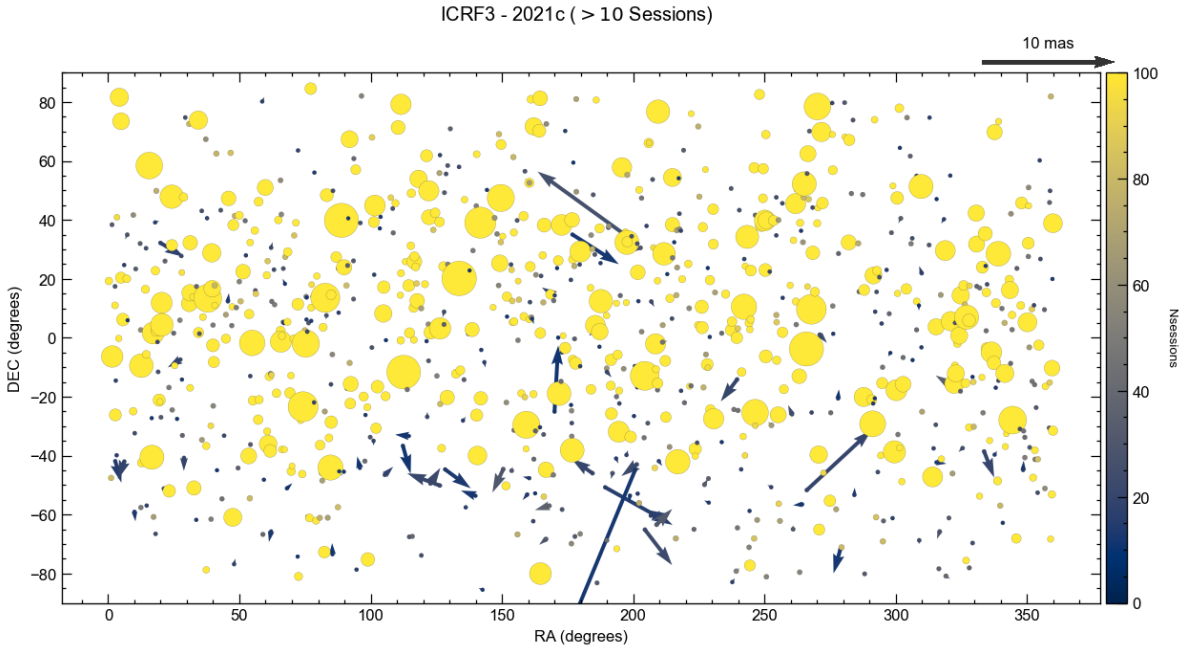

Fig. 5 Global solution usn2021c position differences from ICRF3. The vectors denote the magnitude and direction of the differences. The circle sizes increase and the color changes with the number of observing sessions for a given source, showing that those with large position differences are those with relatively few observations.

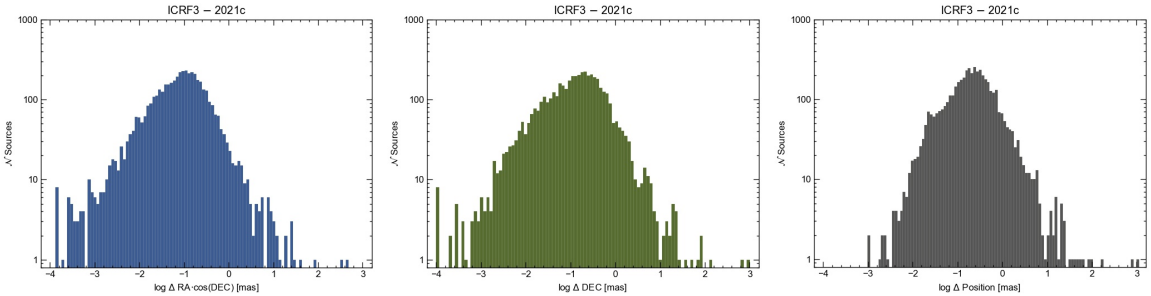

Fig. 6 Log histograms of position differences from ICRF3, determined from the usn2021c global solution. From left to right are distributions for R.A, Dec., and total position difference.

< 0.1 mas, with a median value of ~ 200 microarcsec. The defining sources are better still—99% have differences from ICRF3 of < 1 mas, and 80% have differences < 0.1 mas, with a median of ~ 34 microarcsec.

4 Conclusions

We have a rich set of time series of ICRF3 source positions, estimated from X/S VLBI global solutions. Individual session differences allow us to investigate drifts, discontinuities, and other apparent motion on the sky with the $\sim$ mas precision afforded by VLBI and to capture the inherent measurement variability of the sources. Differences between individual global solutions enable the comparison of large distributions of source positions and large number statistics. The total number of observations—and therefore solved position estimates—is gradually improving for ICRF3 sources in general. This work will be discussed in much greater detail in a forthcoming paper (Cigan et al., *in prep.*).

There are several natural extensions to this work that we are undertaking. We will use the variability

Table 1 Sources with the largest and smallest offsets from ICRF3.

IVS Name	Offset (mas)	$N_{sessions}$
Sources with largest 2021c-ICRF3 offsets		
2028-204	1122.49492	6
1657-298	770.95916	4
1507-246	160.88723	5
1711-251	93.15382	9
0201-440	81.62703	8
Sources with smallest 2021c-ICRF3 offsets		
0537-441	0.00097	2461
0503-043	0.00111	3
1145+268	0.00190	243
2318+049	0.00203	1378
0345+460	0.00203	276
Defining Sources with largest 2021c-ICRF3 offsets		
0809-493	1.29111	22
0918-534	1.16438	12
0700-465	0.83915	19
1718-259	0.68037	25
0742-562	0.63549	10
Defining Sources with smallest 2021c-ICRF3 offsets		
2318+049	0.00203	1378
0307+380	0.00250	442
0552+398	0.00351	4550
0800+618	0.00373	544
0235+164	0.00380	1058

in the time series to investigate potential excess variance not captured by the formal solution error. Comparison with ICRF3 K-band VLBI positions will be interesting for investigating how source position varies with observed frequency—which could be due to angular resolution, inherent astrophysical properties of the objects, or other reasons. We will also utilize images (e.g., from FRIDA[2]) to investigate extended structure. We also plan to compare our radio VLBI time series of source positions to those determined in the optical by Gaia, which provide an independent set of positions in a distinct part of the spectrum but potentially arise from different parts of the astrophysical sources.

[2] https://crf.usno.navy.mil/FRIDA

Acknowledgements

This work supports USNO's ongoing research into the celestial reference frame and geodesy. The National Radio Astronomy Observatory is a facility of the National Science Foundation operated under cooperative agreement by Associated Universities, Inc. The authors acknowledge use of the Very Long Baseline Array under the U.S. Naval Observatory's time allocation.

References

1. Charlot P., Jacobs C. S., Gordon D., Lambert S., de Witt A., Böhm J., Fey A. L., et al., 2020, *The third realization of the International Celestial Reference Frame by very long baseline interferometry*, A&A, 644, A159. doi:10.1051/0004-6361/202038368

Comparing Images of ICRF Sources at X-, K-, and Q-band

Lucas R. Hunt[1,2], Aletha de Witt[3], David Gordon[2], Christopher S. Jacobs.[4], Megan C. Johnson[2]

Abstract We have undertaken an exploratory Q-band (43 GHz) imaging-astrometry project targeting the K-band ICRF sources in three sessions each of 24 hours using the Very Long Baseline Array. The project's goal is to compare images and astrometry from X, K, and Q-bands in order to study the optimal frequency band for CRF observations. The sources were observed as closely as possible in time, typically within a week, in order to minimize temporal variations in source structure. We will show how source structure compares between all three bands and show the interplay between source structure, resolution, and astrometry. We hope to use the results from our campaign to determine if pursuit of a Q-band CRF is worthwhile.

1 Introduction

The third realization of the International Celestial Reference Frame (ICRF3) was the first to be defined at three bands: S/X (2.3/8.4 GHz), K (24 GHz), and X/Ka (8.4/32 GHz) bands [2]. The two higher frequency reference frames allow for higher resolution, and with enough observations, higher positional precision. Sources in the higher frequency reference frames can also be used as calibrators when observing other objects (e.g. water masers at K-band) [6] and for Ka-band spacecraft navigation [8]. The first set of observations for the K-band realization of ICRF3 used the Very Long Baseline Array (VLBA) in 2002 and also included observations used to generate a reference frame solution at Q-band (43 GHz) [7].

The Q-band observations were initially paired with K-band observations, where a source was observed at K-band then Q-band with a short pause in the middle. It was an unsuccessful attempt to use data from the two frequency bands to remove ionospheric effects from the group delay measurement [7]. Positions were determined for 131 of the 172 sources observed at Q-band, for a success rate of $\sim$76%. As mentioned above, the K-band observations eventually became part of ICRF3, but the Q-band observations were the only observations of their kind.

The VLBA has improved data recording rates from 128 Mbps to 4,096 Mbps since the initial observations were taken in 2002 and 2003, and we were inspired to revisit the possibility of generating a reference frame solution at Q-band. A Q-band reference frame is tempting because the higher resolution at higher frequencies would allow for a more precise reference frame with enough observations. We need to determine if enough sources are visible at Q-band to generate a reference frame and if the higher resolution breaks up sources into multiple components where it would be difficult to determine a single position [4]. To assess the viability of a Q-band reference frame, we observed K-band ICRF3 sources at S-, X-, K-, and Q-band (S-band was omitted from this analysis in the interest of time). Our goal was to determine how many sources we might be able to detect and how source structure varies between the different frequency bands. In §2 of this paper, we describe the observations, calibration, and imaging of the data. In §3 we outline our findings from the imaging. Finally in §4 we provide a summary.

1. Computational Physics Incorporated
2. United States Naval Observatory
3. South African Radio Astronomy Observatory
4. NASA Jet Propulsion Laboratory, California Institute of Technology

2 Data

The observations were made using the VLBA [9] with a different set up for each observed frequency. See Table 1 for in depth details on the observing setup. Each experiment ran for 24 hours, with the X-band occurring on 16 April, 24 May, and 13 June using the VLBA's dichroic system, K-band observations occurring on 18 April, 23 May, and 12 June, and Q-band observations occurring on 19 April, 25 May, and 13 June.

The schedules were written using the scheduling program SCHED[1] using the hour angle selection mode in order to do both astrometry and imaging. To optimize imaging, most sources were visited in three scans per observation with a scan length of 1.5 minutes, while new sources had a scan length of 2 minutes. Figure 1 shows the number of sources targeted and imaged in each observation.

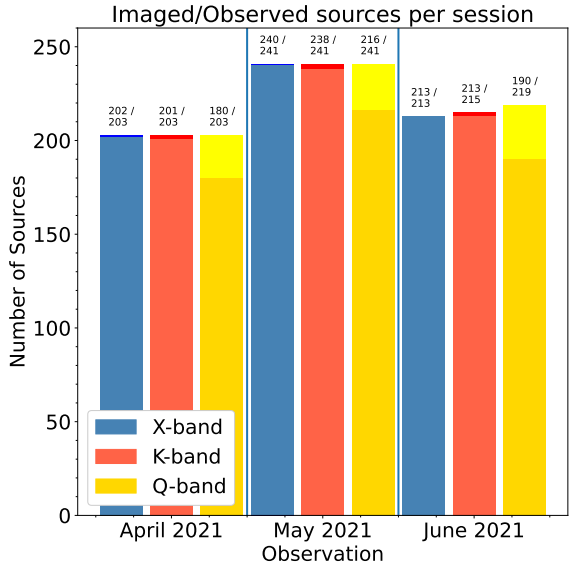

Fig. 1 The number of sources observed in each session. The X-band data is always in blue, the K-band data in red, and the Q-band data in yellow. The numbers above each bar indicate the number of sources imaged on the top and the number of sources observed on the bottom. The different shades of color for each bar also represent the number of sources observed and the number of sources imaged in each session.

The data were calibrated using NRAO's Astronomical Image Processing System (AIPS; [5]) following standard calibration procedures. More details will be available in [3]. The calibrated data were then split into individual source files and imaged using Difmap [10]. The imaging process started with a point source model, and iterated through a CLEAN and self-calibration cycle until the residual image was noise-like.

3 Analysis

In the end we targeted 453, 454, and 458 unique sources at X-, K-, and Q-band respectively. We successfully imaged 406, 449, and 452 sources, successfully detecting 99.7%, 98.9%, and 88.6% of sources at X-, K-, and Q-band respectively. This is an improvement over the $\sim$76% of sources detected in the original Q-band reference frame experiments [7]. Distribution of total flux density for each source is shown in Figure 2. The median clean fluxes are 338, 293, and 215 mJy and the mean clean fluxes are 657, 648, and 439 mJy at X, K, and Q-bands, respectively. Sources are fainter at higher frequencies but are still bright enough at Q-band that we are able to detect a significant fraction of sources. This indicates that there are likely enough sources to generate a robust reference frame at higher frequencies.

For the rest of the analysis we used a subset of 249 sources with an image quality parameter greater than 0.6 in the three frequency bands in order to minimize the corruption of the comparison from poor data. The image quality was determined using the average of the visibility fraction, resolution fraction, beam fraction, and error fraction. For more information on how these are calculated see deWitt et al. (submitted). We used these images to compare source compactness at different frequencies.

We first looked at compactness by dividing the peak flux by the total flux of the image where the peak flux is the flux density of the brightest pixel in Jy bm^{-1} and the total flux is the sum of the flux of all clean components output from the imaging procedure. If the object was completely point-like, the flux in the image would be in the brightest pixel. The ratio of the peak to total flux tells us how much of the total flux is in the brightest pixel and therefore how point-like the source is. Figure 3 shows the distribution of the peak-to-total flux. The mean values are 0.804, 0.769, and 0.761 at

[1] http://www.aoc.nrao.edu/software/sched/

Table 1 Observation setup.

All Sessions			
Parameter	Q-Band	K-Band	X-Band
Backend System	DDC[1]	DDC[1]	PFB[2]
Total channel windows	4	4	12
Single channel window bandwidth (MHz)	128	128	32
No. of spectral channels per window	256	256	64
Total bandwidth (MHz)	512	512	384
Frequency resolution (MHz)	0.5	0.5	0.5
Polarization	Dual	Dual	RR
Data rate (Gbps)	4	4	2
Sampling resolution (bits)	2	2	2
Channel Frequencies (MHz)	42976.5, 43104.5, 43232.5, 43360.5	23375.75, 23503.75, 23631.75, 23759.75	8443.875, 8475.875, 8507.875, 8539.875, 8603.875, 8635.875, 8699.875, 8731.875, 8795.875, 8827.875, 8859.875, 8891.875

[1]Digital Downconverter
[2]Polyphase Filterbank

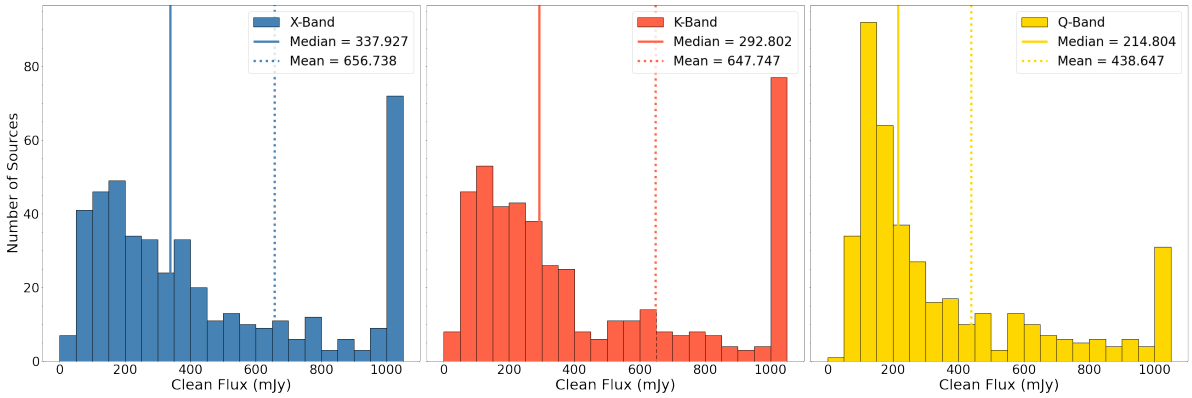

Fig. 2 Distribution of clean flux in sources detected at each frequency. X-band sources are in blue, K-band sources are in red, and Q-band sources are in yellow. All sources brighter than 1000 mJy are included in the bin furthest to the right of each plot, and the median and the mean of the distributions are shown by the solid and dashed lines respectively.

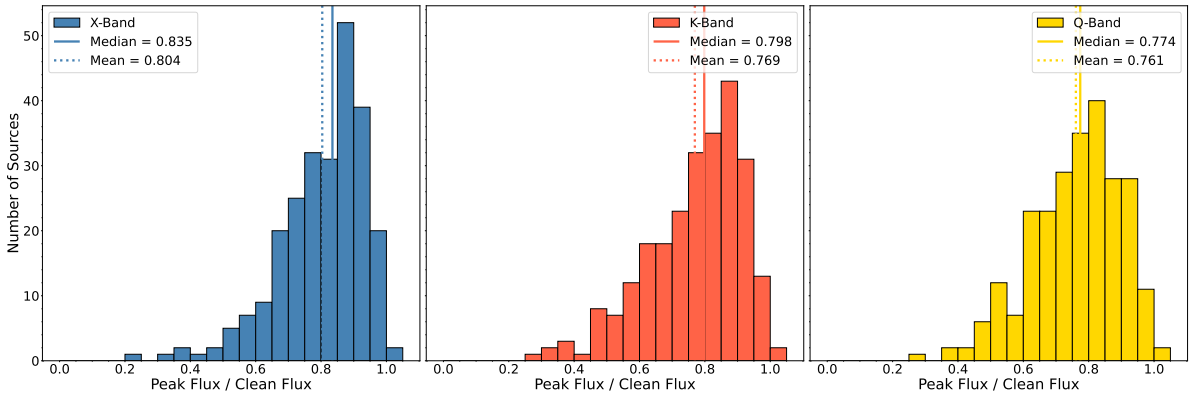

Fig. 3 Distribution of the ratio of peak flux to clean flux. X-band sources are in blue, K-band sources are in red, and Q-band sources are in yellow. The median and the mean of the distributions are shown by the solid and dashed lines respectively.

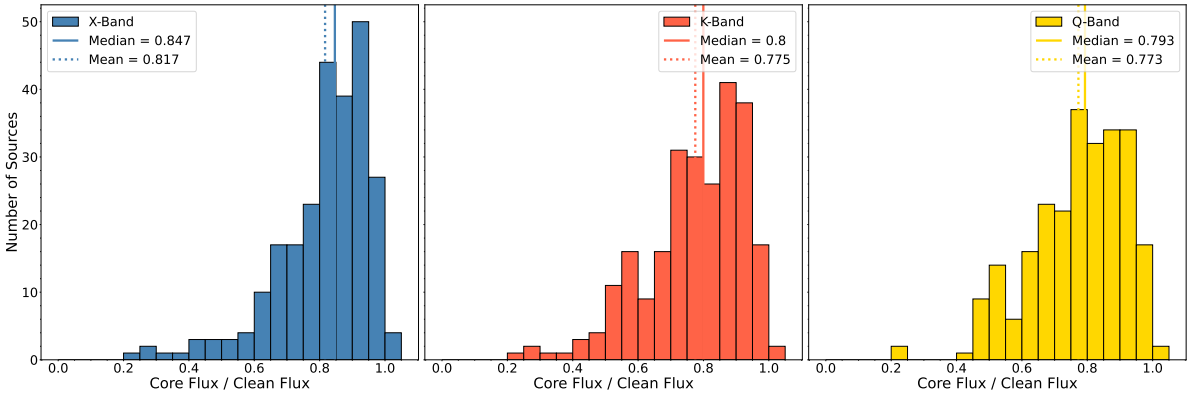

Fig. 4 Distribution of the ratio of core flux to clean flux. X-band sources are in blue, K-band sources are in red, and Q-band sources are in yellow. The median and the mean of the distributions are shown by the solid and dashed lines respectively.

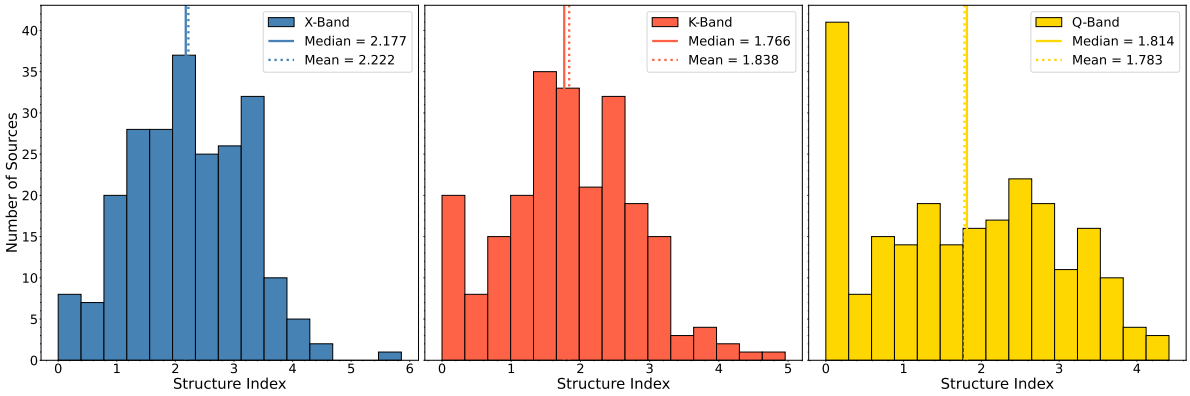

Fig. 5 Distribution of the source structure index. X-band sources are in blue, K-band sources are in red, and Q-band sources are in yellow. The median and the mean of the distributions are shown by the solid and dashed lines respectively. The source structure index is calculated using the logarithmic function, which means that values for the source structure index can be negative. In the case that a source structure index value is negative, we set that value to zero.

X-, K-, and Q-band, respectively, where values closer to 1 indicate a source is more compact.

Next we measured the core flux divided by the clean flux for each image. The core flux is defined as the sum of the clean components within a single beam on a global baseline. Again, the more flux concentrated at the center, the more compact the source is. The frequency of observation determines the beam size, so the core size is different for each frequency band. The beam is 0.71, 0.27, and 0.14 mas for X-, K-, and Q-band respectively. The distribution of core flux to clean flux ratio is shown in Figure 4. The mean value of this ratio is 0.817, 0.775, 0.773 for X-, K-, and Q-band respectively where values closer to 1 indicate a source is more compact.

We finally use the source structure index [1] to determine compactness. The source structure index is the log of the median value of the structure delay corrections derived from Very Long Baseline Interferometry (VLBI) images plus a constant. A higher structure delay indicates there is structure outside of the brightest component, meaning that the source is less compact. The mean values are 2.22, 1.84, and 1.78 for X-, K-, and Q-band, respectively, where lower values indicate that a source is more compact. We note here that we revisited our calculation of the source structure index and were able to fix an error. The distribution in Figure 5 shows the data from the updated calculations.

The peak flux over total flux ratio and the core flux to clean flux ratio show similar distributions across all three bands. The distributions of X-band and K-band

sources typically have a slightly higher mean, indicating the sources are more compact than at Q-band.

The distribution of values for the source structure index seems to show that many Q-band sources actually have a lower source structure index and are as compact at Q-band as they are at K-band. The average source structure index at X-band is slightly higher.

4 Conclusions

In this report we have discussed our exploration of K-band ICRF3 sources at X-, K-, and Q-band. We have shown that we can detect 99% of K-band ICRF3 sources at X and K-band and 87% of K-band ICRF3 sources at Q-band. We see that sources are generally fainter at Q-band, and that is likely the reason we don't detect as many. Finally, our results show nearly equal compactness at all three bands. The compactness is scaled by the beam and therefore by the inverse of the frequency. Thus, our results suggest the potential for improving the VLBI-defined ICRF by moving to higher frequencies and suggest that the improvements scale with frequency, i.e., Q-band is five times better in astrometric precision than X-band.

Acknowledgements

The authors acknowledge use of the Very Long Baseline Array under the US Naval Observatory's time allocation. This work supports USNO's ongoing research into the celestial reference frame and geodesy. The VLBA is operated by the National Radio Astronomy Observatory, which is a facility of the National Science Foundation operated under cooperative agreement by Associated Universities, Inc. The research was carried out in part at the Jet Propulsion Laboratory, California Institute of Technology, under a contract with the National Aeronautics and Space Administration (80NM0018D0004). Copyright 2022 All Rights Reserved. The financial assistance of the South African Radio Astronomy Observatory (SARAO) towards this research is hereby acknowledged.

References

1. Charlot, P. 1990. Radio-Source Structure in Astrometric and Geodetic Very Long Baseline Interferometry. The Astronomical Journal 99, 1309. doi:10.1086/115419.
2. Charlot, P. and 19 colleagues 2020. The third realization of the International Celestial Reference Frame by very long baseline interferometry. Astronomy and Astrophysics 644. doi:10.1051/0004-6361/202038368.
3. Aletha de Witt, Christopher S. Jacobs, David Gordon, Michael Bietenholz, Marisa Nickola, and Alessandra Bertarini 2022 The Astronomical Journal. Submitted.
4. Fomalont, E., Johnston, K., Fey, A., Boboltz, D., Oyama, T., Honma, M. 2011. The Position/Structure Stability of Four ICRF2 Sources. The Astronomical Journal 141. doi:10.1088/0004-6256/141/3/91.
5. Greisen, E. W. 2003. AIPS, the VLA, and the VLBA. Information Handling in Astronomy - Historical Vistas 285, 109. doi:10.1007/0-306-48080-8_7.
6. Immer, K., Reid, M. J., Menten, K. M., Brunthaler, A., Dame, T. M. 2013. Trigonometric parallaxes of massive star forming regions: G012.88+0.48 and W33. Astronomy and Astrophysics 553. doi:10.1051/0004-6361/201220793.
7. Lanyi, G. E. and 12 colleagues 2010. The Celestial Reference Frame at 24 and 43 GHz. I. Astrometry. The Astronomical Journal 139, 1695–1712. doi:10.1088/0004-6256/139/5/1695.
8. Morabito, D. D. 2017. Deep-Space Ka-Band Flight Experience. Interplanetary Network Progress Report 42-211, 1–16.
9. Napier, P. J. and six colleagues 1994. The Very Long Baseline Array. IEEE Proceedings 82, 658–672. doi:10.1109/5.284733.
10. Shepherd, M. C. 1997. Difmap: an Interactive Program for Synthesis Imaging. Astronomical Data Analysis Software and Systems VI 125, 77.

Parsec-scale Jets in AGN: Insights into the Location of the γ-Ray Emission from Geodetic VLBI, *Gaia* EDR3, and Fermi-LAT

S. Lambert[1], A. Pierron[1], H. Sol[2]

Abstract With the advent of the *Gaia* astrometry mission and the constantly improving geodetic VLBI program providing both optical and radio reference frames with precisions better than 0.1 mas, challenging questions arise about identifying which mechanisms are behind the optical emission as well as other emissions at higher energies, especially the γ-ray emission. We use data from *Gaia* EDR3, the radio ICRF3, and GeV fluxes from the Fermi-LAT 4FGL catalog for a sample of about 800 common active galactic nuclei (AGN), dominated by blazars (BL Lac and FSRQs). We investigate the general trends of such populations in terms of geometry, classification, color indices, and GeV emission.

Keywords Reference systems – quasars – technique: interferometrics – technique: *Gaia*

1 Introduction

The observations of the European Space Agency (ESA) *Gaia* astrometry mission (Prusti et al., 2016; Brown et al., 2016) launched in 2013. The constantly improving geodetic very-long-baseline-radio-interferometry (VLBI) program led mainly by the International VLBI Service for Geodesy and Astrometry (IVS, Nothnagel et al., 2017), unveiled the sub-milliarcsecond geometry of the radio and optical emissions of active galactic nuclei (AGN) that constitute the reference points of the celestial reference system. Recent studies, comparing absolute radio and optical astrometry, VLBI imaging, and photometric properties, allowed a first general picture. The radio centroids at 8, 22, and 32 GHz are close to each other (< 0.1 mas) and arranged in order of increasing frequencies towards the inside of the jet, i.e., towards the central black hole, in coherence with a frequency-dependent model of the jet plasma opacity (Lambert et al., 2021). Optical centroids are generally downstream in the jet and are often significantly distant from radio centroids by 0.1 mas to several mas (Kovalev et al., 2017; Plavin et al., 2019; Kovalev et al., 2020; Xu et al., 2021; Lambert et al., 2021). These optical centroids often coincide with a radio component in the jet, often stationary, and can have a high degree of linear polarization in radio and optics, testifying to a well-organized magnetic field typical of a synchrotron emission (Kovalev et al., 2020; Lambert et al., 2021). Conversely, when the *Gaia* centroid is upstream of the jet relative to the radio centroid, we have rather a weak optical polarization suggesting that we see the signature of the accretion disk (Plavin et al., 2019).

The link between the radio-optical geometry and the very high energy (VHE) emission remains unclear. The observed temporal correlation between spectral energy density (SED) in optical and γ suggests a common emission region and correlated mechanisms (e.g., Larionov et al., 2020). In some cases, VHE flares appear to be correlated with VLBI 'events' (variation of the radio core, emergence of a knot, or formation of a stationary knot). In 3C279, Abdalla et al. (2019) deduce that the emission zone is located beyond the broad line region (BLR). This prevents VHE γ photons from being absorbed by ambient background radiation (disk

1. SYRTE, Observatoire de Paris - Université PSL, CNRS, Sorbonne Université, LNE
2. LUTH, Observatoire de Paris - Université PSL, CNRS, Université Paris-Cité

and BLR flux). But this suggests a fairly large emission zone, difficultly explaining the very rapid (sometimes observed) variations. In practice, the observed variabilities remain difficult to reproduce with current 'standard' models, especially if we consider an emission zone far into the jet (and therefore a priori less compact than an area at the base of the jet).

Most of the studies used individual approaches on few well-studied sources. Interestingly, Kramarenko et al. (2022) recently proposed a global approach using hundreds of MOJAVE 15-GHz fluxes (Lister et al., 2018) and Fermi-Large Array Telescope (LAT, Abdollahi et al., 2020) γ fluxes. They suggest that the dominant high-energy production zone is typically located at a distance of several parsecs from the central nucleus, and that quasars have a more distant γ-ray emission region from the central engine and shorter variability time-scale compared to those of BL Lacertae (BL Lac) objects. The time-domain correlation between emission mechanisms at various wavelengths noticed in the above-cited works could have a spatial signature, as the γ emission region could be related in some cases to the optical photocenter observed by *Gaia*, i.e., an active zone emitting non-thermal radiation in the optical band and whose place in the jet can be probed by multiwavelength absolute astrometry. We explore that possibility in this paper by studying the radio-optical geometry of the sources and comparing it with their optical and VHE photometric properties.

2 Data and Their Preparation

Our radio catalog consists of the third realization of the international celestial reference frame (ICRF3, Charlot et al., 2020) restrained to the 4,536 entries at X-band (8.4 GHz). For the optical counterparts, we proceeded with a cross-matching of the full *Gaia* Early Data Release 3 (EDR3) positions (Prusti et al., 2016; Brown et al., 2021) with the ICRF3 positions with a cross-identification radius of 1 arcsecond. We found 3,516 sources with no statistically significant parallaxes. From *Gaia* EDR3, we also collect values for the BP-RP color index. BP-RP is the difference in magnitude between 330–660 nm (BP) and 630–1,000 nm (RP) bands and can usually be used as an indicator of which of the standard accretion disk or the synchrotron jet dominates the optical emission, the latter producing a redder luminosity, the former leading to a bluer source (see, e.g., Plavin et al., 2019).

We obtained the γ 1–100 GeV fluxes and their uncertainties from the Fermi Large Area Telescope (LAT) fourth source catalog data release 3 (4FGL-DR3, Abdollahi et al., 2020, 2022) for 816 sources of our sample. From the same catalog, we recorded the source classification, 488 of the sources being tagged as flat spectrum radio quasars (FSRQ) and another 214 being classified as BL Lac (see Figure 1). The remaining 114 sources are classified as three AGN, three compact steep-spectrum (CSS) radio sources, one Seyfert 1, 12 radio galaxies, one steep spectrum radio quasars (SSRQ), 92 blazar candidates of uncertain type (BCU), and one source of unknown type.

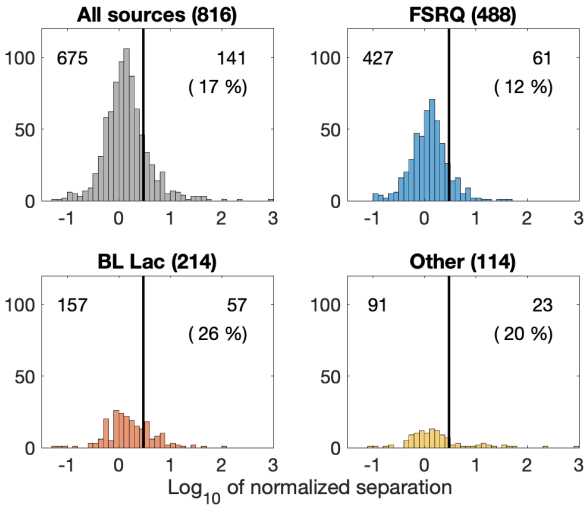

Fig. 1 Distribution of the radio-optical normalized separations (see, e.g., Mignard et al., 2016, about the computation of this quantity) of the source sample. The black, vertical line indicates a normalized separation of 3 (or a separation of 3σ).

Then, we form the radio-optical vector as the difference between the 8-GHz VLBI positions (referred to as X-band centroids) and the *Gaia* EDR3 positions (referred to as optical centroids). The uncertainty on the angular separation is computed using classical spherical astrometry formulae accounting for the correlation between estimates of right ascension and declination in both techniques (see, e.g., Mignard et al., 2016; Charlot et al., 2020). We assume for convenience that the X-band centroid can be considered as the radio core of the VLBI sources.

3 Analysis and Results

The obtained radio-optical angular separations are compared with the BP-RP color index and the γ flux in order to isolate general trends. The joint distributions of these three quantities is studied using several representations in Figures 2 and 3. In the upper plots of Figure 2 all sources are shown with different colors following the spectral class (FSRQ, BL Lac, other). Lower plots of Figure 2 are obtained by taking the medians of the y-axis quantity after dividing the x-scale in five bins containing an equal number of sources. The shaded area represents the standard error on the median. Figure 3 displays kernel smoothing density (KSD) of the distribution patterns of the different representations seen in the upper plots of Figure 2. The density is reported using a color scale from deep blue (less dense) to dark red (very dense) and is scaled for each plot: each map is saturated to its maximum level of density, the density plots intending to show where the sources are and not how many they are. The density is computed first for the whole sample of sources (upper row of Figure 3), then for sources whose radio-optical angular separation (denoted r) is larger or smaller than three times the cumulated uncertainty (σ) on the arc length (second and third rows of Figure 3), and finally for FSRQ and BL Lac (last two rows of Figure 3).

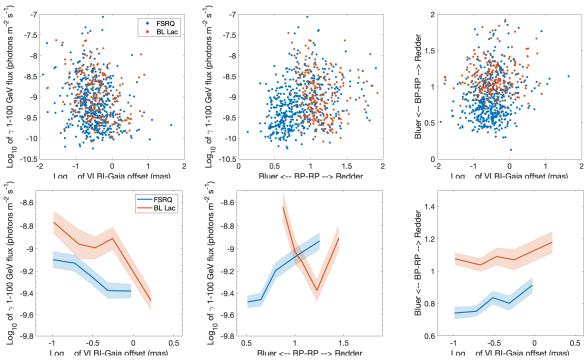

Fig. 2 Joint distributions of radio-optical angular separation, the BP-RP color index, and the γ flux. In the upper row, all sources are displayed. The plots in the lower row represent the median of the y-axis quantity in bins of the x-axis quantity containing equal numbers of sources. The shading gives the uncertainty on the median.

As the radio-optical angular separation increases, the BP-RP color index tends on average to become redder, suggesting that the corresponding optical sources are dominated by the jet, while sources exhibiting short radio-optical angular separations can have an optical emission affected by the presence of a disk. However, at low r such a trend seems mostly due to the FSRQ, which is coherent with the explanation by the bluer emission due to their standard accretion disk contributing to the optical emission located at low offset. For the population of BL Lacs, there is no signature of bluer emission at low r, which appears coherent with the presence of under-luminous accretion disks in such sources. Their BP-RP color index start to become redder only above an offset of about 0.6 mas, which can suggest a general cooling of the population of radiating particles propagating along the jets. Such an effect can also play a role in the case of the FSRQ at large offset, although the effect of the disk emission can dominate the optical radiation at low offset.

The LAT γ flux globally decreases as the radio-optical angular separation increases for the whole pop-

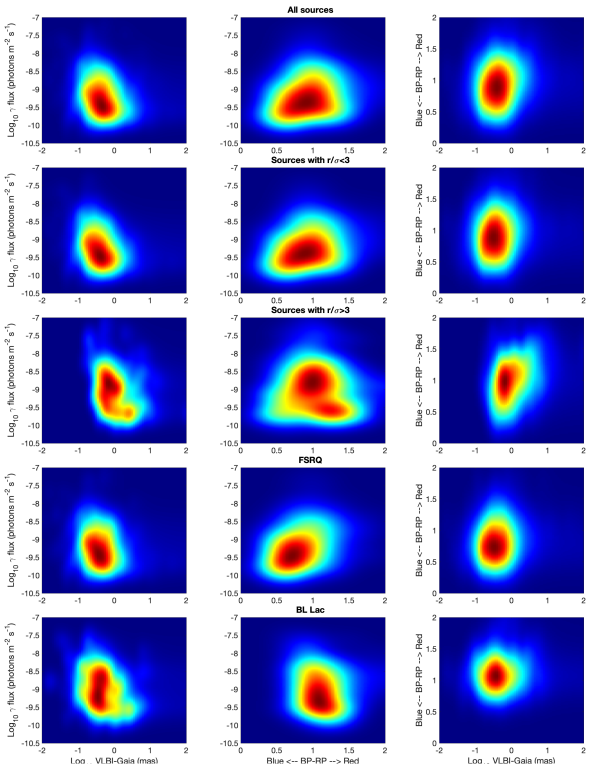

Fig. 3 Kernel smoothing density of distributions of Figure 2 for all sources of the sample (first row), for sources with not significant (second row) and significant (third row) radio-optical separation, for FSRQ (fourth row), and for BL Lac (fifth row).

ulation, dominated by FSRQ. For the population of BL Lacs, the general trend is also a decrease of the γ-ray flux with the offset, but there is a clue of a flux enhancement for offset in the 0.3 to 0.6 mas range. Such an enhancement of the γ-ray flux for sources at intermediate r suggests the presence of an active zone along the jet which dominates both the optical and the γ-ray emission, likely related to one of the radio knots detected in most AGN mapped by VLBI. The highest γ fluxes of the whole population are coinciding with intermediate values of the color index, with an optimal value around BP-RP$\sim$1. Conversely, the bluest sources have the weakest γ fluxes, which can be expected if the accretion disk dominates their MWL emission, and the reddest sources have intermediate γ fluxes, suggesting that an active site in the jet boosts their emission at high energies.

Sources, for which the radio-optical angular separation is not—or poorly—significant ($r/\sigma < 3$), exhibit relatively blue color indices and weak γ fluxes. As shown in Figure 1, this population is dominated by FSRQ and these trends can be partially explained by the influence of the disk emission, which can dominate the optical flux and impose the small value of the radio-optical angular separation, but does not contribute to the γ-ray flux. Then the γ-rays have to come from some other active zone, either from the black hole magnetosphere, or from the jet base or some region downstream in the jet, and the optical counterpart of such non-thermal emission will also contribute to the total optical flux. However, the location of the current *Gaia* photocenter cannot help identifying the location of such non-thermal active site, as long as it is impossible to distinguish between the disk and the radio core positions. In contrast, the group of sources with significant radio-optical angular separations ($r/\sigma > 3$) show two subgroups: one with strong γ fluxes and mid color indices and one with weak γ fluxes and redder color indices, suggesting a weaker non-thermal activity. For these sources at large r, the optical emission fixes the *Gaia* photocenter position and cannot come from the accretion disk, nor from the immediate vicinity of the black hole, and neither from any spherical diffused halo around the central AGN engine. Although the presence of a diffuse asymmetric halo due to the host galaxy could affect the position of the optical photocenter, it is most likely dominated by some active zone(s) in the jet, coherent with their intermediate or redder color indices due to the expected synchrotron power-law jet emission in the optical range. Previous studies of a subsample of sources mapped by the MOJAVE program have shown that this is true for a large percentage of cases showing a spatial coincidence of the *Gaia* photocenter with a radio knot along the jet (Pierron et al., 2021, 2022). Such active non-thermal sites are the best candidates to emit as well the observed γ-ray flux by inverse-Compton processes. The presence of two subgroups is trickier to interpret but could be due to the existence of several active zones. For instance, the confinement shocks with decreasing activity along the jet, of which only the first two would appear in the study of the present AGN sample.

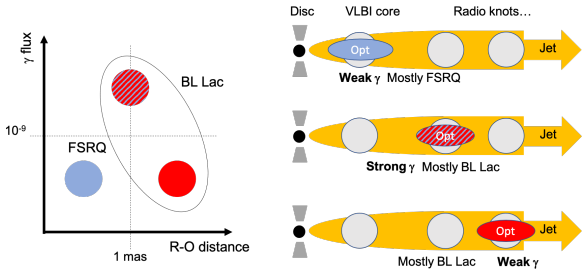

Fig. 4 (Left) Sketch representing the gross locations and color index of FSRQ and BL Lac in a representation following the radio-optical angular distance, the γ flux, and the BP-RP color index. The red (blue) indicates a redder (bluer) color index while the hatched disk means intermediates values of BP-RP. (Right) Sketch of the radio-optical-jet geometry corresponding to the three cases of the left sketch.

FSRQ globally exhibits bluer color indices that can be consistent with an optical emission arising from both the disk and the jet for appropriate parameters of the synchrotron emission. Their γ flux is weaker and is associated with shorter, non significant radio-optical angular separations. BL Lac color indices are globally redder than for FSRQ, consistently with an active jet and a weak disk. Within the BL Lac sample, one can again isolate two groups: (i) weak γ flux and high (red) color index associated with radio-optical angular separations around 1 mas or more, indicating an optical emission downstream in the jet, and (ii) strong γ flux for intermediate color index and relatively shorter radio-optical angular separations (0.1 to less than 1 mas), indicating an optical emission close to the VLBI core, possibly downstream but within the first parsec. The loci of the three cases (FSRQ, BL Lac group (i), BL Lac group (ii)) in the plane corresponding to the

radio-optical separation versus the γ flux are sketched in the left panel of Figure 4.

Interpreting the optical centroid as dominated by the non-thermal emission along the jet, it seems reasonable to associate this region with the γ emission zone for large radio-optical offsets when it is also associated with a radio knot. However, more work is needed to conclude about the position of the γ emission region for short radio-optical offsets. Indeed, it would need to distinguish the offset between the radio core and the optical center and therefore improve the absolute astrometry measurement within few tens of μas or less by reducing systematics of each technique and aligning rigorously the maps with the radio reference frame (that are, moreover, at different wavelengths).

4 Conclusion

In this study, we used two highest standards of absolute astrometry techniques—geodetic VLBI and *Gaia*—as well as photometric measurements including the results of the Fermi LAT spatial observatory. We showed the link between the γ flux and the location and color index of the optical centroid: globally weaker γ fluxes correspond to either FSRQ with short, non significant radio-optical offsets or BL Lac with radio-optical angular separations around 1 mas or more; in contrast, stronger γ fluxed are recorded for BL Lac with shorter but non-zero radio-optical offsets (0.1 to less than 1 mas), indicating an optical emission close to the VLBI core, likely downstream but within the first parsec.

As next steps that would improve our preliminary conclusions, it will be necessary to introduce redshifts and other individual characteristics of the sources, including more detailed classifications—in particular for LBL, IBL, and HBL in order to analyze possible trends in terms of blazar sequence—and geometrical parameters of jet (inclination) in order to consider the geometry in the frame of the source rather than in the one of the observer. The next *Gaia* releases and next ICRF versions—more observations, improved network, multifrequency—will reduce the systematics again, diminish the positional error, increase the sample, and allow to explore closer to the core. A coordination of the observing program of geodetic VLBI with other observations of AGN in the optical and γ (including ground-based photometric monitoring) would be welcome. From this synergy between astrogeodesy and astrophysics, we do expect that improving reference frames will improve the modeling of AGN jets and, conversely, that improving modeling of AGN jets will improve the reference frames.

Acknowledgements

This work has made use of data from the European Space Agency (ESA) mission *Gaia* (https://www.cosmos.esa.int/gaia), and processed by the *Gaia* Data Processing and Analysis Consortium (DPAC). Funding for the DPAC was provided by national institutions, in particular the institutions participating in the *Gaia* Multilateral Agreement. This research has made use of the NASA/IPAC Extragalactic Database (NED), which is funded by the National Aeronautics and Space Administration and operated by the California Institute of Technology.

References

Abdalla H, Adam R, Aharonian F, et al. (2019) Constraints on the emission region of 3C 279 during strong flares in 2014 and 2015 through VHE γ-ray observations with H.E.S.S. Astronomy & Astrophysics 627:A159

Abdollahi S, Acero F, Ackermann M, et al. (2020) Fermi large area telescope fourth source catalog. The Astrophysical Journal Supplement Series 247(1):33

Abdollahi S, Acero F, Baldini L, et al. (2022) Incremental fermi large area telescope fourth source catalog. The Astrophysical Journal Supplement Series, accepted for publication

Brown AGA, Vallenari A, Prusti T, et al. (2016) *Gaia* Data Release 1. Summary of the astrometric, photometric, and survey properties. Astronomy & Astrophysics 595:A2

Brown AGA, Vallenari A, Prusti T, et al. (2021) *Gaia* Early Data Release 3. Summary of the contents and survey properties. Astronomy & Astrophysics 649:A1

Charlot P, Jacobs CS, Gordon D, et al. (2020) The third realization of the International Celestial Reference

Frame by very long baseline interferometry. Astronomy & Astrophysics 644:A159

Kovalev YY, Petrov L, Plavin AV (2017) VLBI-*Gaia* offsets favor parsec-scale jet direction in active galactic nuclei. Astronomy & Astrophysics 598:L1

Kovalev YY, Zobnina DI, Plavin AV, Blinov D (2020) Optical polarization properties of AGNs with significant VLBI-*Gaia* offsets. Monthly Notices of the Royal Astronomical Society: Letters 493(1):L54

Kramarenko I, Pushkarev A, Kovalev Y, et al. (2022) A decade of joint MOJAVE-Fermi AGN monitoring: localisation of the gamma-ray emission region. Monthly Notice of the Royal Astronomical Society 510:469

Lambert S, Liu N, Arias EF, et al. (2021) Parsec-scale alignments of radio-optical offsets with jets in AGNs from multifrequency geodetic VLBI, *Gaia* EDR3, and the MOJAVE program. Astronomy & Astrophysics 651:A64

Larionov VM, Jorstad SG, Marscher AP, et al. (2020) Multiwavelength behaviour of the blazar 3C 279: decade-long study from γ-ray to radio. Monthly Notices of the Royal Astronomical Society 492(3):3829

Lister ML, Aller MF, Aller HD, et al. (2018) MOJAVE. XV. VLBA 15 GHz total intensity and polarization maps of 437 parsec-scale AGN jets from 1996 to 2017. Astronomical Journal 234(1):12

Mignard F, Klioner S, Lindegren L, et al. (2016) *Gaia* Data Release 1. Reference frame and optical properties of ICRF sources. Astronomy & Astrophysics 595:A5

Nothnagel A, Artz T, Behrend D, Malkin Z (2017) International VLBI Service for Geodesy and Astrometry. Journal of Geodesy 91(7):711

Pierron A, Lambert S, Sol H (2021) Insights into AGN parsec-scale emission from radio to GeV gamma rays from VLBI, *Gaia* EDR3, and Fermi-. Journées du Programme National des Hautes Energies, Paris, France

Pierron A, Lambert S, Sol H (2022) Parsec-scale jets in AGN: identification of the optical emission with radio knots. Astronomy & Astrophysics, in preparation

Plavin AV, Kovalev YY, Petrov LY (2019) Dissecting the AGN disk-jet system with joint VLBI-*Gaia* analysis. The Astrophysical Journal 871(2):143

Prusti T, de Bruijne JHJ, Brown AGA, et al. (2016) The *Gaia* mission. Astronomy & Astrophysics 595:A1

Xu MH, Lunz S, Anderson JM, et al. (2021) Evidence of the *Gaia*-VLBI position differences being related to radio source structure. Astronomy & Astrophysics 647:A189

Session 5

Extending the Use of VLBI to Frame Ties, Deep Space Exploration and Other Areas

IVS IAG SUOMEN AKATEMIA

NLS FINNISH GEOSPATIAL RESEARCH INSTITUTE FGI

Observing GPS Satellite Signals in L-Band with a Realistic Global VLBI Network: A Simulation Study

David Schunck, Lucia McCallum

Abstract In the latest realization of the International Terrestrial Reference Frame 2014 (ITRF2014), significant differences are found between tie vectors computed from global-scale space geodesy estimates and terrestrial local ties. As these discrepancies represent one of the most relevant limitations on the quality of the ITRF, the frame ties need to be improved. A promising concept is the establishment of ties via co-location satellites, so-called space ties. However, no dedicated satellite missions are currently in operation. In this paper, we perform a simulation study using geodetic L-band antennas to perform observations of GPS satellites with the Very Long Baseline Interferometry (VLBI) technique. The aim is to investigate the usefulness of utilizing the currently available geodetic infrastructure to tie the VLBI and satellite frames. We achieve station position repeatabilities of about 9 mm to 13 mm with n experiment length of 24 hours. When increasing the experiment length to 48 hours the average repeatability goes down to 6.7 mm. The results indicate that these observations provide results that are not precise enough to tie together the VLBI and satellite frames.

Keywords VLBI, Satellites, Frame Tie

1 Introduction

In ITRF2014, the tie vectors computed from global-scale space geodesy estimates show significant differences to terrestrial local ties (Altamimi et al., 2016). It is believed that most of these discrepancies are related to technique systematic errors rather than local ties. The current ITRF realization is well outside the required accuracy, and as such it is a major error source for observations which are referenced to it. For further improvements of the ITRF, the consistency between local ties and space geodesy estimates needs to be improved as they represent one of the most relevant limitations on the quality of the ITRF (Boucher et al., 2015). A promising and well accepted concept is the additional establishment of ties via co-location satellites, so-called space ties (Rothacher et al., 2009). These ties would be independent of local ties and, therefore, allow the detection of technique-specific biases (Plag, H.-P. and Pearlman, M., 2009). However, no comparable satellite mission is currently in operation. By observing signals emitted by GPS satellites with VLBI, one can make use of the currently available geodetic infrastructure. This approach would build the frame tie between the VLBI and satellite systems. Although first test observations of satellites have successfully been performed, they have not been performed with a global network aiming towards tying the two frames together.

The aim of this paper is to investigate the usefulness of utilizing the current geodetic infrastructure to tie the VLBI and satellite frames by performing VLBI observations of the GPS satellites with a global network of L-band antennas. We present a study simulating and analyzing these observations. In Section 2, the simulation study is described. The results are shown in Section 3. The findings are summarized and discussed in Section 4.

School of Natural Sciences, University of Tasmania

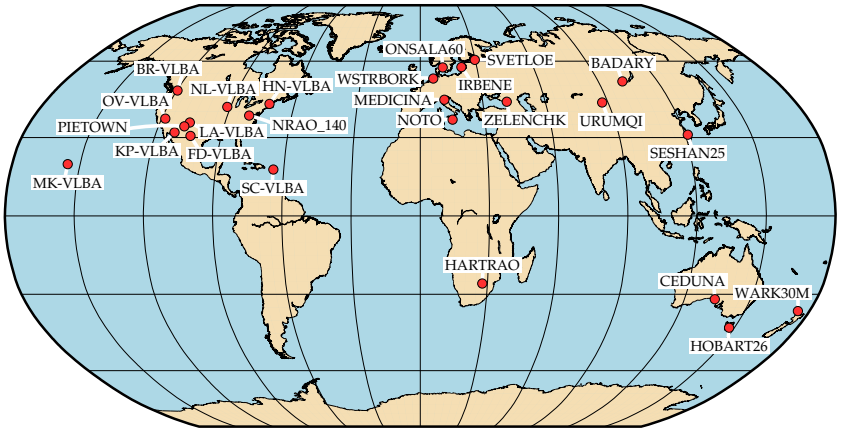

Fig. 1 Global network consisting of 25 stations utilized in the simulation study.

2 Simulation Study

A more detailed description of the network and used GPS satellites is given in Section 2.1 and Section 2.2, respectively. Firstly, as described in Section 2.3, we created an observation schedule. The length of the schedule was chosen to be 24 hours. Based on the schedule the VLBI observations were simulated using the main observation errors and the standard procedure. The simulations are described in Section 2.4. In Section 2.5, the desired parameters are estimated in a least squares adjustment drawing upon the simulations. Section 2.6 presents how the results of the estimation are evaluated.

2.1 Global Station Network

The requirement for a station to be part of the global network is that it be equipped with an adequate L-band receiver to collect signals of GPS satellites. As shown in Figure 1, we found 25 stations that are utilized in this simulation study. Some of these stations have proven to be capable of tracking and recording GNSS satellites in a VLBI experiment (Tornatore et al., 2014; Plank et al., 2017). For the remaining stations we will assume that they have the ability to do so, even though they might run into issues when actually observing GPS satellites in L-band. With only four stations in the Southern hemisphere, the network exhibits an undesired inhomogeneity in the distribution of the stations.

2.2 Satellites

The satellites that serve as sources in the simulation comprise the currently available constellation of Global Positioning Service (GPS) satellites. As of April 12, 2022, there were a total of 30 operational satellites. Throughout the simulation experiment the number of visible satellites for all stations varies between 7 and 14 when considering an elevation mask of 5°.

2.3 Scheduling

The scheduling is performed using the VLBI scheduling software VieSched++ (Schartner and Böhm, 2019). The length of the experiment is chosen to be 24 hours. In comparison to quasars, the signals of GPS satellites are extremely strong. Therefore, a scan time of ten seconds produces a sufficient signal-to-noise ratio to perform fringe-fitting. For the scheduling, fill-in mode and subnetting is used, and only GPS satellites serve as sources. In the following the experiment is referred to as `S24GR`. For the experiment the number of scans was scheduled to be 3,574 with a number of 28.3 scans per station per hour. The number of observations is 56,868 with a sky coverage of 0.45. The sky coverage score is a value between 0 and 1, describing how well the sources are distributed above the sky of a station, where 1 represents a perfect distribution.

Table 1 Parameters used to simulate observations, following the method described in Pany et al. (2011)

Clock	
Allan standard deviation	1×10^{-14}@50 min
Tropospheric turbulence	
Initial zenith wet delay	150 mm
Structure constant C_n	1.8×10^{-7} m$^{1/3}$
Effective height of the troposphere	2 km
Wind speed in eastern direction	8 m/s
Wind speed in northern direction	0 m/s
Height increment for integration	200 m
Correlation interval	2 h
Measurement error	
White noise	50 ps

2.4 Simulated Observations

The Vienna VLBI and Satellite Software (VieVS) has been used to perform the simulations (Böhm et al., 2018). The three main stochastic error sources applied in this study are wet tropospheric delay, station clock inaccuracies, and measurement noise. We perform 300 repetitions of the simulation to be able to run subsequent statistical evaluations of the results in terms of mean values and variance. Table 1 gives the characteristic numbers for the models.

2.5 Parameter Estimation

In the least squares adjustment, the Earth orientation parameters were not estimated in the adjustment. Zenith wet delays were estimated as piecewise linear (pwl) offsets every 15 min for each station with 1.5 cm relative constraints. Troposphere gradients to address azimuthal asymmetry were estimated in 15 min intervals with 0.05 cm relative constraints and 0.1 cm absolute constraints. The clocks were set up as 30 min pwl offsets and one rate as well as one quadratic term per clock. The clock estimates are also constrained with 1.3 cm. For estimating station coordinates, a datum has to be defined. The datum is set by the GPS satellites. A no-net-rotation (NNR), no-net-translation (NNT) or no-net-scale (NNS) condition is not applied.

Because the station positions and network configuration of the antennas is known relatively precisely in the VLBI frame, we are introducing additional observations. 21 of the stations in our network have coordinates and standard deviations in the IVS contribution to the ITRF2014. The relative distance d between two stations $s1$ and $s2$ is incorporated as an additional observation for the least squares adjustment, using

$$d = \sqrt{(x_{s2} - x_{s1})^2 + (y_{s2} - y_{s1})^2 + (z_{s2} - z_{s1})^2}. \quad (1)$$

Based on the number of possible combinations $n(n-1)/2$, where n is the number of stations, the relative distances between the 21 stations lead to an additional 210 observations, in the following referred to as soft constraints. The weights of these additional observations are derived by the propagation of the variance for the relative distance from the standard deviations of the coordinates, using

$$\sigma_d^2 = \left(\frac{\partial d}{\partial x_{s1}}\right)^2 \cdot \sigma_{x,s1}^2 + \cdots + \left(\frac{\partial d}{\partial z_{s2}}\right)^2 \cdot \sigma_{z,s2}^2. \quad (2)$$

CEDUNA, IRBENE, WARK30, and WSTRBORK are the four stations not being represented in the IVS input to the ITRF2014 and, therefore, also not included as additional observations due to a lack of stochastic information.

2.6 Evaluation

The parameter that is used to assess the simulation results is the repeatability of antenna coordinates with respect to the true, a priori antenna coordinates. For a better geometrical interpretation the repeatabilities in the dx, dy, and dz components are converted to local east (de), north (dn), and up (du) components. The standard deviation σ of these estimates gives a measure of the expected accuracy of derived antenna coordinates. The standard deviation σ_{du} for n samples with the mean value du_m is calculated as

$$\sigma_{du} = \sqrt{\frac{1}{n-1}\sum_{i=1}^{n}(du_i - du_m)^2}. \quad (3)$$

Furthermore, the repeatability of the 3D antenna position is assessed. The root mean square error is defined as

$$e_{3D} = \sqrt{\sigma_{dx}^2 + \sigma_{dy}^2 + \sigma_{dz}^2} = \sqrt{\sigma_{de}^2 + \sigma_{dn}^2 + \sigma_{du}^2}. \quad (4)$$

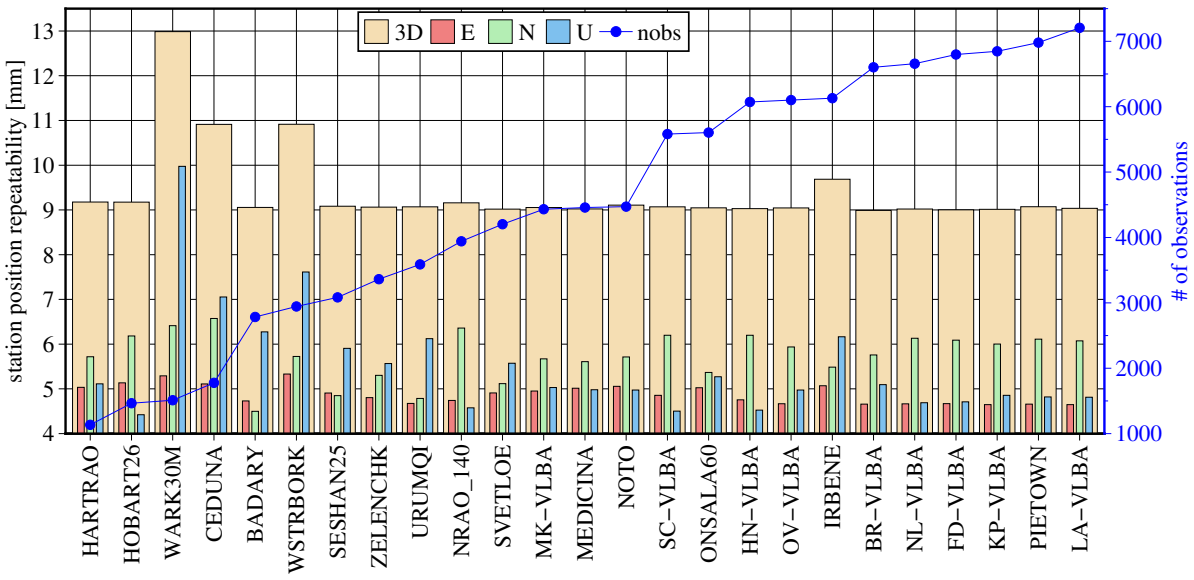

Fig. 2 Station position repeatabilities for the `S24GR` simulation in terms of 3D position rms (*orange*), as well as in the east (*red*), north (*green*) and up (*blue*) components. The *blue* line with the scale on the right gives the number of observations for each station.

3 Results

In Figure 2, the station position repeatabilities are shown when observing a constellation of 30 GPS satellites with a global network of L-band antennas for 24 hours. The results are given as 3D position rms (orange) as well as in the east (red), north (green), and up (blue) components. In addition, the number of observations per station is illustrated. The average and maximum 3D station position repeatabilities are 9.4 mm and about 13 mm, respectively. Overall, they are distributed homogeneously over the stations. This is due to the additionally introduced 210 observations of relative distances between the stations.

The four stations not being included in the soft constraints show a large repeatability in the up component. Large errors in the height are due to the high correlation between the estimated troposphere zenith wet delays and the station height. For the remaining stations the east, north, and up components are relatively similar in magnitude. Introducing the soft constraints makes the station network like a cage with little room for deformation. Stations with a lot of observations being part of a dense regional network (e.g. LA-VLBA) support isolated stations with few observations (e.g. HARTRAO). That leads to the effect that stations with more observations are not significantly more precisely determined than stations with fewer observations.

Most of the antennas are rather large and have a slow slewing speed compared to the new generation VGOS antennas. The determination of the up component of a station coordinate can be increased by increasing the number of observations and distributing them across the sky. This helps in the least squares adjustment to distinguish between the height and troposphere parameters. However, the slow slewing speeds only allow this distinction up to a certain degree. In order to understand how fast slewing antennas would improve the results, we performed an additional simulation `S24GV`, assuming the antennas to be as fast as the new generation VGOS antennas (slew rate 1: 720 degrees per minute, slew rate 2: 360 degrees per minute). Also, another simulation is performed using the original slewing speeds, but the schedule length is increased to 48 hours in `S48GR`.

Assuming antenna slew speeds comparable to the new generation VGOS antennas decreases the average 3D repeatability significantly from 9.4 mm to 5.9 mm. Increasing the length of the schedule from 24 hours to 48 hours also leads to a substantial improvement to 6.7 mm. Furthermore, the impact of the noise is investigated. When neglecting the measurement noise of 50 ps, the average 3D station repeatability goes down from 9.4 mm to 8.7 mm for the 24-hour experiment and from 6.7 mm to 6.0 mm for the 48-hour experiment.

4 Conclusions

The simulation study has shown that observations of GPS satellites enable the derivation of antenna positions in the satellite system with a precision of 9 mm up to 13 mm for a schedule of 24-hour length. Increasing the schedule length to 48 hours improves the precision to 6.7 mm. The slew speed of the antennas is one of the limiting factors. Assuming a slew speed for all antennas comparable to the new generation VGOS antennas improves the average 3D station repeatability to 5.9 mm for a 24-hour schedule. The results show that observations of the GPS satellite constellation with a current infrastructure of L-band antennas in a global network are not precise enough to create the frame tie between the VLBI and GPS systems. The station position repeatabilities are significantly larger as demanded.

A potential problem limiting the results is the sky coverage. The bounded inclination of the GPS constellation of about 55 degrees leads to poor sky coverages for stations that are several tens of degrees away from the equator. A possible solution is to implement the sandwich method with sequences of observations of radio-source–satellite–radio-source. Although not connecting the VLBI and GPS systems, it could improve the troposphere and, hence, the height component estimation. Possible additional error sources such as, e.g., the influence of deficient orbit determination of the target satellites or special characteristics of the transmitter were not included in the investigations above.

Acknowledgements

D. Schunck is grateful for a PhD scholarship by the University of Tasmania and project DE180100245 funded by the Australian Research Council.

References

Altamimi, Z., Rebischung, P., Métivier, L., and Collilieux, X. (2016). ITRF2014: A new release of the International Terrestrial Reference Frame modeling nonlinear station motions. *Journal of Geodesy*, 121:6109–6131.

Boucher, C., Pearlman, M., and Sarti, P. (2015). Global geodetic observatories. *Advances in Space Research*, 55(1):24–39. https://doi.org/10.1016/j.asr.2014.10.011.

Böhm, J., Böhm, S., Boisits, J., Girdiuk, A., Gruber, J., Hellerschmied, A., Krásná, H., Landskron, D., Madzak, M., Mayer, D., McCallum, J., McCallum, L., Schartner, M., and Teke, K. (2018). Vienna VLBI and satellite software (VieVS) for geodesy and astrometry. *Publications of the Astronomical Society of the Pacific*, 130(986):044503.

Pany, A., Böhm, J., MacMillan, D., Schuh, H., Nilsson, T., and Wresnik, J. (2011). Monte Carlo simulations of the impact of troposphere, clock and measurement errors on the repeatability of VLBI positions. *Journal of Geodesy*, 85:39–50. https://doi.org/10.1007/s00190-010-0415-1.

Plag, H.-P. and Pearlman, M. (2009). *Global Geodetic Observing System - Meeting the Requirements of a Global Society on a changing Planet*. Springer-Verlag Berlin Heidelberg.

Plank, L., Hellerschmied, A., McCallum, J., Böhm, J., and Lovell, J. (2017). VLBI observations of GNSS-satellites: from scheduling to analysis. *Journal of Geodesy*, 91:867–880.

Rothacher, M., Beutler, G., Behrend, D., Donnellan, A., Hinderer, J., Ma, C., Noll, C., Oberst, J., Pearlman, M., Plag, H.-P., Richter, B., Schöne, T., Tavernier, G., and Woodworth, P. (2009). The future global geodetic observing system. In *Global Geodetic Observing System*, pages 237–272. Springer, Heidelberg.

Schartner, M. and Böhm, J. (2019). VieSched++: A new VLBI scheduling software for geodesy and astrometry. *Publications of the Astronomical Society of the Pacific*, 131(1002):084501.

Tornatore, V., Haas, R., Casey, S., Duev, D., Pogrebenko, S., and Molera Calvés, G. (2014). *Earth on the Edge: Science for a Sustainable Planet*, chapter Direct VLBI Observations of Global Navigation Satellite System Signals. Spinger-Verlag Berlin Heidelberg.

Adjustment of Galileo Satellite Orbits with VLBI Observations: A Simulation Study

H. Wolf[1], J. Böhm[1], A. Nothnagel[1], U. Hugentobler[2], M. Schartner[3]

Abstract Observing Earth-orbiting satellites and quasars in parallel with Very Long Baseline Interferometry (VLBI) telescopes provides new capabilities such as precise orbit determination (POD) from VLBI observations. As the sensitivity of a satellite observation towards the individual components of the satellite position is dependent on the geometry of the observing stations and the satellite, not all possible satellite observations are equally suitable for orbit determination. We evaluate possible satellite observations in terms of their potential for determining the satellite orbits using Dilution of Precision (DOP) factors, which are indicators for the sensitivities of a satellite observation. We compare the performance of satellite observations having different sensitivities to the satellite position and the precision of the adjusted orbit arc resulting from Monte Carlo simulations of these observations. This study shows that the results of the precision of the adjusted orbit arcs and the values of the DOP factors concur, and therefore possible satellite observations can be evaluated in advance in the scheduling process using DOP factors.

Keywords Galileo, Dilution of Precision factors, satellite orbits, VieSched++, VieVS

1 Introduction

The installation of a Very Long Baseline Interferometry (VLBI) transmitter on one or more Galileo satellites allows the observation of satellites besides natural extra-galactic radio sources with VLBI telescopes. Combining observations to satellites and quasars brings a variety of new possibilities and allows the expansion of the research activities of this highly accurate technique as it enables the connection of the satellite position with the celestial reference frame. This permits the determination of the absolute orientation of the satellite constellation with respect to the International Celestial Reference Frame (ICRF) [3]. Furthermore, it is possible to compare the position of the satellite from VLBI observations with positions obtained from other space geodetic techniques, allowing high precision tying of the different space geodetic techniques. The connection of the different space geodetic techniques via space ties leads to an improvement of the International Terrestrial Reference Frame (ITRF) [1] if the tie vectors on the satellite are known with high accuracy. Moreover, the combination of VLBI observations to quasars and satellites enables Precise Orbit Determination (POD) of these Earth-orbiting satellites [6]. Dilution of Precision (DOP) factors [11] can be used to depict the sensitivity of a satellite observation with VLBI telescopes towards different parameters. In order to reveal the sensitivity of a satellite observation towards the individual components of the satellite position, three intended DOP factors were introduced [12]. These DOP factors can be used to evaluate possible VLBI observations of satellites with respect to their suitability for determining the satellite orbit.

1. TU Wien
2. TU München
3. ETH Zürich

2 Evaluation of Satellite Observations for Orbit Arc Adjustment

In this study, possible satellite observations from a VGOS network are evaluated in terms of their performance for determining the adjustment of satellite orbits. This is done based on two approaches. The first is based on DOP factors, and the second is based on the analysis of simulations. The two different approaches are described in the following subsections.

2.1 Sensitivity Study using DOP Factors

As a first step, satellite observations are investigated in a sensitivity study using DOP factors. These factors are indicators for the change of the observable by a change of a specific parameter and therefore represent the sensitivity of an observation towards this parameter. We use DOP factors for the sensitivity towards the satellite position in the local orbital NTW-frame (see Figure 1), i.e., the normal DOP (NDOP), tangential DOP (TDOP) and cross-track DOP (WDOP). These DOP factors represent the orbital error in the respective component per VLBI measurement error, both in unit of lengths, and are therefore dimensionless. High sensitivities occur due to more suitable geometric configurations of the satellite position and the observing VLBI stations for determining a component of the satellite position, resulting in small values for the respective DOP factor. Therefore, the smaller the values of the DOP factors the higher the sensitivities towards the respective component.

2.2 Simulation Study

In another step, a simulation study is carried out based on schedules including both satellite and quasar observations. These schedules are created with the scheduling software VieSched++ [10] and contain satellite observations for a specific time period of the entire session (e.g., 50 minutes) to one Galileo satellite from all stations from which the satellite is visible during that time period. The remaining part of the schedule is filled with quasar observations. These schedules are simulated 1,000 times using the Vienna VLBI and Satellite Software (VieVS) [2]. The simulations include tropospheric turbulences, station clocks, and white noise [8]. The troposphere is simulated using a tropospheric turbulence parameter C_n with a value of $1.8 \times 10^{-7}\,\mathrm{m}^{-1/3}$ and a tropospheric scale height of 2,000 m [7]. The stochastic error of the station clocks is simulated using random walk and integrated random walk corresponding to 10^{-14} at 50 minutes [4]. In addition, white noise of 20 ps for quasar observations and 50 ps for satellite observations is added.

These simulations are analyzed using VieVS by estimating offsets for the individual components of the satellite position as continuous piecewise linear offsets in a ten-minute interval using relative constraints of 10 cm for each component. The precision of the adjusted arc is studied and assessed in terms of repeatability of the individual components of the satellite position.

3 Results

Our study is based on an arbitrary 24-hour session starting on April 6, 2022 00:00:00 UTC using a network of nine VLBI Global Observing System (VGOS) [9] stations that are currently operational (Figure 2). For the specified network and observing time, two schedules are created including observations of the Galileo satellite GSAT0206 during 50-minute time periods but at different times. In one schedule the satellite scans are scheduled from 00:50:00 to 01:40:00 UTC and in the second schedule from 12:10:00 to 13:00:00 UTC, which are denoted as observation periods A and B, respectively. In the scheduling process,

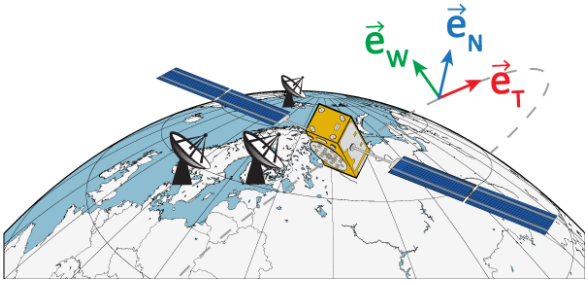

Fig. 1: Local orbital NTW-frame with orthogonal axes, where the N-axis lies in the orbital plane, the T-axis is tangential to the orbit, and the W-axis is orthogonal to the orbital plane.

satellite scans with five seconds of on-source time and 30 seconds in between for calibration and slewing of the antennas are scheduled during these 50 minutes. In the next step, the remaining part of the schedule is filled with quasar observations. It should be noted that quasar observations are also scheduled for stations for which the satellite is not visible during the 50 minutes of satellite scans. During both observation periods, the satellite is visible from a different set of five stations, which are listed in Table 1.

Table 1: Stations where the satellite is visible during the different observation periods.

obs. period A (00:50:00 - 01:40:00)	obs. period B (12:10:00 - 13:00:00)
ISHIOKA	MACGO12M
KOKEE12M	NYALE13S
MACGO12M	RAEGYEB
NYALE13S	WESTFORD
WESTFORD	WETTZ13S

3.1 Results of Sensitivity Study

The results of the sensitivity study, as described in Section 2.1, are shown in Table 2. It is evident that the average value of the NDOP is twenty to thirty times higher compared to the average values of the TDOP and WDOP. This is expected as the sensitivity for the distance is only given by the parallax. Due to the different geometrical configurations of the observing stations and the satellite positions, the values of the DOP factors vary during the two observation periods. The comparison of the DOP values of the different observation periods shows that the average NDOP value is smaller during observation period B but the average TDOP and WDOP values are slightly smaller during the observation period A. This means that the satellite observations during the observation period A are less sensitive to the normal component but more sensitive to the tangential and cross-track components compared to the satellite observations during the observation period B.

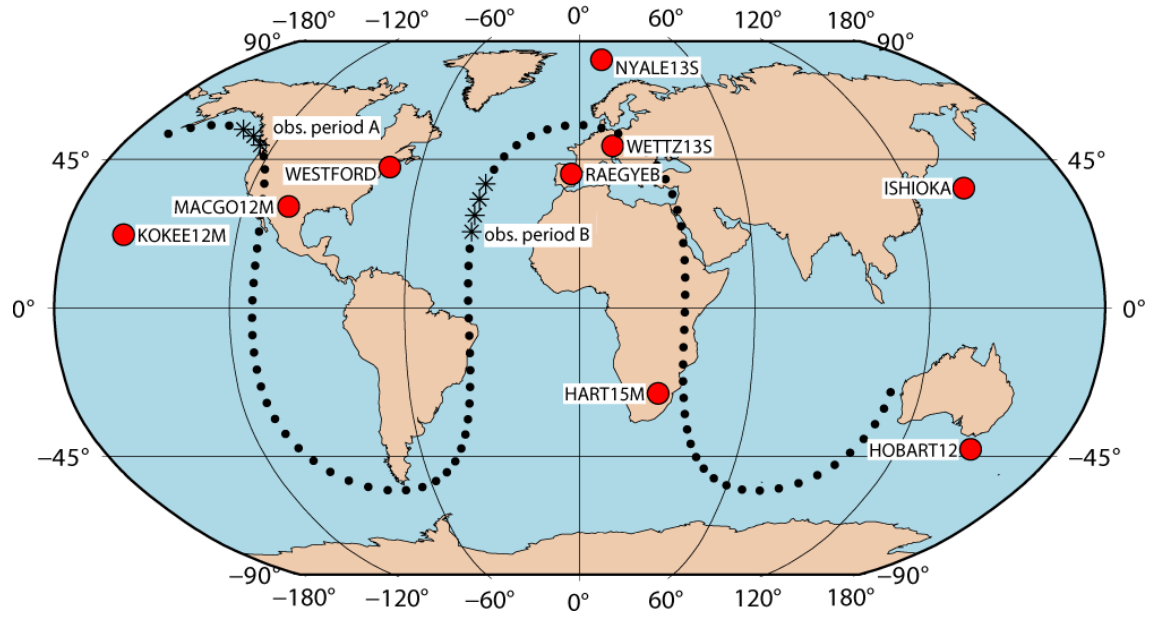

Fig. 2: VGOS station network considered in this study and ground track of the satellite GSAT0206 (E30) during 24 hours starting on April 6, 2022, at 00:00:00 UTC. The dots represent the ground track of the satellite at a 15-minute interval. The asterisks mark the positions of the satellite during the observation periods A and B when satellite scans are scheduled.

Table 2: Average values of the DOP factors (normal N, tangential T, and cross-track W) during the different observation periods.

	#stations	NDOP	TDOP	WDOP
obs. period A (00:50:00 - 01:40:00)	5	46.5	1.6	1.8
obs period B (12:10:00 - 13:00:00)	5	40.7	2.0	2.3

3.2 Results of Simulation Study

As described in Section 2.2, the satellite positions are determined as continuous piecewise linear offsets in each component with ten-minute intervals applying relative constraints of 10 cm. Figure 3 shows the repeatabilities of the estimated offsets from the a-priori orbit (SP3-orbit) for the individual components for each estimation epoch. Comparing the repeatabilities of the normal component during the observation time periods A and B, it is obvious that the accuracy is worse during the observation time period A compared to period B. This concurs with the comparison of the values of the DOP factors, as the NDOP during observation period A is higher and the observations are therefore less sensitive towards the normal component than the observations during time period B. The repeatabilities of the estimated offsets for the tangential and cross-track components are smaller during observation period A than during period B, which again is consistent with the results of the sensitivity study of the corresponding DOP factors as described in Section 3.1.

4 Summary and Discussion

In this study, possible satellite observations from a VGOS network of nine stations to the Galileo satellite GSAT0206 are investigated, first in terms of their sensitivities towards the satellite position and thereafter with regard to the precision of the adjusted orbit arc based on Monte Carlo simulations. The sensitivity analysis of the satellite observations is based on Dilution of Precision factors as indicators for the sensitivity of these observations towards the individual components of the satellite position, namely normal DOP, tangential DOP,

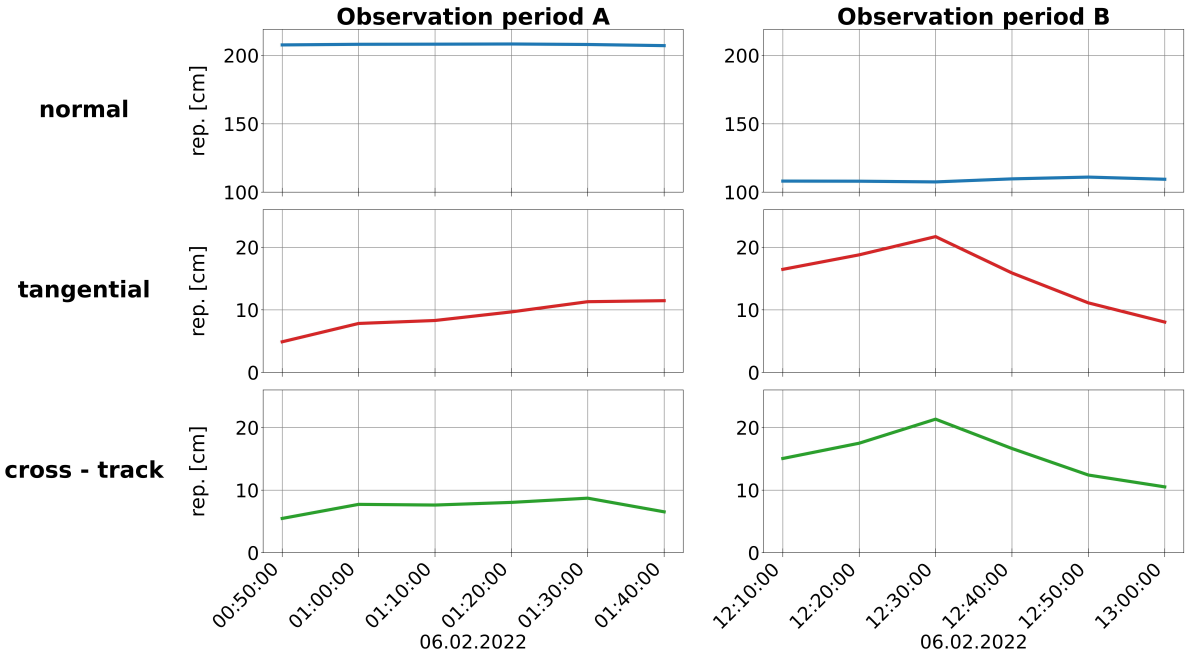

Fig. 3: Repeatability of the estimated offsets of the 1,000 simulations for the individual components (normal, tangential, and cross-track) during the observation periods A and B.

and cross-track DOP. The investigation of the results reveals that satellite observations with high sensitivity towards one of the components of the satellite position exhibit a better repeatability of the estimated offset of the respective component. Therefore, this component can be determined more precisely.

With this study, we further highlight that DOP factors properly represent the precision of satellite observations using VLBI. Therefore, they can be used as an optimization criterion during the scheduling process in order to select satellite scans with high sensitivities to the individual components of the satellite position. In the future, further DOP factors can be introduced, such as a factor for characterizing the quality of the whole schedule for determining the absolute orientation of the satellite constellation.

Acknowledgements

The authors thank the Austrian Science Fund (FWF) for supporting this work within project VLBI2Galileo (P 33925N).

References

1. Z. Altamimi, P. Rebischung, L. Métivier, X. Collilieux (2016), ITRF2014: A new release of the International Terrestrial Reference Frame modeling nonlinear station motions, J. Geophys. Res. Solid Earth, 121, 6109–6131, doi:10.1002/2016JB013098.
2. J. Böhm, S. Böhm, J. Boisits, A. Girdiuk, J. Gruber, A. Hellerschmied, H. Krásná, D. Landskron, M. Madzak, D. Mayer, J. McCallum, L. McCallum, M. Schartner, K. Teke (2018), Vienna VLBI and Satellite Software (VieVS) for Geodesy and Astrometry, Publications of the Astronomical Society of the Pacific, 130, 044503, doi:10.1088/1538-3873/aaa22b.
3. P. Charlot, C. S. Jacobs, D. Gordon, S. Lambert, A. de Witt, J. Böhm, A. L. Fey, R. Heinkelmann, E. Skurikhina, O. Titov, E. F. Arias, S. Bolotin, G. Bourda, C. Ma, Z. Malkin, A. Nothnagel, D. Mayer, D. S. MacMillan, T. Nilsson, R. Gaume (2020), The third realization of the International Celestial Reference Frame by very long baseline interferometry, A&A 644:A159, doi:10.1051/0004-6361/202038368.
4. T. Herring, J. Davis, I. Shapiro (1990) Geodesy by radio interferometry: The application of Kalman Filtering to the analysis of very long baseline interferometry data, Journal of Geophysical Research, 95, 12561-12581, doi:0.1029/JB095iB08p12561.
5. D. Behrend, "Coordinating Center Report", In K. D. Baver, D. Behrend, and K. Armstrong, editors, International VLBI Service for Geodesy and Astrometry 2012 Annual Report, NASA/TP-2013-217511, pages 55–57, 2013.
6. G. Kłopotek, T. Hobiger, R. Haas (2020), Geodetic VLBI for precise orbit determination of Earth satellites: a simulation study, Journal of Geodesy 94:56, doi:10.1007/s00190-020-01381-9.
7. T. Nilsson, R. Haas, G. Elgered (2007), Simulations of atmospheric path delays using turbulence models, Proceedings of the 18th European VLBI for Geodesy and Astrometry Working Meeting, 175–180.
8. A. Pany, J. Böhm, D. MacMillan, H. Schuh, T. Nilsson, J. Wresnik (2011) Monte Carlo simulations of the impact of troposphere, clock and measurement errors on the repeatability of VLBI positions, Journal of Geodesy, 85, 39–50, doi:10.1007/s00190-010-0415-1.
9. W. Petrachenko, H. Schuh, A. Niell, D. Behrend, B. Corey, (2010), VLBI2010: Next generation VLBI system for geodesy and astrometry, In: Kenyon, S., Pacino, M., Marti, U. (eds) Geodesy for Planet Earth, International Association of Geodesy Symposia, vol 136, Springer, Berlin, Heidelberg, doi:10.1007/978-3-642-20338-1_125.
10. M. Schartner, J. Böhm (2019), VieSched++: A New VLBI Scheduling Software for Geodesy and Astrometry, Publications of the Astronomical Society of the Pacific, vol. 131, no. 1002. IOP Publishing, p. 084501, Jun. 18, doi: 10.1088/1538-3873/ab1820.
11. E. R. Swanson (1978), Geometric Dilution of Precision, Annual of Navigation pages, vol 25, 425–429, doi:10.1002/j.2161-4296.1978.tb01345.x
12. H. Wolf, J. Böhm, M. Schartner, U. Hugentobler, B. Soja, A. Nothnagel (2022), Dilution of Precision (DOP) factors for evaluating observations to Galileo satellites with VLBI, Proceedings of IAG Scientific Assembly 2021, International Association of Geodesy Symposia, Springer, in press.

Sources with Significant Astrometric Offsets Between the S/X and K-band Celestial Frames

Aletha de Witt[1], Christopher S. Jacobs[2], David Gordon[3], Lucas Hunt[3], Megan Johnson[3]

Abstract The latest astrometric celestial reference frame (CRF) solutions at S/X-band and K-band have 1,014 sources in common, of which 36 are outliers with significant differences between the X- and K-band coordinates. We investigate possible astrophysical reasons for the large differences seen for the 36 outlier sources. These large differences may indicate significant structural differences between S/X and K-band. In order to study the astrophysical differences, we conducted multi-epoch, quasi-simultaneous S/X and K-band astrometric and imaging observations using the Very Long Baseline Array (VLBA). These images allow us to directly compare the source structure at X- and K-band, and to compare the direction of the extended emission from our imaging to the astrometric offset direction obtained from our CRF solutions.

Keywords Astrometry, VLBI, ICRF, AGN, jets, X-band, 8 GHz, K-band, 24 GHz

1 Introduction

Comparing the latest S/X (2022 Mar 05) and K-band (2022 Feb 07) astrometric celestial reference frame (CRF) solutions (using data back to 1980 for S/X and 2002 for K-band) produced by the United States Naval Observatory (USNO) shows 1,014 sources in common [1], of which 36 are outliers with at least one coordinate where the difference between S/X and K-band is $> 5\sigma$. Of the 36 outliers, there are three sources where the difference in δ are > 5 mas. We believe that these large differences may indicate significant structural differences between X- and K-band.

VLBI images show that Active Galactic Nuclei (AGN) tend to be more core-dominated at higher radio frequencies (e.g., [2]), as the extended structure in the jet tends to fade away with increasing frequency. The main reason why the apparent source structure is a function of frequency in AGN is rooted in their frequency dependent opacity, in particular from synchrotron self-absorption. Typically the core (or base) of an AGN jet is optically thick and has a flat or inverted radio spectra, while the jet is optically thin and has a normal or steep radio spectra. Frequency dependent opacity effects in AGN can also contribute to the frequency dependent shift of the VLBI core position ("core-shift"), with the core or base of the jet moving closer to the central black hole as the frequency increases, e.g., [3]. On the other hand, going to lower frequencies reduces the resolution available to detect structure, thereby desensitizing the baseline to structure. Thus, for some sources, we may only start to resolve individual components at higher radio frequencies.

We investigated possible astrophysical reasons for the large differences seen between the X- and K-band coordinates. We believe that these large differences may indicate significant structural differences between X- and K-band. For this reason we conducted special multi-epoch, quasi-simultaneous S/X and K-band astrometric and imaging observations between September 2020 and June 2021, using the Very Long Baseline Array (VLBA). From these observations we produced high-resolution images from which we derive source structure measures such as the radial extent and structure index, allowing us to directly compare the struc-

1. South African Radio Astronomy Observatory
2. Jet Propulsion Laboratory, California Institute of Technology
3. U.S. Naval Observatory

Table 1 Details of the S/X and K-band VLBA Observations.

Band	Date (2021)	Ref. Freq. (GHz)	Data Rate (Gbps)	Bandwidth	Polarization	$\theta_{\rm VLBA}$ (mas)
S/X-band	16 Apr, 24 May, 13 Jun	2.316	2	4×32 MHz	RCP	3.12
	–	8.668	–	12×32 MHz	–	0.82
K-band	18 Apr, 23 May, 12 Jun	23.568	4	4×128 MHz	RCP/LCP	0.30

ture at X- and K-band. In addition, we compare the direction of the extended emission obtained from model fitting to the astrometric offset direction obtained from the $\alpha\cos\delta$ and δ components. In this paper we present preliminary results from our investigation for 16 of the 36 outlier sources from the sessions that have been imaged so far.

2 Observations, Imaging and Model Fitting

In order to investigate the frequency dependent differences in source structure we conducted a series of ten quasi-simultaneous, multi-epoch S/X and K-band astrometric and imaging observations between September 2020 and June 2021 using the VLBA [4]. The observations were each 24 hours in duration and the data were correlated with the DiFX [5] software correlator at the Array Operations Center in Socorro, New Mexico. The S/X sessions were recorded in right circular polarization with a total data rate of 2 Gbps, and the K-band sessions in dual polarization with a total data rate of 4 Gbps. Data reduction and imaging have been completed thus far for the three S/X and K-band sessions observed between April and June 2021. The details of the observing dates, reference frequencies, observing modes, and angular resolution are given in Table 1.

The data were calibrated in the standard manner with the NRAO's Astronomical Imaging Processing System (AIPS) [6], using a semi-automated approach. An automated pipeline was used for self-calibration, deconvolution (using the standard CLEAN algorithm [7]), and imaging using the Caltech Difference Mapping software (DIFMAP) [8]. Images were produced for a total of 453 sources at X-band and 448 sources at K-band, with some sources having images at multiple epochs.

In addition to the imaging, we also fit a simple two-component, circular Gaussian model to the calibrated visibilities for each source using the MODELFIT task in DIFMAP to get an estimate of the offset and direction of the second brightest component. Estimates of the principal angle of extension of the total emission region ("jet direction") were obtained by fitting a line, going through (0,0), to the CLEAN component locations using a PYTHON script. This method was used to perform both an unweighted and flux-density-weighted fit. Details of our model fitting methods are described in [9].

3 Analysis

3.1 Astrometric Results

Comparing the latest CRF astrometric solutions produced by the USNO at S/X (sx-usno-220305) and K (k-usno-220305) shows 1,014 sources in common with at least two observations and $\sigma < 50$ nrad (~ 10 mas). Comparing the differences in the X- and K-band coordinates from these two catalogs shows 36 outliers with at least one coordinate where the difference is $> 5\sigma$. Note that there is a residual $\Delta\delta$ versus δ slope $= -1.3 \pm 0.1$ μas/deg that was not removed before taking the differences. Removing the 36 outliers leaves 978 sources in common with median inflated position errors of 46 μas in $\alpha\cos\delta$ and 60 μas in δ for X-band and 48 μas in $\alpha\cos\delta$ and 84 μas in δ for K-band.

From the 36 outliers there are three sources where the difference in the X−K coordinates in δ are > 5 mas. The radial X−K offsets of the 36 outliers range between 0.3 and 35 mas. Images have been produced for 16 of the 36 outliers from the observations listed in Table 1, and the radial X−K offsets for this subset of 16 outlier sources range between 0.3 and 2.73 mas.

3.2 Structure Metrics

We evaluate and compare the structure for each source at X- and K-band using various image-based source

structure metrics calculated from the image CLEAN component models (cf. [9]). The flux-density weighted radial extent (R) provides a measure of the source compactness by considering the extent of the source structure weighted by flux density. The median value of R over all sources is 1.82 mas for X and 0.86 mas for K-band, and over the 16 outliers the median values are 5.94 mas for X-band and 3.20 mas for K-band. The structure index (SI) is derived from the median value of the structural delay for each CLEAN component and each intermediate frequency (IF) channel for all possible projected VLBI baselines that could be observed on Earth [10, 11]. The SI indicates the magnitude of the structure of the source: the smaller the SI value, the lower the effect of the source structure, with values of SI > 3 indicating significant source structure. The median value of SI over all sources is 2.36 for X and 1.96 for K-band, and over the 16 outliers the median values are 4.01 for X-band and 3.18 for K-band. These results show that, on average, K-band relative to X is more compact, with the outliers having more extended structure.

3.3 Astrometric Offsets versus Jet Directions

We compare the X-K astrometric offset angle to the angle of the extended emission in the X- and K-band images for all 16 of the outlier sources. We assume that the K-band astrometric position is located at the peak of the K-band image and that the K-band core (versus X-band) would be closer to the central black hole. Thus, we measure the astrometric offset position and angle from the K-band phase center. Table 2 lists for each of the 16 outliers the X-K astrometric offset angle (AOA), the angle of the second brightest X- and K-band component obtained from the model fitting in DIFMAP (DMF), and the principal angle of extension of the X- and K-band total emission region from the flux-density-weighted fit to the CLEAN component locations (wCCF).

We find four sources where all three angles (i.e., the astrometric angle and the angle of the extended emission in the X- and K-band images) agree reasonably well, and five sources where the astrometric offset angle agrees with the angle of the extended emission from the K-band image, but the angle of the extended emission in the X-image is different. There are three sources where the angle of the extended emission in the X- and K-band images agree, but the astrometric offset angle is different. Where the angles don't agree, we find that in most instances the directions are anti-parallel to each other. There are also three sources where none of the angles agree, but in this case the images are all of poor quality and thus our jet direction is poorly determined.

Table 2 X-band versus K-band Offsets (all angles in degrees).

Source	X-K AOA	X DMF	X wCCF	K DMF	K wCCF
0112−017	114.9	130.3	130.0	132.2	132.6
CTA21	−9.9	–	–	–	–
3C84	−169.2	−173.0	−176.6	162.2	173.5
0723−008	−55.6	−8.8	−23.9	152.1	152.3
0729−222	−82.8	−94.2	−93.7	80.8	−109.1
0850+581	133.0	143.9	149.4	152.6	151.6
1156−094	124.3	−87.8	−88.0	–	−90.1
1214+588	115.5	118.9	118.4	−59.1	−58.4
3C286	−142.8	48.0	–	51.3	50.1
OQ208	50.0	23.9	30.1	–	118.3
3C309.1	−29.3	169.3	169.2	168.3	166.2
1600+335	−168.1	15.3	16.7	−3.8	−1.1
1710-269	131.9	78.0	−101.2	−87.2	−90.2
2037−253	−102.6	−69.4	−62.1	129.3	−19.4
2128−123	−150.4	−151.9	−149.3	−151.0	−150.9
3C454.3	−118.0	−106.4	−107.9	−72.5	−79.2

Figures 1 and 2 show two examples of sources for which all three of the angles agree reasonably well. The source 0112−017 (Figure 1) shows the astrometric offset position almost coinciding with the position of the second brightest component identified from the DIFMAP model fitting. Assuming that the astrometric position at X-band is located at the peak of the X-band image, this would imply that the X-band peak coincides with the weaker K-band jet component, with the peak emission at X-band being further down the jet. The source 2128−123 (Figure 2) is another example where all three angles agree reasonably well. For this source, the astrometric offset position (shown in the K-band image) is actually hidden behind the model-fit component.

Figure 3 shows the source 1214+588 as an example where the astrometric offset angle agrees with the angle of extended emission in the K-band image, but the angle of extended emission in the X-band image is different. However, we see that the angle of extended emission in the X-band image is in a direction anti-parallel to the K-band direction, with the angles

within a few degrees of 180° separation. For the source 1214+588 (and others where the X-band angle is in an anti-parallel direction) the X-band core appears to be the weaker X-band emission, and we suspect that we are mis-identifying the X-band core by assuming that the strong component is the core.

The source 3C309.1 (Figure 4) and 1156−094 are examples where the angle of extended emission from X and K images agree, but the astrometric offset angle is different, although we find that it is in a direction anti-parallel to the extended emission. Both sources appear to have very little extended emission, also seen from other epoch images at K-band [9].

4 Conclusions

Comparison of our most recent CRF astrometric catalogs shows 36 of 1,014 sources have statistically significant detections of astrometric offset. Sixteen of the 36 outliers have images at both X- and K-band, from multi-epoch, quasi-simultaneous S/X and K-band astrometric and imaging observations using the VLBA. Structure metrics derived from the image CLEAN component models show that the outliers tend to be the sources with more extended structures. The comparison of both imaging and astrometric results shows that large astrometric offsets have a strong tendency to be aligned along the jet direction of the source. Where the angles do not line up because they are anti-parallel, we suspect that the core may not be the strongest component in one of the images.

Future work: The next step will be to complete the imaging of the remaining seven quasi-simultaneous S/X and K-band VLBA observing sessions enabling the comparison of source structure and astrometric offset positions for the remaining 20 outlier sources.

Acknowledgements

The S/X results made extensive use of the International VLBI Service (IVS) data sets [12]. The S/X and K-band data sets also made extensive use of the VLBA [4] which is managed by the National Radio Astronomy Observatory (NRAO), funded by the National Science Foundation (NSF), and operated under cooperative agreement by Associated Universities. The authors gratefully acknowledge use of the VLBA under the USNO's time allocation. This work supports USNO's ongoing research into the celestial reference frame and geodesy. AdW was supported by the South African Radio Astronomy Observatory (SARAO), a facility of the National Research Foundation (NRF) of South Africa. DG, LH, and MJ were supported by the U.S. Naval Observatory (USNO). CJ's work was supported by the Jet Propulsion Laboratory, California Institute of Technology, under a contract with the National Aeronautics and Space Administration (80NM0018D0004).

References

1. Gordon, D., de Witt, A. & Jacobs, C. S., 12th IVS General Meeting, Helsinki, Finland (virtual), 31 Mar 2022. Current CRF Status at X/S and K Bands.
2. Charlot, P., et al., AJ, 139, 5, 1713–1779, 2010. The Celestial Reference Frame at 24 and 43 GHz. II. Imaging.
3. Sokolovsky, K. V., et al., A&A, 532, A38, 2011. A VLBA survey of the core shift effect in AGN jets.
4. Napier, P. J., in ASP Conf. Series, Zensus, J. A., Diamond, P. J., Napier, P. J., Eds.; ASP: San Francisco, CA, USA, 82, p. 59, 1995. VLBA Design.
5. Deller, A. T., et al., PASP 119, 318, 2007. DiFX: A Software Correlator for VLBI Using Multiprocessor Computing Environments.
6. Greisen, E. W., ed. A. Heck, 285, Dordrecht: Kluwer Academic Publishers, 109–125, 2003. AIPS, the VLA, and the VLBA.
7. Hogböm, J. A., A&A suppl., 15, 417, 1974. Aperture Synthesis with a Non-Regular Distribution of Interferometer Baselines.
8. Shepherd, M. C., in ASP Conf. Series, vol. 125, eds. G. Hunt and H. Payne, 77, 1997. Difmap: an Interactive Program for Synthesis Imaging
9. de Witt, A., et al., 'The Celestial Reference Frame at K-band: Imaging. I. The First 28 Epochs.', AJ, 2022, in press.
10. Fey, A. & Charlot, P., ApJ Suppl., 111,1, 95–142,1997. VLBA Observations of Radio Reference Frame Sources. II. Astrometric Suitability Based on Observed Structure.
11. Shabala, S., et al., J. Geod., 89, 9, 873–886, 2015. Simulating the effects of quasar structure on parameters from geodetic VLBI.
12. Schuh, H. & Behrend, D., J. Geodyn., 61, 68–80, 2012. VLBI: A fascinating technique for geodesy and astrometry.

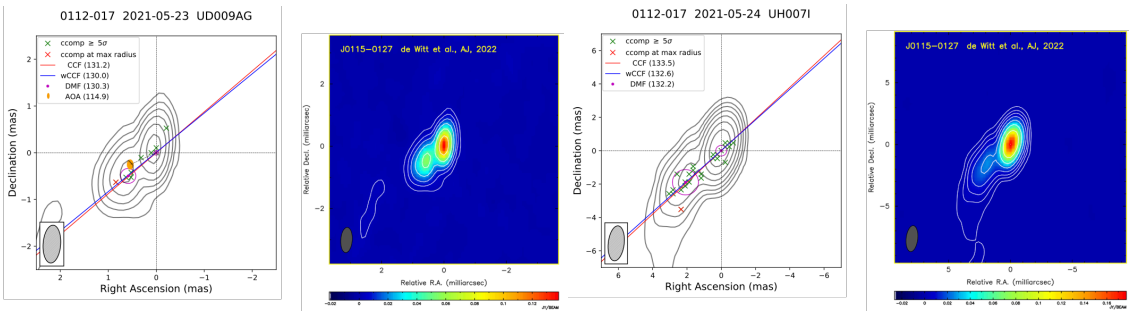

Fig. 1 Contour maps (in grey) and images of 0112−017 (J0115−0127) at K-band (left) and X-band (right).

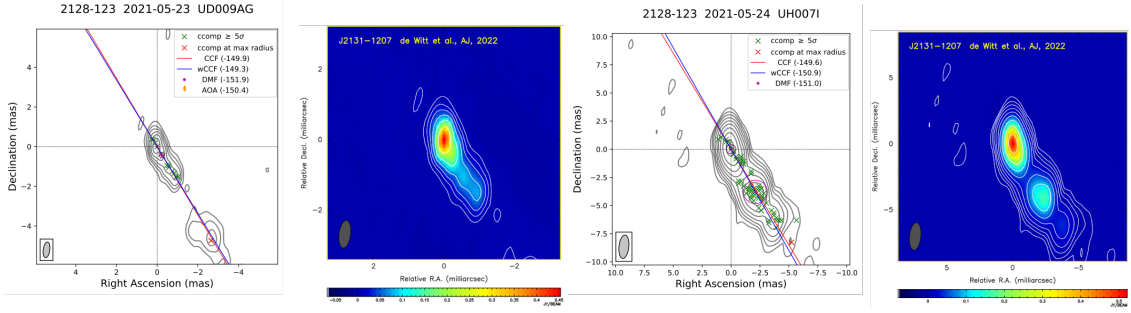

Fig. 2 Contour maps (in grey) and images of 2128−123 (J2131−1207) at K-band (left) and X-band (right).

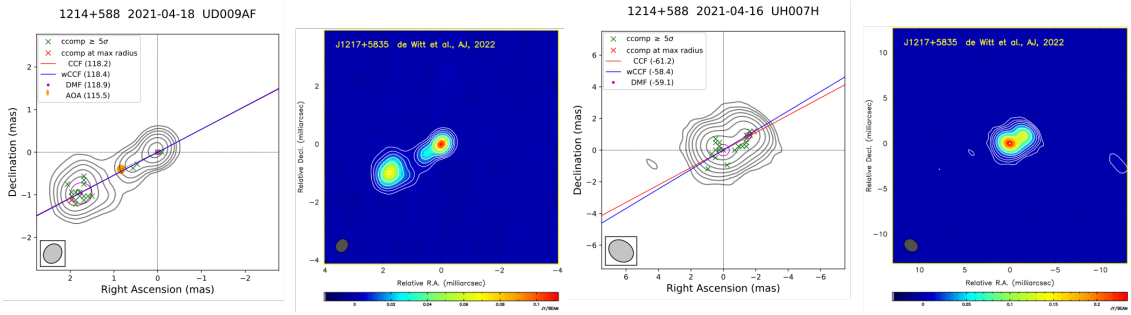

Fig. 3 Contour maps (in grey) and images of 1214+588 (J1217+5835) at K-band (left) and X-band (right).

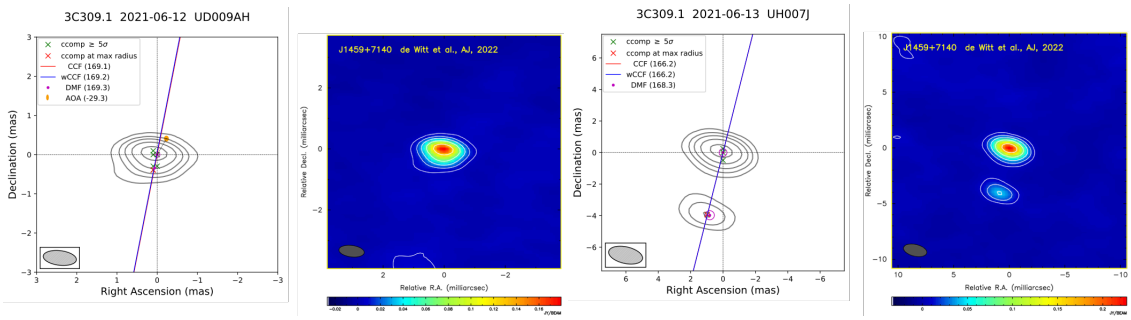

Fig. 4 Contour maps (in grey) and images of 3C309.1 (J1459+7140) at K-band (left) and X-band (right). Contour maps are overlaid with the line of best fit from the unweighted (CCF, blue line) and flux-density-weighted (wCCF, red line) linear fits through the locations of the image CLEAN components. The image CLEAN components (ccomp) are indicated with green crosses and the component with maximum distance from the phase center is indicated by a red cross. The position and size of the DIFMAP model-fit components (DMF) are indicated with magenta circles. The position of the astrometric offset angle (AOA) is indicated with a yellow ellipse with the minor and major axis representing the error in the $\alpha \cos \delta$ and δ differences. Position angles are given in the plot legend.

Evaluate the ICRF3 Axes' Stability via Extragalactic Source Position Time Series

Niu Liu[1,2], Sébastien Lambert[3], Felicitas Arias[3], Jia-Cheng Liu[1], Zi Zhu[1]

Abstract We present an updated study on assessing the stability of the axes of the third generation of the International Celestial Reference Frame (ICRF3) in terms of linear drift and scatter, based on the extragalactic source position time series from analyses of archival Very Long Baseline Interferometry observations. Our results show that the axes of the ICRF3 are stable at a level of 10 to 20 microseconds of arc, and this does not degrade after the adoption of the ICRF3 when observations from new networks are included. We also show that the commonly used method of deriving the position time series (four-step solution) is robust.

Keywords Reference systems, astrometry, techniques: interferometric, quasars: general

1 Introduction

The apparent positions of extragalactic sources are known to vary with time due to their intrinsic evolution. This kind of astrometric instability will cause an orientation variation to the axes of the celestial reference frame that are defined by positions of extragalactic sources, a phenomenon known as the celestial frame instability [1]. Recent studies based on the extragalactic source position time series measured by Very Long Baseline Interferometry (VLBI) suggest that sources that were considered stable are likely to become unstable as long as they are observed for a longer time span [2]. As a result, it is necessary to regularly monitor the astrometric behavior of extragalactic sources and the stability of the axes of the VLBI celestial frame.

We updated our previous work [3] on the evaluation of the ICRF3 axes' stability by extending the VLBI observations to 2022 and also by examining the robustness of the method for deriving the position time series. All the data and the codes (in the PYTHON Jupyter notebook) to reproduce the results of this work can be accessed publicly online[1].

2 Data

We used observations in 7,146 VLBI regular sessions made between November 1979 and December 2021 that are publicly available at the Data Center[2] of the International VLBI Service for Geodesy and Astrometry [4]. These data were processed with the Calc/Solve software [5] in the global solution mode.

To produce the position time series for each source, the observed sources were divided into N subsets in a manner so that each subset contains the same number of ICRF3 defining sources and non-defining sources and the sky distribution is as identical and uniform as possible. Then, N separate VLBI global solutions were carried out treating the positions of the sources in each respective subset as sessionwise parameters, thus providing the position time series for these sources. These

1. School of Astronomy and Space Science, Key Laboratory of Modern Astronomy and Astrophysics (Ministry of Education), Nanjing University, Nanjing 210023, P. R. China
2. School of Earth Sciences and Engineering, Nanjing University, Nanjing 210023, P. R. China
3. SYRTE, Observatoire de Paris, Université PSL, CNRS, Sorbonne Université, LNE, Paris, France

[1] https://git.nju.edu.cn/neo/icrf3-axis-stability-2022

[2] ftp://ivsopar.obspm.fr/vlbi/ivsdata/vgosdb

N solutions together provided the position time series for the full source sample. We may call this method of producing the source position time series as the "N-step" method. Different values of N were used by various authors; for example, $N = 4$ in [6] and $N = 10$ in [2]. In this work, we set N to 4, 8, 12, 16, and 20 in order to test the robustness of the "N-steps" method in deriving the position time series and also to estimate the influence of the different choices of N on the evaluation of the ICRF3 axes' stability.

Finally, we obtained position time series for 6,032 extragalactic sources, including all 303 ICRF3 defining sources, which were considered in this work. The median number of observed sessions and the median of the mean observing epoch for the ICRF3 defining sources were 157 and 2013.5, respectively. The observation time span ranged from 4.13 a year to 42.06 a year.

3 Analysis

We adopted the same methods as used in [3] to evaluate the stability of the ICRF3 axes. On the one hand, we estimated the spin of ICRF3, that is, the change rate of the orientation of the ICRF3 axes, through the apparent proper motion field of extragalactic sources, the latter being derived from the position time series. The value of spin multiplied by the length of the observation period offered an estimate of the stability of the ICRF3 axes. On the other hand, we constructed yearly representations of the ICRF3 by annually averaging the source positions within a one-year window, and we studied the temporal variation in the orientation of the axes of these yearly celestial frames, which assessed the stability of the ICRF3 axes from another aspect.

3.1 Spin of ICRF3

The apparent proper motion was estimated by the least-squares fitting to a linear motion model as

$$\begin{bmatrix} \alpha(t) \\ \delta(t) \end{bmatrix} = \begin{bmatrix} \mu_\alpha \\ \mu_\delta \end{bmatrix} (t - t_0) + \begin{bmatrix} \alpha(t_0) \\ \delta(t_0) \end{bmatrix}, \qquad (1)$$

where t_0 was set to be the mean observing epoch. Data points whose distances to the mean position were three times greater than the corresponding uncertainties were removed from the position time series before fitting. The inverse of the full covariance matrix of each data point position time series was used as the weight. Figure 1 presents the distributions of the apparent proper motion for the ICRF3 defining sources based on different position time series solutions, in which noticeable differences can be found in the declination component. Nearly half of the sources show an apparent proper motion greater than $30\,\mu\mathrm{as\,yr}^{-1}$ in the right ascension or the declination. To examine the statistical significance of these apparent proper motions, we plotted the distribution of the total apparent proper motion μ and its significance X_μ from the 20-step solution as an example in Figure 2, where limits of $\mu \leq 10\,\mu\mathrm{as\,yr}^{-1}$ and $X_\mu \leq 3$ filter out approximately 20% of sources. The source located in the upper right corner with $\mu \simeq 0.8\,\mathrm{mas\,yr}^{-1}$ and $X_\mu \simeq 21.5$ is 2220−351, which may need to be studied further.

We modeled the apparent proper motion filed by the first degree of the vector spherical harmonics (VSH) [7] as

$$\begin{aligned} \mu_\alpha \cos\delta = & -\omega_\mathrm{x} \cos\alpha \sin\delta - \omega_\mathrm{y} \sin\alpha \sin\delta + \omega_\mathrm{z} \cos\delta \\ & - g_\mathrm{x} \sin\alpha + g_\mathrm{y} \cos\alpha, \\ \mu_\delta = & +\omega_\mathrm{x} \sin\alpha - \omega_\mathrm{y} \cos\alpha \\ & - g_\mathrm{x} \cos\alpha \sin\delta - g_\mathrm{y} \sin\alpha \sin\delta + g_\mathrm{z} \cos\delta, \end{aligned} \qquad (2)$$

where $\boldsymbol{\omega} = (\omega_\mathrm{x}, \omega_\mathrm{y}, \omega_\mathrm{z})^\mathrm{T}$ stands for the spin of the celestial frame and $\boldsymbol{g} = (g_\mathrm{x}, g_\mathrm{y}, g_\mathrm{z})^\mathrm{T}$ represents the dipolar pattern due to, for example, the Galactic aberration effect [8]. These parameters were estimated via a least-square fitting to the apparent proper motions of all the ICRF3 defining sources, weighted by the inverse of their covariance matrix, and these results are shown in Figure 3. Different position time series gave consistent results, that is, only the spin around the Y-axis deviated from zero by approximately $0.4\,\mu\mathrm{as\,yr}^{-1}$ to $0.5\,\mu\mathrm{as\,yr}^{-1}$ considering the associated formal uncertainties. We also determined the spin parameters from a bootstrap resampling analysis based on 1,000 randomly picked samples to obtain a realistic estimate of the parameter uncertainties, which were found to be approximately $0.7\,\mu\mathrm{as\,yr}^{-1}$. Figure 4 displays the apex locations of the spin and glide vectors, which are close to the directions of the Galactic anticenter and the Galactic center, respectively. The possible explanation is that

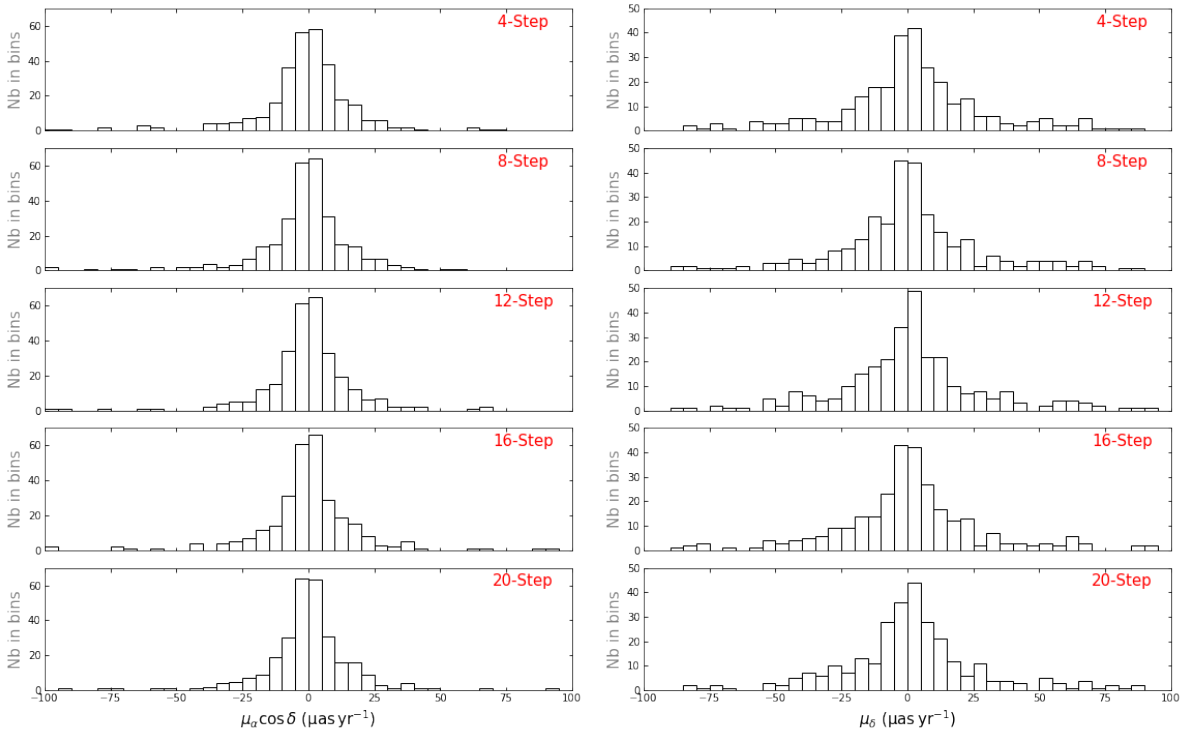

Fig. 1 Distributions of apparent proper motions in right ascension (*left*) and declination (*right*) for the ICRF3 defining sources based on position time series from different solutions.

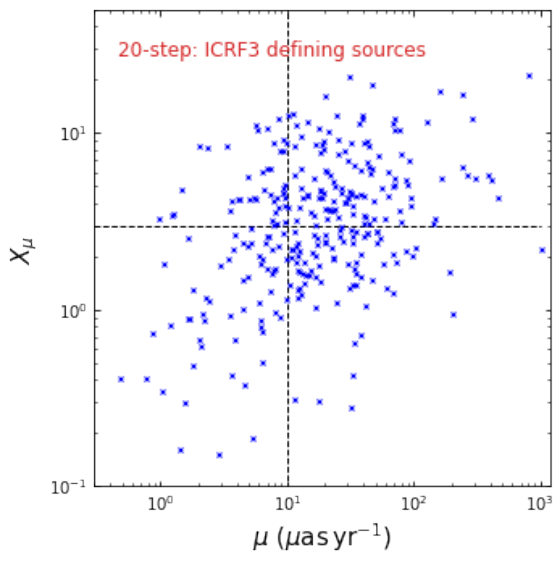

Fig. 2 Distribution of the total apparent proper motion against its significance from the 20-step solution.

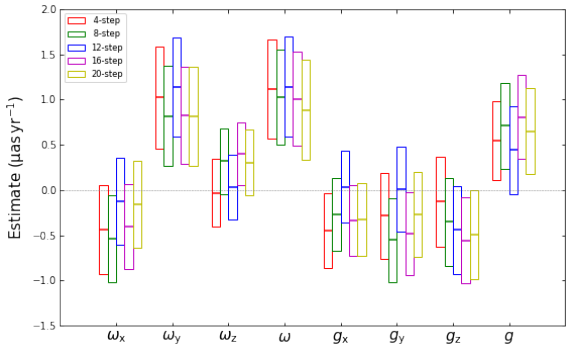

Fig. 3 Estimate of the spin and glide parameters.

there is some residual Galactic aberration effect in the ICRF3, which requires further investigation.

Considering the observation period of approximately 42 years and the nonzero deviation of 0.4 μas yr^{-1} – 0.5 μas yr^{-1} for the spin of ICRF3, the accumulated deformation in the direction of the ICRF3 axes is on the order of 10 μas – 20 μas.

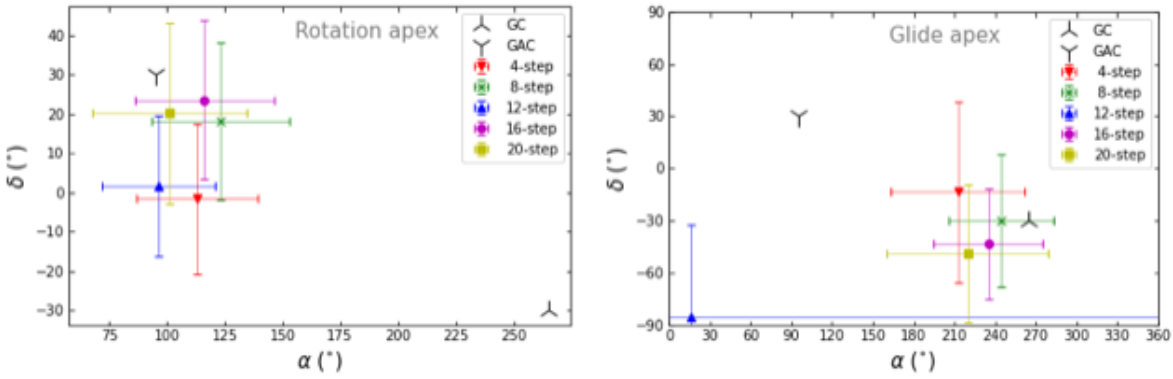

Fig. 4 Location of the apexes of the spin (*left*) and glide (*right*) vectors.

3.2 Variation in the ICRF3 Axes Orientations

The annual representations of ICRF3 were constructed by the mean positions of the ICRF3 defining sources within each one-year observing window. The orientation offsets of these yearly celestial reference frames with respect to ICRF3 were estimated by a weighted least-squares fitting of the first degree of the VSH that is similar to Equation (2). Figure 5 displays the temporal variations of the orientation of the yearly celestial frame axes. Different position time series solutions gave consistent results. We computed the weighted root-mean-squares (WRMS) of the orientation offsets and tabulated them in Table 1. The WRMS is approximately 10 µas – 20 µas over the whole observation span, and it is reduced to no greater than 10 µas if only considering post-2019 data; that is, the adoption of the ICRF3 as the fundamental celestial reference frame.

Table 1 Weighted root-mean-squares of orientation offsets of the yearly celestial reference frames with respect to the ICRF3 in the unit of microseconds of arc.

Solution	1979 – 2022			1995 – 2022			2018 – 2022		
	ε_x	ε_y	ε_z	ε_x	ε_y	ε_z	ε_x	ε_y	ε_z
4-step	18	19	12	13	15	7	4	7	7
8-step	16	17	12	12	13	7	7	7	8
12-step	16	17	13	11	13	8	6	7	6
16-step	17	17	12	12	14	8	5	8	7
20-step	16	16	12	12	13	8	6	7	7

4 Conclusions

We evaluate the stability of the ICRF3 axes based on the VLBI observations between November 1979 and December 2021, which is found to be at 10 µas – 20 µas. We also find that the commonly used four-step method of deriving the position time series is sufficiently robust.

Acknowledgements

This work is supported by the National Natural Science Foundation of China (NSFC), under grant Nos. 11833004 and 12103026, and by the China Postdoctoral Science Foundation (grant No. 2021M691530).

References

1. Lambert, S. B., Dehant, V., & Gontier, A.-M. 2008, A&A, 481, 535. doi:10.1051/0004-6361:20078489
2. Gattano, C., Lambert, S. B., & Le Bail, K. 2018, A&A, 618, A80. doi:10.1051/0004-6361/201833430
3. Liu, N., Lambert, S. B., Arias, E. F., et al. 2022, A&A, 659, A75. doi:10.1051/0004-6361/202142632
4. Nothnagel, A., Artz, T., Behrend, D., et al. 2017, Journal of Geodesy, 91, 711. doi:10.1007/s00190-016-0950-5
5. Ma, C., Clark, T. A., Ryan, J. W., et al. 1986, AJ, 92, 1020. doi:10.1086/114232
6. Lambert, S. 2013, A&A, 553, A122. doi:10.1051/0004-6361/201321320
7. Mignard, F. & Klioner, S. 2012, A&A, 547, A59. doi:10.1051/0004-6361/201219927
8. Liu, J. C. & Liu, N. 2020, Acta Astronomica Sinica, 61, 10

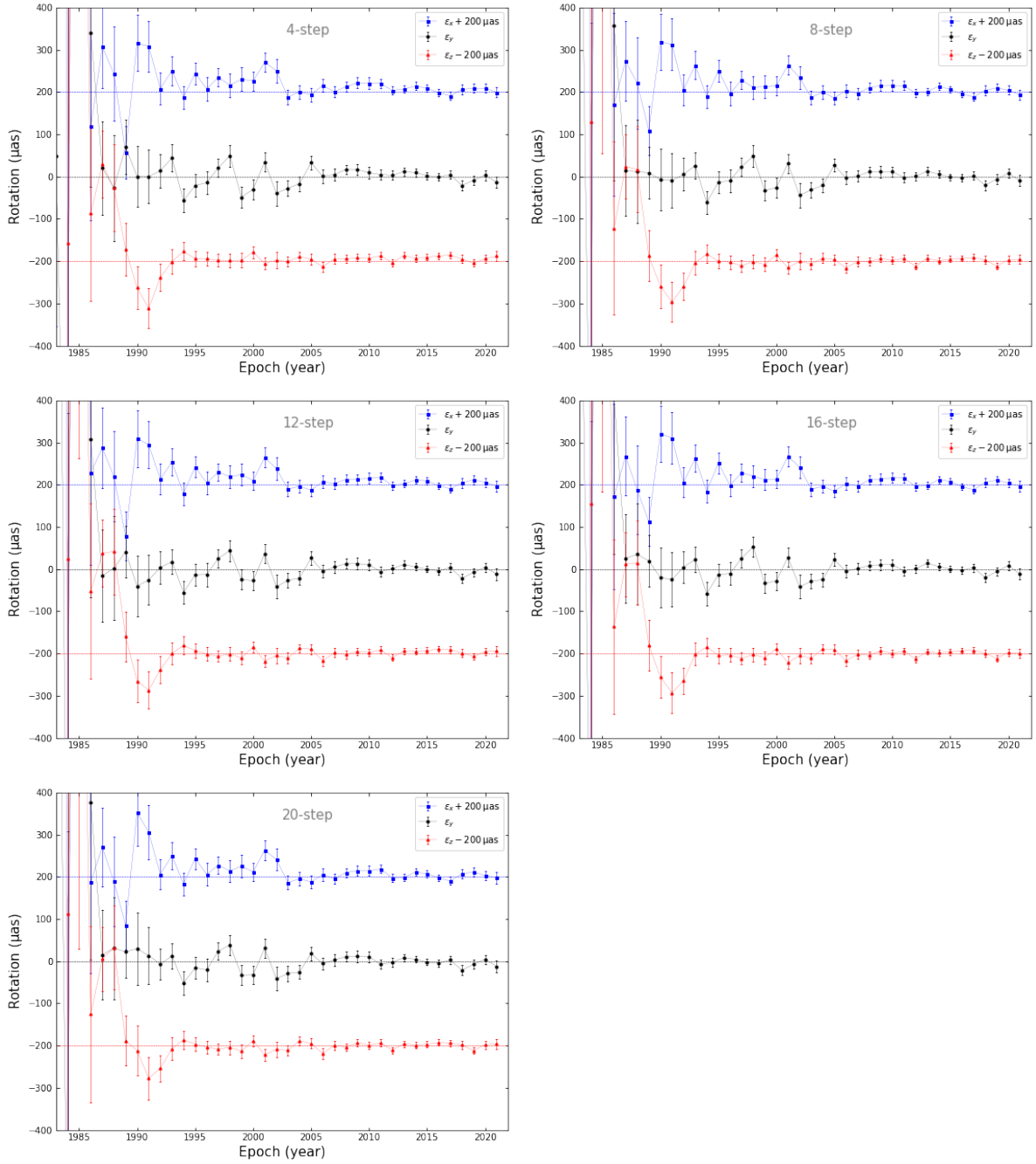

Fig. 5 Orientation offsets of yearly celestial frames with respect to the ICRF3.

ICRF3 Position and Proper Motion of Sagittarius A* from VLBA Absolute Astrometry

David Gordon[1], Alet de Witt[2], Christopher S. Jacobs[3]

Abstract Sagittarius A* (Sgr A*) is a strong compact radio source believed to be powered by a super-massive black hole at the galaxy's center. We have measured its precise coordinates as a function of time in the ICRF3 frame at K-band (24 GHz) using absolute astrometry with the VLBA. The proper motion determined allows us to estimate solar motion in and out of the galactic plane.

Keywords Sgr A*, proper motion, astrometry, VLBA

1 Introduction

The Sagittarius A* (hereafter Sgr A*) radio source is believed to be powered by a super-massive black hole at the galaxy's center [5, 4]. Precisely locating it and measuring its proper motion in the IAU's official ICRF3 [1] celestial reference frame is important in defining the galactic coordinate system, in studies of galactic structure, kinematics and dynamics, and for identification with nearby sources in the radio and IR. Extinction by gas and dust in the galactic plane prevents observing it optically. In the radio region it gets smeared out by plasma in the galactic plane, making it unobservble by VLBI at the lower frequencies, such as the traditional X/S (8.4/2.3 GHz) geodetic band. In this paper we report on the analysis of a 16-year span of VLBA observations of Sgr A* at K-band (24 GHz).

1. US Naval Observatory
2. South African Radio Astronomy Observatory
3. NASA Jet Propulsion Laboratory, California Institute of Technology

2 Observations

Our K-band collaboration has observed Sgr A* at 45 epochs in K-band (24 GHz) absolute astrometry sessions on the VLBA, beginning in November 2017. These 24-hour sessions were made in an effort to generate, maintain, and expand the ICRF3 [1] at K-band, and each typically observed Sgr A* along with ∼225 extragalactic ICRF sources. These sessions were all made in the VLBI absolute astrometry mode, where many sources are observed all over the sky and large arcs between sources are solved for in order to locate each source in an inertial coordinate system, which in our case is the ICRF3 frame. Sgr A*, being just one of many sources targeted in each session, was observed for typically three scans totalling only 4.5 minutes, and taking up less than 0.5% of the total observing time in each session.

These sessions are only part of a much larger set of K-band VLBI sessions that were used to generate the ICRF3-K catalog [1] in 2018 and now to maintain and expand it. The larger data set contains VLBA sessions from 2002–2007 from the work of [7] and three sessions from the original processing at the Goddard Space Flight Center of the Galactic Plane Survey [8] sessions in 2006, two of which observed Sgr A*. Thus we have a 16-year span, from June 2006 through February 2022, of K-band VLBA absolute astrometry observations of Sgr A*. Due to the smearing by plasma in the galactic plane, observations of Sgr A* are somewhat limited at K-band. Sgr A* gets resolved out on the long VLBA baselines to MK-VLBA and SC-VLBA, as well as on most of the HN-VLBA and BR-VLBA baselines, thus limiting the precision of individual measurements.

3 Analysis

The Sgr A* data was taken from a recent K-band solution at USNO of the full data set of 150 K-band sessions spanning 2002–2022. In this solution, we solved for a single average position for 1,035 extragalactic ICRF sources, while the position of Sgr A* was solved for individually in each of its 47 epochs. Ionosphere corrections were computed and applied from GNSS ionosphere maps, as given in [1]. Alignment with ICRF3 was accomplished by imposing a no-net-rotation constraint on 258 ICRF3 defining sources that were well observed at K-band. This gave us a time series of the positions of Sgr A* in the ICRF3 frame. The resulting Right Ascension and Declination positions of Sgr A* are plotted in Figure 1. These positions are offset from

$$17^{\rm h}45^{\rm m}40^{\rm s},\ -29^\circ00'28''.$$

Solving for the RA and Dec slopes gives us the proper motion of Sgr A*. We get:

RA proper motion = -3.144 ± 0.044 mas/yr
Dec proper motion = -5.626 ± 0.080 mas/yr

And solving for the position at 2015.0 gives us the J2000 position of Sgr A* at the 2015.0 proper motion epoch in the ICRF3 frame:

$$\text{RA} = 17^{\rm h}45^{\rm m}40.^{\rm s}034051 \pm 0.^{\rm s}000017$$
$$\text{Dec} = -29^\circ00'28.''21583 \pm 0.''00045$$

For other epochs, add -0.000239665 sec/yr in RA and -0.0056255 arcsec/yr in Dec. The 2015.0 epoch is chosen for consistency with the 2015.0 galactic aberration epoch of ICRF3.

Our absolute astrometry measurement agrees well with the phase referencing (relative astrometry) measurement by [10] of -3.156 mas/yr $\pm$ 0.006 mas/yr and -5.585 mas/yr $\pm$ 0.010 mas/yr. Their relative astrometry measurement is able to achieve smaller uncertainties because of the very small angles between Sgr A* and the phase referencing calibrator sources, and because their observations were made at Q-band (43 GHz), where Sgr A* is smeared out only $\sim$1/3 as much as at K-band, and because they observed Sgr A* and two nearby phase referencing sources for much longer periods ($\sim$eight hours in each of 23 epochs spanning 18 years) than our observations ($\sim$4.5 minutes in each of 47 sessions). However, their relative astrometry measurements are not able to accurately locate Sgr A* in the ICRF3 frame since there are no nearby ICRF3 sources. Also, phase referencing can be subject to systematic errors from calibrator position variations due to source structure or other effects, though these are expected to be small at Q-band.

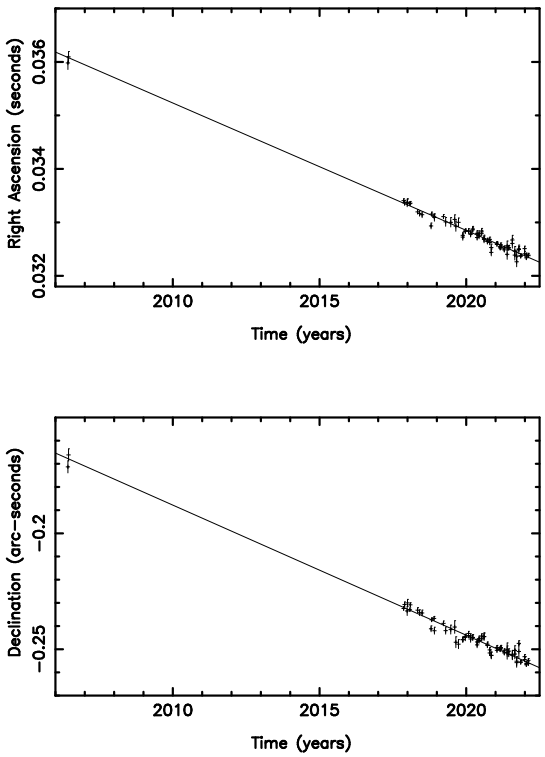

Fig. 1: Positions of Sgr A* from 2006–2022, offset from $17^{\rm h}45^{\rm m}40^{s},\ -29^\circ00'28''$.

Combining the RA and Dec proper motions gives a total proper motion vector of 6.44 $\pm$ 0.09 mas/yr at a position angle of 209.2° $\pm$ 0.7°. This differs from the 211.4° position angle of the galactic plane by some 2.2° $\pm$ 0.7°, indicating out-of-the-plane proper motion of $\sim$0.25 $\pm$ 0.08 mas/year. If we assume a circular orbit for the Sun about the galactic center and a recent value for the distance to the galactic center of 8.15 kpc [3, 6, 9], our proper motion measurement yields a velocity of 249 $\pm$ 4 km/sec for the Sun within the galactic plane. And if attributed to solar motion, the $\sim$2.2° deviation from the galactic plane indicates out-of-the-plane solar motion of 9.7 $\pm$ 3.1 km/sec towards the north galactic pole. This is in fairly good agreement with the recent value of 7.26 $\pm$ 0.36 obtained by [2].

4 Conclusions

Using absolute astrometry at K-band on the VLBA, we have found the proper motion of Sgr A* to be -3.144 ± 0.044 mas/yr in Right Ascension and -5.626 ± 0.080 mas/yr in Declination. And its position in the ICRF3 frame as a function of time is:

$$17^{\mathrm{h}}45^{\mathrm{m}}40.^{\mathrm{s}}034051 - 0.^{\mathrm{s}}000239665 * (year - 2015.0)$$
$$-29^{\circ}00'28.''21583 - 0.''0056255 * (year - 2015.0)$$

The position uncertainty is at approximately the 0.5 mas level due to limitations imposed by the interstellar medium. K-band sessions are continuing on the VLBA approximately monthly and, although Sgr A* is not observed every time, these results can be expected to slowly but steadily improve.

Acknowledgements

The authors gratefully acknowledge use of the Very Long Baseline Array since 2017 under the US Naval Observatory's time allocation. This work supports USNO's ongoing research into the celestial reference frame and geodesy. The VLBA is operated by the National Radio Astronomy Observatory, a facility of the National Science Foundation and operated under cooperative agreement by Associated Universities, Inc. This research was partly supported by the South African Radio Astronomy Observatory (SARAO), a facility of the National Research Foundation (NRF) of South Africa. Part of this research was carried out at the Jet Propulsion Laboratory, California Institute of Technology, under a contract with the National Aeronautics and Space Administration (80NM0018D0004).

References

1. Charlot, P., Jacobs, C.S., Gordon, D., Lambert, S., de Witt, A., Bohm, J., Fey, A.L., Heinkelmann, R., Skurikhina, E., Titov, O., Arias, E.F., Bolotin, S., Bourda, G., Ma, C., Malkin, Z., Nothnagel, A., Mayer, D., MacMillan, D.S., Nilsson, T., and Gaume, R., 2020, Astronomy and Astrophysics, 644, A159.
2. Ding, P-J., Zhu, Z. and Jia-Cheng Liu, J-C., 2019, Res. Astron. Astrophys., 19, 068.
3. Do, T., Hees, A., Ghez, A., et al. 2019, Science, 365, 664.
4. Genzel, F., Eisenhauer, F., & Gillessen, S., 2010, Rev. Mod. Phys., 82, 3121–3195.
5. Ghez, A.M., Salim, S., Weinberg, N.N., et al., 2008, Astrophysical Journal, 689, 1044–1062.
6. Gravity Collaboration, Abuter, R., Amorim, A., et al. 2019, Astronomy and Astrophysics, 625, 10.
7. Lanyi, G.E., Boboltz, D.A., Charlot, P., et al., 2010, Astronomical Journal, 139, 1695–1712.
8. Petrov, L., Kovalev, Y. Y., Fomalont, E. B., Gordon, D., 2011, Astronomical Journal, 142, 35.
9. Reid, M. J., Menten, K. M., Brunthaler, A., et al. 2019, Astrophysical Journal, 885, 131.
10. Reid, M. J. and Brunthaler, A., 2020, Astrophysical Journal, 892:39.

Astrometric Positions of Gravitational Lensed System 1422+231

Ming Hui Xu[1,2,3], Tuomas Savolainen[1,2,4], Niu Liu[5], Alet de Witt[6], Susanne Lunz[3], Robert Heinkelmann[7], Harald Schuh[3,7]

Abstract A gravitational lensing event can occur when a gravitational field of, e.g., a cluster of galaxies, distorts and magnifies the light from a distant, background galaxy that is almost in the same line of sight as the lensing mass. Among the ∼500 discovered gravitational lensed systems, the European Space Agency mission Gaia has detected at least one lensed image in ∼300 of these systems and released their astrometric parameters in EDR3. According to research, high accuracy VLBI observations to determine the relative positions between possible lensed images were carried out for 25 lensed systems. The lensed images refer to the various visible components in the field of view in the direction of the lensing system. Because these multiple lensed images of a source are typically a few arcseconds or less apart on the sky, they can be imaged on one map. This allows to determine the relative positions between them with an accuracy of tens of microarcseconds. This may enhance the study of the position differences between radio and optical, given that the multiple lensed images of an individual source are detected by both VLBI and Gaia. We report on the astrometric positions from historical VLBI observations, the results from the latest VLA observations, and the Gaia EDR3 results. We focus on the lensed system 1422+231, for which high-accuracy relative positions for the complete set of its lensed images are available from geodetic VLBI observations conducted in the 1990s. This study aims to understand the VLBI/Gaia position differences seen for 1422+231 and to potentially improve the modeling of the gravitationally lensed system, 1422+231, using more accurate astrometric positions from radio and optical.

Keywords 1422+231, Gaia EDR3, phase referencing, geodetic VLBI, VLA

1 Introduction

Among the ∼500 discovered gravitational lensed systems, the European Space Agency mission Gaia[1] has detected at least one component for ∼300 of these systems. According to our research, VLBI observations were carried out to determine the high accuracy relative positions between the multiple images detected in 25 systems so far. In these 25 systems, however, there are only four sources for which Gaia EDR3 has detected one image: 0218+358, 1030+074, 1152+199, and 2108+213; and only two sources with more than one image detected: 1422+231 and 0957+561. The latter two sources were popular targets in geodetic VLBI observations from ∼20 years ago, with major contributions from the Mark III system in the 1990s (Clark et al., 1985).

(1) Aalto University Metsähovi Radio Observatory, Metsähovintie 114, FI-02540 Kylmälä, Finland
(2) Aalto University Department of Electronics and Nanoengineering, PL15500, FI-00076 Aalto, Finland
(3) Technische Universität Berlin, Institut für Geodäsie und Geoinformationstechnik 10553, Berlin, Germany
(4) Max-Planck-Institut für Radioastronomie, Auf dem Hügel 69, 53121 Bonn, Germany
(5) School of Astronomy and Space Science, Nanjing University, Nanjing, 210023, PR China
(6) South African Radio Astronomy Observatory, 1740 Krugersdorp, South Africa
(7) Deutsches GeoForschungsZentrum (GFZ), Potsdam, Telegrafenberg, 14473 Potsdam, Germany

[1] https://sci.esa.int/web/gaia

This source was first reported to be a gravitational lensed system, consisting of four components (denoted A, B, C, and D) with a maximum image separation of 1.3 arcseconds, by Patnaik et al. (1992) using VLA + MERLIN. The background radio source is believed to be associated with a 15.5-mag quasar at a redshift of 3.62. The optical follow-up observations made by Remy et al. (1993) found optical images for all four radio components and no other images (i.e., for the lensing source), providing further evidence to support this source to be a gravitational lensed system. Besides the relative position of these components, the authors also gave the photometric information (V, R, and i). Yee & Ellingson (1994) and Bechtold & Yee (1995) made high-resolution maps of this source and found galaxies (G) at z $\sim$ 0.4 that are likely to be the lenses (see also, Kundicet et al. 1997; Tonry 1998).

The imaging and spectroscopic analyses given in Hammer et al. (1995) suggest that the lensing galaxy is a spiral galaxy. Impey et al. (1996) presented observations from the Hubble Space Telescope (HST) of this system and reported that the photometric properties of the lensing galaxy are consistent with an elliptical galaxy. Patnaik et al. (1999) used the VLBA and the 100-m telescope at Effelsberg to observe this system and provided new measurements of the relative positions for the components in radio. All the aforementioned publications provide astrometric information (relative or absolute) for B1422+231. Besides these observations, other authors (for example, Hogg & Blandford (1994)) constructed a theoretical model for the system. There are many studies about this system aiming to investigate why the ratio of the flux of component A over that of component B is not consistent at different frequencies. While component A is roughly as bright as component B in the radio, the optical flux of component A is only about 0.8 of that of component B. Several possible explanations were provided in, e.g., Hogg & Blandford (1994); Narasimha & Patnaik (1994); Kormann, Schneider & Bartelmann (1994); and Mao & Schneider (1998)). Polarization images were derived by Patnaik et al. (1999).

2 Astrometric Positions at Optical

High-accuracy optical positions were obtained using the sub-arcsecond imaging spectrograph of the Canada-France-Hawaii Telescope in May 1994, as listed in Table 1.

Table 1 Relative position at optical wavelengths in 1994.3 (Units: mas).

Image	r (mag)	$\Delta\alpha\cos(\delta)$ (mas)	$\Delta\delta$ (mas)
A	16.69±0.01	389 ± 3	304 ± 3
B	16.37±0.01	0 ± 3	0 ± 3
C	17.15±0.01	-337 ± 3	-755 ± 3
D	20.11±0.07	930 ± 20	-780 ± 20

The EDR3 data release provides the currently most accurate optical positions from the Gaia mission. The relative positions were calculated and listed in Table 2.

3 Astrometric Positions at Radio

The most accurate radio positions were provided by Patnaik et al. (1999) based on phase referencing observations using the VLBA and Effelsberg antennas at 8.4 GHz. The results are listed in Table 3.

By comparing Tables 2 and 3, significant changes are seen from 1997.5 at radio to 2016 at optical for the relative positions between components A and B by 12.6 mas and between components C and B by 4.0 mas.

4 Position Differences due to Relative Motions between the Images?

The relative positions of the four images of the system 1422+231 as seen by VLBI phase referencing and Gaia have differences that are far larger than their uncertainties. There are two possibilities for these differences: (1) the positions of these lensed images changed from 1997.6 to 2016; (2) there is a large difference between the optical and radio positions of the background source. In order to separate these possibilities, we analyzed the VLA observations of 1422+231 taken on 2018-02-27, to derive the relative positions of the images at a time closer to the reference epoch of the Gaia positions, as shown in Figure 1.

The parameters from model fitting in DIFMAP is shown in Table 4. These results confirm that the relative positions between these four images from 1997.5

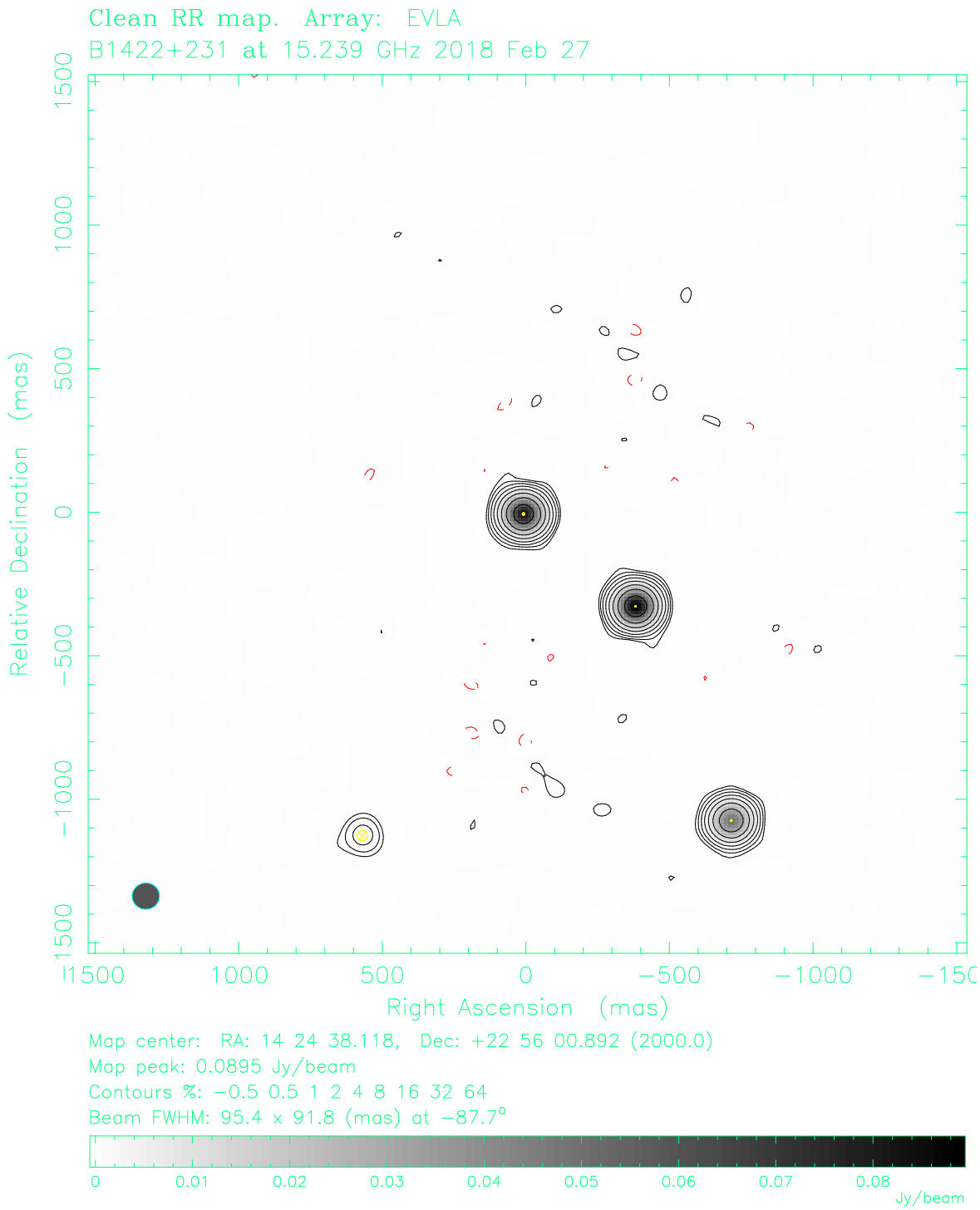

Fig. 1 VLA map of the system 1422+231 at 15.2 GHz in 2018-02-27 obtained in this work. The bottom-left component is image D, and the other three components are A, B, and C from top to bottom, respectively. Their relative positions at radio in 1997.6 are shown in Table 1, and in Table 2 at optical from Gaia in 2016. The relative positions determined from this map are shown in Table 4.

Table 2 Absolute and relative positions of the four images of the lensed system 1422+231 from Gaia EDR3 with the reference epoch of 2016.0. The relative positions derived from radio imaging observations are the arc lengths on the celestial sphere. The differential coordinates calculated from the absolute positions like Gaia EDR3 should thus be transferred to be the arc length for right ascension when they are compared to the radio results. The last two columns are the transferred relative positions from Gaia.

	Absolute position				Relative position (mas)		
Image	α	σ_α (mas)	δ	σ_δ (mas)	$\Delta\alpha$	$\Delta\alpha\cos(\delta)$	$\Delta\delta$
A	$14^h\,24^m\,38^s.1182088$	±0.38	$22^\circ\,56'\,00''.880164$	±0.43	426.6	392.9	307.5
B	$14^h\,24^m\,38^s.0897688$	±0.98	$22^\circ\,56'\,00''.572641$	±0.94	0	0	0
C	$14^h\,24^m\,38^s.0656072$	±0.06	$22^\circ\,55'\,59''.821368$	±0.06	-362.4	-333.8	-751.3
D	$14^h\,24^m\,38^s.1587172$	±70.6	$22^\circ\,55'\,59''.771852$	±46.1	1034.2	952.5	-800.8

Table 3 Relative positions of the four images of the lensed system 1422+231 from phase referencing observations in 1997.5 (Patnaik et al., 1999). The uncertainties were believed to be better than 0.1 mas.

Image	Total flux (mJy)	$\Delta\alpha\cos(\delta)$ (mas)	$\Delta\delta$ (mas)
A	152±2	389.25	319.98
B	164±2	0	0
C	81±1	−333.88	−747.71
D	5±0.5	950.65	−802.15

to 2018.1 do not change, at least at the milliarcsecond level. We may conclude that the differences in the relative positions between Patnaik et al. (1999) and Gaia EDR3 are due to the position difference of the background source between radio and optical observations.

Table 4 Relative positions of the four images of the lensed system 1422+231 from VLA observations in 2018 as determined from the map in Figure 1. Formal errors are reported by DIFMAP.

Image	Total flux (mJy)	$\Delta\alpha\cos(\delta)$ (mas)	$\Delta\delta$ (mas)
A	82.7±0.1	390.6 ± 0.06	321.1 ± 0.06
B	90.0±0.1	0 ± 0.06	0 ± 0.05
C	48.1±0.1	-333.0 ± 0.11	-746.3 ± 0.10
D	2.9±0.1	950.0 ± 2.00	-799.5 ± 1.90

5 Outlook and Future Work

The position difference of the background source between radio and optical, after being affected by gravitational lensing, shows different phenomena for the four images: the difference in the relative position is 12.6 mas for the image pair of A and B between radio and optical, and 4.0 mas for the pair of C and B. The uncertainty of the position of component D is rather large at both optical and radio. The relative positions show significant differences between optical and radio.

No significant movements among the images were detected over 20 years at optical or radio wavelengths for 1422+231. However, geodetic VLBI observations of this sources may provide additional information to validate the results.

Acknowledgements

This research was supported by the Academy of Finland project No. 315721 and the DFG grant No. HE59372-2.

References

1. Cornachione, M. A., Morgan, C. W., Millon, M., et al. 2020, ApJ, 895, 125
2. Ducourant, C., Wertz, O., Krone-Martins, A., et al. 2018, A&A, 618, A56
3. Hammer, F., Rigaut, F., Angonin-Willaime, M. C., & Vanderriest, C. 1995, A&A, 298, 737
4. Hogg, D. W. & Blandford, R. D. 1994, MNRAS, 268, 889
5. Impey, C. D., Foltz, C. B., Petry, C. E., Browne, I. W. A., & Patnaik, A. R. 1996, ApJ, 462, L53
6. Morgan, N. D., Caldwell, J. A. R., Schechter, P. L., et al. 2004, AJ, 127, 2617
7. Patnaik, A. R., Browne, I. W. A., Walsh, D., Chaffee, F. H., & Foltz, C. B. 1992, MNRAS, 259, 1P
8. Patnaik, A. R., Kemball, A. J., Porcas, R. W., & Garrett, M. A. 1999, MNRAS, 307, L1
9. Remy, M., Surdej, J., Smette, A., & Claeskens, J. F. 1993, A&A, 278, L19
10. Yee, H. K. C. & Ellingson, E. 1994, AJ, 107, 28

Author Index

IVS IAG SUOMEN AKATEMIA

NLS FINNISH GEOSPATIAL RESEARCH INSTITUTE FGI

Author Index